Structure-Reactivity Principles of Alkali Metal Amides: Sodium Diisopropylamide, Lithium Hexamethyldisilazide, and Lithium Diisopropylamide

A Dissertation

Presented to the Faculty of the Graduate School

of Cornell University

In Partial Fulfillment of the Requirements for the Degree of

Doctor of Philosophy

by

Russell Frank Algera

August 2017

Structure-Reactivity Principles of Alkali Metal Amides: Sodium Diisopropylamide, Lithium Hexamethyldisilazide, and Lithium Diisopropylamide

Russell Frank Algera, Ph. D.

Cornell University 2017

Alkali metal amide structure-reactivity principles of foundational importance to synthetic chemists are described herein with an emphasis on sodium diisopropylamide (Chapters 1–4), lithium hexamethyldisilazide (Chapter 5), and lithium diisopropylamide (Chapter 6).

Organosodium reagents are notably underdeveloped contrasting with the highly popular organolithium variants, which pervade the literature in capacities ranging from nucleophiles to strong non-nucleophilic bases. This is due in part to documented inferior solubility and stability of alkylsodiums and sodium amides. Nonetheless, scant reports on the reactivity of sodium diisopropylamide (NaDA)—primarily concerned with preparation and crystallography—suggested some regiochemical and reactivity advantages relative to LDA. NaDA in DMEA is highly soluble, stable, resistant to solvent decomposition, and easily prepared. The application of MCV afforded a uniform assignment of symmetric dimer in all solvents. Solvation of NaDA was addressed using a combination of solubility measurements, solvent exchanges, and DFT computations. NaDA/THF effectively metalates 1,4-dienes and isomerizes alkenes, and the corresponding mechanisms were ascertained, providing a glimpse into sodium coordination chemistry. Highly *Z*-selective isomerizations were observed for allyl ethers under conditions that compare

favorably to those of existing protocols. NaDA/THF readily metalates a variety of arenes, and the mechanisms illuminate the influence of substituents on inductive, mesomeric, steric, and chelate effects.

Lithium hexamethyldisilazide (LiHMDS)-mediated enolization of (+)-4-benzyl-3-propionyl-2-oxazolidinone is described in Chapter 5. This enolization shows unusual sensitivity to the choice of hydrocarbon cosolvent (hexane versus toluene) and to isotopic labeling, from which four distinct mechanisms were identified.

The kinetics of lithium diisopropylamide (LDA) in tetrahydrofuran under non-equilibrium conditions are reviewed in Chapter 6. Three distinct topics include: (1) methods and strategies used to deconvolute complex reaction pathways, (2) conclusions about organolithium reaction mechanisms, and (3) perspectives on the concept of rate limitation.

BIOGRAPHICAL SKETCH

The author is from East Amherst, NY, where he completed primary and secondary education in the Williamsville Central School District. The author undertook undergraduate studies at Canisius College (Buffalo, NY) in August of 2008 and performed research in the laboratory of Dr. Timothy M. Gregg concerning rhodium(II) dicarboxylate-mediated cyclopropanation. After receiving a B. S. in Chemistry in May of 2012, the author moved to Cornell University where he pursued graduate studies in the laboratory of Prof. David B. Collum, earning a M. S. in August of 2014 and completing requirements for receipt of a Ph. D. in Summer 2017.

To My Grandparents: Frank and Santina Algera, and Sheldon and Ruth Bender

ACKNOWLEDGMENTS

In this section, I wish to acknowledge individuals that collectively enabled me to produce this document.

Professor David Collum has supported my scientific endeavors since joining his laboratory in November of 2012. Despite a lackluster performance in coursework, he chose not to dismiss my application; for this, I am grateful. Semi-formal meetings quickly gave way to daily discussions ranging topics from chemical kinetics to current literature to historic organosodium chemistry to other active projects in the group, and even economics. I have benefitted tremendously from his broad experience in physical organic chemistry and organic synthesis. I also acknowledge my committee members, Professors Geoffrey Coates and Brett Fors.

Members of the Collum group—past and present—have substantially influenced the course of my graduate education. When I began work in earnest, Evan Tallmadge introduced me to Schlenk line and air-free techniques essential to a practicing organometallic chemist and patiently provided answers to my incessant questions. As time progressed, Evan became an untiring sounding board for inquires and ideas. Dr. Joseph Renny provided early encouragement. As I began a project concerning catalysis of LDA-mediated ortholithiations, Jun Liang introduced me to ReactIR and rapid-inject NMR reaction monitoring; he good-naturedly spent hours discussing intricate details of rate limitation. Laura Tomasevich kept the group running at pace by coordinating regular group events. Angela Bruneau insisted that I obtain a personal copy of Mathematica, a useful tool as it turned out. Jacqueline Perodeau gave useful input throughout the time we overlapped. Michael Houghton's disarming manner often belies his talents; the group benefitted from his tips and tricks. Dr. Yun Ma and I collaborated closely on the sodium diisopropylamide project; I profited from her suggestions and observing her experiments in real time. Kyle Mack has been a valuable office and lab mate and I'd like to think we mutually advanced by consistently vetting each other's ideas. Janis Jermaks has been continually helpful and is a highly skilled synthetic chemist. Dr. Gabriel Reyes-Rodríguez and I collaborated on LiHMDS-mediated enolization; his unwavering optimism was inspiring through all stages of the study. Both Zirong Zhang and Yuhui Zhou made impressive strides in their first years of study; their results are integral to our group's recent surge of activity. Ryan Woltornist and Jackson Clark are the newest additions to the group and already show great potential; I look forward to following their work.

Outside of the Collum group, Dr. Ivan Keresztes was particularly helpful for configuring NMR experiments, as was Anthony Condo.

I wish to acknowledge my family and regret I cannot comprehensively do so. My Aunt Marie and Uncle Bernie (rest in peace) provided enthusiastic support and reassurance through many phases of my life, and even gave me my first chemistry set. The Spencers have been encouraging as well.

My parents have provided unconditional support and guidance through all of my endeavors. I am forever indebted to their selflessness and generosity and realize that this acknowledgement can at best serve as a superficial reflection.

TABLE OF CONTENTS

Chapter 1

Sodium Diisopropylamide in *N,N*-Dimethylethylamine: Reactivity, Selectivity, and Synthetic Utility

Sodium Diisopropylamide in *N,N*-Dimethylethylamine: Reactivity, Selectivity, and Synthetic Utility

Abstract

The reactivities and chemoselectivities of sodium diisopropylamide (NaDA) in *N,N*-dimethylethylamine (DMEA) are compared with those of lithium diisopropylamide (LDA) in tetrahydrofuran (THF). Metalations of arenes, epoxides, ketones, hydrazones, dienes, and alkyl and vinyl halides are represented. The positive attributes of NaDA–DMEA include high solubility, stability, resistance to solvent decomposition, and ease of preparation. The high reactivities and chemoselectivities often complement those of LDA–THF.

Introduction

This paper is the first in a series describing illustrative metalations by sodium diisopropylamine (NaDA) dissolved in *N*,*N*-dimethylethylamine (DMEA). The key insight is that NaDA is highly soluble and stable in trialkylamines (eq 1.1) and *can be prepared in 15 min*. The utility of NaDA–DMEA is illustrated by showing that its metalations have rates that far exceed those of LDA–THF but give comparable yields and selectivities that are often complementary. To our surprise, we have witnessed no solubility problems with NaDA dissolved in several trialkylamines or with the resulting metalated intermediates. From these results, we argue that synthetic chemists should revisit NaDA.

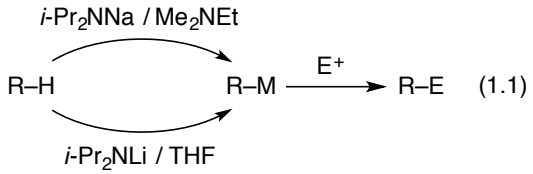

Background. The preparation of lithium diisopropylamide (LDA) by Levine and co-workers[1] in 1949 introduced soluble, highly reactive amide bases to the repertoire of synthetic organic chemists. Metalations with LDA began to flourish in the 1960s,[2] and LDA became one of the most prominent reagents in organic synthesis.[3] Levine[4] first synthesized NaDA in 1959 by reacting phenylsodium and diisopropylamine. Improved preparations include those of Lochmann[6] (using LDA–*t*-BuONa[5] or *n*-BuNa–diisopropylamine prepared from *n*-BuLi–*t*-BuONa) and Wakefield[7] (using a sodium metal–isoprene-based reduction). More recently, Mulvey and co-workers[8] have drawn attention to the merits of sodium chemistry by developing new reagents for synthesis and providing an excellent review of these heavy alkali metal bases. Most reports of NaDA focus on exploration for its own sake,[9] however, and only a few appear to be consumer-driven applications of NaDA to solve specific problems.[10,11]

Why has NaDA languished in relative obscurity? Ambiguities about composition—sodium bases versus mixed-metal "superbases"—have been largely resolved,[6a] and such details certainly would not have deterred synthetic chemists pursuing reactivity and selectivity. The reported thermal instability of solid NaDA[7]—resolved by refrigeration—also seems insufficient to curb the interest of the synthetic organic community. We suspect the major obstacle to be the scarcity of solvents that afford both high solubility and resistance to base-mediated decomposition.[9b,12] This presumption prompted us to examine DMEA and related trialkylamines.

Results

NaDA was prepared by modifying Wakefield's procedure[7] using sodium dispersion in toluene, isoprene, and diisopropylamine, all in DMEA. The sodium dispersion served as both a drying agent for all reagents and a reductant, allowing millimolar-scale synthesis without specialized glassware in 15 min and multiples of that scale in 30 min. (The longer reaction time stems from an exotherm demanding slower addition.) The resulting amide solution can be used directly, stored for later use at –20 °C, or recrystallized to give a white solid. Upgrading purity via recrystallization had a negligible influence on reactivity.

Metalations of representative organic substrates are summarized in Table 1. The yields are of isolated, purified products unless noted otherwise.[13] The relative reactivities of NaDA–DMEA and LDA–THF were assessed with either IR or NMR spectroscopies by measuring pseudo-first-order rate constants or initial rates for 0.10 M solutions of base. The relative rate constants (k_{rel}) for NaDA–DMEA versus LDA–THF are often lower limits because LDA is too unreactive or NaDA is too reactive to measure. Large temperature differences demanded by the two reagents prompt us to crudely (but conservatively) use a 2-fold correction for every 10 °C degrees.[14]

Table 1. Reactions of Substrates with NaDA[a]

	Substrate	Conditions	E^+	Product	k_{rel}	Yield
1	*n*-$C_8H_{17}Br$	1.2 equiv NaDA 0 °C	—	*n*-C_6H_{13} 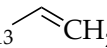	5	87%
2	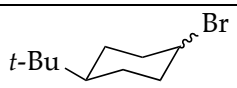	1.2 equiv NaDA –78 °C	—	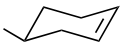	>500	80%
3	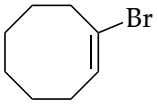	1.2 equiv NaDA 0 °C	—	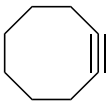	5	87%

4	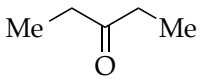	1.1 equiv NaDA –78 °C	TMSCl	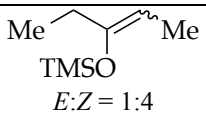 *E*:*Z* = 1:4	N/A	61%
5		1.2 equiv NaDA –78 °C	CH_3I		>300	78%
6	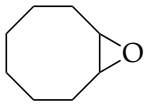	1.3 equiv NaDA rt	H_2O	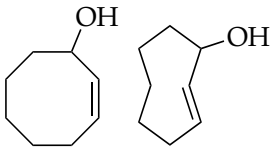 cis:trans = 10:1	>500	80%
7	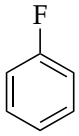	1.1 equiv NaDA –78 °C	CO_2	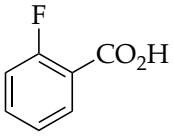	N/A	60%
8	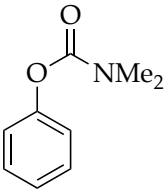	1.2 equiv NaDA –78 °C	H_2O	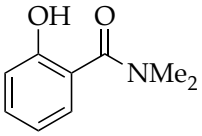	>200	92%
9	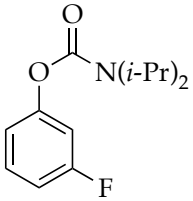	1.2 equiv NaDA –78 °C	CH_3OD	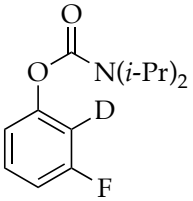	>500	94%
10	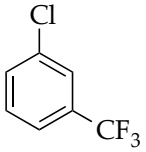	1.2 equiv NaDA –78 °C	CH_3OD	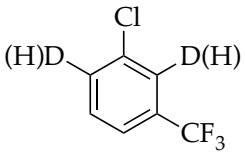 2-*d*:6-*d* = 6:1	1000	92%
11		1.1 equiv NaDA 0 °C	TIPSCl	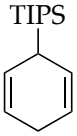	>100	82%
12	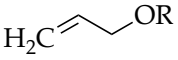 R = Me, Ph, $SiMe_3$	1.1 equiv NaDA 0 °C	—	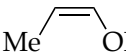 *Z*:*E* > 50:1	>1000	83% R = Ph

[a] k_{rel}, relative rate constant; NaDA, sodium diisopropylamide; rt, room temperature; TIPSCl, triisopropylchlorosilane

Discussion

The substrates in Table 1 were chosen to enable a broadly based comparison of NaDA–DMEA and LDA–THF. The dehydrohalogenations in entries 1–3 of Table 1 offer striking contrasts. Whereas *n*-octyl bromide (entry 1) undergoes clean NaDA-mediated elimination (>100:1), LDA–THF elicits elimination and S_N2-like substitution (eq 1.2).[15] Competing substitution–elimination pathways have plagued analogous eliminations of *n*-alkyl halides.[16] Putative trans-diaxial elimination of conformationally anchored *cis*-4-*tert*-butylcyclohexyl bromide (entry 2) is highly effective with NaDA. Surprisingly, the equatorial form eliminates with nearly equal efficiency ($k_{axial}/k_{equatorial}$ = 5), contrasting with the absence of *any* equatorial elimination by LDA at 25 °C.[17] We suspect that a carbenoid mechanism may be involved.[18] The comparable rates of NaDA–DMEA and LDA–THF[17] for dehydrohalogenations in entries 1 and 3 are outliers in Table 1.

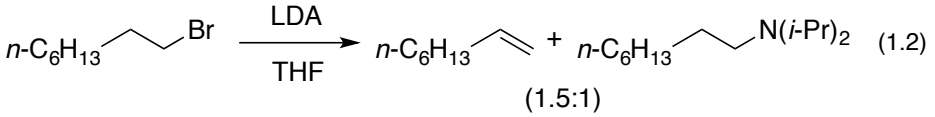

(1.2)

Enolization of 3-pentanone (entry 4) is too fast to monitor at standard temperatures. Although the selectivity for NaDA–DMEA is low, it is reversed relative to the 3:1 *E*/*Z* selectivity observed for LDA–THF.[19] In contrast to ketones, LDA-mediated hydrazone metalations are remarkably slow (entry 5) but are markedly faster with NaDA–DMEA. Trapping the resulting sodium salt with MeI, however, shows a modest 5:1 axial selectivity compared with that for the lithium salt (>15:1).[13e]

Cyclooctene oxide elimination (entry 6) provided the most unexpected result by giving clean elimination to cyclooctenols in a 10:1 cis:trans selectivity. We can find no precedent for such a base-mediated elimination to give the trans isomer.[13f] LDA–THF, by contrast, is much

slower (requiring reflux) and gives low yields of *cis*-2-cyclooctenol and bicyclo[3.3.0]octan-1-ol in >13:1 selectivity,[20] the latter presumably deriving from carbenoid chemistry.

Orthometalation is the most obvious application of NaDA and has received some attention.[9,10] Metalation of fluorobenzene (entry 7) is incomplete at equilibrium, as shown by partial carbonation and by monitoring the reaction with ^{19}F NMR spectroscopy. Precipitation of the arylsodium is observed at approximately 1.0 M at –78 °C. The appearance of benzyne products only at temperatures above –30 °C is notable and surprising.

The rapid orthometalation of the carbamate by NaDA–DMEA (in contrast to LDA–THF) in entry 8 makes the arylsodium observable;[13h] the Snieckus–Fries rearrangement[21] served as an internal quench to illustrate the efficacy of the metalation. The facile haloarene metalations in entries 9 and 10 again underscore a surprising reluctance of the arylsodium to form benzyne at temperatures below –30 °C. Compared with the ~1:1 mixture observed for LDA, the regioselectivity in entry 10 that favors metalation at the 6-position rather than at the doubly activated 2-position is higher,[22] but facile equilibration[22,23] even at –78 °C affords the 2-sodiated intermediate as the exclusive form, as shown via quenching and ^{19}F NMR spectroscopy.

Metalations of 1,4-cyclohexadiene (entry 11) with subsequent silylation can been carried out, albeit slowly, with LDA–THF, but literature reports all use alkyllithiums.[24] Especially notable here is the use of THF as an added ligand *after* metalation but *before* silylation; attempts to silylate without adding THF failed with significant loss of yield owing to aromatization and protonation of the sodium salt. Although allyl methyl, phenyl, and trimethylsilyl ethers are not observably metalated by NaDA (entry 12), facile rearrangement to *Z*-(1-propenyl) ethers as the sole kinetic product compares favorably to a method using *t*-BuOK–DMSO at >70 °C that gives

10–20:1 *Z* selectivity and is fast when compared to the recently reported an analogous procedure using LDA by Su and Williard.[25]

Conclusion

Organosodium chemistry has witnessed brief periods of activity[26] followed by long periods of quiescence. We are hoping to regenerate interest. NaDA in DMEA can be prepared in only minutes, shows excellent solubility properties, and is stable as a concentrated stock solution for months with refrigeration. Metalations are breathtakingly fast in many instances, affording surprisingly soluble sodiated products. Importantly, ongoing studies show that DMEA and related trialkylamines are weakly bound to NaDA, which allows facile substitution with stoichiometric quantities of more conventional ligands such as THF, 1,2-dimethoxyethane, and *N,N,N′,N′*-tetramethylethylenediamine either *before or after the metalation*. Subsequent reports will show that these ligands often accelerate already rapid metalations by orders of magnitude. The merit of post-metalation ligand substitution is illustrated by the need for THF addition when trapping a dienyl anion with triisopropylchlorosilane. Applications and affiliated reaction mechanisms will be described in due course. Most important, we have yet to uncover any chronic limitations.

Experimental

Reagents and solvents. DMEA, hexane, and THF were distilled from blue or purple solutions containing sodium benzophenone ketyl. All products in Table 1 have been prepared previously[13] or are commercially available.

Sodium diisopropylamide: *N,N*-dimethylethylamine (4.0 mL) and diisopropylamine (0.50 mL, 3.5 mmol) were added to a 15 mL pear-shaped flask. To this flask was added sodium dispersion in toluene (3.0 mL, 35 mmol), which produced effervescence for approximately 10 s. With stirring, isoprene (175 mL, 1.75 mmol) was added over the course of 1 min. Stirring was halted after 5 min, and insoluble materials were allowed to settle, which yielded a yellow supernatant. Variations in the quality (age) of the sodium dispersion can lengthen reaction time. The resulting NaDA solution can be used directly or stored at –20 °C. The reaction was shown to be quantitative by monitoring NaDA formation (d 3.2–3.3 ppm, septet) and the disappearance of diisopropylamine (d 2.8–2.9 ppm, octet). Alternatively, the method of Kofron[27] was used to titrate the resulting NaDA solution. Diphenylacetic acid (20.0 mg, 0.094 mmol) and 1.0 mL dry THF were added to a vial. Then, the NaDA–DMEA solution was added dropwise at room temperature until yellow coloration persisted, marking the end point of the titration. (The presumed sodium carboxylate can precipitate as a white solid that, interestingly, redissolves with a second equivalent of NaDA, which suggests that the enediolate is soluble.) The results of this titration provide a NaDA titer up to 1.2 times that anticipated if the loss of highly volatile DMEA occurs during NaDA preparation.

IR spectroscopic analyses. IR spectra were recorded by using an in situ IR spectrometer fitted with a 30-bounce, silicon-tipped probe. The spectra were acquired in 16 scans at a gain of 1 and a resolution of 4 cm^{-1}. A representative reaction was carried out as follows: The IR probe was inserted through a nylon adapter and O-ring seal into an oven-dried, cylindrical flask fitted with a magnetic stir bar and a T-joint. The T-joint was capped with a septum for injections and a nitrogen line. After evacuation under full vacuum, heating, and flushing with nitrogen, the flask was charged with NaDA (62 mg, 0.50 mmol) in 4.9 mL DMEA and cooled in a dry ice–acetone

bath prepared with fresh acetone. After recording a background spectrum, we added substrate stock (100 μL, 0.50 mmol) with stirring. For the most rapid reactions, IR spectra were recorded every 6 s.

NMR spectroscopic analyses. NMR samples for monitoring reactions were prepared by using stock solutions and sealed with partial vacuum or under ambient argon pressure with two natural rubber septa. Standard ^{1}H and ^{19}F NMR spectra were recorded at 500 and 470 MHz, respectively. In the case of ^{1}H NMR spectroscopic analysis, the loss of NaDA and formation of diisopropylamine can be monitored (vide supra) in addition to characteristic changes corresponding to substrate.

Chapter 1 References and Footnotes

1. Hammell, M.; Levine, R. *J. Org. Chem.* **1950**, *15*, 162.

2. Creger, P. L. *J. Am. Chem. Soc.* **1967**, *89*, 2500.

3. (a) Bakker, W. I. I.; Wong, P. L.; Snieckus, V. Lithium Diisopropylamide. In *e-EROS*; Paquette, L. A., Ed.; Wiley: New York, 2001. (b) Clayden, J. *Organolithiums: Selectivity for Synthesis*; Baldwin, J. E., Williams, R. M., Eds.; Pergamon Press: New York, 2002. (c) Hartung, C. G.; Snieckus, V. In Modern Arene Chemistry; Astruc, D. Ed.; Wiley- VCH, Weinheim, 2002; Chapter 10. (d) http://chem.wisc.edu//areas/reich/group/index.htm.

4. Raynolds, S.; Levine, R. *J. Am. Chem. Soc.* **1959**, *82*, 472.

5. (a) Lochmann, L.; Trekoval, J. *J. Organomet. Chem.* **1979**, *179*, 123. (b) Lochmann, L.; Janata, M. *Eur. J. Chem.* **2014**, *12*, 537.

6. (a) Lochmann, L.; Pospíšil, J.; Lím, D. *Tetrahedron Lett.* **1966**, *2*, 257. (b) Lochmann, L. *Eur. J. Inorg. Chem.* **2000**, 1115.

7. Barr, D.; Dawson, A. J.; Wakefield, B. J. *J. Chem. Soc., Chem. Commun.* **1992**, 204.

8. Mulvey, R. E.; Robertson, S. D. *Angew. Chem., Int. Ed.* **2013**, *52*, 11470.

9. (a) Munguia, T.; Bakir, Z. A.; Cervantes-Lee, F.; Metta-Magana, A.; Pannell, K. H. *Organometallics* **2009**, *28*, 5777. (b) Andrews, P. C.; Barnett, N. D. R.; Mulvey, R. E.; Clegg, W.; O'Neil, P. A.; Barr, D.; Cowton, L.; Dawson, A. J.; Wakefield, B. J. *J. Organomet. Chem.* **1996**, *518*, 85.

10. (a) Boeckman, R. K.; Boehmler, D. J.; Musselman, R. A. *Org. Lett.* **2001**, *3*, 3777. (b) LaMontagne, M. P.; Ao, M. S.; Markovac, A.; Menke, J. R. *J. Med. Chem.*, **1976**, *19*, 363. (c) Bond, J. L.; Krottinger, D.; Schumacher, R. M.; Sund, E. H.; Weaver, T. J. *J. Chem. Eng. Data.* **1973**, *18*, 349. (d) Levine, R.; Raynolds, S. *J. Org. Chem.* **1960**, *25*, 530. (e) Mamane, V.; Louërat, F.; Iehl, J.; Abboud, M.; Fort, Y. *Tetrahedron*. **2008**, *64*, 10699. (f) Baum, B. M.; Levine, R. *J. Heterocyclic Chem*. **1966**, *3*, 272. (g) Tsuruta, T. *Makromol. Chem*., **1985**, *13*, 33. (h) Andrikopoulos, P. C.; Armstrong, D. R.; Clegg, W.; Gilfillan, C. J.; Hevia, E.; Kennedy, A. R.; Mulvey, R. E.; O'Hara, C. T.; Parkinson, J. A.; Tooke, D. M. *J. Am. Chem. Soc.* **2004**, *126*, 11612.

11. Inorganic chemists have found NaDA useful for installing the diisopropylamido moiety into transition metal coordination spheres: Spallek, T; Heß, O.; Meermann-Zimmermann, M.; Meermann, C.; Klimpel, M. G.; Estler, F.; Schneider, D.; Scherer, W.; Tafipolsky, M.; Törnroos, K. W.; Maichle-Mössmer, C.; Sirsch, P.; Anwander, R. *Dalton Trans.* **2016**, *45*, 13750.

12. To circumvent solubility issues, Mioskowski and co-workers generated *n*-BuNa in the presence of arenes to achieve orthometalation: Gissot, A.; Becht, J. M.; Desmurs, J. R.; Pévère, V.; Wagner, A.; Mioskowski, C. *Angew. Chem., Int. Ed. Engl.* **2002**, *41*, 340.

13. The products in Table 1 that are not commercially available but have been prepared previously are listed according to table entry number as follows: (a) entry 2: Scott, W. J.; Stille, J. K. *J. Am. Chem. Soc.* **1986**, *108*, 3033. (b) entry 3: Chen, W.; Wang, D.; Dai, C.; Hamelberg, D.; Wang, B. *Chem. Commun.* **2012**, *48*, 1736. (c) entry 4: Tirpak, R. E; Rathke, M. W. *J. Org. Chem.* **1982**, *47*, 5099. (d) entry 5: Corey, E. J., Enders, D. *Tetrahedron Lett*. **1976**, *17*, 3. (e) entry 6: Whitham, G. H.; Wright, M. *J. Chem. Soc. C* **1971**, 883. (f) entry 8: García, F.; McPartlin, M.; Morey, J. V.; Nobuto, D.; Kondo, Y.; Naka, H.; Uchiyama, M.; Wheatley, A. E. H. *Eur. J. Org. Chem.* **2008**, 644. (g) entry 9: Singh, K. J.; Collum, D. B. *J. Am. Chem. Soc.* **2006**, *128*, 13753. (h) entry 11: Landais, Y.; Zekri, E. *Eur. J. Org. Chem.* **2002**, 4037. (i) entry 12: Taskinen, E. *Tetrahedron* **1993**, *49*, 11389.

14. We often find a 3-fold rate change with each 10 °C to be a better approximation.

15. Contrary to our perception, LDA-mediated dehydrohalogenations are conspicuously underrepresented in the published literature for vague reasons. (a) Nikitin, K. V.; Andryukhova, N. P. *Can. J. Chem*. **2004**, *82*, 571. (b) Vinick, F. J.; Desai, M. C.; Jung, S.; Thadeio, P. *Tetrahedron Lett*. **1989**, *30*, 787. (c) Altman, J.; Wilchek, M. *J. Heterocyclic Chem*. **1988**, *25*, 915. (d) For references to amide-mediated dehydrohalogenations and reviews on eliminations, see: Kopka, I. E.; Nowak, M. A.; Rathke, M. W. *Synth. Commun.* **1986**, *16*, 27. (e) Also, see ref 17.

16. (a) Smith, M.; March, J. *March's Advanced Organic Chemistry: Reactions, Mechanisms, and Structure*, 6th ed.; Wiley-Interscience: New York, 2007; Chapters 10, 17 . (b) Carey, F. A.; Sundberg, R. J. *Advanced Organic Chemistry*, 5th ed.; Springer: New York, 2007; Chapters 4, 5. (c) Saunders, W. H., Jr.; Cockerill, A. F. *Mechanisms of Elimination Reactions*; John Wiley & Sons: New York, 1973; Vol. II, pp 60–68. (d) Baciocchi, E. in *The Chemistry of Halides, Pseudo Halides and Azides, Supplement D*; Patai, S., Rappoport, Z., Eds.; Wiley: Chichester, U.K., 1983.

17. Ma, Y.; Ramírez, A.; Singh, K. J.; Keresztes, I.; Collum, D. B. *J. Am. Chem. Soc.* **2006**, *128*, 15399.

18. Cristol, S. J.; Whittemore, C. A. *J. Org. Chem.* **1969**, *34*, 705.

19. (a) Ireland, R. E.; Mueller, R. H.; Willard, A. K. *J. Am. Chem. Soc.* **1976**, *98*, 2868. (b) Miller, D. J.; Saunders, W. H., Jr. *J. Org. Chem.* **1982**, *47*, 5039. (c) Xie, L. F.; Saunders, W. H. *J. Am. Chem. Soc.* **1991**, *113*, 3123.

20. (a) Boeckman, R. K. *Tetrahedron Lett*. **1977,** *49*, 4281. (b) Apparu, M.; Barrelle, M. *Tetrahedron* **1978**, *34*, 1541. Whitesell, J. K.; White, P. D. *Synthesis* **1975**, 602.

21. (a) Sibi, M. P.; Snieckus, V. *J. Org. Chem.* **1983**, *48*, 1935. (b) Snieckus, V. *Chem. Rev.* **1990**, *90*, 879. (c) Hartung, C. G.; Snieckus, V. In *Modern Arene Chemistry*; Astruc, D., Ed.; Wiley-VCH: Weinheim, 2002; Chapter 10. (d) Zhao, Y.; Snieckus, V. *J. Am. Chem. Soc.* **2014**, *136*, 11224.

22. Hoepker, A. C.; Gupta, L.; Ma, Y.; Faggin, M. F.; Collum, D. B. *J. Am. Chem. Soc.* **2011**, *133*, 7135.

23. (a) Cottet, F.; Schlosser, M. *Eur. J. Org. Chem.* **2004**, 3793. (b) Trecourt, F.; Mallet, M.; Marsais, F.; Quéguiner, G. *J. Org. Chem* **1988**, *53*, 1367. (c) Gros, P. C.; Fort, Y. *Eur. J. Org. Chem.* **2009**, 4199. (d) Fukuda, T.; Ohta, T.; Sudo, E.; Iwao, M. *Org. Lett.* **2010**, *12*, 2734. (e) Viciu, M.; Gupta, L.; Collum, D. B. *J. Am. Chem. Soc.* **2010**, *132*, 6361.

24. Landais, Y.; Zekri, E. *Tetrahedron Lett.* **2001**, *42*, 6547.

25. (a) Taskinen, E. *Tetrahedron* **1993**, *48*, 11389. (b) Su, C.; Williard, P. G. *Org. Lett.* **2010**, *12*, 5378.

26. For an interesting historical perspective on organoalkali metal chemistry, see: (a) Seyferth, D. *Organometallics* **2006**, *25*, 2. (b) Seyferth, D. *Organometallics* **2009**, *28*, 2.

27. Kofron, W. G.; Baclawski, L. M. *J. Org. Chem.* **1976**, *41*, 1879.

Chapter 2

Sodium Diisopropylamide:

Aggregation, Solvation, and Stability

Sodium Diisopropylamide:

Aggregation, Solvation, and Stability

Abstract

The solution structure, stabilities, physical properties, and reactivities of sodium diisopropylamide (NaDA) in a variety of coordinating solvents are described. NaDA is stable for months as a solid or as a 1.0 M solution in *N*,*N*-dimethylethylamine (DMEA) at –20 °C. A combination of NMR spectroscopic and computational studies show that NaDA is a disolvated symmetric dimer in DMEA, *N,N*-dimethyl-*n*-butylamine, and *N*-methylpyrrolidine. Tetrahydrofuran (THF) readily displaces DMEA, affording a tetrasolvated cyclic dimer at all THF concentrations. Dimethoxyethane (DME) and *N,N,N′,N′*-tetramethylethylenediamine (TMEDA) quantitatively displace DMEA, affording doubly chelated symmetric dimers. The trifunctional ligands *N,N,N′,N″,N″*-pentamethyldiethylenetriamine and diglyme bind the dimer as bidentate rather than tridentate ligands. Relative rates of solvent decompositions are reported, and rate studies for the decomposition of THF and DME are consistent with monomer-based mechanisms.

Introduction

Several groups, most recently that of Mulvey, have underscored the merits of sodium dialkylamides,[1,2] but the response of the synthetic organic community remains muted compared with the enthusiastic embrace of lithium diisopropylamide (LDA) and related lithium dialkylamides.[3] Sodium diisopropylamide (NaDA) is an excellent case in point. Since the initial preparation of NaDA by Levine in 1959[4] and subsequent improved preparations,[5] NaDA has languished in relative obscurity, appearing in the literature only a dozen times over half a century.[6] This scarcity is somewhat perplexing on first inspection. NaDA is easily prepared, stable as a solid if refrigerated, and a powerful Brønsted base.[5,6] We surmised that potential users must be leery of the rapid destruction of standard ethereal solvents by NaDA and its insolubility in inert hydrocarbons. In short, NaDA is inconvenient.

In our first paper of this series, we reported that 1.0 M solutions of NaDA in neat *N,N*-dimethylethylamine (DMEA) or DMEA–hydrocarbon mixtures are stable for weeks at room temperature and for months under refrigeration.[7] Moreover, NaDA–DMEA can be prepared in 15 min from technical-grade reagents without pre-purification or pre-drying. Metalations of a dozen substrates with a broad range of functionality have shown that NaDA–DMEA is often orders of magnitude more reactive than LDA–THF toward orthometalations, dehydrohalogenations, diene metalations, and epoxide eliminations.[7] The stereo- and chemoselectivities of the two bases are also complementary. Even concerns that the sodiated intermediates and products in DMEA might be insoluble have proved unfounded. Overall, the results of our initial studies were highly encouraging, and, as a referee noted, ″running reactions in trialkylamine solvent is not crazy.″

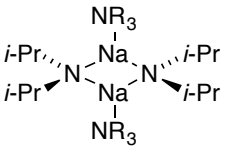

1a; $NR_3 = Me_2NEt$
1b; $NR_3 = Me_2N$-*n*-Bu
1c; NR_3 = N-methylpyrrolidine

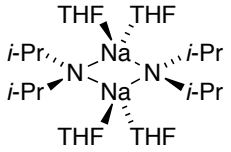

1d

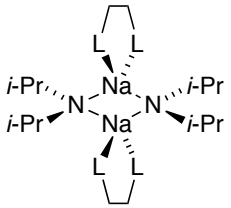

1e; $L = NMe_2$
1f; L = OMe

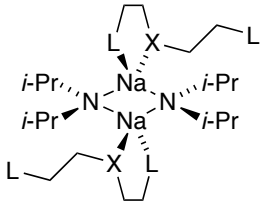

1g; $L = NMe_2$, X = NMe
1h; L = OMe, X = O

In this second paper, we examine the solution structure and stability of NaDA solvated by DMEA, other trialkylamines, and a number of synthetically important coordinating ligands including tetrahydrofuran (THF), *N,N,N′,N′*-tetramethylethylenediamine (TMEDA), and 1,2-dimethoxyethane (DME). The cyclic dimer motif (**1a–h**) is the only detectable form. DMEA is substitutionally labile, which is a critical prerequisite for the addition of other ligands before metalation to modulate the reactivity of NaDA and after metalation to control reactivity of the resulting sodium salts. Mechanistic studies of solvent decomposition offer the first glimpse into NaDA reactivity. This paper is intended to detail the structural foundations underpinning NaDA structure–reactivity–selectivity principles of potential interest to synthetic organic chemists.

Results

Methods. We modified the dissolving metal method first described by Wakefield and co-workers[5a] by using kinetically inert and solubilizing DMEA as the bulk solvent.[5,7] Although the procedure affords 1.0 M stock solutions of NaDA adequate for synthetic applications, a

precautionary crystallization from DMEA–hexane was included for spectroscopic and rate studies. We hasten to add that the typical user will detect little or no difference between the pre- and post-purified reagent.

Given the absence of resolved ^{23}Na–^{15}N coupling owing to the quadrupolar ^{23}Na nucleus and with an eye toward expanding the application of the method of continuous variations (MCV) to aggregated organometallic species lacking NMR-active metal nuclei, we turned to MCV to assign the solution structure.[8,9] In short, an ensemble generated from constitutionally similar species of unknown aggregation number ($\mathbf{A}_n$ and $\mathbf{B}_n$, eq 2.1) is monitored with NMR spectroscopy as a function of mole fraction X_A or X_B. The number of heteroaggregates attests to the aggregation state. Plotting the relative proportions versus mole fraction affords a Job plot confirming the assignment.

$$\mathbf{A}_n + \mathbf{B}_n \Longrightarrow \mathbf{A}_n + \mathbf{A}_{n-1}\mathbf{B}_1 + \mathbf{A}_{n-2}\mathbf{B}_2 + \ldots + \mathbf{B}_n \qquad (2.1)$$

For this study, NaDA was paired with sodium dicyclohexylamide (NaDCA)[5c,10] and sodium isopropylcyclohexylamide (NaICA).[9a] NaICA was previously suggested to be dimeric, as evidenced by two stereoisomers (*cis*-**2** and *trans*-**2**, eq 2.2; Cy = cyclohexyl).[9a] We confirmed the dimer assignment for NaICA and showed that both NaDA and NaDCA are dimers **1** and **3**, respectively, by examining NaDA–NaICA and NaDA–NaDCA mixtures using ^{13}C and ^{15}N NMR spectroscopies. NaDA–NaDCA pairings are superior and are emphasized below. Considerable data for the NaDA–NaICA pairings are archived in the supporting information. Although ^{1}H NMR spectroscopy proved especially valuable in MCV-based studies of sodium enolates,[9a,11] the resolution was inadequate for the study of sodium dialkylamide aggregation.

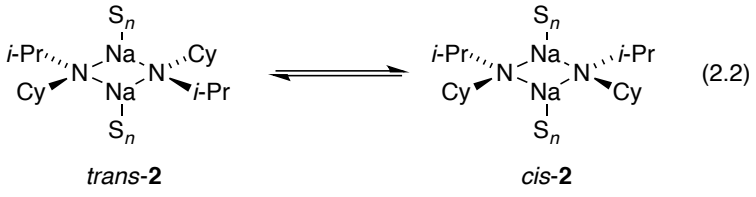

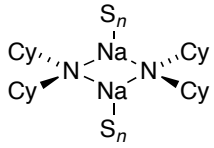

3

The strategies and quantitative insights into solution solvation numbers of NaDA are notable in our opinions. Confirmations and experimentally elusive details are provided with density functional theory (DFT) computations at the B3LYP/6–31G(d) level,[12] with single-point calculations at the MP2 level of theory.[13]

Solution Structure: NaDA in DMEA and related amines. ^{13}C NMR spectra of NaDA–NaDCA mixtures in DMEA showed the dimer ensemble depicted in eq 2.3 with resolution of all ^{13}C methine resonances of the isopropyl and cyclohexyl moieties (Figure 2.1a). A plot of the relative integrations of **1**, **3**, and **4** afforded the Job plot illustrated in Figure 2.2, which is characteristic of statistically distributed dimers.

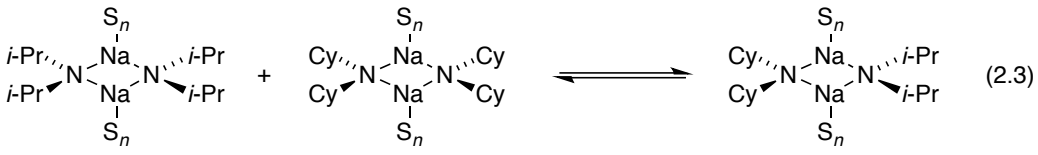

1 **3** **4**

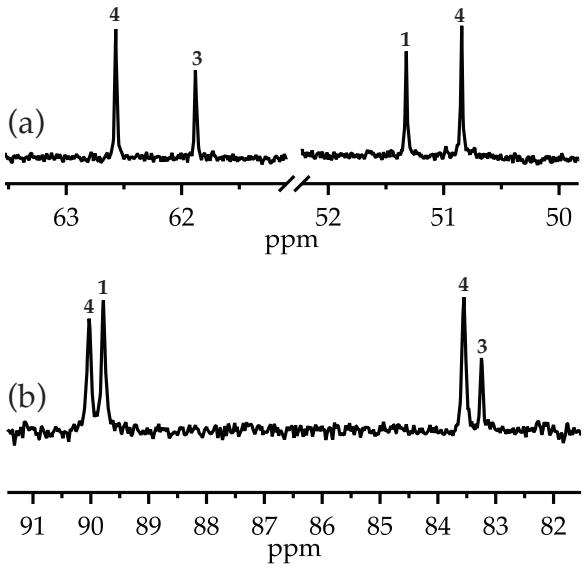

Figure 2.1. NMR spectra of a ~1:1 mixture (0.10 M total titer) of sodium diisopropylamide (NaDA; **1**) and sodium dicyclohexylamide (NaDCA; **3**) in neat dimethylethylamine (DMEA) affording heterodimer **4**. (a) ^{13}C NMR spectrum recorded at –80 °C; (b) ^{15}N NMR spectrum using [^{15}N]NaDA and [^{15}N]NaDCA recorded at –100 °C.

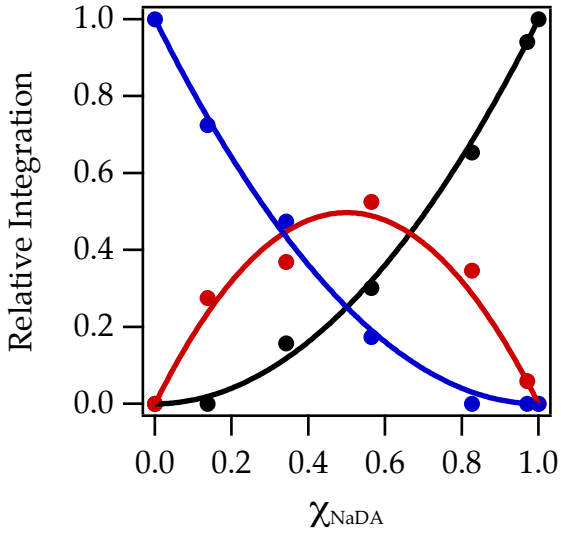

Figure 2.2. Job plot showing relative integrations of the ^{13}C resonances of **1** (black), **3** (blue), and **4** (red) versus the measured[14] mole fraction of NaDA (X_{NaDA}) for mixtures of NaDCA and NaDA in neat DMEA at –80 °C.

A ^{15}N NMR spectrum of a 1:1 mixture of [^{15}N]NaDA and [^{15}N]NaDCA shows signals corresponding to two homodimers and a heterodimer distributed statistically (Figure 2.1b). A Job plot based on ^{15}N NMR data is analogous to that shown in Figure 2.2 (supporting information).

MCV analyses using the NaDA–NaICA mixtures (eq 2.4) were effective, but they have been largely relegated to supporting information. Several interesting observations are worth noting, however. The ^{13}C NMR data resolved two methinyl resonances in each of the two NaICA homodimers as well as the four methinyl resonances in heterodimer **5** (eq 2.2), readily affording the corresponding Job plot. ^{15}N NMR spectroscopy using [^{15}N]NaDA and [^{15}N]NaICA showed that the ^{15}N resonances of the homo- and heteroaggregated NaICA fragments are poorly resolved, whereas homo- and heteroaggregated NaDA fragments are well-resolved. Poor resolution on one pair is not critical;[9a] the resulting Job plot is consistent with a statistical distribution of dimers.

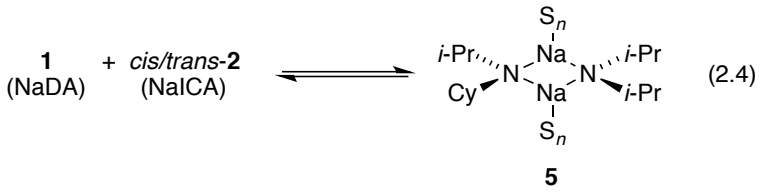

(2.4)

^{13}C and ^{15}N NMR spectroscopic investigations of the NaDA–NaDCA pair in *N,N*-dimethylbutylamine (DMBA) and *N*-methylpyrrolidine showed that NaDA is dimeric (supporting information). DFT computations showed that sequential solvation of dimeric NaDA by DMEA is highly exothermic and affords disolvate **1a**, but no minima corresponding to tri- or tetrasolvated dimers were found. The sterically less demanding and computationally simpler Me_3N gave similar results. This outcome contrasts sharply with ethereal and multidentate ligands (*vide infra*).

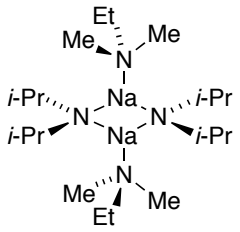

1a

Owing to our experience with DFT computations in lithium chemistry, we were comfortable with the assignment of **1a** as disolvated. Nonetheless, we applied several experimental methods to determine the solvation as follows. Proton diffusion-ordered NMR spectroscopy (^{1}H-DOSY), first applied to organolithium aggregates by Williard,[15] is now proliferating within the field[16] and has been applied to organosodiums.[17] Underlying assumptions about molecular shape and influence on the diffusion constant have always left us uneasy, however.

We examined the structure of NaDA in DMEA using the double bipolar pulse pair stimulated echo sequence with convection compensation pulse sequence to measure the diffusion coefficients of NaDA dissolved in DMEA. An analogous experiment independently measured diffusion coefficients for DMEA, THF, tetramethylsilane, anisole, 1,3-dimethoxybenzene, and 18-crown-6 to obtain the molecular weights for NaDA shown in Table 2. Although the data recorded at ambient temperature seemed to confirm the disolvated dimer, the molecular weight at –80 °C was 25 % low. Similar temperature dependencies have been noted by others.[16,17] We have no evidence, however, that the reduced value at –80 °C is based on a structural change: low temperature promotes rather than retards solvation owing to negative enthalpy. Also, the

solubility of NaDA in DMEA is nearly temperature-independent. The results from THF solvate **1d** (see Table 1) are discussed below.

Table 1. Molecular Weight (MW) of Sodium Diisopropylamide in Dimethylethylamine and Tetrahydrofuran Determined with ^{1}H Diffusion-Ordered Spectroscopy

Aggregate	Calculated MW	Diffusion MW (–80 °C)	Diffusion MW (rt)
1a	393	298	391
1d	534	565	481

rt, room temperature.

A more traditional probe of solubility provided significant insight.[18] The concentration of DMEA-solubilized NaDA in a suspension of NaDA in toluene-d_8 was monitored as a function of added DMEA using ^{1}H NMR spectroscopy and benzene as an internal standard; the two-phase equilibrium is described in eq 2.5.[19] If DMEA coordinates to and solubilizes NaDA quantitatively ($K_{solv} >> 1$), the concentration of NaDA will be proportional to the concentration of DMEA until full solubility is achieved, with the solvation number being extractable from the slope and the endpoint (eq 2.8). We see this behavior for superior solvents (*vide infra*). In the limit of weak binding ($K_{solv} << 1$), the solubility will be low while manifesting curvature diagnostic of the coordination number (eq 2.9). The measured concentration of NaDA in solution versus added DMEA (Figure 2.3) showed non-limiting behavior: it is upwardly curving with a fit

to eq 2.7 showing disolvated dimer ($n = 2$). Forcing the model to a tetrasolvated dimer ($n = 4$) provided a markedly inferior fit to the data.

$$(A)_{solid} + nS \overset{K_{solv}}{\rightleftharpoons} (A_2S_n)_{solution} \quad (2.5)$$

$$K_{solv} = [A_2S_n]/[S]^n \quad (2.6)$$

$$[A_2S_n] = K_{solv}([S]_0 - n[A_2S_n])^n \quad (2.7)$$

$$[A_2S_n] = [S]_0/n \quad (2.8)$$

$$[A_2S_n] = K_{solv}[S]_0{}^n \quad (2.9)$$

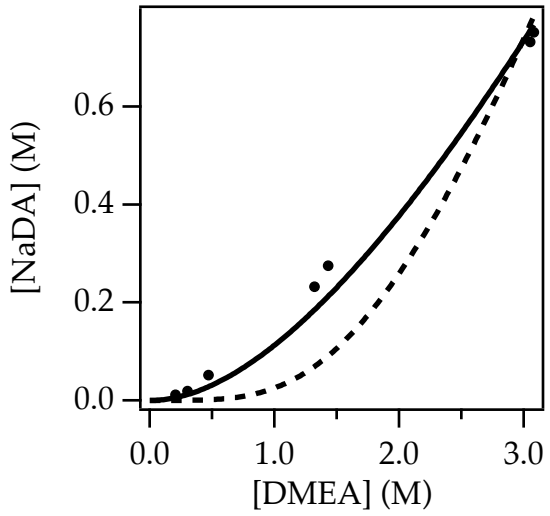

Figure 2.3. Plot of NaDA concentration versus total DMEA concentration in toluene at room temperature fit to equation 7 and presuming one DMEA per sodium (solid line, $n = 2$ [set],[20] $K_{solv} = 0.072 \pm 0.004$) and two DMEA per sodium (dashed line, $n = 4$ [set], $K_{solv} = 0.007 \pm 0.002$).

Thus, recalcitrant solubilization of NaDA by DMEA reflects weak binding. This notion is reinforced by studies of additional monodentate trialkylamines (supporting information). As steric demands increase, the binding constant, K_{solv}, decreases. The poor solubility of NaDA in

triethylamine, for example, stems from weak coordination rather than a low solubility of the doubly solvated dimer. We return to this idea in the discussion.

Solution Structure: NaDA–THF. MCV using ^{13}C and ^{15}N NMR spectroscopies for NaDA–NaICA and NaDA–NaDCA pairs demonstrated that THF-solvated NaDA is dimeric at both low and high THF concentrations (supporting information). As usual, determining the solvation state demanded several strategies. Incremental additions of THF to NaDA in 2.0 M DMEA (Figure 2.4) showed clear saturation of the changing chemical shifts of the methine proton and ^{15}N resonances resulting from ligand substitution consistent with strongly preferential THF coordination. However, curvature with saturation occurring at ≈3.0 equiv of THF per sodium (as opposed to a linear dependence with a sharp endpoint) belied non-quantitative substitution, thereby obscuring the stoichiometry. Fortunately, titration of a suspension of NaDA in toluene, as described for trialkylamines (Figure 2.5 and eqs 5–7), revealed a linear dependence of the measured titer on added THF and a constant 2:1 THF/NaDA ratio in solution up to full solubilization at 2.0 equiv. This outcome is fully consistent with tetrasolvate **1d**.

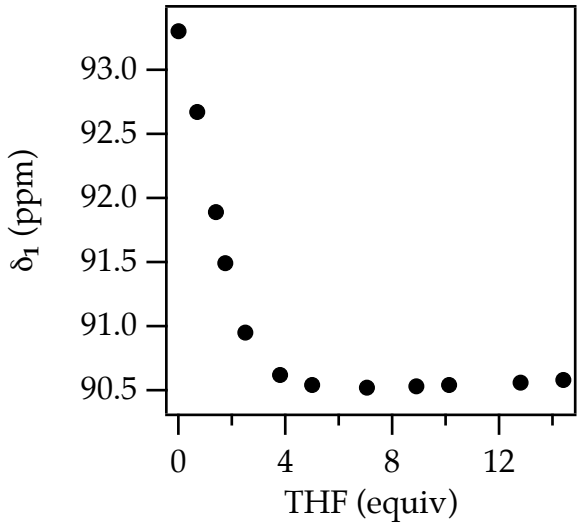

Figure 2.4. Plot of ^{15}N chemical shifts of **1** versus equivalents of tetrahydrofuran (THF) in 2.0 M DMEA–hexane at –80 °C.

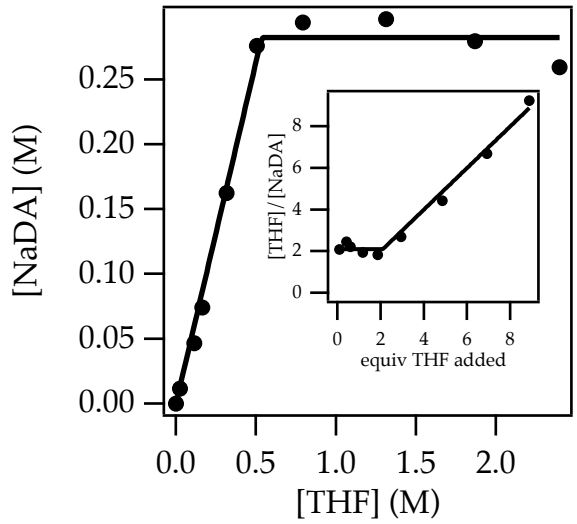

Figure 2.5. Plot of NaDA concentration versus total THF concentration for suspensions of NaDA in toluene at room temperature. The concentration is measured relative to benzene (internal standard). Inset: Plot of THF/NaDA concentration versus equivalents of THF added to the anticipated amount of NaDA at room temperature. The discontinuities correspond to full solubilization.

The tetrasolvated form is also strongly supported computationally (eq 2.10). Given the exothermicity and our experience that DFT computations tend to falter with congested systems, we are confident in the tetrasolvate assignment.

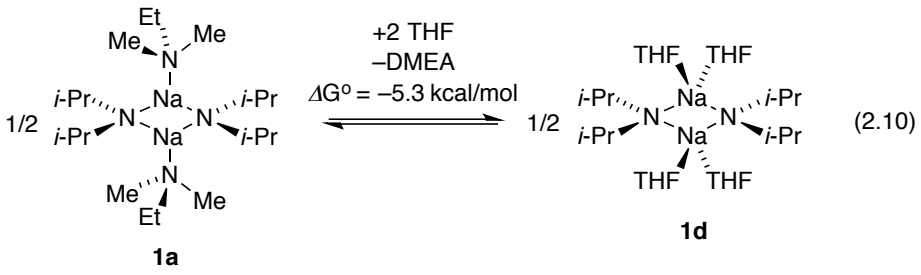

Solution Structure: NaDA–TMEDA. MCV showed that the solution aggregation state of NaDA–TMEDA is akin to the reported doubly chelated crystal structure (supporting information).[6b] We hoped to observe free and bound TMEDA in the slow-exchange limit to directly measure the number of ligands on the bound form, but the exchange was rapid at –100 °C. Two titration methods showed strong coordination by TMEDA and supported a 1:1 proportion of NaDA/TMEDA:

(1) Substitution of DMEA by TMEDA was evidenced by a downfield shift of the methinyl ^{1}H resonance and an upfield shift of the ^{15}N resonance after substitution of TMEDA by DMEA. As found for THF, however, the stoichiometry of the substitution was obscured by non-quantitative binding (supporting information).[19]

(2) Titration of a suspension of NaDA with TMEDA (analogous to that in Figure 2.5) showed a linear dependence of the measured titer on TMEDA concentration, a constant 1:1 proportion of TMEDA to NaDA in solution up to complete dissolution, and a hard solubility endpoint corresponding to 1:1 stoichiometry of TMEDA/NaDA.

DFT computations showed that the displacement of DMEA by chelated TMEDA (eq 2.11) is exothermic. This result contrasts with that observed with LDA, which forms a weakly ligated κ^1-TMEDA-solvated dimer in solution.[21,22,23]

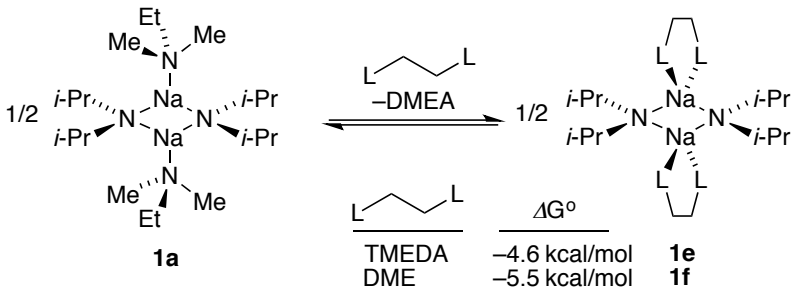

(2.11)

Solution Structure: NaDA–DME. DME acts as an ethereal analog of TMEDA in every respect: (1) ^{13}C NMR spectroscopy in conjunction with MCV showed dimers, (2) incremental addition (akin to those in Figure 2.5) to NaDA–DMEA showed semi-quantitative binding consistent with one DME per sodium, (3) titration of a NaDA suspension showed a linear dependence of the titer on DME with a hard solubility endpoint at 1:1 stoichiometry, and (4) DFT computations supported a highly exothermic substitution of DMEA by DME *without MP2 correction*. We encountered a unique situation in which uncorrected numbers and geometries corroborated experiment, yet MP2 correction provided highly questionable 1.6 kcal/mol/Na solvation energies (eq 2.11) for reasons we failed to identify. We explored a variety of larger basis sets with no obvious improvements. All evidence, including the results of experimental competition studies, suggested that the MP2 correction is indeed spurious.

Doubly chelated dimer **1f** contrasts with LDA, in which two DMEs coordinated to the dimer are unchelated.[21,24,25] We also competed TMEDA and DME by swapping one for the other

at a fixed total ligand concentration corresponding to 2.0 equiv per sodium and monitored the chemical shifts of the time-averaged free and bound ligand. TMEDA is the stronger ligand by approximately 10-fold.

Solution Structure: NaDA with Other Ligands. The results of ^{15}N NMR spectroscopy and MCV showed that trifunctional ligands diglyme and *N,N,N′,N″,N″*-pentamethyldiethylenetriamine (PMDTA) are dimers rather than monomers that could have arisen from tridentate ligation. Their binding affinities slightly greater than those of the bidentate analogs DME and TMEDA were commensurate with only a statistical advantage. Thus, these potentially tridentate ligands function as bidentate ligands, as demonstrated by **1g** and **1h**.[26,27] Computations suggest that the third ligand, although not coordinated to sodium as evidenced by long Na–OMe and Na–NMe_2 bonds, display distinct preferences for orienting the lone pairs toward the sodium nuclei. We discuss the potential synthetic importance of bidentate rather than tridentate coordination below.

We carried out a brief survey of a number of ligands that lacked rigor but provided useful data nonetheless.[28] Ethereal ligands such as Et_2O and 2,5-dimethyltetrahydrofuran substitute for DMEA but much more reluctantly than does THF as expected from binding measurements on lithium amides.[23,26,27] Titration of NaDA/toluene suspensions with anisole displays chemical shift perturbations consistent with binding but no appreciable solubilization, suggesting that anisole is a poor ligand for sodium. The highly dipolar ligand *N,N′*-dimethylpropyleneurea (DMPU) is quickly metalated by NaDA at –80 °C, as evidenced by the rapid appearance of extraneous resonances and diisopropylamine observable with ^{1}H and ^{15}N NMR spectroscopies. The products of these decompositions have not been pursued.[29]

Solvent Decomposition: Products, Rates, and Mechanisms.[30,31] Whether in DMEA or in its solid form, NaDA at room temperature has a half-life of approximately two months, consistent with the thermal sensitivity noted by Wakefield.[5b] This decomposition is mitigated by storage at –20 °C in a standard laboratory freezer. However, facile decompositions of DME and DMPU underscore the possible limitations of NaDA when used in conjunction with standard ethereal solvents. The stability of NaDA in selected solvents at room temperature is illustrated in Table 2.

Table 2: Approximate Half-Life of 0.30 M NaDA in Common Laboratory Solvents at Room Temperature

Ligand[a]	Half-life
DMEA	2 months
TMEDA	1 month
THF	1 h
DME	10 s
DMPU[b]	<<1 s

[a]Neat. [b]0.30 M DMPU in DMEA.

THF decomposition offered our first view of the mechanism of NaDA-mediated metalations. NaDA decomposition in THF–hexane mixtures at 25 °C forms partially soluble *cis* and *trans* alkoxides **7** observable with ^{1}H NMR spectroscopy (Scheme 2.1). Quenching afforded known alcohols **8** and **9** in the proportions shown in Scheme 2.1. The presumed intermediate salt

6 is observed at low (equilibrium) levels owing to facile NaDA-mediated isomerization to **7**; the isomerization of **6** under the reaction conditions was confirmed by adding **8** to NaDA–THF-d_8.

Scheme 2.1. Decomposition of THF

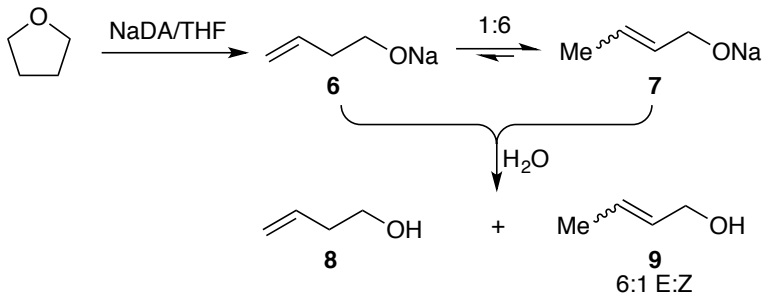

Monitoring the rate of THF decomposition by tracking the loss of **1d** (d3.11 ppm in ^{1}H NMR) and the formation of diisopropylamine showed that the reaction does not follow a first-order decay, which indicated that the decomposition does *not* occur from the observable dimer. Fitting the traces to the nonlinear Noyes equation[32] afforded an average order of 0.68 (Figure 2.6), approximating a half order. Plotting initial rates versus THF concentration revealed a second-order THF dependence (Figure 2.7). The half-order rate constants are nearly independent of the NaDA concentration, albeit with a slight upward drift (Figure 2.8). The idealized rate law[33] (eq 2.12) is consistent with the mechanism described in eq 2.13.[34] Rate-limiting proton transfer was evidenced by a substantial kinetic isotope effect determined by comparing THF to THF-d_8 (k_H/k_D = 6.9).

$$d[A_2(THF)_4]/dt = k[A_2(THF)_4]^{1/2}[THF]^2 \quad (2.12)$$

$$1/2\ A_2(THF)_4 + 2\ THF \xrightarrow{k} [A(THF)_4]^{\ddagger} \quad (2.13)$$

(**1d**)

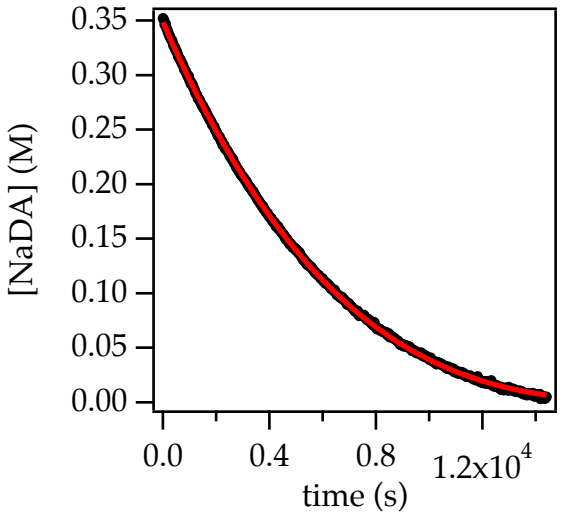

Figure 2.6. Plot of NaDA concentration versus time for the decomposition of THF (Scheme 2.1) of NaDA at 25 °C. The red curve depicts an unweighted least-squares fit to the function $f(t) = [a^{1-n} - kt(1-n)]^{[1/(1-n)]}$: $a = 0.3484 \pm 0.0002$; $k = 1.061 \times 10^{-5} \pm 9 \times 10^{-8}$; $n = 0.698 \pm 0.002$.

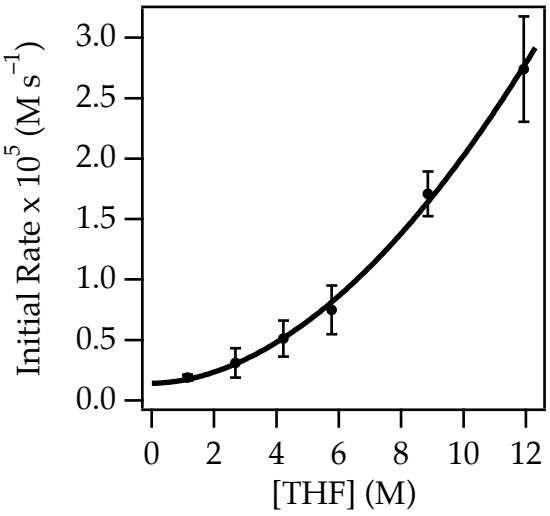

Figure 2.7. Plot of initial rates versus THF concentration for the decomposition of THF (Scheme 2.1) in 0.20 M NaDA at 25 °C. The curve depicts an unweighted least-squares fit to the function $f(x) = ax^b + c$: $a = 0.025 \pm 0.008$; $b = 1.9 \pm 0.1$; $c = 0.14 \pm 0.05$.

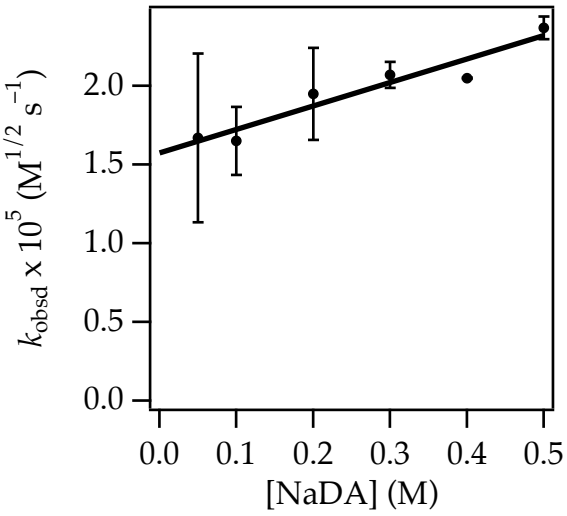

Figure 2.8. Plot of pseudo-*half*-order rate constants (k_{obsd}) versus NaDA concentration for the decomposition of THF (Scheme 2.1) in neat THF at 25 °C. The curve depicts an unweighted least-squares fit to the function $f(x) = ax + b$: $a = 1.5 \pm 0.2$; $b = 1.57 \pm 0.07$.

The $[AS_4]^{‡}$ stoichiometry is consistent with an a deprotonation via transition structure **11**–α to generate oxacarbenoid **12** as a precursor to carbene **13** (Scheme 2.2).[35] Alternatively, a b metalation whether via a concerted E2-like elimination or **11**-b discrete carbanion **14** with post-rate-limiting elimination to **6a** is plausible. Although the isomerization and consequent scrambling dissuaded us from sophisticated isotopic labeling studies, we collected evidence supporting the carbenoid pathway. Comparing THF to THF-d_4 (**15**)[36] afforded $k_H/k_D \sim 6$ suggesting a rate limiting C-H(D) cleavage at the 3 position, but it does not distinguish the two possible mechanisms. Monitoring a mixture of NaDA, THF, and *i*-Pr_2ND by ^1H and ^2H NMR spectroscopies shows isotopic exchange at the a protons of THF, consistent with a deprotonation. The comparable rates of exchange and decomposition suggest that neither metalation nor insertion are dominantly rate limiting. The existence of discrete carbene **13**, however, is not even assured.

Scheme 2.2. Mechanism of THF Decomposition

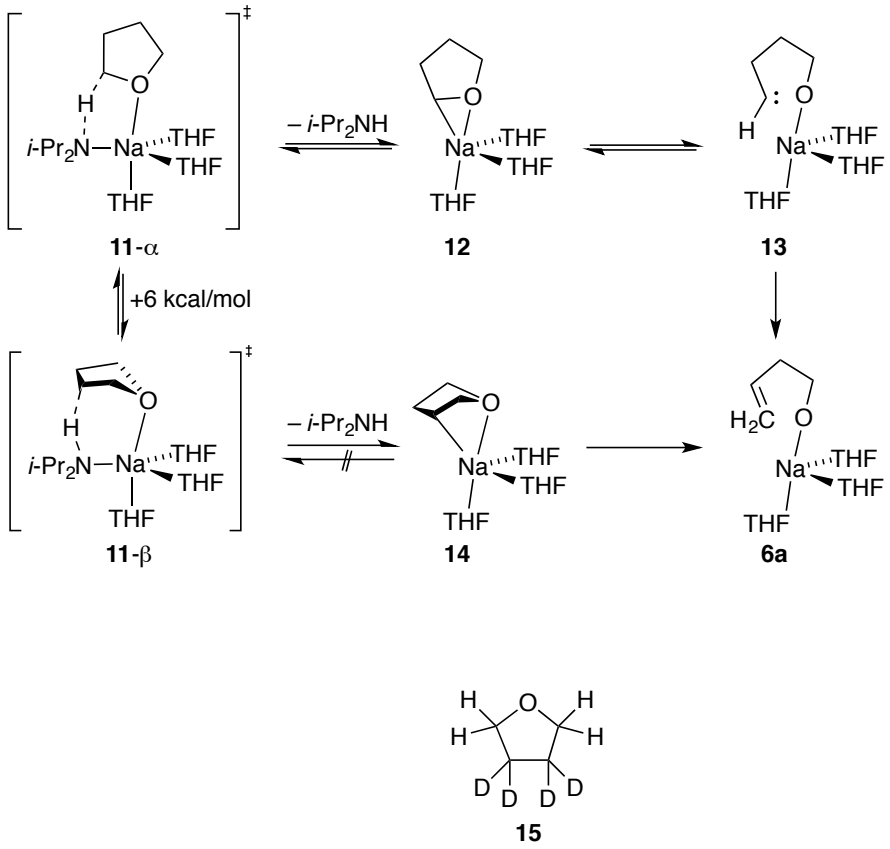

NaDA in DME–toluene undergoes decomposition to give methyl vinyl ether and sodium methoxide (eq 2.14). Following the proton resonance of **1f** at d1.10 ppm shows that the decay approximates a half-order rather than a first-order decay (akin to Figure 2.6). Fitting multiple decays to the nonlinear Noyes equation[32] to ascertain the order by best fit affords an average order of 0.52. Plotting the half-order rate constants versus NaDA concentration showed some upward drift (akin to that in Figure 2.7). A plot of k_{obsd} versus DME concentration approximated first order with a slight upward curvature (Figure 2.9), possibly hinting at either low contributions from a more highly solvent-dependent pathway or more generalized medium effects. The structure of **1f** in conjunction with the idealized[33] rate law (eq 2.15) afforded the

generic mechanism in eq 2.16. The doubly solvated monomer-based transition state, $[A(DME)_2]^{‡}$, is isostructural to THF-based **11** when ligand hapticity is considered. Although DFT computations showed **16** and **17** to be computationally viable, **16** was preferred by ~21 kcal/mol. The low coordination number—the absence of a $^{+}Na(DME)_3$ fragment[37]—argues against a free-ion-based mechanism.

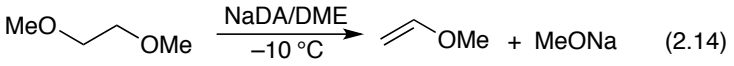

(2.14)

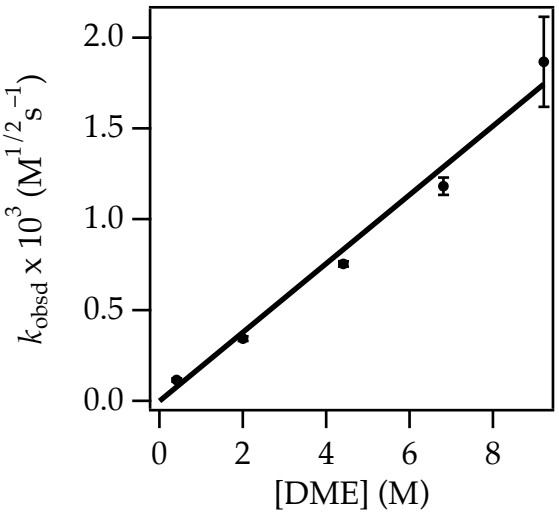

Figure 2.9. Plot of k_{obsd} versus dimethoxyethane (DME) concentration for the decomposition of DME (eq 2.12) in 0.40 M NaDA at –10 °C. The curve depicts an unweighted least-squares fit to the function $f(x) = ax$: $a = 0.189 \pm 0.008$.

$$-d[A_2(DME)_2]/dt = k[A_2(DME)_2]^{1/2}[DME]^1 \qquad (2.15)$$

$$1/2\ A_2(DME)_2 + DME \longrightarrow [A(DME)_2]^{‡} \qquad (2.16)$$

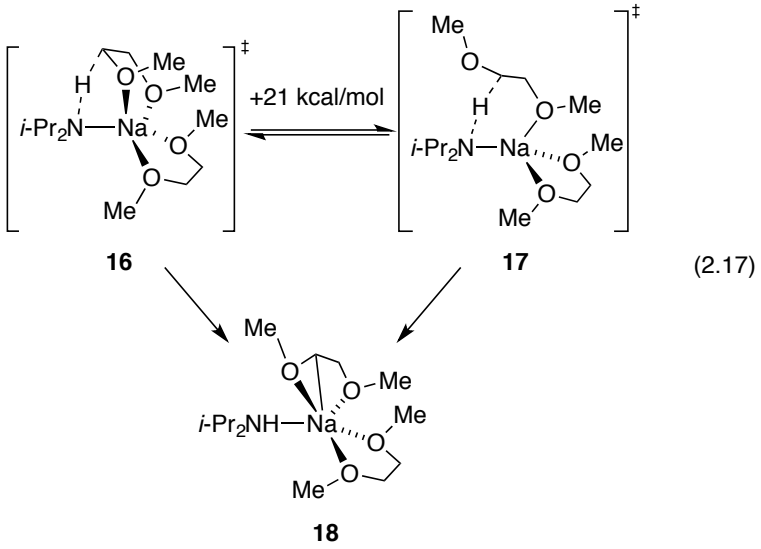

(2.17)

Discussion

The first paper in this series showed NaDA is a highly efficacious Brønsted base when compared with LDA. Our seemingly trivial but potentially consequential contribution at the outset was to show that NaDA is soluble and stable in DMEA and related minimally hindered trialkylamines. We previously asserted that simple trialkylamines have been largely overlooked as ligands for lithium salts, an oversight we attribute to the unfortunate urge to use them in concert with—rather than to the exclusion of—strongly coordinating ethereal ligands.[38]

The structural studies described in this second paper lay foundations for subsequent studies that will dovetail synthetic organic applications with mechanistic investigations. We must suppress the almost irresistible urge to rely on analogy to lithium amides. Parallel behaviors exist, but such analogies are imperfect and demand, at a minimum, experimental support.

Structures. A survey of NaDA reveals cyclic dimers in solutions containing a number of standard coordinating ligands, analogous to the dominance of LDA dimers (Scheme 2.3).[21] Even the smallest trialkylamines are so sterically demanding as to afford disolvated dimers of NaDA (**1a**–**1c**) akin to those of LDA. Compared with lithium, however, the larger sodium can

accommodate more ligands. LDA dimer, for example, *never* exceeds one solvent per lithium in the solid[39] or solution state[21] (see **19**) and is trisolvated endothermically by THF in silico.[40] Even bifunctional ligands such as DME and TMEDA remain unchelated on the LDA dimer (**20**).[21] By contrast, NaDA in THF forms tetrasolvated dimer **1d**, and both DME and TMEDA readily chelate dimeric NaDA (**1e** and **1f**).[6b] All substitute DMEA exothermically (see eqs 6 and 7).

Scheme 2.3. Comparison of NaDA and LDA Structures.

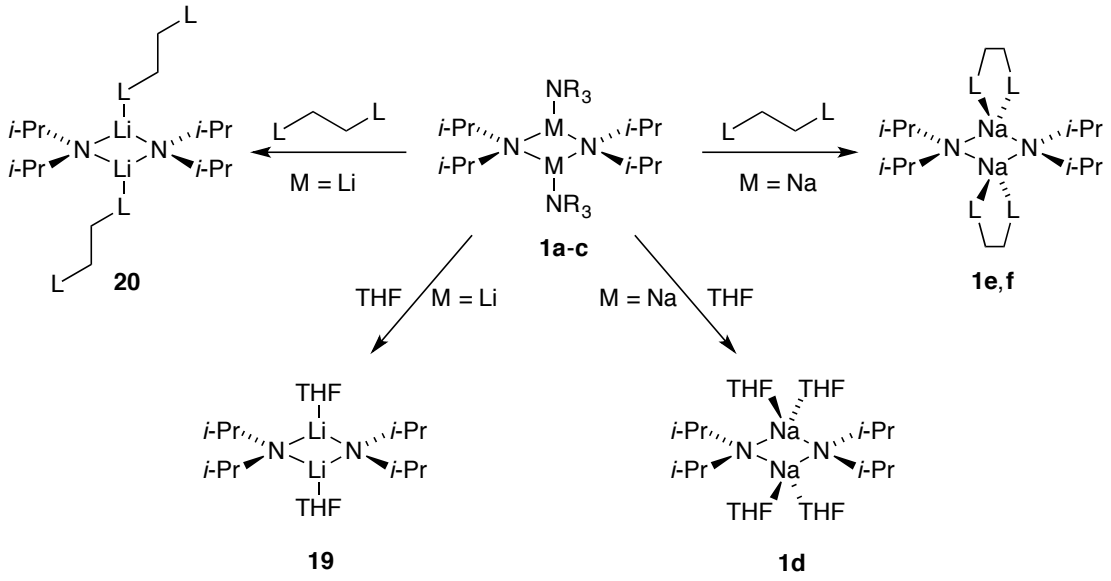

Comments on Methods. We use a combination of tactics to understand structure–reactivity relationships and develop new strategies whenever possible. MCV as a method to study aggregation, for example, has its origins in early work from several laboratories[11] and has been of enormous importance to us for studying aggregation in systems in which M–X coupling is not observable.[8,9] To this end, our expansion of the method to include ^{13}C and ^{15}N as observable nuclei is new and noteworthy.

We also explored DOSY as a means to ascertain the structure of NaDA using functional molecular weights as a proxy. DOSY is increasingly popular,[15,16,17] and our results could be considered supportive. That said, however, we remain cautious owing to significant (up to 25 %) temperature-dependent changes in measured molecular weights that do not appear to derive from changes in structure.

Solvent Decomposition. We investigated the decomposition of THF and DME to understand the limitations of standard ethereal solvents as ligands for NaDA (Table 2) and get a first peek at the mechanism of NaDA-mediated metalations. THF decomposition occurred via tetrasolvated-monomer-based a-elimination (**11**). Although isotope effects show rate-limiting cleavage of the C-H(D) bonds at the β position (Scheme 2.2), unambiguous differentiation of a carbene-derived a-elimination (**11**-α) rather an E2-like β-metalation (**11**-β) was elusive owing to isotopic scrambling. From a synthetic organic (applications) perspective, the high solvent order shows that decomposition can be suppressed by using low ethereal ligand concentrations. Analogous rate suppression allows LDA/THF/hydrocarbon solutions to be sold commercially.

Facile decomposition of DME (eq 2.12) proceeded via a disolvated-monomer-based transition structure. Both **16** and **17** are computationally viable, with **16** energetically preferred. The suppression of decomposition at low DME concentrations is especially crucial if DME is to find a niche given its lability and relatively high cost (see Table 2).

Thoughts on Solubilities. One might argue that our interest in the solubilities of NaDA in trialkylamines is excessive, but applications of NaDA–R_3N mixtures are predicated on the fact that high-molarity stock solutions are easily prepared, handled, and stored. Sodiated intermediates must also be soluble to be of value to synthetic chemists. There is, however, a previously undisclosed and subtle motivation for confirming NaDA solubility: ongoing rate

studies of NaDA-mediated metalations in trialkylamines display odd rate behaviors that we cannot reconcile easily. Such discussions are beyond the scope of this paper but add to our obsession.

The solubility studies underscored some basic principles of alkali metal salt solubilities that, although not unprecedented, warrant further discussion. NaDA is highly soluble in DMEA and DMEA–hexane yet poorly soluble in triethylamine and TMEDA–hexane at low temperatures: why? This question is nuanced and is summarized in eq 2.18.

$$(A_\infty)_{solid} + nS \underbrace{\overset{K_{solv}(1)}{\rightleftharpoons}}_{\text{primary shell}} (A_2S_n)_{solution} \underbrace{\overset{1/K_{solv}(2)}{\rightleftharpoons}}_{\text{secondary shell}} (A_2S_n)_{solid} \qquad (2.18)$$

Dissolving unsolvated solid NaDA, denoted as $(A_\infty)_{solid}$, to form solubilized disolvated dimer stems largely from the enthalpy of primary shell solvation:[41,42] the ligand must bind strongly enough to overcome the enthalpy of lattice deaggregation. The fact that the solubility of NaDA in trialkylamines is nearly temperature-independent shows that the two large enthalpic contributions cancel. The overall high solubility shows that $(A_2S_n)_{solution}$ is favorable relative $(A_2S_n)_{solid}$ and $(A_\infty)_{solid}$. Triethylamine, on the other hand, does not bind well; the poor solubility of NaDA correlates with a small binding constant, $K_{solv}(1)$, rather than an inherent insolubility of A_2S_n reflected in $K_{solv}(2)$. The failure of primary shell solvation causes the insolubility of NaDA in triethylamine.

By contrast, TMEDA binds strongly: $K_{solv}(1)$ is large. However, doubly chelated dimer **1e** (A_2S_n in eq 2.13) has limited solubility at low temperature. Therefore, to the extent that A_2S_n (and almost every organic molecule) is more soluble at high temperature, the solubilization of

$(A_2S_n)_{solid}$ dimer is entropy-dominated.[43] The failure of secondary shell solvation causes the insolubility of NaDA in TMEDA–hexane.

Synthetic Implications. In our first contribution,[7] we emphasized the merits of NaDA–DMEA for metalations owing to its ease of handling and resistance to base-mediated solvent decomposition.[30,31] However, the substitutional lability of trialkylamines is also synthetically important. In forthcoming papers, we will explore the effects of ethereal ligand additions to NaDA–DMEA mixtures. Ongoing studies show that THF elicits large accelerations relative to that of NaDA–DMEA while the metalation rate far exceeds the THF decomposition rate. The short half-life of NaDA in ethereal stock solutions by no means precludes their use as additives. Mono- and difunctional ethers readily displace coordinated DMEA in NaDA–DMEA stock solutions. Moreover, when robust trialkylamines are required to force a recalcitrant metalation, the resulting salts—arylsodiums, for example—can be treated with ethereal ligands after the metalation to modulate their reactivities. Again, the ligand substitution will be highly favorable.

Hemilabile Trifunctional Ligands. Trifunctional PMDTA and diglyme afford dimeric NaDA bound only as bidentate ligands (**1g** and **1h**). This outcome segues to a topic of long-standing interest: hemilabile ligands.[44] In contrast to transition metal chemists attempting to build weakly chelating di- and polyfunctional ligands that readily liberate coordination sites,[45] we approach hemilability by identifying ligands that chelate selectively in the transition state to optimize accelerations.[44] Imagine, for example, transformations in which fleeting intermediates bearing a trifunctional ligand (eq 2.19) are markedly accelerated by transition-state stabilization that is *not* offset by ground-state stabilization. The reader might also realize that we have evidence to support this notion.

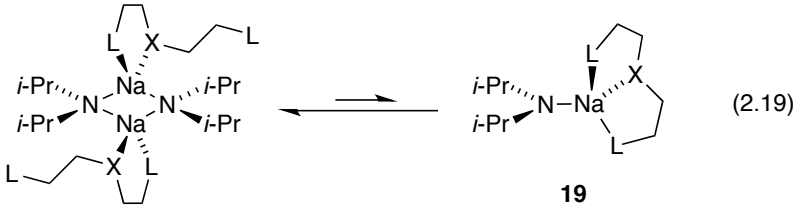

(2.19)

19

1g; L = NMe_2, X = NMe
1h; L = OMe, X = O

Conclusions

We are enthusiastic about the promise of NaDA–DMEA mixtures to solve metalation problems that plague synthetic chemists. NaDA is both convenient and demonstrably effective. It can be prepared in minutes using standard glassware and stored for months with refrigeration as 1.0 M DMEA solutions. Metalation rates are typically orders of magnitude higher than those for LDA–THF.[7] The obvious limitations include the higher costs and unpleasant odors of trialkylamines, but neither precludes application to difficult metalations. Another point that should not be overlooked is that DMEA is substitutionally labile. Stronger ligands, even potentially expensive ligands, can be added *before* the metalation to accelerate it—they do—or *after* the metalation to modulate the reactivity of the resulting sodiated intermediate. Furthermore, quite unlike LDA, NaDA shows little tendency to form mixed aggregates.[21] We are encouraged by the well-defined aggregation and solvation states described herein that are required to unravel the mechanistic details of NaDA-mediated metalations and correlate them with selectivities.

Experimental

Reagents and solvents. THF, DME, diethyl ether, TMEDA, PMDTA, diglyme, hexane, and all trialkylamines were distilled from blue or purple solutions containing sodium benzophenone ketyl. [^{15}N]diisopropylamine,[46] [^{15}N]dicyclohexylamine,[47] and [^{15}N]isopropylcyclohexylamine[48] have been described previously. NaDA was prepared from diisopropylamine, isoprene, DMEA, and sodium dispersion using a modified[7] procedure first reported by Wakefield.[5b] A precautionary crystallization was used for the work described herein. Solutions of NaDA were titrated using a literature method.[49] NaICA was prepared with an optimized dissolving-metal-based preparation analogous to that used to prepare NaDA.[7, 9a]

NaDCA. NaDCA is more conveniently prepared using *n*-butylsodium[50] rather than sodium dispersion because of its lower solubility. To a dry 15 mL pear flask charged with *n*-butylsodium (33.0 mg, 0.413 mmol) was added DMEA (3.3 mL) at room temperature. On complete dissolution of the *n*-butylsodium, neat dicyclohexylamine (66.0 μL, 0.33 mmol) was added to provide a stock solution. ^{13}C NMR spectrum (125.72 MHz, DMEA) δ 61.9, 41.6, 27.3, 26.7; ^{15}N NMR spectrum (50.66 MHz, DMEA) 86.9.

NMR Spectroscopic Analyses. NMR samples for reaction monitoring were routinely prepared using stock solutions of NaDA and sealed under partial vacuum. DMEA-free solutions of NaDA with added ligands used DMEA-free crystallized NaDA. Samples were routinely flame-sealed except when used in experiments involving serial titration with a coordinating ligand. Standard ^{1}H, ^{13}C, and ^{15}N spectra were recorded on a 500 MHz spectrometer at 500, 125.79, and 50.66 MHz, respectively. The ^{13}C, and ^{15}N resonances were referenced to the CH_2O resonance of THF at –90 °C (67.57 ppm), and neat Me_2NEt at –90 °C (25.7 ppm), respectively.

Chapter 2 References and Footnotes

1. Mulvey, R. E.; Robertson, S. D. *Angew. Chem.* **2013**, *52*, 11470.

2. Schlosser, M. In *Organometallics in Synthesis : A Manual*. Schlosser, M., Ed.; Wiley: New York, 2002; Chapter 1.

3. (a) Bakker, W. I. I.; Wong, P. L.; Snieckus, V. Lithium Diisopropylamide. In *e-EROS*; Paquette, L. A., Ed.; Wiley: New York, 2001. (b) Clayden, J. *Organolithiums: Selectivity for Synthesis*; Baldwin, J. E., Williams, R. M., Eds.; Pergamon Press: New York, 2002. (c) Hartung, C. G.; Snieckus, V. In Modern Arene Chemistry; Astruc, D. Ed.; Wiley- VCH, Weinheim, 2002; Chapter 10. (d) Collum, D. B.; McNeil, A. J.; Ramírez, A. *Angew. Chem., Int. Ed.* **2007**, *46*, 3002.

4. Raynolds, S.; Levine, R. *J. Am. Chem. Soc.* **1959**, *82*, 472.

5. (a) Lochmann, L.; Trekoval, J. *J. Organomet. Chem.* **1979**, *179*, 123. (b) Barr, D.; Dawson, A. J.; Wakefield, B. J. *J. Chem. Soc., Chem. Commun.* **1992**, 204. (c) Lochmann, L.; Janata, M. *Cent. Eur. J. Chem.* **2014**, *12*, 537.

6. (a) Munguia, T.; Bakir, Z. A.; Cervantes-Lee, F.; Metta-Magana, A.; Pannell, K. H. *Organometallics* **2009**, *28*, 5777. (b) Andrews, P. C.; Barnett, N. D. R.; Mulvey, R. E.; Clegg, W.; O'Neil, P. A.; Barr, D.; Cowton, L.; Dawson, A. J.; Wakefield, B. J. *J. Organomet. Chem.*

1996, *518*, 85. (c) Boeckman, R. K.; Boehmler, D. J.; Musselman, R. A. *Org. Lett.* **2001**, *3*, 3777. (d) LaMontagne, M. P.; Ao, M. S.; Markovac, A.; Menke, J. R. *J. Med. Chem.* **1976**, *19*, 363. (e) Bond, J. L.; Krottinger, D.; Schumacher, R. M.; Sund, E. H.; Weaver, T. J. *J. Chem. Eng. Data* **1973**, *18*, 349. (f) Levine, R.; Raynolds, S. *J. Org. Chem.* **1960**, *25*, 530. (g) Mamane, V.; Louërat, F.; Iehl, J.; Abboud, M.; Fort, Y. *Tetrahedron*. **2008**, *64*, 10699. (h) Baum, B. M.; Levine, R. *J. Heterocyclic Chem*. **1966**, *3*, 272. (i) Tsuruta, T. *Makromol. Chem*. **1985**, *13*, 33.

7. Ma, Y.; Algera, R. F.; Collum, D. B. *J. Org. Chem.* **2016**, *81*, 11312.

8. (a) Renny, J. S.; Tomasevich, L. L.; Tallmadge, E. H.; Collum, D. B. *Angew. Chem., Int. Ed.* **2013**, *52*, 11998. (b) Weingarten, H.; Van Wazer, J. R. *J. Am. Chem. Soc.* **1965**, *87*, 724. (c) Goralski, P.; Legoff, D.; Chabanel, M. *J. Organomet. Chem.* **1993**, *456*, 1. (d) Goralski, P.; Chabanel, M. *Inorg. Chem.* **1987**, *26*, 2169.

9. (a) Tomasevich, L. L.; Collum, D. B. *J. Am. Chem. Soc.* **2014**, *136*, 9710. (b) Liou, L. R.; McNeil, A. J.; Ramírez, A.; Toombes, G. E. S.; Gruver, J. M.; Collum, D. B. *J. Am. Chem. Soc.* **2008**, *130*, 4859.

10. Bartoň, J.; Kašpar, M.; Růžička, V. *Collect. Czech. Chem. Commun.* **1982**, *47*, 594.

11. Kissling, R. M.; Gagne, M. R. *J. Org. Chem.* **2001**, *66*, 9005.

12. (a) Frisch, M. J.; et al. Gaussian 09, Revision A.02; Gaussian, Inc.: Wallingford, CT, 2009. (b) "Perspectives on Computational Organic Chemistry". Streitwieser, A. *J. Org. Chem.* **2009** *74*, 4433.

13. For a particularly incisive comparison of methods for calculating alkali metal solvation using both explicit and continuum models of solvation (including lithium and sodium solvated by THF and DME), see: Ziegler, M. J.; Madura, J. D. *J. Solution Chem*. **2011**, *40*, 1383.

14. Measuring the mole fraction within only the ensemble of interest rather than the overall mole fraction of NaDA added to the samples eliminates the distorting effects of impurities.

15. (a) Li, D.; Keresztes, I.; Hopson, R.; Williard, P. G. *Acc. Chem. Res.* **2009**, *42*, 270. (b) Kagan, G.; Li, L.; Hopson, R.; Williard, P. G. *Org. Lett.* **2010**, *12*, 520. (c) Su, S.; Hopson, R.; Williard, P. G. *J. Org. Chem.* **2013**, *78*, 11733. (d) Guang, J.; Hopson, R.; Williard, P. G. *J. Org. Chem.* **2015**, *80*, 9102. (e) Guang, J.; Liu, Q. P.; Hopson, R.; Williard, P. G. *J. Am. Chem. Soc.* **2015**, *137*, 7347. (f) Su, G.; Guang, J.; Li, W.; Wu, K.; Hopson, R.; Williard, P. G. *J. Am. Chem. Soc.* **2014**, *136*, 11735.

16. (a) Armstrong, D. R.; Harris, C. M. M.; Kennedy, A. R.; Liggat, J. J.; McLellan, R.; Mulvey, R. E.; Urquhart, M. D. T.; Robertson, S. D.
Chem.–Euro. J. **2015**, *21*, 14410. (b) Neufeld, R.; John, M.; Stalke, D. *Angew. Chem., Int. Ed.* **2015**, *54*, 6994. (c) Hamdoun, G.; Sebban, M.; Cossoul, E.; Harrison-Marchand, A.; Maddaluno, J.; Oulyadi, H. *Chem. Commun.* **2014**, *50*, 4073. (d) Armstrong, D. R.; Garden, J. A.; Kennedy,

A. R.; Leenhouts, S. M.; Mulvey, R. E.; O'Keefe, P.; O'Hara, C. T.; Steven, A. *Chem.–Euro. J.* **2013**, *19*, 13492. (e) Lecachey, B.; Duguet, N.; Oulyadi, H.; Fressigne, C.; Harrison-Marchand, A.; Yamamoto, Y.; Tomioka, K.; Maddaluno, J. *Org. Lett.* **2009**, *11*, 1907.

17. DOSY has been used to study sodium 2,2,6,6-tetramethylpiperidide: Armstrong, R.; Garcia-Alvarez, P.; Kennedy, A. R.; Mulvey, R. E.; Robertson, S. D. *Chem. Eur. J.* **2011**, *17*, 6725.

18. (a) Bloor, E. G.; Kidd R. G. *Can. J. Chem.* **1968**, *46*, 3425. (b) Erlich, R. H.; Popov, A. I. *J. Am. Chem. Soc*. **1971**, *93*, 5620. (c) Arnett, E. M.; Ko, H. C.; Minasz, R. J. *J. Phys. Chem.* **1972**, *76*, 2474. (d) Herlem, M.; Popov, A. I. *J. Am. Chem. Soc.* **1972**, *94*, 1431. (e) Kintzinger, J. P.; Lehn, J. M. *J. Am. Chem. Soc.* **1974**, *96*, 3313. (f) Van Geet, A. L. *J. Am. Chem. Soc.* **1972**, *94*, 5583. (g) Templeman, G. J.; Van Geet A. L. *J. Am. Chem. Soc.* **1972**, *94*, 5578.

19. (a) Cheema, Z. W.; Gibson, G. W.; Eastham, J. F. *J. Am. Chem. Soc.* **1963**, *85*, 3517. (b) Eastham, J. F.; Gibson, G. W. *J. Am. Chem. Soc.* **1963**, *85*, 2171. (c) Settle, F. A.; Haggerty, M.; Eastham, J. F. *J. Am. Chem. Soc.* **1964**, *86*, 2076. (d) Waack, R. Doran, M. A.; Stevenson, P. E. *J. Am. Chem. Soc.* **1966**, *88*, 2109. (e) Bartlett, P. D.; Goebel, C. V.; Weber, W. P. *J. Am. Chem. Soc.* **1969**, *91*, 7425. (f) Lewis, H. L.; Brown, T. L. *J. Am. Chem. Soc.* **1970**, *92*, 4664. (g) Popov, A. I. *Pure Appl. Chem.* **1975**, *41*, 275. (h) Sergutin, V. M.; Zgonnik, V. N.; Kalninsh, K. K. *J. Organomet. Chem.* **1979**, *170*, 151. (i) Kminek, I.; Kaspar, M.; Trekoval, J. *Coll. Czech. Chem. Commun.* **1981**, 1132. (j) Sunner, J.; Kebarle, P. *J. Am. Chem. Soc.* **1984**, *106*, 6135. (k) Wanat, R. A.; Collum, D. B.; Van Duyne, G.; Clardy, J.; DePue, R. T. *J. Am. Chem. Soc.* **1986**, *108*, 3415. (l) Kallman, N.; Collum, D. B. *J. Am. Chem. Soc.* **1987**, *109*, 7466.

20. The value of *n* is preset to give an analytically solvable form to which the data can be fitted explicitly.

21. Collum, D. B. *Acc. Chem. Res.* **1993**, *26*, 227.

22. Monodentate TMEDAs on lithium are common. For recent examples, see: (a) Jin, K. J.; Collum, D. B. *J. Am. Chem. Soc.* **2015**, *137*, 14446. (b) Zhang, S.; Zhan, M.; Zhang, W.-X.; Xi, Z. *Organometallics* **2013**, *32*, 4020. (c) Aharonovich, S.; Botoshanski, M.; Rabinovich, Z.; Waymouth, R. M.; Eisen, M. S. *Inorg. Chem.* **2010**, *49*, 1220. (d) Andrews, P. C.; Koutsaplis, M.; Robertson, E. G. *Organometallics* **2009**, *28*, 1697. (e) Clegg, W.; Graham, D. V.; Herd, E.; Hevia, E.; Kennedy, A. R.; McCall, M. D.; Russo, L. *Inorg. Chem.* **2009**, *48*, 5320.

23. Sodium coordinated by an h^1-TMEDA: Kennedy, A. R.; Mulvey, R. E.; O'Hara, C. T.; Robertson, S. D.; Robertson, G. M. *Acta Crystallogr., Sect. E: Struct. Rep. Online* **2012**, *68*, m1468.

24. Monodentate DMEs on lithium are common. For recent examples, see: (a) Majumdar, M.; Omlor, I.; Yildiz, B.; Azizoglu, A.; Huch, V.; Scheschkewitz, D. *Angew. Chem., Int. Ed.* **2015**, *54*, 8746. (b) Schowtka, B.; Gorls, H.; Westerhausen, M. *Z. Anorg. Allg. Chem.* **2014**, *640*, 907. (c) Seo, D. M.; Boyle, P. D.; Allen, J. L.; Han, S.-D.; Jonsson, E.; Johansson, P.; Henderson, W. A. *J. Phys. Chem. C* **2014**, *118*, 18337. (d) Ren, W.; Deng, X.; Zi, G.; Fang, D.-C. *J. Chem. Soc., Dalton Trans.* **2011**, *40*, 9662. (e) Beck, J. F.; Neshat, A.; Schmidt, J. A. R. *Eur. J. Inorg. Chem.*

2010, 5146. (f) Lewis, R. A.; Wu, G.; Hayton, T. W. *J. Am. Chem. Soc.* **2010**, *132*, 12814. (g) Volpe, E. C.; Manke, D. R.; Bartholomew, E. R.; Wolczanski, P. T.; Lobkovsky, E. B. *Organometallics* **2010**, *29*, 6642.

25. Sodium coordinated by an h^1-DME: Gallo, E.; Solari, E.; Floriani, C.; Chiesi-Villa, A.; Rizzoli, C. *Inorg. Chem.* **1997**, *36*, 2178.

26. (a) Ali, A.; Langer, M.; Lorenz, V.; Hrib, C. G.; Hilfert, L.; Edelmann, F. T. *J. Organomet. Chem.* **2015**, *776*, 163. (b) Al-Harbi, A.; Rong, Y.; Parkin, G. *Inorg. Chem.* **2013**, *52*, 10226. (c) Neander, S.; Kornich, J.; Olbrich, F. *J. Organomet. Chem.* **2002**, *656*, 89. (d) Bock, H.; Gharagozloo-Hubmann, K.; Holl, S.; Sievert, M. *Z. Naturforsch., B: Chem. Sci.* **2000**, *55*, 1163. (e) Bock, H.; Arad, C.; Nather, C. *J. Organomet. Chem.* **1996**, *520*, 1. (f) Bock, H.; Arad, C.; Nather, C.; Gobel, I.; John, A. *Z. Naturforsch., B: Chem. Sci.* **1996**, *51*, 1391. (g) Bock, H.; Arad, C.; Nather, C.; Gobel, I. *Helv. Chim. Acta* **1996**, *79*, 92. (h) Gallo, E.; Solari, E.; De Angelis, S.; Floriani, C.; Re, N.; Chiesi-Villa, A.; Rizzoli, C. *J. Am. Chem. Soc.* **1993**, *115*, 9850. (i) Mulvey, R. E.; Clegg, W.; Barr, D.; Snaith, R. *Polyhedron* **1986**, *5*, 2109.

27. There are approximately a dozen instances in which PMDTA binds as a bidentate rather than the highly preferred tridentate motif:
Armstrong, D. R.; Brouillet, E. V.; Kennedy, A. R.; Garden, J. A.; Granitzka, M.; Mulvey, R. E.; Trivett, J. J. *J. Chem. Soc., Dalton Trans.* **2014**, *43*, 14409.

28. (a) Titration of a NaDA suspension with *trans-N,N,N',N'*-tetramethylcyclohexanediamine (TMCDA) shows a linear dependence of the titer on TMCDA with a hard solubility endpoint at a 2:1 stoichiometry, which contrasts with the 1:1 proportions for TMEDA (supporting information). MCV did not reveal spectral distortions consistent with heteroaggregation when paired with NaICA, which implicated a doubly chelated monomer.[28b] However, preliminary rate data on a metalation (unpublished) suggested a fractional-order dependence on NaDA, which argues for a requiste dimer deaggregation. h^2-TMCDA on sodium: (b) TMCDA-solvated LDA in hydrocarbons is monomeric: Remenar, J. F.; Lucht, B. L.; Collum, D. B. *J. Am. Chem. Soc.* **1997**, *119*, 5567. (c) Ojeda-Amador, A. I.; Martinez-Martinez, A. J.; Kennedy, A. R.; Armstrong, D. R.; O'Hara, C. T. *Chem. Commun.* **2017**, *53*, 324. (d) Garcia-Alvarez, P.; Kennedy, A. R.; O'Hara, C. T.; Reilly, K.; Robertson, G. M. *J. Chem. Soc., Dalton Trans.* **2011**, *40*, 5332.

29. (a) Mukhopadhyay, T.; Seebach, D. *Helv. Chim. Acta* **1982**, *65*, 385. (b) Sun, X.; Collum, D. B. *J. Am. Chem. Soc.* **2000**, *122*, 2459.

30. (a) Melchior, M. T.; Klemann, L. P.; Whitney, T. A.; Langer, A. W., Jr. *Am. Chem. Soc., Polym. Preprints* **1972**, *13*, 649. (b) Koehler, F. H.; Hertkorn, N.; Bluemel, J. *Chem. Ber.* **1987**, *120*, 2081. (c) Bates, R. B.; Kroposki, L. M.; Potter, D. E. *J. Org. Chem.* **1970**, *37*, 560. Stanetty, P.; Koller, H.; Mihovilovic, M. *J. Org. Chem.* **1992**, *57*, 6833. (d) Melchior, M. T.; Klemann, L. P.; Whitney, T. A.; Langer, A. W., Jr. *Am. Chem. Soc., Polym. Preprints* **1972**, *13*, 649. (e) Koehler, F. H.; Hertkorn, N.; Bluemel, J. *Chem. Ber.* **1987**, *120*, 2081. (f) Kopka, I. E.; Fataftah, Z. A.; Rathke, M. W. *J. Org. Chem.* **1987**, *52*, 448.

31. Studies of base-mediated solvent decomposition: (a) Holm, T. *Acta Chem. Scand.* **1978**, *32B*, 162. (b) Bates, T. F.; Clarke, M. T.; Thomas, R. D. *J. Am. Chem. Soc.* **1988**, *110*, 5109. (c) Raposo, M. L.; Fernández-Nieto, F.; Garcia-Rio, L.; Rodríguez-Dafonte, P.; Paleo, M. R.; Sardina, F. J. *Chem. Eur. J*. **2013**, *19*, 9677. (d) Corset, J.; Castellà-Ventura, M.; Froment, F.; Strzalko, T.; Wartski, L. *J. Raman Spectrosc*. **2002**, *33*, 652.

32. We occasionally turn to a method based on a nonlinear least-squares fit to the non-linear variant[32a] of the Noyes equation:[32b]

$$[\text{substrate}] = \{(n-1)k_{\text{obsd}}t + [\text{substrate}]_0^{(1-n)}\}^{1/(1-n)}$$

The adjustable parameter *n* corresponds to the reaction order in the decaying substrate. (a) Briggs, T. F.; Winemiller, M. D.; Collum, D. B.; Parsons, R. L., Jr.; Davulcu, A. K.; Harris, G. D.; Fortunak, J. D.; Confalone, P. N. *J. Am. Chem. Soc.* **2004**, *126*, 5427. (b) Noyes, A. A. *Am. Chem. J.* **1897**, *19*, 766.

33. We define the idealized rate law as that obtained by rounding the observed reaction orders to the nearest rational order.

34. The rate law provides the stoichiometry of the transition structure relative to that of the reactants: Edwards, J. O.; Greene, E. F.; Ross, J. *J. Chem. Educ.* **1968**, *45*, 381.

35. Leading references to oxacarbenoids: (a) Boche, G; Lohrenz, J. C. W. *Chem Rev.* **2001**, *101*, 697. Boche, G.; Bosold, F.; Lohrenz, J. C. W.; Opel, A.; Zulauf, P. *Chem. Ber.* **1993**, *126*, 1873. Baumgartner, T.; Gudat, D.; Nieger, M.; Niecke, E.; Schiffer, T. J. *J. Am. Chem. Soc.* **1999**, *121*, 5953.

36. (a) Bissell, E. R.; Finger, M. *J. Org. Chem.* **1959**, *24*, 1259. (b) Yang, Y. K.; Bergman, R. G. *Organometallics* **1985**, *4*, 129.

37. There are an enormous number of documented $^{+}Na(THF)_6$ and $^{+}Na(h^2\text{-}DME)_3$ gegenions. For an example of both see: Livingstone, Z.; Hernan-Gomez, A.; Baillie, S. E.; Armstrong, D. R.; Carrella, L. M.; Clegg, W.; Harrington, R. W.; Kennedy, A. R.; Rentschler, E.; Hevia, E. *J. Chem. Soc., Dalton Trans.* **2016**, *45*, 6175.

38. For an example and extensive leading references to applications of simple (monofunctional) trialkylamines in organolithium chemistry, see: Godenschwager, P.; Collum, D. B. *J. Am. Chem. Soc.* **2008**, *130*, 8726.

39. Williard, P. G.; Salvino, J. M. *J. Org. Chem.* **1993**, *58*, 1.

40. Hoepker, A. C.; Collum, D. B. *J. Org. Chem.* **2011**, *76*, 7985.

41. Manifestation of a steric effect as an entropic contribution has been referred to as "population control".[42a] Previous authors have concluded that differences in penchants for ion solvation stem from entropic effects.[42b,c]

42. (a) Winans, R. E.; Wilcox, C. F., Jr. *J. Am. Chem. Soc.* **1976**, *98*, 4281. (b) Lucht, B. L.; Collum, D. B. *J. Am. Chem. Soc.* **1995**, *117*, 9863. (c) Strong, J.; Tuttle, T. R., Jr. *J. Phys. Chem.* **1973**, *77*, 533.

43. It may be instructive for some to note that simple thermochemical expression, $\Delta G = \Delta H - T\Delta S$, seems to bait many into believing that the temperature dependence of an equilibrium (or any ratio of relative rates) is inherently entropic. However, when combined with a second thermochemical cornerstone, $\Delta G = -RT\ln K_{eq}$, we find that $\ln K_{eq} = -\Delta H/RT + \Delta S/R$. We see that the existence and direction of a temperature dependence derives exclusively from the enthalpic term. A species is promoted by lowering the temperature if and only if it is enthalpically preferred.

44. Ramírez, A.; Sun, X.; Collum, D. B. *J. Am. Chem. Soc.* **2006**, *128*, 10326 and references cited therein.

45. (a) Angell, S. E.; Rogers, C. W.; Zhang, Y.; Wolf, M. O.; Jones, W. E. *Coord. Chem. Rev.* **2006**, *250*, 1829. (b) Braunstein, P.; Naud, F. *Angew. Chem., Int. Ed.* **2001**, *40*, 680. (c) Slone, C. S.; Weinberger, D. A.; Mirkin, C. A. *Progr. Inorg. Chem.* **1999**, *48*, 233.

46. Ma, Y.; Hoepker, A. C.; Gupta, L.; Faggin, M. F.; Collum, D. B. *J. Am. Chem. Soc.* **2010**, *132*, 15610.

47. Aubrecht, K. B.; Collum, D. B. *J. Org. Chem.* **1996**, *61*, 8674.

48. Galiano-Roth, A. S.; Michaelides, E. M.; Collum, D. B. *J. Am. Chem. Soc.* **1988**, *110*, 2658.

49. Kofron, W. G.; Baclawski, L. M. *J. Org. Chem.* **1976**, *41*, 1879.

50. Lochmann, L.; Pospisil, J.; Lim, D. *Tetrahedron Lett.* **1966**, *7*, 257.

Chapter 2 Appendix

I. NMR spectroscopic studies

II. Rate studies

I. NMR spectroscopic studies

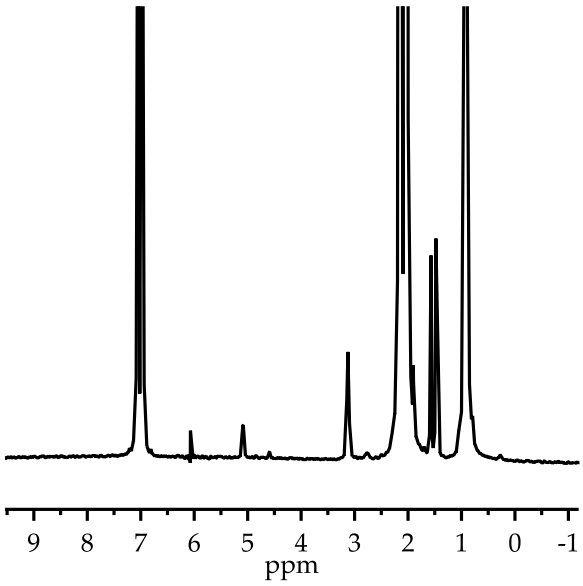

Figure A.2.1. ^{1}H NMR spectrum of 600 uL extract of 0.50 M NaDA in DMEA prepared from 4.0 mL DMEA, 0.50 mL diisopropylamine (1 equiv), 3.0 mL sodium dispersion (30% w/w) in toluene, and 175 uL isoprene (0.50 equiv). Aside from the solvent resonances the only remaining signals are affiliated with 2-methyl-2-butene (δ 5.08, δ 1.57, δ 1.48, δ 1.45) and NaDA (δ 3.12, δ 0.90).

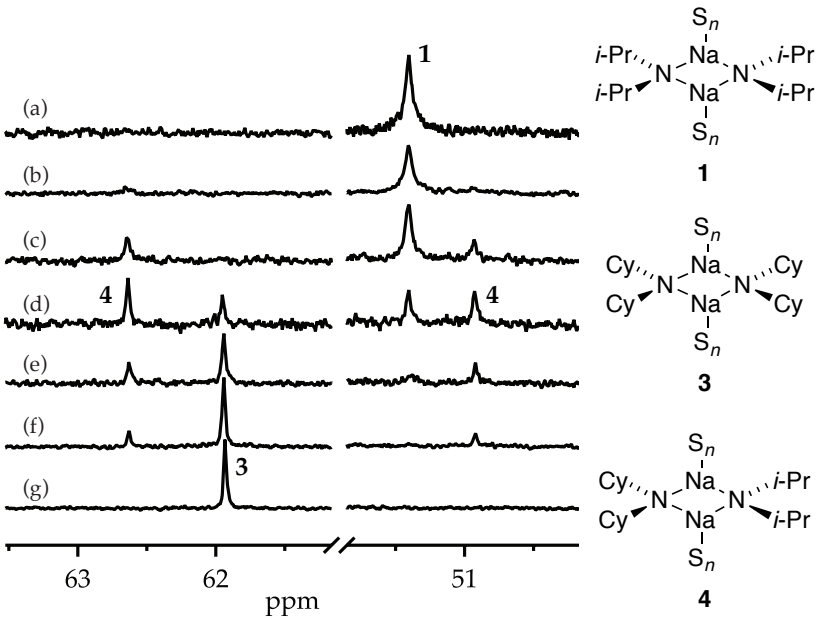

Figure A.2.2.[13]C NMR spectra for 0.20 M solutions of NaDA and NaDCA in DMEA with varying χ_{NaDA} at –80 °C. The measured mole fractions, χ_{NaDA}, in (a)–(g) are 1.00, 0.97, 0.82, 0.56, 0.34, 0.14, and 0.00, respectively.

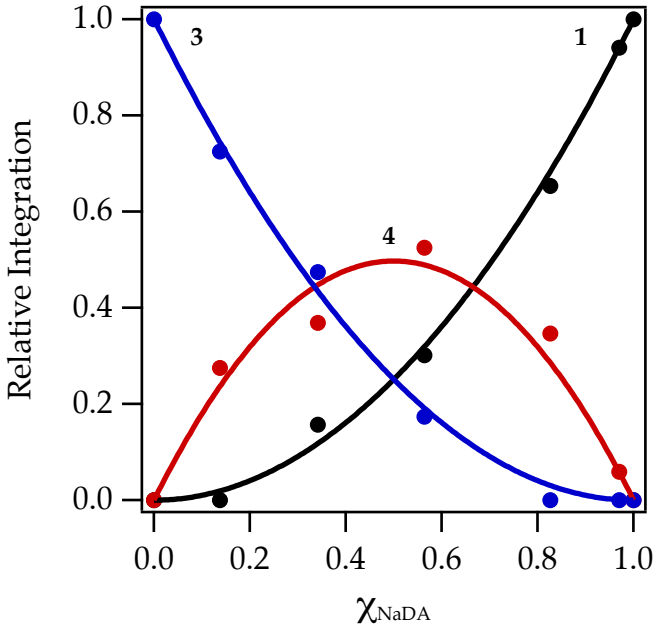

Figure A.2.3.Job plot showing the relative integrations versus the measured mole fraction of NaDA for 0.20 M solutions of NaDA and NaDCA in DMEA with varying χ_{NaDA} at –80 °C. Fitting the data to an aggregating dimer ensemble affords $K_{eq} = 4 \pm 1$.

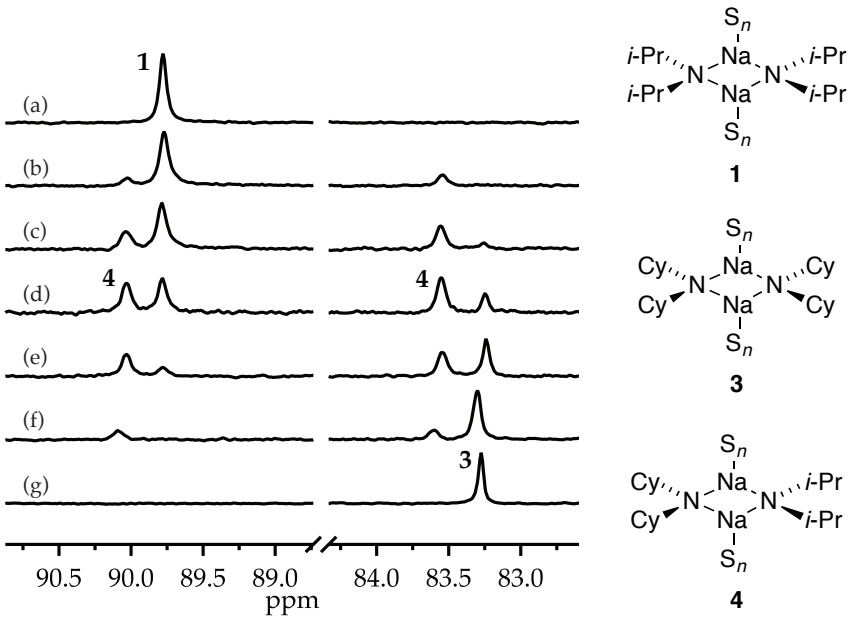

Figure A.2.4.[15]N NMR spectra for 0.10 M solutions of NaDA and NaDCA in DMEA with varying χ_{NaDA} at –100 °C. The measured mole fractions, χ_{NaDA}, in (a)–(g) are 1.00, 0.86, 0.71, 0.58, 0.40, 0.17, and 0.00, respectively.

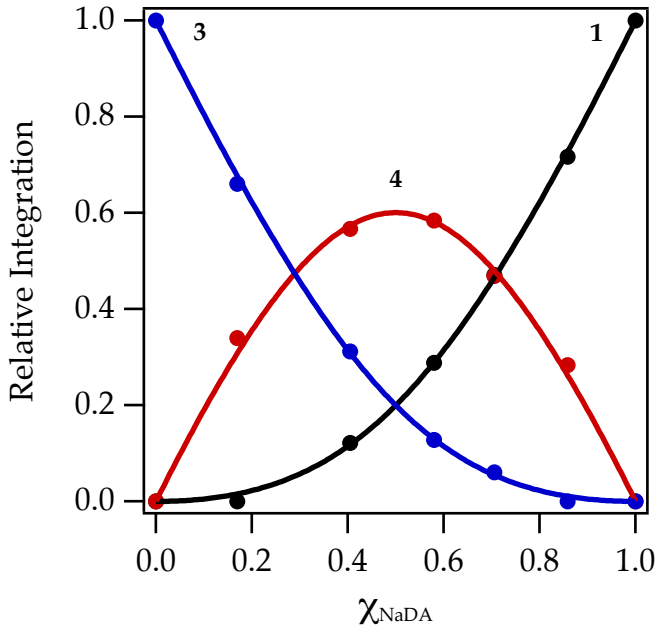

Figure A.2.5.Job plot showing the relative integrations versus the measured mole fraction of NaDA for 0.10 M solutions of NaDA and NaDCA in DMEA with varying χ_{NaDA} at –100 °C. Fitting the data to an aggregating dimer ensemble affords $K_{eq} = 9.0 \pm 0.9$.

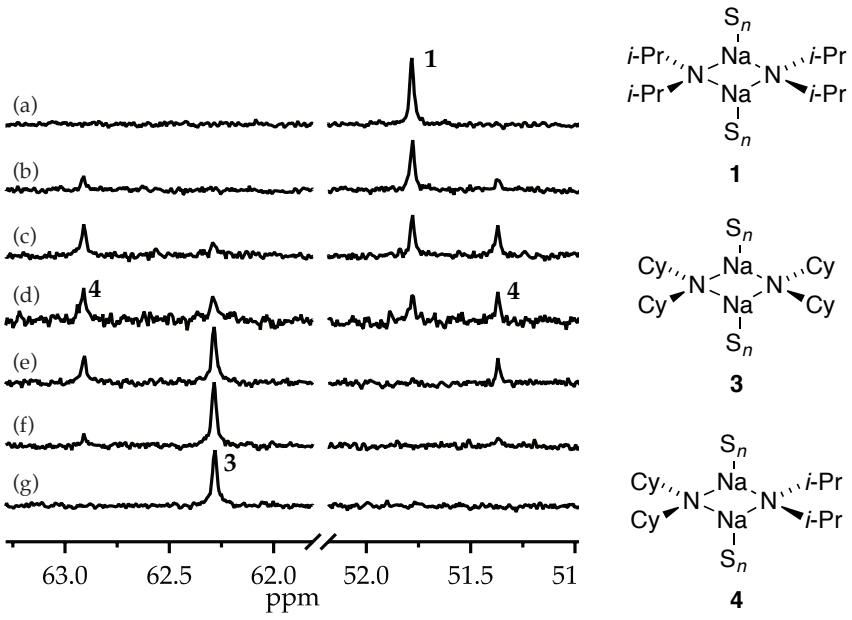

Figure A.2.6. ^{13}C NMR spectra for 0.10 M solutions of NaDA and NaDCA in DMBA with varying χ_{NaDA} at –80 °C. The measured mole fractions, χ_{NaDA}, in (a)–(g) are 1.00, 0.97, 0.82, 0.56, 0.34, 0.14, and 0.00, respectively.

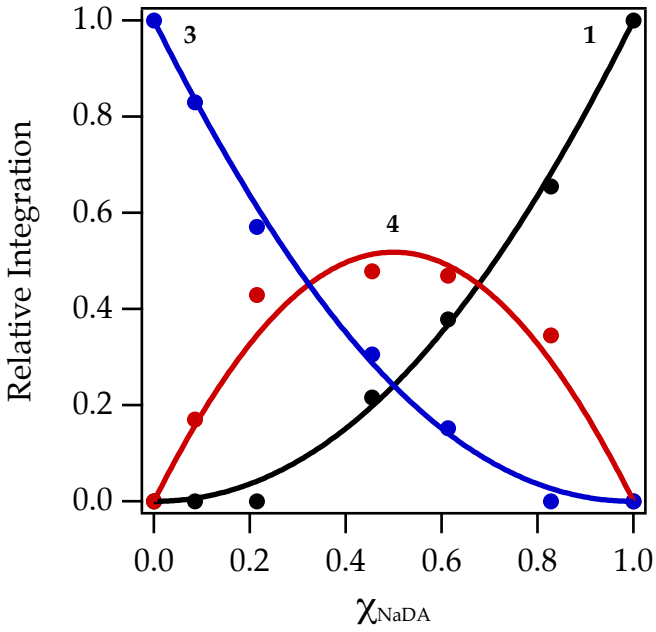

Figure A.2.7.Job plot showing the relative integrations versus the measured mole fraction of NaDA for 0.10 M solutions of NaDA and NaDCA in DMBA with varying χ_{NaDA} at –80 °C. Fitting the data to an aggregating dimer ensemble affords $K_{eq} = 5 \pm 1$.

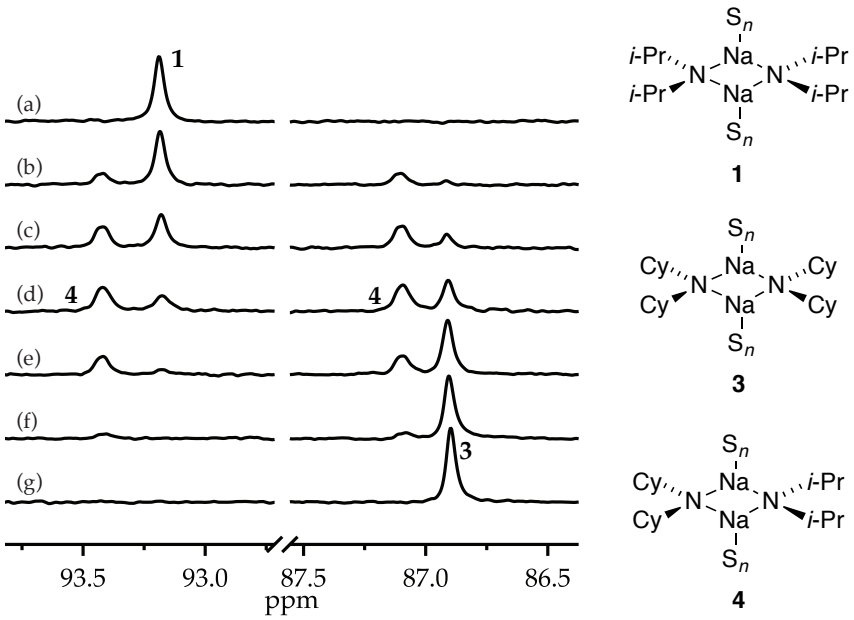

Figure A.2.8.[15]N NMR spectra for 0.10 M solutions of NaDA and NaDCA in DMBA with varying χ_{NaDA} at –80 °C. The measured mole fractions, χ_{NaDA}, in (a)–(g) are 1.00, 0.78, 0.60, 0.47, 0.30, 0.11, and 0.00, respectively.

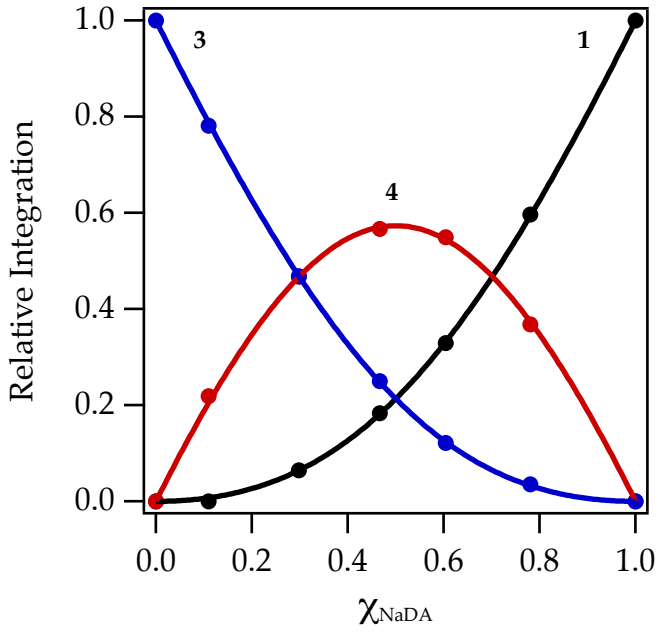

Figure A.2.9.Job plot showing the relative integrations versus the measured mole fraction of NaDA for 0.10 M solutions of NaDA and NaDCA in DMBA with varying χ_{NaDA} at –80 °C. Fitting the data to an aggregating dimer ensemble affords $K_{eq} = 7.2 \pm 0.3$.

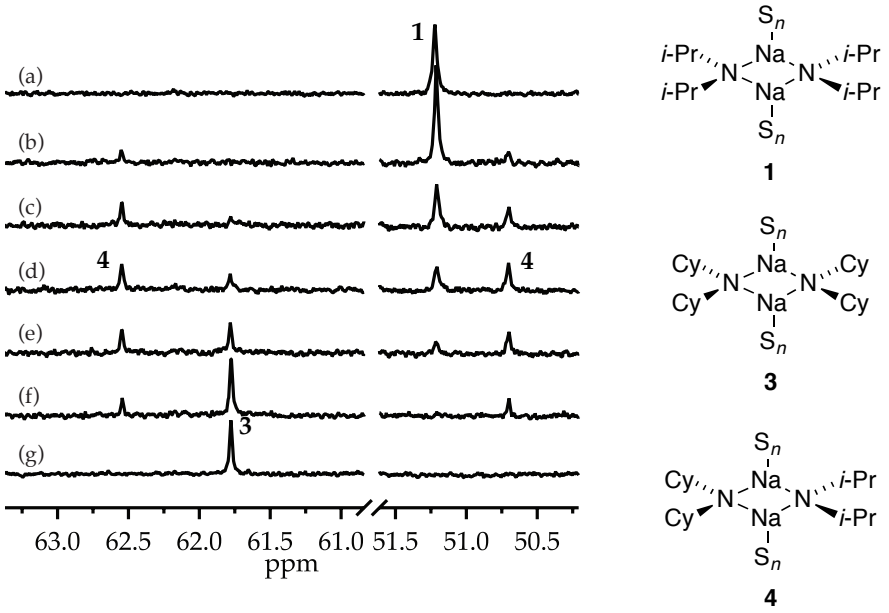

Figure A.2.10.[13]C NMR spectra for 0.10 M solutions of NaDA and NaDCA in *N*-methylpyrrolidine with varying χ_{NaDA} at –80 °C. The measured mole fractions, χ_{NaDA}, in (a)–(g) are 1.00, 0.94, 0.72, 0.59, 0.36, 0.17, and 0.00, respectively.

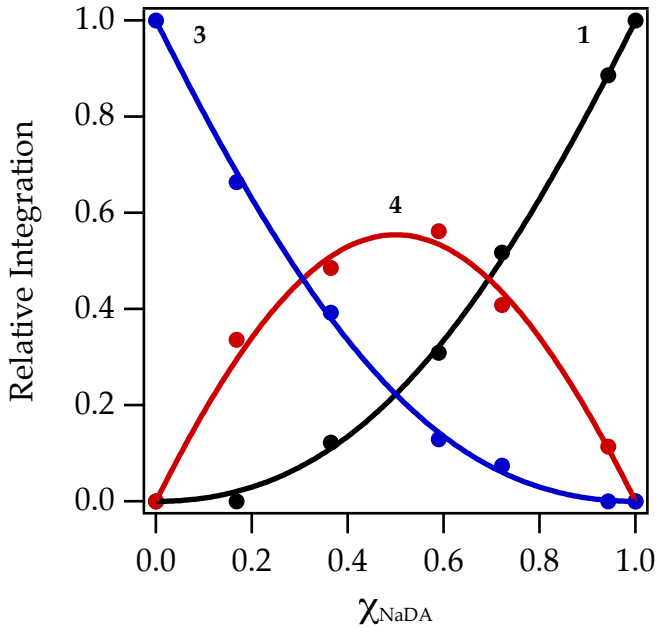

Figure A.2.11.Job plot showing the relative integrations versus the measured mole fraction of NaDA for 0.10 M solutions of NaDA and NaDCA in *N*-methylpyrrolidine with varying χ_{NaDA} at –80 °C. Fitting the data to an aggregating dimer ensemble affords $K_{eq} = 6.2 \pm 0.9$.

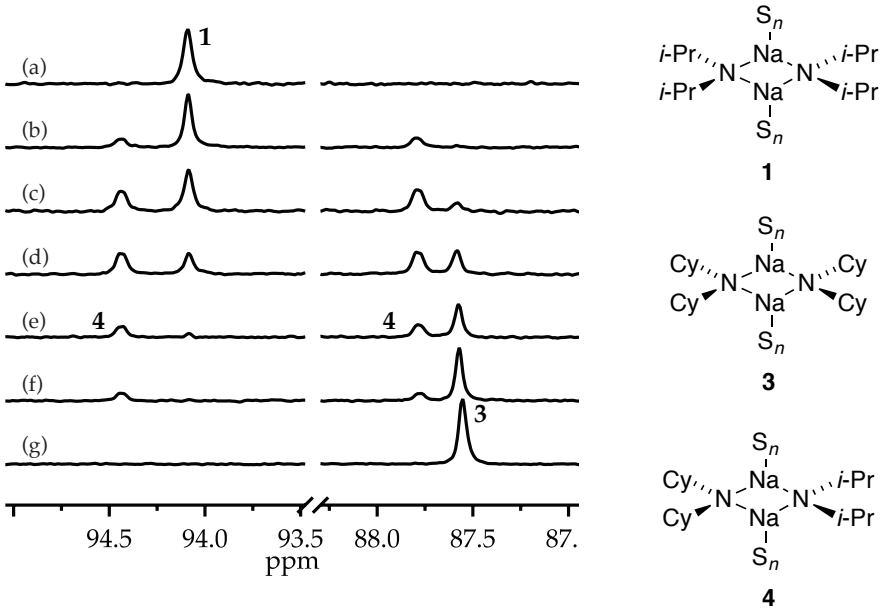

Figure A.2.12.[15]N NMR spectra for 0.10 M solutions of NaDA and NaDCA in *N*-methylpyrrolidine with varying χ_{NaDA} at –85 °C. The measured mole fractions, χ_{NaDA}, in (a)–(g) are 1.00, 0.83, 0.65, 0.54, 0.28, 0.15, and 0.00, respectively.

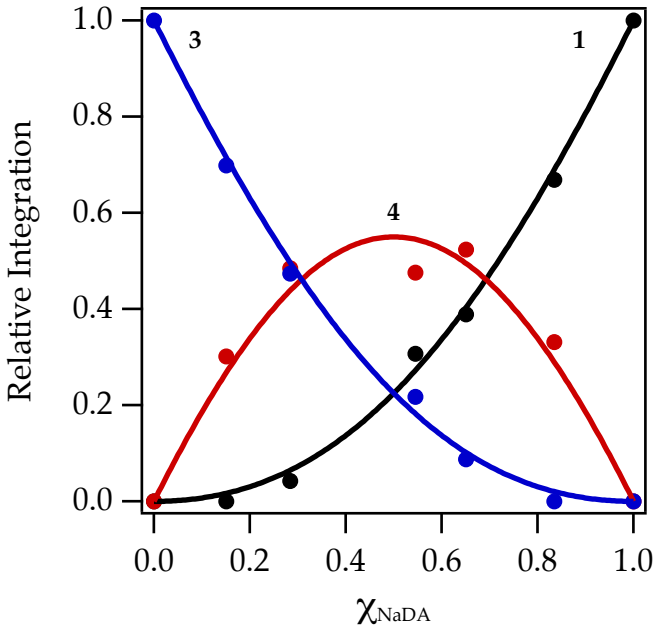

Figure A.2.13.Job plot showing the relative integrations versus the measured mole fraction of NaDA for 0.10 M solutions of NaDA and NaDCA in *N*-methylpyrrolidine with varying χ_{NaDA} at –85 °C. Fitting the data to an aggregating dimer ensemble affords $K_{eq} = 6 \pm 1$.

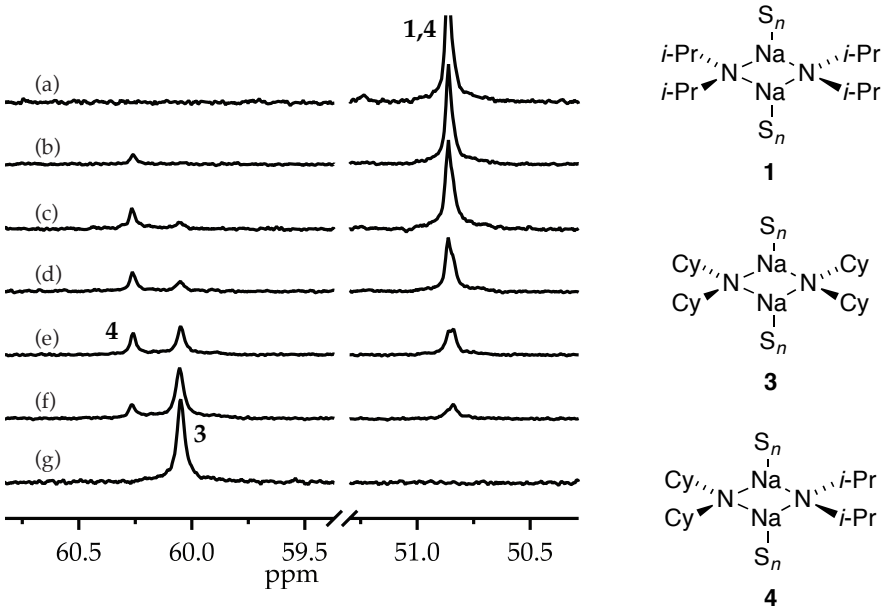

Figure A.2.14.[13]C NMR spectra for 0.30 M solutions of NaDA and NaDCA in 6.15 M THF/hexane with varying χ_{NaDA} at –100 °C. The measured mole fractions, χ_{NaDA}, in (a)–(g) are 1.00, 0.91, 0.83, 0.66, 0.31, 0.16, and 0.00, respectively.

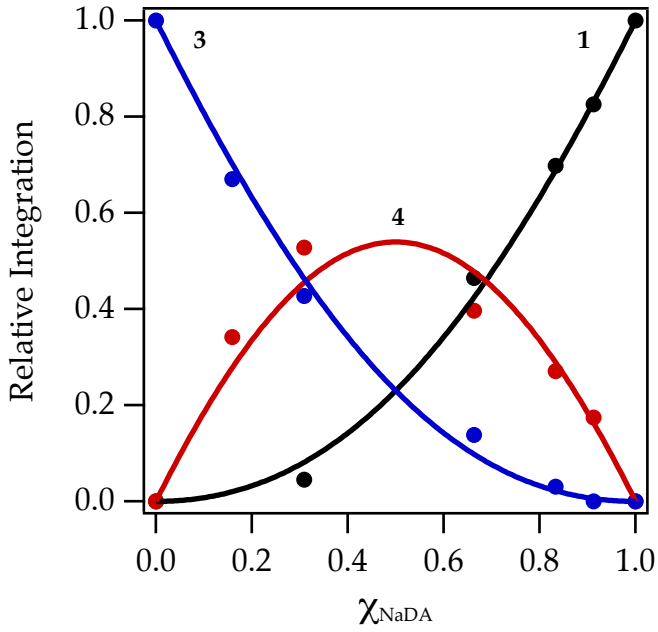

Figure A.2.15.Job plot showing the relative integrations versus the measured mole fraction of NaDA for 0.30 M solutions of NaDA and NaDCA in 6.15 M THF/hexane with varying χ_{NaDA} at –100 °C. Fitting the data to an aggregating dimer ensemble affords $K_{eq} = 6 \pm 2$.

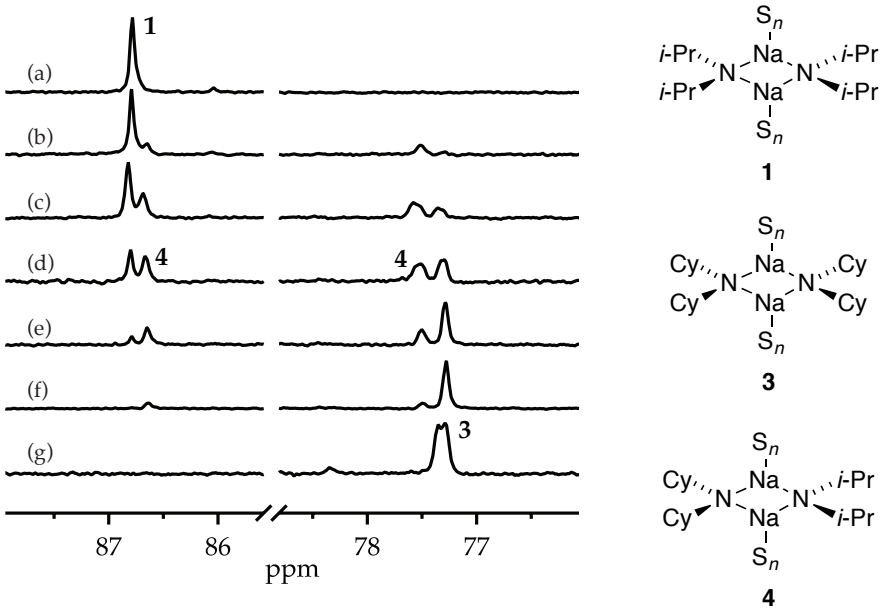

Figure A.2.16.[15]N NMR spectra for 0.086 M solutions of NaDA and NaDCA in 1.76 M THF/DMEA with varying χ_{NaDA} at –100 °C. The measured mole fractions, χ_{NaDA}, in (a)–(g) are 1.00, 0.81, 0.64, 0.52, 0.27, 0.11, and 0.00, respectively. Apparent duplication in spectrum (g) is an irreproducible artifact.

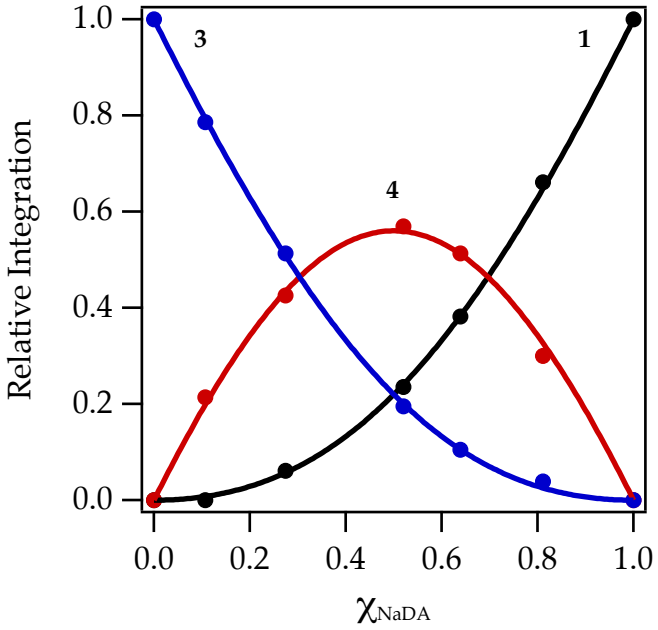

Figure A.2.17.Job plot showing the relative integrations versus the measured mole fraction of NaDA for 0.086 M solutions of NaDA and NaDCA in 1.76 M THF/DMEA with varying χ_{NaDA} at –100 °C. Fitting the data to an aggregating dimer ensemble affords $K_{eq} = 6.5 \pm 0.5$.

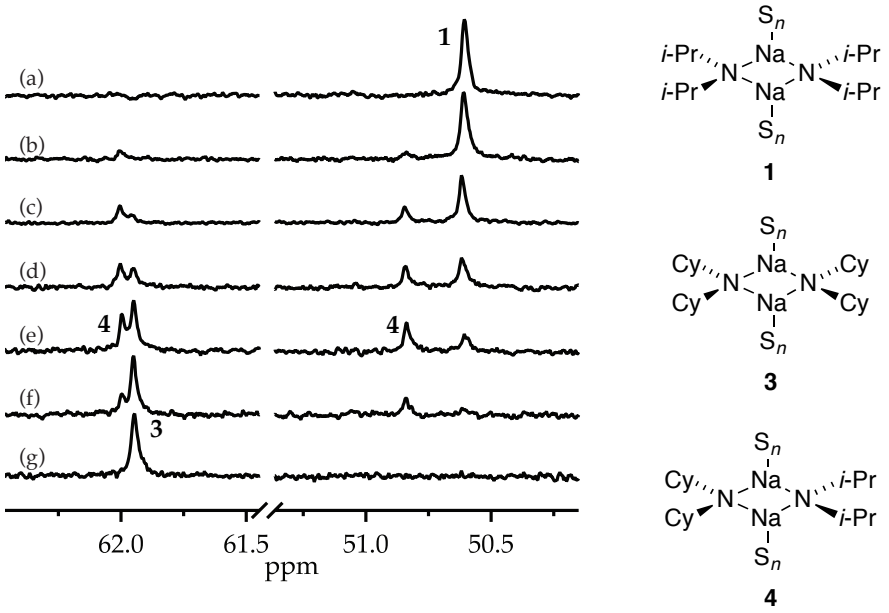

Figure A.2.18.[13]C NMR spectra for 0.17 M solutions of NaDA and NaDCA in 1.37 M 1,2-dimethoxyethane/DMEA with varying χ_{NaDA} at –80 °C. The measured mole fractions, χ_{NaDA}, in (a)–(g) are 1.00, 0.94, 0.76, 0.59, 0.33, 0.23, and 0.00, respectively.

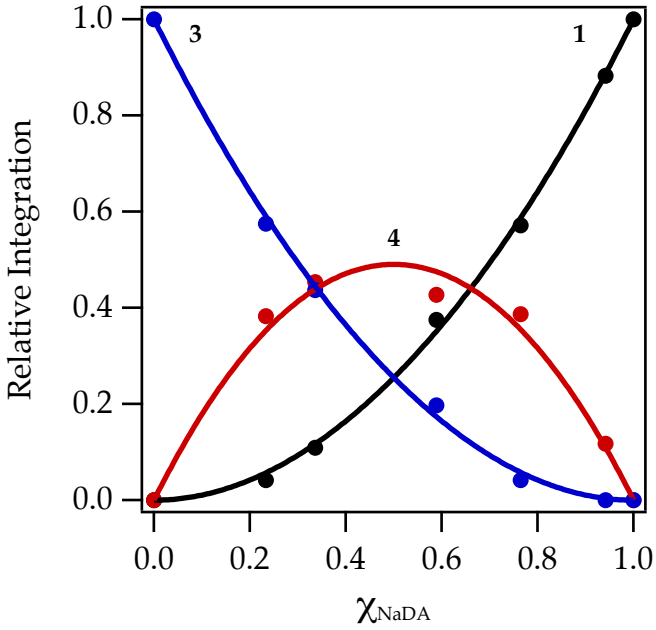

Figure A.2.19.Job plot showing the relative integrations versus the measured mole fraction of NaDA for 0.17 M solutions of NaDA and NaDCA in 1.37 M 1,2-dimethoxyethane/DMEA with varying χ_{NaDA} at –80 °C. Fitting the data to an aggregating dimer ensemble affords $K_{eq} = 3.7 \pm 0.6$.

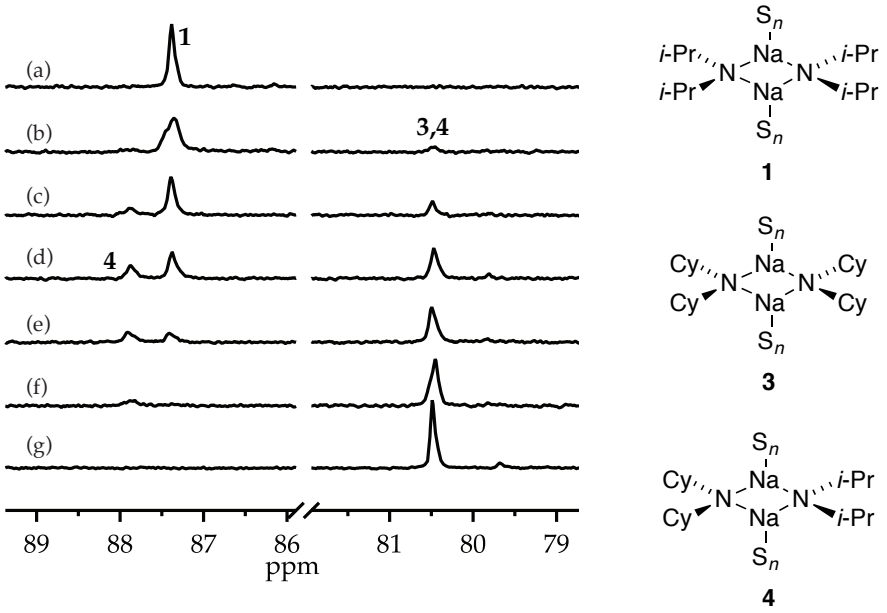

Figure A.2.20.[15]N NMR spectra for 0.086 M solutions of NaDA and NaDCA in 1.37 M 1,2-dimethoxyethane/DMEA with varying χ_{NaDA} at –100 °C. The measured mole fractions, χ_{NaDA}, in (a)–(g) are 1.00, 0.94, 0.76, 0.59, 0.33, 0.23, and 0.00, respectively.

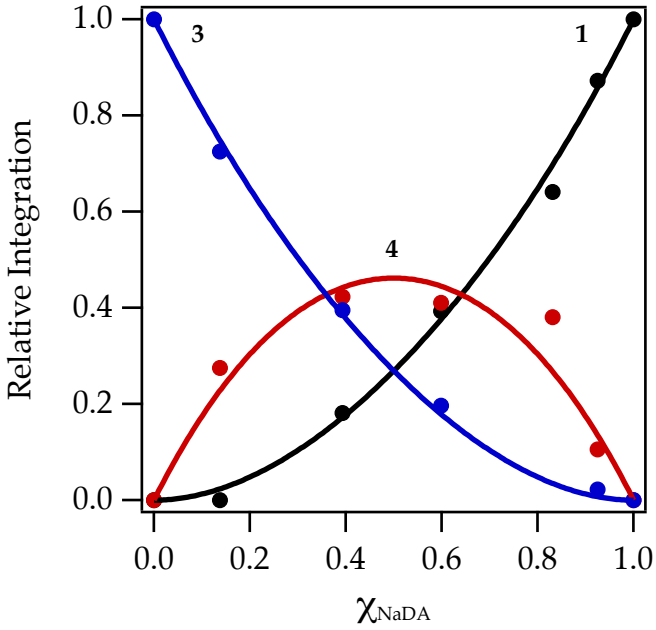

Figure A.2.21.Job plot showing the relative integrations versus the measured mole fraction of NaDA for 0.086 M solutions of NaDA and NaDCA in 1.37 M 1,2-dimethoxyethane/DMEA with varying χ_{NaDA} at –100 °C. Fitting the data to an aggregating dimer ensemble affords $K_{eq} = 2.9 \pm 0.9$.

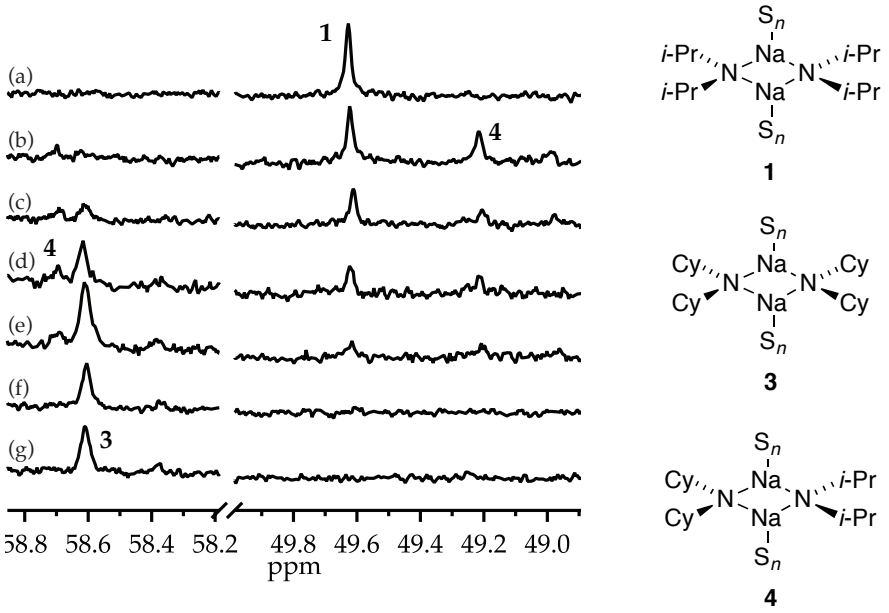

Figure A.2.22.[13]C NMR spectra for 0.086 M solutions of NaDA and NaDCA in 0.95 M TMEDA/DMBA with varying χ_{NaDA} at –80 °C. The measured mole fractions, χ_{NaDA}, in (a)–(g) are 1.00, 0.68, 0.69, 0.47, 0.14, 0.06, and 0.00, respectively.

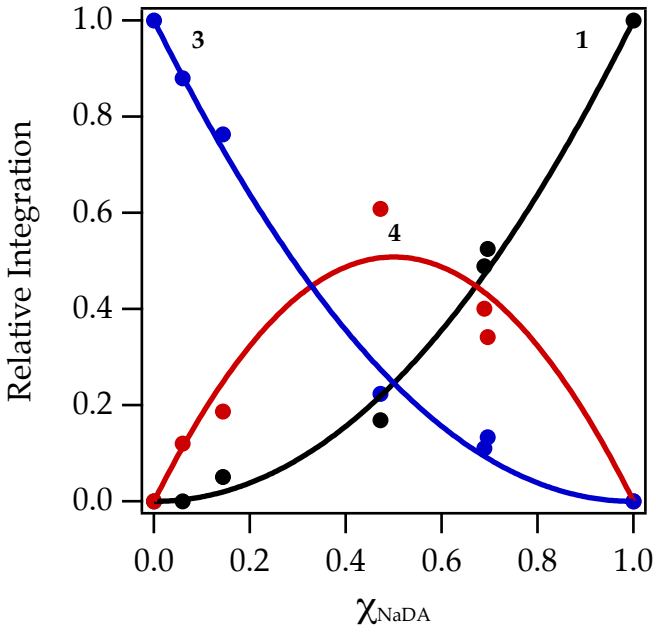

Figure A.2.23.Job plot showing the relative integrations versus the measured mole fraction of NaDA for 0.086 M solutions of NaDA and NaDCA in 0.95 M TMEDA/DMBA with varying χ_{NaDA} at –80 °C. Fitting the data to an aggregating dimer ensemble affords $K_{eq} = 4 \pm 1$.

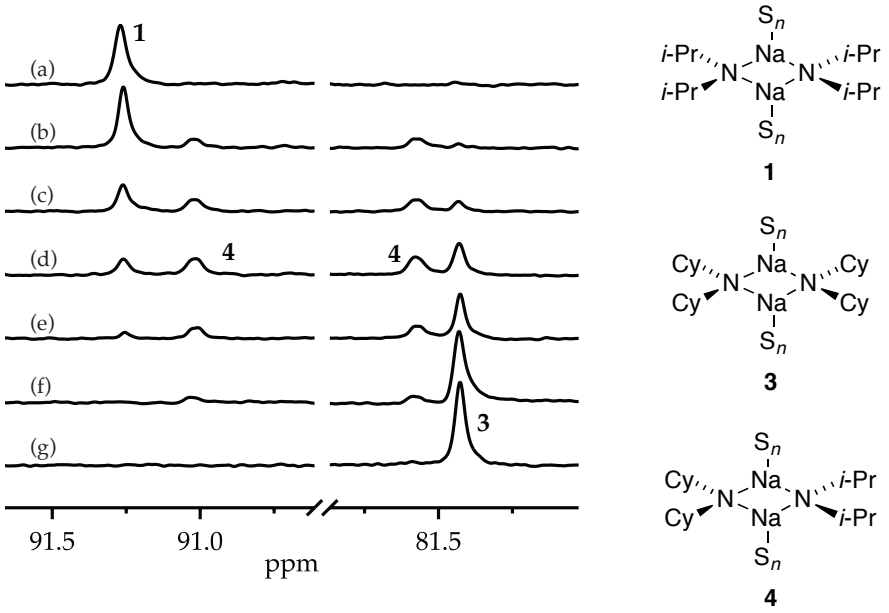

Figure A.2.24.[15]N NMR spectra for 0.086 M solutions of NaDA and NaDCA in 0.95 M TMEDA/DMBA with varying χ_{NaDA} at –80 °C. The measured mole fractions, χ_{NaDA}, in (a)–(g) are 1.00, 0.81, 0.62, 0.42, 0.27, 0.08, and 0.00, respectively.

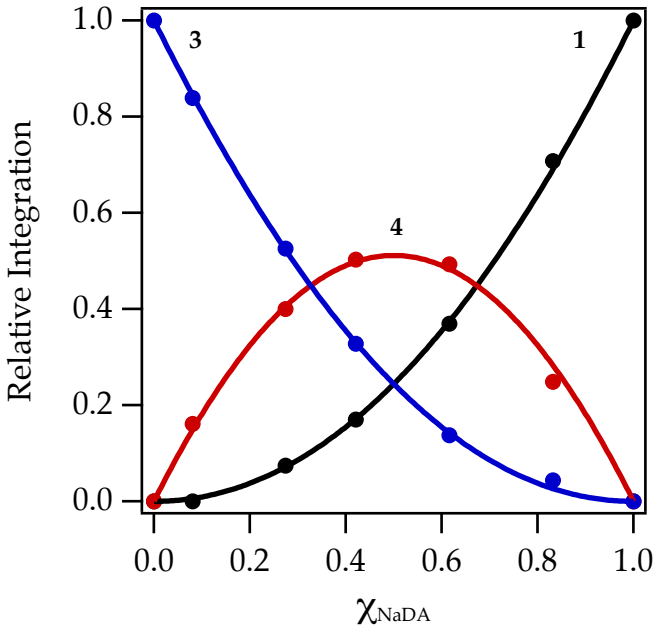

Figure A.2.25.Job plot showing the relative integrations versus the measured mole fraction of NaDA for 0.086 M solutions of NaDA and NaDCA in 0.95 M TMEDA/DMBA with varying χ_{NaDA} at –80 °C. Fitting the data to an aggregating dimer ensemble affords $K_{eq} = 4.4 \pm 0.4$.

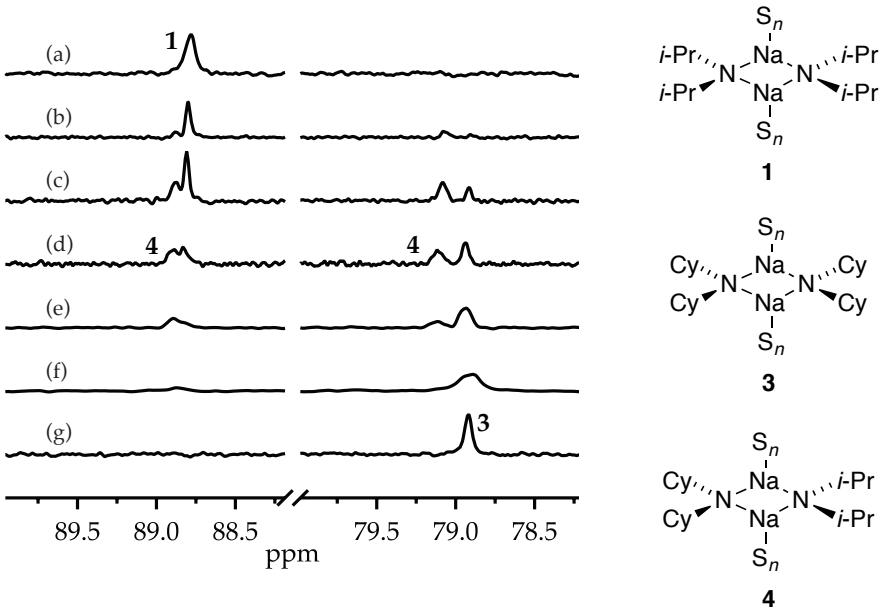

Figure A.2.26.[15]N NMR spectra for 0.086 M solutions of NaDA and NaDCA in 0.68 M PMDTA/DMEA with varying χ_{NaDA} at –80 °C. The measured mole fractions, χ_{NaDA}, in (a)–(g) are 1.00, 0.79, 0.63, 0.50, 0.31, 0.13, and 0.00, respectively.

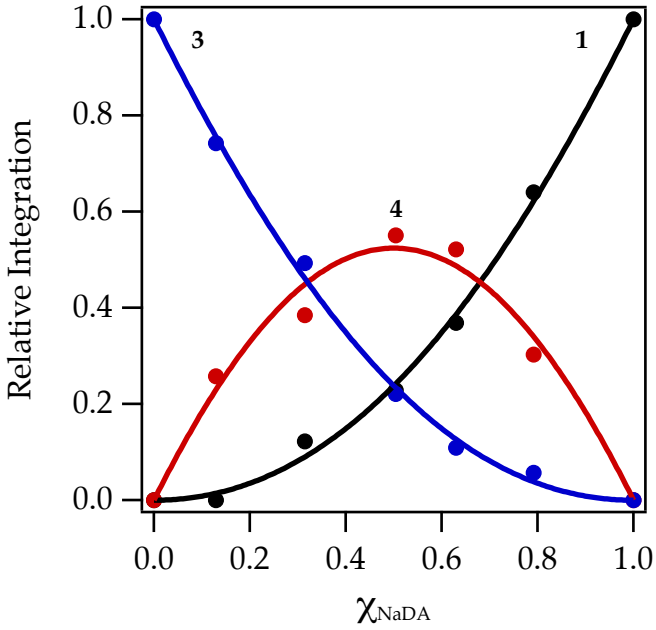

Figure A.2.27.Job plot showing the relative integrations versus the measured mole fraction of NaDA for 0.086 M solutions of NaDA and NaDCA in 0.68 M PMDTA/DMEA with varying χ_{NaDA} at –80 °C. Fitting the data to an aggregating dimer ensemble affords $K_{eq} = 4.9 \pm 0.9$.

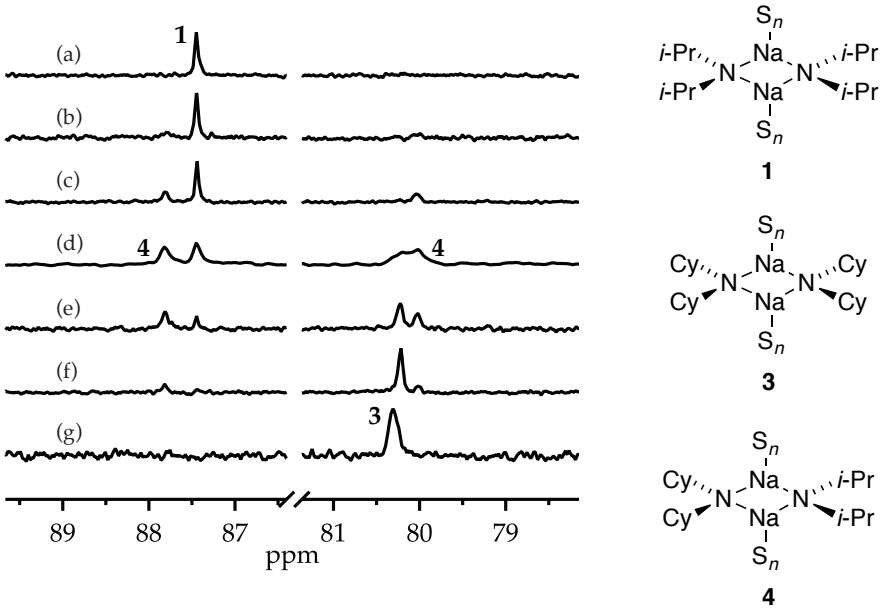

Figure A.2.28. ^{15}N NMR spectra for 0.086 M solutions of NaDA and NaDCA in 1.00 M diglyme/DMEA with varying χ_{NaDA} at –80 °C. The measured mole fractions, χ_{NaDA}, in (a)–(g) are 1.00, 0.88, 0.76, 0.44, 0.35, 0.14, and 0.00, respectively.

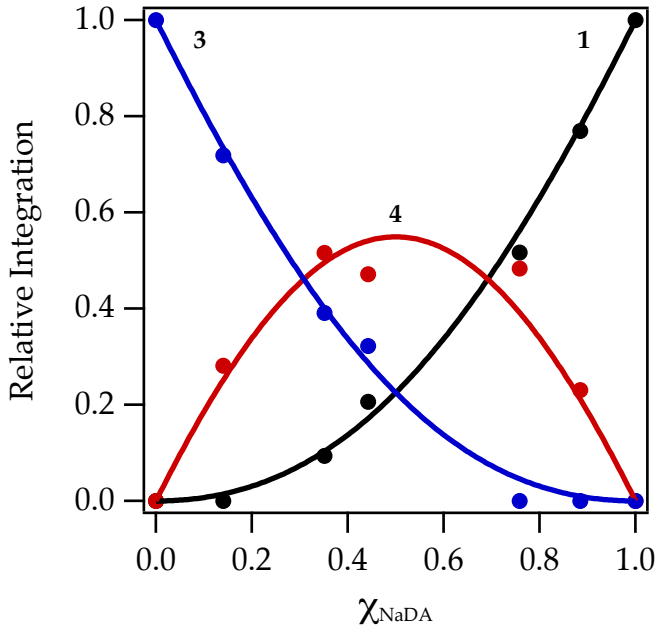

Figure A.2.29.Job plot showing the relative integrations versus the measured mole fraction of NaDA for 0.086 M solutions of NaDA and NaDCA in 1.00 M diglyme/DMEA with varying χ_{NaDA} at –80 °C. Fitting the data to an aggregating dimer ensemble affords $K_{eq} = 6 \pm 2$.

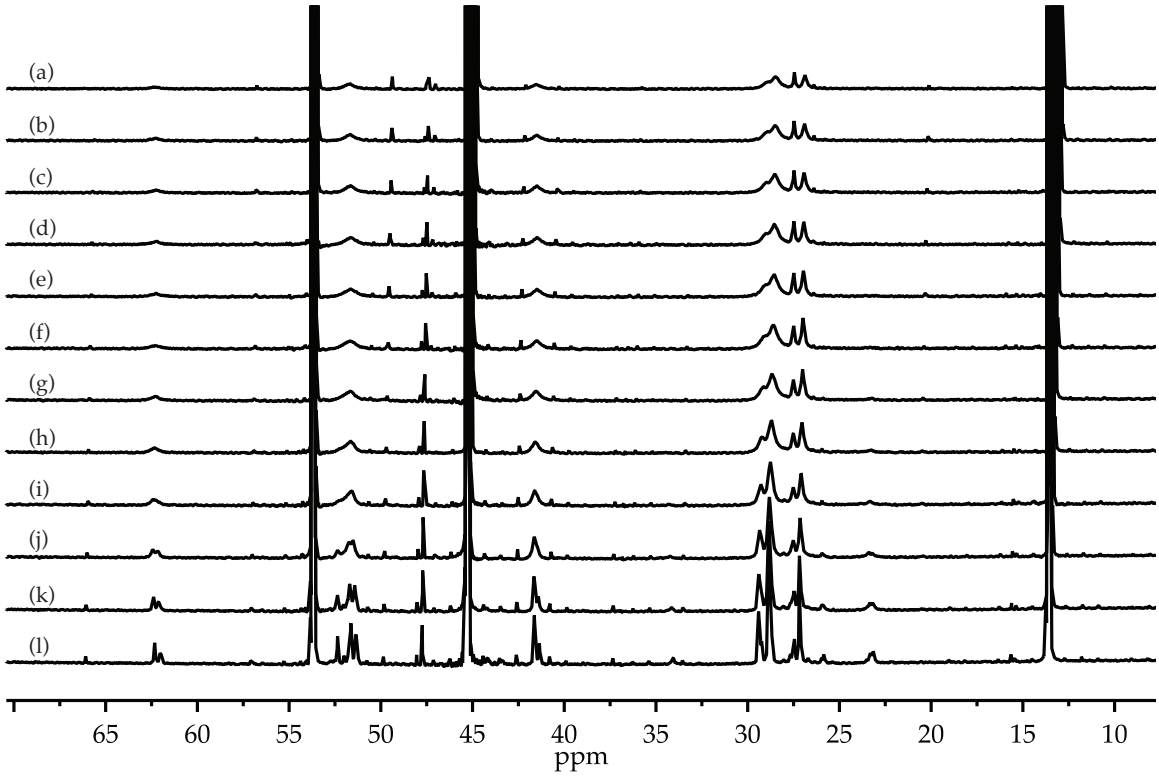

Figure A.2.30.Variable temperature ^{13}C NMR spectra for a mixture of 0.35 M NaDA and 0.35 M NaICA in DMEA with 10% v/v benzene-d_6 as an internal standard. The temperatures are (a) +10 °C, (b) 0 °C, (c) –10 °C, (d) –20 °C, (e) –30 °C, (f) –40 °C, (g) –50 °C, (h) –60 °C, (i) –70 °C, (j) –80 °C, (k) –90 °C, and (l) –99 °C respectively. These spectra demonstrate highly fluxional aggregate subunit exchange.

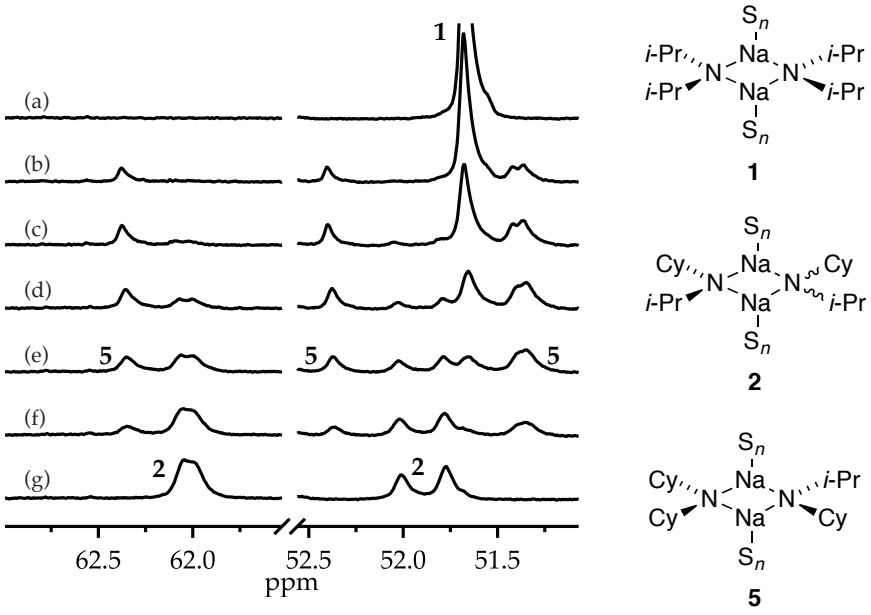

Figure A.2.31.[13]C NMR spectra for 0.50 M solutions of NaDA and NaICA in DMEA with varying χ_{NaDA} at –98 °C. The measured mole fractions, χ_{NaDA}, in (a)–(g) are 1.00, 0.87, 0.72, 0.55, 0.36, 0.15, and 0.00, respectively.

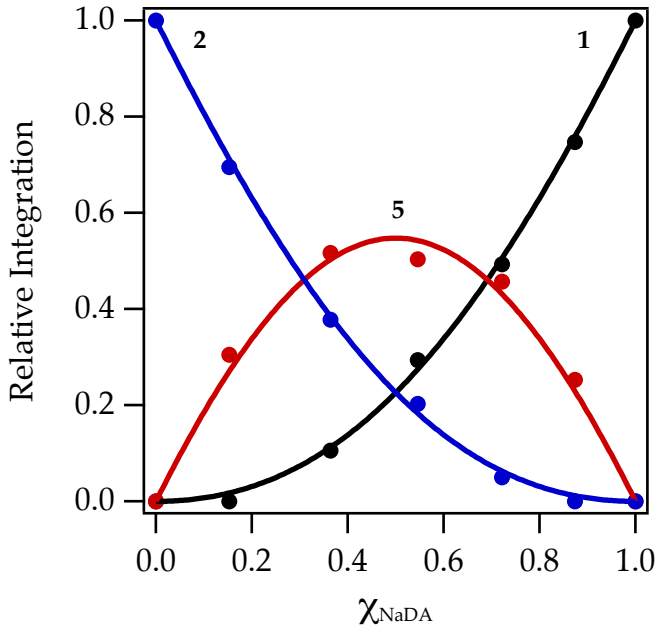

Figure A.2.32.Job plot showing the relative integrations versus the measured mole fraction of NaDA for 0.50 M solutions of NaDA and NaICA in DMEA with varying χ_{NaDA} at –98 °C. Fitting the data to an aggregating dimer ensemble affords $K_{eq} = 5.9 \pm 0.9$.

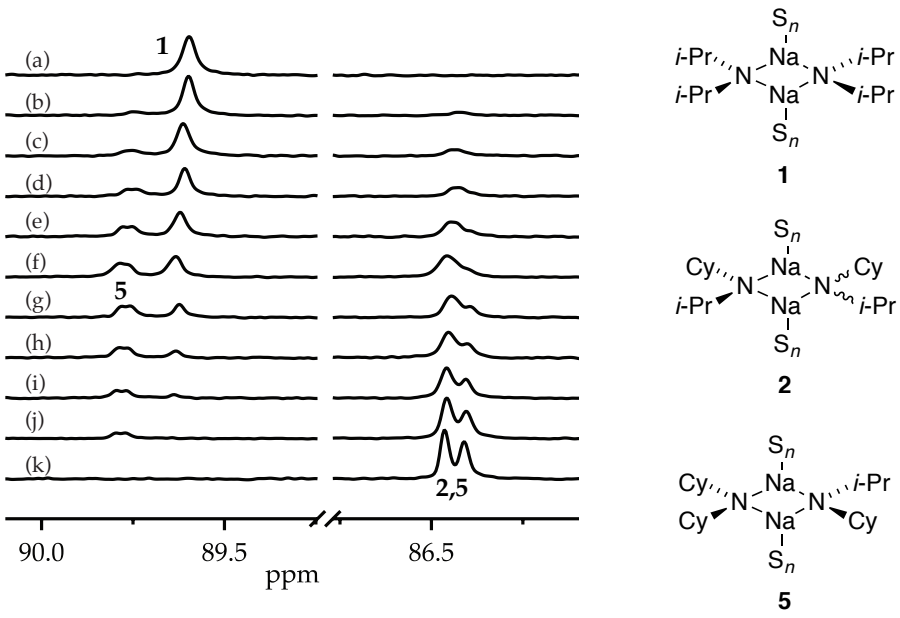

Figure A.2.33.[15]N NMR spectra for 0.30 M solutions of NaDA and NaICA in DMEA with varying χ_{NaDA} at −109 °C. The measured mole fractions, χ_{NaDA}, in (a)–(k) are 1.00, 0.91, 0.82, 0.72, 0.67, 0.56, 0.44, 0.28, 0.27, 0.12, and 0.00, respectively.

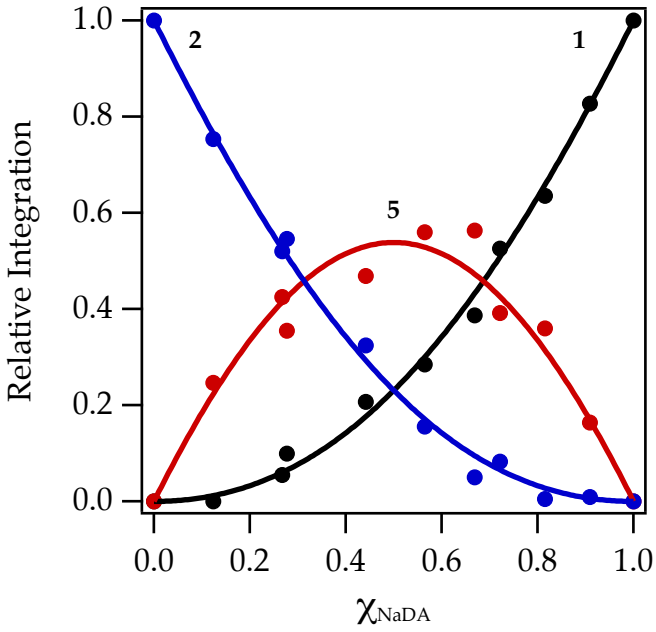

Figure A.2.34.Job plot showing the relative integrations versus the measured mole fraction of NaDA for 0.30 M solutions of NaDA and NaICA in DMEA with varying χ_{NaDA} at −109 °C. Fitting the data to an aggregating dimer ensemble affords $K_{eq} = 5 \pm 1$.

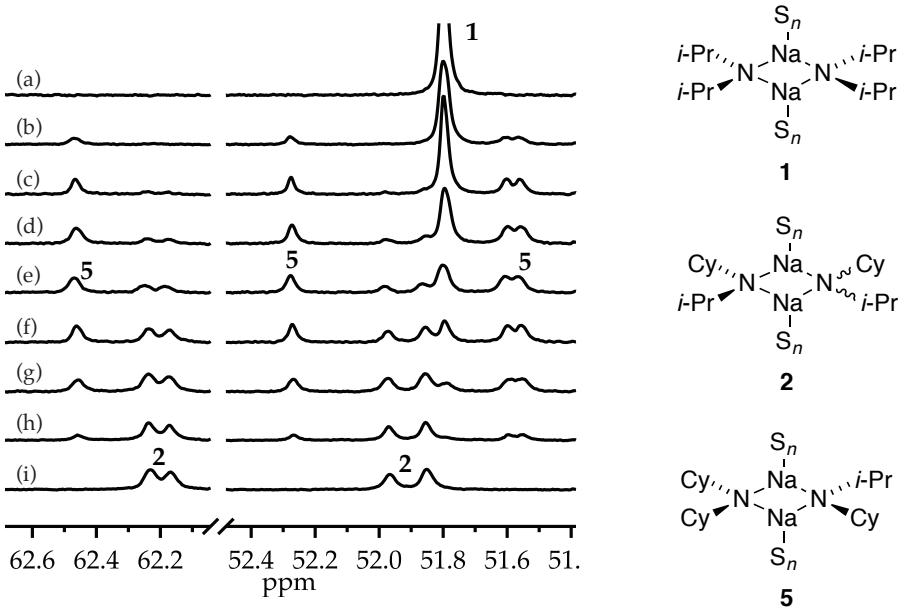

Figure A.2.35.[13]C NMR spectra for 0.31 M solutions of NaDA and NaICA in DMBA with varying χ_{NaDA} at –100 °C. The measured mole fractions, χ_{NaDA}, in (a)–(i) are 1.00, 0.88, 0.77, 0.62, 0.52, 0.36, 0.27, 0.11, and 0.00, respectively.

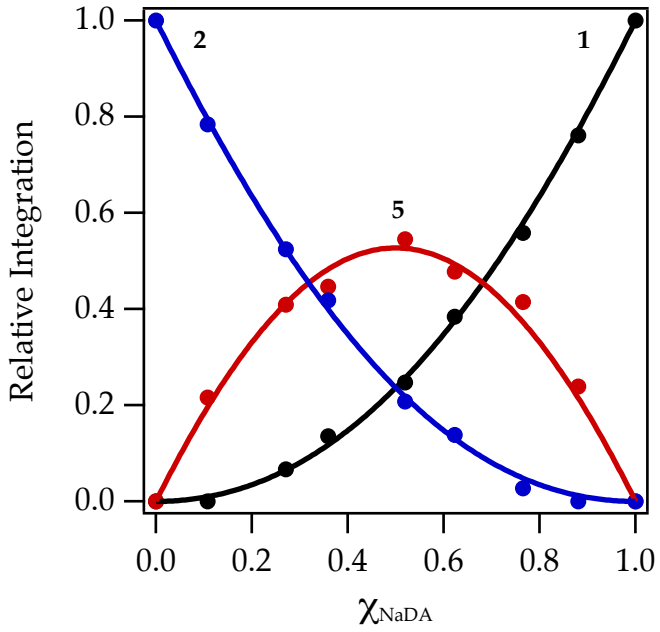

Figure A.2.36.Job plot showing the relative integrations versus the measured mole fraction of NaDA for 0.31 M solutions of NaDA and NaICA in DMBA with varying χ_{NaDA} at –100 °C. Fitting the data to an aggregating dimer ensemble affords $K_{eq} = 5.0 \pm 0.5$.

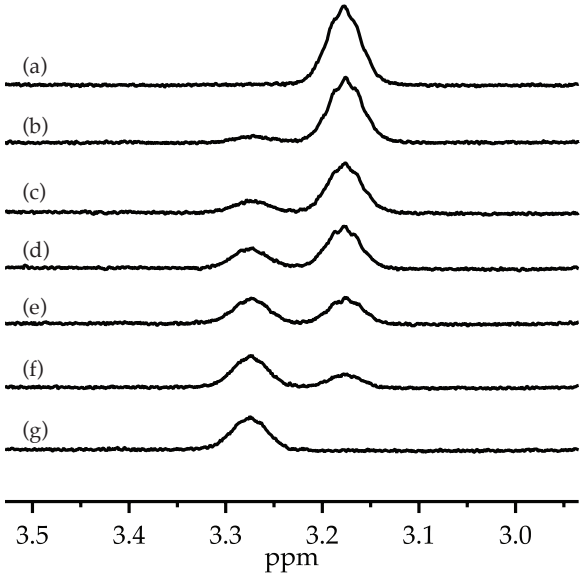

Figure A.2.37.[1]H NMR spectra for 0.10 M solutions of NaDA and NaICA in TMCDA/DMEA with varying χ_{NaDA} at 21 °C. The measured mole fractions, χ_{NaDA}, in (a)–(g) are 1.00, 0.82, 0.67, 0.50, 0.33, 0.16, and 0.00, respectively. The absence of time-averaged resonance perturbation is taken to imply monomeric NaDA.

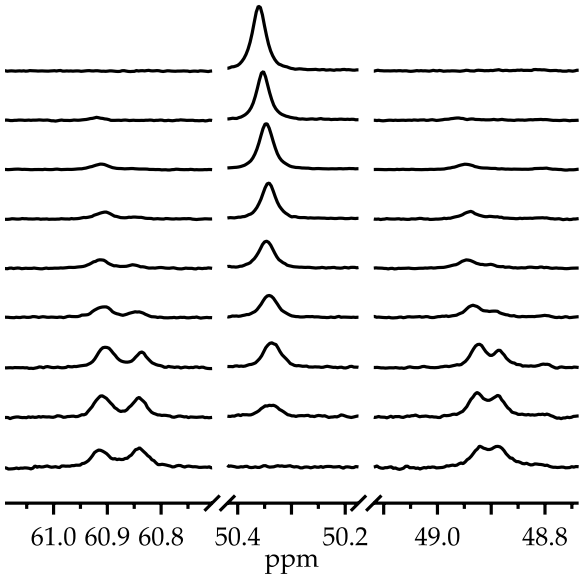

Figure A.2.38.[13]C NMR spectra for 0.40 M solutions of NaDA and NaICA in 0.40 M TMEDA/DMEA with varying χ_{NaDA} at –80 °C. Due to poor resolution of homo- from heteroaggregates a Job plot was not extracted from this data.

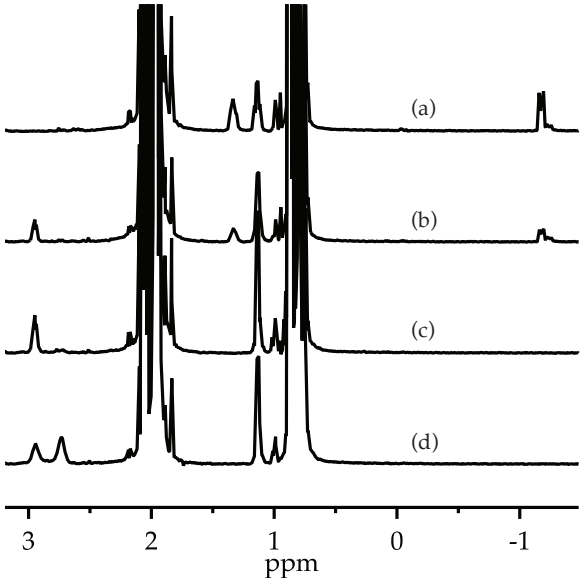

Figure A.2.39.[1]H NMR spectra for 0.40 M solutions of *n*-BuNa in DMEA with 10% v/v benzene-d_6 varying diisopropylamine at –80 °C. The equivalents of diisopropylamine in (a)–(d) are 0.00, 0.50, 1.0, and 2.0, respectively. The spectra show quantitative conversion of *n*-BuNa into NaDA up to 1.0 equiv diisopropylamine with concomitant appearance of *n*-butane resonances.

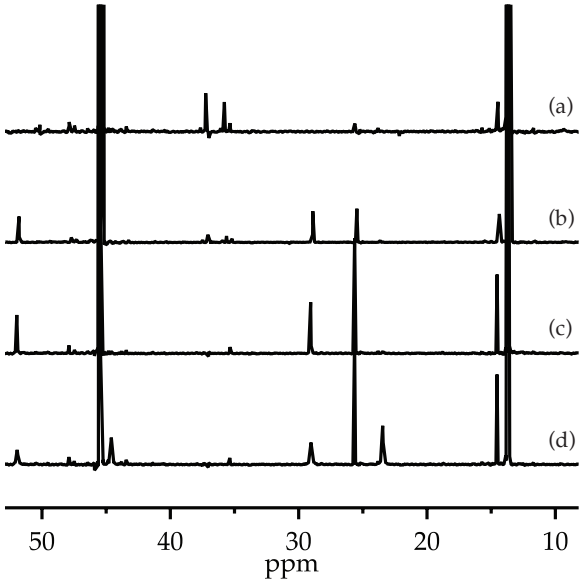

Figure A.2.40.[13]C NMR spectra for 0.40 M solutions of *n*-BuNa in DMEA with 10% v/v benzene-d_6 varying diisopropylamine at –80 °C. The equivalents of diisopropylamine in (a)–(d) are 0.00, 0.50, 1.0, and 2.0, respectively. The spectra show quantitative conversion of *n*-BuNa into NaDA up to 1.0 equiv diisopropylamine with concomitant appearance of *n*-butane resonances.

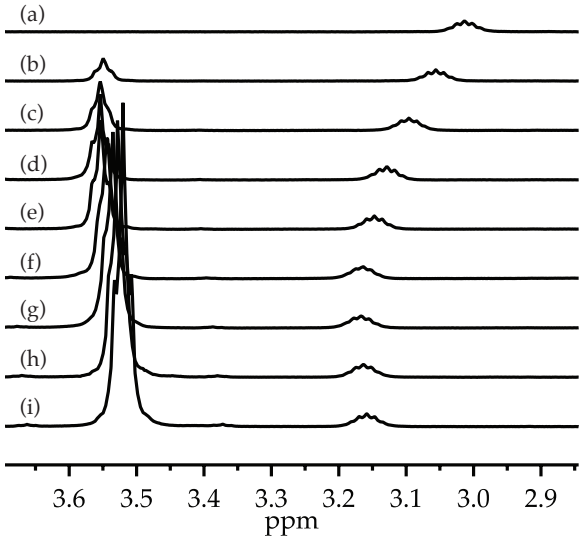

Figure A.2.41.[1]H NMR spectra for 0.30 M solutions of NaDA in DMBA with 10% v/v benzene-d_6 varying THF at –80 °C. The equivalents of THF in (a)–(i) are 0.00, 0.63, 1.19, 1.885, 2.44, 3.77, 5.025, 5.975, and 7.325, respectively.

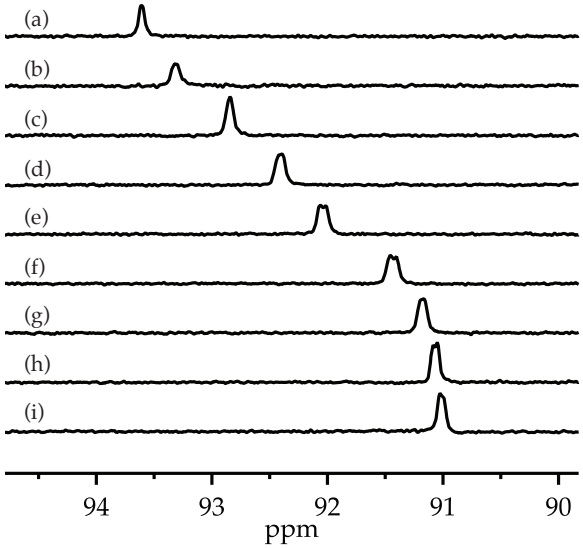

Figure A.2.42.[15]N NMR spectra for 0.30 M solutions of NaDA in DMBA with 10% v/v benzene-d_6 varying THF at –80 °C. The equivalents of THF in (a)–(i) are 0.00, 0.63, 1.19, 1.885, 2.44, 3.77, 5.025, 5.975, and 7.325, respectively.

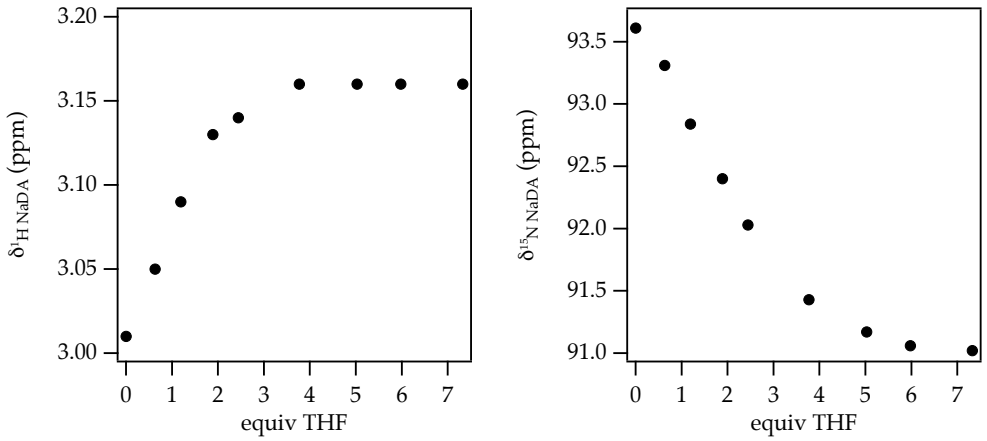

Figure A.2.43.Plots of chemical shift affiliated with NaDA for 0.30 M solutions of NaDA in DMBA with 10% v/v benzene-d_6 varying THF at –80 °C. Non-quantitative substitution is evidenced by chemical shift saturation at >3.0 equiv THF/Na.

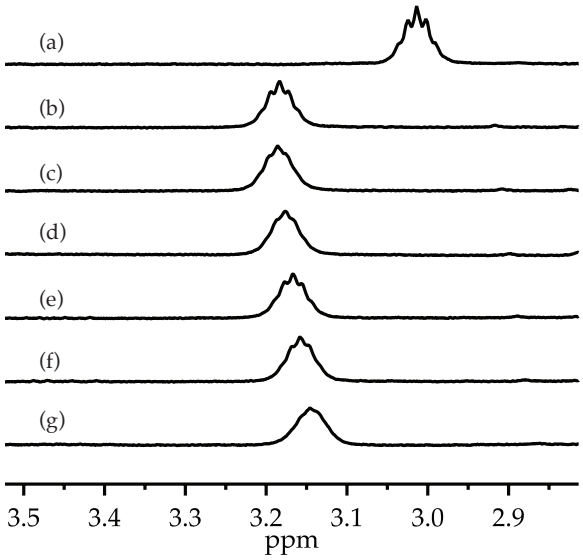

Figure A.2.44.[1]H NMR spectra for 0.25 M solutions of NaDA in DMBA with 10% v/v benzene-d_6 varying TMEDA at –80 °C. The equivalents of TMEDA in (a)–(g) are 0.00, 0.50, 1.0, 2.0, 3.0, 4.0, and 5.0, respectively.

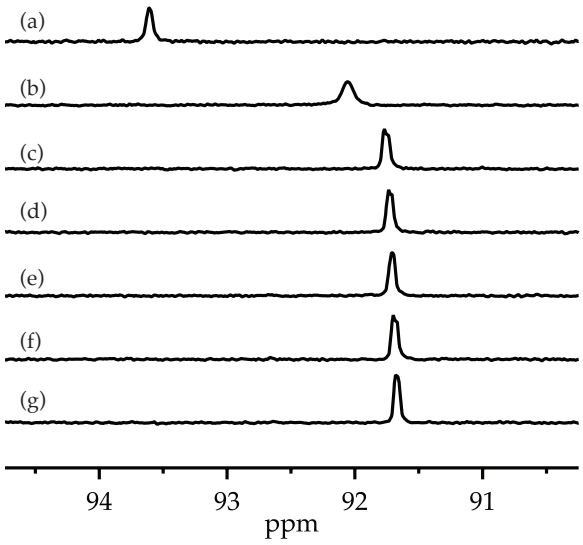

Figure A.2.45.[15]N NMR spectra for 0.25 M solutions of NaDA in DMBA with 10% v/v benzene-d_6 varying TMEDA at –80 °C. The equivalents of TMEDA in (a)–(g) are 0.00, 0.50, 1.0, 2.0, 3.0, 4.0, and 5.0, respectively.

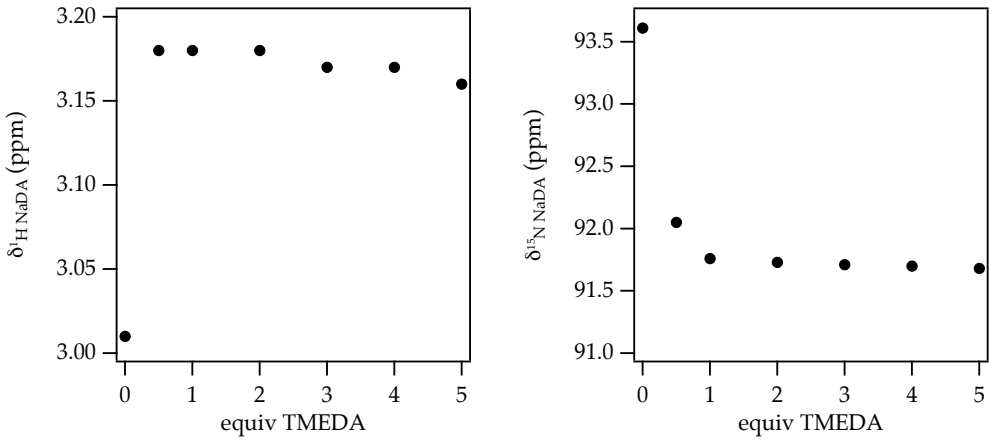

Figure A.2.46.Plots of chemical shift affiliated with NaDA for 0.30 M solutions of NaDA in DMBA with 10% v/v benzene-d_6 varying THF at –80 °C.

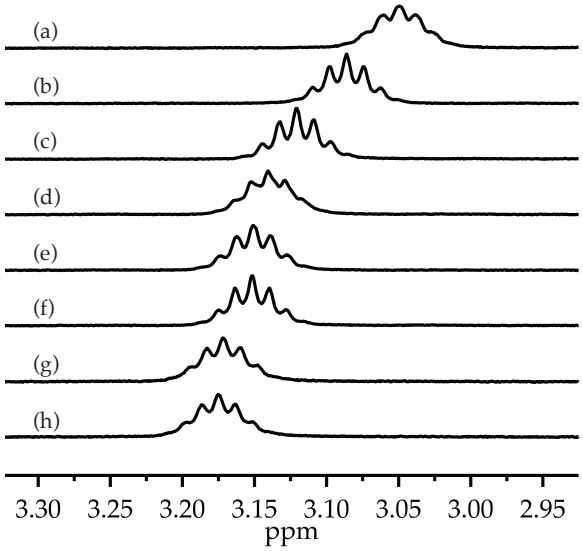

Figure A.2.47.[1]H NMR spectra for 0.30 M solutions of NaDA in DMBA with 10% v/v benzene-d_6 varying TMCDA at –30 °C. The equivalents of TMCDA in (a)–(h) are 0.00, 0.55, 1.08, 1.58, 2.15, 2.09, 5.99, and 7.72, respectively.

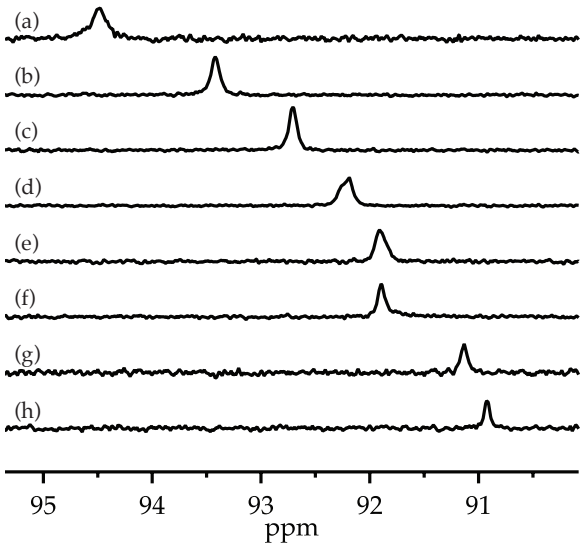

Figure A.2.48.[15]N NMR spectra for 0.30 M solutions of NaDA in DMBA with 10% v/v benzene-d_6 varying TMCDA at –30 °C. The equivalents of TMCDA in (a)–(h) are 0.00, 0.55, 1.08, 1.58, 2.15, 2.09, 5.99, and 7.72, respectively.

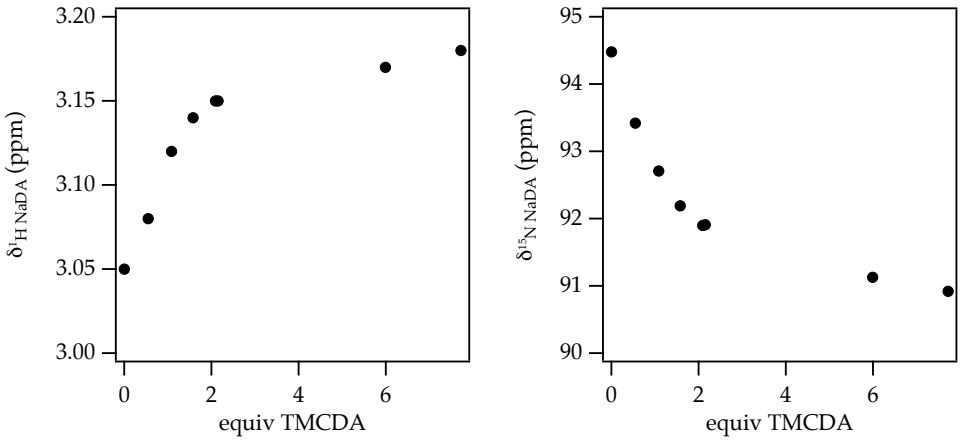

Figure A.2.49.Plots of chemical shift affiliated with NaDA for 0.30 M solutions of NaDA in DMBA with 10% v/v benzene-d_6 varying TMCDA at –30 °C. Non-quantitative substitution is evidenced by chemical shift saturation at >3.0 equiv TMCDA/Na.

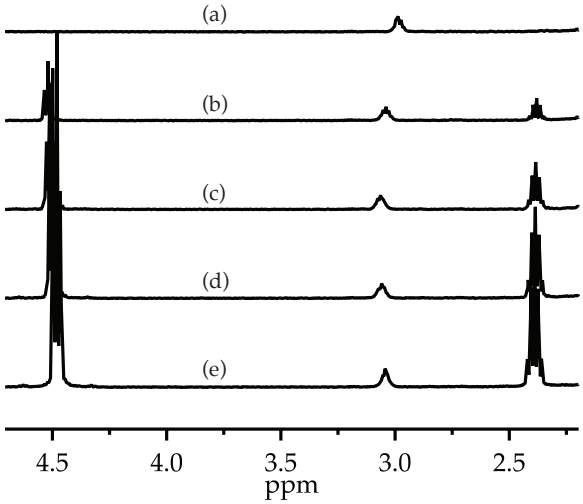

Figure A.2.50.[1]H NMR spectra for 0.30 M solutions of NaDA in DMEA with 10% v/v benzene-d_6 varying oxetane at –80 °C. The equivalents of oxetane in (a)–(e) are 0.00, 0.79, 2.09, 3.09, and 5.10, respectively.

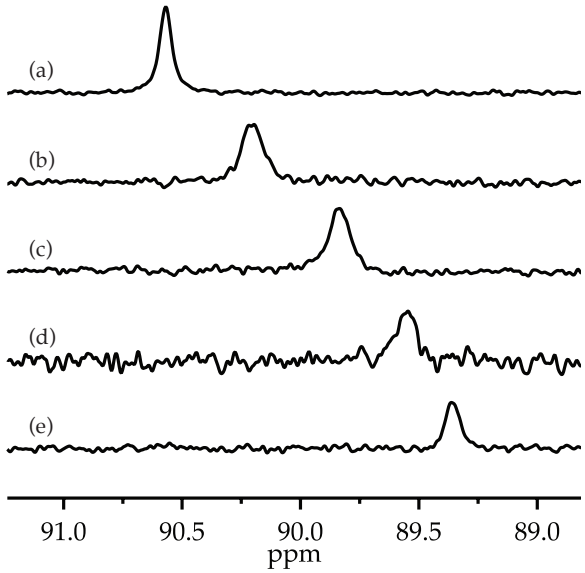

Figure A.2.51.[15]N NMR spectra for 0.30 M solutions of NaDA in DMEA with 10% v/v benzene-d_6 varying oxetane at –80 °C. The equivalents of oxetane in (a)–(e) are 0.00, 0.79, 2.09, 3.09, and 5.10, respectively.

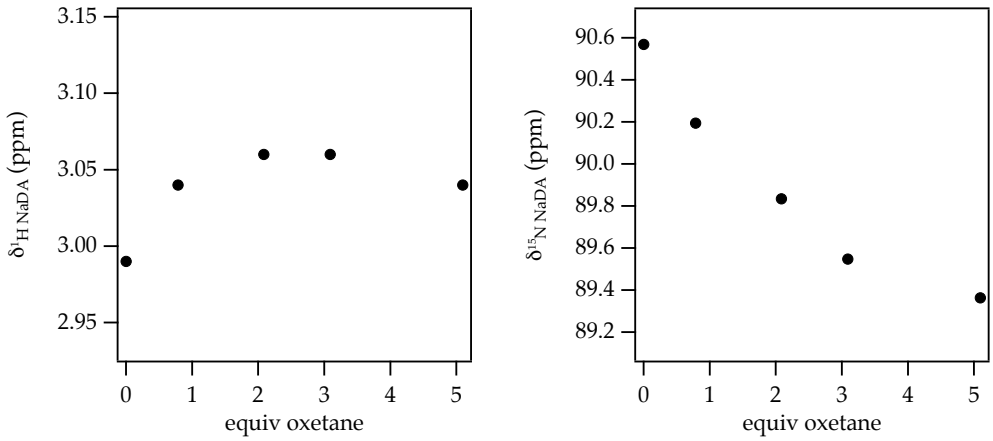

Figure A.2.52.Plots of chemical shift affiliated with NaDA for 0.30 M solutions of NaDA in DMEA with 10% v/v benzene-d_6 varying oxetane at –80 °C. Non-quantitative substitution is evidenced by chemical shift saturation at >3.0 equiv oxetane/Na.

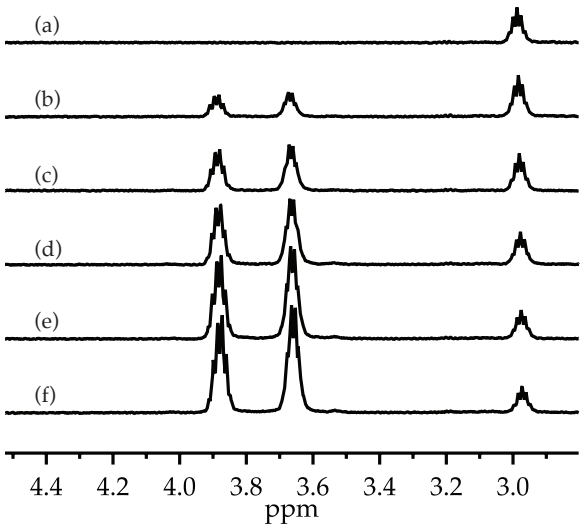

Figure A.2.53.[1]H NMR spectra for 0.30 M solutions of NaDA in DMEA with 10% v/v benzene-d_6 varying 2,5-dimethyltetrahydrofuran at –80 °C. The equivalents of 2,5-dimethyltetrahydrofuran in (a)–(f) are 0.00, 1.20, 2.74, 4.36, 7.30, and 9.03, respectively.

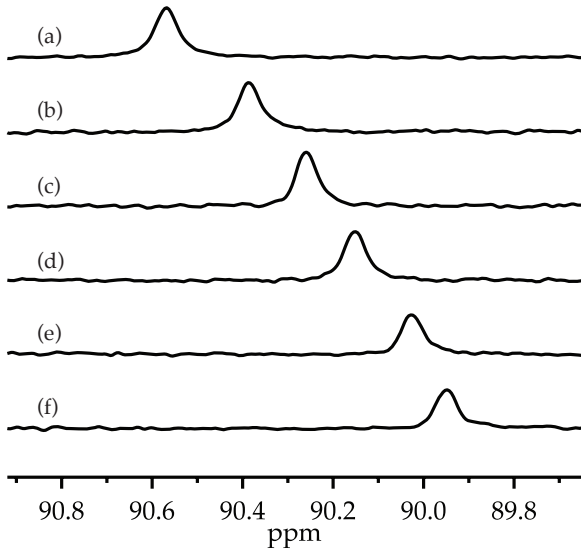

Figure A.2.54.[15]N NMR spectra for 0.30 M solutions of NaDA in DMEA with 10% v/v benzene-d_6 varying 2,5-dimethyltetrahydrofuran at –80 °C. The equivalents of 2,5-dimethyltetrahydrofuran in (a)–(f) are 0.00, 1.20, 2.74, 4.36, 7.30, and 9.03, respectively.

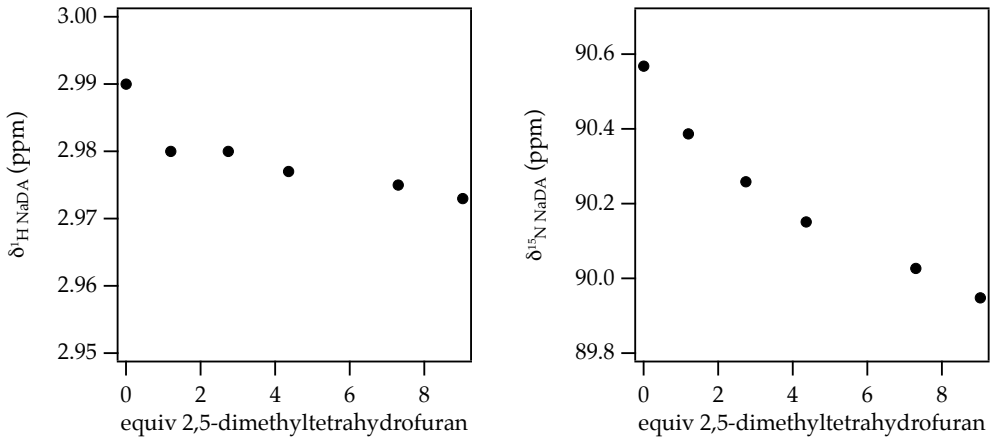

Figure A.2.55.Plots of chemical shift affiliated with NaDA for 0.30 M solutions of NaDA in DMEA with 10% v/v benzene-d_6 varying 2,5-dimethyltetrahydrofuran at –80 °C.

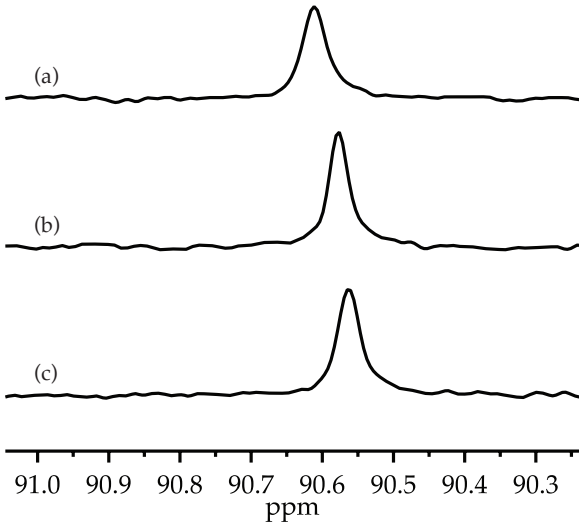

Figure A.2.56.[15]N NMR spectra for 0.30 M solutions of NaDA in DMEA with 10% v/v cyclohexane-d_{12} varying anisole at –80 °C. The equivalents of anisole in (a)–(c) are 0.00, 1.35, and 2.55, respectively.

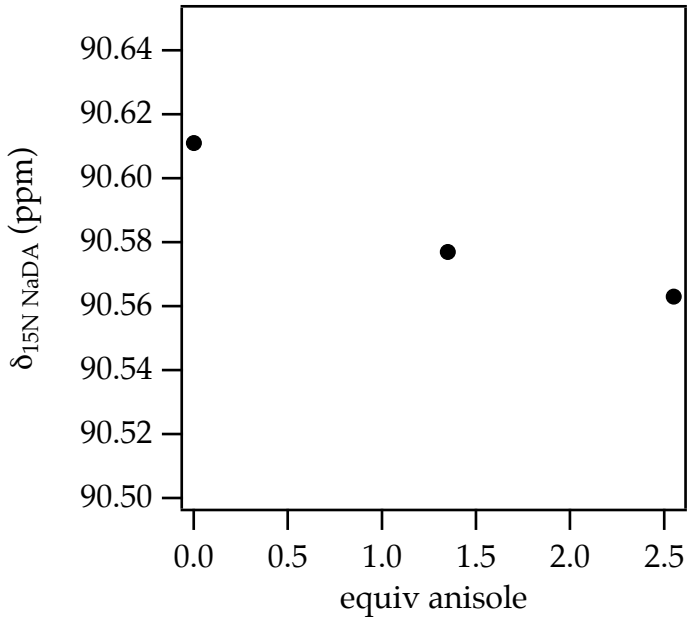

Figure A.2.57.Plots of chemical shift affiliated with NaDA for 0.30 M solutions of NaDA in DMEA with 10% v/v cyclohexane-d_{12} varying anisole at –80 °C.

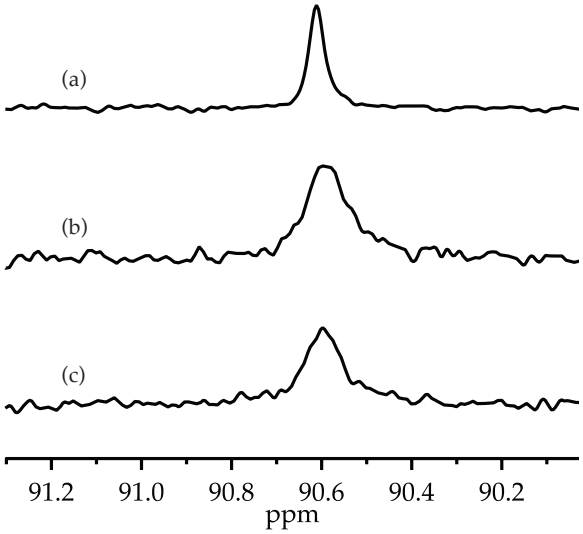

Figure A.2.58.[15]N NMR spectra for 0.30 M solutions of NaDA in DMEA with 10% v/v cyclohexane-d_{12} varying benzotrifluoride at –80 °C. The equivalents of benzotrifluoride in (a)–(c) are 0.00, 1.30, and 2.92, respectively.

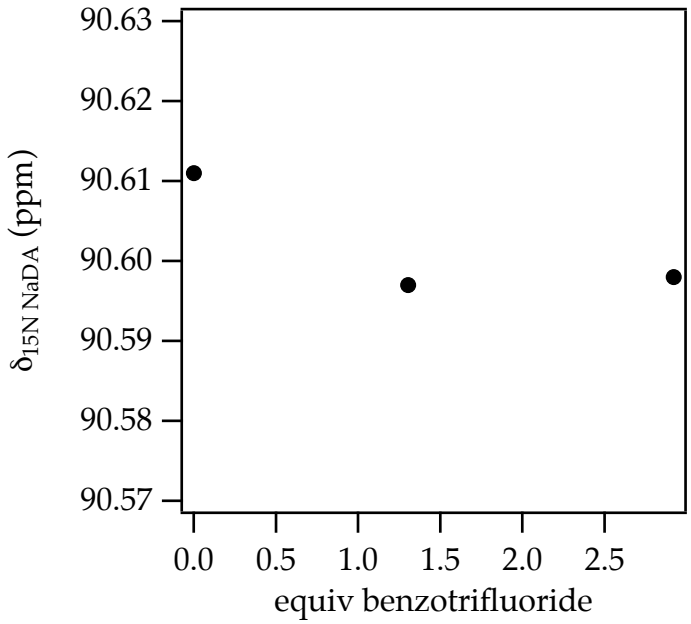

Figure A.2.59.Plots of chemical shift affiliated with NaDA for 0.30 M solutions of NaDA in DMEA with 10% v/v cyclohexane-d_{12} varying benzotrifluoride at –80 °C.

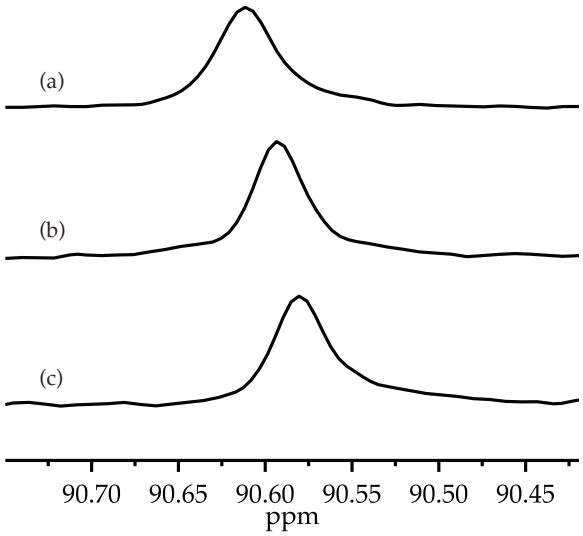

Figure A.2.60.[15]N NMR spectra for 0.30 M solutions of NaDA in DMEA with 10% v/v cyclohexane-d_{12} varying anisole at –80 °C. The equivalents of chlorobutane in (a)–(c) are 0.00, 1.30, and 2.92, respectively.

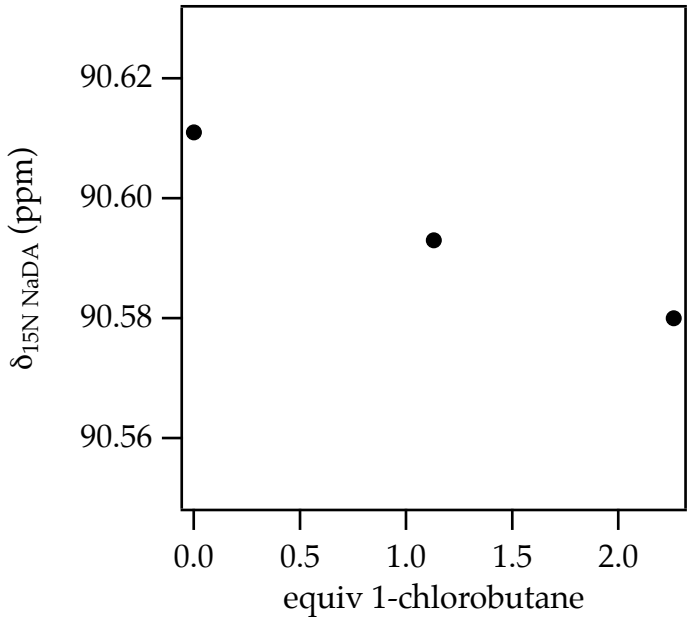

Figure A.2.61.Plots of chemical shift affiliated with NaDA for 0.30 M solutions of NaDA in DMEA with 10% v/v cyclohexane-d_{12} varying chlorobutane at –80 °C.

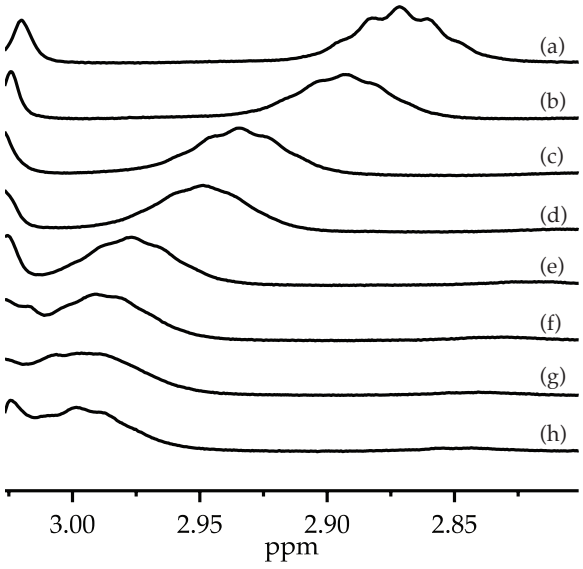

Figure A.2.62.[1]H NMR spectra for 0.10 M solutions of NaDA in *N,N*-diethylmethylamine with 10% v/v cyclohexane-d_{12} varying THF at –80 °C. The equivalents of THF in (a)–(h) are 0.00, 0.63, 0.78, 1.35, 1.83, 2.11, 2.78, and 3.56, respectively.

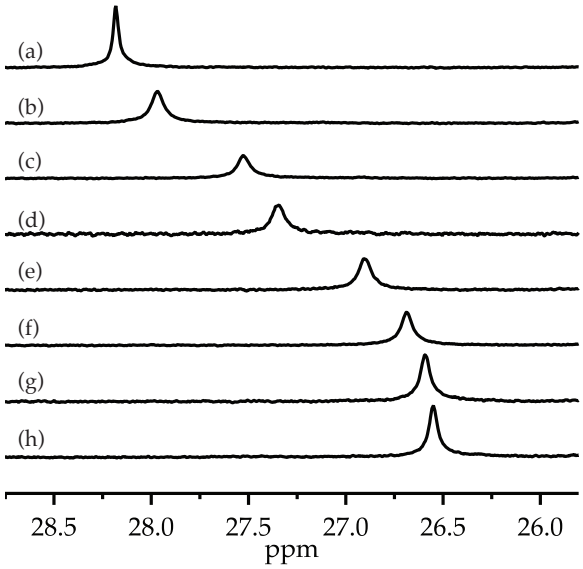

Figure A.2.63.[13]C NMR spectra for 0.10 M solutions of NaDA in *N,N*-diethylmethylamine with 10% v/v cyclohexane-d_{12} varying THF at –80 °C. The equivalents of THF in (a)–(h) are 0.00, 0.63, 0.78, 1.35, 1.83, 2.11, 2.78, and 3.56, respectively.

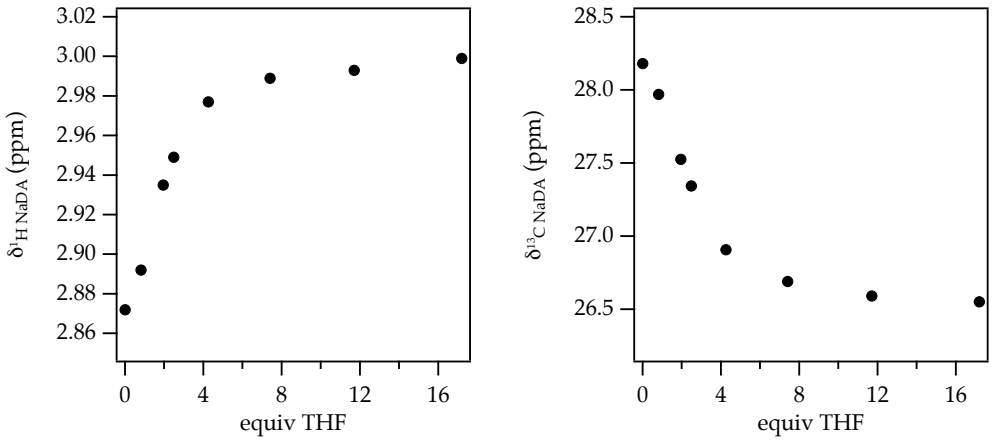

Figure A.2.64.Plots of chemical shift affiliated with NaDA for 0.10 M solutions of NaDA in *N,N*-diethylmethylamine with 10% v/v cyclohexane-d_{12} varying THF at –80 °C. Non-quantitative substitution is evidenced by chemical shift saturation at >3.0 equiv THF/Na despite the weaker binding affinity of *N,N*-diethylmethylamine relative to *N,N*-dimethylethylamine.

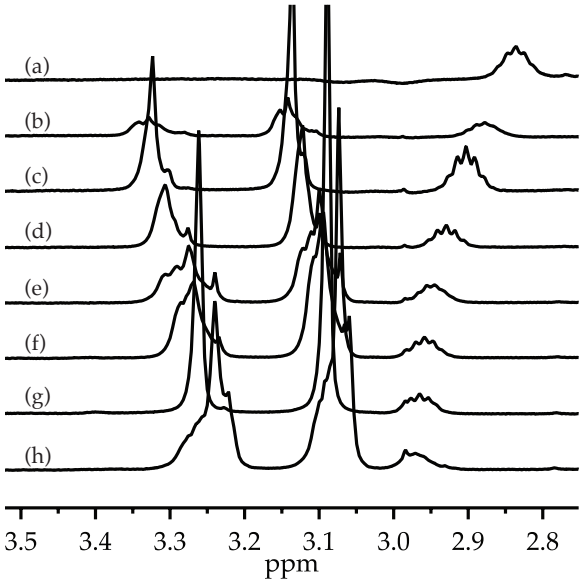

Figure A.2.65.[1]H NMR spectra for 0.10 M solutions of NaDA in DMEA with 10% v/v cyclohexane-d_{12} varying 1,2-dimethoxyethane at –80 °C. The equivalents of DME in (a)–(h) are 0.00, 0.63, 0.78, 1.35, 1.83, 2.11, 2.78, and 3.56, respectively.

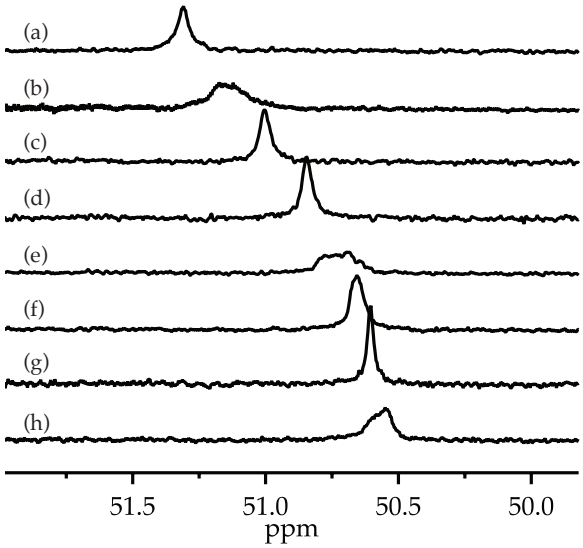

Figure A.2.66.[13]C NMR spectra for 0.10 M solutions of NaDA in DMEA with 10% v/v cyclohexane-d_{12} varying 1,2-dimethoxyethane at –80 °C. The equivalents of DME in (a)–(h) are 0.00, 0.63, 0.78, 1.35, 1.83, 2.11, 2.78, and 3.56, respectively.

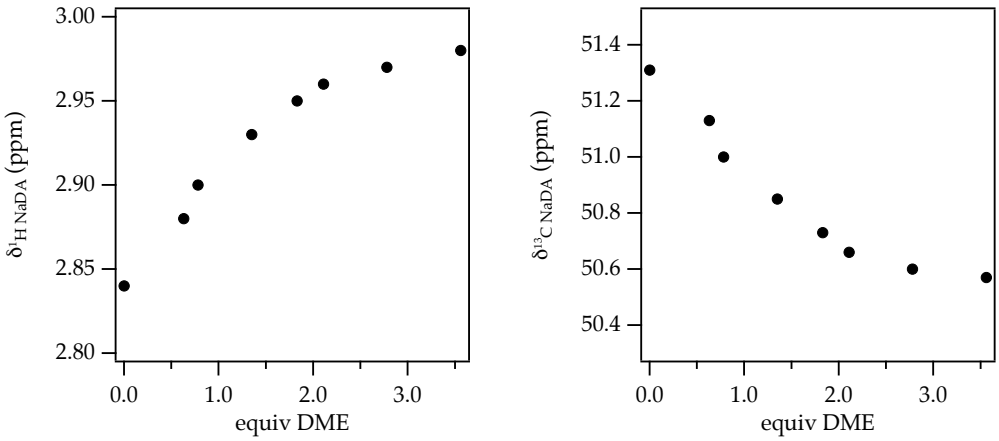

Figure A.2.67.Plots of chemical shift affiliated with NaDA for 0.10 M solutions of NaDA in DMEA with 10% v/v cyclohexane-d_{12} varying DME at –80 °C. Non-quantitative substitution is evidenced by chemical shift saturation at >3.0 equiv DME/Na.

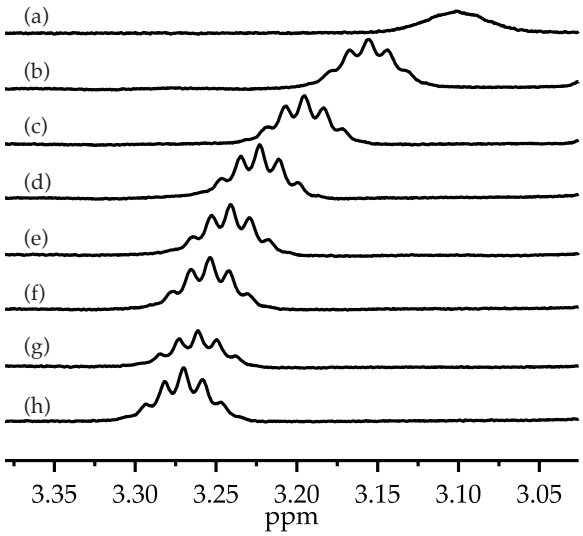

Figure A.2.68.[1]H NMR spectra for 0.10 M solutions of NaDA in DMEA with 10% v/v cyclohexane-d_{12} varying TMEDA at –40 °C. The equivalents of TMEDA in (a)–(h) are 0.00, 0.37, 0.83, 1.43, 1.87, 3.04, 4.61, and 4.99, respectively.

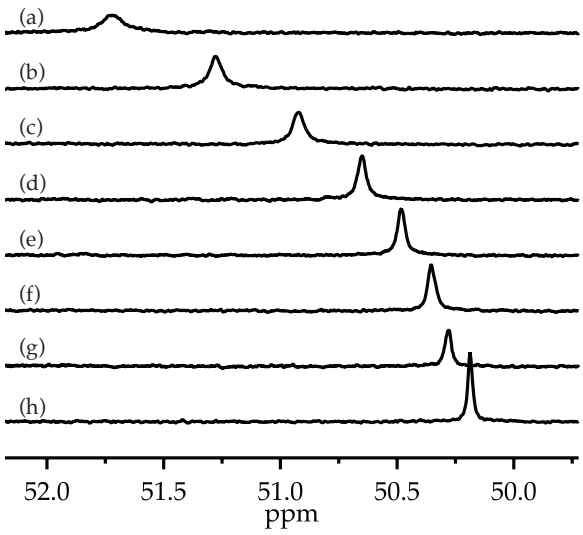

Figure A.2.69.[13]C NMR spectra for 0.10 M solutions of NaDA in DMEA with 10% v/v cyclohexane-d_{12} varying TMEDA at –40 °C. The equivalents of TMEDA in (a)–(h) are 0.00, 0.37, 0.83, 1.43, 1.87, 3.04, 4.61, and 4.99, respectively.

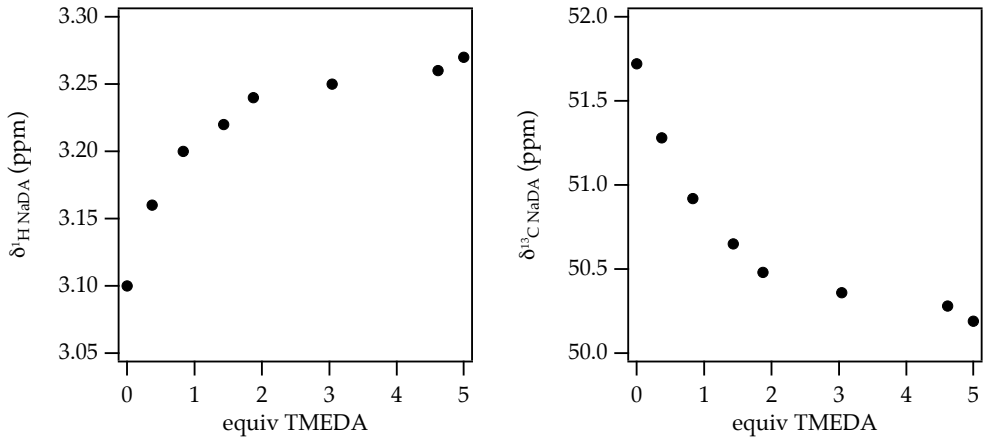

Figure A.2.70.Plots of chemical shift affiliated with NaDA for 0.10 M solutions of NaDA in DMEA with 10% v/v cyclohexane-d_{12} varying TMEDA at –40 °C.

Figures 71 and 72 describe a solvent swap between TMEDA and DME and are fit to the following equilibrium (with the somewhat restrictive but simplifying assumption to exclude a mixed solvate):

$$A_2(TMEDA)_2 \ + \ 2\ DME \ \underset{}{\overset{K_{eq}}{\rightleftharpoons}} \ A_2(DME)_2 \ + \ 2\ TMEDA$$

Assuming that the resonances affiliated with $A_2(TMEDA)_2$ and $A_2(DME)_2$ are time-averaged:

$$\begin{aligned}\delta_{obs} &= \delta_{A_2(TMEDA)_2}\chi_{A_2(TMEDA)_2} + \delta_{A_2(DME)_2}\chi_{A_2(DME)_2} \\ &= \delta_{A_2(TMEDA)_2}\left(1-\chi_{A_2(DME)_2}\right) + \delta_{A_2(DME)_2}\chi_{A_2(DME)_2} \\ &= \delta_{A_2(TMEDA)_2} + \left(\delta_{A_2(DME)_2} - \delta_{A_2(TMEDA)_2}\right)\chi_{A_2(DME)_2} \\ &= \delta_{A_2(TMEDA)_2} + \Delta\delta\chi_{A_2(DME)_2}\end{aligned}$$

What remains is to calculate $\chi_{A_2(DME)_2}$ as a function of χ_{DME}:

$$\begin{aligned}K_{eq} &= \frac{\left[A_2(DME)_2\right]\left[TMEDA\right]^2}{\left[A_2(TMEDA)_2\right]\left[DME\right]^2} \\ &= \frac{\chi_{A_2(DME)_2}\left(2(1-\chi_{DME}) - (1-\chi_{A_2(DME)_2})\right)^2}{\left(1-\chi_{A_2(DME)_2}\right)\left(2\chi_{DME} - \chi_{A_2(DME)_2}\right)^2}\end{aligned}$$

The factor of 2 appearing in the numerator and denominator represents the relative stoichiometry of solvent to NaDA. The fitting expression as input into Igor Pro is:

```
f(xd) = a+b*((1/(6*(1+keq)))*(2*(-2+keq+4*xd+4*keq*xd)+(2*2^(1/3)*((1-
2*xd)^2+keq^2*(1-2*xd)^2+keq*(-7-8*xd+8*xd^2)))/(2-12*xd+24*xd^2-
16*xd^3-2*keq^3*(-1+2*xd)^3+keq*(33-36*xd+72*xd^2-48*xd^3)-
3*keq^2*(7+12*xd-24*xd^2+16*xd^3)+3*Sqrt(3)*Sqrt(keq*(1+keq)^2*(8*(-
1+xd)*(-1+2*xd)^3+8*keq^2*xd*(-1+2*xd)^3+keq*(-1+80*xd+48*xd^2-
256*xd^3+128*xd^4))))^(1/3)+2^(2/3)*(2-12*xd+24*xd^2-16*xd^3-2*keq^3*(-
1+2*xd)^3+keq*(33-36*xd+72*xd^2-48*xd^3)-3*keq^2*(7+12*xd-
24*xd^2+16*xd^3)+3*Sqrt(3)*Sqrt(keq*(1+keq)^2*(8*(-1+xd)*(-
1+2*xd)^3+8*keq^2*xd*(-1+2*xd)^3+keq*(-1+80*xd+48*xd^2-
256*xd^3+128*xd^4))))^(1/3)))
```

(a)

where xd represents χ_{DME}, keq represents K_{eq}, a represents $\delta_{A_2(TMEDA)_2}$, and b represents $\Delta\delta$.

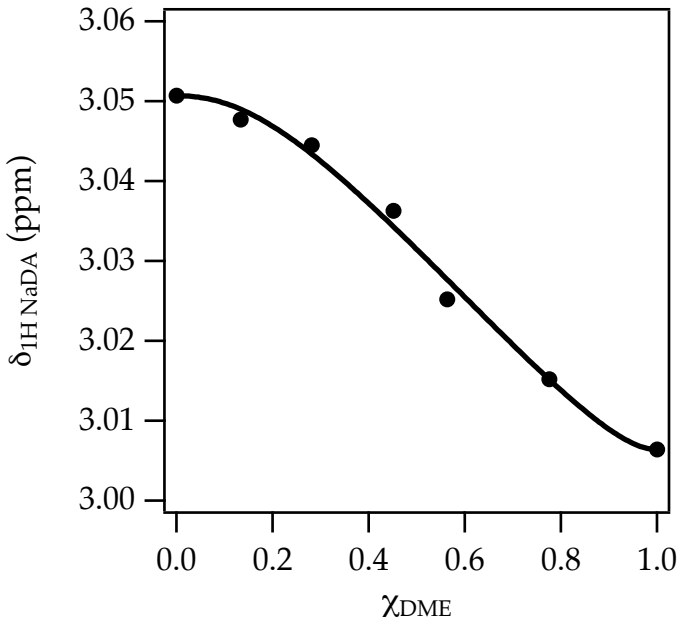

Figure A.2.71.Plot of ^{1}H NMR chemical shift affiliated with NaDA for 0.10 M solutions of NaDA in DMEA with 2 equiv added ligand varying the mole fraction of DME with TMEDA at –80 °C. A best-fit to equation (a) gives K_{eq} = 0.5 ± 0.1; a = 3.0507; b = –0.0443.

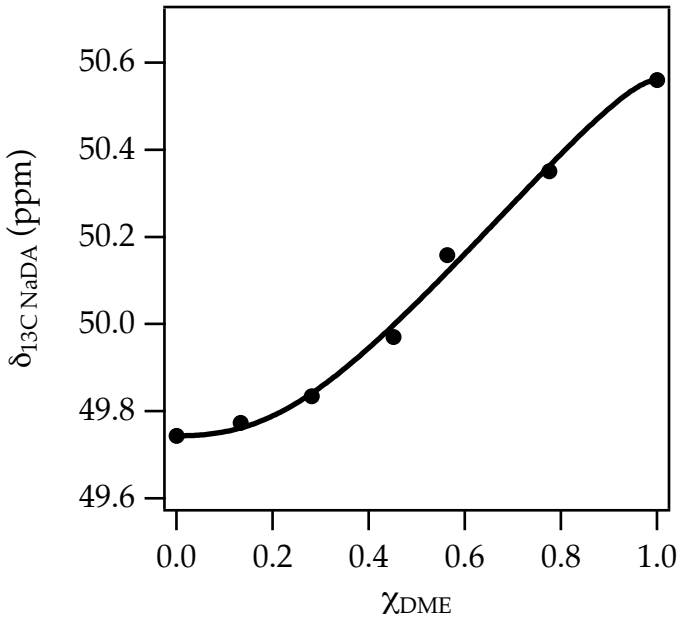

Figure A.2.72.Plot of ^{13}C NMR chemical shift affiliated with NaDA for 0.10 M solutions of NaDA in DMEA with 2 equiv added ligand varying the mole fraction of DME with TMEDA at –80 °C. A best-fit to equation (a) gives K_{eq} = 0.21 ± 0.04; a = 49.744; b = 0.8166.

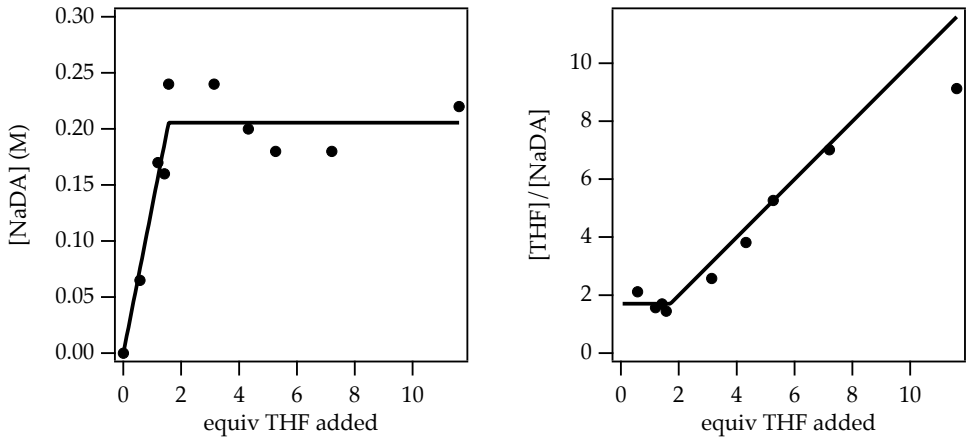

Figure A.2.73.Plots of (a) NaDA solubility vs THF concentration and (b) [THF]/[NaDA] vs THF concentration with solid NaDA suspended in cyclohexane-d_{12} internally standardized with benzene.

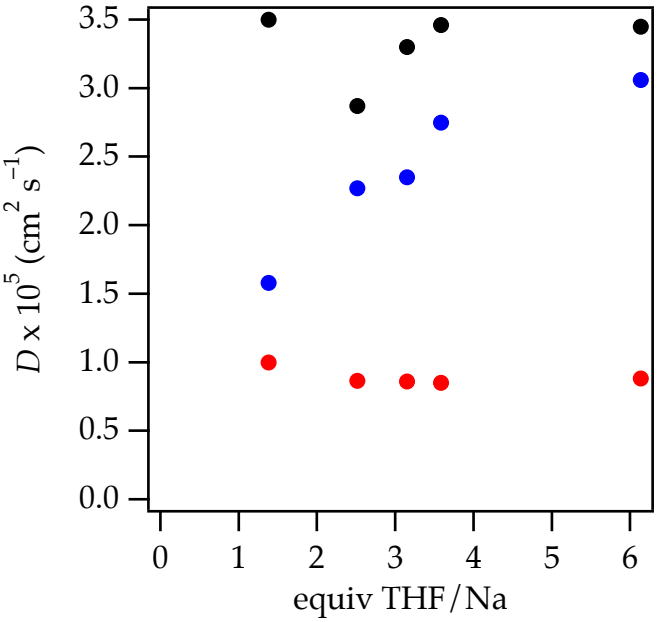

Figure A.2.74.Plot of diffusion constant (NaDA = red points, THF = blue, and benzene = black points) vs equivalents of THF per unit normality of NaDA at 25 °C. THF was titrated into a suspension of NaDA/cyclohexane-d_{12} containing benzene as an internal standard. These data show that below 2 equiv THF/Na the diffusion coefficient of THF approximates that of NaDA implying that all THF is bound. Above 2 equiv THF/Na, the diffusion coefficient of THF rises to that of free, consistent with time-averaging. Furthermore, the diffusion coefficient of NaDA remains invariant.

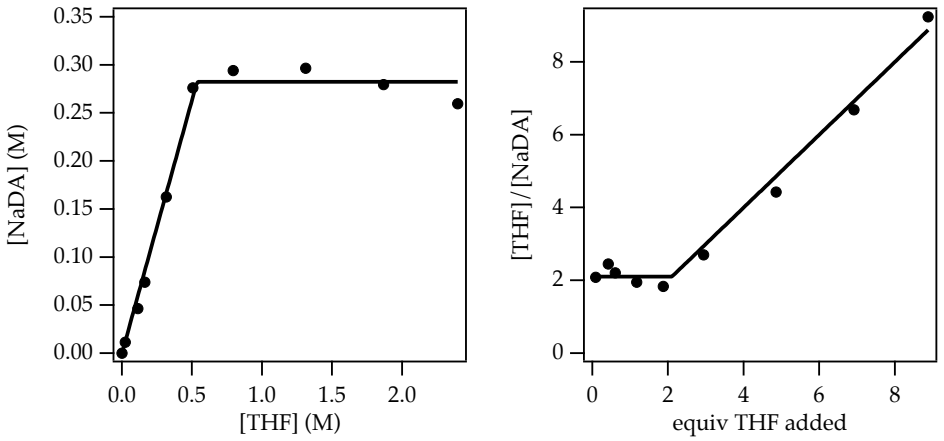

Figure A.2.75.Plots of (a) NaDA solubility vs THF concentration and (b) [THF]/[NaDA] vs THF concentration with solid NaDA suspended in toluene-d_8 internally standardized with benzene. Both plots support a 2:1 THF:NaDA stoichiometry.

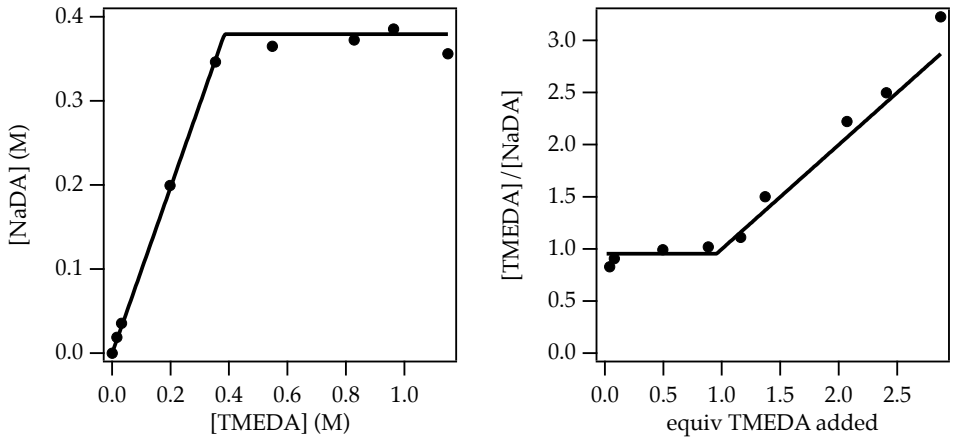

Figure A.2.76.Plots of (a) NaDA solubility vs TMEDA concentration and (b) [TMEDA]/[NaDA] vs THF concentration with solid NaDA suspended in toluene-d_8 internally standardized with benzene. Both plots support a 1:1 TMEDA:NaDA stoichiometry.

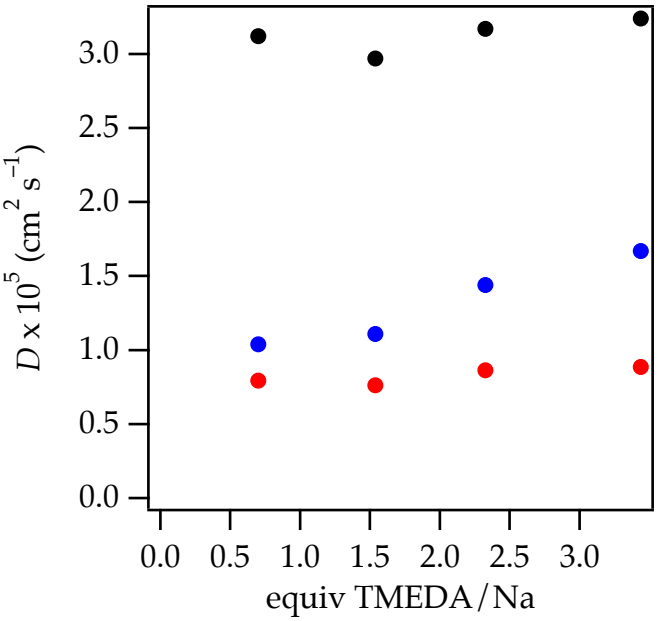

Figure A.2.77.Plot of diffusion constant (NaDA = red points, TMEDA = blue, and benzene = black points) vs equivalents of TMEDA per unit normality of NaDA at 25 °C. TMEDA was titrated into a suspension of NaDA/cyclohexane-d_{12} containing benzene as an internal standard. These data show that below 1 equiv TMEDA/Na the diffusion coefficient of TMEDA approximates that of NaDA implying that all TMEDA is bound. Above 1 equiv TMEDA/Na, the diffusion coefficient of TMEDA rises to that of free, consistent with time-averaging. Furthermore, the diffusion coefficient of NaDA remains invariant.

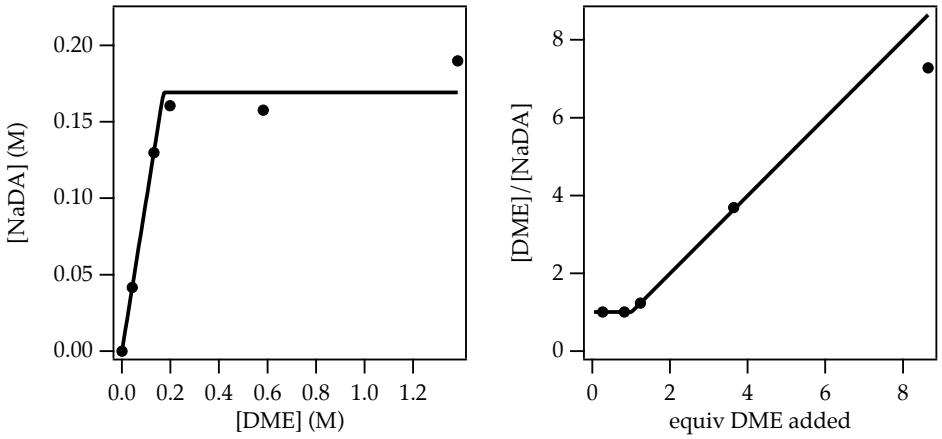

Figure A.2.78.Plots of (a) NaDA solubility vs DME concentration and (b) [DME]/[NaDA] vs DME concentration with solid NaDA suspended in toluene-d_8 internally standardized with benzene. Both plots support a 1:1 DME:NaDA stoichiometry.

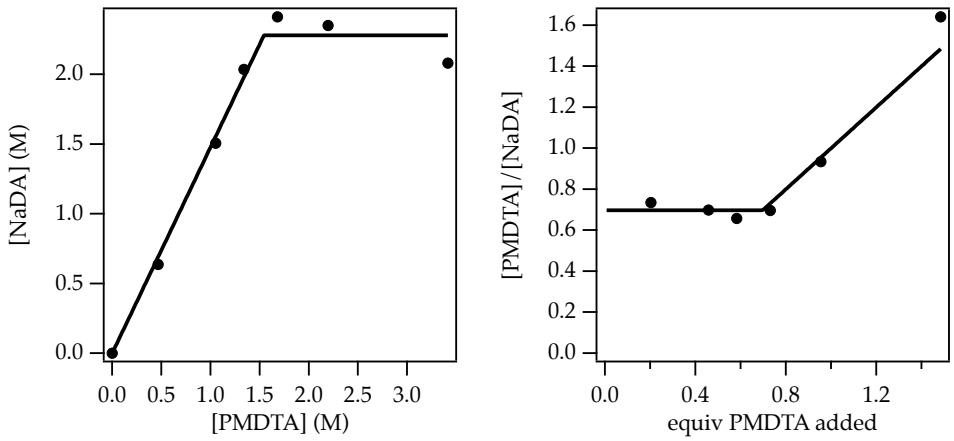

Figure A.2.79.Plots of (a) NaDA solubility vs PMDTA concentration and (b) [PMDTA]/[NaDA] vs PMDTA concentration with solid NaDA suspended in toluene-d_8 internally standardized with benzene. Both plots support substoichiometric binding of PMDTA to NaDA consistent with measurable solubility of both $A_2(PMDTA)_1$ and $A_2(PMDTA)_2$.

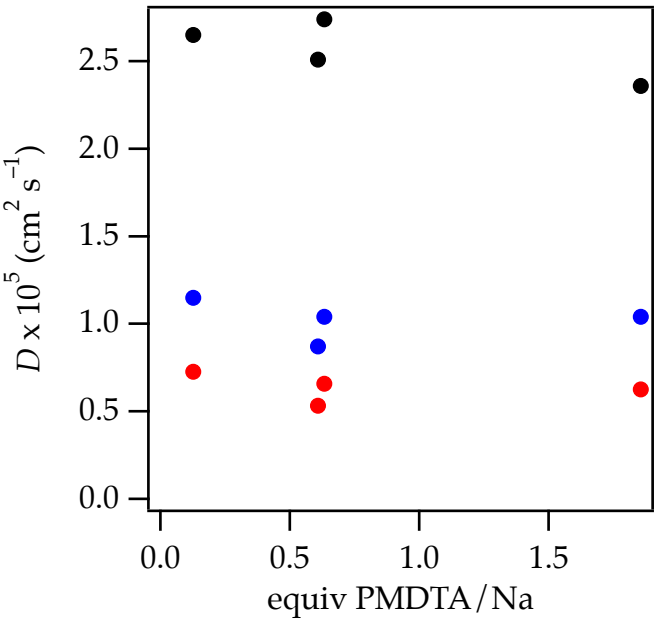

Figure A.2.80.Plot of diffusion constant (NaDA = red points, PMDTA = blue, and benzene = black points) vs equivalents of PMDTA at 25 °C. PMDTA was titrated into a suspension of NaDA/cyclohexane-d_{12} containing benzene as an internal standard.

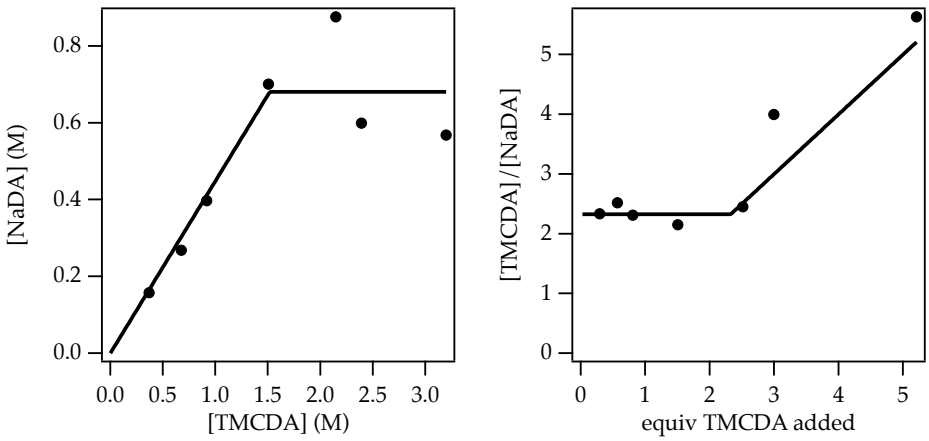

Figure A.2.81.Plots of (a) NaDA solubility vs TMCDA concentration and (b) [TMCDA]/[NaDA] vs TMCDA concentration with solid NaDA suspended in toluene-d_8 internally standardized with benzene. Both plots support a 2:1 TMCDA:NaDA stoichiometry.

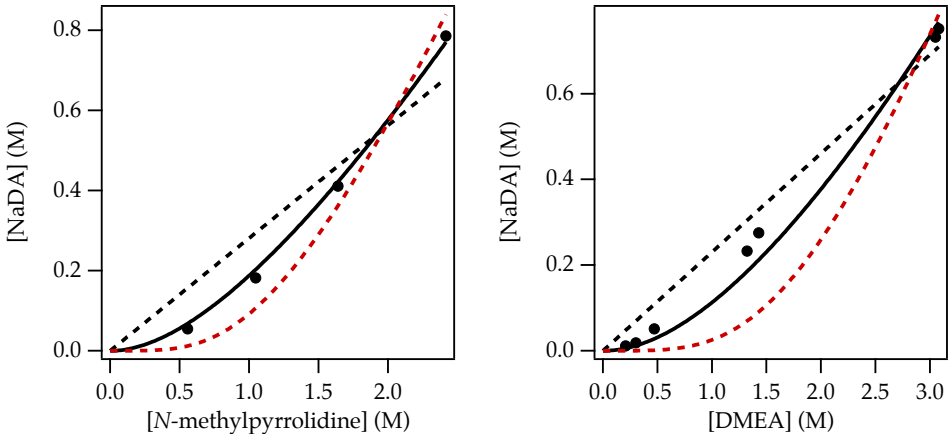

Figure A.2.82.Plots of NaDA solubility vs trialkylamine concentration with solid NaDA suspended in toluene-d_8 internally standardized with benzene. See equation 7 in manuscript. (Solid black line: best fit to disolvated dimer, Black dashed line: best fit to monosolvated dimer, red dashed line: best fit to tetrasolvated dimer). Both plots suggest a stoichiometry of 2 trialkylamine/NaDA dimer.

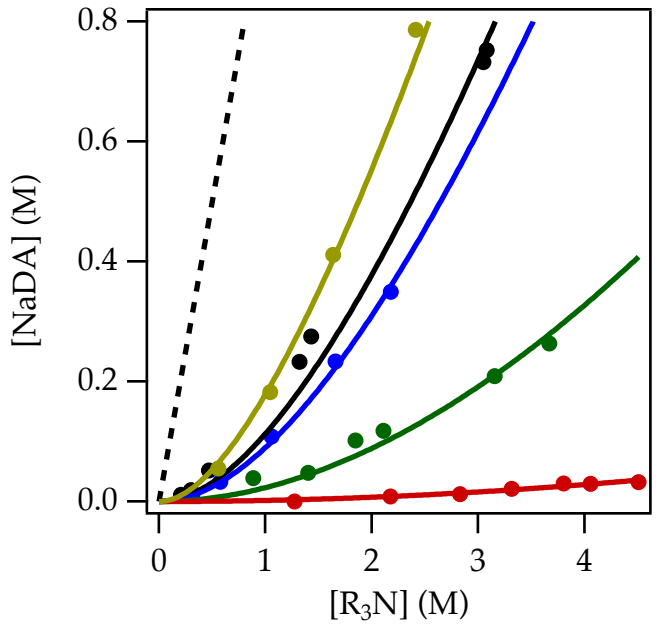

Figure A.2.83.Plot of NaDA solubility vs trialkylamine concentration with solid NaDA suspended in toluene-d_8 internally standardized with benzene. The dashed line represents quantitative solubilization to disolvated dimer. All traces represent unweighted least-squares fits to [NaDA]=(1/K_{solv}+4[R_3N]–Sqrt(1+8K_{solv}[R_3N])/K_{solv})/4 according to to disolvated dimer in equilibrium with solid NaDA. The trialkylamines and corresponding equilibrium constants are: *N*-methylpyrrolidine (yellow trace, K_{solv} = 0.132 ± 0.005); DMEA (black trace, K_{solv} = 0.102 ± 0.003); DMBA (blue trace, K_{solv} = 0.054 ± 0.001); *N,N*-diethylmethylamine (green trace, K_{solv} = 0.0121 ± 0.0007); and triethylamine (red trace, K_{solv} = 0.00089 ± 0.00004).

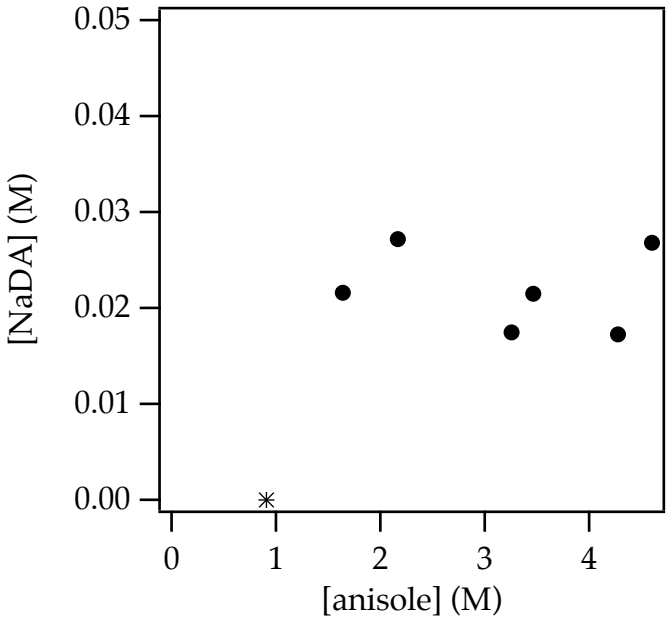

Figure A.2.84.Plot of NaDA solubility vs anisole concentration with solid NaDA suspended in toluene-d_8 internally standardized with benzene. Anisole does not appreciably solubilize NaDA.

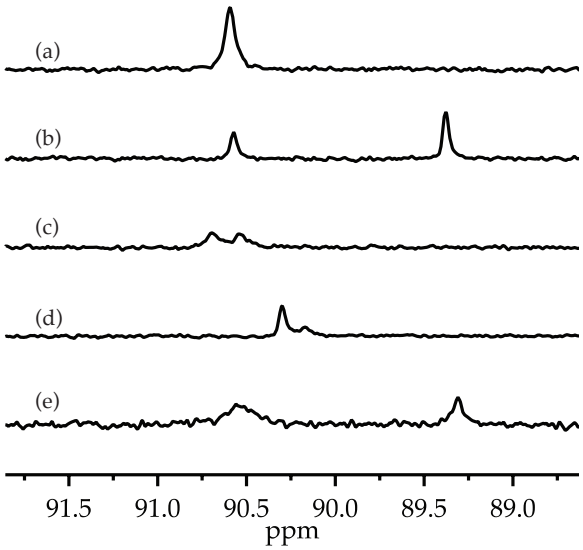

Figure A.2.85.[15]N NMR spectra for total titer of 0.30 M solutions of NaDA in DMEA with 10% v/v benzene-d_6 or cyclohexane-d_{12} recorded at –80 °C for (a) NaDA, and with (b) equimolar (b) NaTMP, (c) sodium *cis*-2,6-dimethylpiperidide, (d) sodium diisobutylamide, and (e) sodium hexamethyldisilazide. Heteroaggregation within the class of sodium amides is notable.

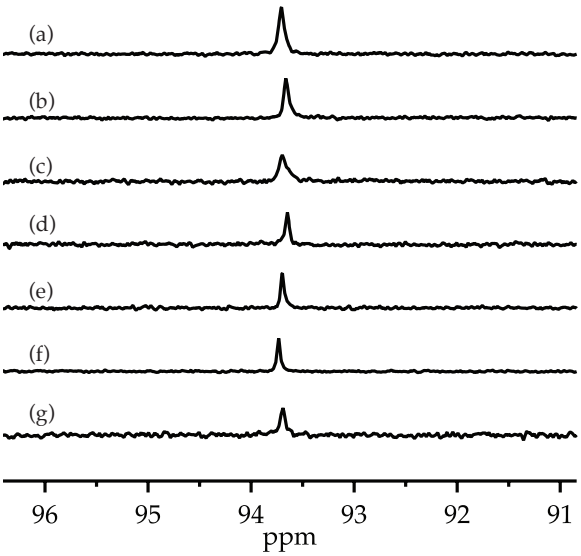

Figure A.2.86.[15]N NMR spectra for 0.30 M solutions of NaDA in DMEA with 10% v/v benzene-d_6 or cyclohexane-d_{12} recorded at –80 °C with equimolar (b) *n*-BuNa, (c) 2,6-dimethoxyphenylsodium, (d) sodium cycloheptenolate, (e) sodium *iso*-butoxide, (f) sodium *tert*-butoxide, and (g) sodium phenolate. Absence of resolved heteroaggregation is notable.

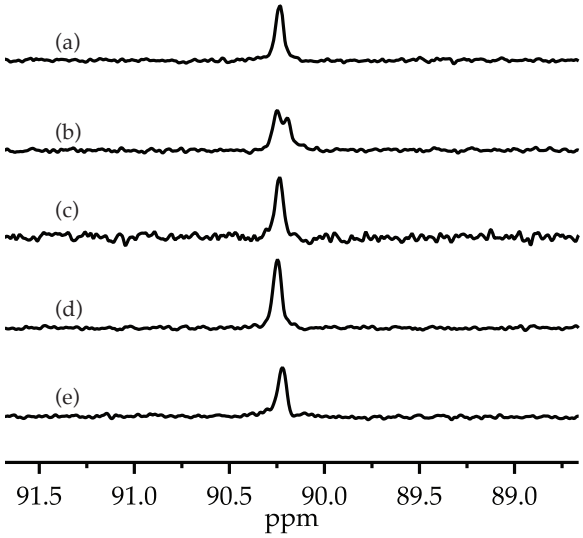

Figure A.2.87.[15]N NMR spectra for 0.40 M total base titer of NaDA in THF with 10% v/v cyclohexane-d_{12} with varying equimolar sodium salts at –80 °C. The salts in are (b) sodium isopropylcyclohexylamide, (c) sodium hexamethyldisilazide, (d) sodium *tert*-butoxide, and (e) sodium *iso*-butoxide. The absence of apparent mixed aggregation for NaHMDS is notable.

II. Rate Studies

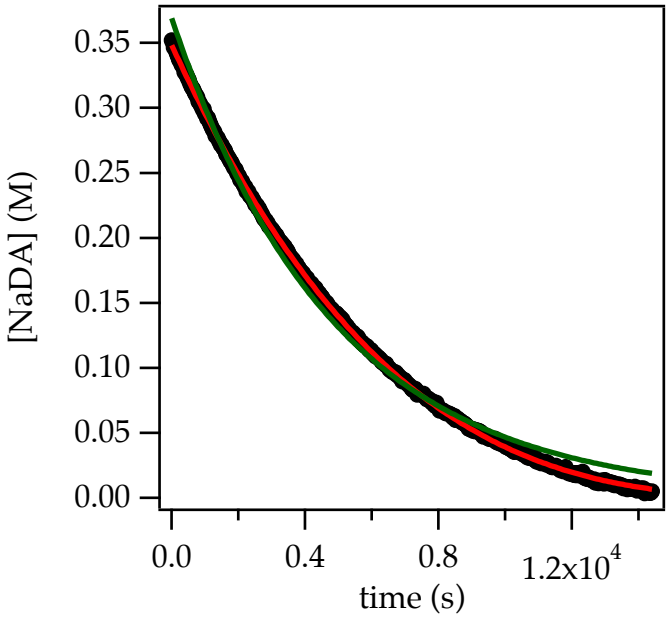

Figure A.2.88.Plot of NaDA concentration vs time in neat THF at 25 ºC followed with ^{1}H NMR. The green curve depicts an unweighted least-squares fit to the function $f(t) = ae^{-kt}$: a = 0.369 ± 0.004; k = (2.07 ± 0.01) × 10^{-4}. The red curve depicts an unweighted least-squares fit to the function $f(t) = ([A]_0^{(1-n)} - kt(1-n))^{1/(1-n)}$: $[A]_0$ = 0.3484 ± 0.0002; n = 0.698 ± 0.002, k = (1.061 ± 0.009) × 10^{-5}.

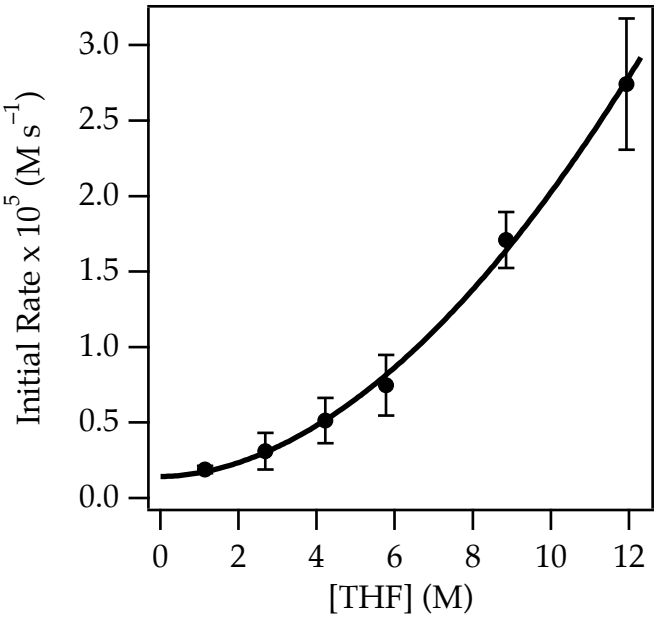

Figure A.2.89.Plot of initial rates vs THF concentration for the decomposition of THF with 0.20 M NaDA at 25 ºC. The curve depicts an unweighted least-squares fit to the function $f(x) = ax^b + c$: $a = (2.5 \pm 0.8) \times 10^{-2}$; $b = 1.9 \pm 0.1$; $c = (1.4 \pm 0.5) \times 10^{-1}$.

[THF] (M)	Initial rate × 10^5 (M s^{-1})	Standard deviation × 10^5 (M s^{-1})
1.1	0.19	0.02
2.7	0.3	0.1
4.2	0.5	0.1
5.8	0.7	0.2
8.9	1.7	0.2
11.9	2.7	0.4

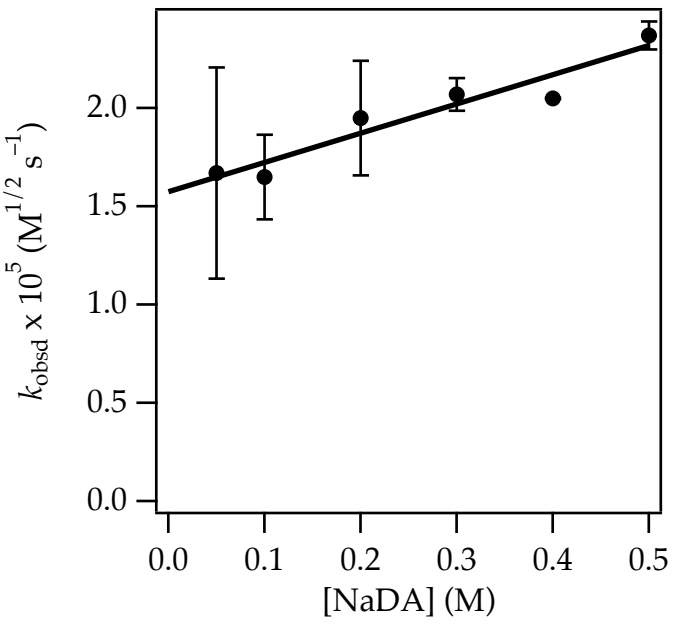

Figure A.2.90.Plot of half-order rate constants vs NaDA concentration for the decomposition of THF in neat THF at 25 ºC. The curve depicts an unweighted least-squares fit to the function $f(x) = ax + b$: $a = 1.5 \pm 0.2$; $b = 1.58 \pm 0.07$.

[NaDA] (M)	$k_{obsd} \times 10^5$ ($M^{1/2}$ s^{-1})	Standard deviation $\times 10^5$ ($M^{1/2}$ s^{-1})
0.05	1.7	0.5
0.10	1.7	0.2
0.20	2.0	0.3
0.30	2.07	0.08
0.40	2.05	0.003
0.50	2.37	0.07

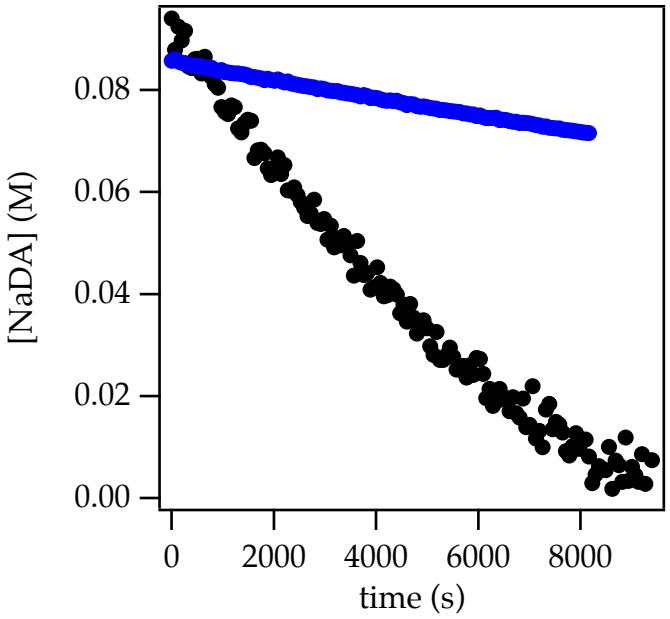

Figure A.2.91.Plot of NaDA concentration versus time in neat THF (black trace) and in neat THF-d_8 (blue trace) at 25 °C followed by ^{1}H NMR. This corresponds to an isotope effect of $k_H/k_D = 7.2$.

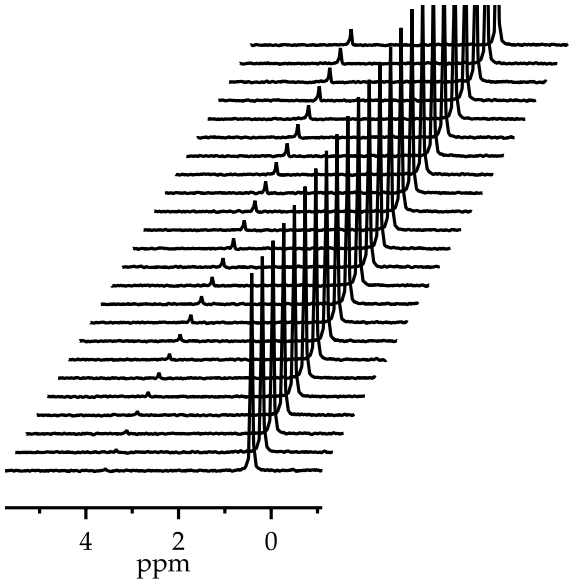

Figure A.2.92.^{2}H NMR spectra of 0.20 M NaDA in 6.15 M THF and 3.57 M *N*-deuteriodiisopropylamine at 25 °C over the course of 1.3 hours. Appearance of a deuterium resonance at 3.58 ppm represents selective isotopic exchange into the alpha position of THF.

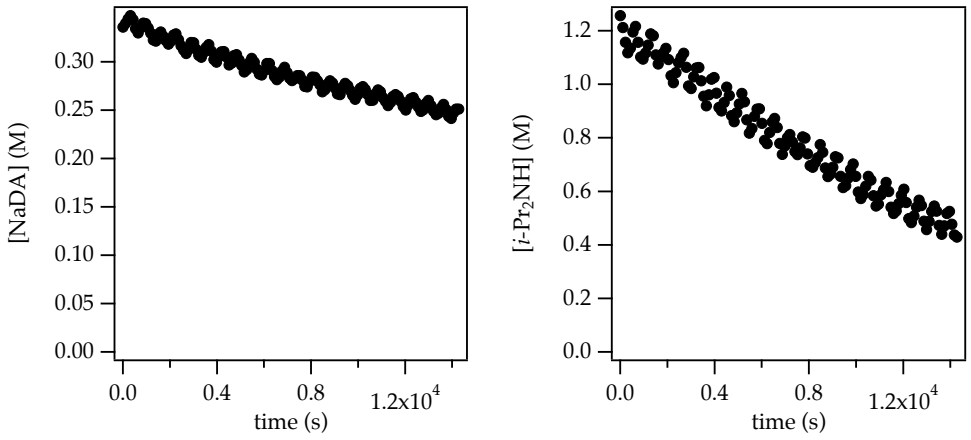

Figure A.2.93.Plots of NaDA and *N*-protiodiisopropylamine isotopologue concentration versus time in 10.3 M THF-d_8 at 25 °C. These demonstrate competitive NaDA decomposition and NaDA-mediated isotopic exchange of THF and diisopropylamine.

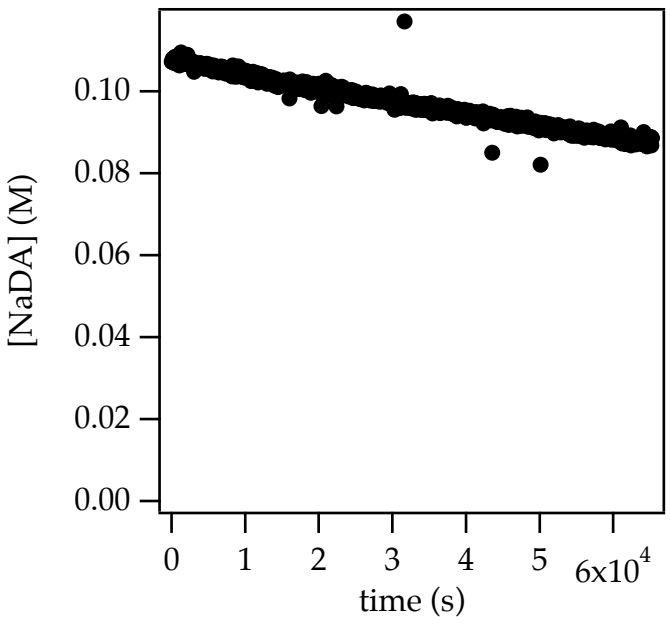

Figure A.2.94.Plot of NaDA concentration versus time in 2.3 M 3,3,4,4-tetradeuteriotetrahydrofuran/hexane at 25 °C. This rate of decomposition corresponds to an isotope effect of $k_H/k_D = 6$.

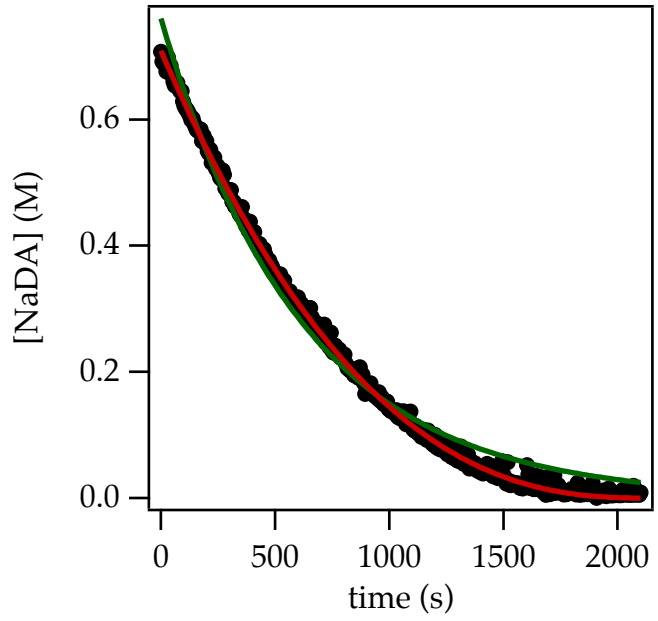

Figure A.2.95.Plot of NaDA concentration vs time in 4.41 M 1,2-dimethoxyethane at –10 ºC. The green curve depicts an unweighted least-squares fit to the function $f(t) = ae^{-kt}$: $a = 0.76 \pm 0.005$; $k = (1.63 \pm 0.01) \times 10^{-3}$. The red curve depicts an unweighted least-squares fit to the function $f(t) = ([A]_0^{(1-n)} - kt(1-n))^{1/(1-n)}$: $[A]_0 = (1.63 \pm 0.01) \times 10^{-3}$; $n = 0.605 \pm 0.007$, $k = (1.00 \pm 0.009) \times 10^{-3}$.

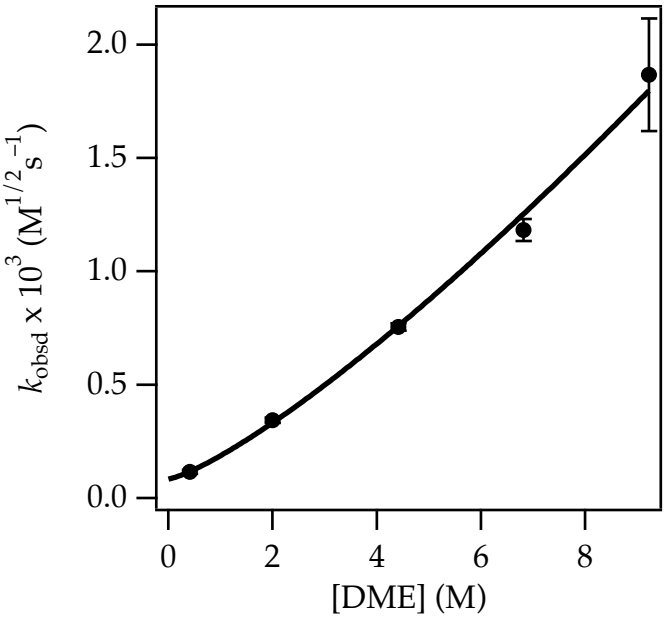

Figure A.2.96.Plot of k_{obsd} vs DME concentration for the decomposition of DME with 0.40 M NaDA at –10 ºC. The curve depicts an unweighted least-squares fit to the function $f(x) = ax^b + c$: $a = 0.10$; $b = 1.3$; $c = 0.08$.

[DME] (M)	$k_{obsd} \times 10^3$ ($M^{1/2}$ s^{-1})	Standard deviation $\times 10^3$ ($M^{1/2}$ s^{-1})
0.41	0.116	0.009
2.00	0.34	0.01
4.41	0.75	0.02
6.81	1.18	0.05
9.22	1.9	0.2

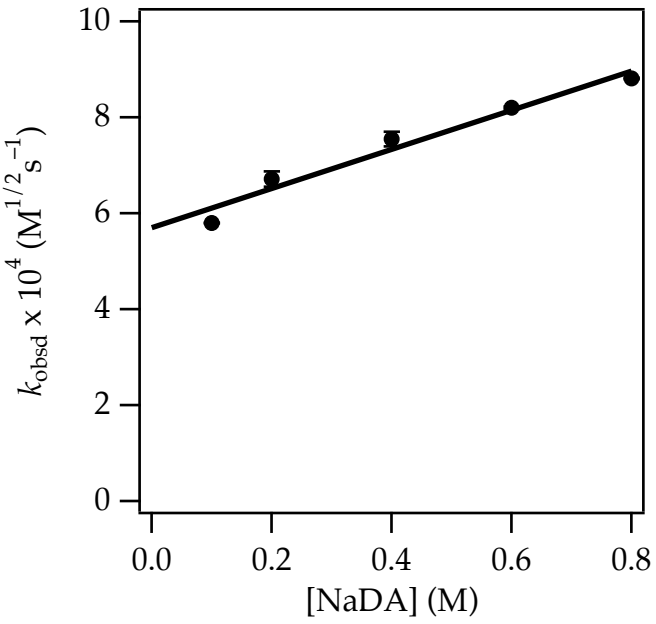

Figure A.2.97.Plot of k_{obsd} vs NaDA concentration in 4.41 M 1,2-dimethoxyethane at –10 ºC. The green curve depicts an unweighted least-squares fit to the function $f(x) = ax + b$: $a = 4.1 \pm 0.5$; $k = 5.7 \pm 0.2$.

[NaDA] (M)	$k_{obsd} \times 10^3$ ($M^{1/2}$ s^{-1})	Standard deviation $\times 10^3$ ($M^{1/2}$ s^{-1})
0.10	5.801	0.006
0.20	6.7	0.2
0.40	7.5	0.2
0.60	8.20	0.02
0.80	8.81	0.02

Chapter 3

Sodium Diisopropylamide in Tetrahydrofuran:

Selectivities, Rates, and Mechanisms of

Alkene Isomerizations and Diene Metalations

Sodium Diisopropylamide in Tetrahydrofuran: Selectivities, Rates, and Mechanisms of Alkene Isomerizations and Diene Metalations

Abstract

Sodium diisopropylamide in tetrahydrofuran is an effective base for the metalation of 1,4-dienes and isomerization of alkenes. Dienes metalate via tetrasolvated sodium amide monomers, whereas 1-pentene is isomerized by trisolvated monomers. Facile, highly *Z*-selective isomerizations are observed for allyl ethers under conditions that compare favorably to those of existing protocols. The selectivity is independent of the substituents on the allyl ethers; rate and computational data show that the rates, mechanisms, and roles of sodium–oxygen contacts are substituent-dependent. The competing influences of substrate coordination and solvent coordination to sodium are discussed.

Introduction

Sodium diisopropylamide (NaDA) is a case study of reagent popularity within the synthetic organic community. First prepared by Levine in 1959,[1] NaDA is demonstrably more reactive than lithium diisopropylamide (LDA).[2] During the intervening half century, however, NaDA has been used in approximately a dozen studies,[3] whereas LDA is probably used thousands of times *daily*. What explains this huge disparity? We believe inconvenience plays a role: NaDA is insoluble in inert hydrocarbons and unstable in solubilizing ethereal solvents, which makes it difficult to handle as stock solutions.

From previous studies of lithium amides solvated by simple trialkylamines[4]—an overlooked and underappreciated class of solvents—we surmised that NaDA might be soluble and stable. Indeed, 1.0 M solutions of NaDA in *N,N*-dimethylethylamine (DMEA), *N,N*-dimethylbutylamine, or *N*-methylpyrrolidine are homogeneous and stable for weeks at room temperature and for months and possibly years with refrigeration. *NaDA/trialkylamine solutions can be prepared in 15 min from unpurified commercial reagents*, however, which means that long-term storage is unnecessary. As strange as it may sound, organosodium chemistry is likely in its infancy.[5,6]

Our first study illustrated the synthetic importance of NaDA in DMEA by metalating a dozen functionally diverse substrates and comparing the rates and selectivies with LDA in tetrahydrofuran (THF).[7] Subsequent structural studies showed that NaDA is dimeric when solvated by a number of mono-, di-, and trifunctional solvents.[8] Tetrasolvated dimer **1** is germane to the work described herein.

The current study explored NaDA-mediated metalations of alkenes and dienes in THF to probe the role of aggregation and solvation (Scheme 3.1). We examined whether potentially coordinating substituents influence rate and mechanism through direct sodium–ligand interactions or through induction.

Scheme 3.1. Summary of alkene and diene metalation with NaDA/THF.

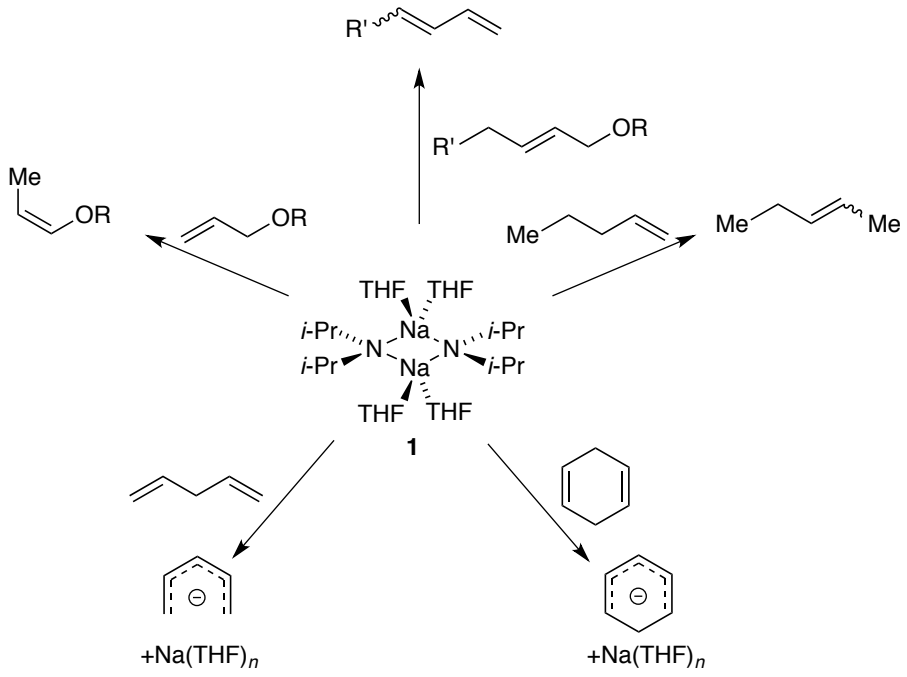

Results

General. Stock solutions of 1.0 M NaDA in DMEA were prepared as described previously.[7] (The importance of using fresh sodium dispersion cannot be overstated.) NaDA was crystallized from DMEA/hexane for spectroscopic and rate studies despite no evidence that this added precaution has a significant effect.[8] Solutions of NaDA in neat DMEA containing >4.0 equiv of THF contained exclusively (>95%) THF solvate **1**.[8]

The metalation and isomerization rates were monitored by following the alkene and diene absorbances using a combination of in situ IR[9] and ^{1}H NMR spectroscopies. Control experiments showed that DMEA and hexane could be used interchangeably as cosolvents without detectable changes in reactivity. The temperature for IR spectroscopy was controlled using baths

comprising ice/water (0 °C), dry ice/acetone (–78 °C), liquid nitrogen/methanol (–95 °C), and liquid nitrogen/Et_2O (–116 °C). The reproducibility of the latter two temperatures surprised us.

Rate studies were carried out at standard yet variable concentrations of NaDA (0.025–0.40 M) and THF (1.00–12.3 M) in either DMEA or hexane cosolvent, whereas the substrate concentrations were typically low (0.0050 M) to maintain pseudo-first-order conditions. Non-linear least-squares fits to the decays of the substrate afforded pseudo-first-order rate constants (k_{obsd}). The method of initial rates was used when pseudo-first-order conditions were not rigorously established. Reactions with equimolar base and substrate showed no evidence of autocatalysis or autoinhibition.

1-Pentene Isomerization. The metalation of 1-pentene with NaDA/THF to provide pentenyl sodium is endothermic. Nonetheless, facile isomerization of 1-pentene was observed in the presence of NaDA/THF at 25 °C via the presumed intermediacy of pentenyl sodium. Monitoring with ^{1}H NMR spectroscopy showed an initial formation of 2-pentene as a 1:1 cis/trans mixture that slowly equilibrated to a 1:4 cis/trans mixture (eq 3.1; see Figure 3.1). The proportions of *cis*- and *trans*-2-pentene at early conversion were independent of THF and NaDA concentrations, confirming that both are formed via isomeric transition states. Plots of the initial rates for the loss of 1-pentene versus THF concentration (Figure 3.2) and NaDA concentration (Figure 3.3) revealed first- and half-order dependencies, respectively. The overall rate law described by eq 3.2 is consistent with a trisolvated-monomer-based transition structure, $[A(THF)_3]^{‡}$ (eqs 2 and 3; 'A' denotes a NaDA subunit).[10]

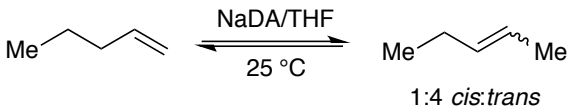

(3.1)

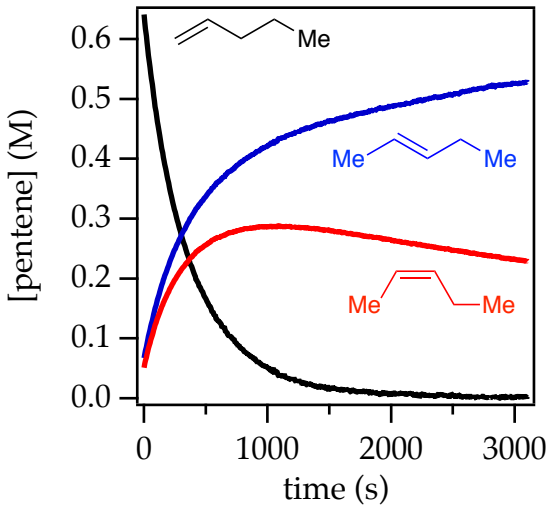

Figure 3.1. Plot of alkene concentration versus time measured with ^{1}H NMR spectroscopy for the isomerization of 0.76 M 1-pentene with 0.18 M NaDA and 0.59 M diisopropylamine in 8.83 M THF/hexane at 25 °C. The traces show 1-pentene (black), *trans*-2-pentene (blue), and *cis*-2-pentene (red) at partial equilibration.

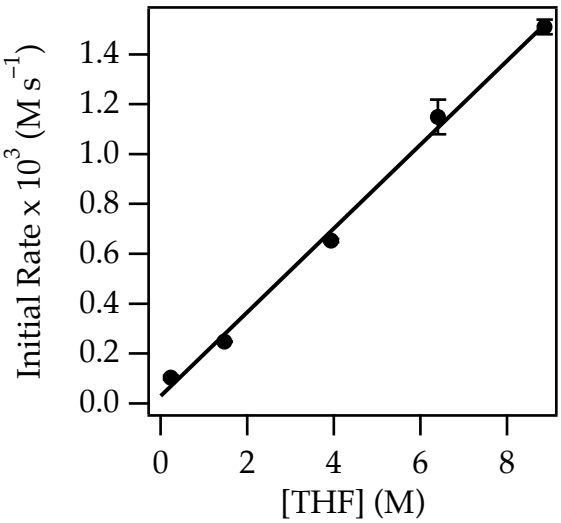

Figure 3.2. Plot of initial rates versus THF concentration for the isomerization of 0.76 M 1-pentene (eq 3.1) with 0.18 M NaDA and 0.59 M diisopropylamine in hexane cosolvent at 25 °C. The curve depicts an unweighted least-squares fit to the function $f(x) = ax + b$: $a = 0.168 \pm 0.006$; $b = 0.03 \pm 0.03$.

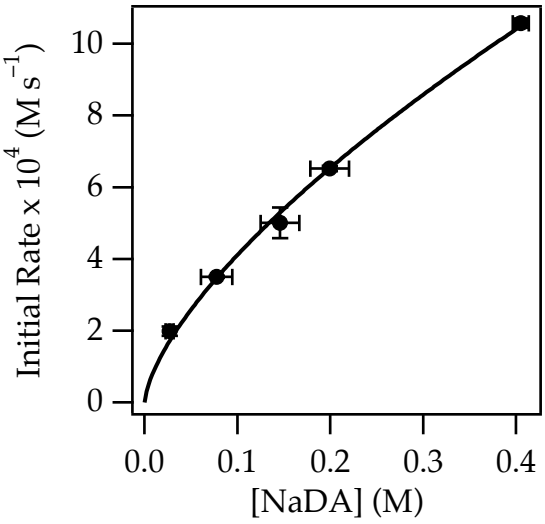

Figure 3.3. Plot of initial rates versus NaDA concentration for the isomerization of 0.76 M 1-pentene (eq 3.1) with 0.59 M diisopropylamine in 3.93 M THF/hexane at 25 °C. The curve depicts an unweighted least-squares fit to the function $f(x) = ax^b$: $a = 19.2 \pm 0.8$; $b = 0.67 \pm 0.03$. Covariance is used because the NaDA titer was measured.

$$-\text{d[1-pentene]}/\text{d}t = k\text{[1-pentene][THF][A}_2\text{(THF)}_4\text{]}^{1/2} \qquad (3.2)$$

$$1/2\ \text{A}_2\text{(THF)}_4 + \text{THF} + \text{1-pentene} \longrightarrow [\text{A(THF)}_3\cdot\text{1-pentene}]^{\ddagger} \qquad (3.3)$$

The reaction coordinate for metalation was examined using density functional theory (DFT) calculations at the B3LYP/6–31G(d) level of theory with single-point MP2 calculations.[11] Transition structures ***Z*-2** and ***E*-2**, affording *cis*- and *trans*-2-pentene, respectively, predicted a modest trans selectivity (eq 3.4) that was not borne out experimentally. A distinct p interaction between sodium and the developing allyl anion was visible in both cases.[12]

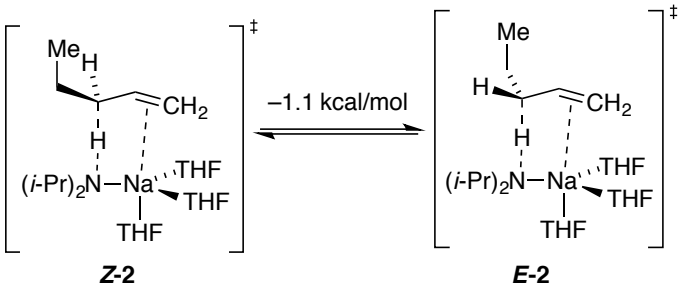

***Z*-2** ***E*-2** (3.4)

Allyl Ether Isomerizations. NaDA-mediated metalations of allyloxy ethers **3a**–**d** are also endothermic, but the catalyzed isomerizations afforded enol ethers **4a**–**d**[13] in synthetically useful >50:1 *Z*:*E* selectivities (eq 3.5). Analogously selective isomerizations have been reported by Williard and co-workers[14] using LDA/THF but are >1000-fold slower.[15] Monitoring the isomerization of allyl methyl ether with NaDA in THF at –116 °C revealed a first-order THF dependence and half-order NaDA dependence (supporting information), which implicated a trisolvated-monomer-based metalation (eqs 6 and 7). DFT computations showed a strong preference for transition structure ***Z*-5a** relative to ***E*-5a**. Distinct methoxy–sodium interactions were observed in lieu of the allyl–sodium interactions observed with simple alkenes (eq 3.8). The energies were consistent with the *Z* selectivity.

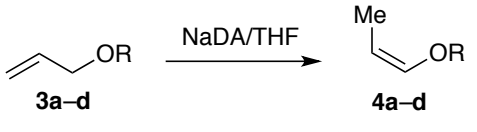

3a–d **4a–d** (3.5)

a; R = Me ; –116 °C
b; R = $SiMe_3$; –78 °C
c; R = Si(*t*-Bu)Me_2; –78 °C
d; R = Si(*i*-Pr)$_3$; 0 °C
} >50:1 *Z*:*E*

$$-d[\mathbf{3a}]/dt = k[\mathbf{3a}][THF][A_2(THF)_4]^{1/2} \quad (3.6)$$

$$1/2\ A_2(THF)_4 + THF + \mathbf{3a} \longrightarrow [A(THF)_3 \cdot (\mathbf{3a})]^{\ddagger} \quad (3.7)$$

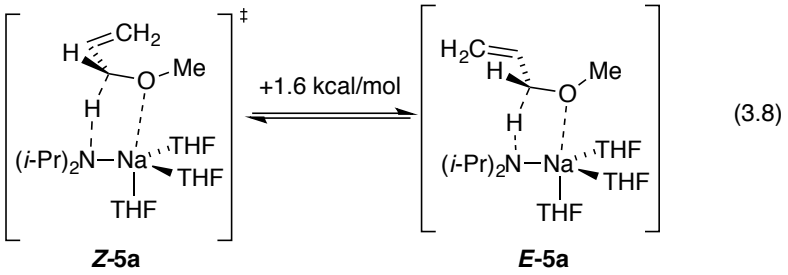

***Z*-5a** ***E*-5a** (3.8)

Trimethylsilyl groups are often suggested to suppress O–Li interactions owing to a combination of steric and electronic effects,[16] and the *tert*-butyldimethylsilyl moiety is larger. Of course, this conventional wisdom gleaned largely from empirical evidence—even if true—may not apply to organosodium reagents. In the event, the highly *Z*-selective isomerizations (eq 3.5) occurred at the approximate relative rates: methyl (1), trimethylsilyl (10^{-1}), *tert*-butyldimethylsilyl (10^{-2}), and triisopropylsilyl (10^{-4}). Rate studies (supporting information) revealed that the trimethylsilyl ether isomerized at –78 °C via monomer-based transition structure $[A(THF)_3(\mathbf{3b})]^{\ddagger}$, which is analogous to that for the isomerization of allyl methyl ether; the high *Z* preference is reflected in eq 3.9. A small non-zero intercept was consistent with $[A(THF)_2(\mathbf{3b})]^{\ddagger}$. The *tert*-butyldimethylsilyl ether isomerized at –78 °C and was shown kinetically to occur via a *disolvated* monomer, $[A(THF)_2(\mathbf{3c})]^{\ddagger}$, while retaining a high *Z* preference supported computationally (eq 3.10). Given that the loss of primary shell solvation is typically endothermic by >5 kcal/mol, the rate reduction is surprisingly muted. The

triisopropylsilyl ether isomerized at 0 °C and was shown kinetically to metalate via trisolvated monomer $[A(THF)_3(\mathbf{3d})]^{‡}$ while retaining the *Z* selectivity observed experimentally and supported computationally (eq 3.11). We return to the role of stereoelectronic control and changing solvation numbers in the discussion.

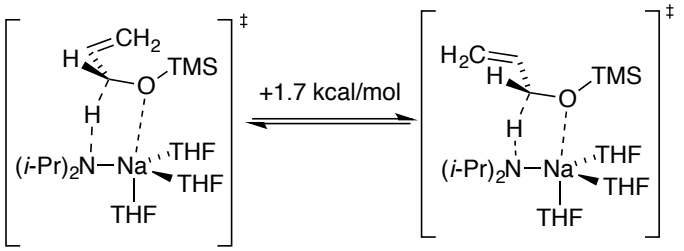

***Z*-5b** ***E*-5b** (3.9)

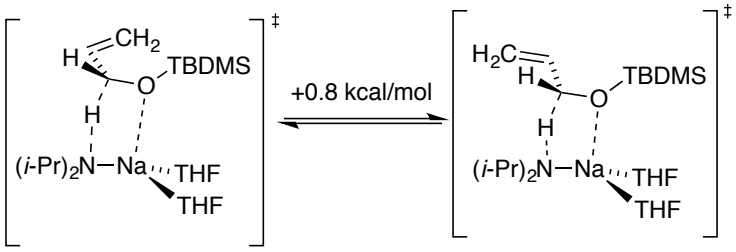

***Z*-5c** ***E*-5c** (3.10)

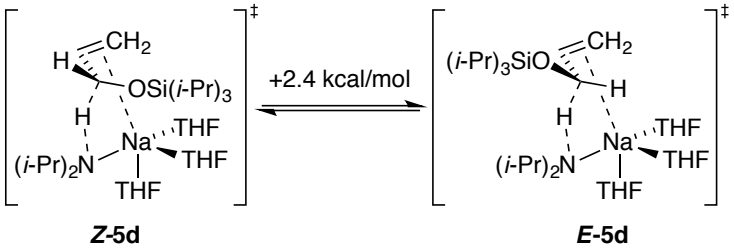

***Z*-5d** ***E*-5d** (3.11)

Isomerization of allyloxy-*tert*-butyldimethylsilane **3c** using NaDA in neat THF containing 3 equiv of $(i\text{-Pr})_2$ND with monitoring by ^{1}H NMR spectroscopy showed <20% deuterium incorporation in ***Z*-4c**, indicating that the proton transfer is intramolecular. The sequence in Scheme 3.2 is computationally viable. The Na–N contact stretches to ~3.5 Å computationally en route to ***Z*-8c** while the proton reorients toward the allyl anion terminus.

Scheme 3.2. Intramolecular proton transfer in allyloxy to enol ether conversion.

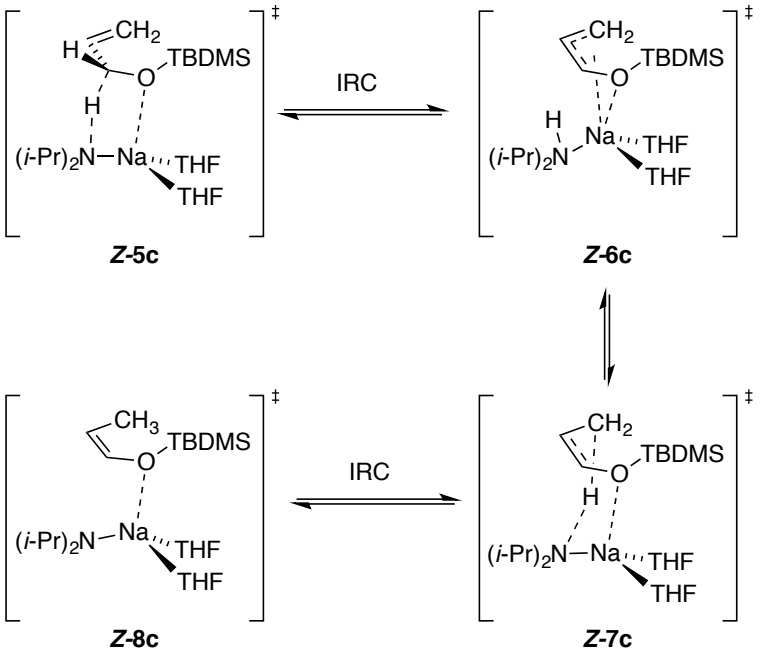

Isomerization: Catalysis. The isomerizations described above, although carried out stoichiometrically in the rate studies, were inherently catalytic in NaDA. The simplicity of a catalytic protocol is illustrated in eq 3.12. Treatment of *neat* allyloxytrimethylsilane with 6.5% NaDA monitored with ^{1}H NMR spectroscopy showed quantitative conversion to **4b** in 30–60

seconds at room temperature. Compared with other protocols, this preparation is a remarkably simple one for a useful synthon.[14,17]

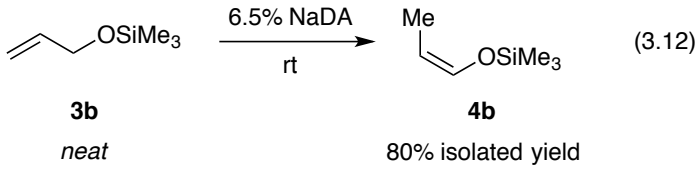

(3.12)

Allyloxy 1,4-Eliminations. The high *Z* selectivity for allyl ether isomerization prompted us to examine substituted allyl ethers as putative substrates, but 1,4-eliminations intervened (eqs 13 and 14) to the exclusion of isomerization. The volatile alkenes in eq 3.13 were formed cleanly as shown by ^{1}H NMR spectroscopy. Myrcene (**10**) was isolated pure in excellent yield.

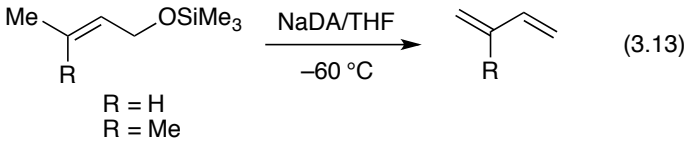

(3.13)

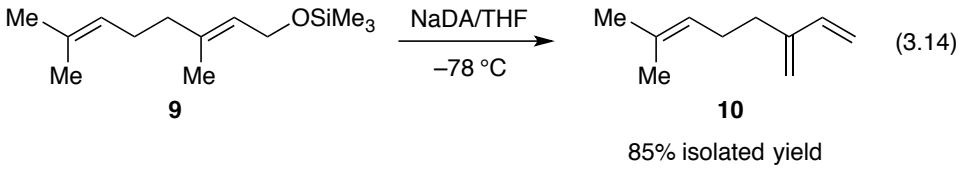

(3.14)

Diene Metalations. 1,4-Dienes are sufficiently acidic to metalate exothermically with NaDA in THF (eq 3.15) and afford synthetically useful dienyl sodiums at rates that outpace those of alternative deprotonations with BuLi/TMEDA and LDA/THF. Monitoring the reaction of 1,4-cyclohexadiene with NaDA in 2.0–10 M THF at –95 °C showed a loss of substrate (1642 cm^{-1}) and the formation of the cyclohexadienyl sodium (1558 cm^{-1}). The transformation was confirmed by trapping the resulting sodium salt with TIPSCl.[7] Rate studies using IR

spectroscopy (supporting information) showed a first-order dependence on diene, half-order dependence on NaDA, and second-order dependence on THF (eq 3.16) consistent with a tetrasolvated-monomer-based transition structure as depicted in eq 3.17. Although the $A(THF)_4$ fragment in isolation was computationally viable, attempts to calculate **11** consistently led to the extrusion of a THF ligand, which afforded trisolvate **12** displaying a distinct p-allyl sodium interaction. Rate studies of the metalation of 1,4-pentadiene revealed an entirely analogous $[A(THF)_4 \cdot (diene)]^{\ddagger}$ stoichiometry and a p-bonded $[A(THF)_3 \cdot (diene)]^{\ddagger}$ transition structure computationally (supporting information). Attempted metalations of 1,3-cyclohexadiene appeared to afford polymer under relatively forcing conditions (0 °C) instead as might be expected.[18] That the dienes formed during the eliminations (eqs 13 and 14) did not polymerize appreciably is less surprising than their reluctance to metalate.

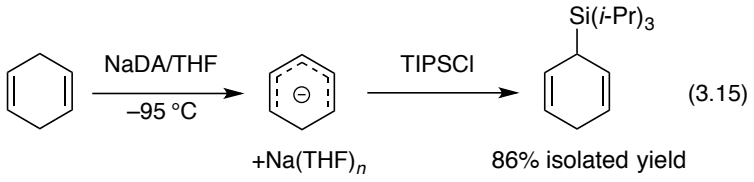

(3.15)

$$-d[diene]/dt = k[diene][THF]^2[A_2(THF)_4]^{1/2} \qquad (3.16)$$

$$1/2\ A_2(THF)_4 + 2THF + diene \longrightarrow [A(THF)_4 \cdot (diene)]^{\ddagger} \qquad (3.17)$$

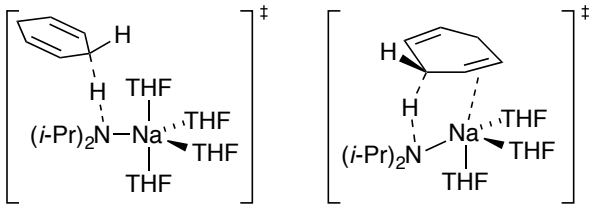

11 **12**

Discussion

The first paper in this series promulgated NaDA/DMEA as an easily prepared, effective Brønsted base that compares favorably to LDA/THF.[7] A second paper described detailed structural studies of NaDA in various standard coordinating solvents[8] as a foundation for the current mechanistic study and those that will follow. The temptation to rely on analogies of sodium amides to lithium amides owing to decades of experience is fraught with risk.[19] Parallel behaviors of lithium and sodium do exist, but they are imperfect and require experimental support. The mechanistic studies described herein begin to examine the relationships among organosodium aggregation, solvation, reactivity, mechanism, and selectivity.

The current study probed a combination of the synthetic utility and underlying mechanism of NaDA/THF-mediated reactions of alkenes and dienes. NaDA cleanly and rapidly metalates 1,4-dienes, but synthetic chemists often resort to using alkyllithiums.[20,21] By contrast, metalations of simple alkenes and allyloxy ethers are endothermic, yet facile isomerizations underscore synthetic opportunities and provide an opportunity to study fundamental principles of sodium coordination chemistry.

Diene Metalation. NaDA metalates 1,4-cyclohexadiene and 1,4-pentadiene to form dienylsodiums rapidly and quantitatively. Both react via tetrasolvated monomers; transition structure **11** is emblematic. 1,4-Cyclohexadiene reacts approximately 10-fold slower than 1,4-pentadiene, presumably owing to unproductive substituents as well as the suboptimal alignment of the C–H bond with the p system. Tetrasolvation in the rate-limiting transition structures contrasts with the trisolvation observed with alkene isomerizations.

The synergies of kinetics and computations offer excellent opportunities to test theory–experiment correlations, which is crucial for our fledgling studies of sodium amides. In this case,

however, the correlation proved imperfect: all attempts to find tetrasolvated transition structure **11** afforded trisolvate **12**, which resulted from the extrusion of a THF ligand with the formation of a p-allyl sodium interaction. It is plausible that the transition structure includes four solvents (demonstrated kinetically) *and* the p interaction predicted computationally. DFT often fails to replicate highly solvated lithiums.[22]

1-Pentene Isomerization. Despite the inherent endothermicity of alkene metalations, mechanistic details were obtained from studies of the isomerization of 1-pentene to *cis*- and *trans*-2-pentenes (eq 3.1). The kinetic formation of both stereoisomers in equal proportions is followed by a slower stereochemical equilibration (Figure 3.1). Rate studies showing trisolvated-monomer-based transition structures are supported by computational studies showing ***Z*-2** and ***E*-2** transition structures manifesting distinct p-allyl sodium interactions. A predicted kinetic preference for ***E*-2** is not observed experimentally.

Allyloxy Isomerizations: Mechanistic Chameleons. The series of NaDA/THF-mediated allyl ether (CH_2=$CHCH_2OR$) isomerizations (eq 3.5) constitutes the most interesting portion of this study. Rates of isomerization correlate with apparent steric effects following the order R = Me > $SiMe_3$ > Si(*t*-Bu)Me_2 > Si(*i*-Pr)$_3$. The underlying mechanistic differences, however, are far more nuanced (eqs 8–11). Methyl and $SiMe_3$ moieties are essentially interchangeable, reacting via a trisolvated-monomer-based transition structure depicted generically as $\mathbf{A}^{\ddagger}$ with prominent Na–O interactions to the exclusion of Na–C p-allyl contacts. The decidedly larger Si(*t*-Bu)Me_2 group metalates significantly more slowly via a *disolvated* monomer, $\mathbf{B}^{\ddagger}$, while retaining the putative Na–O contact. The notoriously large Si(*i*-Pr)$_3$ (TIPS) moiety blocks the Na–O contact, replacing it with an Na–C p-allyl interaction, which allows it to return to a trisolvated monomer ($\mathbf{C}^{\ddagger}$).

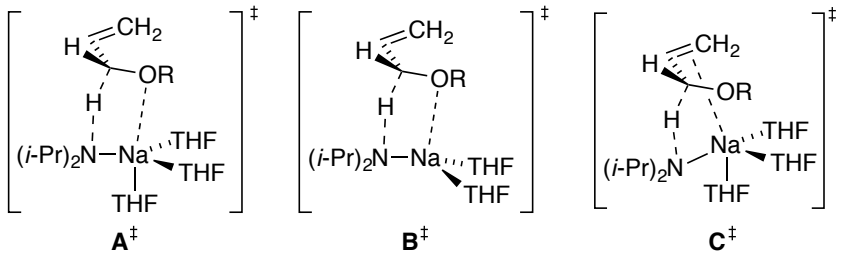

Scheme 3.3 offers an alternative perspective on the interplay among allyloxy RO–Na coordination, steric bulk, and solvation number. We have taken the liberty of normalizing the energies of the reactants to a common level. Transition structures $\mathbf{A}^{‡}$, $\mathbf{B}^{‡}$, and $\mathbf{C}^{‡}$ are color-coded. Moving from left to right reflects increasing steric demand and decreasing relative rate constants (k_{rel}). The energy of $\mathbf{A}^{‡}$, which is stabilized by both trisolvation and a Na–O contact with the allyloxy fragment, is sterically sensitive. The intermediate steric demand of the Si(*t*-Bu)Me_2 moiety sacrifices a stabilizing Na–THF interaction to retain the Na–O contact with the allyloxy. In the limit of high steric demand, the Na–O contact is inaccessible, which reveals the inferior Na–C contact ($\mathbf{C}^{‡}$) while returning to trisolvation. Transition structure $\mathbf{C}^{‡}$ is insensitive to the steric demands of the R group, which make it dominant by default for the TIPS ether.

Scheme 3.3. Qualitative barriers for the isomerization of allyloxy ethers via differing transition structures.

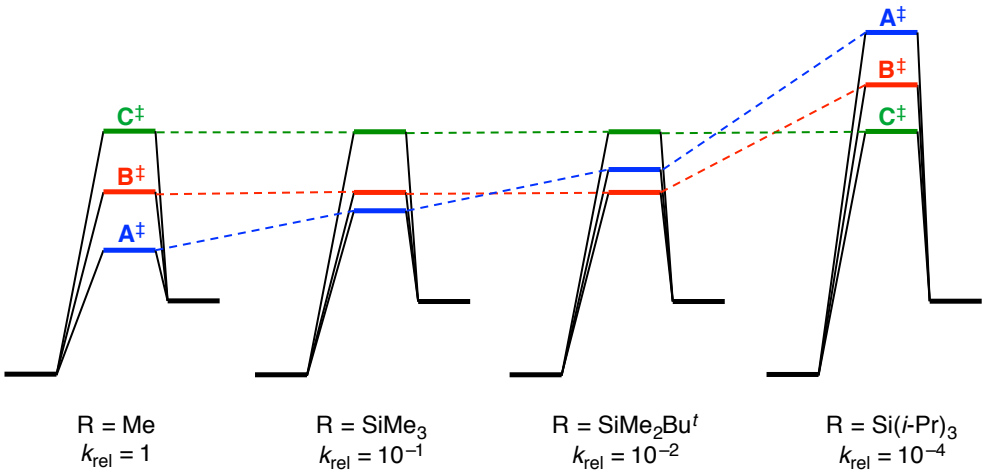

Allyloxy Isomerization: Origin of *Z* Selectivity. The contrasteric isomerization of allyl ethers to provide *Z*-(1-propenyl) ethers (eq 3.5) tempts us to invoke a privileged role for NaDA in this transformation, but *Z*-selective isomerizations have been noted with *t*-BuOK/DMSO[17] and LDA/THF.[14] An overlay of the computed pro-*Z* and pro-*E* transition structures (***Z*-5** and ***E*-5**, respectively) reveals complete superposition of the $A(THF)_3$ fragment, with the sole distinction being the terminal methylene orientation. Given that transition states **5a**–**d** are product-like in accord with the Hammond postulate, we directed our attention toward stereoelectronic preferences endemic to the putative allylsodium intermediate. Geometric preferences within this class of allyl anions have been addressed both experimentally[23] and computationally.[24] Compared with ***E*-11**, ***Z*-11** shows a greater spatial overlap—and consequent stabilization—of the allyl anion π manifold with the O–R σ* orbital. The transition-state energy differences cited in eqs 8–11 are reflected in the calculated relative energies of allyl anions ***Z*-13** and ***E*-13** and are consistent with this highly simplified, purely stereoelectronic model.[25]

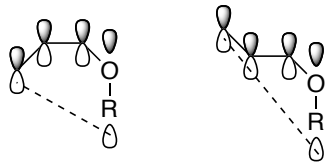

***Z*-13** ***E*-13**

Alloxy Isomerization: Competing Elimination. Although the efficient and highly *Z*-selective isomerization of allyl ethers **4a**–**d** (eq 3.5) is notable given the potential importance of these compounds as synthons,[26] we were admittedly disappointed that substituted analogs including **9** undergo 1,4-elimination (eqs 13 and 14).

Conclusion

NaDA/THF observably metalates dienes and transiently metalates alkenes and allyloxy ethers. The NaDA-mediated isomerization of 1-pentene shows no stereoselectivity. By contrast, the >50:1 *Z*-selective isomerization of allyl ethers is synthetically noteworthy. Rate and computational data revealed the roles of solvation and aggregation, which are key for understanding organosodium coordination chemistry. The current investigation reinforces our enthusiasm for NaDA to effect difficult metalations that plague synthetic chemists. That it can be prepared as stock solutions in trialkylamines in minutes using standard glassware and stored for months with refrigeration amplifies its appeal.[7]

Experimental

Reagents. NaDA was prepared from diisopropylamine, isoprene, and sodium dispersion by using a modified[7] procedure first reported by Wakefield.[3a] Despite little evidence of improved efficacy, NaDA was crystallized from DMEA/hexane as an added measure.[8] THF, hexane, and DMEA were vacuum-transferred from purple solutions of sodium benzophenone ketyl. Air- and moisture-sensitive materials were manipulated under argon using standard glovebox, vacuum line, and syringe techniques. The substrates were commercially available or prepared with standard protocols.[27]

IR Spectroscopic Analyses. IR spectra were recorded using an in situ IR spectrometer fitted with a 30-bounce, silicon-tipped probe. The spectra were acquired in 16 scans at a gain of 1 and a resolution of 4 cm^{-1}. A representative reaction was carried out as follows: The IR probe was inserted through a nylon adapter and O-ring seal into an oven-dried, cylindrical flask fitted with a magnetic stir bar and a T-joint. The T-joint was capped with a septum for injections and a nitrogen line. After evacuation under full vacuum, heating, and flushing with nitrogen, the flask was charged with NaDA (62 mg, 0.50 mmol) in THF/DMEA (4.9 mL) and cooled in a dry ice–acetone bath prepared with fresh acetone. After a background spectrum was recorded, ether **3b** (0.050 mmol) was added with stirring. For the most rapid reactions, IR spectra were recorded every 6 s with monitoring of the absorbance at 1510 cm^{-1} over the course of the reaction.

NMR Spectroscopy. All samples for reaction monitoring and structure elucidation were prepared using stock solutions and sealed under partial vacuum. Standard ^{1}H and ^{13}C NMR spectra were recorded at 500 and 125.79 MHz, respectively.

Myrcene (10). To a stirred solution of NaDA (500 mg, 4.06 mmol) in THF (15 mL) at –78 °C was added geraniol trimethylsilyl ether **9** (836 mg, 3.70 mmol). After 5 h at –78 °C, the

reaction was quenched with water and partitioned between water and pentane. The crude extract was chromatographed on silica with pentane (R_f = 0.5) and the fractions were concentrated to afford myrcene (428 mg, 85% yield) to identical to that reported in the literature (^{1}H and ^{13}C NMR).[28]

Enol ether 4b: neat isomerization. To a NMR tube charged with solid NaDA (71 mg, 0.58 mmol) was added neat allyloxytrimethylsilane (1.5 mL, 8.9 mmol) at room temperature. After 1 minute, the crude reaction mixture was vacuum-transferred to a receiving flask cooled with dry ice–acetone to provide 0.982 g (84% yield) of product enol ether **4b** contaminated by ~5% diisopropylamine.

Chapter 3 References and Footnotes

1. Raynolds, S.; Levine, R. *J. Am. Chem. Soc.* **1959**, *82*, 472.

2. (a) Lochmann, L.; Janata, M. *Eur. J. Chem.* **2014**, *12*, 537. (b) Lochmann, L. *Eur. J. Inorg. Chem.* **2000**, 1115. (c) Lochmann, L.; Trekoval, J. *J. Organomet. Chem.* **1979**, *179*, 123. (d) Lochmann, L.; Pospíšil, J.; Lím, D. *Tetrahedron Lett.* **1966**, *2*, 257.

3. (a) Barr, D.; Dawson, A. J.; Wakefield, B. J. *J. Chem. Soc., Chem. Commun.* **1992**, 204. 9. (b) Andrews, P. C.; Barnett, N. D. R.; Mulvey, R. E.; Clegg, W.; O'Neil, P. A.; Barr, D.; Cowton, L.; Dawson, A. J.; Wakefield, B. J. *J. Organomet. Chem.* **1996**, *518*, 85. (c) Munguia, T.; Bakir, Z. A.; Cervantes-Lee, F.; Metta-Magana, A.; Pannell, K. H. *Organometallics* **2009**, *28*, 5777. (d) Boeckman, R. K.; Boehmler, D. J.; Musselman, R. A. *Org. Lett.* **2001**, *3*, 3777. (e) LaMontagne, M. P.; Ao, M. S.; Markovac, A.; Menke, J. R. *J. Med. Chem.* **1976**, *19*, 363. (f) Bond, J. L.; Krottinger, D.; Schumacher, R. M.; Sund, E. H.; Weaver, T. J. *J. Chem. Eng. Data.* **1973**, *18*, 349. (g) Levine, R.; Raynolds, S. *J. Org. Chem.* **1960**, *25*, 530. (e) Mamane, V.; Louërat, F.; Iehl, J.; Abboud, M.; Fort, Y. *Tetrahedron*. **2008**, *64*, 10699. (h) Baum, B. M.; Levine, R. *J. Heterocyclic Chem*. **1966**, *3*, 272. (i) Tsuruta, T. *Makromol. Chem*. **1985**, *13*, 33. (h) Andrikopoulos, P. C.; Armstrong, D. R.; Clegg, W.; Gilfillan, C. J.; Hevia, E.; Kennedy, A. R.; Mulvey, R. E.; O'Hara, C. T.; Parkinson, J. A.; Tooke, D. M. *J. Am. Chem. Soc.* **2004**, *126*, 11612.

4. (a) Zhao, P.; Collum, D. B. *J. Am. Chem. Soc.* **2003**, *125*, 4008. (b) Lucht, B. L.; Collum, D. B. *J. Am. Chem. Soc.* **1996**, *118*, 2217. (c) Remenar, J. F.; Lucht, B. L.; Collum, D. B. *J. Am. Chem. Soc.* **1997**, *119*, 5567. (d) Bernstein, M. P.; Collum, D. B. *J. Am. Chem. Soc.* **1993**, *115*, 8008. (e) Godenschwager, P.; Collum, D. B. *J. Am. Chem. Soc.* **2008**, *130*, 8726.

5. Mulvey, R. E.; Robertson, S. D. *Angew. Chem., Int. Ed.* **2013**, *52*, 11470.

6. For an interesting historical perspective on organoalkali metal chemistry, see: (a) Seyferth, D. *Organometallics* **2006**, *25*, 2. (b) Seyferth, D. *Organometallics* **2009**, *28*, 2.

7. Ma, Y.; Algera, R. F.; Collum, D. B. *J. Org. Chem.* **2016**, *81*, 11312.

8. Algera, R. F.; Ma, Y.; Collum, D. B. *J. Am. Chem. Soc.* **2017**, *139*, xxASAP.

9. (a) Rein, A. J.; Donahue, S. M.; Pavlosky, M. A. *Curr. Opin. Drug Discov. Dev.* **2000**, *3*, 734. (b) Connolly, T. J.; Hansen, E. C.; MacEwan, M. F. *Org. Process Res. Dev.* **2010**, *14*, 466.

10. The rate law provides the stoichiometry of the transition structure relative to that of the reactants: Edwards, J. O.; Greene, E. F.; Ross, J. *J. Chem. Educ.* **1968**, *45*, 381.

11. Frisch, M. J.; *et al. GaussianVersion 3.09*; revision A.1; Gaussian, Inc.: Wallingford, CT, 2009.

12. Haeffner, F.; Houk, K. N.; Schulze, S. M.; Lee, J. K. *J. Org. Chem*. **2003**, *68*, 2310.

13. (a) **4a**: Leung, D. H.; Bergman, R. G.; Raymond, K. N. *J. Am. Chem. Soc.* **2007**, *129*, 2746; (b) **4b**: Heathcock, C. H.; Buse, C. T.; Kleschick, W. A.; Pirrung, M. C.; Sohn, J. E.; Lampe, J. *J. Org. Chem.* **1980**, *45*, 1066; (c) **4c**: Su, C.; Williard, P. G. *Org. Lett.* **2010**, *12*, 5378.; (d) **4d**: Guha, S. K.; Shibayama, A.; Abe, D.; Sakaguchi, M.; Ukaji, Y.; Inomata, K. *Bull. Chem. Soc. Jpn.* **2004**, *77*, 2147.

14. Su, C.; Williard, P. G. *Org. Lett.* **2010**, *12*, 5378.

15. The acceleration was estimated assuming a factor 2 per 10 °C with the adjustment for the relative rates. This is likely to be an underestimate.

16. (a) Hattori, K.; Yamamoto, H. *J. Org. Chem.* **1993**, *58*, 5301. (b) Rücker, C. *Chem. Rev.* **1995**, *95*, 1009. (c) Williard, P. G.; Hintze, M. J. *J. Am. Chem. Soc.* **1987**, *109*, 5539.

17. (a) Taskinen, E. *Tetrahedron* **1993**, *48*, 11389. (b) *J. Am. Chem. Soc.* **1961**, *83*, 1701. (c) Martinez-Erro, S.; Sanz-Marco, A; Gómez, A. B.; Vázquez-Romero, A.; Ahlquist, M. S. G.; Martín-Matute, B. *J. Am. Chem. Soc.* **2016**, *138*, 13408.

18. Hsieh, H. L.; Quirk, R. P. *Anionic Polymerization: Principles and Practical Applications*; Marcel Dekker: New York, 1996.

19. Collum, D. B.; McNeil, A. J.; Ramírez, A. *Angew. Chem., Int. Ed.* **2007**, *46*, 3002.

20. (a) Simonneau, A.; Oestreich, M. *Angew. Chem., Int. Ed.* **2013**, *52*, 11905. (b) Fujioka, H.; Sawama, Y.; Kotoku, N.; Ohnaka, T.; Okitsu, T.; Murata, N.; Kubo, O.; Li, R.; Kita, Y. *Chem.–Eur. J.* **2007**, *13*, 10225. (c) Landais, Y.; Zekri, E. *Tetrahedron Lett.* **2001**, *42*, 6547.

21. It appears to be unreported, but 1,4-dienes can be metalated with LDA. Literature procedures use alkyllithiums.[17]

22. Reyes-Rodríguez, G. J.; Algera, R. F.; Collum, D. B. *J. Am. Chem. Soc.* **2017**, *139*, 1233.

23. (a) Taskinen, E. *J. Chem. Soc., Perkin Trans. 2* **2001**, 1824. (b) Bank, S.; Schriesheim, A.; Rowe, C. A. *J. Am. Chem. Soc.* **1965**, *87*, 3244. (c) Haag, W. O.; Pines, H. *J. Am. Chem. Soc.* **1960**, *82*, 387.

24. (a) Mangelinckx, S.; Giubellina, N.; De Kimpe, N. *Chem. Rev*. **2004**, *104*, 2353. (b) Schleyer, P. v. R.; Dill, J. D.; Pople, J. A.; Hehre, W. J. *Tetrahedron* **1977**, *33*, 2497.

25. This stereoelectronic model rationalizes the outcome of 1-pentene isomerization, for which poorer overlap of the allyl anion π manifold with C–H(C) σ* results in minimal disproportionate stabilization and consequent stereorandom isomerization.)

26. (a) Denmark, S. E. and Ghosh, S. K. *Angew. Chem., Int. Ed.* **2001** *40*, 4759. (b) Lim, S. M.; Hill, N.; Myers, A. G. *J. Am. Chem. Soc.* **2009**, *131*, 5763. (c) Wang, X.; Meng, Q.; Nation, A. J.; Leighton, J. L *J. Am. Chem. Soc.* **2002**, *124*, 10672. (d) Schumacher, R.; Reissig, H. U. *Synlett* **1996**, 1121.

27. **9**; De Carvalho, M. E.; Meunier, B. *Nouv. J. Chim.* **1986**, *10*, 223.

28. Myrcene is commercially available with ^{1}H and ^{13}C NMR spectra reported by Sigma-Aldrich.

Chapter 3 Appendix

I. Rate studies

I. Rate Studies

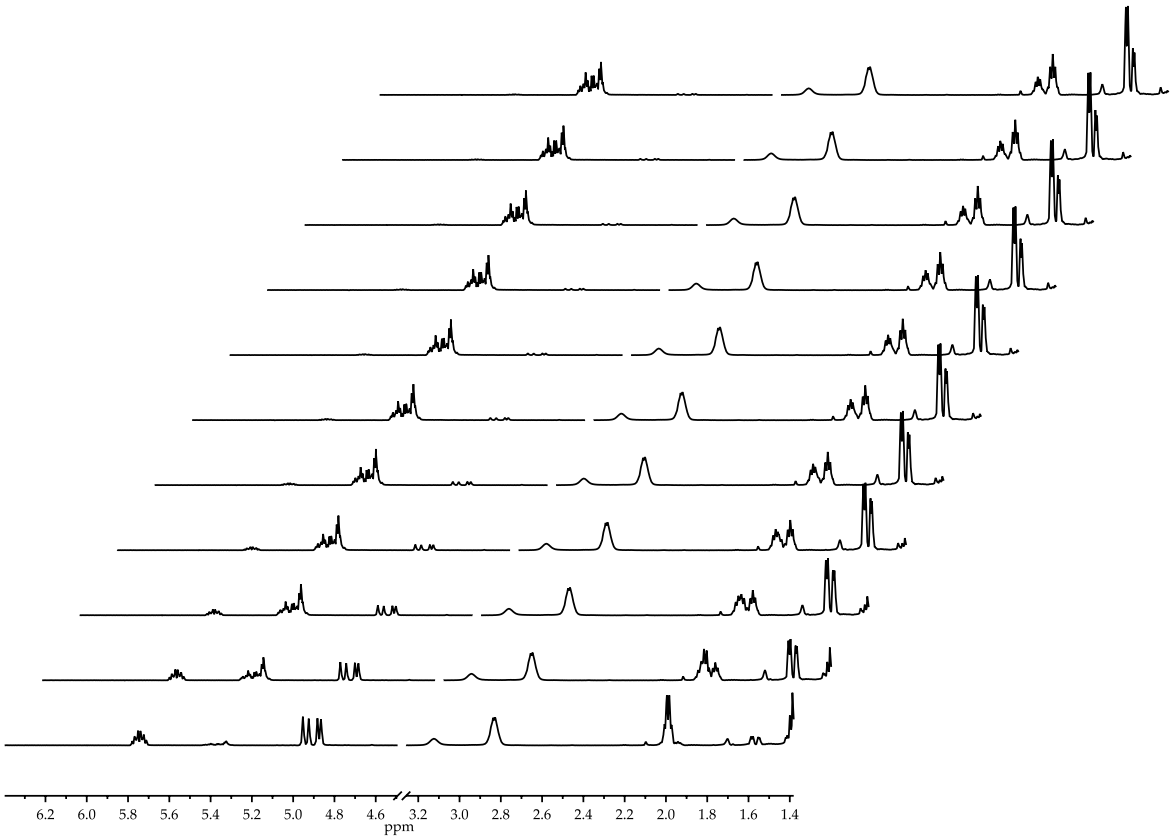

Figure A.3.1. Representative plot of pentene concentration versus time (^{1}H NMR) for the isomerization of 0.76 M 1-pentene with 0.18 M NaDA and 0.59 M diisopropylamine in 8.83 M THF/hexane at 25 °C. Each interval represents 300 seconds.

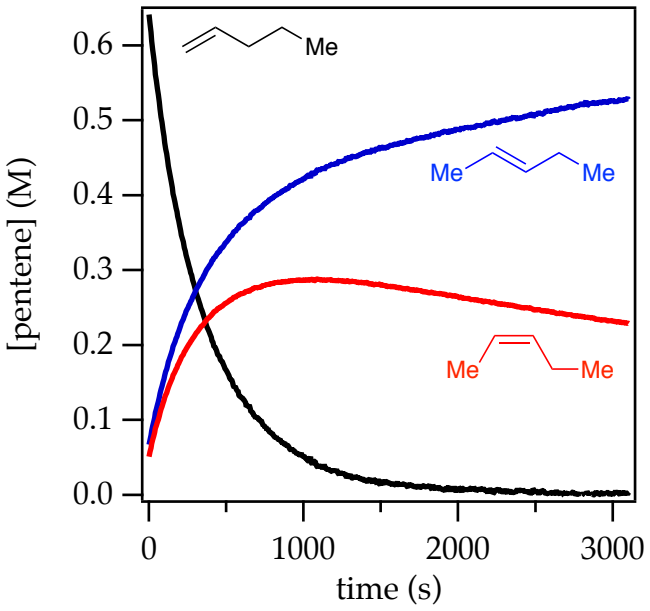

Figure A.3.2.Plot of alkene concentration versus time (^{1}H NMR) for the isomerization of 0.76 M 1-pentene with 0.18 M NaDA and 0.59 M diisopropylamine in 8.83 M THF/hexane at 25 °C. The black trace represents 1-pentene, the blue trace represents *trans*-2-pentene, and the red trace represents *cis*-2-pentene.

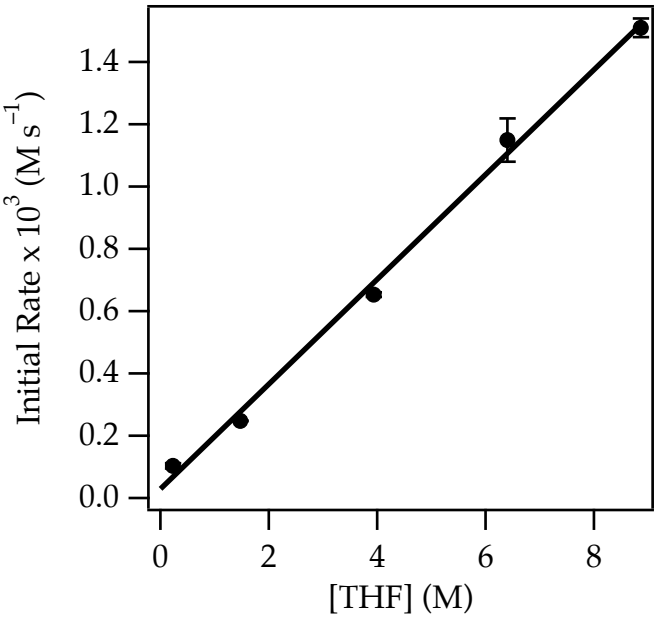

Figure A.3.3.Plot of initial rate versus THF concentration for the isomerization of 0.76 M 1-pentene (Equation 1) with 0.18 M NaDA and 0.59 M diisopropylamine in hexane cosolvent at 25 °C. The curve depicts an unweighted least-squares fit to the function $f(x) = ax + b$: $a = 0.168 \pm 0.006$; $b = 0.03 \pm 0.03$.

[THF] (M)	Initial Rate × 10^3 (M s^{-1})	Standard deviation × 10^3 (M s^{-1})
0.23	0.104	0.008
1.47	0.248	0.0007
3.93	0.653	0.007
6.40	1.15	0.07
8.86	1.51	0.03

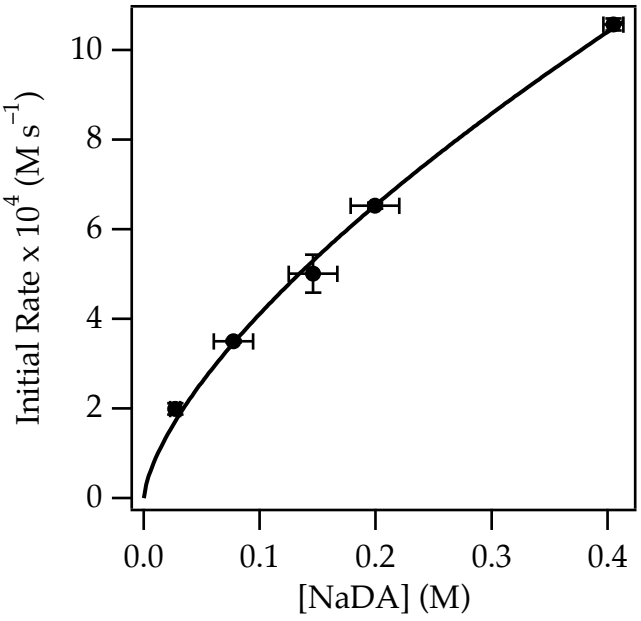

Figure A.3.4.Plot of initial rate versus NaDA concentration for the isomerization of 0.76 M 1-pentene (Equation 1) with 0.59 M diisopropylamine in 3.93 M THF/hexane at 25 °C. The curve depicts an unweighted least-squares fit to the function $f(x) = ax^b$: a = 19.2 ± 0.8; b = 0.67 ± 0.03. The covariance represents measured titer of NaDA.

[NaDA] (M)	Initial Rate × 10^4 (M s^{-1})	Standard deviation × 10^4 (M s^{-1})
0.027	2.0	0.1
0.080	3.50	0.03
0.15	5.0	0.4
0.20	6.53	0.07
0.405	10.6	0.1

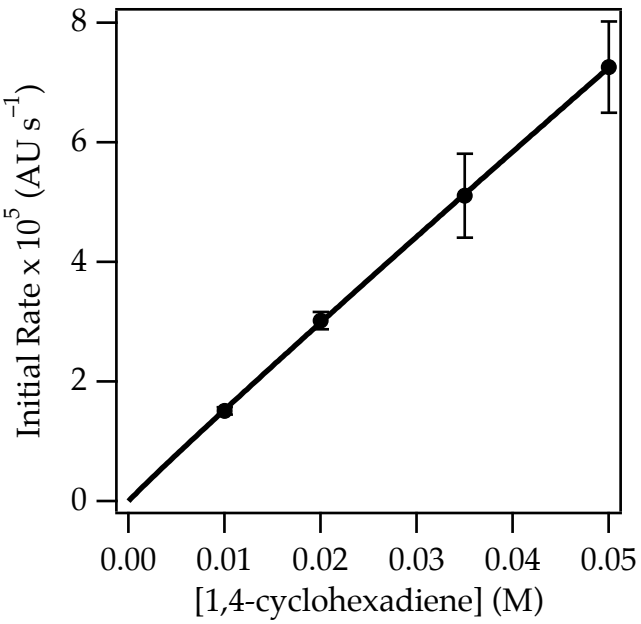

Figure A.3.5.Plot of initial rate versus concentration of 1,4-cyclohexadiene following product growth at 1558 cm^{-1} with 0.10 M NaDA in 6.04 M THF/DMEA at –95 °C. The curve depicts an unweighted least-squares fit to the function $f(x) = ax^b$: $a = 132 \pm 4$; $b = 0.968 \pm 0.009$.

[alkene] (M)	Initial Rate × 10^5 (AU s^{-1})	Standard deviation × 10^5 (AU s^{-1})
0.010	1.51	0.06
0.020	3.0	0.1
0.035	5.1	0.7
0.050	7.3	0.8

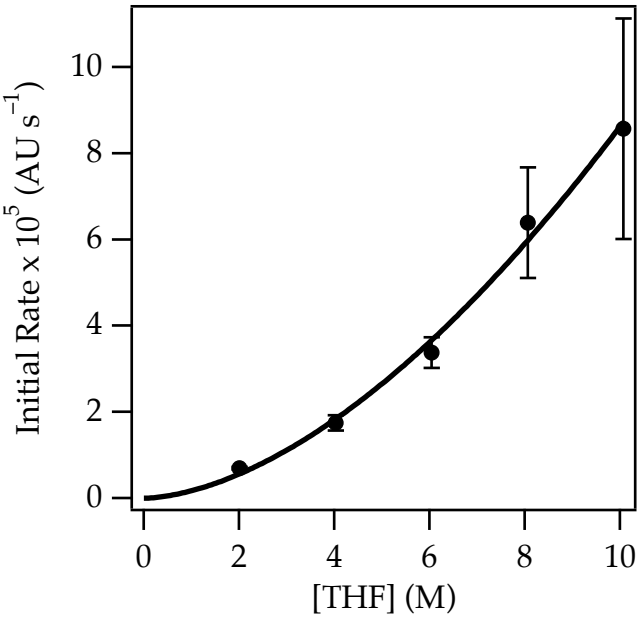

Figure A.3.6.Plot of initial rate versus concentration of THF following product growth at 1558 cm^{-1} with 0.10 M NaDA and 0.020 M 1,4-cyclohexadiene in DMEA cosolvent at –95 °C. The curve depicts an unweighted least-squares fit to the function $f(x) = ax^b$: $a = 0.17 \pm 0.05$; $b = 1.7 \pm 0.1$.

[THF] (M)	Initial Rate × 10^5 (AU s^{-1})	Standard deviation × 10^5 (AU s^{-1})
2.01	0.696	0.03
4.03	1.75	0.2
6.04	3.38	0.4
8.06	6.39	1
10.1	8.57	3

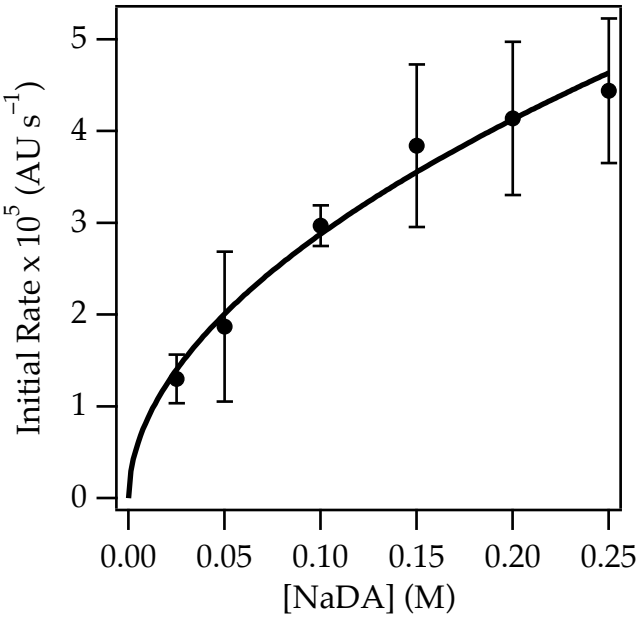

Figure A.3.7.Plot of initial rate versus concentration of NaDA following product growth at 1558 cm^{-1} with 0.020 M 1,4-cyclohexadiene in 6.04 M THF/DMEA at –95 °C. The curve depicts an unweighted least-squares fit to the function $f(x) = ax^b$: $a = 9.53 \pm 0.8$; $b = 0.52 \pm 0.05$.

[NaDA] (M)	Initial Rate × 10^5 (M s^{-1})	Standard deviation × 10^5 (M s^{-1})
0.025	1.3	0.3
0.05	1.87	0.8
0.10	2.97	0.2
0.15	3.84	0.9
0.20	4.14	0.8
0.25	4.44	0.8

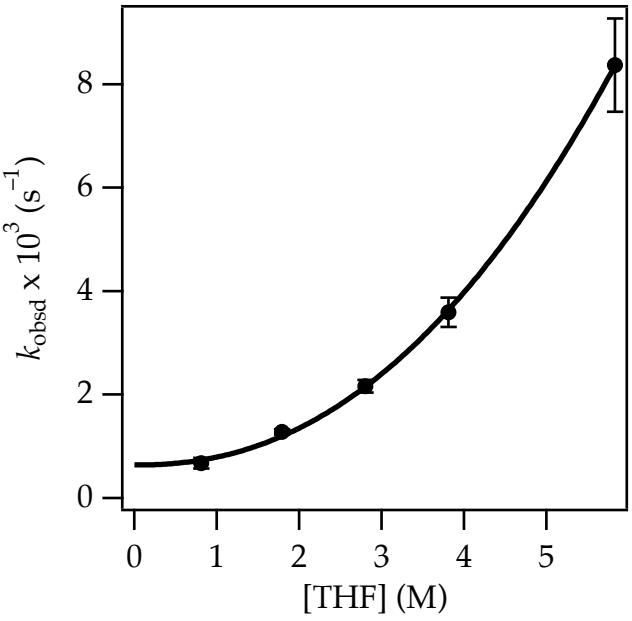

Figure A.3.8.Plot of k_{obsd} versus concentration of THF following product growth with 0.10 M NaDA and 0.020 M 1,4-pentadiene at –116 °C. The curve depicts an unweighted least-squares fit to the function $f(x) = ax^b + c$: $a = 0.15 \pm 0.02$; $b = 2.23 \pm 0.07$; $c = 0.64 \pm 0.08$. The THF order depicted here is consistent with and supportive of the elevated THF order observed in the metalation of 1,4-cyclohexadiene.

[THF] (M)	$k_{obsd} \times 10^3$ (s^{-1})	Standard deviation $\times 10^3$ (s^{-1})
0.81	0.7	0.1
1.79	1.28	0.05
2.80	2.2	0.1
3.81	3.6	0.3
5.83	8.4	0.9

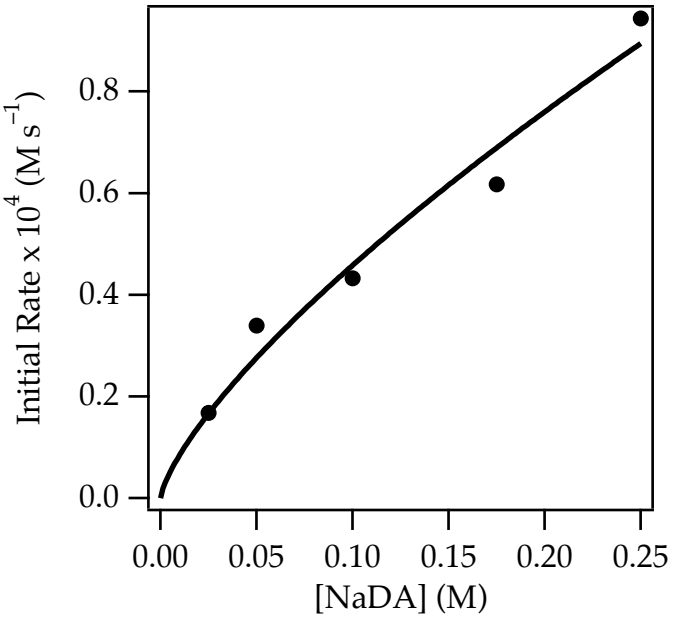

Figure A.3.9.Plot of initial rate versus concentration of NaDA following product growth with 0.020 M 1,4-pentadiene in 2.80 M THF/DMEA at –116 °C. The curve depicts an unweighted least-squares fit to the function $f(x) = ax^b$: $a = 2.5 \pm 0.5$; $b = 0.7 \pm 0.1$.

[NaDA] (M)	Initial Rate × 10^4 (s^{-1})
0.025	0.167
0.05	0.339
0.1	0.433
0.175	0.617
0.25	0.944

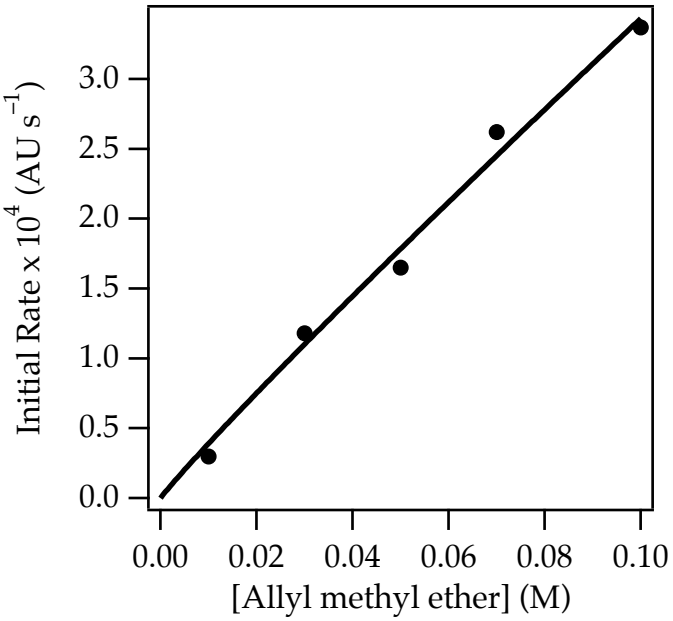

Figure A.3.10.Plot of initial rate versus concentration of allyl methyl ether following product growth at 1674 cm^{-1} (methyl enol ether) with 0.10 M NaDA in 5.5 M THF/DMEA at –116 °C. The curve depicts an unweighted least-squares fit to the function $f(x) = ax$: $a = 35 \pm 1$.

[allyl methyl ether] (M)	Initial Rate × 10^4 (AU s^{-1})
0.010	0.299
0.030	1.18
0.050	1.65
0.070	2.62
0.10	3.37

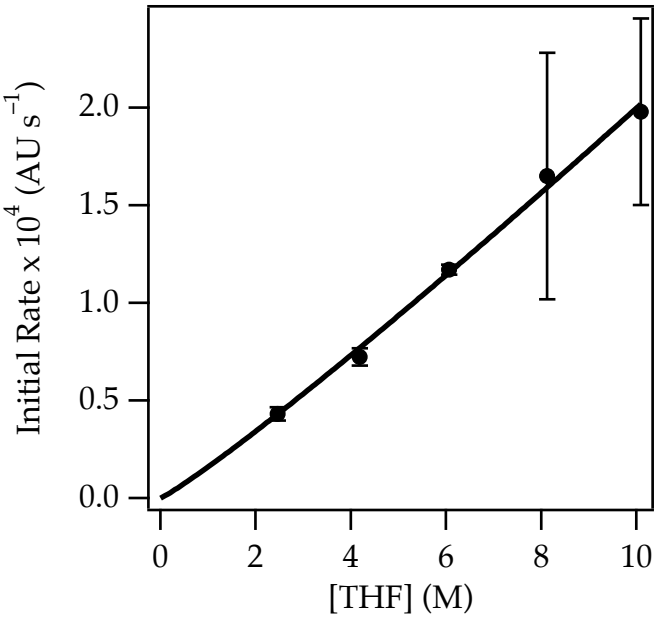

Figure A.3.11.Plot of initial rate versus concentration of THF following product growth at 1674 cm^{-1} (methyl enol ether) with 0.10 M NaDA and 0.030 M allyl methyl ether at –116 °C. The curve depicts an unweighted least-squares fit to the function $f(x) = ax^b$: $a = 0.16 \pm 0.02$; $b = 1.10 \pm 0.05$.

[THF] (M)	Initial Rate × 10^4 (AU s^{-1})	Standard deviation × 10^4 (AU s^{-1})
2.46	0.43	0.03
4.18	0.72	0.04
6.06	1.17	0.03
8.12	1.7	0.6
10.1	2.0	0.5

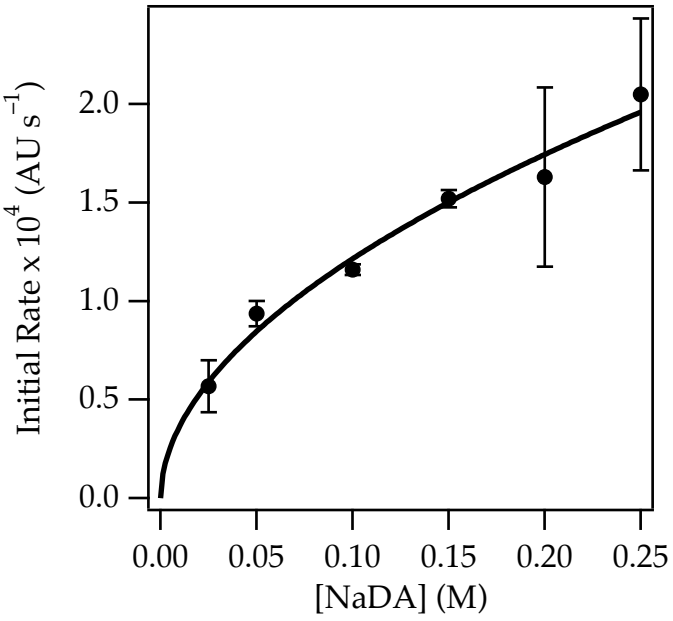

Figure A.3.12.Plot of initial rate versus concentration of NaDA following product growth at 1674 cm^{-1} (methyl enol ether) with 0.030 M allyl methyl ether in 5.5 M THF/DMEA at –116 °C. The curve depicts an unweighted least-squares fit to the function $f(x) = ax^b$: $a = 4.0 \pm 0.3$; $b = 0.52 \pm 0.05$.

[NaDA] (M)	Initial Rate × 10^4 (AU s^{-1})	Standard deviation × 10^4 (AU s^{-1})
0.025	0.6	0.1
0.05	0.94	0.06
0.10	1.16	0.03
0.15	1.52	0.04
0.20	1.6	0.5
0.25	2.1	0.4

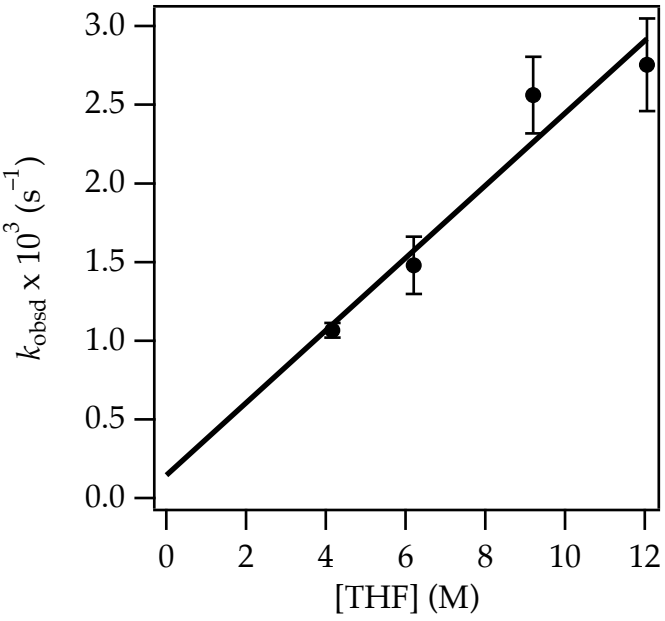

Figure A.3.13.Plot of k_{obsd} versus THF concentration following product growth at 1601 cm^{-1} (trimethylsilyl enol ether) with 0.010 M allyloxytrimethylsilane in hexane cosolvent at –78 °C. The curve depicts an unweighted least-squares fit to the function $f(x) = ax + b$: $a = 0.23 \pm 0.04$; $b = 0.14 \pm 0.4$.

[THF] (M)	$k_{obsd} \times 10^3$ (s^{-1})	Standard deviation $\times 10^3$ (s^{-1})
4.16	1.07	0.05
6.20	1.5	0.2
9.20	2.6	0.2
12.05	2.8	0.3

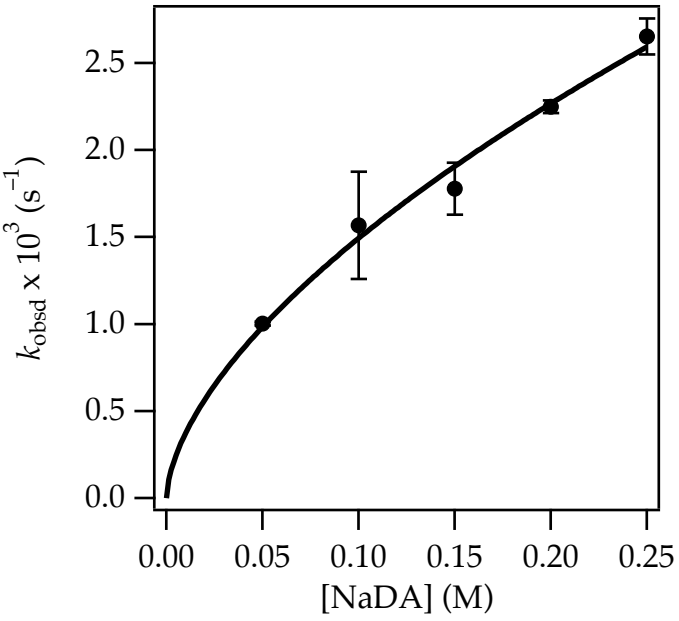

Figure A.3.14.Plot of k_{obsd} versus NaDA concentration following product growth at 1601 cm^{-1} (trimethylsilyl enol ether) with 0.010 M allyloxytrimethylsilane in 6.0 M THF/hexane at –78 °C. The curve depicts an unweighted least-squares fit to the function $f(x) = ax^b$: $a = 6.0 \pm 0.6$; $b = 0.60 \pm 0.05$.

[NaDA] (M)	$k_{obsd} \times 10^3$ (s^{-1})	Standard deviation $\times 10^3$ (s^{-1})
0.05	1.00	0.01
0.10	1.6	0.3
0.15	1.8	0.1
0.20	2.25	0.04
0.25	2.7	0.1

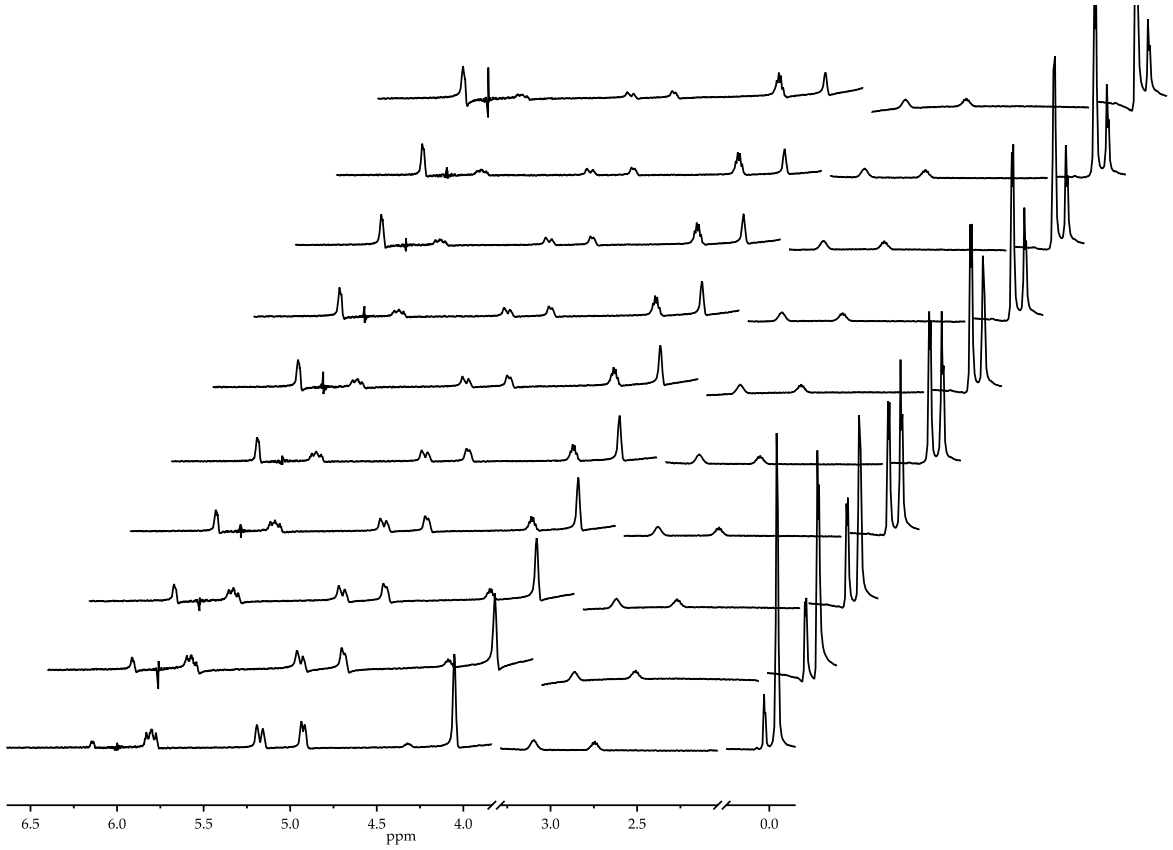

Figure A.3.15. ^{1}H NMR spectra of 0.78 M allyloxy-*tert*-butyldimethylsilane with 0.27 M NaDA in neat THF at –80 °C. Each spectrum corresponds to an interval of 881 seconds.

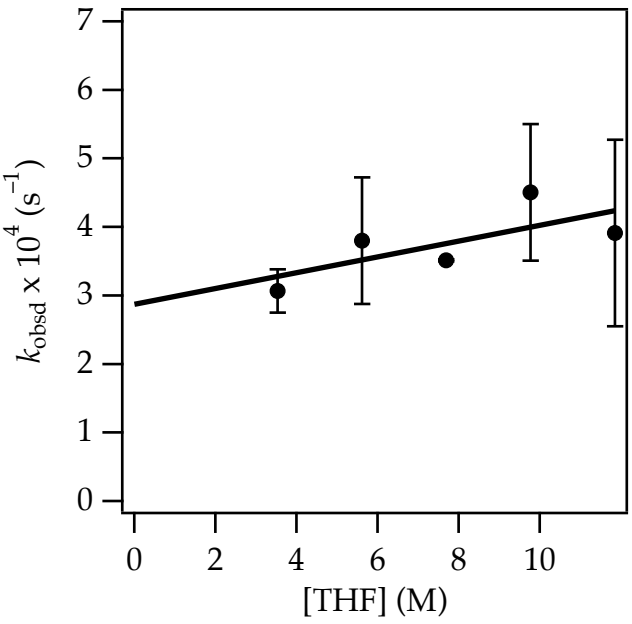

Figure A.3.16.Plot of k_{obsd} versus THF concentration following product growth at 1664 cm^{-1} (*tert*-butyldimethylsilyl enol ether) with 0.010 M allyloxy-*tert*-butyldimethylsilane in 6.00 M THF/hexane at –78 °C. The curve depicts an unweighted least-squares fit to the function $f(x) = ax + b$: $a = 0.12 \pm 0.06$; $b = 2.9 \pm 0.5$.

[THF] (M)	$k_{obsd} \times 10^4$ (s^{-1})	Standard deviation $\times 10^4$ (s^{-1})
3.53	3.1	0.3
5.61	3.8	0.9
7.69	3.51	0.01
9.77	4.5	1
11.9	3.9	1.4

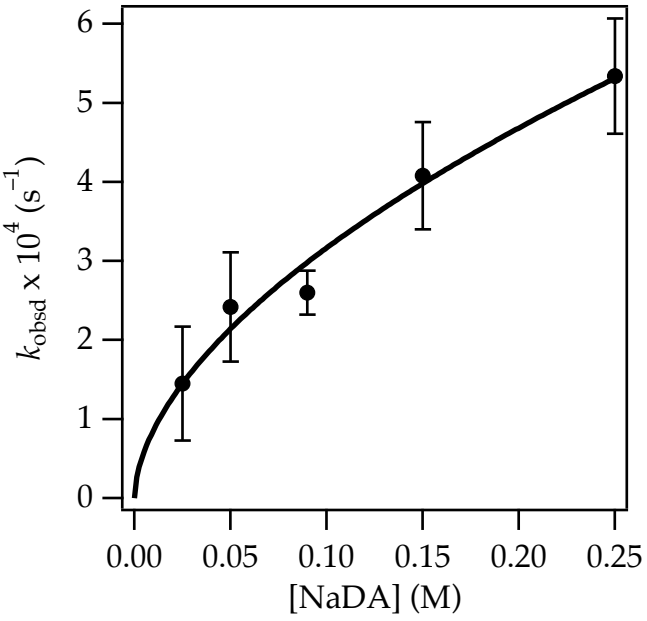

Figure A.3.17.Plot of initial rate versus NaDA concentration following product growth at 1664 cm^{-1} (*tert*-butyldimethylsilyl enol ether) with 0.010 M allyloxy-*tert*-butyldimethylsilane in 6.0 M THF/hexane at –78 °C. The curve depicts an unweighted least-squares fit to the function $f(x) = ax^b$: $a = 12 \pm 1$; $b = 0.56 \pm 0.06$.

[NaDA] (M)	$k_{obsd} \times 10^4$ (s^{-1})	Standard deviation $\times 10^4$ (s^{-1})
0.025	1.5	0.7
0.050	2.4	0.7
0.090	2.6	0.3
0.15	4.1	0.7
0.25	5.3	0.7

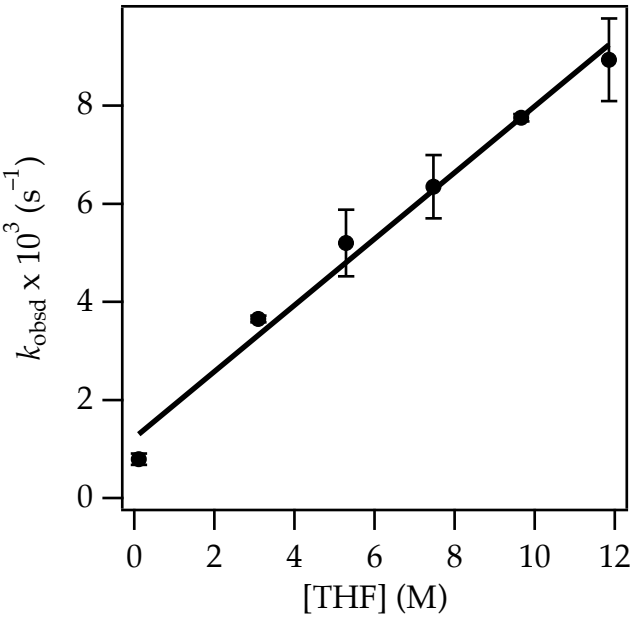

Figure A.3.18.Plot of k_{obsd} versus THF concentration following product growth at 1661 cm^{-1} (triisopropylsilyl enol ether) with 0.010 M allyloxytriisopropylsilane and 0.10 M NaDA with hexane cosolvent at 0 °C. The curve depicts an unweighted least-squares fit to the function $f(x) = ax + b$: $a = 0.68 \pm 0.04$; $b = 1.2 \pm 0.3$.

[THF] (M)	$k_{obsd} \times 10^3$ (s^{-1})	Standard deviation $\times 10^3$ (s^{-1})
0.11	0.8	0.1
3.09	3.66	0.07
5.28	5.2	0.7
7.47	6.3	0.6
9.66	7.76	0.07
11.9	8.9	0.8

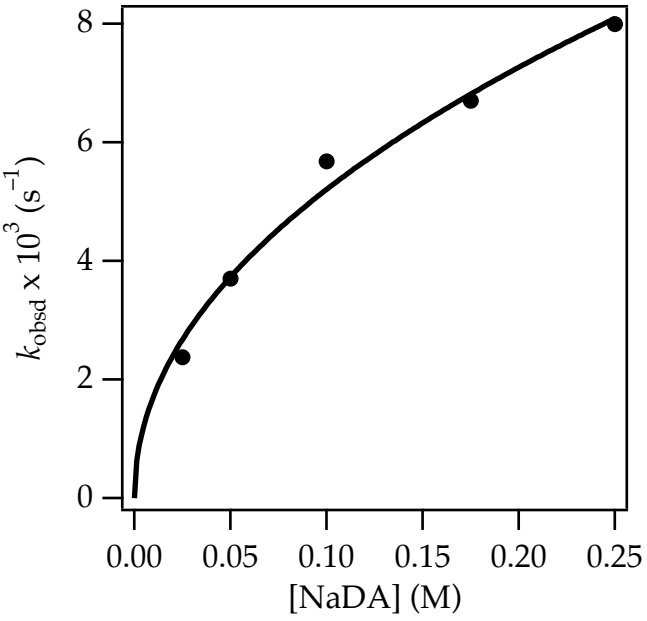

Figure A.3.19.Plot of k_{obsd} versus NaDA concentration following product growth at 1661 cm^{-1} (triisopropylsilyl enol ether) with 0.010 M allyloxytriisopropylsilane in 5.28 M THF/hexane at 0 °C. The curve depicts an unweighted least-squares fit to the function $f(x) = ax + b$: $a = 0.68 \pm 0.04$; $b = 1.2 \pm 0.3$.

[NaDA] (M)	$k_{obsd} \times 10^3$ (s^{-1})
0.025	2.38
0.050	3.70
0.10	5.68
0.175	6.70
0.25	7.99

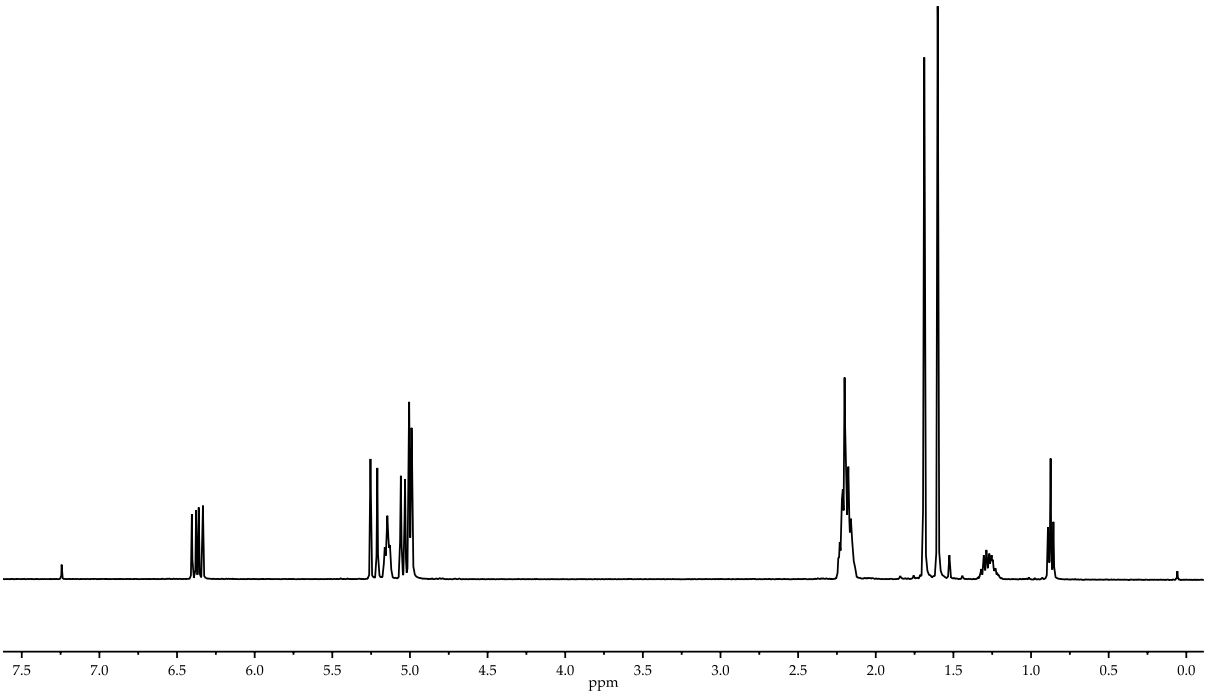

Figure A.3.20.[1]H NMR spectrum ($CDCl_3$) of myrcene recovered from reaction of NaDA/THF with trimethylsilyl ether of geraniol. Resonances at δ 0.85 ppm and δ 1.35 ppm correspond to residual pentane from chromatography.

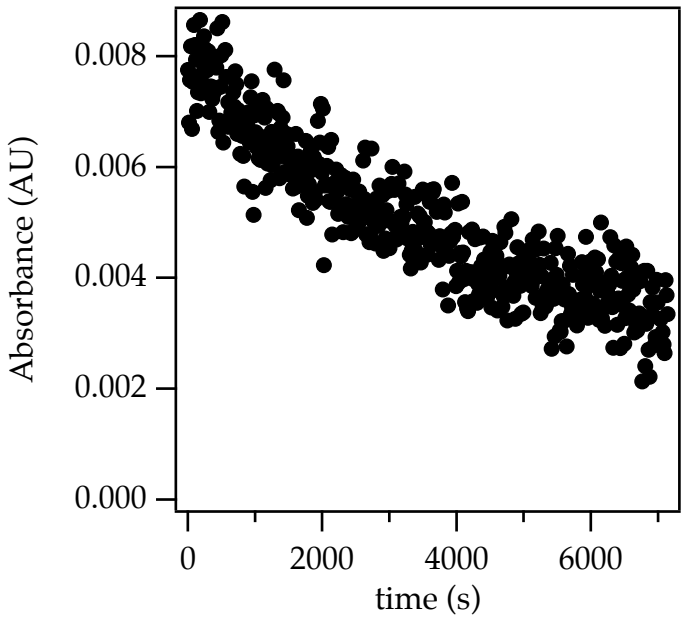

Figure A.3.21.Representative concentration trace showing loss of 0.050 M geraniol TMS ether **6** with 0.10 M NaDA in neat THF at –78 °C (monitored by ReactIR).

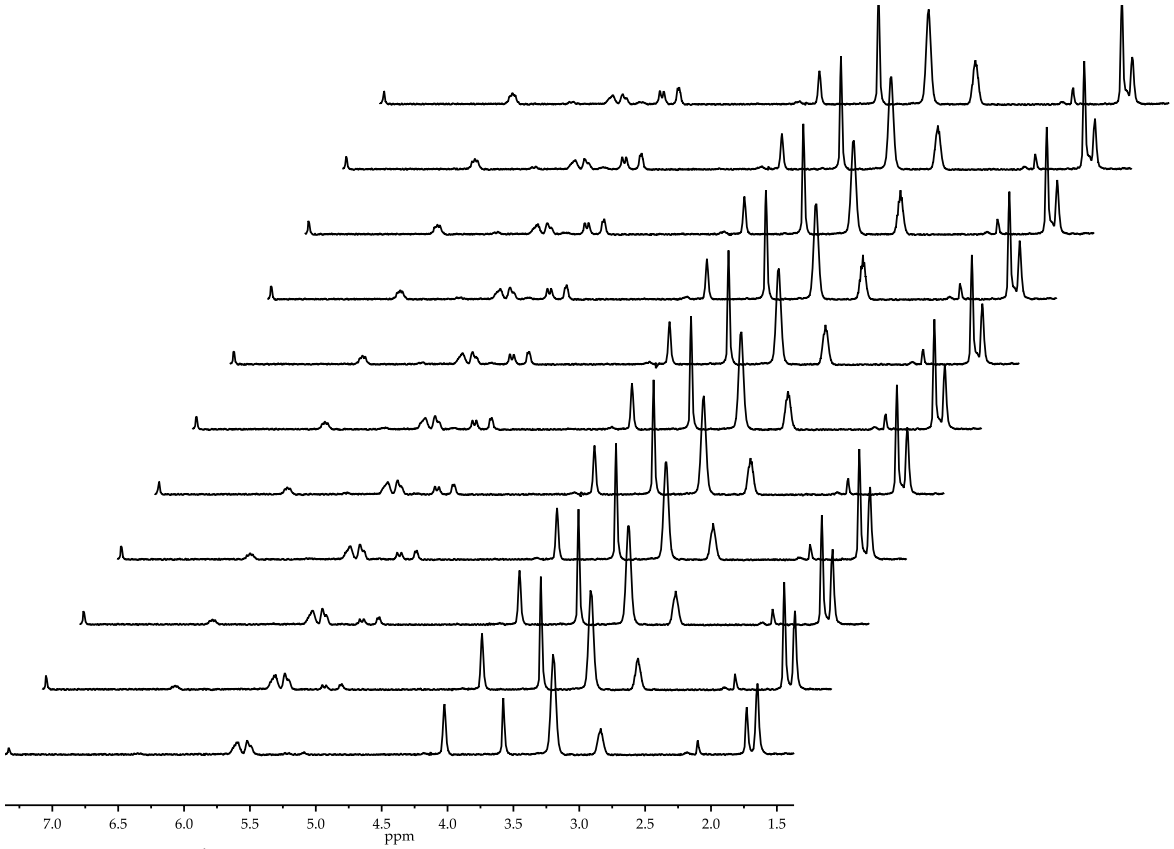

Figure A.3.22. ^{1}H NMR spectra of 0.090 M trimethylsilyl ether of crotyl alcohol with 0.32 M NaDA in neat THF at –60 °C. Each spectrum corresponds to an interval of 263 seconds. These spectra are consistent with stoichiometric consumption of NaDA to give 1,3-butadiene.

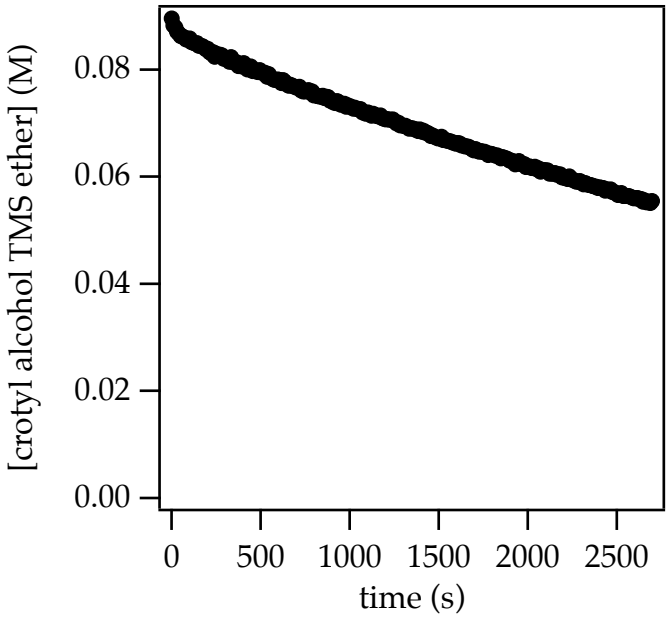

Figure A.3.23.Concentration of 0.090 M trimethylsilyl ether of crotyl alcohol with 0.32 M NaDA in neat THF at –60 °C.

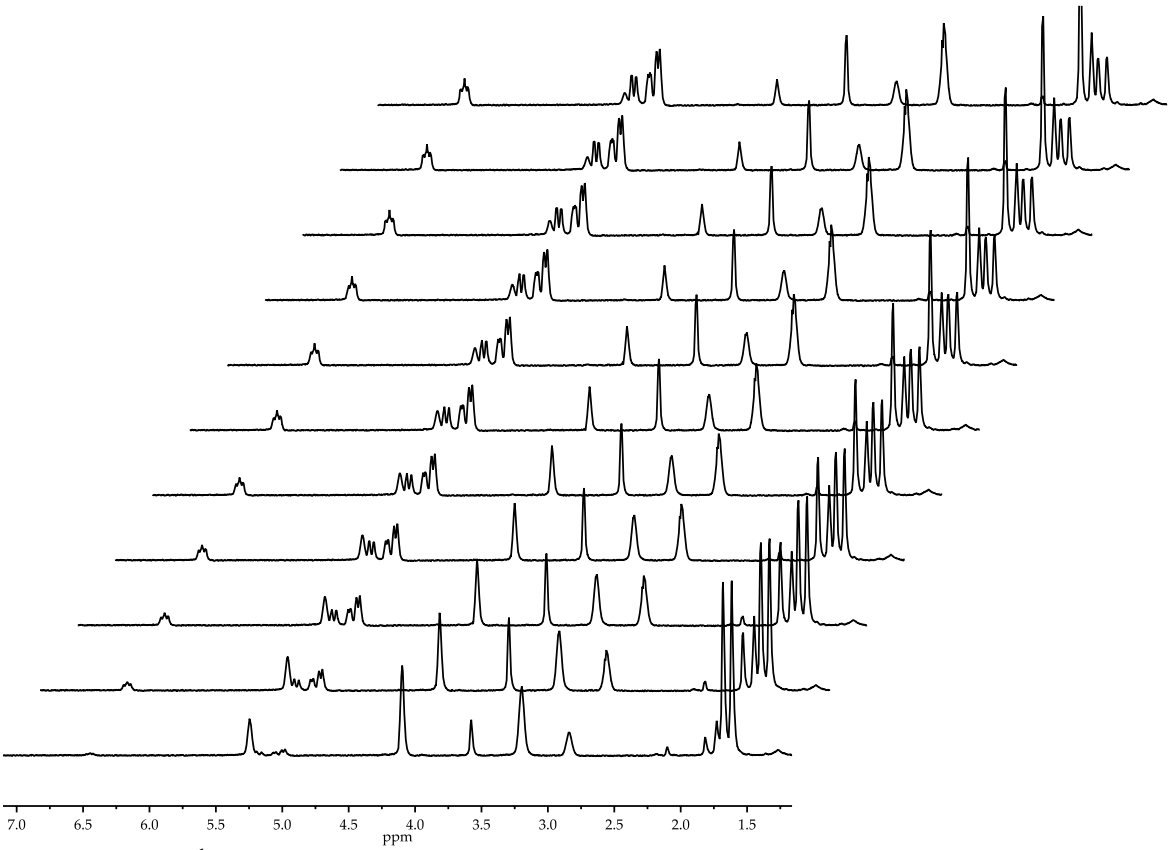

Figure A.3.24. ^{1}H NMR spectra of 0.23 M trimethylsilyl ether of prenol with 0.30 M NaDA in neat THF at –60 °C. Each spectrum corresponds to an interval of 131 seconds. These spectra are consistent with stoichiometric consumption of NaDA to give isoprene.

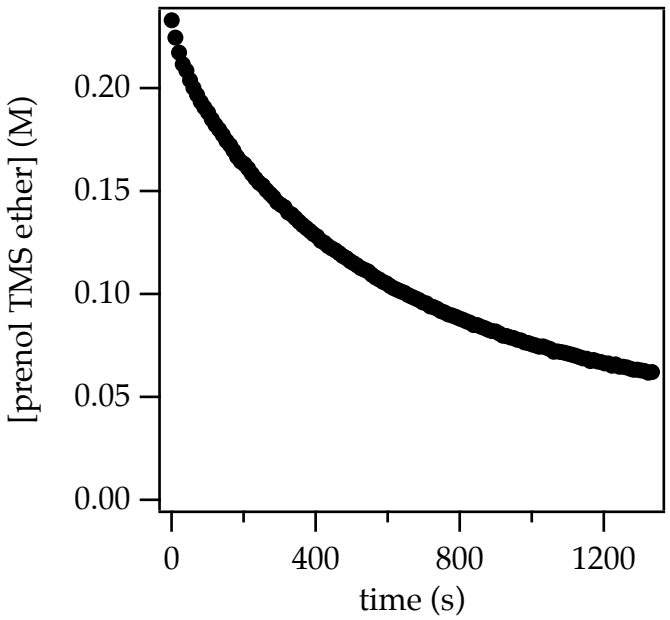

Figure A.3.25.Concentration of 0.23 M trimethylsilyl ether of prenol with 0.30 M NaDA in neat THF at –60 °C.

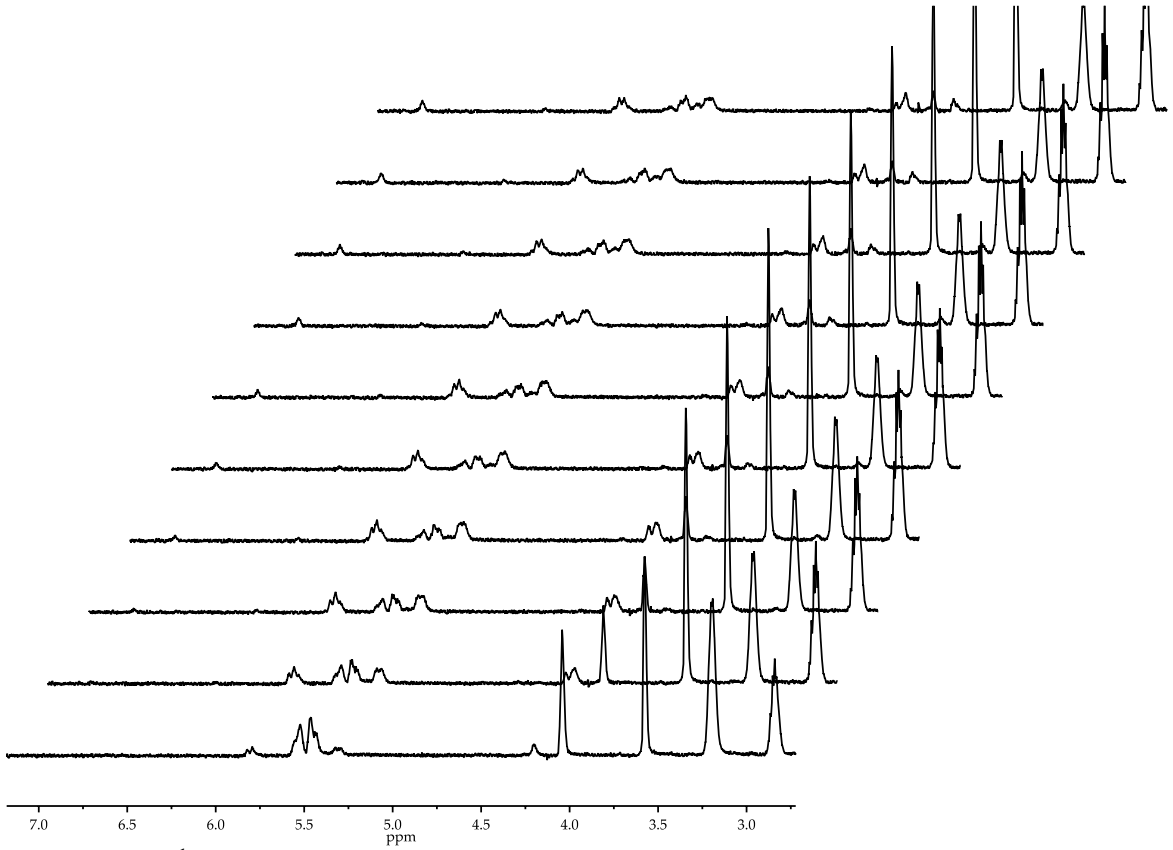

Figure A.3.26. ^{1}H NMR spectra of 0.080 M trimethylsilyl ether **8** with 0.19 M NaDA in neat THF at –40 °C. Each spectrum corresponds to an interval of 626 seconds. These spectra are consistent with stoichiometric consumption of NaDA to give several products.

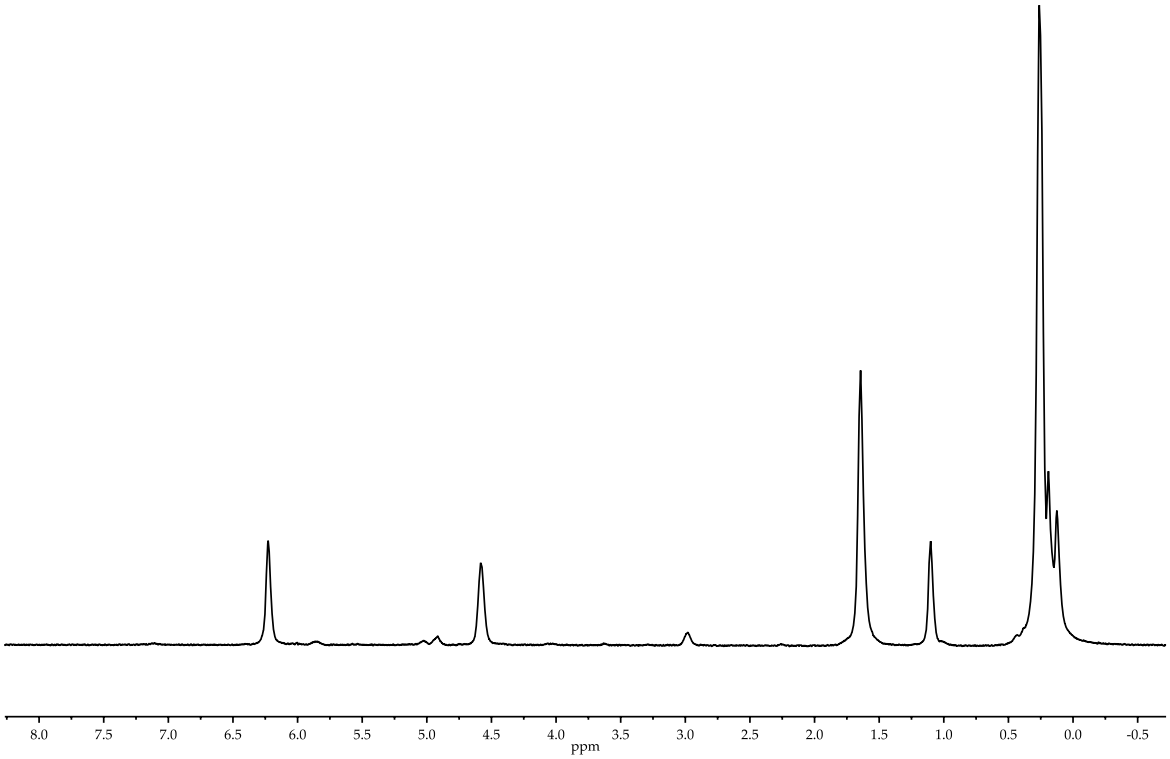

Figure A.3.27. ^{1}H NMR spectrum of isomerization of 1.5 mL neat allyloxytrimethylsilane with 7 mol % NaDA at room temperature after one minute. The resonances at 2.9 ppm and 1.1 ppm are consistent with diisopropylamine.

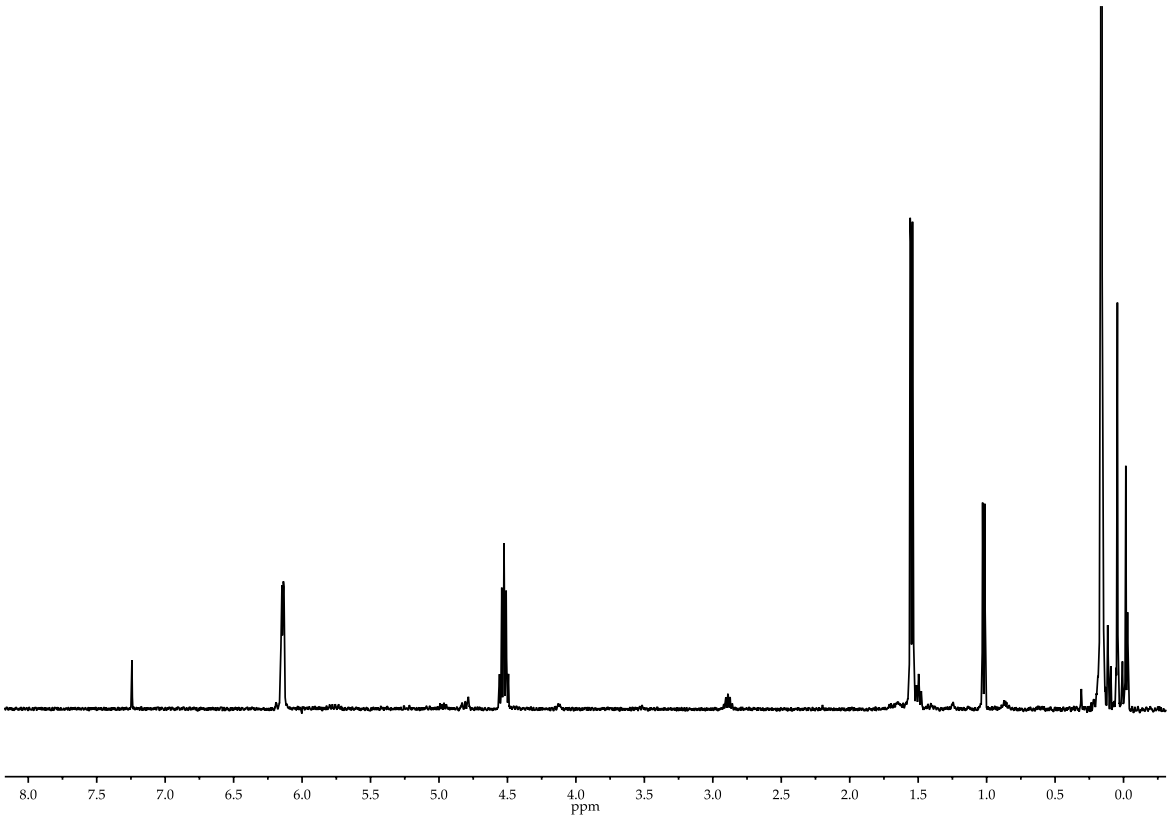

Figure A.3.28. ^{1}H NMR spectrum ($CDCl_3$) of isolated material (distillation) from isomerization of 1.5 mL neat allyloxytrimethylsilane with 7 mol % NaDA at room temperature after one minute.

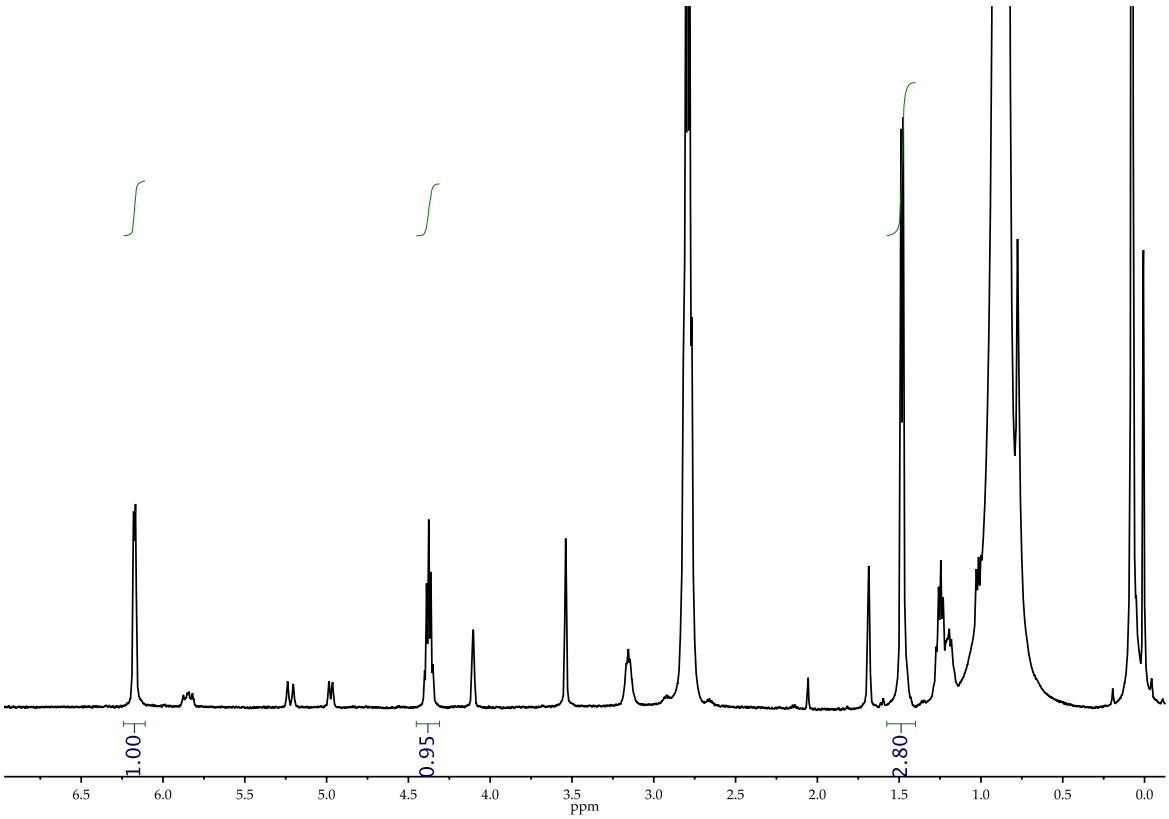

Figure A.3.29.[1]H NMR spectrum of partial isomerization of 0.47 M allyloxy-*tert*-butyldimethylsilane with 0.094 M NaDA and 1.43 M DN*i*-Pr_2 in THF-d_8. That the relative integration of the terminal methyl (~1.4 ppm) is significantly above 2 is consistent with predominant retention of protons from substrate without trapping of the allylsodium intermediate by DN*i*-Pr_2.

Chapter 4

Sodium Diisopropylamide:

Selectivities, Rates, and Mechanisms of Arene Metalations

Sodium Diisopropylamide:

Selectivities, Rates, and Mechanisms of Arene Metalations

Abstract

Sodium diisopropylamide (NaDA)-mediated metalations of arenes in THF/hexane or THF/Me_2NEt solutions are described. A survey of >40 benzenoid and pyridine-based arenes with a range of substituents demonstrates the efficacy and regioselectivity of metalation. The metalations of activated disubstituted arenes and selected monosubstituted arenes are rapid at –78 °C. Rate studies of 1,3-dimethoxybenzene and related methoxylated arenes show exclusively monomer-based orthometalations with two or three coordinated THF ligands. Rate studies of isotopic exchange of benzene and monosubstituted arenes with weakly activating groups reveal analogous di- and trisolvated monomer-based metalations. Substituent dependencies reveal cooperative inductive, mesomeric, steric, and chelate effects are described.

Introduction

In 1908 Schorigin reported that ethylsodium metalates benzene, constituting the first example of an organosodium-mediated arene metalation.[1] Progress accelerated with seminal studies by Gilman in the 1930s and Morton in the 1940s to explore highly reactive aryl- and alkylsodiums.[2,3,4] Renewed activity in organosodium chemistry appeared sporadically with the emergence of mixed-alkali-metal super bases[5] and, most recently, structural studies of Mulvey and coworkers.[6] Of course, there are a number of sodium-based reagents used routinely. In contrast to organolithium chemistry, however, organosodium chemistry has been in a protracted period of relative quiescence. Sodium diisopropylamide (NaDA) is an excellent case in point.

Whereas lithium diisopropylamide (LDA) is used hundreds if not thousands of times *daily*, we can find only a dozen reports of NaDA over the six decades since the first report by Levine and coworkers in 1959.[7,8] It is difficult to know with confidence why this is the case, but the 2017 *Wikipedia* entry probably captures the essence of the problem by noting that organosodium reagents are "limited in part due to competition from organolithium compounds" and that they are "poorly soluble."[9]

We have begun a program to examine synthetic, structural, and mechanistic organosodium chemistry that centers on the chemistry of NaDA.[10] In the first paper of the series, we showed that 1.0 M solutions of NaDA in *N,N*-dimethylethylamine (DMEA) can be prepared in minutes using technical-grade reagents (eq 4.1).[10a] Subsequent studies probed the stability and solubility of NaDA in a range of solvents—dimers **1** and **2** are germane to the work described below[10b]—as well as the reactivity of NaDA toward alkenes and dienes.[10c] The most obvious application of NaDA—metalation of substituted arenes—must have been examined by somebody and possibly even reported, but our failure to find an example underscores a glaring omission (eq 4.2).[11] We describe herein NaDA-mediated arene sodiation from a synthetic organic and mechanistic perspective.[12]

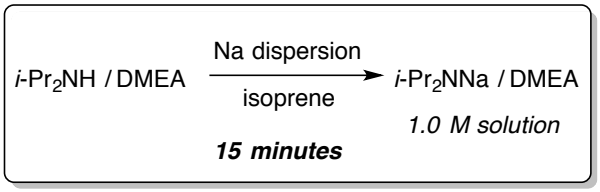

(4.1)

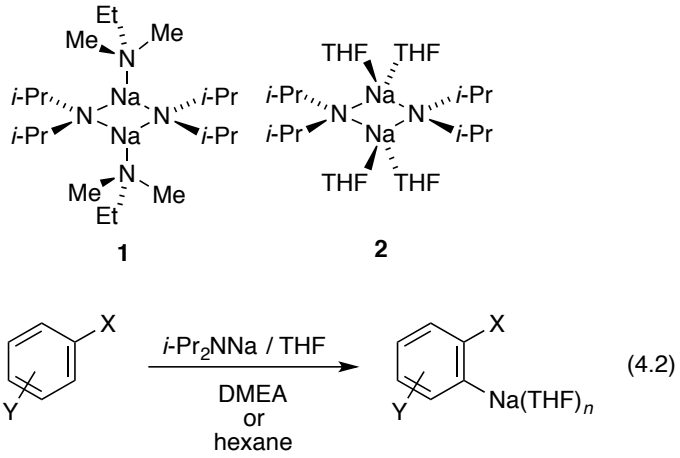

Results

Methods. NaDA was prepared and purified by a modified literature procedure.[8a,10a] It can be handled as a white solid or as a 1.0 M solution in DMEA, both of which are stable for weeks at 25 °C and months at –20 °C.[10a,b] Control experiments show that NaDA/THF/DMEA and NaDA/THF/hexane are operationally indistinguishable, consistent with the weak donicity of trialkylamines and exergonic substitution by THF.[13,14] We use the two cosolvents interchangeably but favor NaDA/THF/hexane only because of our specific interests in structural and mechanistic studies. The typical practitioner is likely to find NaDA/DMEA stock solutions convenient.

Arene metalations were monitored using ^{1}H, ^{2}H, ^{19}F NMR, or *in situ* IR spectroscopies.[15,16] By habit and protocols tied to rate studies, we routinely carry out metalations with 0.10 M NaDA, although metalations of 0.50–1.0 M arene occur without detectable precipitation of the arylsodiums in most instances.[17] Arenes can be cataloged as those that metalate instantaneously at –78 °C (Chart 4.1), slowly enough to monitor at –78 °C (Chart 4.2), detectably only through isotopic exchange (Chart 4.3), and destructively (Chart 4.4). Metalations of substrates in Charts 4.1–4 using other bases have been reported.[12]

Chart 4.1. Substrates that rapidly metalate.

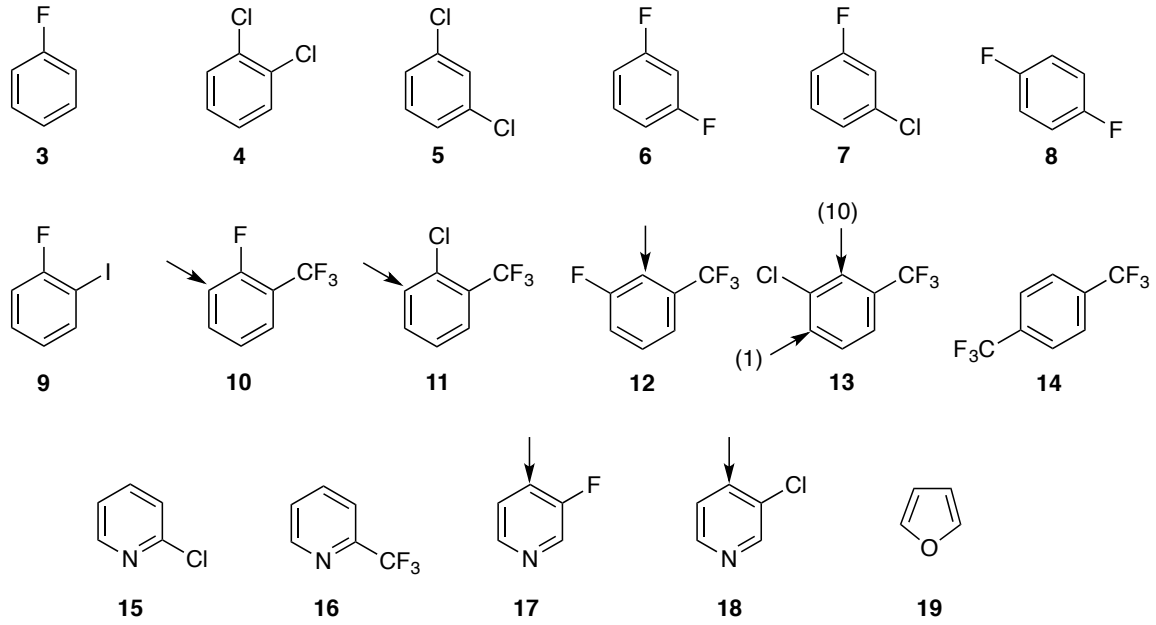

Chart 4.2. Substrates that metalate at measurable rates.

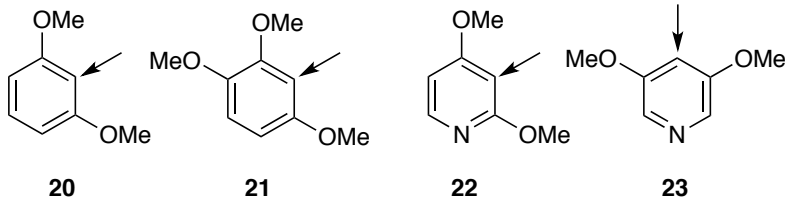

Chart 4.3. Substrates that transiently metalate.

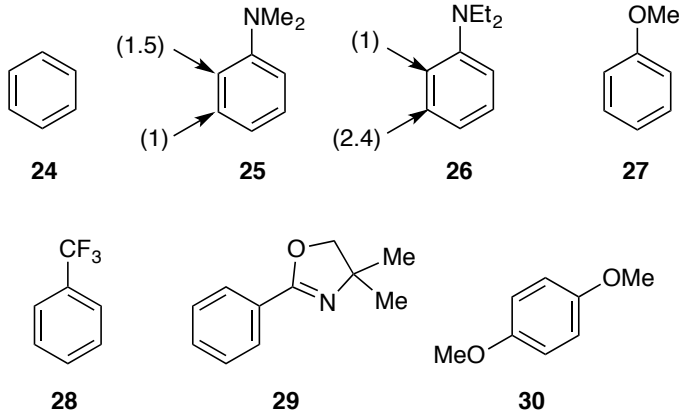

Chart 4.4. Substrates that degrade on metalation.

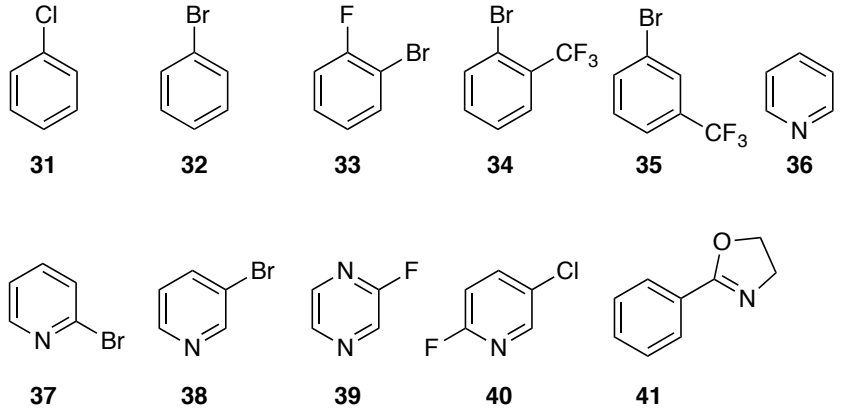

Regioselectivity and Reversible Metalation. The regioselectivities for substrates in Charts 4.1 and 4.3 are implicitly ortho or doubly ortho. Selectivities that are less obvious are indicated by arrows with affiliated selectivities. Whether the selectivities are kinetically or thermodynamically controlled *cannot* be ascertained unless an equilibration is explicitly detected. A rare example is the ~1:5 selectivity for metalation of **13** at –116 °C that reverses to a 10:1 selectivity on standing at –116 °C (eq 4.3). Such an isomerization would be undetectable at –78 °C.

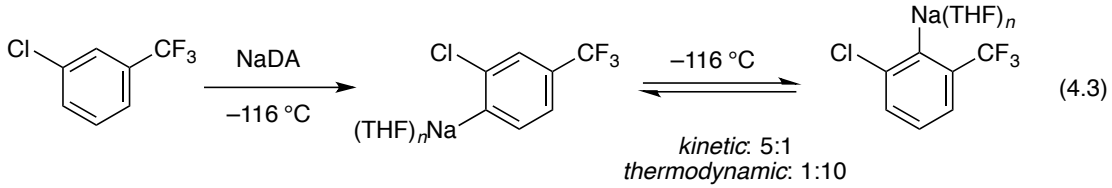

(4.3)

Kinetics and Mechanism of Arene Metalation.[18] The muted reactivity of arenes in Chart 4.2 allowed us to monitor rates under pseudo-first-order conditions in which the substrate is the limiting reagent (0.010 M). Metalation of 1,3-dimethoxybenzene (**20**, eq 4.4) at –78 °C by NaDA in THF/hexane follows a clean decay to partial conversion at equilibrium (Figure 4.1). Plotting initial rate vs THF concentration (Figure 4.2) shows a linear dependence with a substantial non-zero intercept. The rates monitored versus NaDA concentration (Figure 4.3) afford an approximate half-order dependence. The idealized rate law[19] (eq 4.5) and assignment of NaDA as tetrasolvated dimer **2**[10b] are consistent with dominant disolvated monomer-based metalation depicted generically in eq 4.6.[20] The collective data on THF dependencies (below) suggest that the first-order dependence is likely to be a primary shell solvation step consistent with low levels of an intervening trisolvated monomer-based metalation (eq 4.7).

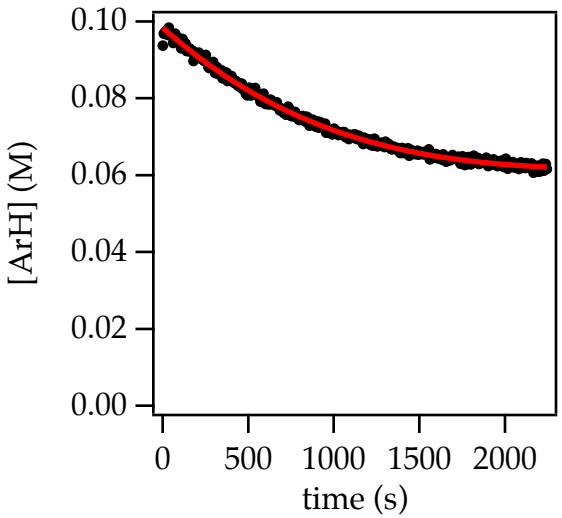

Figure 4.1. Plot of 1,3-dimethoxybenzene (**20**, ArH) concentration versus time for stoichiometric orthometalation with 0.10 M NaDA in 5.83 M THF/hexane at –78 °C. The curve depicts an unweighted least-squares fit to the function[18,21] $[ArH] = \{[ArH]_0^{1-n} + k(n-1)t\}^{1/(1-n)} +$

$[ArH]_\infty$: $[ArH]_0 = 0.0368 \pm 0.0004$; $n = 0.71 \pm 0.03$; $k = (4.1 \pm 0.4) \times 10^{-4}$; $[ArH]_\infty = 0.0616 \pm 0.0003$. The deviation from 1.5-order behavior (first order in arene and one-half order in NaDA) is likely due to mild autocatalysis.

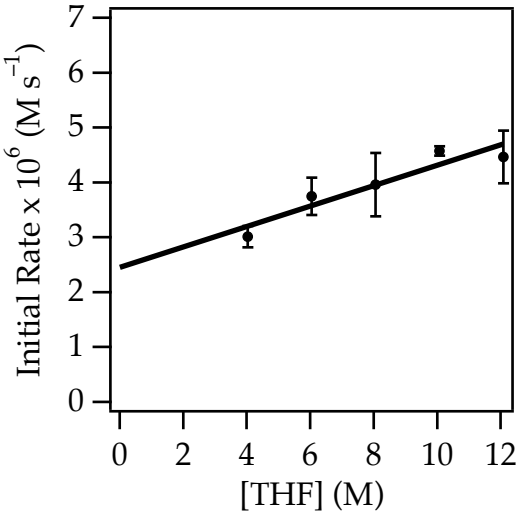

Figure 4.2. Plot of initial rate versus THF concentration for the orthometalation of 0.010 M 1,3-dimethoxybenzene (**20**) with 0.10 M NaDA at –78 °C. The curve depicts an unweighted least-squares fit to the function $f(x) = ax + b$: $a = 0.19 \pm 0.04$; $b = 2.5 \pm 0.03$.

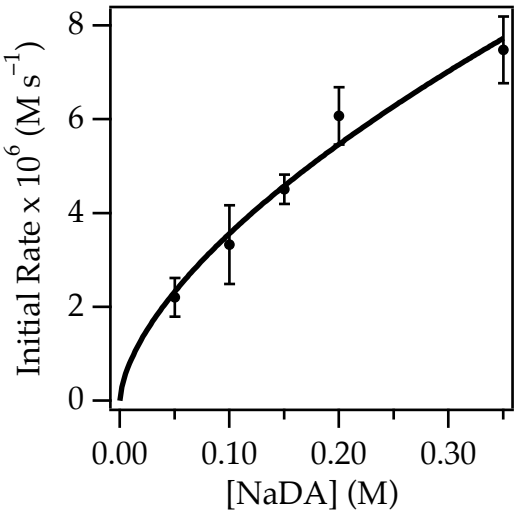

Figure 4.3. Plot of initial rate versus NaDA concentration for the orthometalation of 0.010 M 1,3-dimethoxybenzene in 6.0 M THF/hexane at –78 °C. The curve depicts an unweighted least-squares fit to the function $f(x) = ax^b$: $a = 15 \pm 2$; $b = 0.62 \pm 0.07$.

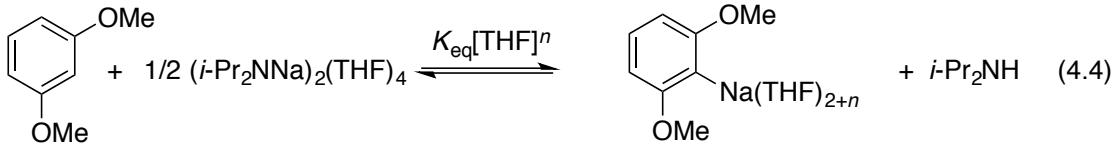

(4.4)

$$-d[ArH]/dt = (k\,[THF]^0 + k'[THF]^1)\,[A_2S_4]^{1/2}[ArH]^1 \qquad (4.5)$$

$$1/2\ A_2(THF)_4 + ArH \longrightarrow [A(THF)_2 \cdot ArH]^{\ddagger} \qquad (4.6)$$

$$1/2\ A_2(THF)_4 + THF + ArH \longrightarrow [A(THF)_3 \cdot ArH]^{\ddagger} \qquad (4.7)$$

Rate studies using 1,2,4-trimethoxybenzene (**21**) show a threefold higher rate than with **20** via an otherwise analogous mechanism and incomplete conversion at equilibrium (Supporting Information). Unlike **20**, metalation of high concentrations of **21** reveals autocatalysis in the form of a sigmoidal decay (Figure 4.4). Decays at lower arene concentrations are nearly

exponential (Figure 4.4, inset). An approximate[22] first-order dependence of initial rates on ArNa is consistent with the intermediacy of a fleeting NaDA-ArNa mixed-aggregate (eq 4.8).[23] Curiously, arylsodium **21-Na** also catalyzes the metalation of **20**, whereas **20-Na** does *not* catalyze the metalation of **21**.

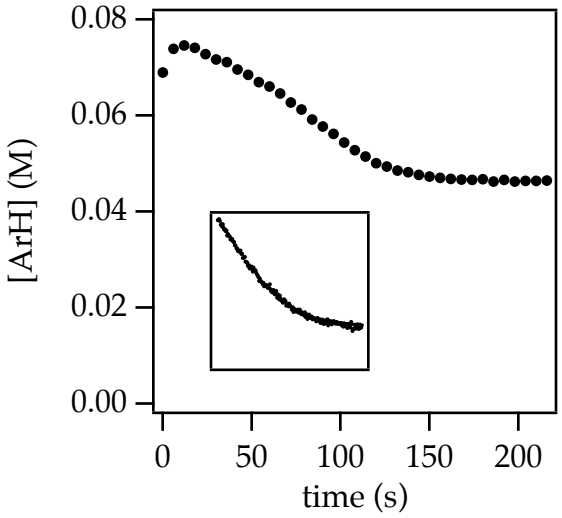

Figure 4.4. Plot of 1,2,4-trimethoxybenzene (**21**, ArH) concentration versus time for metalation of 0.080 M ArH with 0.10 M NaDA in neat THF at –78 °C. Inset: Plot of arene concentration versus time (0–1200 seconds) for metalation of low concentrations (0.010 M) ArH with 0.10 M NaDA in neat THF at –78 °C.

$$1/2\ \mathbf{2} + \mathrm{ArNa} \rightleftharpoons [(i\text{-Pr})_2\mathrm{NNa{\bullet}ArNa}] \xrightarrow{+\mathrm{ArH}} 2\ \mathrm{ArNa} \qquad (4.8)$$

Kinetics and Mechanism of Isotopic Exchange. The influence of arene substituents on rates, mechanisms, and selectivities of metalation was examined by monitoring deuterium exchange (eq 4.9) using ^{2}H NMR spectroscopy for substrates that metalate only transiently (endergonically) (Chart 4.3).[24] Monitoring initial rates precludes multiple exchanges and

minimizes the slower but detectable exchange with a protons in THF.[10b] The regiochemistries (arrows in Chart 4.3) attest to competitive steric, chelation, inductive, and p effects (discussed below).

$$\underset{\text{(excess)}}{\text{ArH} + i\text{-Pr}_2\text{ND}} \overset{\text{NaDA}}{\rightleftharpoons} \text{ArD} + i\text{-Pr}_2\text{NH} \qquad (4.9)$$

ArH: $PhNEt_2$ < $PhNMe_2$ < PhH < PhOMe < $PhCF_3$ < **29**
k_{rel}: (1.0) (1.5) (10) (5×10^3) (10^4) (2×10^4)

Rate studies show approximate half-order NaDA dependencies in all cases, signifying monomer-based metalations. The plots of rates versus THF concentrations show substrate-dependent contributions of zeroth- and first-order dependencies attributed to di- and trisolvated monomer-based metalations to the regioselectivities (Figures 4.5–8). $PhNEt_2$ shows marked attenuation of ortho metalation rates relative to $PhNMe_2$ while leaving meta metalation unchanged. $PhCF_3$ shows evidence of exchange into the para position, but only at elevated temperatures (–20 °C). Supporting information has full details.

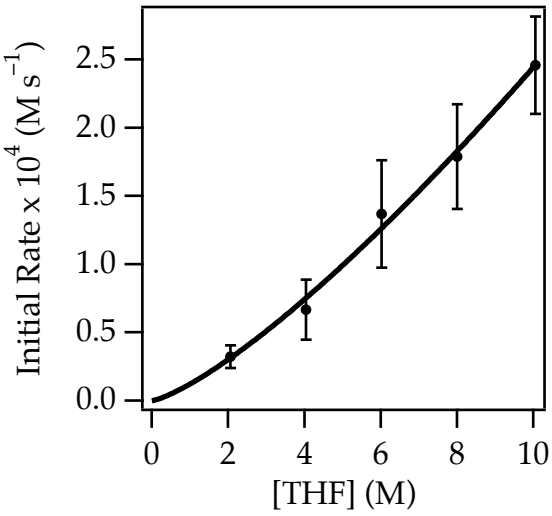

Figure 4.5. Plot of initial rate versus THF concentration for the isotopic exchange of 0.23 M benzene with 0.10 M NaDA and 1.04 M *i*-Pr_2ND in hexane cosolvent at 25 °C. The curve depicts an unweighted least-squares fit to the function $f(x) = ax^b$: $a = 0.12 \pm 0.02$; $b = 1.30 \pm 0.02$.

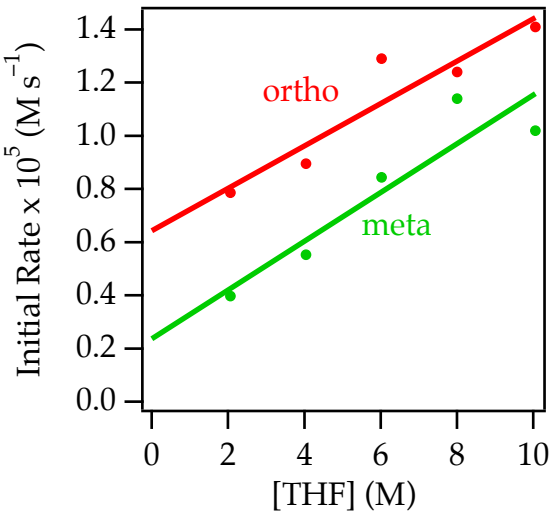

Figure 4.6. Plot of initial rate versus THF concentration for the isotopic exchange of 0.44 M *N,N*-dimethylaniline (**25**) with 0.10 M NaDA and 0.79 M *i*-Pr_2ND in hexane cosolvent at 25 °C.

The curves depict unweighted least-squares fits to the function $f(x) = ax + b$: ortho: ($a = 0.08 \pm 0.02$; $b = 0.6 \pm 0.1$); meta: ($a = 0.09 \pm 0.02$; $b = 0.2 \pm 0.1$).

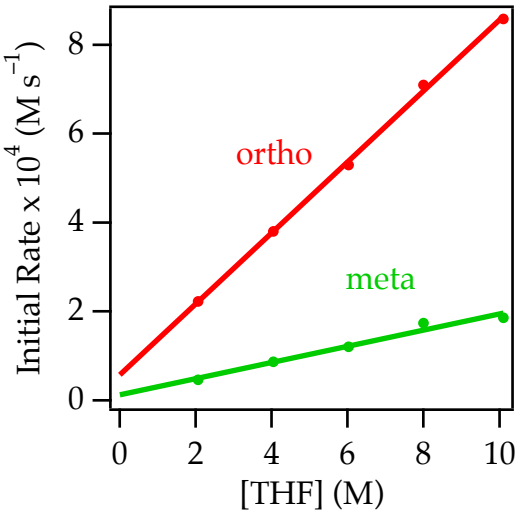

Figure 4.7. Plot of initial rate versus THF concentration for the isotopic exchange of 0.45 M α,α,α-trifluorotoluene (**28**) with 0.10 M NaDA and 0.79 M *i*-Pr_2ND in hexane cosolvent at –40 °C. The curves depict unweighted least-squares fits to the function $f(x) = ax + b$: ortho: ($a = 0.80 \pm 0.02$; $b = 0.6 \pm 0.1$); meta: ($a = 0.18 \pm 0.02$; $b = 0.1 \pm 0.1$).

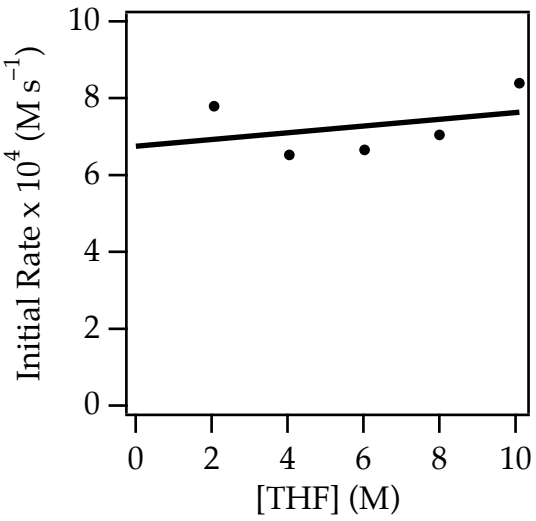

Figure 4.8. Plot of initial rate versus THF concentration for the ortho-selective isotopic exchange of 0.32 M 4,4-dimethyl-2-phenyl-2-oxazoline (**29**) with 0.10 M NaDA and 0.79 M *i*-Pr_2ND in hexane cosolvent at –40 °C. The curve depicts an unweighted least-squares fit to the function $f(x) = ax + b$: $a = 0.09 \pm 0.1$; $b = 6.8 \pm 0.9$.

Discussion

We examined NaDA-mediated metalations of >40 arenes grouped by those that metalate instantaneously at –78 °C (Chart 4.1), at tractable rates (Chart 4.2), via fleeting arylsodiums (Chart 4.3), and destructively (Chart 4.4). These metalations collectively confront issues and questions that are recognizable to those versed in base-mediated arene functionalization.[10]

The Case for Sodium. NaDA is easy to prepare as stable 1.0 M solutions in trialkylamines (DMEA) and is readily isolated as a white solid.[10a,b] The steric demands of trialkylamines[13,14] allow for exergonic substitution by standard ethereal ligands either before or after metalation. Adding >3 equiv THF to NaDA/DMEA quantitatively converts DMEA-solvated dimer **1** to THF-solvated dimer **2**.[10b] Rates of arene metalations using NaDA/THF are

often so rapid that few were slow enough to study mechanistically. The absence of previously cited NaDA-mediated arene metalations underscores the degree to which the community may have overlooked organosodium chemistry. With that said, the full advantages of NaDA will take time to emerge.

Regioselectivities. The selectivities in Charts 4.1–3 are singly or doubly ortho unless otherwise indicated by arrows. This story is not so simple, however. The issue of regiochemical equilibration in ortholithiations has surfaced previously,[26] been studied mechanistically,[27] and rears its ugly head here. Explicit kinetic versus thermodynamic control was documented for arene **13** (eq 4.3). However, we cannot rule out the possibility that many arylsodiums equilibrate rapidly; the kinetic vs thermodynamic preferences remain unresolved. This ambiguity is more persistent in many studies of regioselectivity than many realize. We suspect from limited data—it is more of a hunch than an observation—that isomerization may be more prevalent using NaDA than LDA.

Over the decades practitioners of orthometalations have surveyed relative directing effects of arene substituents largely through internal competitions of ortho-, meta-, and para-disubstituted arenes **42**, **43**, and **44**, respectively.[12] Empirically observed fast versus slow metalations add to the story.

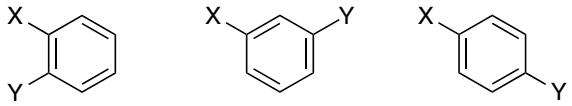

42 **43** **44**

These experiments are well suited to those seeking to render othometalations predictable. However, there are latent approximations in using such disubstituted arenes because *inductive, resonance, steric, and chelation effects are not always restricted to the ortho position.* How do

meta and para substituents influence the rates of ortho metalations? In short, the effects are additive and underdetermined in such seemingly simple regiochemical competitions. It is in this context that we are enamored with the isotopic exchange studies of the transiently metalated substrates in Chart 4.3.[24,25] Monosubstituted arenes present no such additivities, and observable meta and para exchanges reveal long range effects that cannot be ignored. We should add that entirely regioselective orthometalations of arenes **27** and **29** do *not* tell us anything about long range effects, only that the influence at the ortho position is large by comparison (dominant). The rate of benzene exchange provides a benchmark for rates of meta and para metalation.

One can discern separate contributions at play: (1) $PhCF_3$ (**28**) shows a distribution suggesting that CF_3 exerts a dominantly inductive influence, as noted by Mulvey using *n*BuNa;[11] (2) comparing the relative rates of benzene (**24**) and $PhNMe_2$ (**25**) shows that anilines are overall *deactivated* toward metalation (even with the statistical effects included) with the most marked inhibition at the para position suggesting a destabilizing resonance effect; and (3) comparing $PhNMe_2$ (**25**) and $PhNEt_2$ (**26**) confirms that steric effects retard orthometalation, tacitly promoting meta substitution. The conclusions that should not surprise many are as follows: resonance effects inhibit ortho and para metalation; inductive effects promote ortho, meta, and para metalation in that order; steric effects inhibit only orthometalation; and chelation (substituent coordination to sodium) promotes only orthometalation.

Decompositions. There were, of course, a few failures (Chart 4.4). Benzyne formation poses a problem in some cases (unless it is the targeted outcome).[28] Stabilized orthohalo arylsodiums derived from most substrates in Chart 4.1 illustrate elimination to form benzyne is not a chronic problem. In several cases we saw limited darkening of the solutions that seems to

accompany decomposition, but the NMR spectra of the arylsodiums and successful deuterations revealed no major problems.

Although the failures in Chart 4.4 could stem from benzyne formation, we cannot exclude $[Ar–Br–NR_2]^-$ adducts,[29] electron-transfer-based reductions,[30] or migration (halogen dancing).[31] Arenes **38**–**40** share a 3-halopyridine motif that may present special problems contrasting with the successful 2-halo arene metalations in Chart 4.1, possibly owing to enhanced electrophilicity. Nucleophilic addition to pyridines, especially self-condensation,[32] is a problem we hoped to avoid.

The CF_3 substituent seems particularly sensitive to destruction, possibly owing to formation of benzocyclopropene studied by Billups.[33] Interestingly, $PhCF_3$ should be highly sensitive to decomposition, but NaDA-mediated isotopic exchange was readily achieved. Several doubly activated forms including **14** and **16** showed darkening but no direct evidence of destruction.

Oxazoline **41** appears to undergo facile elimination of the saturated heterocycle backbone, which often elicits use of 4,4-dimethylated analog **29**. Only one group—that of Collum and coworkers—has reported the LDA-mediated orthometalation of **41**.[34] Suspecting the LDA result might be an error, we repeated the metalation and, indeed, confirmed the error (probably owing to inadequate supervision and oversight).[34] Nonetheless, alkyllithiums and lithium 2,2,6,6-tetramethylpiperidide orthometalate **41** without competing decomposition.[35,36]

Mechanisms. Rate studies of observable metalations of **20** and **21** as well as of isotopic exchange via fleeting anions derived from **24**–**30** all show approximately half-order dependencies on NaDA consistent with monomer-based metalations. Plots of rates versus THF concentrations showing non-zero intercepts and linear dependencies on THF concentration are

consistent with di- and trisolvated monomers, respectively.[18] One could ascribe minor THF dependencies to medium effects, but the absence of dependence in some cases (Figure 4.8) and striking dependence in others (Figures 4.5 and 4.7) argue strongly for primary shell solvation. We add that secondary-shell effects are generally small using *lithium* bases.[18,37] We can glean some insights about substituent dependencies by noting the relative contributions of the two solvation states.

Metalation of benzene, a cornerstone to any discussion of arene metalation, occurs via a trisolvated monomer-based mechanism shown by density functional theory (DFT) computations to be **45**.[38] Slight upward curvature in Figure 4.5 suggests a contributing tetrasolvate. Although DFT is unsupportive, we are reluctant to dismiss such a mechanism because we have found transition states based on five- and even six-coordinate sodiums to be computationally viable in other instances.[10c]

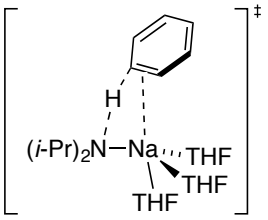

45

Metalations of **20** and **21** with meta-disposed methoxy moieties reveal a mixture of di- and trisolvate consistent with encroaching steric demand. DFT computations show discrete MeO–Na interactions both in **46** and **47** and predict a distinct preference for trisolvation (eq 4.10) that is *not* borne out experimentally (Figure 4.2). Analogous studies of *n*-butyllithium/TMEDA-mediated metalations showed no experimental or computational evidence of methoxy-lithium contacts. Anisole, a less congested variant of **20** and **21**, shows MeO–Na contacts and no significant bias for di- versus trisolvate experimentally and computationally (eq

4.11). The somewhat baffling quantitative difference in eqs 4.10 and 4.11 was explored extensively with no obvious explanation.

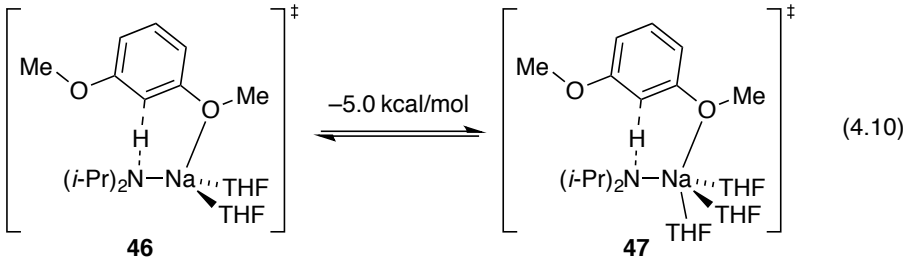

46 **47** (4.10)

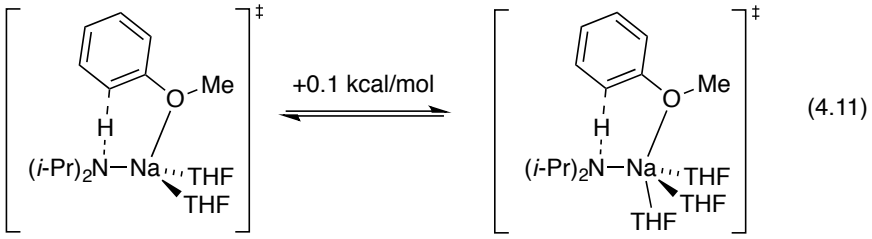

48 **49** (4.11)

$PhCF_3$ behaves as an inductively activated benzene, facilitating metalations at all positions. Orthometalation represents a potential battle between steric inhibition versus activation through induction and Na–F interaction (chelation). DFT computations support such an interaction (**50**), but the resulting regioselectivity suggests it cannot be as highly stabilizing as predicted (eq 4.12).

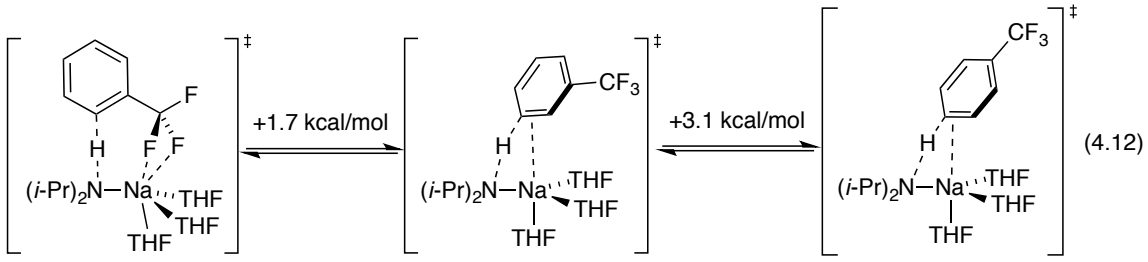

50 **51** **52** (4.12)

Metalations of anilines **25** and **26** are especially interesting. Anilines are notoriously poor directing groups, a fact readily ascribed to weak Lewis basicity of the dimethylamino moiety and

high steric effects.[12] Although early studies using alkylsodiums suggest anilines are acidic relative to benzene,[2] we find both **25** and **26** metalate more slowly than benzene. DFT computations of orthometalation (**53**) show evidence of an N–Na contact, but it could merely reflect minimization of steric effects. The de facto preference for meta metalation results from inhibited ortho and para metalation. Evidence of both di- and trisolvation even at the benzene-like meta position is somewhat perplexing given benzene shows evidence of only trisolvated monomer.

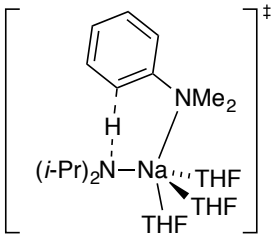

53

Oxazoline **29** appears to be a prime candidate for a chelation-directed orthometalation, which is implicated by high rates and dominant disolvated-monomer-based pathway. Previous studies of the lithium analog suggest the N–Li contact is likely preferred relative to the O–Li contact.[39,40] Indeed, DFT computations show a >6 kcal/mol preference for the N–Na interaction shown in **54** despite the steric demands imparted by the methyl moieties. The proton transfer in transition structure **54** displays significant distortion with the arene C–H bond deviating 17 degrees out of the benzene plane with an accompanying 19 degree rotation of the oxazoline moiety relative to the benzene fragment. This potentially strong directing group appears to be laboring to achieve optimal alignment.

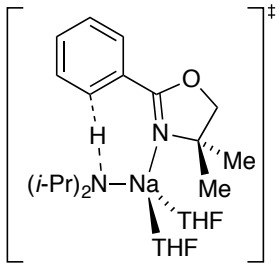

54

Conclusion

NaDA-mediated arene metalations are much faster than with LDA. With that said, time will tell if investigators facing specific challenges will find such accelerations advantageous. That NaDA is trivial to prepare and handle ought to bolster its appeal. We also suspect reactions of the resulting arylsodiums are ripe for development. Metathesis with other metal salts such as copper chloride or zinc chloride for subsequent couplings will occur under "salt-free" conditions given the insolubility of NaCl.[41,42] In anticipation of such interest, we began studying the solution structures of the arylsodiums generated herein thinking the task would be easy and discovered it was a research project in its own right. For now, we can say that NaDA-mediated metalations of arenes generally work well and are mechanistically tractable.

Experimental

IR spectroscopic analyses. IR spectra were recorded using an in situ IR spectrometer fitted with a 30-bounce, silicon-tipped probe. The spectra were acquired in 16 scans at a gain of 1 and a resolution of 4 cm^{-1}. A representative reaction was carried out as follows: The IR probe was inserted through a nylon adapter and O-ring seal into an oven-dried, cylindrical flask fitted with a magnetic stir bar and a T-joint. The T-joint was capped by a septum for injections and a nitrogen line. After evacuation under full vacuum, heating, and flushing with nitrogen, the flask

was charged with NaDA (60.4 mg, 0.49 mmol) in THF/hexane (4.9 mL) and cooled in a dry ice–acetone bath prepared with fresh acetone. After recording a background spectrum, a stock solution of arene **20** (100 mL, 0.049 mmol) was added with stirring. For the most rapid reactions, IR spectra were recorded every 6 s with monitoring of the absorbance at 1493 cm^{-1} over the course of the reaction.

NMR Spectroscopy. NMR samples for reaction monitoring were routinely prepared using stock solutions of NaDA and flame sealed under partial vacuum. DMEA-free solutions of NaDA with added ligands used DMEA-free crystallized NaDA. Standard ^{1}H, ^{2}H, and ^{13}C NMR spectra were recorded on a 500 MHz spectrometer at 500, 76.7, and 125.7 MHz, respectively. The ^{1}H, ^{2}H, and ^{13}C resonances were referenced to the C*H*$_2$O resonance of THF at –80 °C (3.58 ppm), the C*D*(H)O resonance of THF at –80 °C (3.58 ppm), and the *C*H$_2$O resonance of THF at –80 °C (67.57 ppm), respectively.

Density Functional Computations. Density functional theory (DFT) calculations were carried out at the B3LYP/6–31G(d) level with single-point calculations at the MP2 level of theory.[38] Transition structures were confirmed by a single negative frequency.

Arene Metalations: Method A. A representative reaction was carried out as follows: Sodium dispersion in toluene (3.0 mL, 35 mmol) in a 15 mL pear-shaped flask was washed three times with DMEA (2.0 mL each) with removal of the supernatants by syringe. A final aliquot of DMEA was added (3.6 mL) and followed by diisopropylamine (1.05 mL, 7.5 mmol). After cooling to 0 °C, isoprene (380 μL, 3.75 mmol) was added. The solution was allowed to warm to rt over the course of 20 minutes, after which the stirring was halted and insoluble materials were allowed to settle providing a yellow supernatant. A dried vial was charged with this stock solution (2.9 mL, 4.4 mmol), to which THF (5.0 mL) was added and cooled to –78 °C. Neat 1,2-

dichlorobenzene (382 μL, 3.4 mmol) was added with stirring for 30 sec and subsequently quenched with 1.00 mL MeOD. After warming to rt, the reaction mixture was diluted with water and pentane. The organic layer was washed with water (4 × 5 mL), dried over sodium sulfate, and concentrated. The crude product was chromatographed in neat pentane (Rf = 0.7) to provide 1,2-dichlorobenzene (270 mg, 55% mass recovery) with 80% deuteration at the ortho position. The extent and regiochemistry of proton loss was taken to represent the metalation event.

Arene Metalations: Method B. A representative reaction was carried out as follows: a dried vial flushed with argon was sequentially charged with solid NaDA (49 mg, 0.400 mmol) and THF (1.00 mL) and cooled to –78 °C. Neat 1,2-dichlorobenzene (42 mL, 0.38 mmol) was added with stirring for 10 sec and subsequently quenched with 500 mL MeOD. Neat cyclohexene (100 mL) was added to the flask to serve as an internal standard. After warming to rt, a portion of the sample was transferred to an NMR tube for analysis as noted above.

Chapter 4 References and Footnotes

1. Schorigin, P. *Ber.* **1908**, *41*, 2711.

2. Benkeser, R. A.; Foster, D. J.; Sauve, D. M.; Nobis, J. F. *Chem. Rev*. **1957**, *57*, 867.

3. (a) Schlosser, M. *Angew. Chem., Int. Ed.* **1964**, 3, 287. (b) Schlosser, M. *Angew. Chem., Int. Ed.* **1964**, 3, 362. (c) Mordini, A. In *Comprehensive Organometallic Chemistry III*; Mingos, D. M. P.; Crabtree, R. H., Eds; Elsevier, 2007, vol. *9*, p 3. (d) Annual surveys: Glaze, W. H. *Organometal. Chem. Rev.* **1971**, *8*, 319 and references cited therein. (e) Jonczyk, A.; Kowalkowska, A. In *Science of Synthesis, 8b: Category 1*, Organometallics; Majewski, M. and Snieckus, V., Eds. Thieme: New York, 2006, vol 8b, p 1141.

4. For an interesting historical perspective on organoalkali metal chemistry, see: (a) Seyferth, D. *Organometallics* **2006**, *25*, 2. (b) Seyferth, D. *Organometallics* **2009**, *28*, 2.

5. Schlosser, M. *Pure Appl. Chem.* **1988**, *60*, 1627.

6. Mulvey, R. E.; Robertson, S. D. *Angew. Chem., Int. Ed.* **2013**, *52*, 11470.

7. Raynolds, S.; Levine, R. *J. Am. Chem. Soc.* **1959**, *82*, 472.

8. (a) Barr, D.; Dawson, A. J.; Wakefield, B. J. *J. Chem. Soc., Chem. Commun.* **1992**, 204. (b) For an attempted comprehensive bibliography of NaDA, see reference 10a.

9. https://en.wikipedia.org/wiki/Organosodium_chemistry

10. (a) Ma, Y.; Algera, R. F.; Collum, D. B. *J. Org. Chem.* **2016**, *81*, 11312. (b) Algera, R. F.; Ma, Y.; Collum, D. B. *J. Am. Chem. Soc.* **2017**, *139*, 7921. (c) Algera, R. F.; Ma, Y.; Collum, D. B. *J. Am. Chem. Soc.* **2017**, *139*, xxASAP.

11. For other forms of orthosodiations, see references 1–6.

12. (a) Gschwend, H. W.; Rodriguez, H. R. *Org. React.* (*N. Y.*) **1979**, *26*, 1. (b) Snieckus, V. *Chem. Rev.* **1990**, *90*, 879. (c) Ager, D. J.; Prakash, I.; Schaad, D. R. *Chem. Rev.* **1996**, *96*, 835. (d) Clayden, J. *Organolithiums: Selectivity for Synthesis*; Tetrahedron Organic Chemistry, Vol. 23; Pergamon: Oxford, 2002. (e) Haag, B.; Mosrin, M.; Ila, H.; Dr. Vladimir Malakhov, V.; Knochel, P. *Angew. Chem., Int Ed.* **2011**, *50*, 9794.

13. For early studies revealing poor coordination of trialkylamines to organolithium aggregates, see: Settle, F. A.; Haggerty, M.; Eastham, J. F. *J. Am. Chem. Soc.* **1964**, *86*, 2076. Lewis, H. L.; Brown, T. L. *J. Am. Chem. Soc.* **1970**, *92*, 4664. Brown, T. L.; Gerteis, R. L.; Rafus, D. A.; Ladd, J. A. *J. Am. Chem. Soc.* **1964**, *86*, 2135. Quirk, R. P.; Kester, D. E. *J. Organomet. Chem.* **1977**, *127*, 111.

14. Discussion of cone angle and steric demands of trialkylamines: (a) Seligson, A. L.; Trogler, W. C. *J. Am. Chem. Soc.* **1991**, *113*, 2520. (b) Choi, M.-G.; Brown, T. L. *Inorg. Chem.* **1993**, *32*, 1548. (c) Widenhoefer, R. A.; Buchwald, S. L. *Organometallics* **1996**, *15*, 3534.

15. Rein, A. J.; Donahue, S. M.; Pavlosky, M. A. *Curr. Opin. Drug Discov. Dev.* **2000**, *3*, 734. (b) Defernez, M.; Wilson, R. *Anal. Chem.* **1997**, *69*, 1288. (c) Brodmann, T.; Koos, P.; Metzger, A.; Knochel, P.; Ley, S. V. *Org. Process Res. Dev.* **2012**, *16*, 1102. (d) Connolly, T. J.; Hansen, E. C.; MacEwan, M. F. *Org. Process Res. Dev.* **2010**, *14*, 466.

16. Review describing ^{19}F NMR spectroscopy in organometallic chemistry: Espinet, P.; Albeniz, A. C.; Casares, J. A.; Martinez-Ilarduya, J. M. *Coord. Chem. Rev.* **2008**, *252*, 2180.

17. On standing at 1.0 M in THF at –78 °C, 2-fluorophenylsodium precipitates.

18. (a) Collum, D. B.; McNeil, A. J.; Ramírez, A. *Angew. Chem., Int. Ed.* **2007**, *46*, 3002. (b) Algera, R. F.; Gupta, L.; Hoepker, A. C.; Liang, J.; Ma, Y.; Singh, K. J.; Collum, D. B. *J. Org. Chem.* **2017**, *82*, 4513.

19. We define the idealized rate law as that obtained by rounding the observed reaction orders to the nearest rational order.

20. The rate law provides the stoichiometry of the transition structure relative to that of the reactants: Edwards, J. O.; Greene, E. F.; Ross, J. *J. Chem. Educ.* **1968**, *45*, 381.

21. Fit is a non-linear variant of the Noyes equation[20a,b] that has been rarely used.[20,cd] (a) Noyes, A. A. *Am. Chem. J.* **1897**, *19*, 766. (b) Casado, J.; Lopez-Quintela, M. A.; Lorenzo-Barral, F. M. *J. Chem. Educ.* **1986**, *63*, 450. (c) Briggs, T. F.; Winemiller, M. D.; Collum, D. B.; Parsons, R. L., Jr.; Davulcu, A. K.; Harris, G. D.; Fortunak, J. D.; Confalone, P. N. *J. Am. Chem. Soc.* **2004**, *126*, 5427.

22. At low ArH concentration the initial rates display a clear first-order dependence; at high ArH concentrations the early onset of autocatalysis disproportionately accelerates beyond that expected for a first-order dependence.

23. Extensive review of structural studies of alkali metal mixed aggregates: Harrison-Marchand, A.; Mongin, F. *Chem. Rev.* **2013**, 113, 7470.

24. (a) Streitwieser, A.; Shah, K.; Reyes, J. R.; Zhang, X.; Davis, N. R.; Wu, E. C. *J. Phys. Chem. A* **2010**, *114*, 8793. (b) Streitwieser, A., Jr.; Lawler, R. G. *J. Am. Chem. Soc.* **1965**, *87*, 5388.

25. Hall, G. E.; Piccolini, R.; Roberts, J. D. *J. Am. Chem. Soc.* **1955**, *77*, 4540.

26. (a) Cottet, F.; Schlosser, M. *Eur. J. Org. Chem.* **2004**, 3793. (b) Bridges. A. J.; Patt, W. C.; Stickney, T. M. *J. Org. Chem.* **1990**, *55*, 773. (c) Fukuda, T.; Ohta, T.; Sudo, E.; Iwao, M. *Org. Lett.* **2010**, *12*, 2734. (d) Comins, D. L.; LaMunyon, D. H. *Tetrahedron Lett.* **1988**, *29*, 773. (e)

Trécourt, F.; Marsais, F.; Güngör, T.; Quéguiner, G. *J. Chem. Soc., Perkin Trans. 1* **1990**, 2409. (g) Gros, P. C.; Fort, Y. *Eur. J. Org. Chem.* **2009**, 4199. (f) Cottet, F.; Marull, M.; Lefebvre, O.; Schlosser, M. *Eur. J. Org. Chem.* **2003**, 1559. (g) Güngör, T.; Marsais, F.; Quéguiner, G. *J. Organomet. Chem.* **1981**, *215*, 139.

27. (a) Viciu, M. S.; Gupta, L.; Collum, D. B. *J. Am. Chem. Soc.* **2010**, *132*, 6361. (b) Hoepker, A. C.; Gupta, L.; Ma, Y.; Faggin, M. F.; Collum, D. B. *J. Am. Chem. Soc.* **2011**, *133*, 7135.

28. (a) Dyke, A. M.; Hester, A. J.; Lloyd-Jones, G. C. *Synthesis* **2006**, 4093. (b) Pellissier, H.; Santelli, M. *Tetrahedron* **2003**, *59*, 701. (c) Wenk, H. H.; Winkler, M.; Sander, W. *Angew. Chem., Int. Ed.* **2003**, *42*, 502. (d) Nájera, C.; Sansano, J. M.; Yus, M. *Tetrahedron* **2003**, *59*, 9255. (e) Leroux, F.; Schlosser, M. *Angew. Chem., Int. Ed.* **2002**, *41*, 4272.

29. Reich, H. J. *Chem. Rev.* **2013**, *113*, 7130.

30. (a) Benkeser, R. A.; DeBoer, C. E. *J. Org. Chem.*, **1956**, 21, 281. (b) Majewski, M.; Gleave, D. M. *J. Organomet. Chem.* **1994**, *470*, 1.

31. Schnuerch, M.; Spina, M.; Khan, A. F.; Mihovilovic, M. D.; Stanetty, P. *Chem. Soc. Rev.* **2007**, *36*, 1046.

32. Ma, Y.; Breslin, S.; Keresztes, I.; Lobkovsky, E.; Collum, D. B. *J. Org. Chem.* **2008**, *73*, 9610 and references cited therein.

33. Billups, W. E. *Acc. Chem. Res*. **1978**, *11*, 245.

34. Gupta, L.; Hoepker, A. C.; Singh, K. J.; Collum, D. B. *J. Org. Chem.* **2009**, *74*, 2231.

35. (a) Allen, J. V.; Bower, J. F.; Williams, J. M. J. *Tetrahedron: Asymmetry* **1994**, *5*, 1895. (b) Holz, J.; Monseesb, A.; Kadyrovc, R.; Börner, A. *Synlett* **2007**, *2007,* 599.

36. Mack, K. A.; Collum, D. B., unpublished.

37. The distinction of primary versus secondary shell solvation is routinely achieved using polar, but poorly coordinating di- and tetramethyltetrahydrofurans instead of hexane as media. Unfortunately, these solvents are rapidly destroyed by NaDA.[8b]

38. Frisch, M. J.; *et al. GaussianVersion 3.09*; revision A.1; Gaussian, Inc.: Wallingford, CT, 2009.

39. Sammakia, T.; Latham, H. A. *J. Org. Chem.* **1996**, *61*, 1629.

40. (a) Stol, M.; Snelders, D. J. M.; de Pater, J. J. M.; van Klink, G. P. M.; Kooijman, H.; Spek, A. L.; van Koten, F. *Organometallics* **2005**, *24*, 743. (b) Jayasuriya, K.; Alster, J.; Politzer, P. *J. Org. Chem.* **1988**, *53*, 677. (c) Chadwick, S. T.; Ramírez, A.; Gupta, L.; Collum, D. B. *J. Am. Chem. Soc.* **2007**, *129*, 2259.

41. Inorganic chemists have found NaDA useful for installing the diisopropylamido moiety into transition metal coordination spheres: Spallek, T; Heß, O.; Meermann-Zimmermann, M.; Meermann, C.; Klimpel, M. G.; Estler, F.; Schneider, D.; Scherer, W.; Tafipolsky, M.; Törnroos, K. W.; Maichle-Mössmer, C.; Sirsch, P.; Anwander, R. *Dalton Trans.* **2016**, *45*, 13750.

42. (a) Lipshutz, B. H.; Ellsworth, E. L.; Behling, J. R.; Campbell, A. L. *Tetrahedron Lett.* **1988**, *29*, 893. (b) Bertz, S. H.; Gibson, C. P.; Dabbagh, G. *Organometallics* **1988**, *7*, 227.

Chapter 4 Appendix

I. Rate studies

II. NMR Spectroscopy

I. Rate Studies

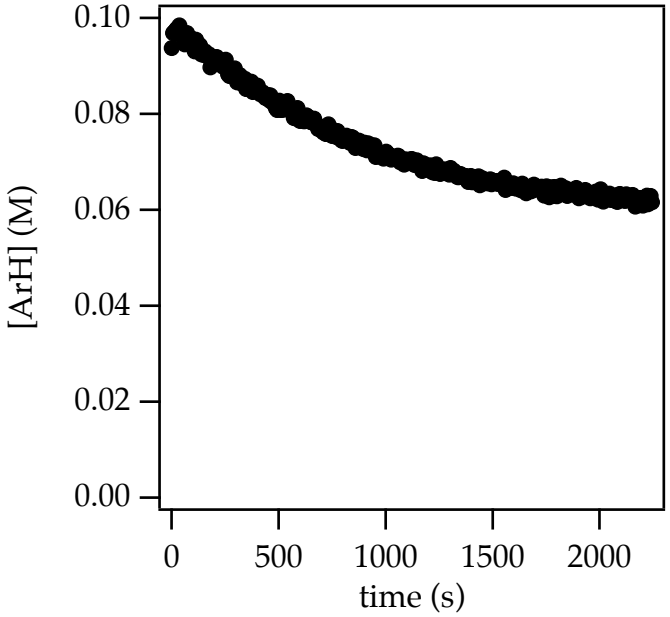

Figure A.4.1.Plot of 1,3-dimethoxybenzene (ArH) concentration versus time (ReactIR) for metalation with 0.10 M NaDA in 5.83 M THF/hexane at –78 °C. Incomplete metalation reflects near thermoneutrality.

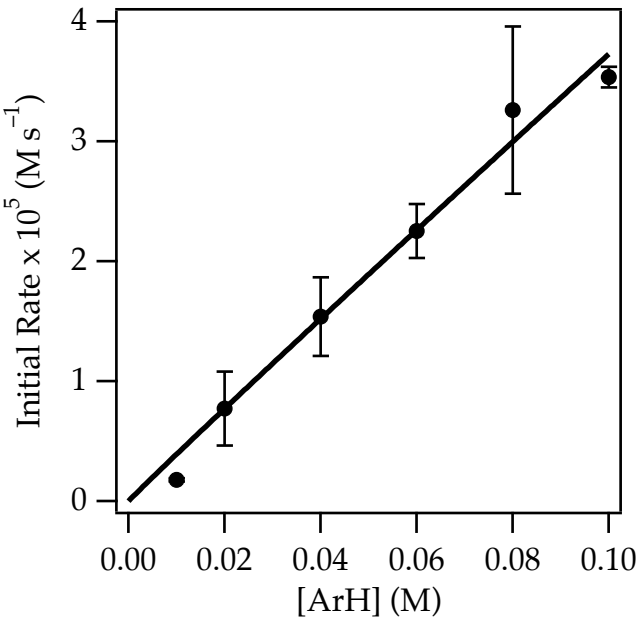

Figure A.4.2.Plot of initial rate versus 1,3-dimethoxybenzene concentration (ArH) for the metalation with 0.10 M NaDA in 6.02 M THF/hexane at –78 °C. The curve depicts an unweighted least-squares fit to the function $f(x) = ax$: $a = 37 \pm 1$.

[ArH] (M)	Initial Rate × 10^5 (M s^{-1})	Standard deviation × 10^5 (M s^{-1})
0.010	0.18	0.01
0.020	0.8	0.3
0.040	1.5	0.3
0.060	2.3	0.2
0.080	3.3	0.7
0.100	3.54	0.08

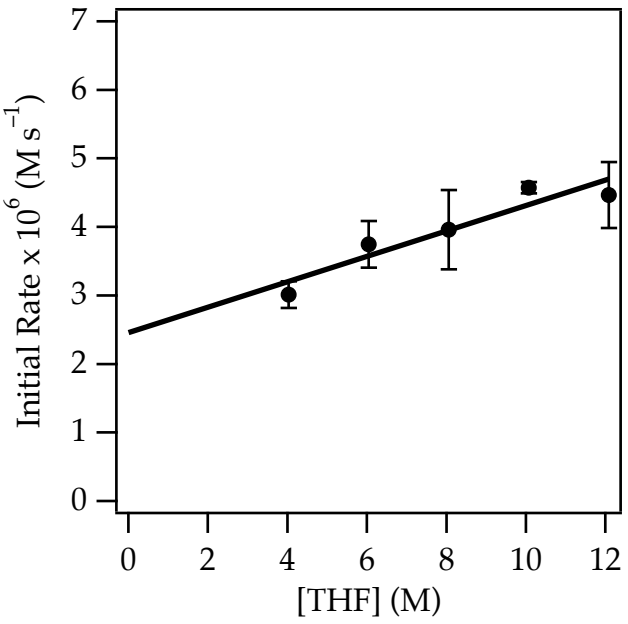

Figure A.4.3.Plot of initial rate versus THF concentration for the metalation of 0.010 M 1,3-dimethoxybenzene with 0.10 M NaDA in hexane cosolvent at –78 °C. The curve depicts an unweighted least-squares fit to the function $f(x) = ax + b$: $a = 0.19 \pm 0.04$; $b = 2.5 \pm 0.3$.

[THF] (M)	Initial Rate × 10^6 (M s^{-1})	Standard deviation × 10^6 (M s^{-1})
4.03	3.0	0.2
6.04	3.7	0.3
8.05	4.0	0.6
10.1	4.58	0.08
12.1	4.5	0.5

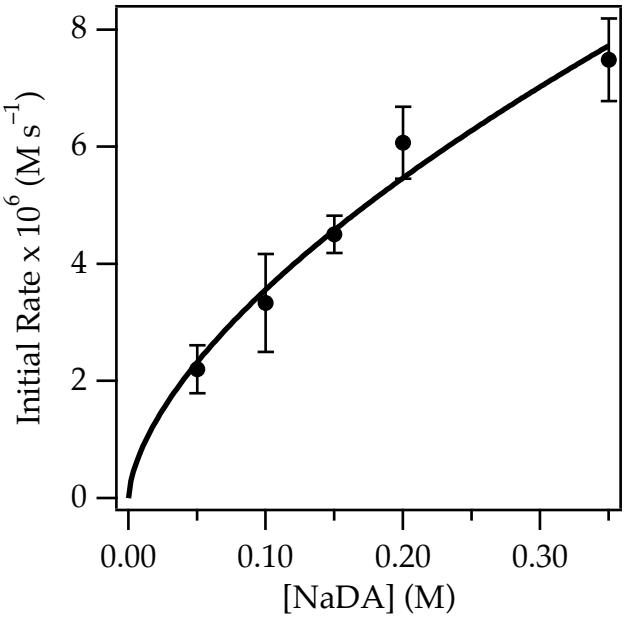

Figure A.4.4.Plot of initial rate versus NaDA concentration for the metalation of 0.010 M 1,3-dimethoxybenzene in 6.0 M THF/hexane at –78 °C. The curve depicts an unweighted least-squares fit to the function $f(x) = ax^b$: $a = 15 \pm 2$; $b = 0.62 \pm 0.07$.

[NaDA] (M)	Initial Rate × 10^6 (M s^{-1})	Standard deviation × 10^6 (M s^{-1})
0.050	2.2	0.4
0.10	3.3	0.8
0.15	4.5	0.3
0.20	6.1	0.6
0.35	7.5	0.7

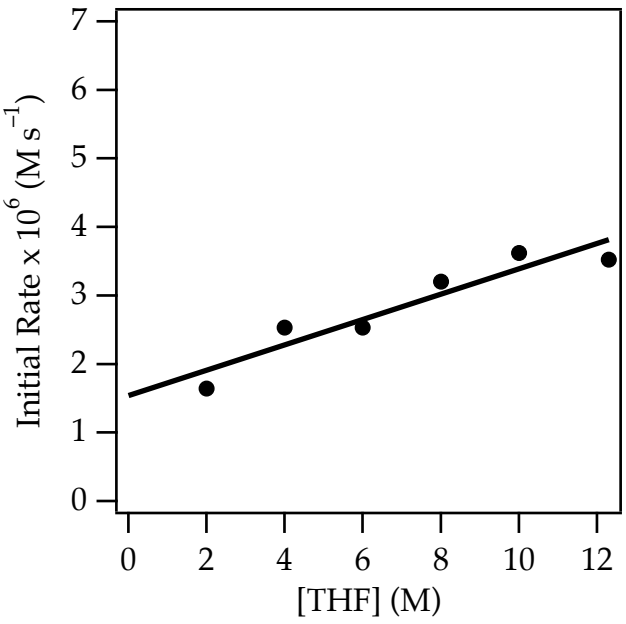

Figure A.4.5.Plot of initial rate versus THF concentration for the metalation of 0.010 M 1,3-dimethoxybenzene with 0.10 M NaDA in DMEA cosolvent at –78 °C. The curve depicts an unweighted least-squares fit to the function $f(x) = ax + b$: $a = 0.19 \pm 0.03$; $b = 1.5 \pm 0.3$. That the rates or behavior are not significantly different from those collected in hexane cosolvent suggests that cosolvent is inconsequential.

[THF] (M)	Initial Rate × 10^6 (M s^{-1})
2.00	1.65
4.00	2.54
6.00	2.53
8.00	3.21
10.0	3.62
12.3	3.53

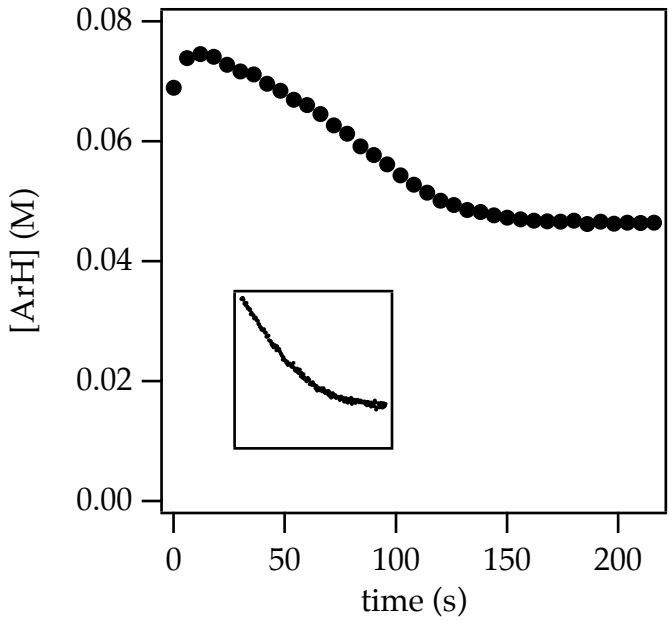

Figure A.4.6.Plot of 1,2,4-trimethoxybenzene (ArH) concentration versus time (ReactIR) for metalation of 0.080 M ArH with 0.10 M NaDA in neat THF at –78 °C. Inset: Plot of 1,2,4-trimethoxybenzene (ArH) concentration versus time (time to completion is ~1200 seconds) for metalation of 0.010 M ArH with 0.10 M NaDA in neat THF at –78 °C. The sigmoidal behavior at high concentration is indicative of autocatalysis.

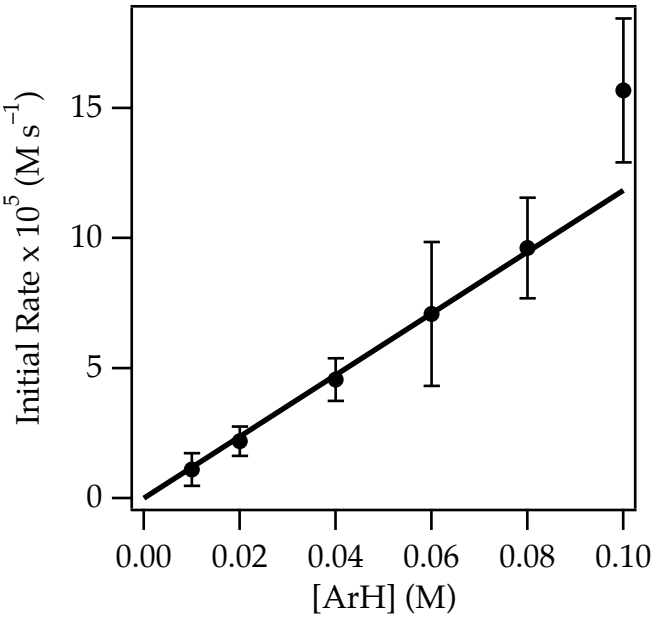

Figure A.4.7.Plot of initial rate versus 1,2,4-trimethoxybenzene concentration (ArH) for the metalation with 0.10 M NaDA in neat THF at –78 °C. The curve depicts an unweighted least-squares fit to the function $f(x) = ax$: $a = 118 \pm 1$. The point corresponding to [ArH] = 0.10 M is omitted from the fit because of the early onset of autocatalytic acceleration.

[ArH] (M)	Initial Rate × 10^5 (M s^{-1})	Standard deviation × 10^5 (M s^{-1})
0.010	1.1	0.6
0.020	2.2	0.6
0.040	4.6	0.8
0.060	7	3
0.080	10	2
0.10	16	3

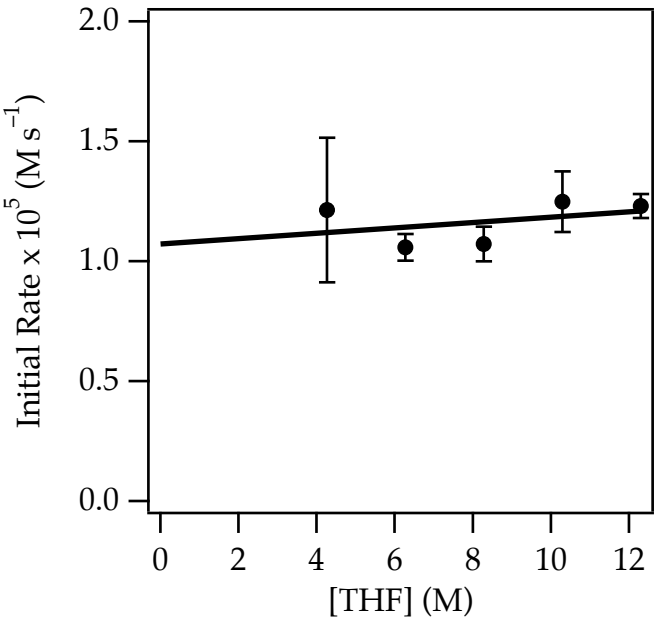

Figure A.4.8.Plot of initial rate versus THF concentration for the metalation of 0.010 M 1,2,4-trimethoxybenzene with 0.10 M NaDA in hexane cosolvent at –78 °C. The curve depicts an unweighted least-squares fit to the function $f(x) = ax + b$: $a = 0.01 \pm 0.02$; $b = 1.1 \pm 0.1$.

[THF] (M)	Initial Rate × 10^5 (M s^{-1})	Standard deviation × 10^5 (M s^{-1})
4.26	1.2	0.3
6.27	1.06	0.06
8.28	1.07	0.07
10.3	1.2	0.1
12.3	1.23	0.05

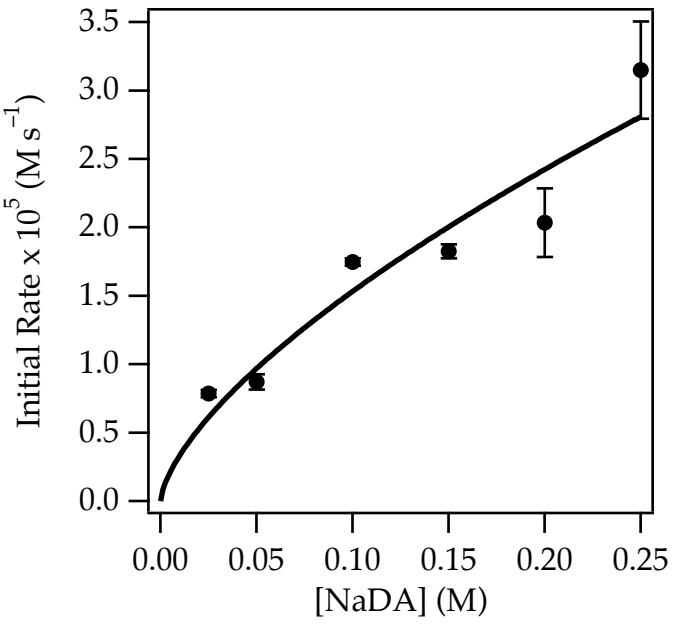

Figure A.4.9.Plot of initial rate versus NaDA concentration for the metalation of 0.010 M 1,2,4-trimethoxybenzene in 6.0 M THF/hexane at –78 °C. The curve depicts an unweighted least-squares fit to the function $f(x) = ax^b$: $a = 7 \pm 2$; $b = 0.66 \pm 0.1$.

[NaDA] (M)	Initial Rate × 10^5 (M s^{-1})	Standard deviation × 10^5 (M s^{-1})
0.025	0.79	0.03
0.050	0.87	0.06
0.10	1.75	0.03
0.15	1.83	0.05
0.20	2.0	0.3
0.25	3.2	0.4

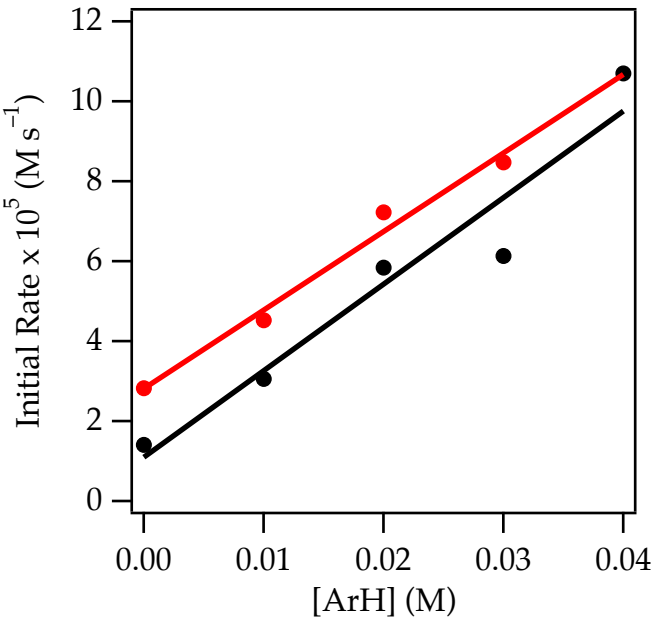

Figure A.4.10.Plot of initial rate versus previous cumulative concentration of added 1,2,4-trimethoxybenzene (ArH) for metalation in neat THF at –78 °C. The curves depict unweighted least-squares fits to the function $f(x) = ax + b$: (Black trace: [NaDA] = 0.10 M ; $a = 220 \pm 30$; $b = 1.1 \pm 0.8$) ; (Red trace: [NaDA] = 0.25 M ; $a = 200 \pm 20$; $b = 2.8 \pm 0.4$). In the event, a background spectrum was collected followed by addition of 0.010 M ArH. Upon completion, the collection was aborted and the process of serial injection was repeated. In the absence of autocatalysis, the initial rate should decrease reflecting the loss of NaDA titer. This experiment shows compensation for NaDA titer loss with autocatalysis, the expected positive NaDA dependence of initial rate in the absence of preformed arylsodium, and a surprising insensitivity of slope to initial NaDA titer.

[ArH] (M) (0.10 M NaDA)	Initial Rate × 10^5 (M s^{-1})	[ArH] (M) (0.25 M NaDA)	Initial Rate × 10^5 (M s^{-1})
0.000	1.41	0.000	2.83
0.010	3.06	0.010	4.52
0.020	5.84	0.020	7.22
0.030	6.13	0.030	8.48
0.040	10.7		

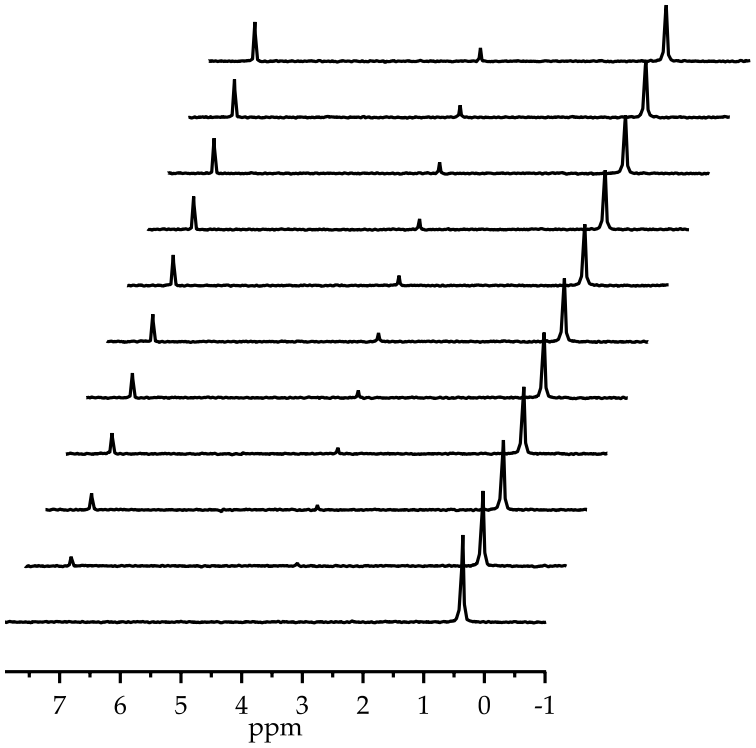

Figure A.4.11.Stacked ^{2}H NMR spectra for isotopic exchange of 0.23 M benzene (δ 7.15) with 0.10 M NaDA and 1.04 M *i*-Pr_2ND (δ 0.37) in 10.1 M THF (δ 3.42) at –78 °C. The concomitant emergence of benzene and THF resonances is consistent with competitive rates of exchange.

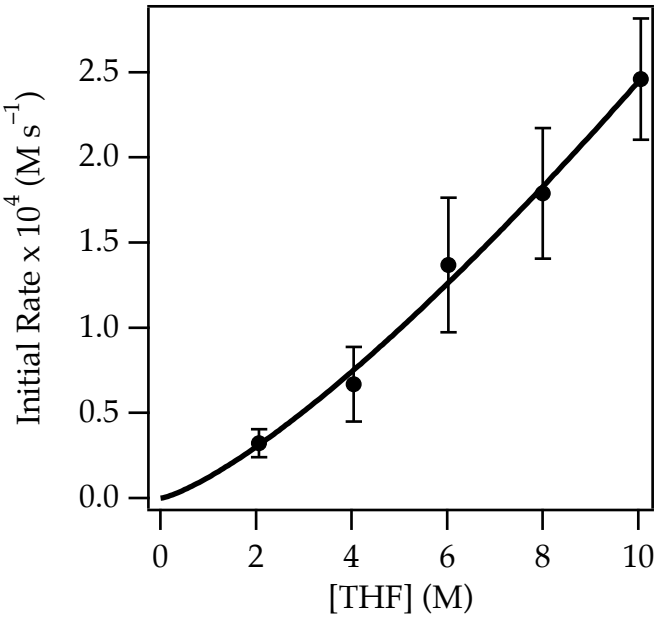

Figure A.4.12.Plot of initial rate versus THF concentration for the isotopic exchange of 0.23 M benzene with 0.10 M NaDA and 1.04 M *i*-Pr_2ND in hexane cosolvent at 25 °C. The curve depicts an unweighted least-squares fit to the function $f(x) = ax^b$: $a = 0.12 \pm 0.02$; $b = 1.30 \pm 0.09$.

[THF] (M)	Initial Rate × 10^4 (M s^{-1})	Standard deviation × 10^4 (M s^{-1})
2.06	0.32	0.08
4.04	0.7	0.2
6.02	1.4	0.4
8.00	1.8	0.4
10.1	2.5	0.4

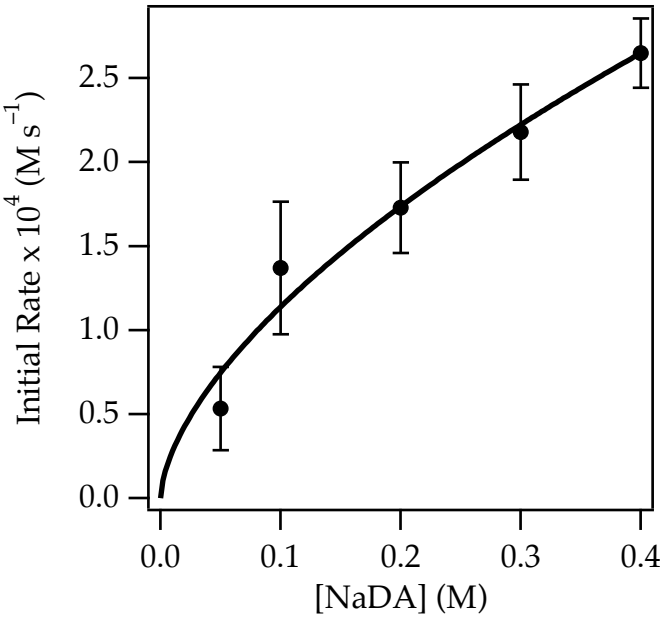

Figure A.4.13.Plot of initial rate versus NaDA concentration for the isotopic exchange of 0.23 M benzene and 1.04 M *i*-Pr_2ND in 6.02 M THF/hexane at 25 °C. The curve depicts an unweighted least-squares fit to the function $f(x) = ax^b$: $a = 4.6 \pm 0.6$; $b = 0.61 \pm 0.09$.

[NaDA] (M)	Initial Rate × 10^4 (M s^{-1})	Standard deviation × 10^4 (M s^{-1})
0.050	0.5	0.2
0.10	1.4	0.4
0.20	1.7	0.3
0.30	2.2	0.3
0.40	2.7	0.2

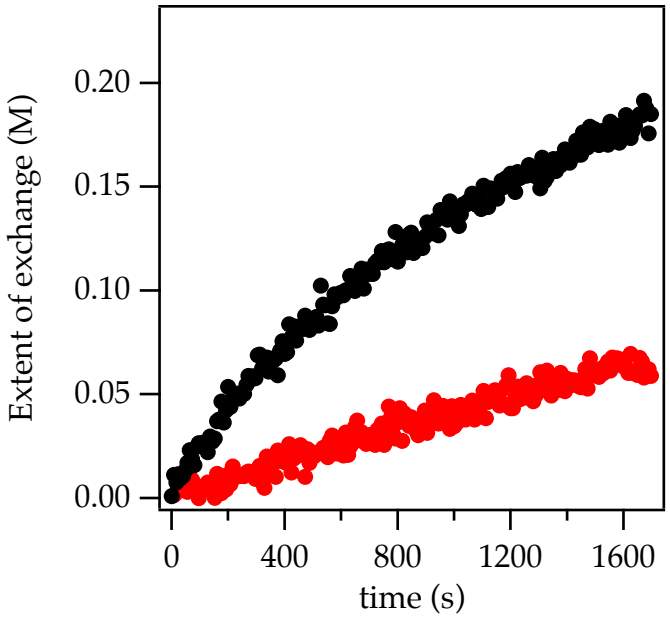

Figure A.4.14.Plot of benzene isotopologue concentration (black trace: benzene-h_6 and *i*-Pr_2ND; red trace: benzene-d_6 and *i*-Pr_2NH) versus time for the isotopic exchange of 0.23 M benzene with 0.10 M NaDA and 1.04 M diisopropylamine in 10.1 M THF at 25 °C. These plots collectively attest to an isotope effect of $k_H/k_D = 6.3$.

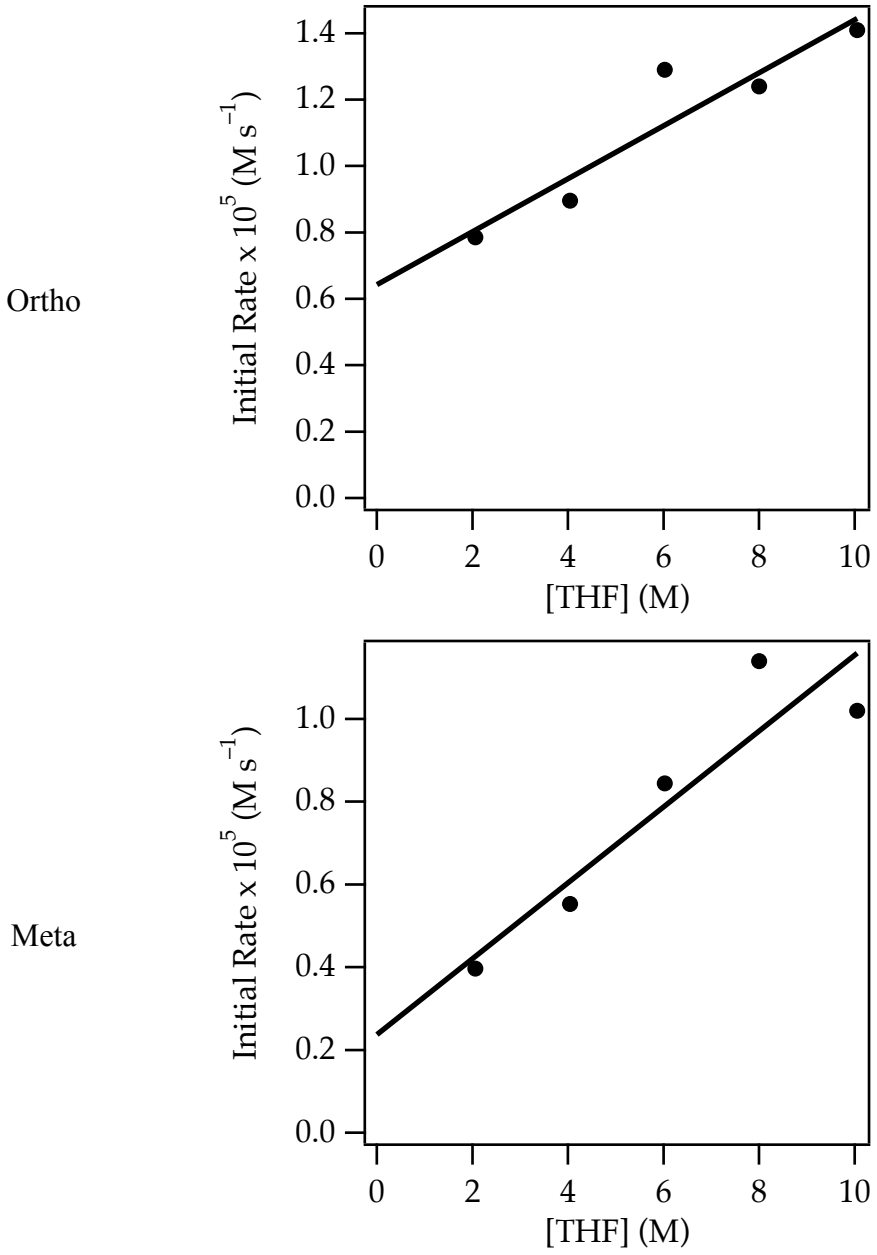

Figure A.4.15.Plot of initial rate versus THF concentration for the isotopic exchange of 0.44 M *N*,*N*-dimethylaniline with 0.10 M NaDA and 0.79 M *i*-Pr_2ND in hexane cosolvent at 25 °C. The curves depict unweighted least-squares fits to the function $f(x) = ax + b$: Ortho: ($a = 0.08 \pm 0.02$; $b = 0.6 \pm 0.1$); Meta: ($a = 0.09 \pm 0.02$; $b = 0.2 \pm 0.1$).

[THF] (M)	Ortho Initial Rate × 10^5 (M s^{-1})	Meta Initial Rate × 10^5 (M s^{-1})
2.06	0.786	0.397
4.04	0.896	0.553
6.02	1.29	0.844
8.00	1.24	1.14
10.1	1.41	1.02

Ortho

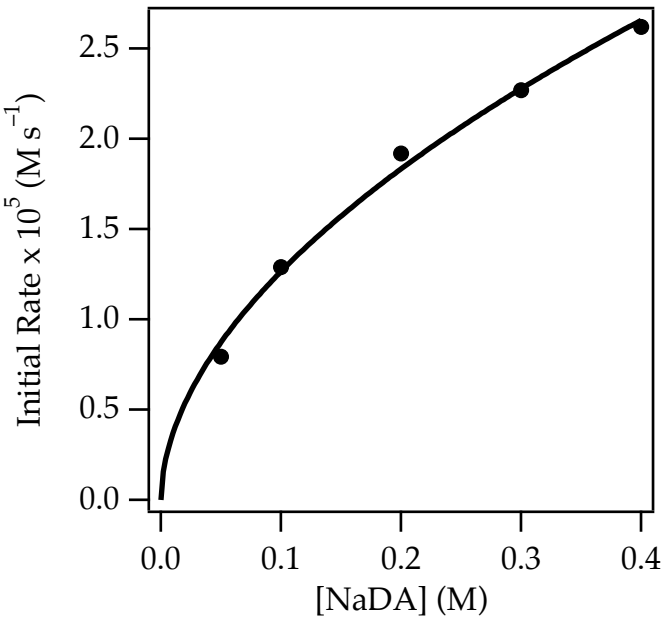

Meta

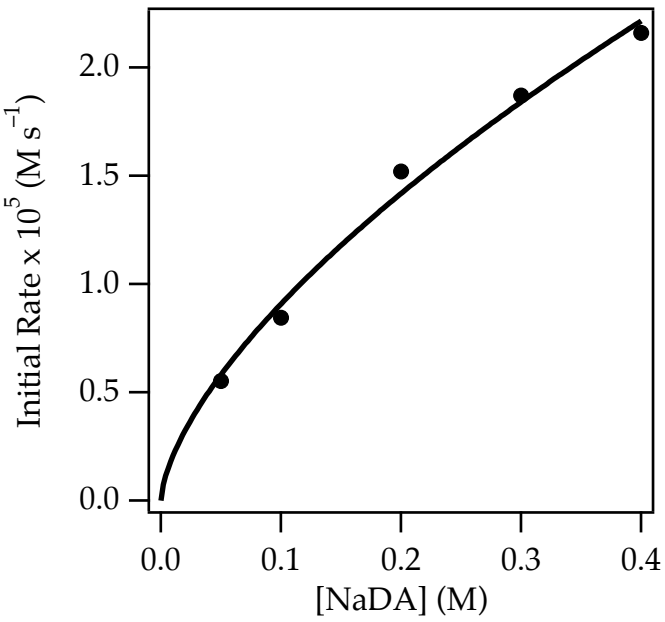

Figure A.4.16.Plot of initial rate versus NaDA concentration for the isotopic exchange of 0.44 M *N*,*N*-dimethylaniline with 0.79 M *i*-Pr_2ND in 6.02 M THF/hexane at 25 °C. The curves depict unweighted least-squares fits to the function $f(x) = ax^b$: Ortho: (a = 4.3 ± 0.2; b = 0.53 ± 0.03); Meta: (a = 4.0 ± 0.3; b = 0.65 ± 0.05).

[NaDA] (M)	Ortho Initial Rate × 10^5 (M s^{-1})	Meta Initial Rate × 10^5 (M s^{-1})
0.050	0.793	0.553
0.10	1.29	0.844
0.20	1.92	1.52
0.30	2.27	1.87
0.40	2.62	2.16

Ortho

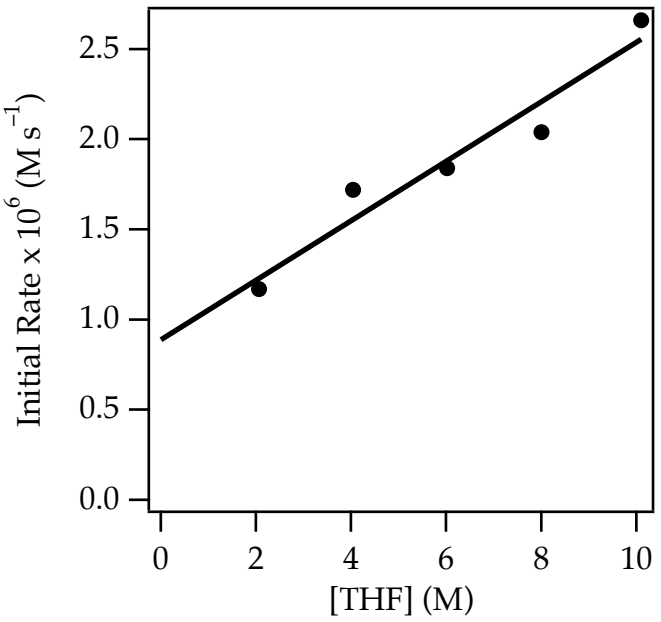

Meta

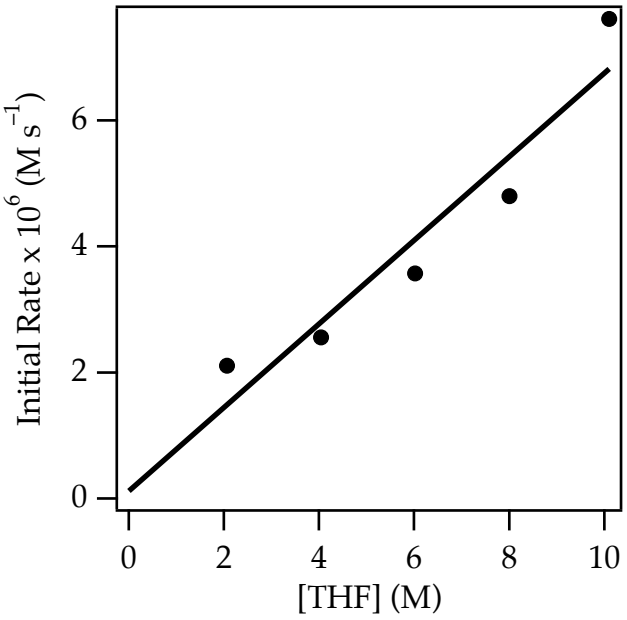

Figure A.4.17.Plot of initial rate versus THF concentration for the isotopic exchange of 0.35 M *N*,*N*-diethylaniline with 0.10 M NaDA and 0.79 M *i*-Pr_2ND in hexane cosolvent at 25 °C. The curves depict unweighted least-squares fits to the function $f(x) = ax + b$: Ortho: ($a = 0.16 \pm 0.02$; $b = 0.9 \pm 0.2$); Meta: ($a = 0.6 \pm 0.1$; $b = 0.1 \pm 0.8$).

[THF] (M)	Ortho Initial Rate × 10^6 (M s^{-1})	Meta Initial Rate × 10^6 (M s^{-1})
2.06	1.17	2.11
4.04	1.72	2.56
6.02	1.84	3.57
8.00	2.04	4.8
10.1	2.66	7.61

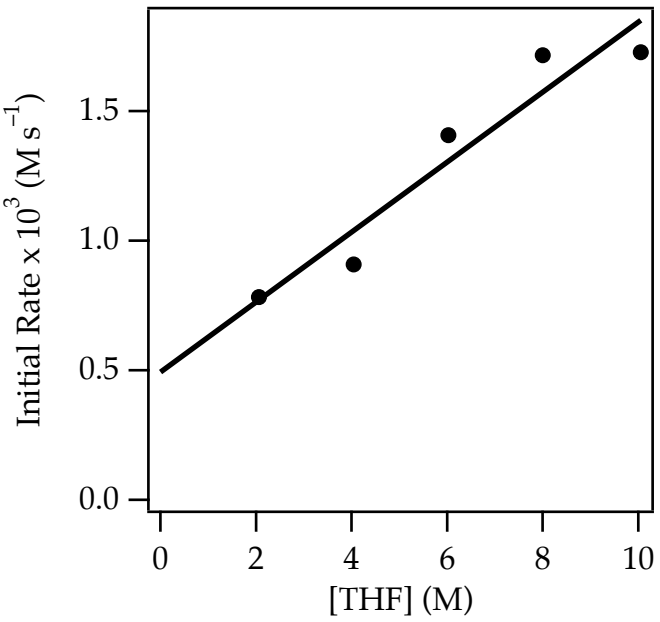

Figure A.4.18.Plot of initial rate versus THF concentration for the ortho selective isotopic exchange of 0.51 M anisole with 0.10 M NaDA and 0.79 M *i*-Pr_2ND in hexane cosolvent at –20 °C. The curve depicts an unweighted least-squares fit to the function $f(x) = ax + b$: $a = 0.12 \pm 0.02$; $b = 0.5 \pm 0.2$.

[THF] (M)	Initial Rate × 10^3 (M s^{-1})
2.06	0.782
4.04	0.908
6.02	1.41
8.00	1.72
10.1	1.73

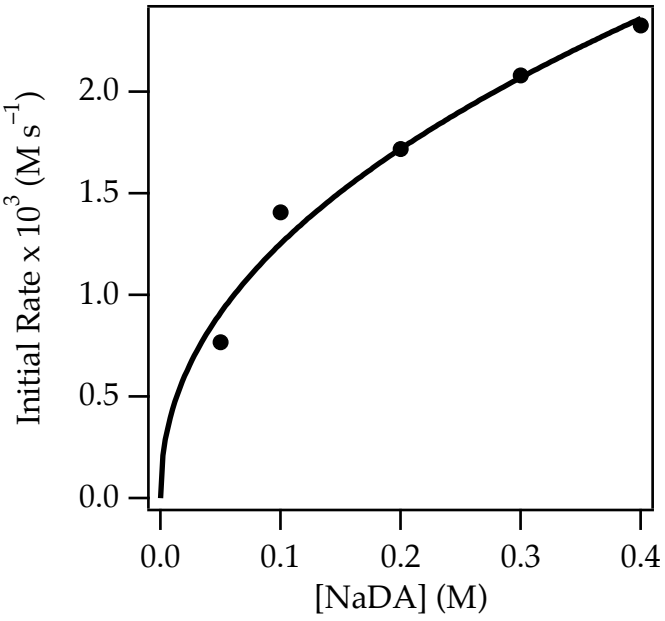

Figure A.4.19.Plot of initial rate versus NaDA concentration for the ortho selective isotopic exchange of 0.51 M anisole and 0.79 M *i*-Pr_2ND in 6.02 M THF/hexane at –20 °C. The curve depicts an unweighted least-squares fit to the function $f(x) = ax^b$: $a = 3.6 \pm 0.3$; $b = 0.46 \pm 0.06$.

[NaDA] (M)	Initial Rate × 10^3 (M s^{-1})
0.050	0.768
0.10	1.41
0.20	1.72
0.30	2.08
0.40	2.33

Ortho

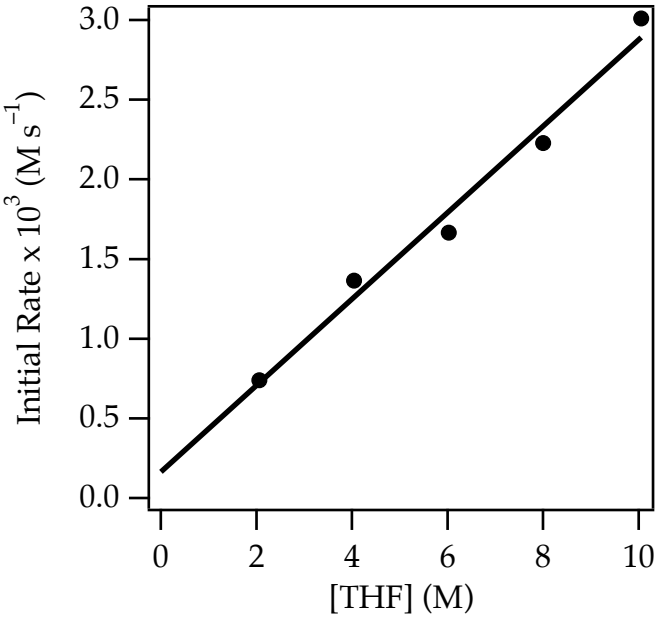
Initial Rate x 10^3 (M s^{-1})
3.0
2.5
2.0
1.5
1.0
0.5
0.0
0
2
4
6
8
10
[THF] (M)

Meta

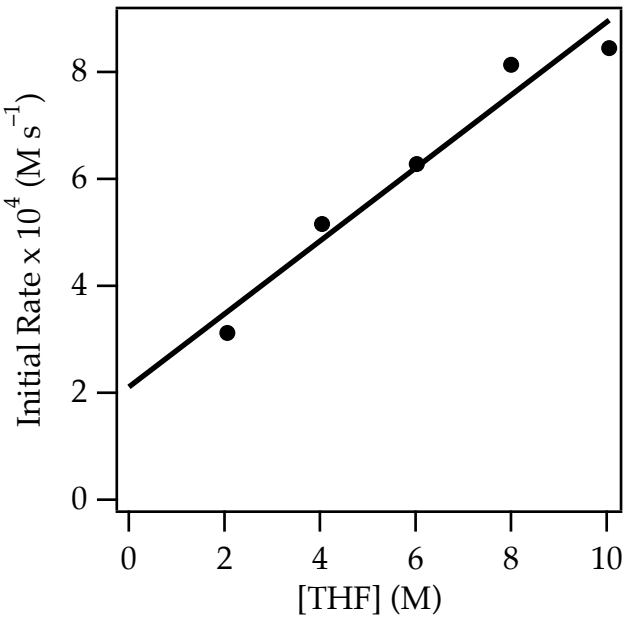
Initial Rate x 10^4 (M s^{-1})
8
6
4
2
0
0
2
4
6
8
10
[THF] (M)

Para

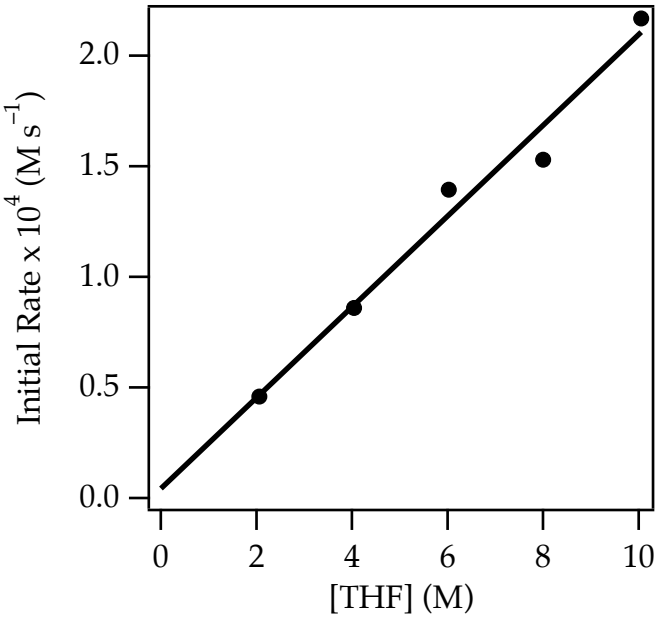

Figure A.4.20.Plot of initial rate versus THF concentration for the isotopic exchange of 0.45 M benzotrifluoride with 0.10 M NaDA and 0.79 M *i*-Pr_2ND in hexane cosolvent at –20 °C. The curves depict unweighted least-squares fits to the function $f(x) = ax + b$: Ortho: ($a = 0.27 \pm 0.02$; $b = 0.2 \pm 0.1$); Meta: ($a = 0.68 \pm 0.08$; $b = 2.1 \pm 0.6$); Para: ($a = 0.21 \pm 0.02$; $b = 0.04 \pm 0.1$).

[THF] (M)	Ortho × 10^3 (M s^{-1})	Meta × 10^4 (M s^{-1})	Para × 10^4 (M s^{-1})
2.06	0.740	3.12	0.459
4.04	1.37	5.16	0.859
6.02	1.67	6.28	1.39
8.00	2.23	8.14	1.53
10.1	3.01	8.45	2.17

Ortho

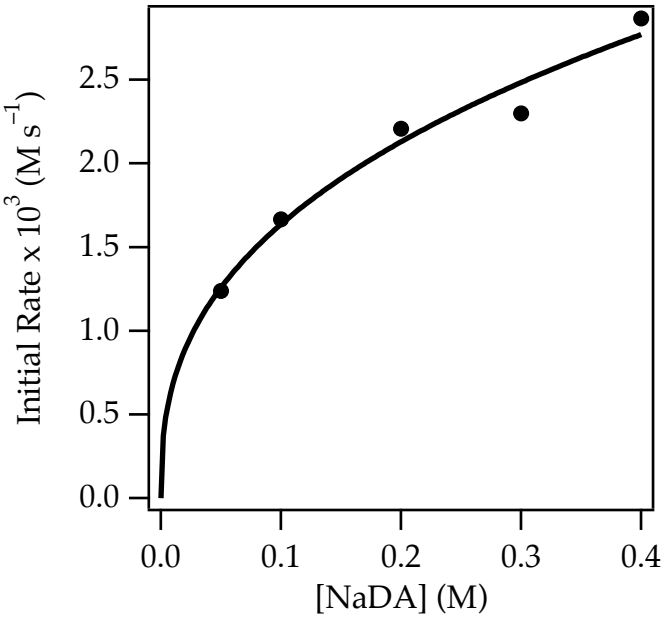
Initial Rate x 10^3 (M s^{-1})
2.5
2.0
1.5
1.0
0.5
0.0
0.0
0.1
0.2
0.3
0.4
[NaDA] (M)

Meta

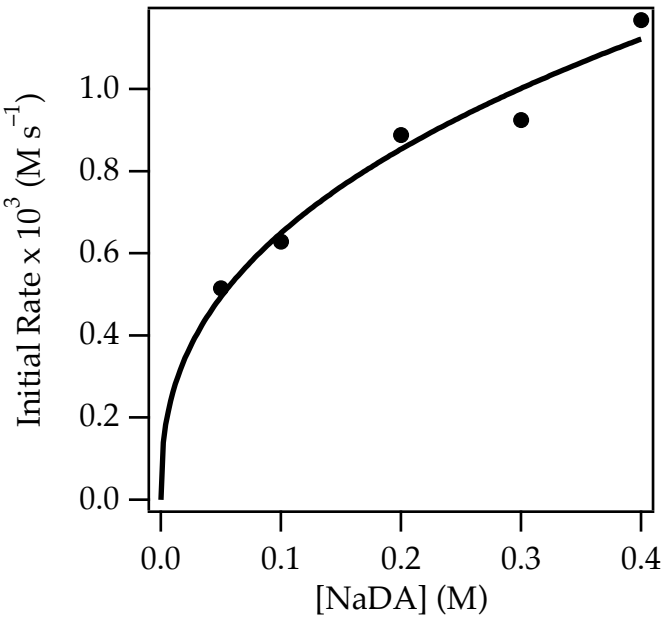
Initial Rate x 10^3 (M s^{-1})
1.0
0.8
0.6
0.4
0.2
0.0
0.0
0.1
0.2
0.3
0.4
[NaDA] (M)

Para

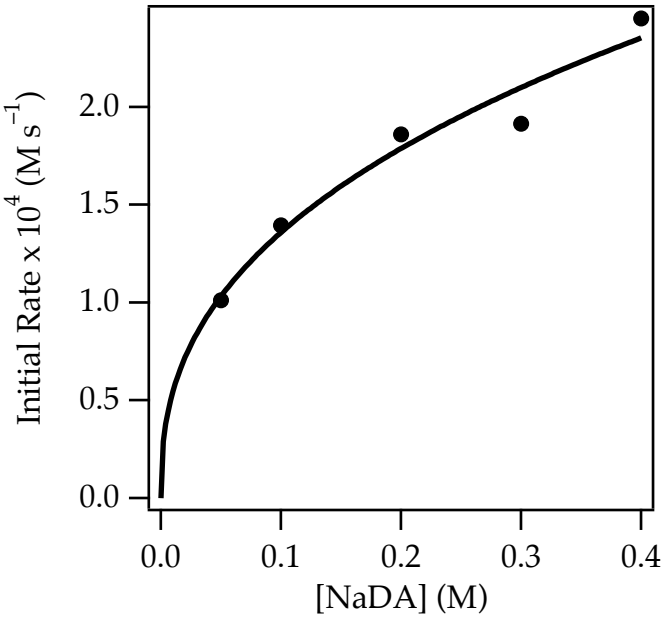

Figure A.4.21.Plot of initial rate versus NaDA concentration for the isotopic exchange of 0.45 M benzotrifluoride with 0.79 M *i*-Pr_2ND in 6.02 M THF/hexane at –20 °C. The curves depict unweighted least-squares fits to the function $f(x) = ax^b$: Ortho: (a = 3.9 ± 0.3; b = 0.38 ± 0.04); Meta: (a = 1.6 ± 0.1; b = 0.40 ± 0.05); Para: (a = 3.4 ± 0.3; b = 0.40 ± 0.05).

[NaDA] (M)	Ortho × 10^3 (M s^{-1})	Meta × 10^3 (M s^{-1})	Para × 10^4 (M s^{-1})
0.050	1.24	0.515	1.01
0.10	1.67	0.628	1.39
0.20	2.21	0.888	1.86
0.30	2.30	0.925	1.91
0.40	2.87	1.17	2.45

Ortho

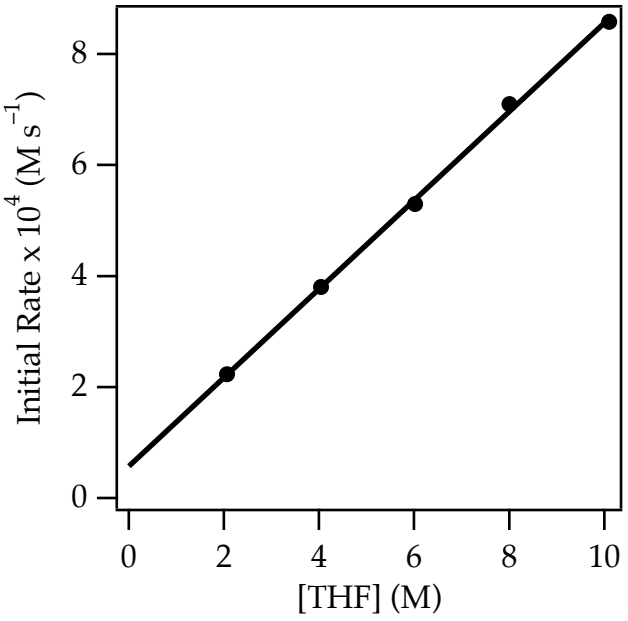

Meta

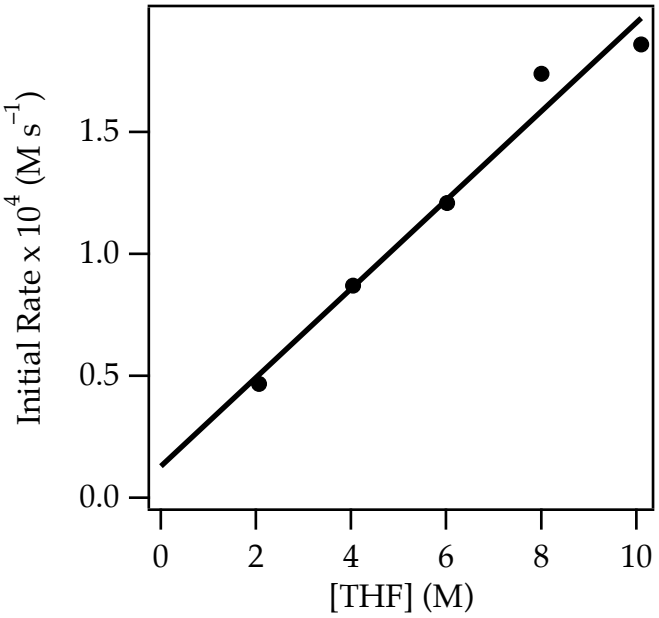

Figure A.4.22.Plot of initial rate versus THF concentration for the isotopic exchange of 0.45 M benzotrifluoride with 0.10 M NaDA and 0.79 M *i*-Pr_2ND in hexane cosolvent at –40 °C. The curves depict unweighted least-squares fits to the function $f(x) = ax + b$: Ortho: ($a = 0.80 \pm 0.02$; $b = 0.6 \pm 0.1$); Meta: ($a = 0.18 \pm 0.02$; $b = 0.1 \pm 0.1$).

[THF] (M)	Ortho × 10^4 (M s^{-1})	Meta × 10^4 (M s^{-1})
2.06	2.23	0.468
4.04	3.81	0.870
6.02	5.30	1.21
8.00	7.10	1.74
10.1	8.59	1.86

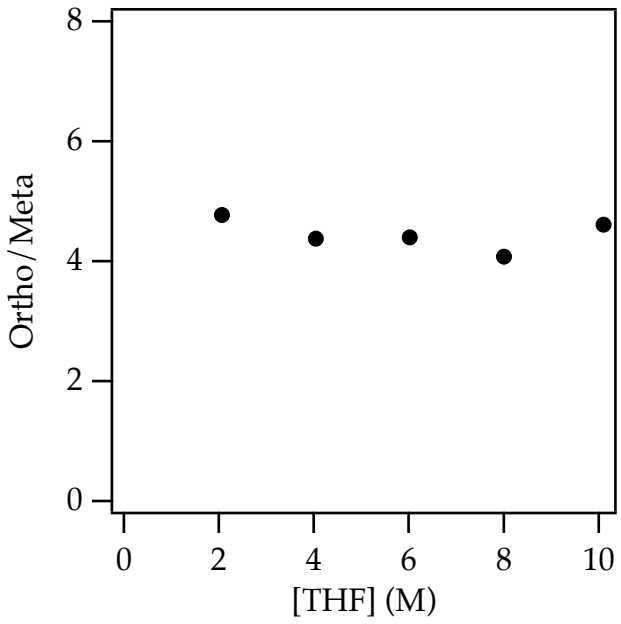

Figure A.4.23.Plot of initial proportions (ratio of initial rates) of ortho and meta deuteration versus THF concentration for the isotopic exchange of 0.45 M benzotrifluoride with 0.10 M NaDA and 0.79 M *i*-Pr_2ND in hexane cosolvent at –40 °C. The invariance demonstrated argues for a common solvate eliciting the exchanges.

[THF] (M)	Ortho:Meta
2.06	4.77
4.04	4.38
6.02	4.40
8.00	4.08
10.1	4.61

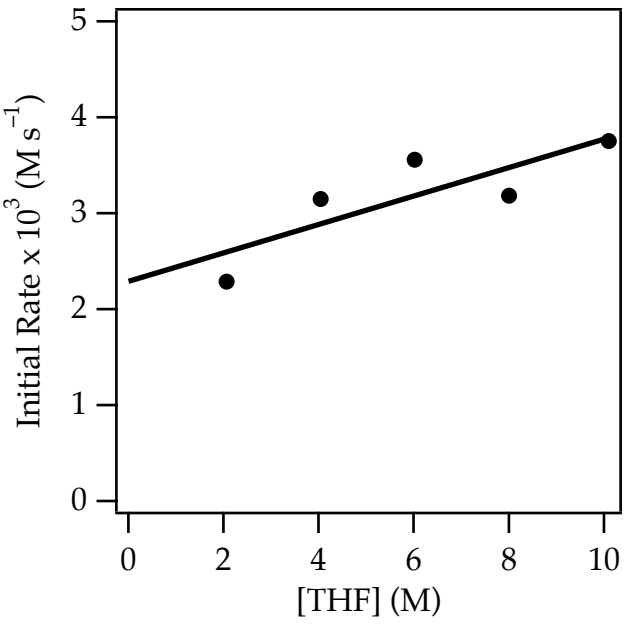

Figure A.4.24.Plot of initial rate versus THF concentration for the ortho selective isotopic exchange of 0.32 M 4,4-dimethyl-2-phenyl-2-oxazoline with 0.10 M NaDA and 0.79 M *i*-Pr_2ND in hexane cosolvent at –20 °C. The curve depicts an unweighted least-squares fit to the function $f(x) = ax + b$: $a = 0.15 \pm 0.06$; $b = 2.3 \pm 0.4$.

[THF] (M)	Initial Rate × 10^3 (M s^{-1})
2.06	2.29
4.04	3.15
6.02	3.56
8.00	3.18
10.1	3.75

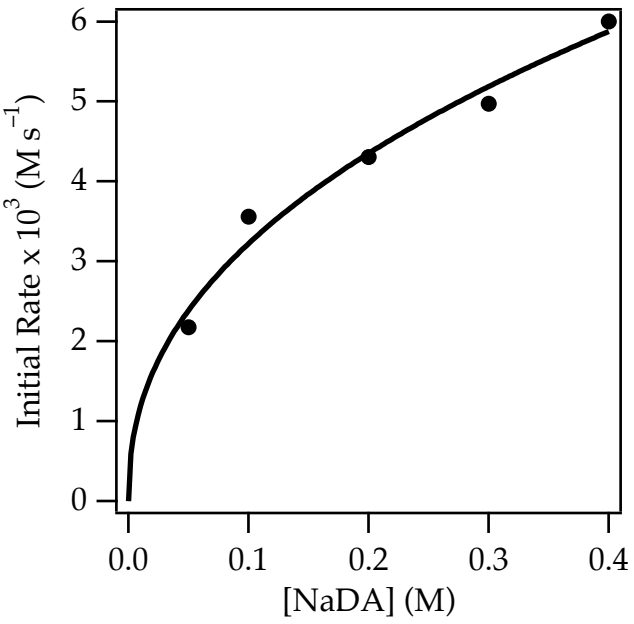

Figure A.4.25.Plot of initial rate versus NaDA concentration for the ortho selective isotopic exchange of 0.32 M 4,4-dimethyl-2-phenyl-2-oxazoline and 0.79 M *i*-Pr_2ND in 6.02 M THF/hexane at –20 °C. The curve depicts an unweighted least-squares fit to the function $f(x) = ax^b$: $a = 8.7 \pm 0.6$; $b = 0.43 \pm 0.05$.

[NaDA] (M)	Initial Rate × 10^3 (M s^{-1})
0.050	2.18
0.10	3.56
0.20	4.31
0.30	4.97
0.40	6.00

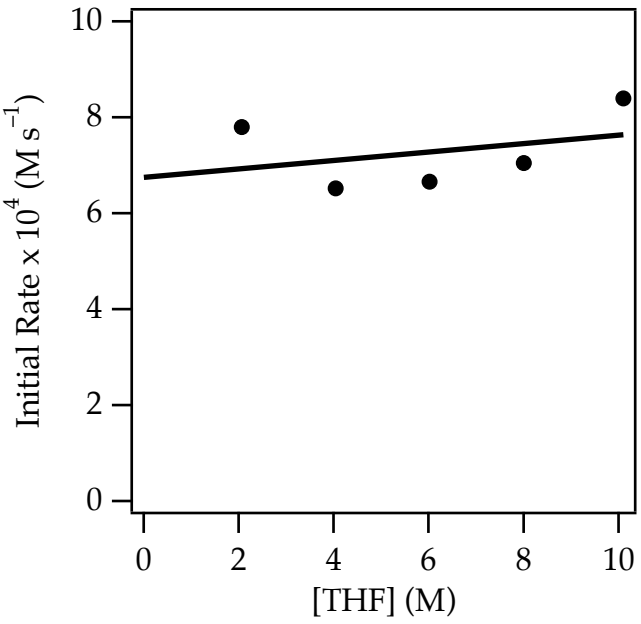

Figure A.4.26.Plot of initial rate versus THF concentration for the ortho selective isotopic exchange of 0.32 M 4,4-dimethyl-2-phenyl-2-oxazoline with 0.10 M NaDA and 0.79 M *i*-Pr_2ND in hexane cosolvent at –40 °C. The curve depicts an unweighted least-squares fit to the function $f(x) = ax + b$: $a = 0.09 \pm 0.1$; $b = 6.8 \pm 0.9$.

[THF] (M)	Initial Rate × 10^4 (M s^{-1})
2.06	7.80
4.04	6.52
6.02	6.66
8.00	7.05
10.1	8.39

III. NMR Spectroscopy

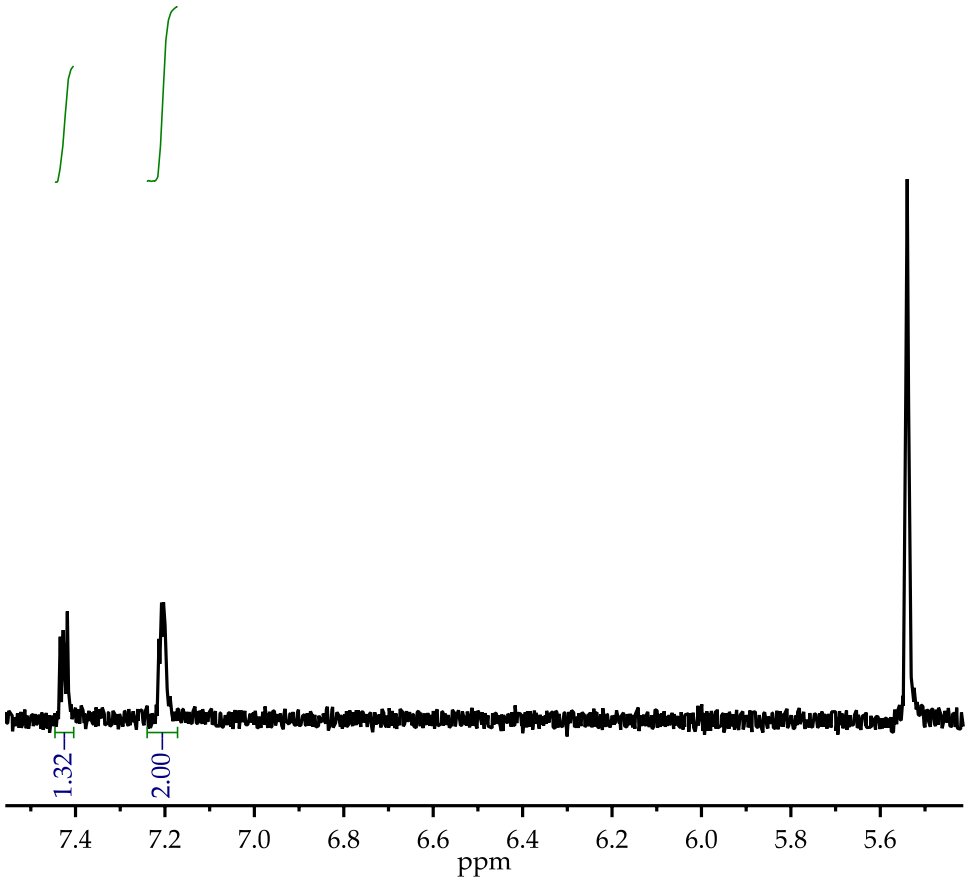

Figure A.4.27.Isolated ^{1}H NMR spectrum for metalation of 0.38 M 1,2-dichlorobenzene with 0.40 M NaDA in 1.00 mL THF at –78 °C after quenching with 500 µL MeOD (100 µL cyclohexene internal standard added at δ 5.54 ppm). Loss of the resonance at δ 7.42 ppm indicates ortho selective metalation.

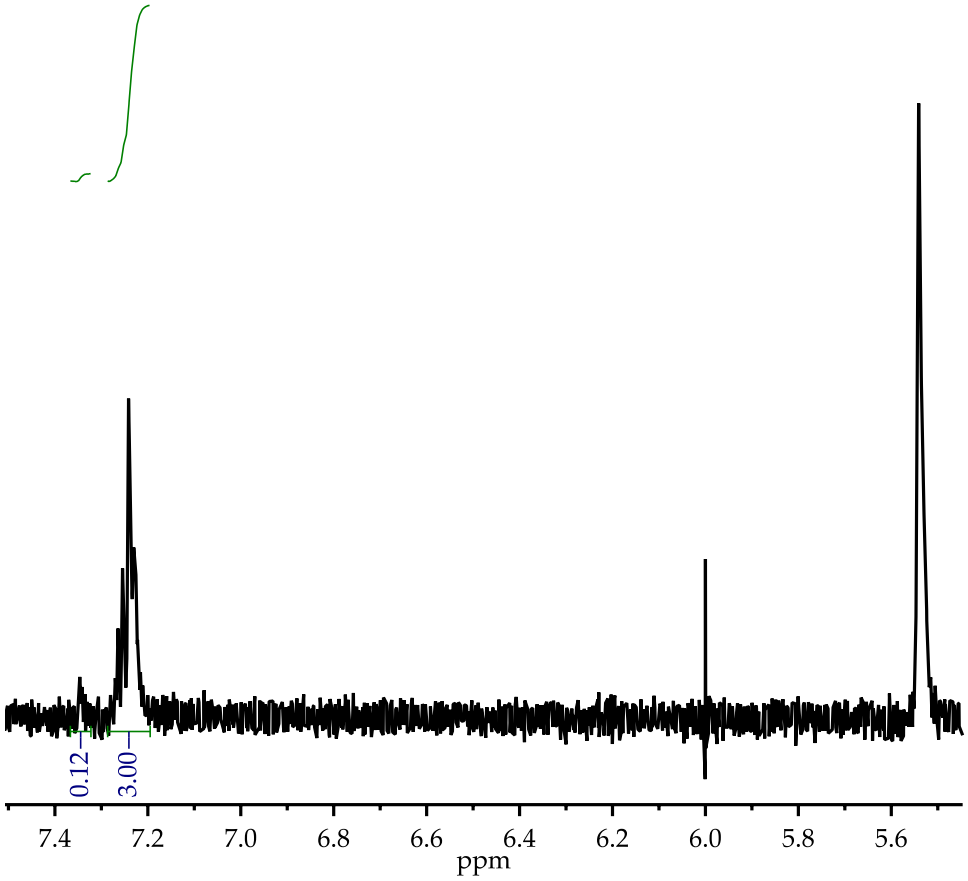

Figure A.4.28.Isolated ^{1}H NMR spectrum for metalation of 0.38 M 1,3-dichlorobenzene with 0.40 M NaDA in 1.00 mL THF at –78 °C after quenching with 500 µL MeOD (100 µL cyclohexene internal standard added at δ 5.54 ppm). Loss of the resonance at δ 7.35 ppm indicates doubly ortho selective metalation.

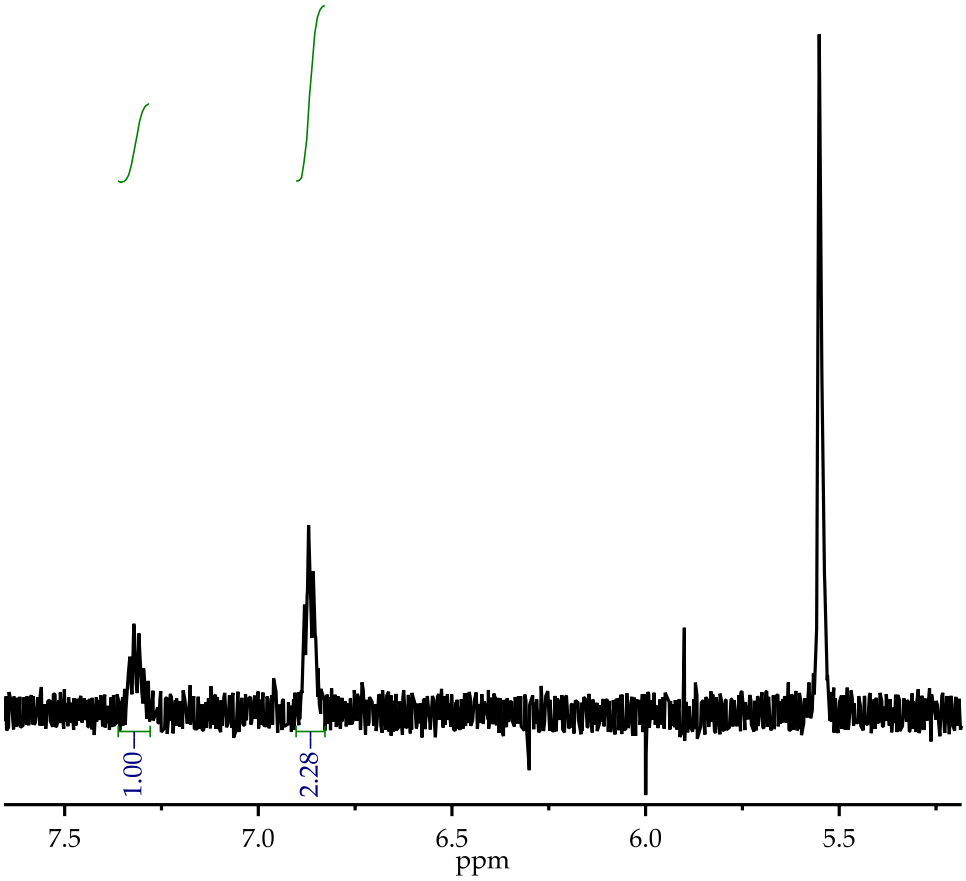

Figure A.4.29.Isolated ^{1}H NMR spectrum for metalation of 0.38 M 1,3-difluorobenzene with 0.40 M NaDA in 1.00 mL THF at –78 °C after quenching with 500 µL MeOD (100 µL cyclohexene internal standard added at δ 5.54 ppm). Loss of the resonance at δ 6.87 ppm is consistent with doubly ortho selective metalation.

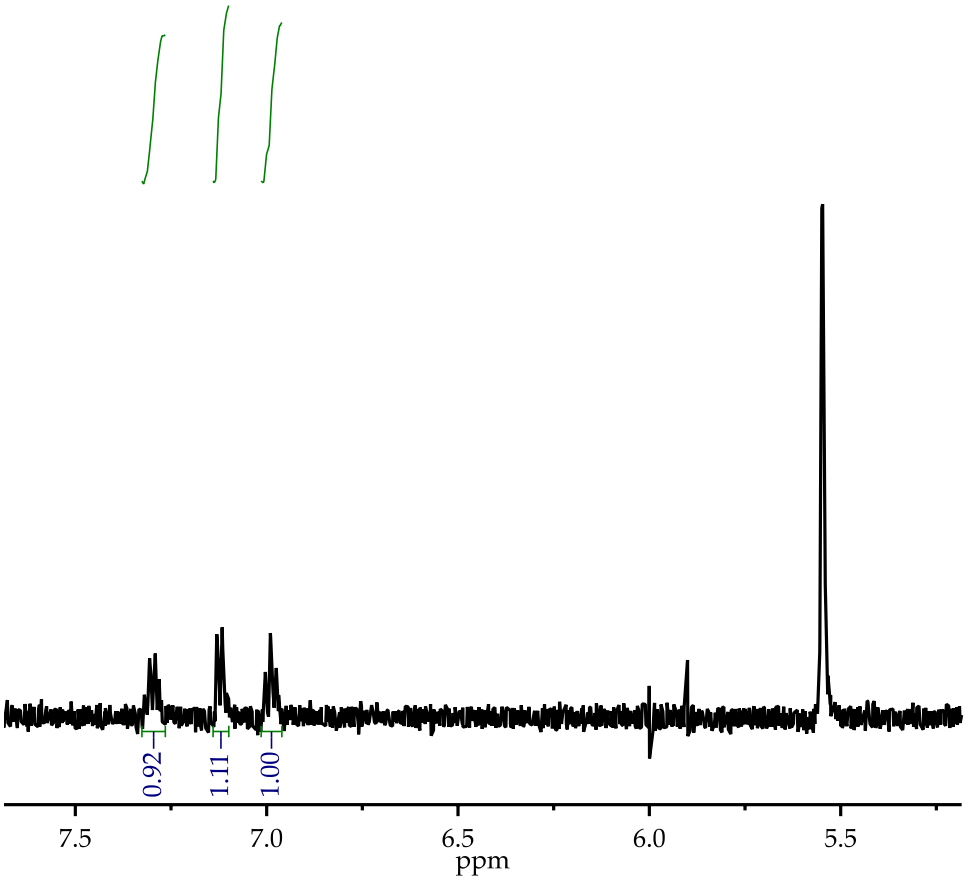

Figure A.4.30.Isolated ^{1}H NMR spectrum for metalation of 0.38 M 1-chloro-3-fluorobenzene with 0.40 M NaDA in 1.00 mL THF at –78 °C after quenching with 500 µL MeOD (100 µL cyclohexene internal standard added at δ 5.54 ppm). Loss of the resonance at δ 7.11 ppm is consistent with doubly ortho selective metalation.

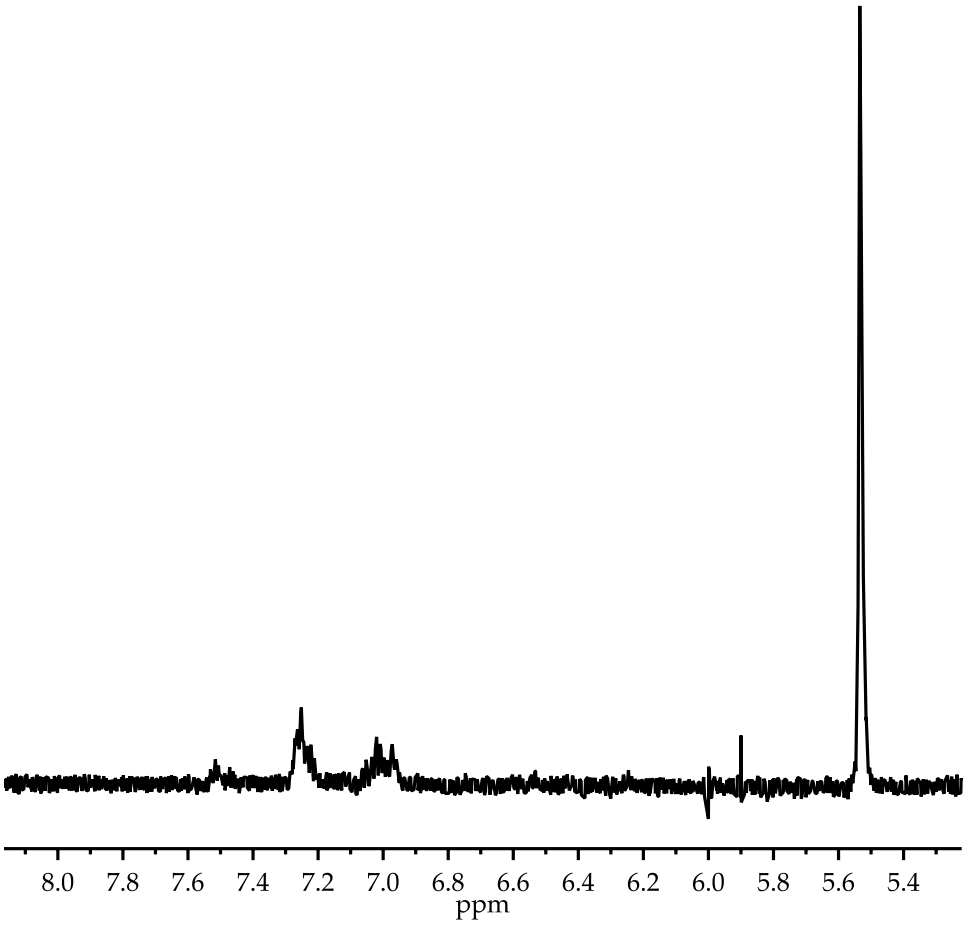

Figure A.4.31.Isolated ^{1}H NMR spectrum for metalation of 0.38 M 1-bromo-2-fluorobenzene with 0.40 M NaDA in 1.00 mL THF at –78 °C after quenching with 500 μL MeOD (100 μL cyclohexene internal standard added at δ 5.54 ppm). The appearance of extraneous resonances is consistent with decomposition.

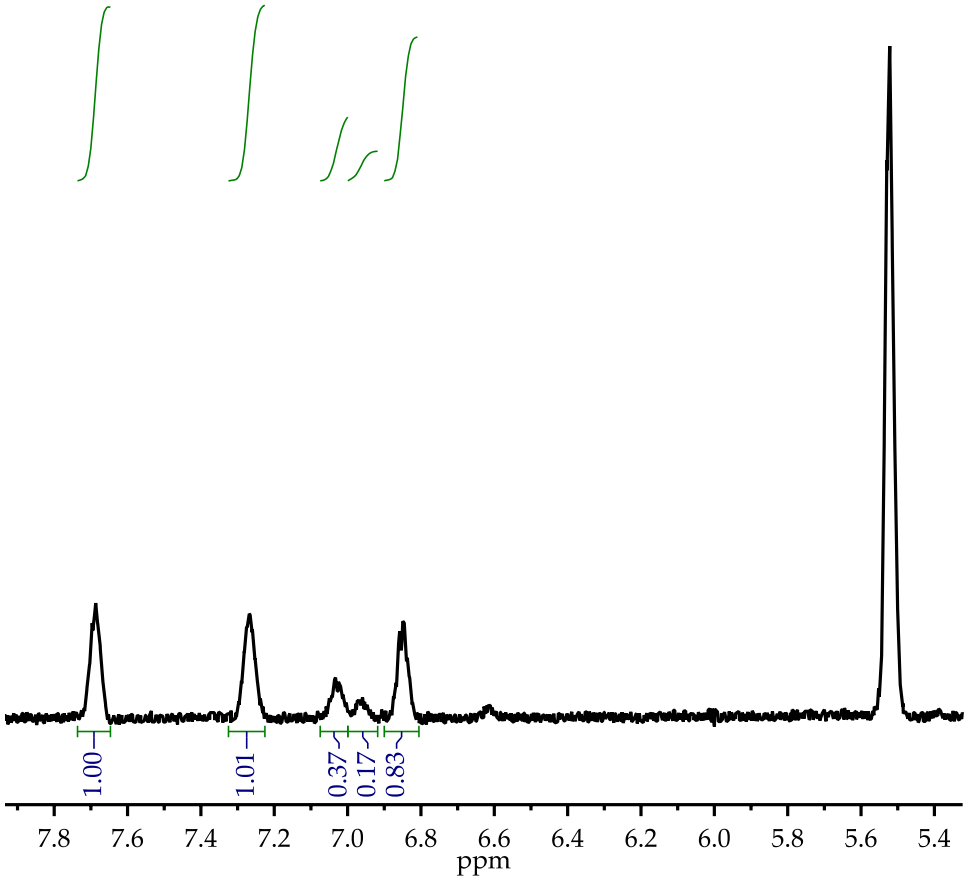

Figure A.4.32.Isolated ^{1}H NMR spectrum for metalation of 0.38 M 1-fluoro-2-iodobenzene with 0.40 M NaDA in 1.00 mL THF at –78 °C after quenching with 500 µL MeOD (100 µL cyclohexene internal standard added at δ 5.54 ppm).

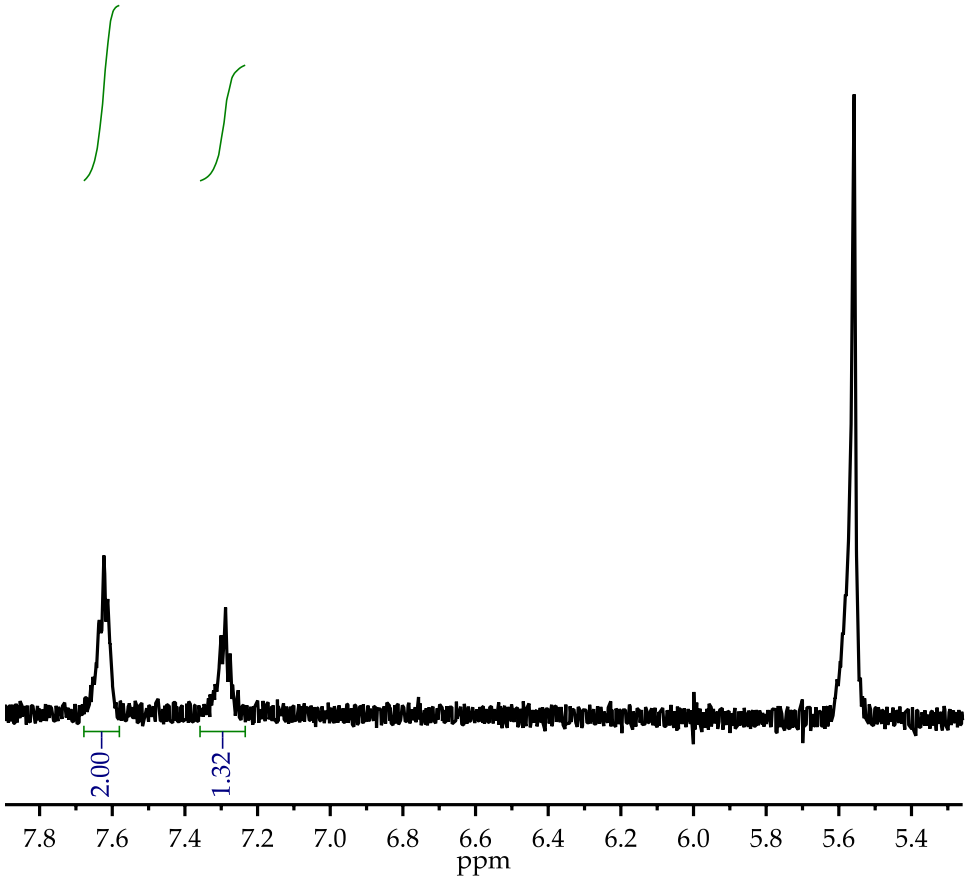

Figure A.4.33.Isolated ^{1}H NMR spectrum for metalation of 0.38 M 2-fluorobenzotrifluoride with 0.40 M NaDA in 1.00 mL THF at –78 °C after quenching with 500 µL MeOD (100 µL cyclohexene internal standard added at δ 5.54 ppm). Loss of the resonance at δ 7.28 ppm is consistent with selective metalation ortho to fluorine.

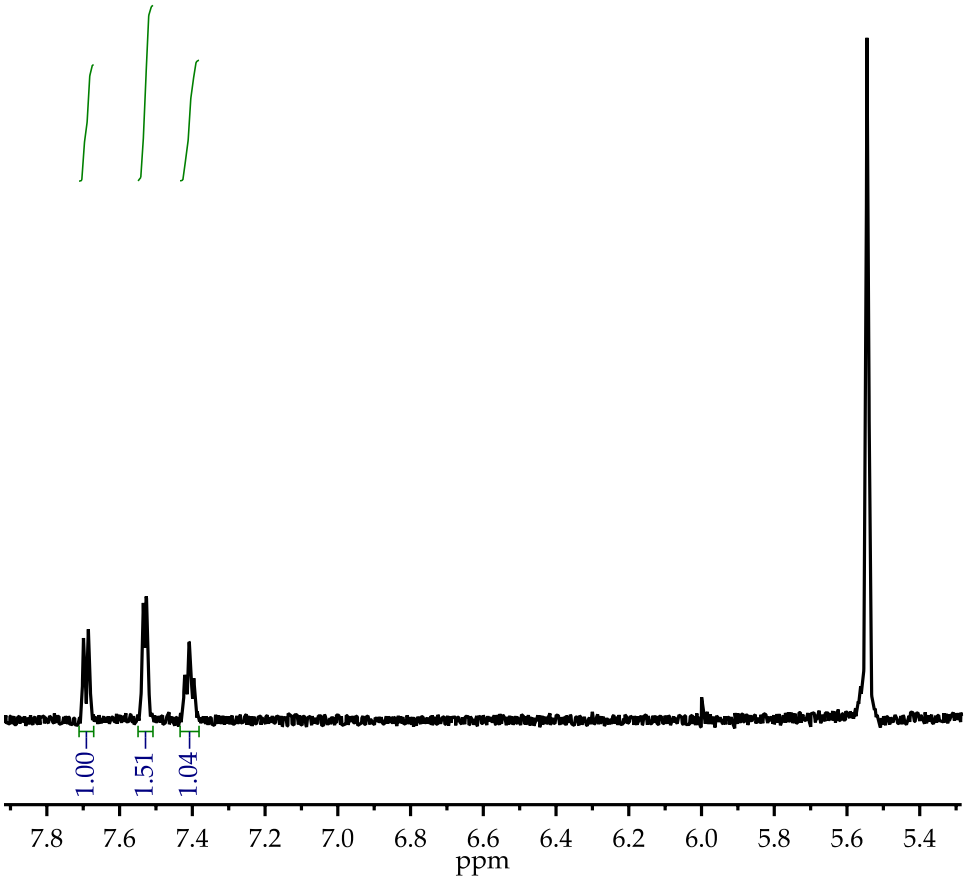

Figure A.4.34.Isolated ^{1}H NMR spectrum for metalation of 0.38 M 2-chlorobenzotrifluoride with 0.40 M NaDA in 1.00 mL THF at –78 °C after quenching with 500 µL MeOD (100 µL cyclohexene internal standard added at δ 5.54 ppm). Loss of the resonance at δ 7.53 ppm is consistent with selective metalation ortho to chlorine.

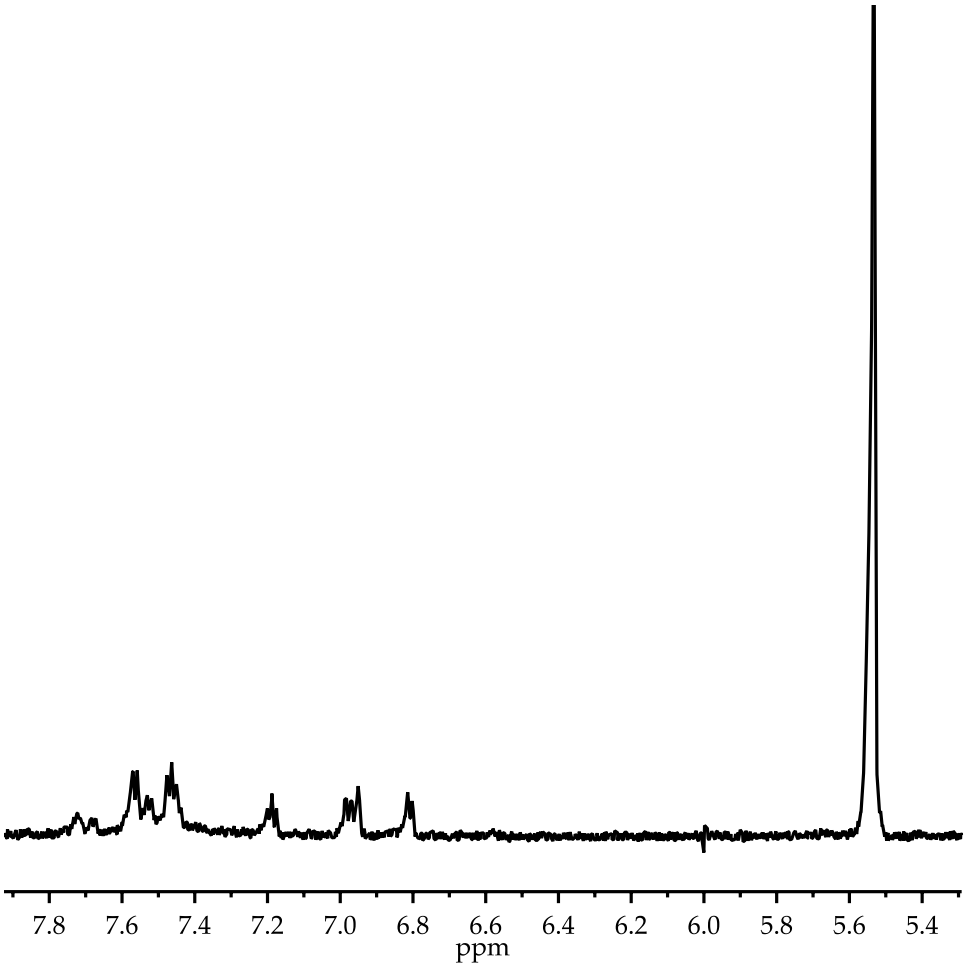

Figure A.4.35.Isolated ^{1}H NMR spectrum for metalation of 0.38 M 2-bromobenzotrifluoride with 0.40 M NaDA in 1.00 mL THF at –78 °C after quenching with 500 μL MeOD (100 μL cyclohexene internal standard added at δ 5.54 ppm). The appearance of extraneous resonances is consistent with decomposition.

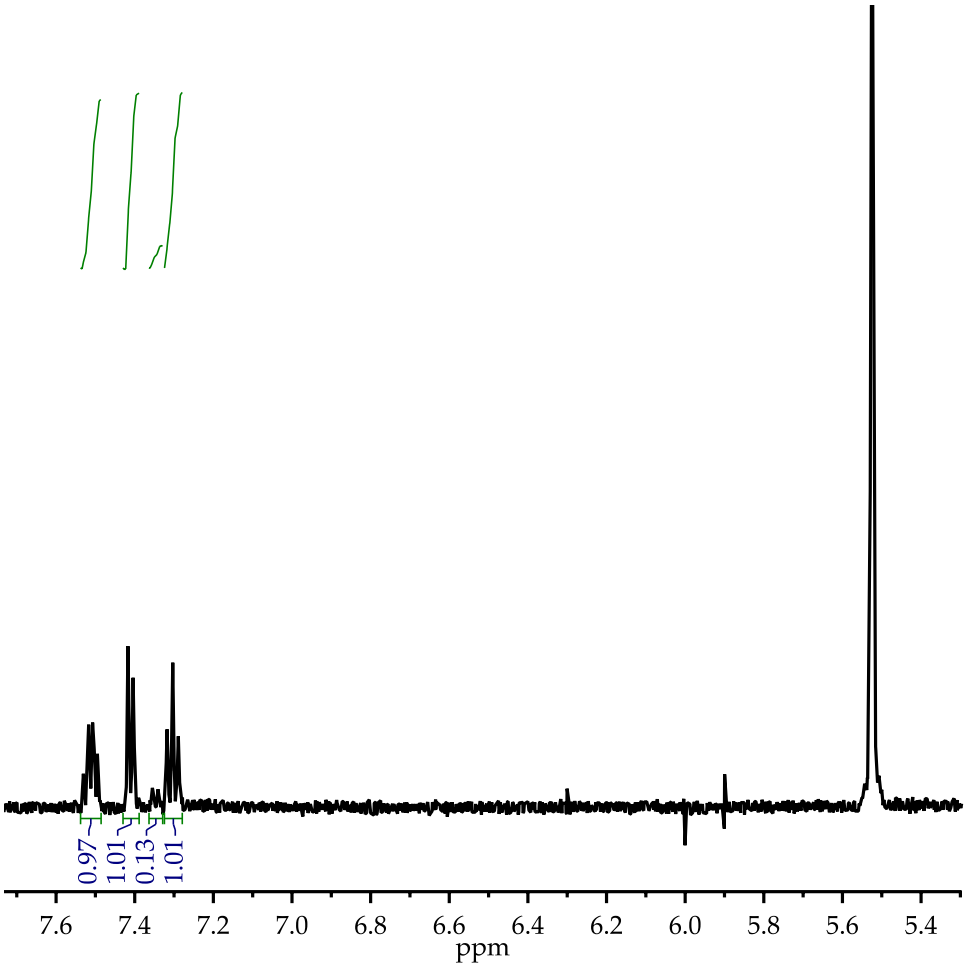

Figure A.4.36.Isolated ^{1}H NMR spectrum for metalation of 0.38 M 3-fluorobenzotrifluoride with 0.40 M NaDA in 1.00 mL THF at –78 °C after quenching with 500 µL MeOD (100 µL cyclohexene internal standard added at δ 5.54 ppm). Loss of the resonance at δ 7.34 ppm indicates doubly ortho metalation.

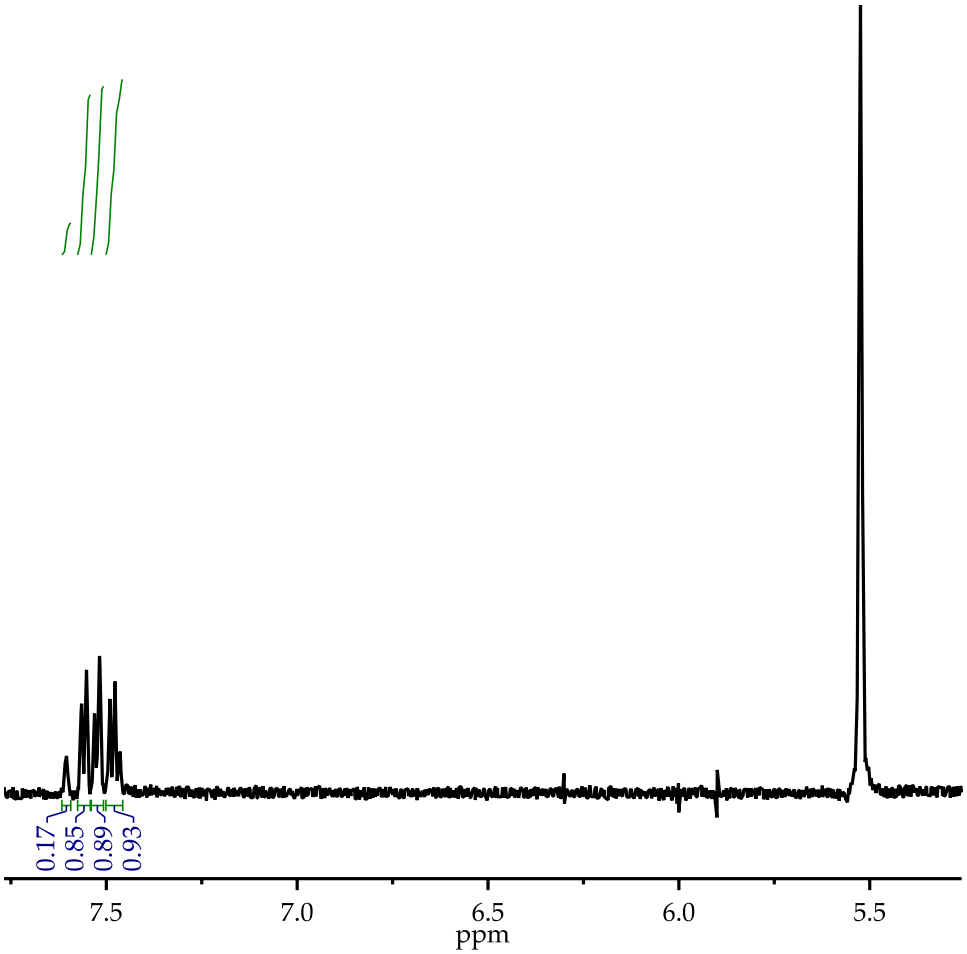

Figure A.4.37.Isolated ^{1}H NMR spectrum for metalation of 0.38 M 3-chlorobenzotrifluoride with 0.40 M NaDA in 1.00 mL THF at –78 °C after quenching with 500 µL MeOD (100 µL cyclohexene internal standard added at δ 5.54 ppm). Loss of the resonance at δ 7.60 ppm indicates doubly ortho metalation.

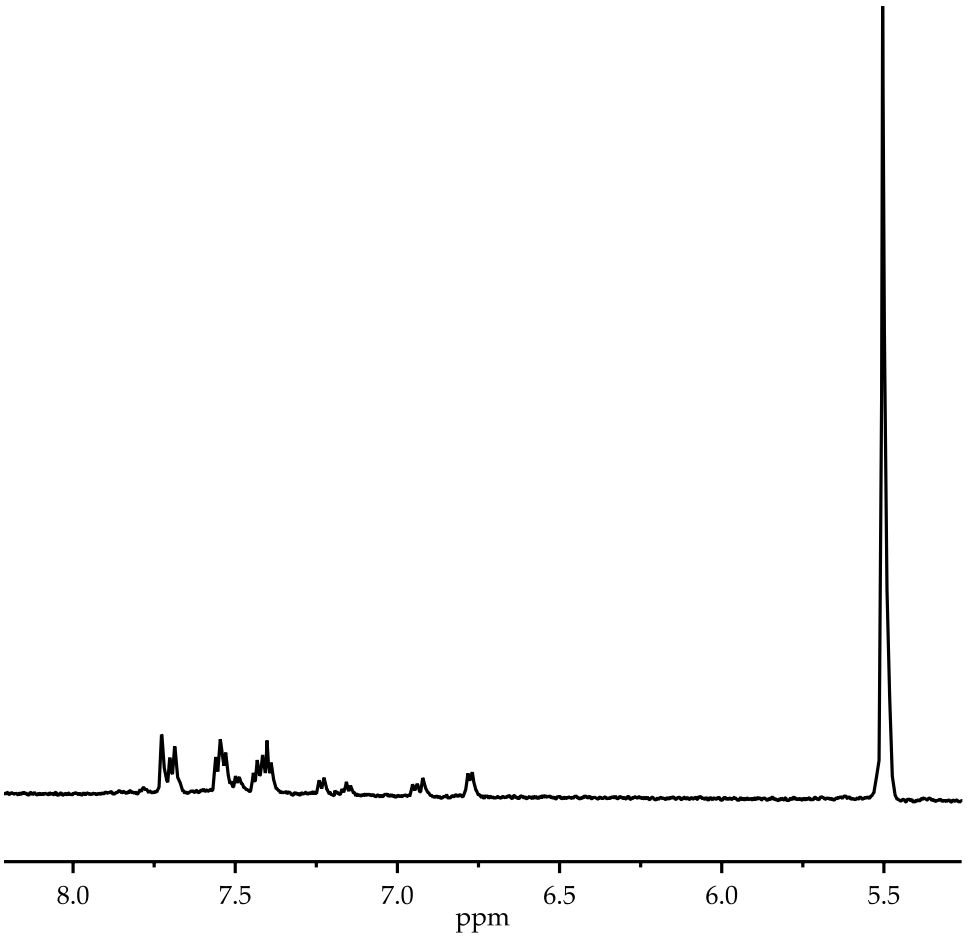

Figure A.4.38.Isolated ^{1}H NMR spectrum for metalation of 0.38 M 3-bromobenzotrifluoride with 0.40 M NaDA in 1.00 mL THF at –78 °C after quenching with 500 μL MeOD (100 μL cyclohexene internal standard added at δ 5.54 ppm). The appearance of extraneous resonances is consistent with decomposition (possibly isomerization).

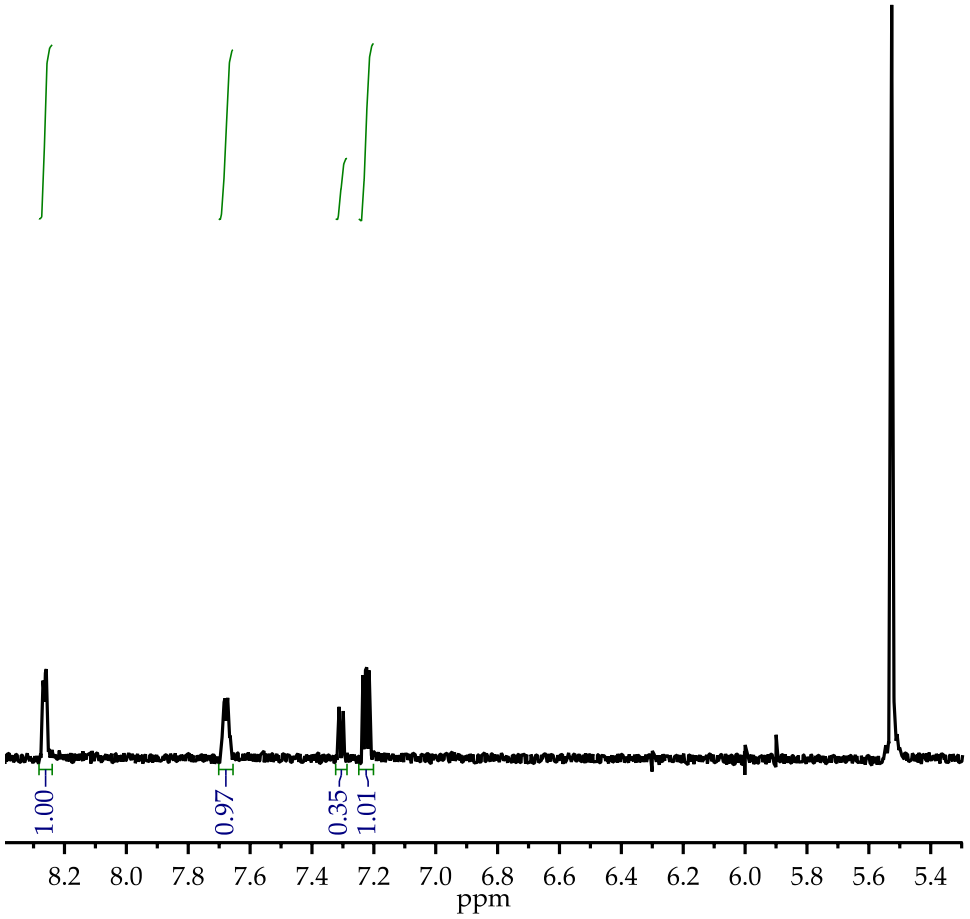

Figure A.4.39.Isolated ^{1}H NMR spectrum for metalation of 0.38 M 2-chloropyridine with 0.40 M NaDA in 1.00 mL THF at –78 °C after quenching with 500 µL MeOD (100 µL cyclohexene internal standard added at δ 5.54 ppm). Loss of the resonance at δ 7.31 ppm indicates ortho metalation to chlorine.

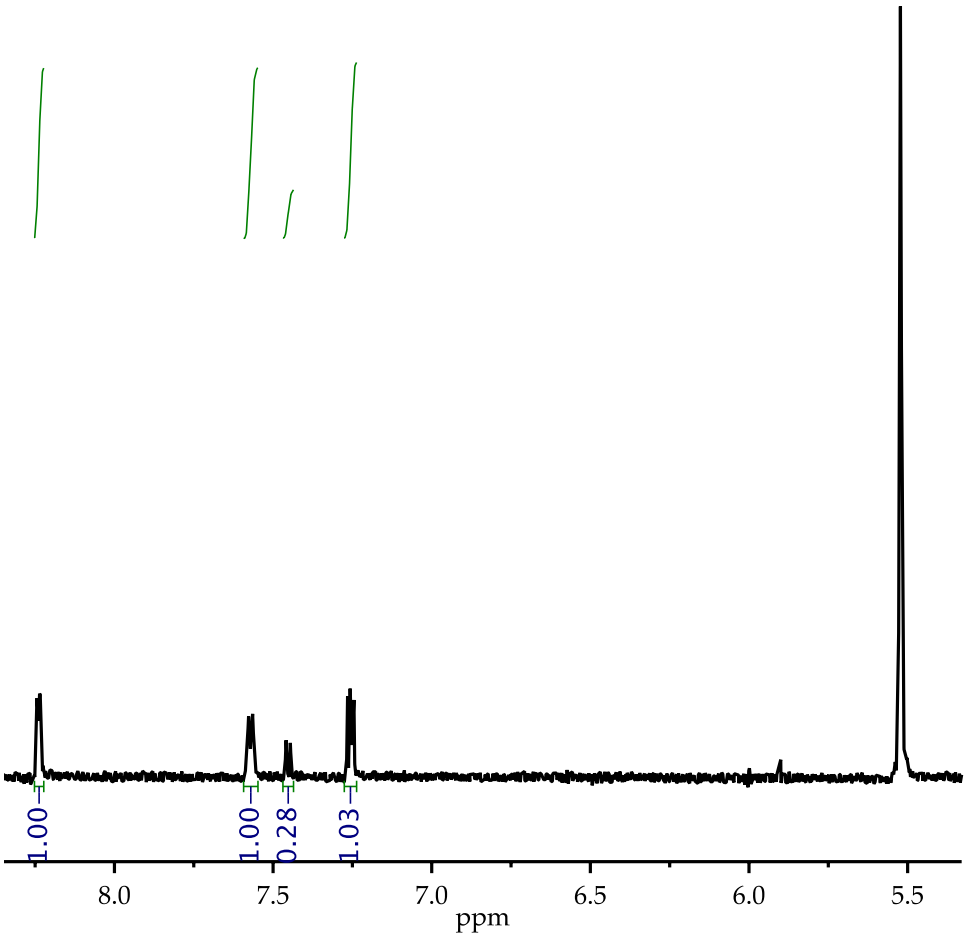

Figure A.4.40.Isolated ^{1}H NMR spectrum for metalation of 0.38 M 2-bromopyridine with 0.40 M NaDA in 1.00 mL THF at –78 °C after quenching with 500 µL MeOD (100 µL cyclohexene internal standard added at δ 5.54 ppm). Loss of the resonance at δ 7.46 ppm indicates ortho metalation to bromine.

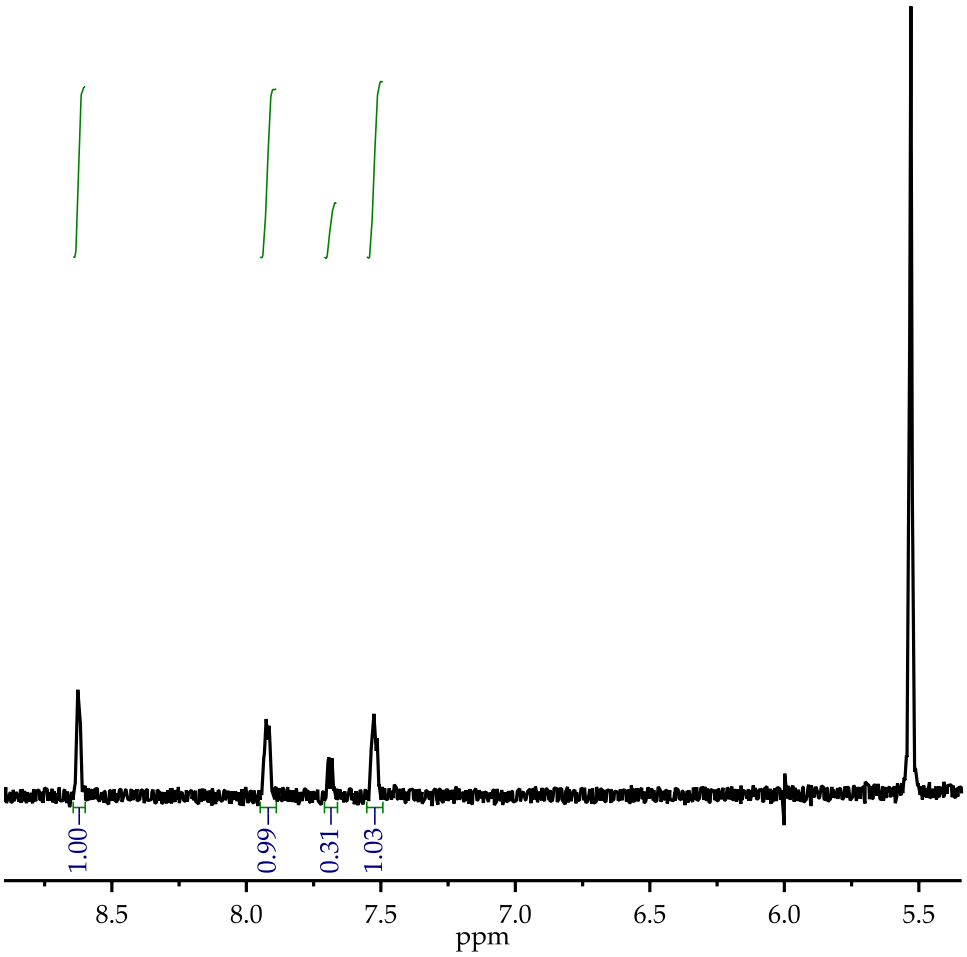

Figure A.4.41.Isolated ^{1}H NMR spectrum for metalation of 0.38 M 2-(trifluoromethyl)pyridine with 0.40 M NaDA in 1.00 mL THF at –78 °C after quenching with 500 µL MeOD (100 µL cyclohexene internal standard added at δ 5.54 ppm). Loss of the resonance at δ 7.69 ppm indicates ortho metalation to CF_3.

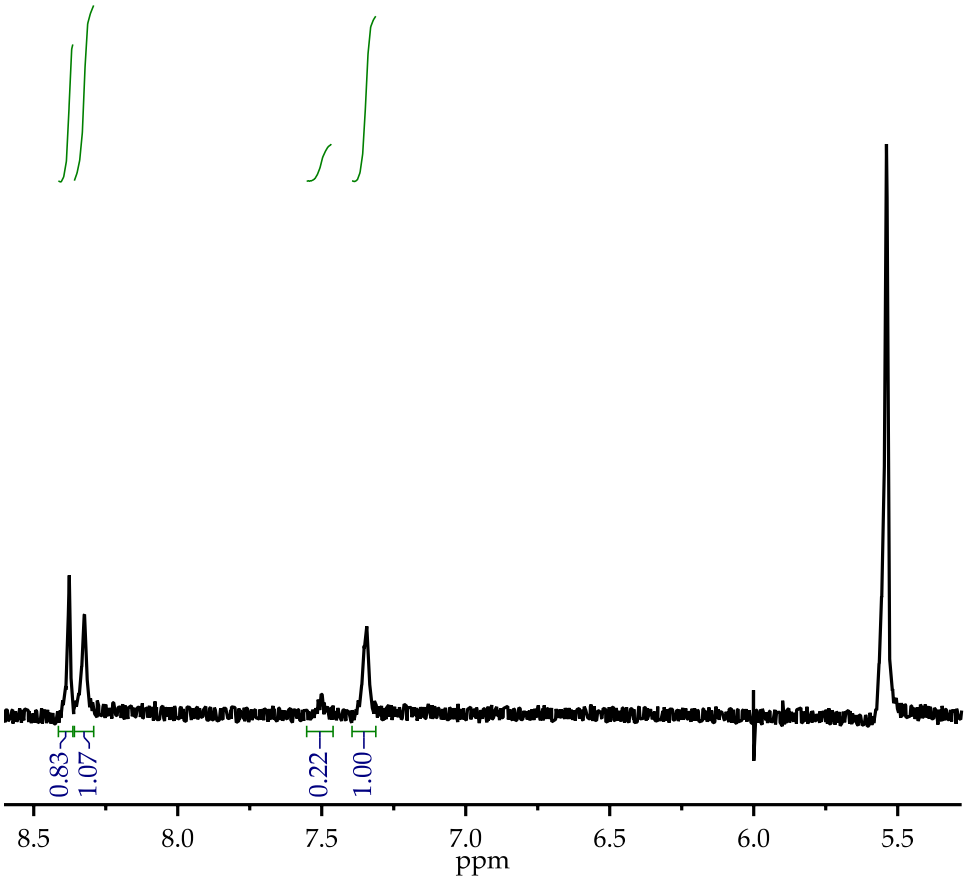

Figure A.4.42.Isolated ^{1}H NMR spectrum for metalation of 0.38 M 3-fluoropyridine with 0.40 M NaDA in 1.00 mL THF at –78 °C after quenching with 500 µL MeOD (100 µL cyclohexene internal standard added at δ 5.54 ppm). Loss of the resonance at δ 7.5 ppm indicates metalation at the 4 position.

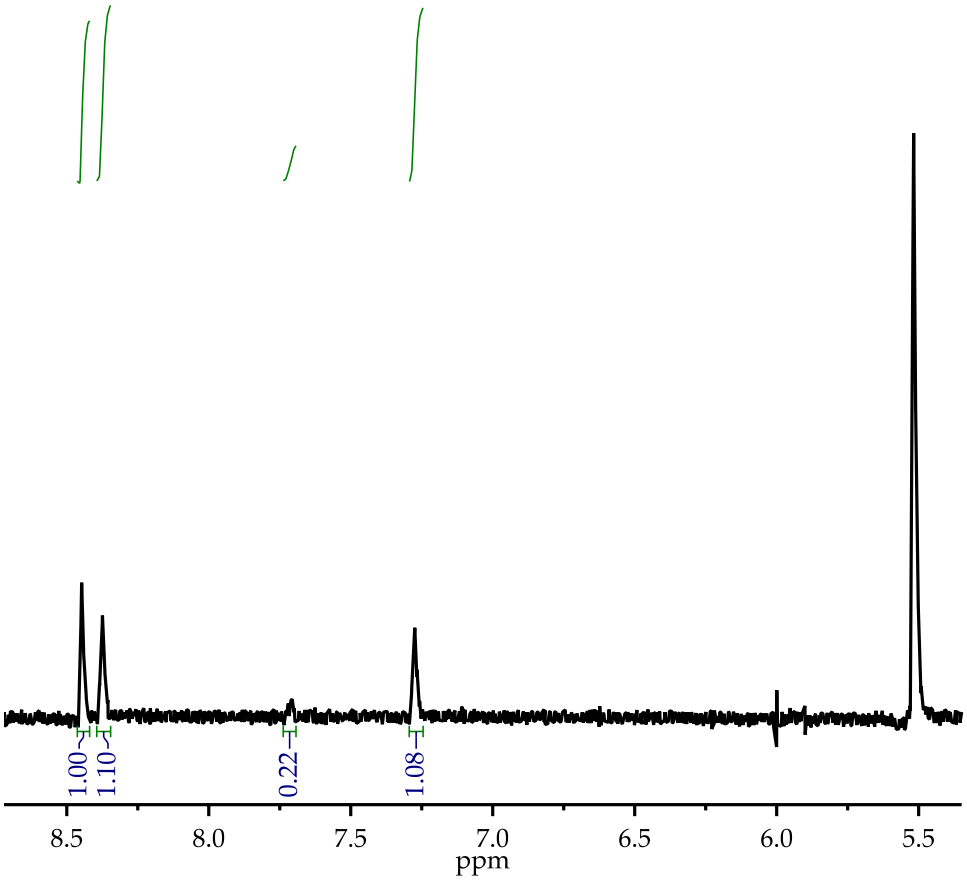

Figure A.4.43.Isolated ^{1}H NMR spectrum for metalation of 0.38 M 3-chloropyridine with 0.40 M NaDA in 1.00 mL THF at –78 °C after quenching with 500 µL MeOD (100 µL cyclohexene internal standard added at δ 5.54 ppm). Loss of the resonance at δ 7.7 ppm indicates metalation at the 4 position.

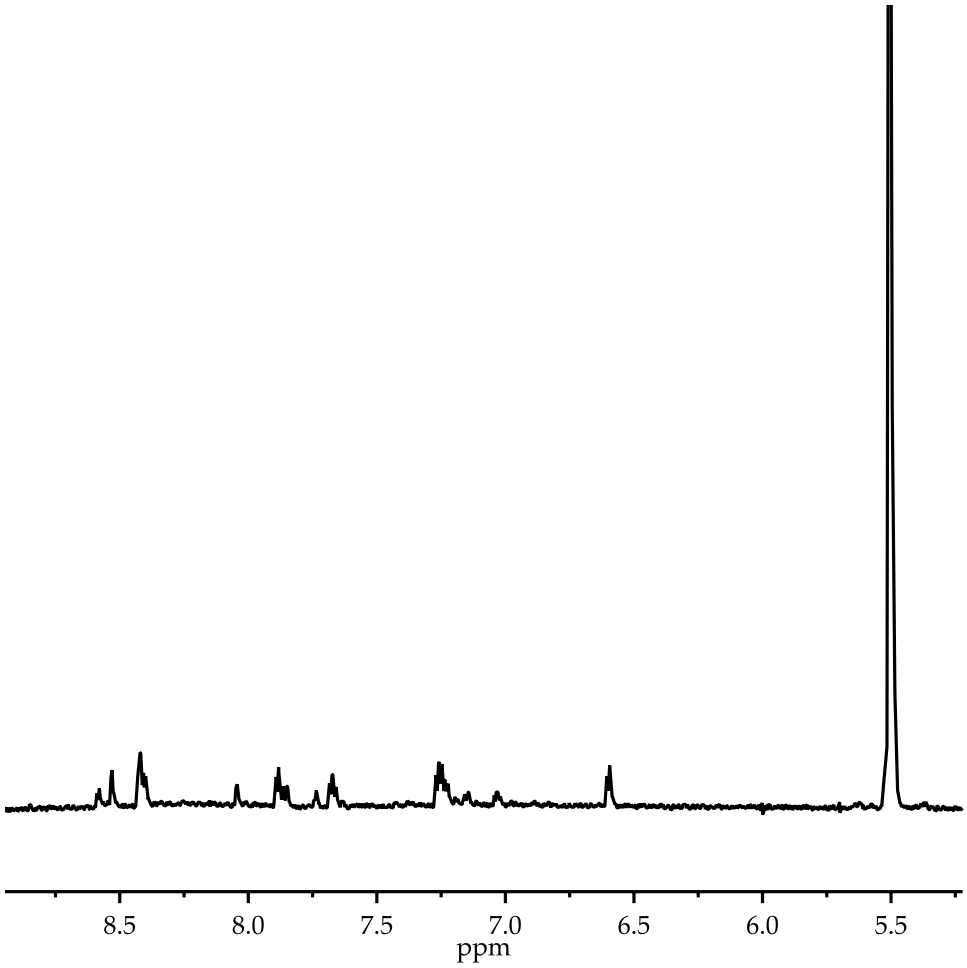

Figure A.4.44.Isolated ^{1}H NMR spectrum for metalation of 0.38 M 3-bromopyridine with 0.40 M NaDA in 1.00 mL THF at –78 °C after quenching with 500 μL MeOD (100 μL cyclohexene internal standard added at δ 5.54 ppm). The appearance of extraneous resonances is consistent with decomposition (possibly isomerization).

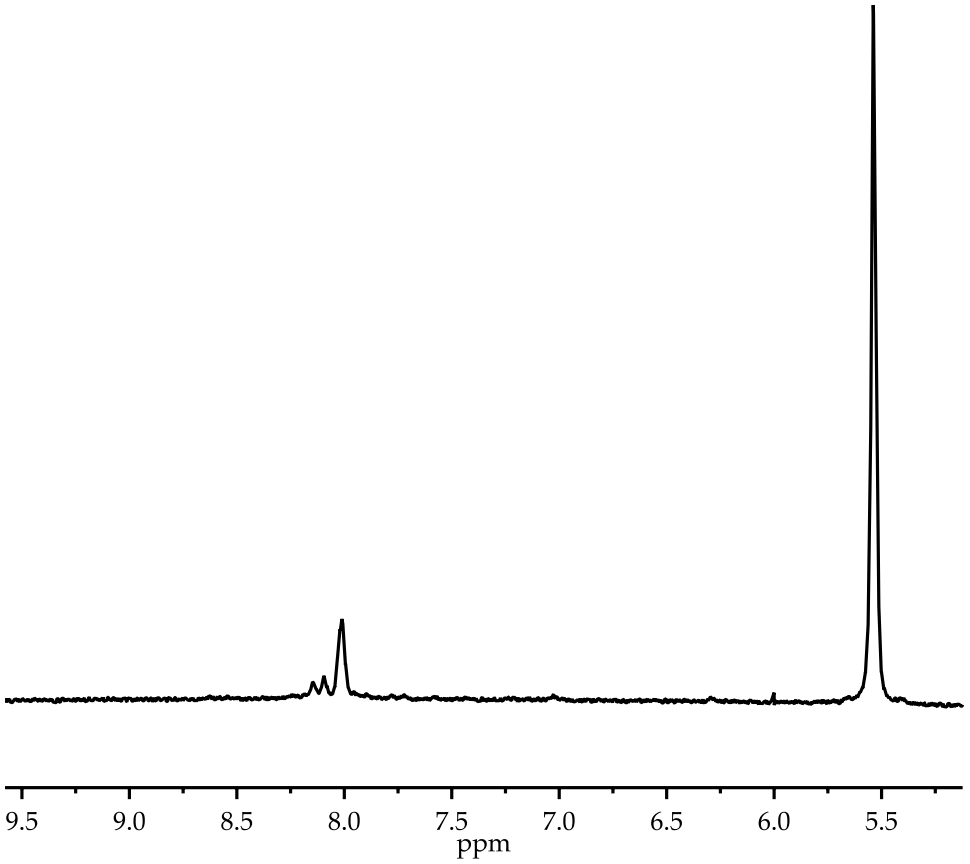

Figure A.4.45.Isolated ^{1}H NMR spectrum for metalation of 0.38 M 2-fluoropyrazine with 0.40 M NaDA in 1.00 mL THF at –78 °C after quenching with 500 μL MeOD (100 μL cyclohexene internal standard added at δ 5.54 ppm). That there are no resonances corresponding to starting material is consistent with decomposition.

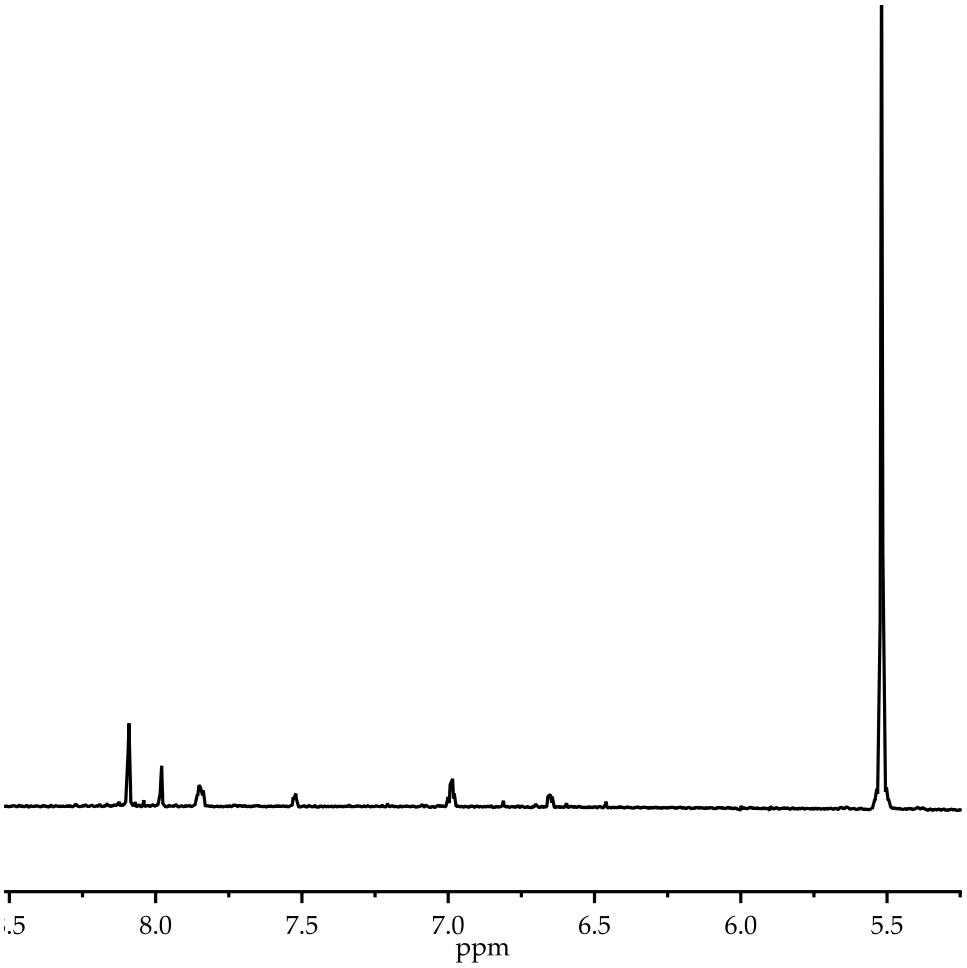

Figure A.4.46.Isolated ^{1}H NMR spectrum for metalation of 0.38 M 5-chloro-2-fluoropyridine with 0.40 M NaDA in 1.00 mL THF at –78 °C after quenching with 500 μL MeOD (100 μL cyclohexene internal standard added at δ 5.54 ppm). That there are no resonances corresponding to starting material is consistent with decomposition (possibly isomerization).

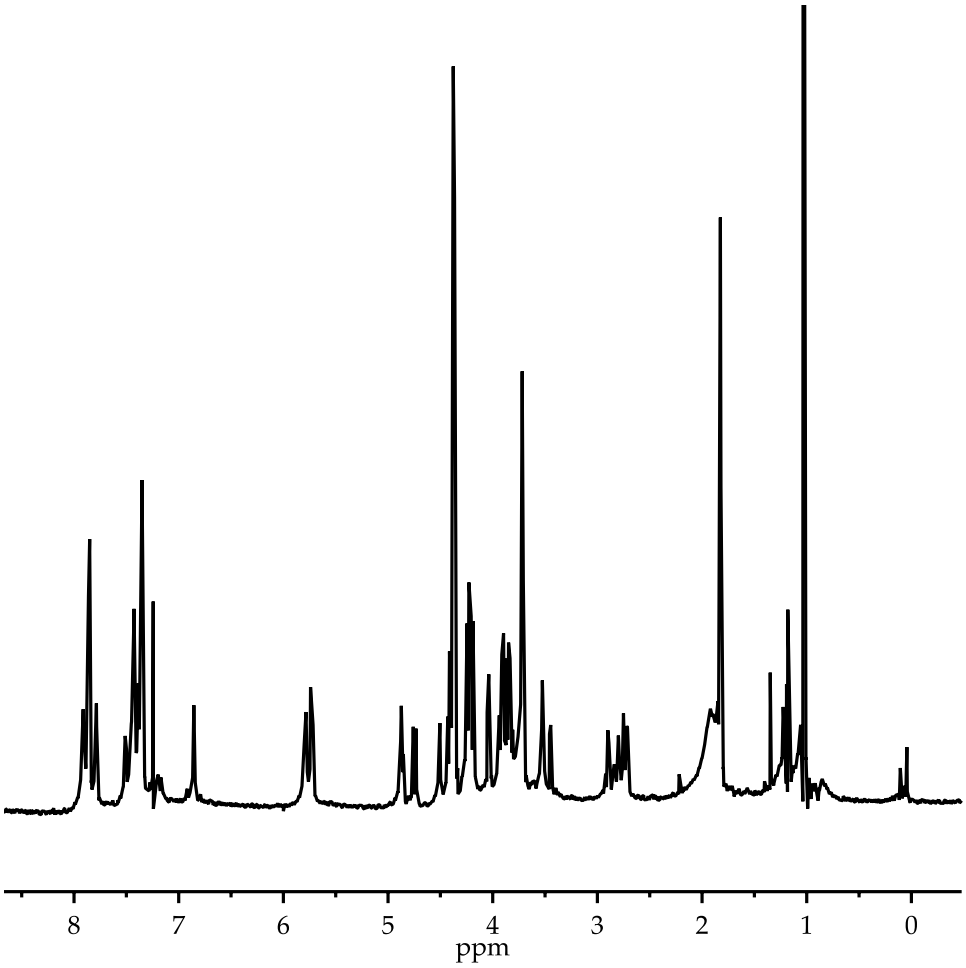

Figure A.4.47.Isolated ^{1}H NMR spectrum for metalation of 0.20 M 2-phenyl-2-oxazoline with 0.22 M NaDA in 1.00 mL THF at –78 °C after quenching with 200 μL MeOD. That there are no resonances corresponding to starting material is consistent with decomposition (likely due to heterocycle metalation).

Chapter 5

Lithium Hexamethyldisilazide Mediated Enolization of Acylated Oxazolidinones: Solvent, Cosolvent, and Isotope Effects on Competing Monomer- and Dimer-Based Pathways

Lithium Hexamethyldisilazide Mediated Enolization of Acylated Oxazolidinones: Solvent, Cosolvent, and Isotope Effects on Competing Monomer- and Dimer-Based Pathways

Abstract

Lithium hexamethyldisilazide (LiHMDS)-mediated enolization of (+)-4-benzyl-3-propionyl-2-oxazolidinone in THF–hydrocarbon mixtures shows unusual sensitivity to the choice of hydrocarbon cosolvent (hexane versus toluene) and to isotopic labeling. Four mechanisms corresponding to monosolvated monomers, trisolvated dimers, octasolvated monomers, and octasolvated dimers were identified. Even under conditions in which the LiHMDS monomer was the dominant observable form, dimer-based metalation was significant. The mechanism-dependent isotope and cosolvent effects are discussed in the context of ground state stabilization and transition-state tunneling.

Introduction

Lithium hexamethyldisilazide (LiHMDS) is second only to lithium diisopropylamide (LDA) in its importance as a lithium amide base in organic chemistry.[1] In light of the low basicity (low pK_b) of LiHMDS relative to that of lithium dialkylamides,[2] one might be tempted to attribute the high efficacy of the former to appreciable concentrations of monomer in neat tetrahydrofuran (THF; eq 5.1).[3,4,5] Although the results of numerous crystallographic,[6] spectroscopic,[3] and computational[7,8,9] studies have been published, only a few affiliated

mechanistic studies have been undertaken.[6,10] In particular, the enolization of 2-methylcyclohexanone has been shown to proceed via a seemingly straightforward disolvated-monomer-based mechanism (eq 5.2) and proves particularly germane to the work described herein.

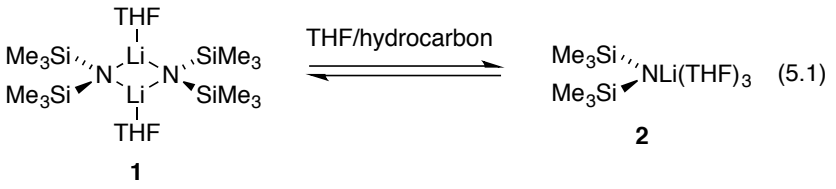

(5.1)

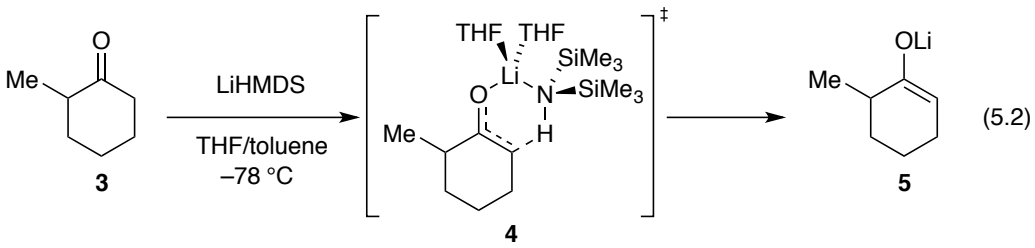

(5.2)

As part of our investigation of oxazolidinone-based enolates,[11] we were drawn to the sequential enolization aldol addition used by Pfizer in a plant-scale preparation of filibuvir.[12] The transformation proved particularly idiosyncratic on this scale.[13,14]

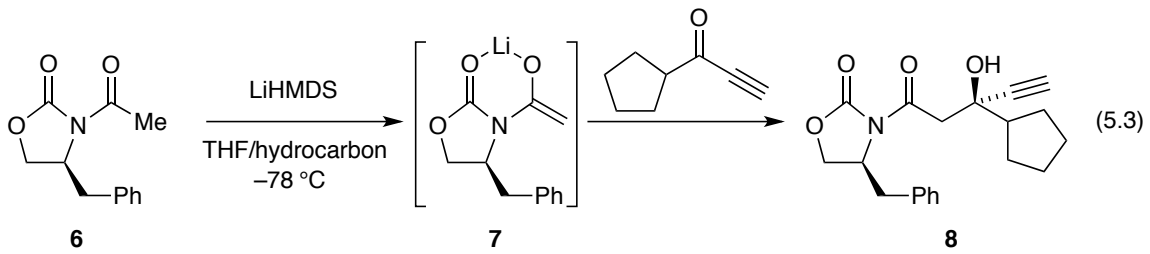

(5.3)

In this paper we describe the mechanisms of LiHMDS-mediated oxazolidinone enolizations. Guided by recent enolate structural studies[11] and a desire to attenuate the metalation rates, we focused on propionate analogue **9** (eq 5.4), fully expecting an uneventful prologue to our study of the Pfizer sequence. What emerged was a complex scenario in which four pathways represented by the four transition structures in Chart 5.1 competed for dominance. Notable observations included the importance of monomers and fully ionized triple ions, which showed the full complement of primary and secondary solvation shells, as well as dimer-based pathways that were significant *even when monomer was the observable form.* Solvation and isotope effects on the rates were considerable, mechanism-dependent, and central to deconvoluting the contributing mechanisms.

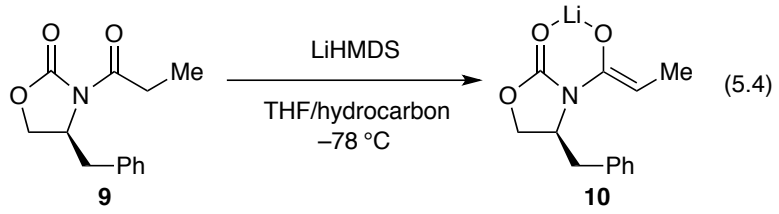

9 **10** (5.4)

Chart 5.1

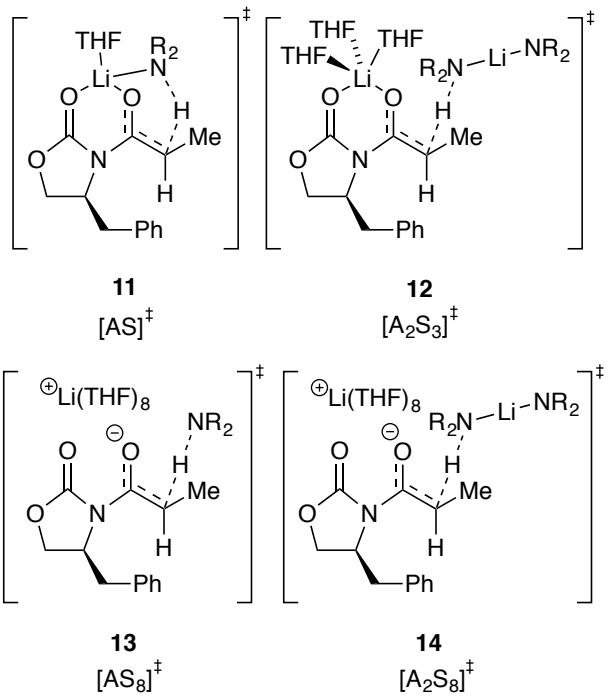

11 $[AS]^{‡}$ **12** $[A_2S_3]^{‡}$

13 $[AS_8]^{‡}$ **14** $[A_2S_8]^{‡}$

Results

Describing complex mechanisms demands literary expediencies such as the plot-spoiling summary in Chart 5.1. We also introduce shorthand in which A is a LiHMDS subunit and S is THF. For example, A_2S_2 refers to dimer **1**, whereas $[A_2S_3]^{‡}$ denotes a trisolvated-dimer-based transition structure such as **12**. Substrates **9** and **9**-d_2 are omitted to minimize clutter.

Enolizations of **9** with recrystallized LiHMDS[15] in THF–hydrocarbon mixtures were monitored using in situ IR spectroscopy[16] to follow the loss of the oxazolidinone absorbance at 1783–1793 cm^{-1} and appearance of an enolate absorbance at 1733–1740 cm^{-1}.[17] We found no evidence of precomplexation except at very low THF concentrations,[18] conditions that were assiduously avoided. Enolizations under pseudo-first-order conditions (0.0050 M substrate)

displayed first-order decays affording fits to $A = A_0e^{-bx} + c$ such that b is the pseudo-first-order rate constant, k_{obsd}, and c is a baseline correction.[19] In a control experiment, zeroing the baseline and injecting a second aliquot of **9** did not change k_{obsd}, which confirmed the absence of autocatalysis.[20] In one instance, initial rates were used instead of k_{obsd} as proxies for rates.[21]

Solvent and Isotope Effects. Deconvoluting the contributing pathways to assemble a unified mechanistic hypothesis depended critically on a combination of cosolvent (hexane versus toluene) and isotopic (**9** versus **9**-d_2) sensitivities that perturbed the *relative* proportions of the contributing pathways. This section delineates the insights gained from the solvent, cosolvent, and isotopic dependencies viewed in isolation from other data and notes salient observations. Critically, as the THF concentration changed from 1.0 M to 12 M,[22] LiHMDS shifted from >99% disolvated dimer A_2S_2 (**1**) to 97% trisolvated monomer AS_3 (**2**), as shown in eq 5.1.[5,23] The equilibrium in eq 5.1 was reexamined to compare the influence of hydrocarbon cosolvent on the dimer–monomer ratio, and no dependencies were detected outside a narrow experimental error. The subsequent sections describe the affiliated LiHMDS orders and construction of the mechanistic and affiliated mathematical models.

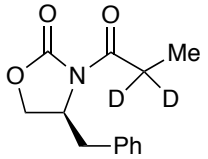

9-d_2

Figures 5.1–3 show plots of the THF-concentration-dependent rates for the lithiation of oxazolidinone **9** and isotopologue **9**-d_2 in THF–hexane and THF–toluene mixtures. One might

expect these rates to be qualitatively similar, but even casual inspection shows that they are not. The curves represent best-fit numerical integrations to *a single model* (*vide infra*). The solvent dependencies, with a few comments and some foreshadowing, are as follows.

(1) A plot of k_{obsd} versus THF concentration in hexane (see Figure 5.1, curve A) displays a striking maximum at 3–4 M THF and an *apparent* plateauing of the rates in neat THF. Qualitatively, the first-order dependence at low THF concentration suggests a mechanism requiring *one* more THF ligand than the number found on A_2S_2 as expected for either $[AS_2]^‡$ or $[A_2S_3]^‡$.[24] The inverse dependence at high THF concentration indicates a dominant pathway in which the observable AS_3 monomer is necessarily oversolvated—*has more solvents than optimal at the maximum*—and thereby requires dissociation of one or more THF ligands en route to enolization. The data fit credibly (albeit imperfectly) to a simple model built on a single AS_2-based metalation (curve not shown), but subsequent data completely undermined such a model. To the contrary, we found no evidence of contributions from $[AS_2]^‡$.

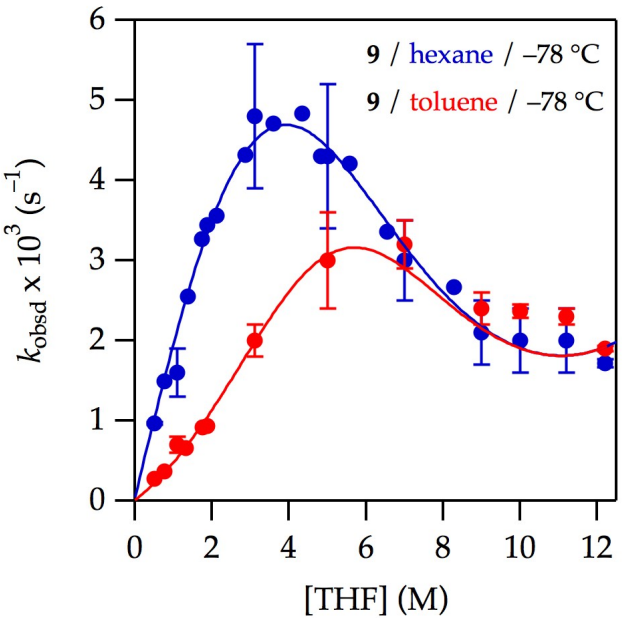

Figure 5.1. Plot of k_{obsd} vs tetrahydrofuran (THF) concentration[25] for the enolization of 0.0050 M oxazolidinone **9** with 0.10 M lithium hexamethyldisilazide (LiHMDS) with THF in hexane (curve A, blue) and toluene (curve B, red) at –78 °C. The curve depicts an unweighted least-squares fit to the composite model described by eq 5.12 (*vide infra*). Curve A (hexane): $[A]_0$ is set at 0.10 M; $K_{eq} = (2.3 \pm 0.2) \times 10^{-4}$; $k_8 = (3.9 \pm 0.1) \times 10^{-2}$; $k_9 = (2 \pm 10) \times 10^{-8}$; k_{10} is set to 2.0×10^{-4}; $k_{11} = (5 \pm 4) \times 10^{-10}$. Curve B (toluene): All parameters carried over from the fit from curve A; additionally, $a = -3.19 \times 10^{-5}$; $b = 3.36 \times 10^{-5}$; c is set at 1.0; and $m = 4.81$.

(2) Enolizations in THF–toluene (see Figure 5.1, red curve B) showed measurable *retardation* by toluene. As discussed below, we entertained a variety of models to account for the suppression of enolization by toluene as well as an upward curvature at low THF concentrations that *appeared* to be emblematic of a higher-order THF-dependent pathway.

(3) Isotopically labeled **9**-d_2 in THF–hexane (see Figure 5.2, curve A) markedly suppressed the dominant pathway(s) and affiliated rate maximum. What had previously appeared to be a saturation of the rate at high THF concentration was clearly the emergence of a highly THF-concentration-dependent pathway. Throughout the study we suspected that a THF-concentration-independent enolization, a non-zero *y*-intercept, might exist, and this plot provided

the most compelling evidence. Notably, the results of selective rate suppression via deuteration suggest that various mechanistic contributions have markedly different isotopic sensitivities.

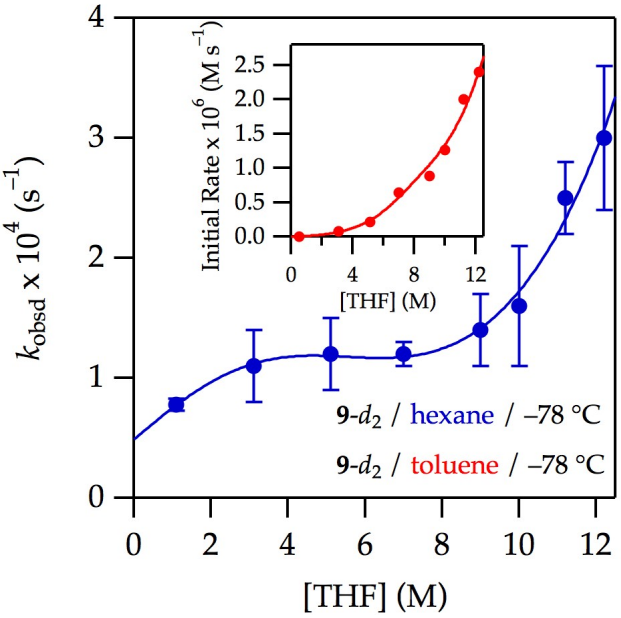

Figure 5.2. Plot of k_{obsd} vs THF concentration for the enolization of 0.0050 M oxazolidinone **9**-d_2 with 0.10 M LiHMDS with THF in hexane or toluene cosolvent at –78 °C. The curves depict unweighted least-squares fits to the model described by eq 5.12 (*vide infra*). Curve A (hexane): $[A]_0$ is set at 0.10 M; $K_{eq} = (1.1 \pm 1) \times 10^{-4}$; $k_8 = (5 \pm 4) \times 10^{-4}$; $k_9 = (8 \pm 20) \times 10^{-9}$; $k_{10} = (2.2 \pm 1) \times 10^{-4}$; $k_{11} = (7 \pm 3) \times 10^{-11}$. Curve B (toluene) measured using initial rates: All parameters carried over from the fit from curve A; additionally, $a = (-2 \pm 1) \times 10^{-4}$; $b = (1.4 \pm 0.9) \times 10^{-4}$; $c = 1.58 \pm 0.06$; and $m = 5$.

(4) A combination of isotopically labeled **9**-d_2 *and* toluene as cosolvent (see Figure 5.2, curve B) suppressed the previously dominant pathway so as to remove the maximum altogether. The data at –78 °C showed no fine structure (subtle curvatures), but the slow enolization demanded initial rates rather than the preferred k_{obsd}. Accordingly, we sought higher-quality measurements at –50 °C. The data in THF–hexane (see Figure 5.3, curve A) measured at –50 °C were quite similar to those obtained at –78 °C. The data in toluene (curve B) approximated a simple high-order THF dependence along with a marginally detectable perturbation. Dismissing

the perturbation as error would have been tempting were it not for the curves in Figures 5.1 and 5.2.

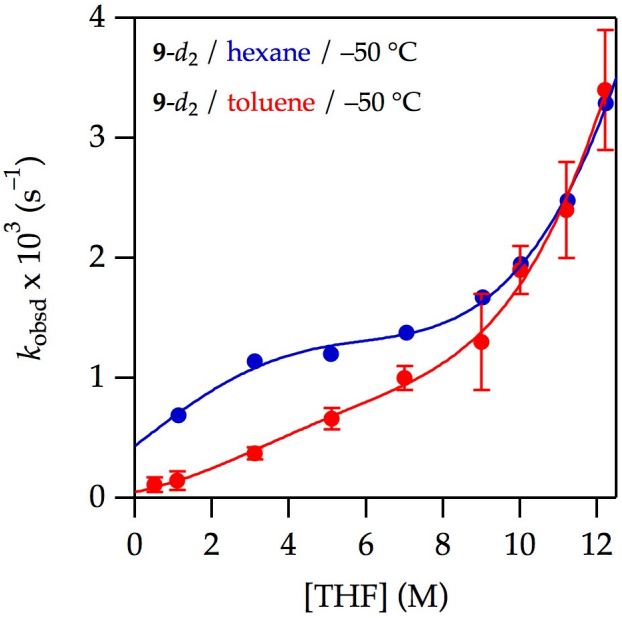

Figure 5.3. Plot of k_{obsd} vs THF concentration for the enolization of 0.0050 M oxazolidinone **9**-d_2 with 0.10 M LiHMDS with THF at –50 ºC in hexane (blue, curve A) and toluene (red, curve B). The curves depict an unweighted least-squares fit to the composite model described by eq 5.12 (*vide infra*). Curve A (hexane): $[A]_0$ is set at 0.10 M; $K_{eq} = (4 \pm 3) \times 10^{-5}$; $k_8 = (5 \pm 1) \times 10^{-3}$; $k_9 = (5 \pm 5) \times 10^{-8}$; $k_{10} = (1.9 \pm 0.6) \times 10^{-3}$; $k_{11} = (4 \pm 1) \times 10^{-10}$. Curve B (toluene): All parameters carried over from the fit from curve A; additionally, $a = -4 \times 10^{-2}$; $b = 9.2 \times 10^{-3}$; $c = 1.04$; and $m = 1.2$.

It is instructive to present the cosolvent and isotope effects from slightly different perspectives. The effect of toluene near the rate maxima is illustrated by a plot of k_{obsd} versus toluene concentration at a fixed 3.1 M THF concentration (Figure 5.4). The fit is essentially an inverse-first-order dependence with provisions for non-zero y-intercepts. The factor of two is energetically trivial, but the influence on the curvatures is not.

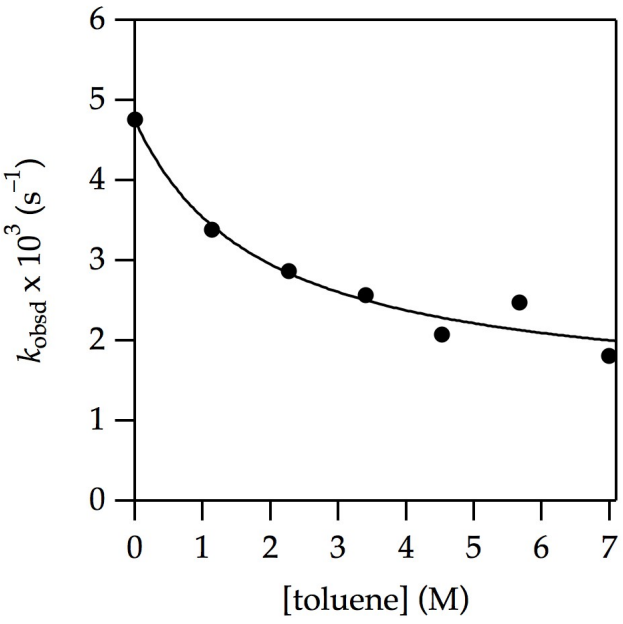

Figure 5.4. Plot of k_{obsd} vs toluene concentration for the enolization of 0.0050 M oxazolidinone **9** with 0.10 M LiHMDS with toluene in 3.1 M THF–hexane at –78 °C. The curve depicts an unweighted least-squares fit to $f(x) = (a + bx)/(1 + cx)^5$; $a = (4.7 \pm 0.2) \times 10^{-3}$; $b = (7 \pm 5) \times 10^{-4}$; and $c = 0.5 \pm 0.2$.

Plotting k_H/k_D versus THF concentration in hexane and toluene, as shown in Figure 5.5 (*note the different temperatures*), reveals a number of critical observations: (1) the isotope effects may seem uncharacteristically large to the casual observer, but such large effects are observed routinely in a number of metalations[26,27]; (2) the existence of a maximum in the isotope effect reveals *at least* three contributing mechanisms that, crudely speaking, correspond to low, intermediate, and high THF concentrations; (3) the maximum isotope effect at the intermediate THF concentrations coincides with the rate maxima that are suppressed by deuteration and toluene; and (4) the odd fine structures in the best-fit curves are consequences of the mathematical model discussed below.

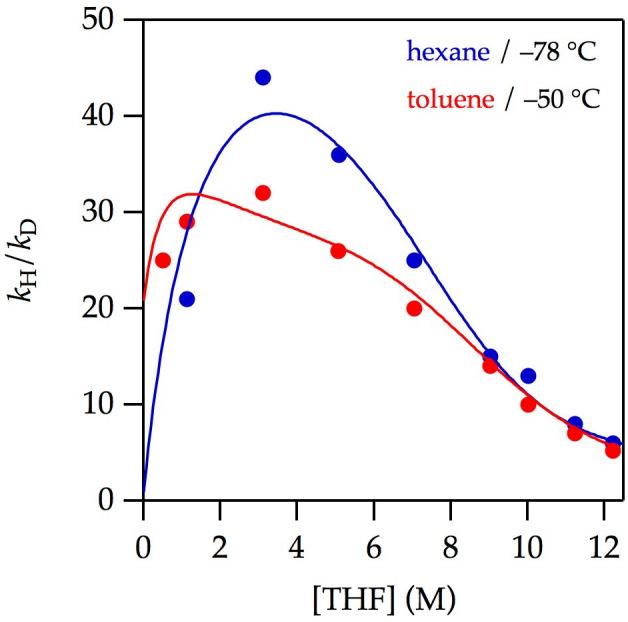

Figure 5.5. Plot of k_H/k_D vs THF concentration for the enolization of 0.0050 M oxazolidinones **9**-d_2 and **9** with 0.10 M LiHMDS with THF at –78 °C in hexane (curve A) and toluene (curve B). The curves are provided by dividing k_{obsd} for **9** by that of **9**-d_2 using the parameters reported in Figures 5.1 and 5.3.

Orders in LiHMDS. Complex mechanisms often call for multidimensional rate studies. The LiHMDS reaction order, for example, varies with changes in THF concentration, choice of hydrocarbon cosolvent, and isotopic labeling, as summarized in Table 1.[28] Note that the LiHMDS orders are confounding without consideration of the observable form of LiHMDS—dimer at low THF concentration and monomer at high—because the stoichiometry of the transition structure is measured *relative to the reactant*.[24]

Table 1. LiHMDS Reaction Order as a Function of Tetrahydrofuran (THF) and Cosolvent Concentrations and Isotopic Labeling

entry	subst	cosolvent	[THF] (M)	order	$[A_m]^‡$
1	**9**	hexane	1.0	1.1 ± 0.1	$[A_2]^‡$
2	**9**	hexane	7.1	1.20 ± 0.04	$[A_2]^‡$, $[A]^‡$
3	**9**	—	12.2 (neat)	1.40 ± 0.03	$[A_2]^‡$, $[A]^‡$
4	**9**	toluene	1.0	0.75 ± 0.04	$[A_2]^‡$, $[A]^‡$
5	**9**	toluene	7.1	1.14 ± 0.05	$[A_2]^‡$, $[A]^‡$
6	**9**-d_2	hexane	3.1	0.76 ± 0.08	$[A_2]^‡$, $[A]^‡$
7	**9**-d_2	---	12.2 (neat)	1.32 ± 0.03	$[A_2]^‡$, $[A]^‡$
8	**9**-d_2	toluene	1.0	0.7 ± 0.1	$[A_2]^‡$, $[A]^‡$

We offer graphical depictions of several LiHMDS orders emblematically. Plotting k_{obsd} versus LiHMDS concentration at low THF concentration (1.0 M) in hexane (see Figure 5.1, left edge of curve A) is cleanly first-order in LiHMDS (Figure 5.6, curve A and Table 1, entry 1). The linear dependence of k_{obsd} in conjunction with spectroscopy showing exclusively (>99%) dimer **1** and a first-order THF dependence implicates lithiation via an $[A_2S_3]^‡$ transition structure. At increasing THF concentrations, which promote the formation of monomer as the observable form, the LiHMDS order increases (Table 1, entries 2 and 3). In neat THF, wherein LiHMDS is 97% monomer, a LiHMDS order of 1.40 (Table 1, entry 3, and Figure 5.7) implicates the composite of first and second orders expected if both monomer- *and* dimer-based metalations contribute. Thus, *the observable AS_3 monomer **2** in conjunction with a LiHMDS order greater than 1.0 indicates that monomer is associating into a dimer to lithiate **9***. However, the curvatures in Figures 5.2 and 5.3 indicate an underlying set of highly solvated transition structures (below).

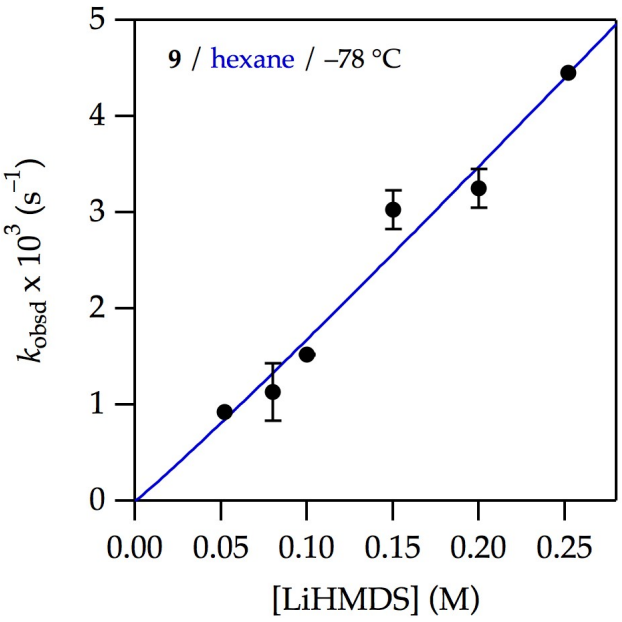

Figure 5.6. Plot of k_{obsd} vs LiHMDS concentration for the enolization of 0.0050 M oxazolidinone **9** with LiHMDS[28] and 1.0 M THF–hexane at –78 °C. The curves depict unweighted least–squares fits to $k_{obsd} = k[\text{LiHMDS}]^n$. $k = (1.9 \pm 0.4) \times 10^{-2}$ s^{-1}; $n = 1.1 \pm 0.1$.

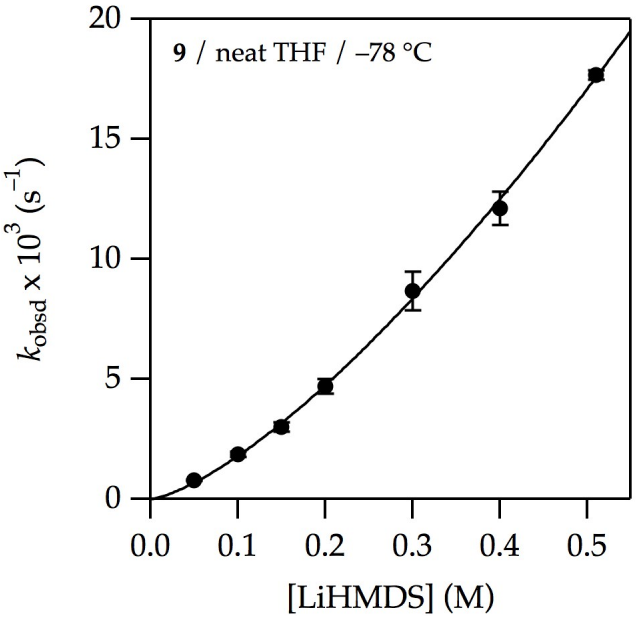

Figure 5.7. Plot of k_{obsd} vs LiHMDS concentration for the enolization of 0.0050 M oxazolidinone **9** with LiHMDS in neat THF at –78 °C. The curve depicts an unweighted least-squares fit to $k_{obsd} = k[\text{LiHMDS}]^n$. $k = (4.5 \pm 0.1) \times 10^{-2}$ s^{-1}; $n = 1.40 \pm 0.03$.

Mechanistic Model. Possible contributions to the rate law are generically depicted in eqs 5 and 6 and described mathematically by the generalized rate law in eq 5.7. (Recall that substrate **9** has been omitted for simplicity.) Eq 5.7 includes provisions for dimer–monomer equilibrium (K_{eq}, eq 5.1) and an indefinite number of mechanisms of arbitrary aggregation and solvation states.

$$A_2S_2 + xS \longrightarrow [A_2S_{2+x}]^{\ddagger} \tag{5.5}$$

$$1/2\ A_2S_2 + yS \longrightarrow [AS_{1+y}]^{\ddagger} \tag{5.6}$$

$$k_{obsd} = \sum_i k_i \left([A_2S_2]^{\frac{a_i}{2}} [S]^{s_i - a_i} \right) \text{ such that}$$

$$[A_2S_2] = \left(\frac{4[A]_0 + K_{eq}[S]^4 - \sqrt{K_{eq}}[S]^2 \sqrt{K_{eq}[S]^4 + 8[A]_0}}{8} \right) \tag{5.7}$$

The maximum in the plot of kinetic isotope effects versus THF concentration demands the involvement of *at least* three lithiation pathways. When including the added constraints of the dependencies on THF and LiHMDS concentrations, cosolvent, and isotopic substitution, the subset of mechanisms required to *fit all data*, in particular, the functions for THF dependencies in Figures 5.1–3, includes only four pathways (eqs 8–11), as described mathematically by eq 5.12. Of course, other minor pathways may contribute, but only eqs 8–11 are consistent with the constraints of Occam's razor.[29]

The THF–toluene fits pivot about the fits for the enolization of **9** and **9**-d_2 in THF–hexane. Thus, K_{eq} corresponds to the equilibrium constant in eq 5.1. The four rate constants (k_8–k_{11}) are numbered according to the equation number for which they are affiliated (eqs 8–11). K_{eq} and k_8–k_{11} are adjustable parameters. The value 12.3–[THF] represents the proportion of toluene scaled to neat THF concentration, 12.3 M. Whereas the $[A_2S_3]^‡$ stoichiometry (affiliated with k_8) is preset based on simulations demonstrating its importance, n is an adjustable parameter that can be left to ascertain the highly solvated contributions for the plots in Figures 5.2 and 5.3. Within these plots, the curvatures provide data that strongly support contributions from AS_n and A_2S_n, such that n approximates 8. We therefore set the value of n to 8. The curves in Figure 5.1, by contrast, lack adequate fine structure in the high THF region to extract n as an adjustable parameter; n is necessarily preset at 8 from the other data. Fits of the THF–toluene data in Figures 5.1–3 use the values of K_{eq} and k_8–k_{11} and apply a toluene-dependent weighting function, f[S], to the rates measured in toluene as described below.

$$A_2S_2 + S \longrightarrow [A_2S_3]^‡ \qquad (5.8)$$

$$A_2S_2 + (n\text{-}2)S \longrightarrow [A_2S_n]^‡ \qquad (5.9)$$

$$1/2\ A_2S_2 \longrightarrow [AS]^‡ \qquad (5.10)$$

$$1/2\ A_2S_2 + (n\text{-}1)S \longrightarrow [AS_n]^‡ \qquad (5.11)$$

$$k_{\text{obsd}} = f\left([\text{S}]\right)\left(\left(k_8[\text{S}] + k_9[\text{S}]^6\right)[\text{A}_2\text{S}_2] + \left(k_{10} + k_{11}[\text{S}]^7\right)[\text{A}_2\text{S}_2]^{\frac{1}{2}}\right)$$

$$\text{where } f\left([\text{S}]\right) = \begin{cases} 1 \text{ for hexane} \\ \dfrac{a\left(12.3 - [\text{S}]\right)^m}{1 + b\left(12.3 - [\text{S}]\right)^m} + c \text{ for toluene} \end{cases}$$

such that

$$[\text{A}_2\text{S}_2] = \left(\frac{4[\text{A}]_0 + K_{\text{eq}}[\text{S}]^4 - \sqrt{K_{\text{eq}}}[\text{S}]^2\sqrt{K_{\text{eq}}[\text{S}]^4 + 8[\text{A}]_0}}{8}\right) \qquad (5.12)$$

We cannot possibly recount in detail the copious trials and errors or even the intimate details of the fits described herein. Supporting information fills at least some of these gaps. The model was constrained, successfully we hasten to add, by demands for a single set of rate and equilibrium constants for multiple fits and a means with which to account for rate suppression by toluene. The evidence demanding these four contributions, however, can be summarized in generalized terms as follows:

(1) $[A_2S_3]^‡$ (eq 5.8) stems from the first-order THF dependencies on THF and LiHMDS concentrations at low THF concentrations in hexane (see Figure 5.1, curve A).

(2) For a protracted period, we believed that $[A_2S_4]^‡$ (eq 5.9) was required to account for the upwardly curving THF dependence at low THF concentrations in toluene (see Figure 5.1, curve B), but this conclusion was, in part, a red herring created by structural flaws in our modeling. We attribute the upward curvature to a *non-linear* influence of toluene (*vide infra*) combined with contributions from the more highly solvated pathways.

(3) The dropping isotope effect in Figure 5.5 demands a pathway emerging near the *y* intercept. $[AS]^{‡}$ (eq 5.10) provides for non-zero intercepts—rates in the limit of no free THF—that are minor at best and, in some cases, difficult to detect. The attribution to $[AS]^{‡}$ rather than $[A_2S_2]^{‡}$ (both fit the solvent-dependent data equally well) derives from fractional LiHMDS orders measured at low THF concentrations (Table 1, entries 4 and 8). Computed barriers, by contrast, argue strongly for the $[A_2S_2]^{‡}$ mechanism instead, and we discuss this disagreement below. Regardless, this term is of minor importance to the modeling and our thinking.

(4) The manifest upward curvatures at high THF concentration depicted in Figure 5.2 in tandem with an elevated LiHMDS order of 1.40 point to the coexistence of highly solvated monomer- and dimer-based transition states. We often invoke ionized fragments when confronted with highly solvated forms, and in this model we presume that the lithium gegenions affiliated with the highly solvated monomer and dimer share a common solvation state. Fitting the THF dependencies in Figure 5.2 while accounting for the elevated LiHMDS order affords an *n* value of 8, which is consistent with that of $[AS_8]^{‡}$ and $[A_2S_8]^{‡}$. Given that the upper limit of the primary coordination sphere of a lithium cation appears to octahedral $^{+}Li(THF)_6$,[30] invoking higher solvates demands contributions from a secondary solvation shell (*vide infra*).[31,32] We hasten to add that a variety of differentially solvated monomer- and dimer-based pathways adequately model the THF concentration dependencies but conflict with the measured LiHMDS orders.

(5) The most challenging problem proved to be that of adequately describing the influence of toluene. In the discussion below, we ponder the role of ground and transition state effects, which guided our thinking in subtle ways. Early studies simply let k_8–k_{11} float to values for THF–toluene data and THF–hexane independently, but that allowance is structurally flawed

because the *k* values are necessarily constant, whereas the rates are necessarily dependent on toluene concentration.

We reverse-engineered a toluene weighting function by ascertaining the function necessary to impose a successful fit constrained by using a single set of rate constants (Figure 5.8). Although this model is non-predictive and of limited pedagogical value, it adequately describes the influence of toluene as a cosolvent. Models that assigned explicit stoichiometric roles to toluene and included provisions for differential ground state and transition state stabilization had potential to offer molecular-level insights, but they were unjustifiably intricate compared with the empirically determined toluene weighting function *f*[S] in Figure 5.8.

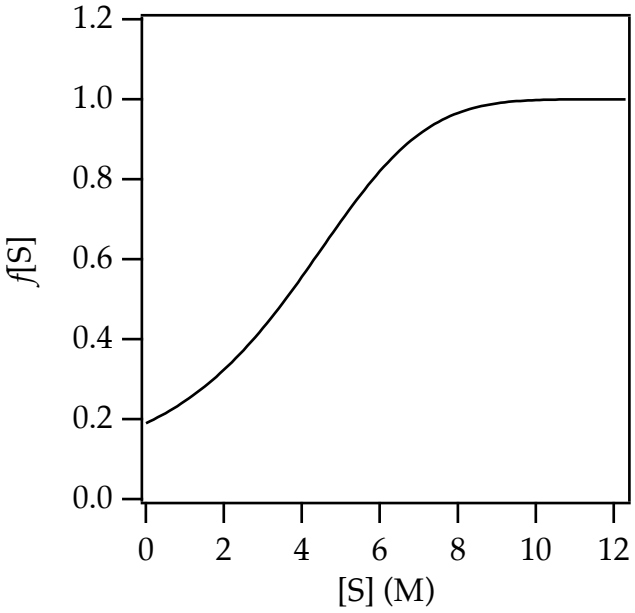

Figure 5.8. Representative plot of *f*[S] versus S (THF); all parameters carried over from the fit in Figure 5.1, curve B.

Computations. Transition structures corresponding to those described by eqs 8–11 (Chart 5.1) were examined with density functional theory (DFT) calculations at the B3LYP/6–

31G(d) level with single-point calculations at the MP2 level of theory.[33] The computational study was far more extensive than can be justifiably described herein. (See the supporting information for additional results.) The transition structures in Chart 5.1 provide pleasing depictions and confirmation of some level of viability, but thermochemical insights are limited by the non-isodesmic relationships.[34]

The $[AS_8]^‡$ and $[A_2S_8]^‡$ structures were well beyond the scope of our computational approach. We could not calculate the putative $^+LiS_6$ core structure despite undeniable experimental support,[30] let alone probe secondary-shell solvation. Highly ionic structures also showed electron correlation problems.[35] The calculated barriers for $[A_2S_3]^‡$ and $[AS]^‡$ showed a decidedly large (>8 kcal/mol/lithium) preference for the dimer. Even in this instance, however, large energy differences for such non-isodesmic comparisons were unsurprising.[36] We invoked $[AS]^‡$ in place of $[A_2S_2]^‡$ owing to the fractional LiHMDS order observed experimentally. $[A_2S_2]^‡$ (**15**), however, was chemically intuitive, showed a N–H–C alignment approximating 180°, and was only +4.7 kcal/mol/lithium less stable than the more highly solvated $[A_2S_3]^‡$. When confronted with large theory–experiment disagreements, we instinctively go with experiment, but we do so with pause in this case.

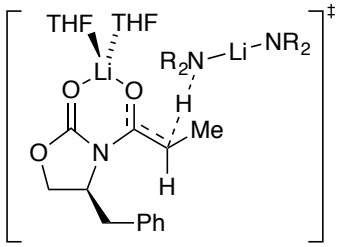

15
$[A_2S_2]^‡$

One complicating and potentially critical question was which diastereotopic proton in **9a**, H_{syn} or H_{anti}, was abstracted. H_{anti} was the computationally preferred proton for computationally viable transition structures **11** and **12** (2.5 and 5.6 kcal/mol, respectively). There are potential implications to synthesis that may prove important.

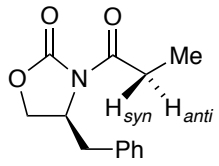

9a

Discussion

Summary. In light of the seemingly straightforward enolization of 2-methylcyclohexanone in eq 5.1, the complexity of the metalation of **9** in THF–hydrocarbon mixtures emerged unexpectedly. The maximum in the rates obtained using THF–hexane (see Figure 5.1, curve A) is startling on first inspection, but it is qualitatively consistent with the simple case of an AS_2-based pathway accompanied by a shifting ground state (eq 5.1). At low THF concentration, the A_2S_2 dimer would be undersolvated, causing a positive order in THF, whereas at high THF concentration, the observable AS_3 monomer would be oversolvated, causing an inverse dependence.[37] A fit to such a model was tolerable, though not stupendous. Switching from THF–hexane to THF–toluene, however, suppressed the maximum (see Figure 5.1, curve B), rendering the simple AS_2-based metalation untenable. Deuteration (**9**-d_2) further attenuated the dominant pathway (see Figures 5.2 and 5.3) and accentuated the complexity by offering views of additional enolization mechanisms. Of particular import, two highly THF-

concentration-dependent pathways not easily detected using **9** in THF–hexane became prominent using **9**-d_2 in THF–hexane and were dominant for **9**-d_2 in THF–toluene.

The THF concentration dependencies and cosolvent effects in conjunction with multiply measured LiHMDS reaction orders led to a model comprising four mechanisms: $[AS]^{‡}$, $[A_2S_3]^{‡}$, $[AS_8]^{‡}$, and $[A_2S_8]^{‡}$. (Substrates **9** and **9**-d_2 are omitted from the transition structures to reduce clutter.) We hasten to add that THF-concentration-dependent isotope effects (see Figure 5.5) *required* the involvement of *at least* three mechanisms; the final model containing four is reasonable. Additional mechanisms may be involved, but a *single mathematical model including these four along with a correction for toluene versus hexane fit the data in Figures 5.1–3*. The forthcoming discussion fleshes out the details and concludes with thoughts on why the oxazolidinone enolization is hypersensitive to seemingly trivial changes in conditions.

Correlating Stoichiometry with Structure. Rate studies establish stoichiometries at the rate-limiting transition structures,[24] and computations add insights into structure and other experimentally elusive details. The experimentally determined high per-lithium solvation numbers pushed us to invoke free-ion-based pathways: a simple free ion **13** and fully ionized triple ion **14**. Triple ions,[38] including LiHMDS-derived triple ions,[3] are well-documented. Spectroscopic evidence also indicated an ionized LiHMDS monomer: a free ion or solvent-separated ion pair.[39] Nonetheless, the $^{+}LiS_8$ gegenion in **14** defied computation, which may be shocking to some. In defense of the hypothesis, we first note that $^{+}Li(THF)_6$ is documented crystallographically.[30] The high-order dependence on THF concentration is unusual by any standard, but it is not without support. We observed a *seventh*-order dependence for Ph_2NLi alkylations in 1988 consistent with a decasolvated cation, $^{+}Li(THF)_{10}$.[32] In that instance, we invoked secondary-shell effects stemming from the requisite ionization of a solvent-separated

ion pair. Conductivity studies show that full ionization of the $LiClO_4$ separated ion pair is significantly endothermic,[40] presumably requiring considerable secondary-shell solvation (eq 5.13). The secondary shells of aprotic solvents have been discussed[31,32] and are suggested to be marginally sensitive to steric effects and not particularly well-ordered but might still require orderly THF dipole alignment about the cation.

$$X^-//^+Li(THF)_6 + n\text{THF} \rightleftharpoons X^- + {}^+Li(THF)_6\bullet(THF)_n \qquad (5.13)$$

A marginally detectable basal reactivity in the limit of low THF concentration was attributed to **11** (Chart 5.1) because of an observed fractional order in LiHMDS. It posed an interesting theory–experiment conflict, however, in that computations suggested that A_2S_2-dimer-based transition structure **15** was viable. We also found **15** to be intuitively appealing, which is admittedly unscientific. When confronted with a large experiment–theory disagreement, we instinctively favor experiment, but not always with great confidence. Fortunately, this particular disagreement was of limited importance.

Syn versus Anti Deprotonation. The rate-limiting proton transfers in transition structures **11** and **12** represent anti deprotonation as defined in **9a**; the corresponding syn counterparts are 2.5 and 5.6 kcal/mol less stable, respectively, with the exception of a slight syn preference in **13**. Are these relative *syn–anti* selectivities important? In the current context, no, but we offer an interesting thought: if one wished to quaternize an Evans enolate at the alpha carbon with high stereocontrol,[41] a requisite stereoselective enolization would depend on the facial preference for deprotonation (eq 5.14), which would in turn require mechanistic control. For now, however, this thought is just passing.[42]

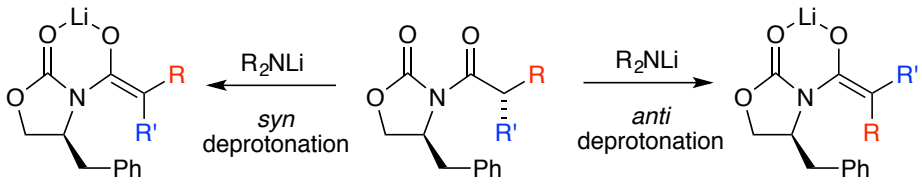

(5.14)

Contributions to the Reaction Coordinate. It is instructive to consider the relative importance of the four mechanisms to the overall reaction coordinate. Using the parameters from the fit for the enolization of **9** in hexane (see Figure 5.1, curve A), we plotted the individual contributions versus THF concentration (Figure 5.9). The attribution of $[A_2S_3]^‡$ as the root cause of the maximum in the enolization rate is evident. The *apparent* saturation of the rates at high THF concentration in Figure 5.1 is shown in Figure 5.9 to derive from highly solvated $[AS_8]^‡$ and $[A_2S_8]^‡$ pathways. The data from Figure 5.1 in isolation were insufficient to detect these terms, but the upward curvature became prominent and undeniable through further suppression of the dominant $[A_2S_3]^‡$ pathway (*vide infra*).

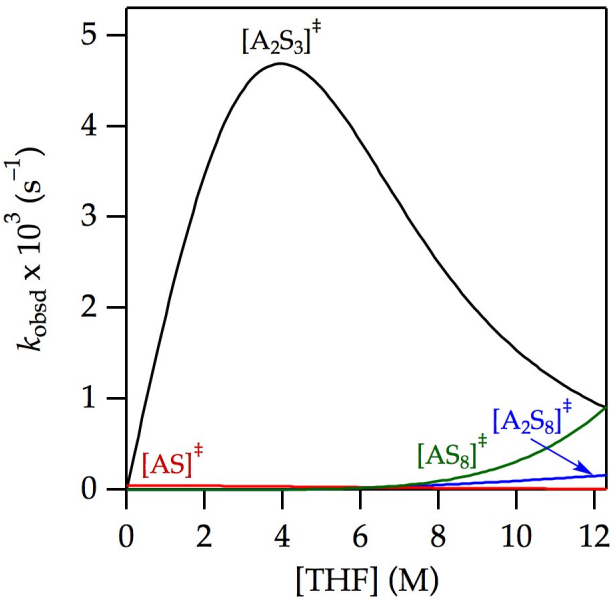

Figure 5.9. Contributions of **$[A_2S_3]^‡$**, $[AS_8]^‡$, $[AS]^‡$, and $[A_2S_8]^‡$ to the enolization of **9** in THF–hexane at –78 °C depicted using the parameters from curve A in Figure 5.1.

Role of Monomer–Dimer Aggregation. An important phenomenon was detected via the rate studies: the $[A_2S_3]^‡$ and $[A_2S_8]^‡$ dimer-based pathways are significant even in neat THF wherein the dimeric LiHMDS is almost nonexistent (3%; eq 5.1).[3] The widely held notion that organolithium aggregates *necessarily* react via deaggregation to highly reactive monomers has given way to a more nuanced view in which aggregates react directly. The enolization described herein, however, is unusual in that *observable monomers aggregate to form more highly reactive dimers.* The precedent for aggregation preceding a transformation is spartan and somewhat idiosyncratic but does exist. The exchange of t**etramethylethylenediamine** from t**etramethylethylenediamine**-solvated LiHMDS monomer was shown to occur via a fleeting disolvated dimer.[39] Similarly, the deaggregation of LDA dimers to monomers was shown to occur, in part, via association to form tetramers.[43] Requisite aggregations *preceding* metalations (eq 5.15) are probably exceptional,[44] but they remind us not to be too dogmatic.

$$n\text{RLi} \underset{\text{substrate}}{\rightleftharpoons} [(\text{RLi})_n] \longrightarrow \text{product} \qquad (5.15)$$

Cosolvent Dependence. The influence of toluene on the individual enolization pathways can be gleaned by using the fitting parameters for the enolization of **9** in toluene (see Figure 5.1, curve B) to generate Figure 5.10. The attenuation of the maximum by toluene relative to hexane derives from the selective attenuation of the $[A_2S_3]^‡$ term (cf. Figures 5.9 and 5.10). The origins of the inhibition are discussed below.

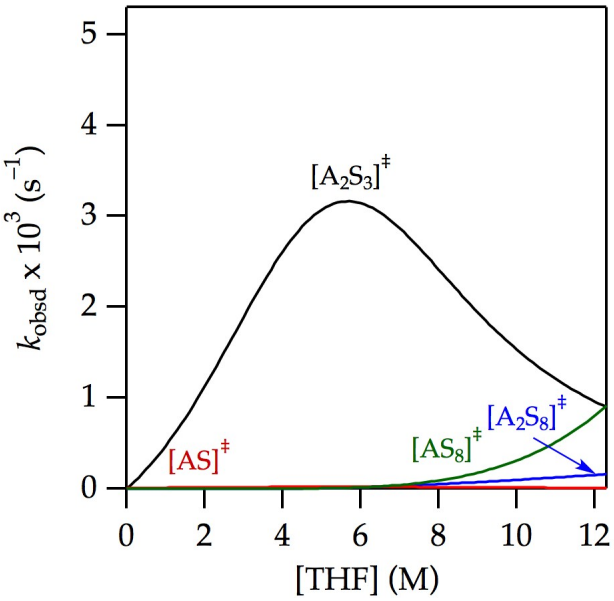

Figure 5.10. Contributions of $\mathbf{[A_2S_3]^‡}$, $[AS_8]^‡$, $[AS]^‡$, and $[A_2S_8]^‡$ to the enolization of **9** in THF–toluene at –78 °C determined using the parameters from curve B in Figure 5.1.

Isotope Effects. THF-concentration-dependent isotope effects (see Figure 5.5) display a maximum that correlates with the maximal rates of dimer-based enolization dominated by transition structure **9** (cf. Figures 5.5 and 5.9.) Using the approach described in the previous

section we found that the fitting parameters for the enolization of **9**-d_2 in hexane from Figure 5.1 (curve A) afford the contributions of $[AS]^{‡}$, $[A_2S_3]^{‡}$, $[AS_8]^{‡}$, and $[A_2S_8]^{‡}$ versus THF concentration (Figure 5.11). The $[A_2S_3]^{‡}$-based metalation is suppressed relative to that of $[AS]^{‡}$ and $[A_2S_8]^{‡}$. In neat THF, the reaction coordinate is dominated by the $[AS_8]^{‡}$ and $[A_2S_8]^{‡}$ pathways. Deuteration *and* the use of toluene accentuate this trend.

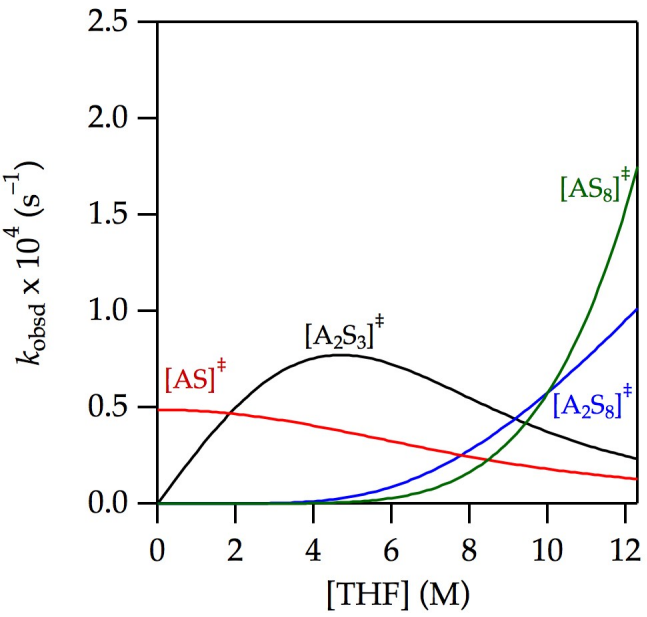

Figure 5.11. Contributions of **$[A_2S_3]^{‡}$**, $[AS_8]^{‡}$, $[AS]^{‡}$, and $[A_2S_8]^{‡}$ to the enolization of **9**-d_2 in THF–hexane at –78 °C determined using the parameters from curve A in Figure 5.2.

Cosolvent Effects: Ground State or Transition State? Inhibition by toluene may be much ado about nothing. It is small when measured in kilocalories per mole, but it piques our interest. We probed the influence of cyclopentane, an aliphatic hydrocarbon analogous to hexane with solubilizing properties more akin to toluene,[45a,46] and found that cyclopentane is a hexane surrogate rather than a toluene surrogate (supporting information). Such aliphatic versus aromatic cosolvent effects are common but not easily explained.[45]

The changes in rate that arise from swapping toluene for hexane *appear* to be mechanism-dependent. We must be careful in our interpretation, however, because no cosolvent effect can occur on either $[AS_8]^‡$ or $[A_2S_8]^‡$ for the pedestrian reason that little or no cosolvent is present when these pathways become prominent. Also, a cosolvent effect on $[AS]^‡$ could be obscured by difficulties in detecting this small term. Thus, the cosolvent can significantly influence rates only within a limited range. Nonetheless, toluene clearly suppresses $[A_2S_3]^‡$-based enolizations and the question remains: why?

It is probably a truism—real truisms are rare—that rate suppression occurs through stabilization of the ground state or destabilization of the transition state. Beyond that, all we have are thoughts and opinions. It is easy to imagine that swapping hexane for toluene could influence the ground and transition states differently. To the extent that a direct relationship exists between the *stability* of a solute and solute *solubility*, toluene should stabilize all reactants, including LiHMDS dimer and monomer, oxazolidinone **9**, and even THF (eq 5.16). For example, to the extent that toluene stabilizes, dissolves if you will, THF better than hexane does, the highly solvated forms should be disproportionately retarded. We argued for such a cosolvent-based stabilization of hexamethylphosphoramide as the source of rate suppression in a previous study.[45b]

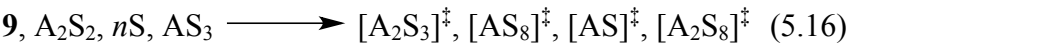

(5.16)

In the present study, many of the models we explore that assign explicit stoichiometric roles to toluene involve the stabilization of both A_2S_2 and AS_3 with the potential consequence of perturbing the monomer–dimer ratio. We examine the equilibrium in eq 5.1[3,4] and find that the

stabilization of LiHMDS dimers and monomers is the same regardless of whether hexane or toluene is used as the cosolvent (supporting information). *Thus, only a generalized ground-state stabilization offers a credible explanation of suppression.* We believe, however, that there is more to the story.

Examining transition state(s), first through a classical lens, we ask: Are transition states differentially stabilized—that is, do they have different solubilities—in toluene than in hexane? The answer is almost certainly yes, which could explain mechanism-dependent cosolvent effects. However, explaining a toluene-induced rate *suppression* requires that the transition state(s) be *more stabilized by hexane than by toluene*. That result would be extremely odd. We considered models based on variable (selective) transition state sensitivities to toluene versus hexane. These models were satisfactory but too contrived, relegating them to archival status in supporting information. However, this finding segues to the next topic: tunneling.

Role of Tunneling. We[26a–d] and others[26e,f] have observed large primary isotope effects (k_H/k_D = 30–60) for lithiations using a variety of bases and substrates. They are definitely odd but not that unusual. Why are the isotope effects large and highly mechanism-dependent? We are loath to jump into discussions of tunneling[47] out of ignorance and the sense that it may be overused to explain classical isotope effects that are simply large. That said, Carpenter and co-workers[48] suggest that tunneling is pervasive. Yet again,[43] we are forced to discuss tunneling.

If we may digress briefly, standard primary isotope effects are attributed to the relative stabilization of the deuterated substrate owing to the zero-point energy of the C–D stretch that disappears as the stretch becomes the reaction coordinate. k_H/k_D is often said to approximate 7 at ambient temperature, which translates to ~20 at –78 °C.[39a] By this account, a primary kinetic isotope effect is an inherent property of the substrate and would be mechanism-*independent*.

Deviations are often ascribed to the coupling of the reaction coordinate with secondary vibrations. However, effects that perturb k_H/k_D to levels above 30–60[26] are certainly larger than normal.

If, however, one invokes quantum mechanical tunneling, the zero-point energy in the ground state and the isotopic sensitivity to tunneling disfavoring deuterium transfer at the transition state[47] work in concert to cause large isotope effects (Figure 5.12). Moreover, a putative hypersensitivity of tunneling to barrier width—magnitude of atomic movement involved in crossing the barrier—would naturally be highly mechanism-dependent.

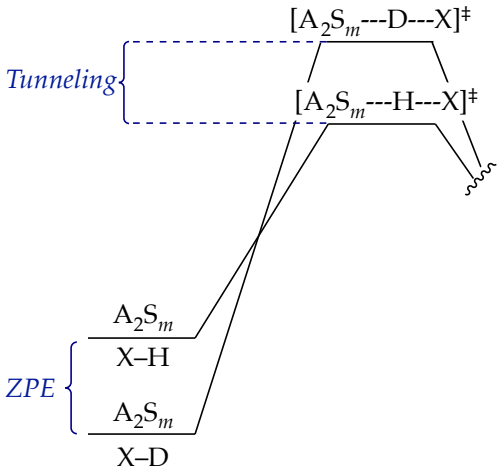

Figure 5.12. Free-energy diagram illustrating the contributions of zero-point energy (ZPE) and tunneling to an observed isotope effect.

Through tunneling, the hydrocarbon cosolvent effects and large isotope effects may dovetail. Solvent effects on tunneling have been discussed.[49] Even secondary-shell effects could influence barrier widths. With that notion in mind, we performed a whimsical experiment to measure the solvent isotope effect[50] with toluene and toluene-d_8 and found that k_H/k_D was 1.15 ± 0.04. We cannot say whether this value is substantial (it seems large to us) or is even true given

the potential for error (although it replicates). We also cannot say why toluene-d_8 would widen a barrier for proton transfer; we are simply making a content-free supposition of differential vibrational coupling to the reaction coordinate. Our enthusiasm for such a supposition is muted by additional experiments.

2-Methylcyclohexanone: Revisited. At the outset, we used the enolization of 2-methylcyclohexanone in eq 5.2 to illustrate "a seemingly straightforward" enolization. We now confess to a deception, albeit with foreshadowing. In our 2004 study, enolizations in THF–*toluene* showed a THF concentration dependence approximating first order with a gentle downward curvature. In the context of a shifting ground state, the curvature could have been dismissed. To our retrospective surprise, however, we had noted the following:

> "However, neither the first-order [THF] dependence nor the substantially incomplete saturation behavior are fully consistent with formation of predominantly trisolvated monomers. . . . We believe the relatively simple THF dependence belies a greater underlying complexity."

Apparently, the absence of a maximum troubled us. We have now replicated the THF–toluene data (Figure 5.13, curve B) and added the analogous THF–*hexane* data (curve A). *There is the missing maximum!* Are the enolizations of **3** and oxazolidinone **9** totally analogous? In a word, no. Spot-checking the LiHMDS orders shows *exclusively* monomer-based enolization across the range of THF concentrations (supporting information). The functions in Figure 5.13 are fit to a mechanism involving $[AS_2]^‡$ and the toluene suppression function described above. Of course, the mechanism could be more complex, and the fit has structural flaws that we are

currently unwilling to pursue.[51] Nonetheless, the hydrocarbon effect is observed *in the absence of detectable dimer mechanisms*. Could there still be a correlation of hydrocarbon effects with isotopically sensitive tunneling? The reported isotope effect in THF–toluene at –78 °C was small (k_H/k_D = 11), but we could not reconstruct the precise conditions under which it was measured. Accordingly, we re-evaluated the isotope effect by comparing **3** and 2,6,6-**3**-d_3 over a range of THF–hexane concentrations and observed a k_H/k_D value of 9–12. Thus, the evidence suggests that the toluene effect is most likely a ground-state stabilization uncorrelated with large isotope effects.

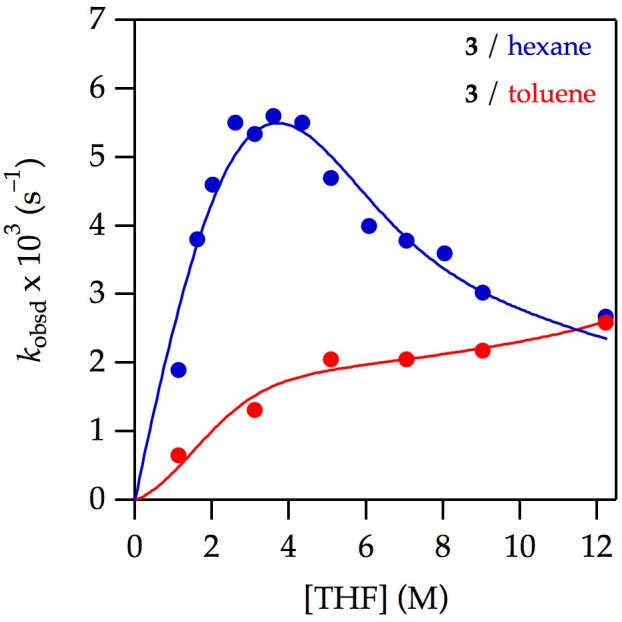

Figure 5.13. Plot of k_{obsd} vs THF concentration for the enolization of 0.0050 M 2-methylcyclohexanone **3** with 0.10 M LiHMDS with THF in hexane (blue) and toluene (red) at –78 °C.

Conclusions

The study described herein, which shows that enolizations of an oxazolidinone by LiHMDS proceed via multiple mechanisms with widely varying solvent, cosolvent, and isotopic sensitivities, has a number of disparate implications. The reaggregation of LiHMDS dimer to form highly reactive dimers has little precedent but is of interest to those debating the influence of aggregation on reactivity. From the vantage point of a structural and mechanistic organolithium chemist, the mechanistic complexity is on the high end but not unprecedented. Rate studies of LDA-mediated metalations have shown that medium effects are usually unimportant; changing THF–hexane proportions over a broad range reveals little or no contributions from the change in polarity.[19] The differences observed with aromatic and aliphatic cosolvents are therefore surprising. However, we and others have noted these differences,[44] which are not well-understood.[52] The large kinetic isotope effects that implicate tunneling are not that rare in strong-base-mediated lithiations,[26] but these lack scrutiny as well.

Our results also underscore some general principles of complex mechanistic studies. The mechanism-dependent isotope effects, in conjunction with hydrocarbon cosolvent effects, proved critical to deconvoluting the complex reaction coordinate. Espenson[53] reminds us that only through complex dependencies can one glean complex mechanisms.

The roles played by synergies cannot be overstated. Traditional kinetic methods based on initial rates and flooding techniques and numerical methods are tremendously powerful when used in concert. The numerical methods cannot be applied robotically, however. They require a combination of patience, judgment, and a moral compass: the desire to get it right, not just get a fit. We sense this final element is often overlooked. Lastly, kinetics methods guide and constrain

the computations while the computations provide details that are experimentally elusive and often unexpected. The combination is greater than the sum of its parts.

From a more synthetic organic perspective, this study was inspired by a plant-scale oxazolidinone enolization–alkylation sequence used by Pfizer that proved challenging during scale-up.[12] Ongoing studies should help us understand whether the mechanistic complexity of enolization contributes to the idiosyncrasies that include LiHMDS batch and source dependencies. The sensitivity of the oxazolidinone enolization to hydrocarbons also reminds us that the choice of cosolvent matters even in reactions involving much more polar solvents. In a pharmaceutical setting in which percent yield, trace impurities, and processing subtleties are overriding economic parameters, the choice of hydrocarbon cosolvent—often toluene versus heptane—may be acutely important.

Experimental

Reagents and Solvents. THF, toluene, and hexane were distilled from blue or purple solutions containing sodium benzophenone ketyl. LiHMDS was prepared as a ligand- and LiCl-free recrystallized solid.[15] Air- and moisture-sensitive materials were manipulated under argon using standard glovebox, vacuum line, and syringe techniques. Oxazolidinone **9** is commercially available, and **9**-d_2 was prepared from 2,2-dideuterio-propionyl chloride following a literature protocol.[54]

(*S*)-(+)-4-benzyl-3-propionyl-2-oxazolidinone-2,2-d_2 (9-d_2). Propionic acid-2,2-d_2 (4.90 mL, 65.7 mmol, 98% D) was added to a flame-dried 100 mL two-neck round-bottom flask and dissolved with 50 mL of dry THF. The solution was stirred and cooled to 0 °C under an argon atmosphere, and sodium hydride (1.89 g, 78.8 mmol, 1.2 equiv) was added slowly by placing a

powder funnel in an open neck and carefully pouring the powder into the reaction via the funnel. *Caution!* Reduce the positive flow of inert gas out of the flask and add the solid slowly in small portions. The funnel was replaced with a stopper, and the reaction mixture was allowed to stir for an additional 15 min. The THF was removed in vacuo, yielding sodium propionate-2,2-d_2 as a white solid. The salt was dried in vacuo (87%) and used immediately in the next step.

A flame-dried 50 mL one-neck round-bottom flask charged with 5.63 g (57.4 mmol) of sodium propionate-2,2-d_2 and 16.5 mL (114.8 mmol, 2 equiv) of phthaloyl chloride was connected through a short-path glass apparatus to a two-neck receiving flask cooled in a dry ice-acetone bath prepared with fresh acetone. The reaction mixture was maintained at 150 °C with vigorous magnetic stirring, and propionyl chloride-2,2-d_2 was allowed to distill into the receiving flask as it formed (74%). The product was used immediately in the next step.

A flame-dried 250 mL one-neck round-bottom flask was charged with (*S*)-(–)-4-benzyl-2-oxazolidinone (5.96 g, 33.6 mmol) and 40 mL of dry THF under an argon atmosphere. The mixture was stirred and cooled to –78 °C using a dry ice-acetone bath prepared with fresh acetone. *n*-Butyllithium (1.6 M solution in hexanes, 25.2 mL, 40.3 mmol, 1.2 equiv) was added dropwise, and the reaction mixture was stirred for 15 min to yield a bright orange solution. Propionyl chloride-2,2-d_2 (3.0 mL, 33.6 mmol) was dissolved in 10 mL of dry THF and added dropwise to the reaction mixture. After 10 min, the cooling bath was removed and the reaction was allowed to warm to 0 °C over 30 min, stirred for an additional 30 min at 0 °C, and quenched with saturated aqueous NH_4Cl. The THF was removed in vacuo, and the mixture was extracted with CH_2Cl_2.

The combined organic layer was dried over Na_2SO_4 and concentrated in vacuo. Flash chromatography yielded 5.58 g (71 %) of **9**-d_2: R*f* = 0.41 in 25% ethyl acetate/hexanes; ^{1}H NMR

(500 MHz, $CDCl_3$) δ 1.19 (s, 3H), 2.75–2.79 (dd, J = 6, 12 Hz, 1H), 3.29–3.32 (dd, J = 6, 12 Hz, 1H), 4.15–4.22 (m, 2H), 4.65–4.69 (m, 1H), 7.20–7.35 (m, 5H); ^{13}C NMR (125.79 MHz, $CDCl_3$) δ 8.2, 37.9, 55.1, 66.2, 127.3, 128.9, 129.4, 135.3, 153.5, 174.1. The ^{13}C NMR spectrum matched that of unlabeled acylated oxazolidinone **9** except for the absence of the peak at δ 29.2 corresponding to the deuterium-substituted C-2. Integration of the ^{1}H NMR spectrum indicated d_2 = 100%. High-resolution mass spectrometry (DART ionization, orbitrap mass analyzer), calcd for $C_{13}H_{13}D_2NO_3$ $[M + H]^+$ = 236.12558, found 236.12666. Deuterium content was evaluated from the relative intensities of m/z = 234 (H + $C_{13}H_{15}NO_3$), m/z = 235 (H + $C_{13}H_{14}DNO_3$), and m/z = 236 (H + $C_{13}H_{13}D_2NO_3$) for **9**, **9**-d_1, and **9**-d_2, respectively, and corrected for the natural abundance of ^{13}C, as measured in the protio standard (**9**). High-resolution mass spectrometry analysis indicated d_2 = 95%.

IR Spectroscopic Analyses. IR spectra were recorded with an in situ IR spectrometer fitted with a 30-bounce, silicon-tipped probe. The spectra were acquired in 16 scans at a gain of 1 and a resolution of 4 cm^{-1}. A representative reaction was carried out as follows: The IR probe was inserted through a nylon adapter and O-ring seal into an oven-dried, cylindrical flask fitted with a magnetic stir bar and a T-joint. The T-joint was capped with a septum for injections and a nitrogen line. After evacuation under full vacuum, heating, and flushing with nitrogen, the flask was charged with LiHMDS (84 mg, 0.50 mmol) in THF–hexane (or toluene, 4.9 mL total volume) and cooled in a dry ice–acetone bath prepared with fresh acetone. After a background spectrum was recorded, oxazolidinone **9** or **9**-d_2 (0.025 mmol in 0.10 mL THF or toluene) was added with stirring. For rapid reactions, IR spectra were recorded every 6 s with monitoring of the absorbance at 1783–1793 cm^{-1} during the course of the reaction.

NMR Spectroscopic Analyses. All NMR samples for reaction monitoring and structure elucidation were prepared using stock solutions and sealed under partial vacuum. Standard ^{1}H, ^{6}Li, and ^{13}C NMR spectra were recorded at 500, 73.57, and 125.79 MHz, respectively.

Chapter 5 References and Footnotes

1. For an incisive review of lithium amides in organic synthesis, see: (a) Eames, J. Product Subclass 6: Lithium Amides. In *Science of Synthesis*; Snieckus, V., Ed.; Thieme; New York, 2006; Vol. 8a, p 173. (b) "Lithium Hexamethyldisilazide". Gray, M.; Snieckus, V.; Lebel, H. In *Handbook of Reagents for Organic Synthesis: Reagents for Silicon-Mediated Organic Synthesis*, Edited by Fuchs, P. L., Wiley: New York, 2011; p 356.

2. (a) Fraser, R. R.; Mansour, T. S. *J. Org. Chem.* **1985**, *50*, 3232. (b) Streitwieser, A.; Facchetti, A.; Xie, L.; Zhang, X.; Wu, E. C. *J. Org. Chem.* **2012**, *77*, 985.

3. Lucht, B. L.; Collum, D. B. *Acc. Chem. Res.* **1999**, *32*, 1035.

4. Lucht, B. L.; Collum, D. B. *J. Am. Chem. Soc.* **1995**, *117*, 9863.

5. (a) Zhao, P.; Condo, A.; Keresztes, I.; Collum, D. B. *J. Am. Chem. Soc*. **2004**, *126*, 3113. (b) Godenschwager, P. F.; Collum, D. B. *J. Am. Chem. Soc.* **2007**, *129*, 12023.

6. For recent or particularly germane examples of crystal structures of solvated LiHMDS, see: (a) Usher, M.; Protchenko, A. V.; Rit, A.; Campos, J.; Kolychev, E. L.; Tirfoin, R.; Aldridge, S. *Chem. Eur. J.* **2016**, *22*, 11685. (b) Nako, A. E.; White, A. J. P.; Crimmin, M. R. *Chem. Sci.* **2013**, *4*, 691. (c) Li, Q.; Zhou, S.; Wang, S.; Zhu, X.; Zhang, L.; Feng, Z.; Guo, L.; Wang, F.; Wei, Y. *Dalton Trans.* **2013**, *42*, 2861. (d) Williard, P. G.; Liu, Q.-Y. *J. Org. Chem.* **1994**, *59*,

1596. (e) Power, P. P.; Xu, X. *J. Chem. Soc., Chem. Commun.* **1984**, 358. (f) Power, P. P. *Acc. Chem. Res.* **1988**, *21*, 147. (g) Henderson, K. W.; Dorigo, A. E.; Liu, Q.-L.; Williard, P. G. *J. Am. Chem. Soc.* **1997**, *119*, 11855. (h) Engelhardt, L. M.; Jolly, B. S.; Junk, P. C.; Raston, C. L.; Skelton, B. W.; White, A. H. *Aust. J. Chem.* **1986**, *39*, 1337. (i) Lappert, M. F.; Slade, M. J.; Singh, A.; Atwood, J. L.; Rogers, R. D.; Shakir, R. *J. Am. Chem. Soc.* **1983**, *105*, 302. (J) Mulvey, R. E.; Robertson, S. D. *Angew. Chem., Int. Ed.* **2013**, *52*, 11470.

7. (a) Honda, K.; Harris, T. V.; Hatanaka, M.; Morokuma, K.; Mikami, K. *Chem. Eur. J.* **2016**, *22*, 8796. (b) Popenova, S.; Mawhinney, R. C.; Schreckenbach, G. *Inorg. Chem.* **2007**, *46*, 3856. (c) Pratt, L. M. *Bull. Chem. Soc. Jpn.* **2005**, *78*, 890. (d) Pratt, L. M.; Streitwieser, A. *J. Org. Chem.* **2003**, *68*, 3830. (e) Romesberg, F. E.; Bernstein, M. P.; Gilchrist, J. H.; Harrison, A. T.; Fuller, D. J.; Collum, D. B. *J. Am. Chem. Soc.* **1993**, *115*, 3475. (f) Sapse, A.-M.; Kaufmann, E.; Schleyer, P. v. R.; Gleiter, R. *Inorg. Chem.* **1984**, *23*, 1569.

8. For the seminal spectroscopic investigations of LiHMDS see: Kimura, B. Y.; Brown, T. L. *J. Organomet. Chem.* **1971**, *26*, 57.

9. For additional physicochemical studies of LiHMDS, see: (a) Wannagat, U. *Adv. Inorg. Chem. Radiochem.* **1964**, *6*, 237. (b) Rogers, R. D.; Atwood, J. L.; Grüning, R. *J. Organomet. Chem.* **1978**, *157*, 229. (c) Mootz, D.; Zinnius, A.; Böttcher, B. A*ngew. Chem., Int. Ed. Engl.* **1969**, *8*, 378. (d) Renaud, P.; Fox, M. A. *J. Am. Chem. Soc.* **1988**, *110*, 5702. (e) Fjeldberg, T.; Lappert, M. F.; Thorne, A. J. *J. Mol. Struct.* **1984**, *125*, 265. (f) Fjeldberg, T.; Hitchcock, P. B.; Lappert, M. F.; Thorne, A. J. *J. Chem. Soc., Chem. Commun.* **1984**, 822. (g) Engelhardt, L. M.; May, A.

S.; Raston, C. L.; White, A. H. *J. Chem. Soc., Dalton Trans.* **1983**, 1671. (h) Williard, P. G.; Liu, Q.-Y.; Lochmann, L. *J. Am. Chem. Soc.* **1992**, *114*, 348. (i) Lochmann, L.; Trekoval, J. *J. Organomet. Chem.* **1975**, *99*, 329. (j) Boche, G.; Langlotz, I.; Marsch, M.; Harms, K.; Frenking, G. *Angew. Chem., Int. Ed., Engl.* **1993**, *32*, 1171. (k) Arnett, E. M.; Moe, K. D. *J. Am. Chem. Soc.* **1991**, *113*, 7068. (l) Arnett, E. M.; Moe, K. D. *J. Am. Chem. Soc.* **1991**, *113*, 7288. (m) Anglehardt, L. M.; Jolly, B. S.; Punk, P.; Raston, C. L. Skelton, B. W.; White, A. H. *Aust. J. Chem.* **1986**, *39*, 133. (n) Arnett, E. M.; Fisher, F. J.; Nichols, M. A.; Ribeiro, A. A. *J. Am. Chem. Soc.* **1990**, *112*, 801. (o) Grimm, D. T.; Bartmess, J. E. *J. Am. Chem. Soc.* **1992**, *114*, 1227. (p) Henderson, K. W.; Dorigo, A. E.; Liu, Q-Y.; Williard, P. G.; Schleyer, P. v. R.; Bernstein, P. R. *J. Am. Chem. Soc.* **1996**, *118*, 1339.

10. For rate studies of the alkylation of LiHMDS/lithium enolate mixed aggregates in THF, see: Kim, Y.-J.; Streitwieser, A. *Org. Lett.* **2002**, *4*, 573.

11. Tallmadge, E. H.; Jermaks, J.; Collum, D. B. *J. Am. Chem. Soc.* **2016**, *138*, 345.

12. Singer, R. A.; Ragan, J. A.; Bowles, P.; Chisowa, E.; Conway, B. G.; Cordi, E. M.; Leeman, K. R.; Letendre, L. J.; Sieser, J. E.; Sluggett, G. W.; Stanchina, C. L.; Strohmeyer, H.; Blunt, J.; Taylor, S.; Byrne, C.; Lynch, D.; Mullane, S.; O'Sullivan, M. M.; Whelan, M. *Org. Process Res. Dev.* **2014**, *18*, 26.

13. For reviews of organolithium chemistry in pharmaceutical process research, see: (a) Farina, V.; Reeves, J. T.; Senanayake, C. H. Song, J. J. *Chem. Rev.* **2006**, *106*, 2734. (b) Wu, G.; Huang,

M. *Chem. Rev.* **2006**, *106*, 2596. (c) Rathman, T. L.; Bailey, W. F. *Org. Process Res. Dev.* **2009**, *13*, 144.

14. For selected examples in which LiHMDS is used on large scale, see: (a) Duan, S.; Place, D.; Perfect, H. H.; Ide, N. D.; Maloney, M.; Sutherland, K.; Price-Wiglesworth, K. E.; Wang, K.; Olivier, M.; Kong, F.; Leeman, K.; Blunt, J.; Draper, J.; McAuliffe, M.; O'Sullivan, M.; Lynch, D. *Org. Process Res. Dev.* **2016**, *20*, 1191. (b) Knight, J.; Guizzetti, S.; Zhao, W.; Schwindeman, J. A.; Zhao, D. *Org. Process Res. Dev.* **2015**, *19*, 1392. (c) Pan, X.; Xu, S.; Huang, R.; Yu, W.; Liu, F. *Org. Process Res. Dev.* **2015**, *19*, 611. (d) Peng, Z.; Ragan, J. A.; Colon-Cruz, R.; Conway, B. G.; Cordi, E. M.; Leeman, K.; Letendre, L. J.; Ping, L.-J.; Sieser, J. E.; Singer, R. A.; Sluggett, G. W.; Strohmeyer, H.; Vanderplas, B. C.; Blunt, J.; Mawby, N.; Meldrum, K.; Taylor, S. *Org. Process Res. Dev.* **2014**, *18*, 36. (e) Rathman, T.; Schwindeman, J. A. *Org. Process Res. Dev.* **2014**, *18*, 1192.

15. For a dissolving metal-based preparation of LiCl-free LiHMDS, see: Tomasevich, L. L.; Collum, D. B. *J. Am. Chem. Soc.* **2014**, *136*, 9710.

16. (a) Rein, A. J.; Donahue, S. M.; Pavlosky, M. A. *Curr. Opin. Drug Discovery Dev.* **2000**, *3*, 734. (b) Eisenbeis, S. A.; Chen, R.; Kang, M.; Barrila, M.; Buzon, R. *Org. Process Res. Dev.* **2015**, *19*, 244, and references cited therein.

17. The absorbance of **9** is solvent dependent in the absence of lithium salts: (a) 1783 cm^{-1} in neat THF ; (b) 1787 cm^{-1} in THF–toluene mixtures; (c) 1793 cm^{-1} in THF–hexane or THF–

cyclopentane mixtures. For detailed analysis of solvent-dependent IR absorbances, see: Reimers, J. R.; Hall, L. E. *J. Am. Chem. Soc.* **1999**, *121*, 3730.

18. Rate measurements at < 0.5 M THF–hexane were complicated by overlapping absorbances of partial substrate-LiHMDS complexation and by poor solubilities. Moreover, solutions containing LiHMDS (0.10 M), and **9**-d_2 (0.005 M) in neat toluene at –78 ^{o}C show absorbances corresponding to a LiHMDS-bound oxazolidinone (1767 and 1680 cm^{-1}) to the exclusion of free oxazolidinone. Serial addition of THF shows full decomplexation at [THF] ≥ 0.15 M (1.5 equiv/LiHMDS).

19. (a) For a treatise on rate studies of lithium amides, see: Collum, D. B.; McNeil, A. J.; Ramírez, A. *Angew. Chem., Int. Ed.* **2007**, *46*, 3002. (b) For detailed review and leading references to the structures and reactivities in organolithium chemistry, see: Reich, H. J. *Chem. Rev.* **2013**, *113*, 7130.

20. Enolization at < 1.0 M THF–cyclopentane showed minor deviations from first-order decays that could be construed as evidence of basal-level autocatalysis. No evidence of mixed aggregation was observed.

21. Casado, J.; Lopez-Quintela, M. A.; Lorenzo-Barral, F. M. *J. Chem. Educ.* **1986**, *63*, 450.

22. LiHMDS concentration refers to the concentration of the monomer subunit (normality)

23. Previous studies[3a] suggest that AS_4 also coexists with AS_3 in neat THF at –78 °C. Although it quantitatively adds perturbations in the modelling, it in no way undermines comparisons of any of the models.

24. The rate law provides the stoichiometry of the transition structure relative to that of the reactants: Edwards, J. O.; Greene, E. F.; Ross, J. *J. Chem. Educ.* **1968**, *45*, 381.

25. THF concentrations are corrected to be just the free (uncoordinated) THF concentration. At high concentrations wherein the correction would become slightly more complex, it also becomes miniscule.

26. (a) Ma, Y.; Breslin, S.; Keresztes, I.; Lobkovsky, E.; Collum, D. B. *J. Org. Chem.* **2008**, *73*, 9610. (b) Hoepker, A. C.; Gupta, L.; Ma, Y.; Faggin, M. F.; Collum, D. B. *J. Am. Chem. Soc.* **2011**, *133*, 7135. (c) Singh, K. J.; Collum, D. B. *J. Am. Chem. Soc.* **2006**, *128*, 13753. (d) Rennels, R. A.; Rutherford, J. L.; Collum, D. B. *J. Am. Chem. Soc.* **2000**, *122*, 8640. (e) Anderson, D. R.; Faibish, N. C.; Beak, P. *J. Am. Chem. Soc.* **1999**, *121*, 7553. (f) Meyers, A. I.; Mihelich, E. D. *J. Org. Chem.* **1975**, *40*, 3158.

27. Isotope effects for LiHMDS-mediated ketone enolizations: (a) Held, G.; Xie, L. F. *Microchem. J.* **1997**, *55*, 261. (b) Xie, L. F.; Saunders, W. H. *J. Am. Chem. Soc.* **1991**, *113*, 3123.

28. Rate measurements above 0.25 M of LiHMDS in 1.0 M THF–hexane at –78 ^{o}C were precluded by poor solubilities, unlike 1.0 M THF–toluene where rates were determined up to 0.40 M LiHMDS.

29. (a) Occam's razor constrains you to employing the simplest mechanism to explain the observables. The often-stated variant that claiming "the simplest model is most likely correct" is an incorrect statement of Occam's intent and, in our opinions, foolish in almost all settings. (b) "Plurality should not be assumed without necessity". Adams, M. M., *William Ockham*; Univ. of Notre Dame Press: Notre Dame, **1987**, p 156. (c) See also: Hoffman, R.; Minkin, V. I.; Carpenter, B. K. *HYLE*: *Int. J. Philos. Chem.* **1997**, *3*, 3.

30. (a) $^{+}$Li(THF)$_6$: Schenk, C.; Schnepf, A. *Angew. Chem., Int. Ed. Engl.* **2007**, *46*, 5314. (b) $^{+}$Li(THF)$_6$: Schenk, C.; Henke, F.; Santiso-Quinones, G.; Krossing, I.; Schnepf, A. *Dalton Trans.* **2008**, 4436.

31. (a) Ohtaki, H.; Radnai, T. *Chem. Rev.* **1993**, *93*, 1157. (b) Chang, S.; Severson, M. W.; Schmidt, P. P. *J. Phys. Chem.*, **1985**, *89*, 2892. (c) Worsfold, D. J.; Bywater, S. *Can. J. Chem.* **1964**, *42*, 2884. (d) Roovers, J. E. L.; Bywater, S. *Macromolecules* **1968**, *1*, 328. (e) Bywater, S.; Worsfeld, D. J. *J. Organometal. Chem.* **1967**, *10*, 1. (f) Also, see reference 45.

32. Depue, J. S.; Collum, D. B. *J. Am. Chem. Soc.* **1988**, *110*, 5524.

33. Frisch, M. J. *et al. GaussianVersion 3.09*; revision A.1; Gaussian, Inc.: Wallingford, CT, 2009.

34. From Wikipedia, an isodesmic reaction is a chemical reaction in which the type of chemical bonds broken in the reactant are the same as the type of bonds formed in the reaction product.

35. Cohen, A. J.; Mori-Sánchez, P.; Yang, W. *Science* **2008**, *321*, 792.

36. The computations use the Gaussian standard state of 1.0 atm. If the THF concentration is corrected to neat THF (approximately 13 M), each solvation step benefits from approximately 2.0 kcal/mol of additional stabilization at- 78 °C (195 K). Pratt, L. M.; Merry, S.; Nguyen, S. C.; Quan, P.; Thanh, B. T. *Tetrahedron* **2006**, *62*, 10821.

37. Even if monomers were the most reactive form, driving an equilibrium to the preferred aggregation state but at the wrong solvation state will inhibit a reaction.

38. For some recent reports of triple ions, see: (a) Kolonko, K. J.; Biddle, M. M.; Guzei, I. A.; Reich, H. J. *J. Am Chem. Soc.* **2009**, *131*, 11525. (b) Jones, A. C.; Sanders, A. W.; Sikorski, W. H.; Jansen, K. L.; Reich, H. J. *J. Am. Chem. Soc.* **2008**, *130*, 6060. (c) Dewan, R.; Datta, B.; Roy, M. C.; Roy, M. N. *Fluid Phase Equil*. **2013**, *358*, 233.

39. Lucht, B. L.; Bernstein, M. P.; Remenar, J. F.; Collum, D. B. *J. Am. Chem. Soc.* **1996**, *118*, 10707.

40. Physicochemical studies of $LiClO_4$ in THF, substituted THF's, and THF/benzene mixtures: (a) Badiali, J.-P.; Cachet, H.; Cyrot, A.; Lestrade, J.-C. *J. Chem. Soc., Farad. Trans.* **1973**, *69*, 1339. (b) Cachet, H.; Cyrot, A.; Fekir, M.; Lestrade, J.-C. *J. Phys. Chem.* **1979**, *83*, 2419. (c) Ashby, E. C.; Dobbs, F. R.; Hopkins, H. P., Jr. *J. Am. Chem. Soc.* **1973**, *95*, 2823. (d) Matsuda, Y.; Morita, M.; Tachihara, F. *Bull. Chem. Soc. Japan* **1986**, *59*, 1967. (e) Delsignore, M.; Maaser, H. E.; Petrucci, S. *J. Phys. Chem.* **1984**, *88*, 2405. (f) Tobishima, S.; Yamaji, A. *Electrochim. Acta* **1983**, *28*, 1067. (g) Bhattacharyya, D. N.; Lee, C. L.; Smid, J.; Szwarc, M. *J. Phys. Chem.* **1965**, *69*, 608. (h) Wong, M. K.; Popov, A. I. *J. Inorg. Nucl. Chem.* **1972**, *34*, 3615.

41. (a) Peddie, V.; Pietsch, M.; Bromfield, K. M.; Pike, R. N.; Duggan, P. J.; Abell, A. D. *Synthesis* **2010**, *11*, 1845. (b) Falck, J. R.; Gao, S.; Prasad, R. N.; Koduru, S. R. *Bioorg. Med. Chem. Lett.* **2008**, 18, 1768. (c) Schmidt, B.; Wildermann, H. *J. Chem. Soc. Perkin Trans.* **2002**, *1*, 1050. (d) Murata, Y.; Kamino, T.; Hosokawa, S.; Kobayashi, S. *Tetrahedron Lett.* **2002**, *43*, 8121. (e) Jacobson, I. C.; Reddy, G. P. *Tetrahedron Lett.* **1996**, *37*, 8263. (f) Less, S. L.; Handa, S.; Millburn, K.; Leadlay, P. F.; Dutton, C. J.; Staunton, J. *Tetrahedron Lett.* **1996**, *37*, 3515.

42. Haesler, J.; Schindelholz, I.; Riguet, E.; Bochet, C. G.; Hug, W. *Nature* **2007**, *446*, 526.

43. Liang, J.; Hoepker, A. C.; Algera, R. F.; Ma, Y.; Collum, D. B. *J. Am. Chem. Soc.* **2015**, *137*, 6292.

44. Reich suspected a requisite pre-aggregation step in the addition of aryllithiums to esters but found it difficult to document definitively: Plessel, K. N.; Jones, A. C.; Wherritt, D. J.; Maksymowicz, R. M.; Poweleit, E. T. Reich, H. J. *Org. Lett.* **2015**, *17*, 2310.

45. (a) Ma, Y.; Ramírez, A.; Singh, K. J.; Keresztes, I.; Collum, D. B. *J. Am. Chem. Soc.* **2006**, *128*, 15399. (b) Godenschwager, P. F.; Collum, D. B. *J. Am. Chem. Soc.* **2007**, *129*, 12023. (c) Chadwick, S. T.; Rennels, R. A.; Rutherford, J. L.; Collum, D. B. *J. Am. Chem. Soc.* **2000**, *122*, 8640. (d) Lucht, B. L.; Collum, D. B. *J. Am. Chem. Soc.* **1996**, *118*, 2217. (e) Wu, S.; Lee, S.; Beak, P. *J. Am. Chem. Soc.* **1996**, *118*, 715. (f) Hsieh, H. L.; Quirk, R. P. *Anionic Polymerization: Principles and Practical Applications*; Marcel Dekker: New York, 1996. (g) Lewis, H. L.; Brown, T. L. *J. Am. Chem. Soc.* **1970**, *92*, 4664.

46. (a) Eliezer, I.; Adida, S. *J. Phys. Chem.* **1973**, *77*, 87. (b) McAuliffe, C. *J. Phys. Chem.* **1966**, *70*, 1267.

47. (a) Kohen, Amnon, and Hans-Heinrich Limbach, eds. *Isotope effects in chemistry and biology*. CRC Press, New York: 2005. (b) Bell, R. P. *The Tunnel Effect in Chemistry*; Chapman & Hall: New York, 1980.

48. Carpenter, B. K. *Nat. Chem.* **2010**, *2* 80.

49. (a) Shimada, S.; Ikeda, Y.; Sasaki, M. *Mem. Konan Univ., Sci. & Eng. Ser.* **2004**, *51*, 141. (b) Wu, A.; Mader, E. A.; Datta, A.; Hrovat, D. A.; Borden, W. T.; Mayer, J. M. *J. Am. Chem. Soc.*

2009, *131*, 11985. (c) Caldin, E. F.; Mateo, S. *J. Chem. Soc., Faraday Trans. 1*, **1975**, *71*, 1876. (d) Kwon, O.-H., Lee, Y.-S., Yoo, B. K.; Jang, D.-J. *Angew. Chem., Int. Ed.* **2006**, *45*, 415.

50. (a) Zong, Y.; McHale, J. L. *J. Chem. Phys.* **1997**, *106*, 4963. (b) Miller, J. R.; Beitz, J. V.; Huddleston, R. K. *J. Am. Chem. Soc.* **1984**, *106*, 5057.

51. Trouble emerges here in that the Keq extracted from the fit is an order of magnitude too high relative to that observed experimentally; the maximum for $[AS_2]^{‡}$ should appear around 5-6 M THF according to the experimentally determined monomer-dimer ratio versus THF.

52. Ma, J. C.; Dougherty, D. A. *Chem. Rev.* **1997**, *97*, 1303.

53. Espenson, J. H. *Chemical Kinetics and Reaction Mechanisms*, 2nd ed.; McGraw-Hill: New York, 1995;

54. Isotopologue **9**-d_2 was prepared using $CH_3CD_2CO_2H$ by a standard procedure: (a) Garg, A.; Khosla, C.; Cane, D. E. *J. Am. Chem. Soc.* **2013**, *135*, 16324. (b) Cane, D. E.; Tan, W.; Ott, W. R. *J. Am. Chem. Soc.* **1993**, *115*, 527. (c) Cane, D. E.; Block, M. H. *J. Am. Chem. Soc.* **1988**, *53*, 4923.

Chapter 5 Appendix

I. NMR spectroscopic studies

II. Mechanistic models

III. Rate studies

VII. Appendix A Revisiting the LiHMDS-mediated enolization of 2-methylcyclohexanone

Chart A.5.1. Substrates and intermediates.

THF

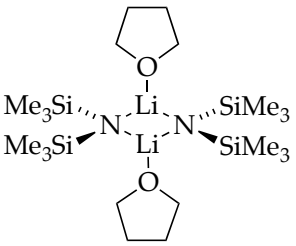

1

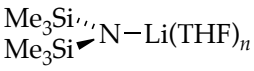

2

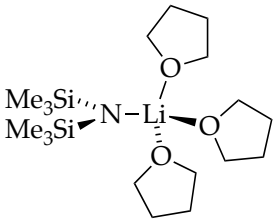

2; $n = 3$

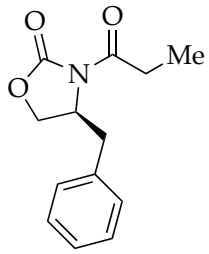

9

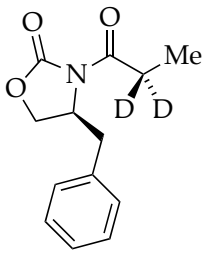

9-d_2

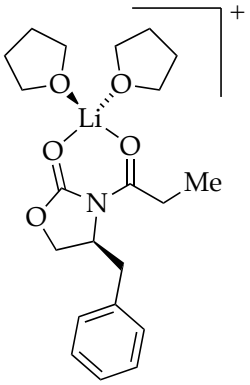

16

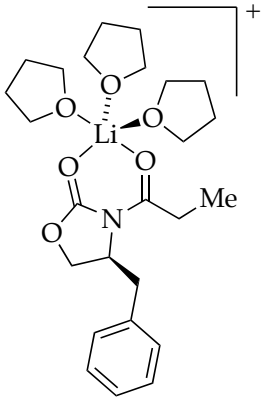

17

I. NMR spectroscopic studies

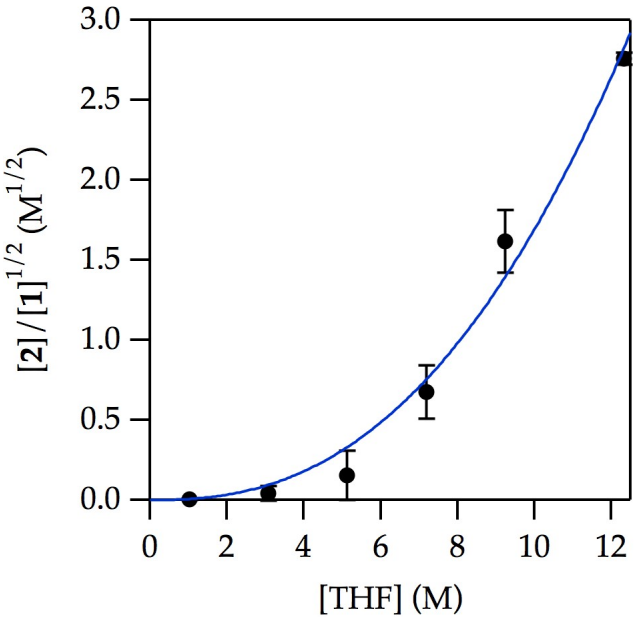

Figure A.5.1. Plot of $[\mathbf{2}]/[\mathbf{1}]^{1/2}$ vs $[\mathrm{THF}]_{total}$ 0.10 M LiHMDS in hexane at –80 °C. The data are fit by nonlinear least-squares methods to the function $[\mathbf{2}]/[\mathbf{1}]^{1/2} = K_{eq}[\mathrm{THF}]^{(n-1)}$ ($K_{eq} = (6.0 \pm 3.9) \times 10^{-3}$, $n = 3.4 \pm 0.3$).

The THF dependence on the $[\mathbf{2}]/[\mathbf{1}]^{1/2}$ ratio has been studied in depth previously (pentane at –80 °C; $K_{eq} = (4.2 \pm 0.8) \times 10^{-3}$; $n = 3.6 \pm 0.2$).[S1]

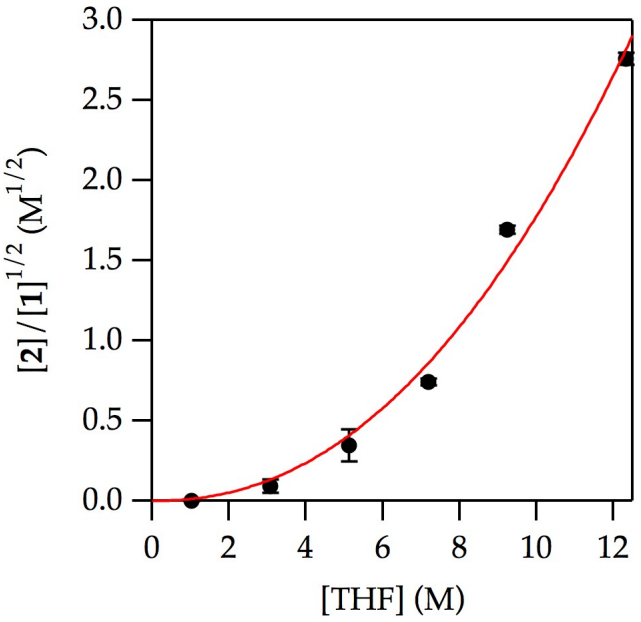

Figure A.5.2. Plot of [**2**]/[**1**]$^{1/2}$ vs [THF]$_{total}$ for 0.10 M LiHMDS in toluene at –80 °C. The data are fit by nonlinear least-squares methods to the function [**2**]/[**1**]$^{1/2}$ = K_{eq} [THF]$^{(n-1)}$ (K_{eq} = (1.1 ± 0.5) × 10^{-2}, n = 3.2 ± 0.2).

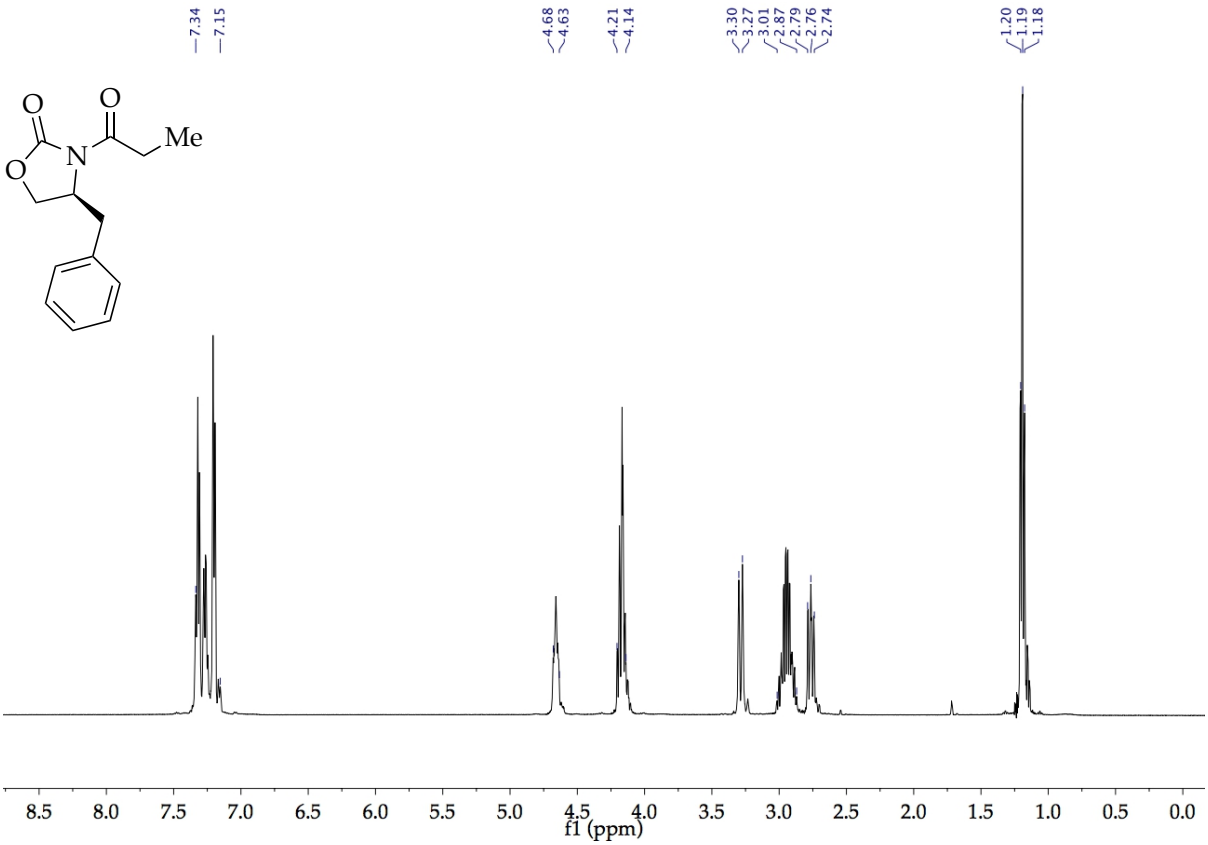

Figure A.5.3. ^{1}H NMR spectrum of oxazolidinone **9** in $CDCl_3$.

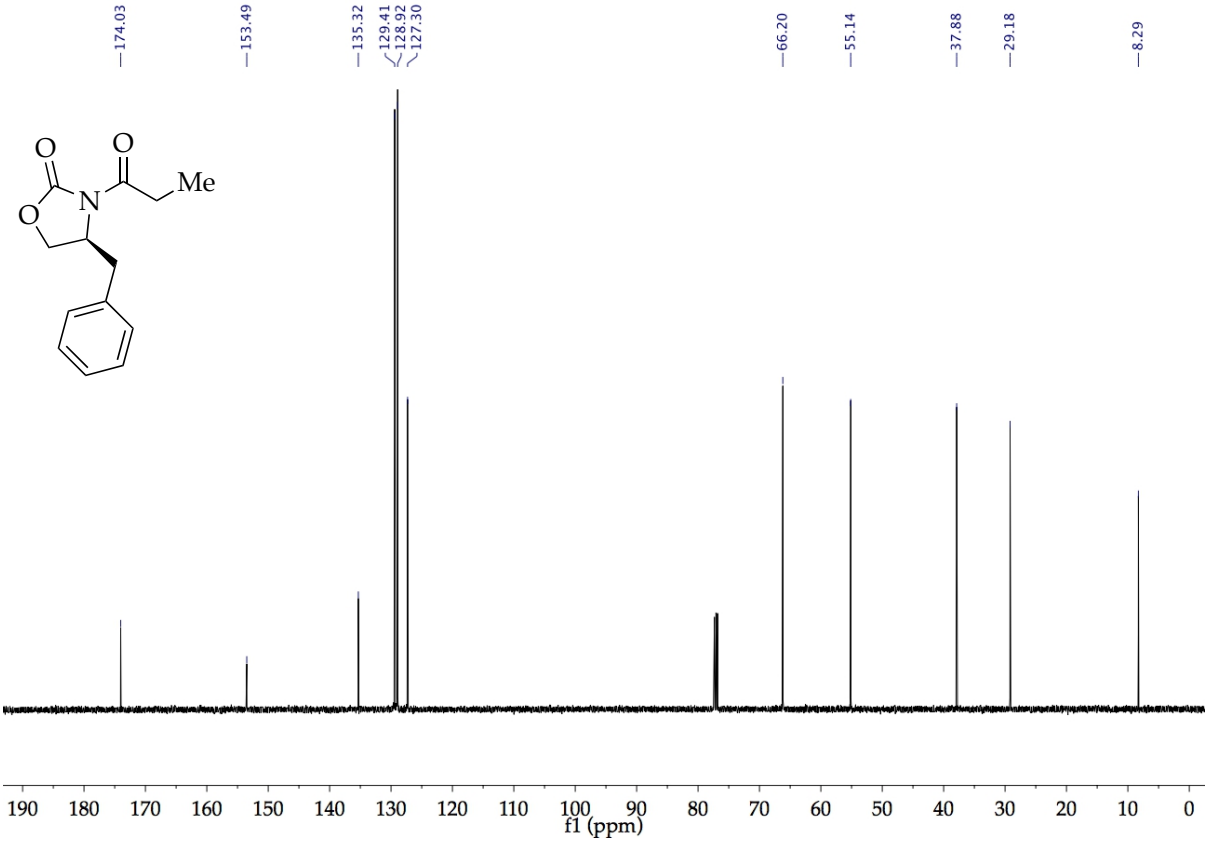

Figure A.5.4. ^{13}C NMR spectrum of oxazolidinone **9** in $CDCl_3$.

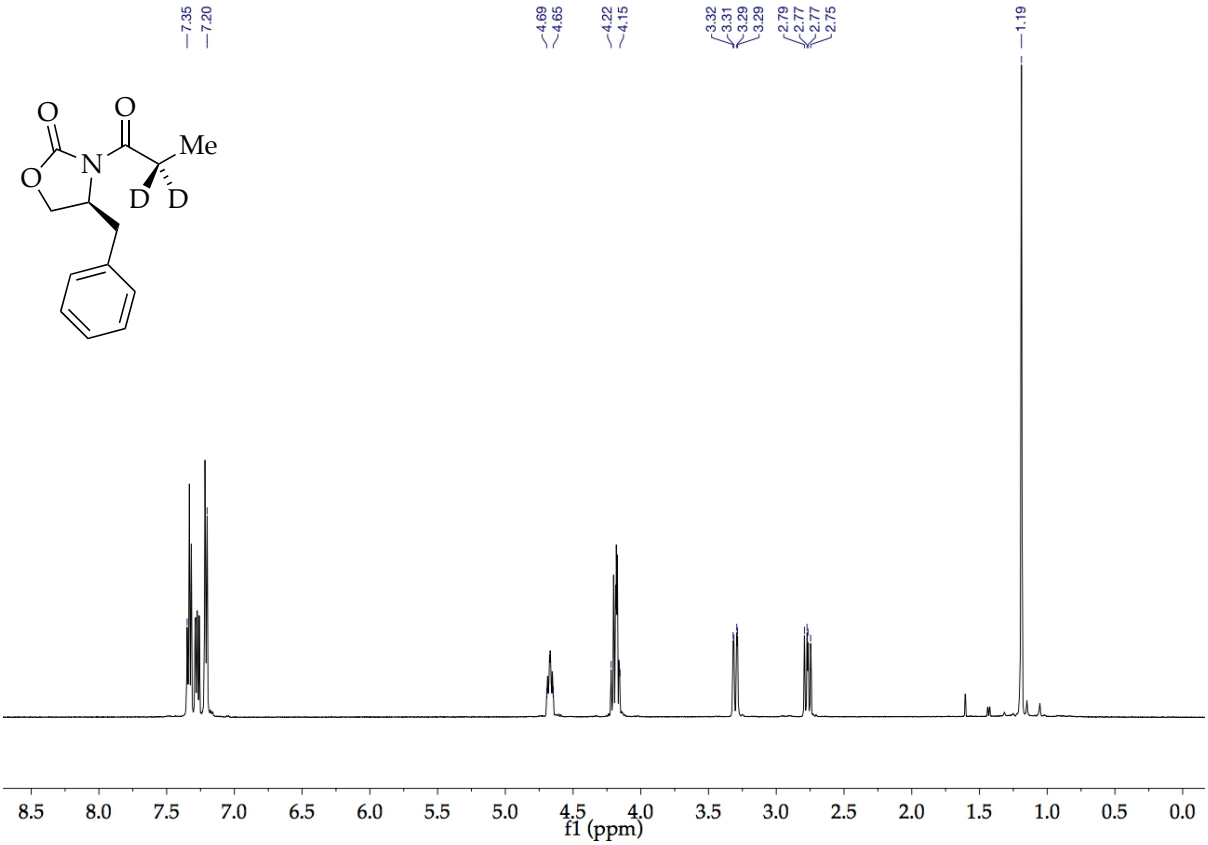

Figure A.5.5. ^{1}H NMR spectrum of oxazolidinone **9**-d_2 in $CDCl_3$.

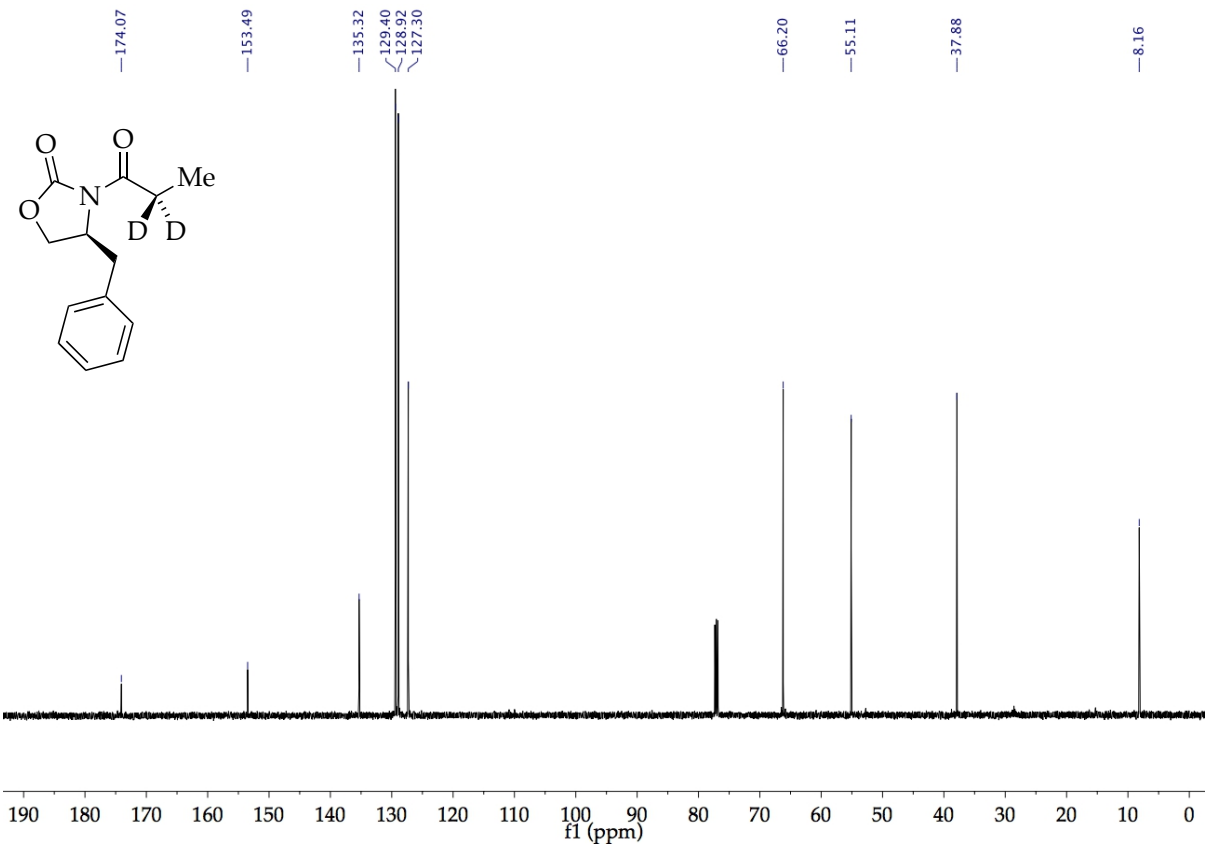

Figure A.5.6. ^{13}C NMR spectrum of oxazolidinone **9**-d_2 in $CDCl_3$.

II. Mechanistic models

i. LiHMDS mechanistic model: Derivations and equations

To simplify mechanistic discussions, we introduce the following shorthand: A = a LiHMDS subunit, and S = THF. For example, A_2S_2 corresponds to disolvated LiHMDS dimer **1**, and AS_3 corresponds to trisolvated LiHMDS monomer **2**.

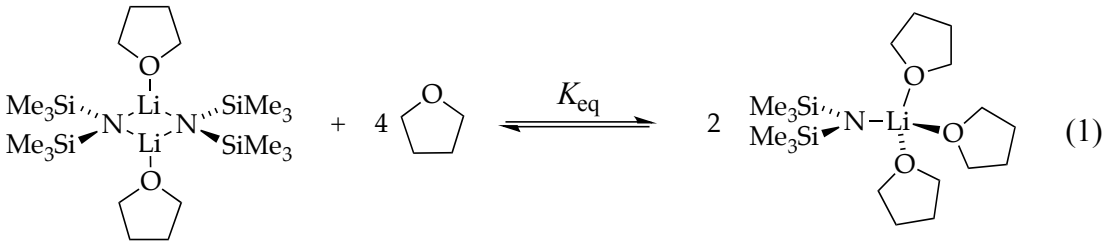

1 **2** (1)

Given $K_{eq} = [AS_3]^2 / \{[A_2S_2][S]^4\}$ and $2[A_2S_2] + [AS_3] = [A]_0$, one can solve for $[A_2S_2]$ as a function of [S]:

$$K_{eq} = \frac{[AS_3]^2}{[A_2S_2][S]^4} = \frac{([A]_0 - 2[A_2S_2])^2}{[A_2S_2][S]^4} \quad (2)$$

Rearranging,

$$4[A_2S_2]^2 - \left(4[A]_0 + K_{eq}[S]^4\right)[A_2S_2] + [A]_0^2 = 0 \quad (3)$$

Applying the quadratic equation to $[A_2S_2]$ gives:

$$[A_2S_2] = \frac{\left(4[A]_0 + K_{eq}[S]^4\right) - \sqrt{\left(4[A]_0 + K_{eq}[S]^4\right)^2 - 16[A]_0^2}}{8} = \frac{4[A]_0 + K_{eq}[S]^4 - \sqrt{K_{eq}}[S]^2\sqrt{K_{eq}[S]^4 + 8[A]_0}}{8} \quad (4)$$

In the case that many distinct aggregates can react at equilibrium and are exclusively non-observable, the following general formula applies:

$$\left[\mathrm{A}_a\mathrm{S}_s\right] \propto \left[\mathrm{A}_2\mathrm{S}_2\right]^{\frac{a}{2}}\left[\mathrm{S}\right]^{s-a} \tag{5}$$

To prove the formula $\left[\mathrm{A}_a\mathrm{S}_s\right] \propto \left[\mathrm{A}_2\mathrm{S}_2\right]^{\frac{a}{2}}\left[\mathrm{S}\right]^{s-a}$ for non-observable species, suppose that $m\mathrm{X} + n\mathrm{Y} \overset{K}{\rightleftharpoons} \mathrm{X}_m\mathrm{Y}_n$. Alternatively stated:

$$\begin{aligned} K &= \frac{\left[\mathrm{X}_m\mathrm{Y}_n\right]}{\left[\mathrm{X}\right]^m\left[\mathrm{Y}\right]^n} \\ &= \frac{\left[\mathrm{X}_m\mathrm{Y}_n\right]}{\left(\left[\mathrm{X}\right]_0 - m\left[\mathrm{X}_m\mathrm{Y}_n\right]\right)^m\left(\left[\mathrm{Y}\right]_0 - n\left[\mathrm{X}_m\mathrm{Y}_n\right]\right)^n} \\ &\approx \frac{\left[\mathrm{X}_m\mathrm{Y}_n\right]}{\left(\left[\mathrm{X}\right]_0\right)^m\left(\left[\mathrm{Y}\right]_0\right)^n} \end{aligned} \tag{6}$$

where $[\mathrm{X}_m\mathrm{Y}_n] << [\mathrm{X}]_0, [\mathrm{Y}]_0$ is invoked in the last step. Rearranging gives the generic form:

$$\left[\mathrm{X}_m\mathrm{Y}_n\right] \propto \left[\mathrm{X}\right]^m\left[\mathrm{Y}\right]^n \tag{7}$$

Assuming the activated complex $\mathrm{A}_a\mathrm{S}_s$•substrate reacts as the rate-limiting step—tantamount to enforcing that all preceding species are at equilibrium—we can write:

$$\begin{aligned} -\frac{\mathrm{d}\left[\text{substrate}\right]}{\mathrm{d}t} &= k'\left[\mathrm{A}_a\mathrm{S}_s \bullet \text{substrate}\right] \\ &= k\left(\left[\mathrm{A}_2\mathrm{S}_2\right]^{\frac{a}{2}}\left[\mathrm{S}\right]^{s-a}\left[\text{substrate}\right]\right) \end{aligned} \tag{8}$$

Therefore, the most general expression that describes reaction out of multiple aggregates is:

$$\begin{aligned} -\frac{\mathrm{d}\left[\text{substrate}\right]}{\mathrm{d}t} &= \left[\text{substrate}\right]\sum_i k_i\left(\left[\mathrm{A}_2\mathrm{S}_2\right]^{\frac{a_i}{2}}\left[\mathrm{S}\right]^{s_i-a_i}\right) \\ &= \left[\text{substrate}\right]\sum_i k_i\left(\left(\frac{4\left[\mathrm{A}\right]_0 + K_{\mathrm{eq}}\left[\mathrm{S}\right]^4 - \sqrt{K_{\mathrm{eq}}}\left[\mathrm{S}\right]^2\sqrt{K_{\mathrm{eq}}\left[\mathrm{S}\right]^4 + 8\left[\mathrm{A}\right]_0}}{8}\right)^{\frac{a_i}{2}}\left[\mathrm{S}\right]^{s_i-a_i}\right) \end{aligned} \tag{9}$$

where i indexes the individual reacting aggregate and k_i is the corresponding rate constant.

To account for the role of cosolvent we assume generically:

$$k_{\text{obsd}} \propto f\left([\text{cosolvent}]\right) \propto f\left(12.3 - [\text{S}]\right) \tag{10}$$

This term accounts for the deviation in THF-concentration dependencies observed when simply varying cosolvent. We hasten to add that f([cosolvent]) is necessarily a function of cosolvent and THF concentrations and settled upon the following form to empirically describe, without attribution, the role of toluene-mediated rate suppression (m is different from the one in eq 6–7):

$$\begin{aligned} f\left([\text{S}]\right) &= \begin{cases} 1 \text{ for hexane} \\ \dfrac{a'[\text{toluene}]^m}{1 + b'[\text{toluene}]^m} + c \text{ for toluene} \end{cases} \\ &= \begin{cases} 1 \text{ for hexane} \\ \dfrac{a\left(12.3 - [\text{S}]\right)^m}{1 + b\left(12.3 - [\text{S}]\right)^m} + c \text{ for toluene} \end{cases} \end{aligned} \tag{11}$$

By including constraints applied by the dependencies on THF and LiHMDS concentration, cosolvent choice, and influence of isotopic substitution, the subset of mechanisms required to *fit all data* reduces to four (eqs 12–15) that are described by eq 16. This is true for *all* fits on plots of k_{obsd} vs [S] for the enolization of oxazolidinones **9** and **9**-d_2.

$$A_2S_2 + S \rightleftharpoons A_2S_3 + \mathbf{9} \xrightarrow{k_8} [A_2S_3\bullet\mathbf{9}]^{\ddagger} \tag{12}$$

$$A_2S_2 + 6S \rightleftharpoons A_2S_8 + \mathbf{9} \xrightarrow{k_9} [A_2S_8\bullet\mathbf{9}]^{\ddagger} \tag{13}$$

$$\tfrac{1}{2}\, A_2S_2 \rightleftharpoons AS + \mathbf{9} \xrightarrow{k_{10}} [AS\bullet\mathbf{9}]^{\ddagger} \tag{14}$$

$$\tfrac{1}{2}\, A_2S_2 + 7S \rightleftharpoons AS_8 + \mathbf{9} \xrightarrow{k_{11}} [AS_8\bullet\mathbf{9}]^{\ddagger} \tag{15}$$

$$k_{\text{obsd}} = f\left(\left[\text{S}\right]\right)\left\{\left(k_8\left[\text{S}\right] + k_9\left[\text{S}\right]^6\right)\left(\frac{4\left[\text{A}\right]_0 + K_{\text{eq}}\left[\text{S}\right]^4 - \sqrt{K_{\text{eq}}}\left[\text{S}\right]^2\sqrt{8\left[\text{A}\right]_0 + K_{\text{eq}}\left[\text{S}\right]^4}}{8}\right) + \right.$$

$$\left.\left(k_{10} + k_{11}\left[\text{S}\right]^7\right)\left(\frac{4\left[\text{A}\right]_0 + K_{\text{eq}}\left[\text{S}\right]^4 - \sqrt{K_{\text{eq}}}\left[\text{S}\right]^2\sqrt{8\left[\text{A}\right]_0 + K_{\text{eq}}\left[\text{S}\right]^4}}{8}\right)^{\frac{1}{2}}\right\} \qquad (16)$$

$$\text{where } f\left(\left[\text{S}\right]\right) = \begin{cases} 1 \text{ for hexane} \\ \dfrac{a\left(12.3 - \left[\text{S}\right]\right)^m}{1 + b\left(12.3 - \left[\text{S}\right]\right)^m} + c \text{ for toluene} \end{cases}$$

Eq 16 is the general equation used for the unweighted least-squares fits on all the plots of k_{obsd} vs [S] for the enolization of oxazolidinones **9** and **9**-d_2.

ii. Discussion of alternative models

We entertained a variety of models to account for the simultaneously shifting LiHMDS orders, isotope effects, and cosolvent dependencies and summarize salient features in this section.

Model	THF dependence **9**	THF dependence **9**-d_2	Isotope Effect	LiHMDS order	Central flaw(s)
$[AS_2]^‡$	✓	✖	✖	✖	Inadequately describes LiHMDS orders at all THF concentrations
$[A_2S_3]^‡$	✓	✖	✖	✖	Does not accommodate rising rates at high THF for **9**-d_2
$[A_2S_3]^‡$, $[AS_n]^‡$	✓	✓	✖	✖	Does not account for drifting isotope effect at low THF
$[AS]^‡$, $[A_2S_3]^‡$, $[AS_n]^‡$	✓	✓	✓	✖	Does not adequately describe LiHMDS dimeric reactivity for **9**-d_2 in neat THF

iii. Toluene-mediated rate suppression: Explicit molecular stabilization

Although the model described above (section i) ascribes no molecular role for the influence of toluene as a cosolvent, to account for explicit stabilization of LiHMDS by toluene involves the following equilibria:

$$A_2S_2 + 4\ S \overset{K_{eq}}{\rightleftharpoons} 2\ AS_3$$

$$A_2S_2 + a\ Tol \overset{K_{Tol}{}^1}{\rightleftharpoons} A_2S_2Tol_a$$

$$AS_3 + b\ Tol \overset{K_{Tol}{}^2}{\rightleftharpoons} AS_3Tol_b$$

One can construct scenarios whereby A_2S_2 alone, not $A_2S_2Tol_a$, sources the reactive forms of LiHMDS while retaining a monomer/dimer ratio consistent with experiment. Although this scheme can successfully replicate the observed toluene suppression, the sigmoidal shape of the toluene suppression function is (in this model) inconsistent with the inverse-first-order dependence of k_{obsd} vs toluene at a fixed THF concentration. The only variations of explicit toluene coordination models that were consistent with all experiments entailed mechanism-dependent sensitivities to toluene. This was implemented by allowing reactivity out of both A_2S_2 and $A_2S_2Tol_a$. We elected to abandon these models due to the adequate description by an arbitrary toluene suppression function.

iv. Simulation of the LiHMDS mechanistic model using *Mathematica*

To construct a generic model for observable differentially solvated dimer and monomer sharing common subunits, consider the following equilibrium:

$$A_2S_n + m\ S \overset{K_{eq}}{\rightleftharpoons} 2\ AS_{(n+m)/2}$$

for which $K_{eq}=[AS_{(n+m)/2}]^2/\{[A_2S_n][S]^m\}$. Within this section, we cordon off *Mathematica* input into boxed tables for which the top line illustrates syntax and the bottom line contains an example of directly executable code. Optional parameters are demarcated by italics. To solve for $[A_2S_n]$ and $[AS_{(n+m)/2}]$ we execute the following expression in *Mathematica*:

Solve[{«equilibrium constant definition(s)», «mass balance expression(s)»}, {«list of components to solve for»}]
Solve[{keq == a^2/(a2*s^m), a0 == 2 a2 + a}, {a2, a}]

```
Solve[{keq == a^2/(a2*s^m), a0 == 2 a2 + a}, {a2, a}]
```

$$\left\{\left\{a2 \to \frac{1}{8}\left(4\,a0 + keq\,s^m + \sqrt{keq}\;s^{m/2}\sqrt{8\,a0 + keq\,s^m}\right),\ a \to \frac{1}{4}\left(-keq\,s^m - \sqrt{keq}\;s^{m/2}\sqrt{8\,a0 + keq\,s^m}\right)\right\},\right.$$
$$\left.\left\{a2 \to \frac{1}{8}\left(4\,a0 + keq\,s^m - \sqrt{keq}\;s^{m/2}\sqrt{8\,a0 + keq\,s^m}\right),\ a \to \frac{1}{4}\left(-keq\,s^m + \sqrt{keq}\;s^{m/2}\sqrt{8\,a0 + keq\,s^m}\right)\right\}\right\}$$

We accept the second root corresponding to the physically realistic circumstance where all concentrations are positive. Given the verifiable assumption that all reactivity proceeds through rate-limiting proton transfer, we can construct a function that describes reactivity out of any number of differentially aggregated and solvated forms. For sake of example we consider the following mechanistic scenario:

$$A_2S_n + x\ S \rightleftharpoons A_2S_{n+x} + \textbf{substrate} \xrightarrow{k_a} [A_2S_{n+x}\bullet\textbf{substrate}]^{\ddagger}$$
$$1/2\ A_2S_n + y\ S \rightleftharpoons AS_{n/2+y} + \textbf{substrate} \xrightarrow{k_b} [AS_{n/2+y}\bullet\textbf{substrate}]^{\ddagger}$$

This scenario translates into the following *Mathematica* input:

«rate expression»/.«physically realistic solution affiliated with ground state»
(ka*s^x*a2+kb*s^y*a2^(1/2))/.{a2->1/8 (4 a0+keq s^m-Sqrt[keq] s^(m/2) Sqrt[8 a0+keq s^m]),a->1/4 (-keq s^m+Sqrt[keq] s^(m/2) Sqrt[8 a0+keq s^m])}

The expression above can be used directly to simulate the kinetic behavior affiliated with this highly generalized mechanism. As written, these inputs must be nested within a Manipulate command that assigns values for the remaining variables. For this system, an appropriate form is:

Manipulate[{«list of expression(s) to manipulate»}, «list of parameters to float according to the form {{«parameter»,«initial value»,"«parameter identifier»"},«low

limit»,«high limit»}»]

(1) Solvent dependence:

Plot[«rate expression»,{s,«low limit»,«high limit»},*PlotRange->{«low limit»,«high limit»}*]
Plot[(ka*s^x*a2+kb*s^y*a2^(1/2))/.{a2->1/8 (4 a0+keq s^m-Sqrt[keq] s^(m/2) Sqrt[8 a0+keq s^m]),a->1/4 (-keq s^m+Sqrt[keq] s^(m/2) Sqrt[8 a0+keq s^m])},{s,0,1}]

(2) Aggregating component dependence:

Plot[«rate expression»,{a0,«low limit»,«high limit»},*PlotRange->{«low limit»,«high limit»}, AxesLabel->{"«independent variable label»","«dependent variable label»"}*]
Plot[(ka*s^x*a2+kb*s^y*a2^(1/2))/.{a2->1/8 (4 a0+keq s^m-Sqrt[keq] s^(m/2) Sqrt[8 a0+keq s^m]),a->1/4 (-keq s^m+Sqrt[keq] s^(m/2) Sqrt[8 a0+keq s^m])},{a0,0,1}]

Nesting these within a Manipulate command gives the following:

```
Manipulate[{Plot[{a2,a}/.{a2->1/8 (4 a0+keq s^m-Sqrt[keq] s^(m/2) Sqrt[8 a0+keq s^m]),a->1/4
(-keq s^m+Sqrt[keq] s^(m/2) Sqrt[8 a0+keq
s^m])},{s,0,1}],Plot[(ka*s^x*a2+kb*s^y*a2^(1/2))/.{a2->1/8 (4 a0+keq s^m-Sqrt[keq] s^(m/2)
Sqrt[8 a0+keq s^m]),a->1/4 (-keq s^m+Sqrt[keq] s^(m/2) Sqrt[8 a0+keq
s^m])},{s,0,1}],Plot[(ka*s^x*a2+kb*s^y*a2^(1/2))/.{a2->1/8 (4 a0+keq s^m-Sqrt[keq] s^(m/2)
Sqrt[8 a0+keq s^m]),a->1/4 (-keq s^m+Sqrt[keq] s^(m/2) Sqrt[8 a0+keq
s^m])},{a0,0,1}]},{{keq,10,"keq"},0,10},{{m,2,"m"},0,2},{{a0,1,"a0"},0,1},{{s,1,"s"},0,1},{{k
a,1,"ka"},0,1},{{x,1,"x"},0,1},{{kb,1,"kb"},0,1},{{y,1,"y"},0,1}]
```

Executing the above code affords the following *Mathematica* output:

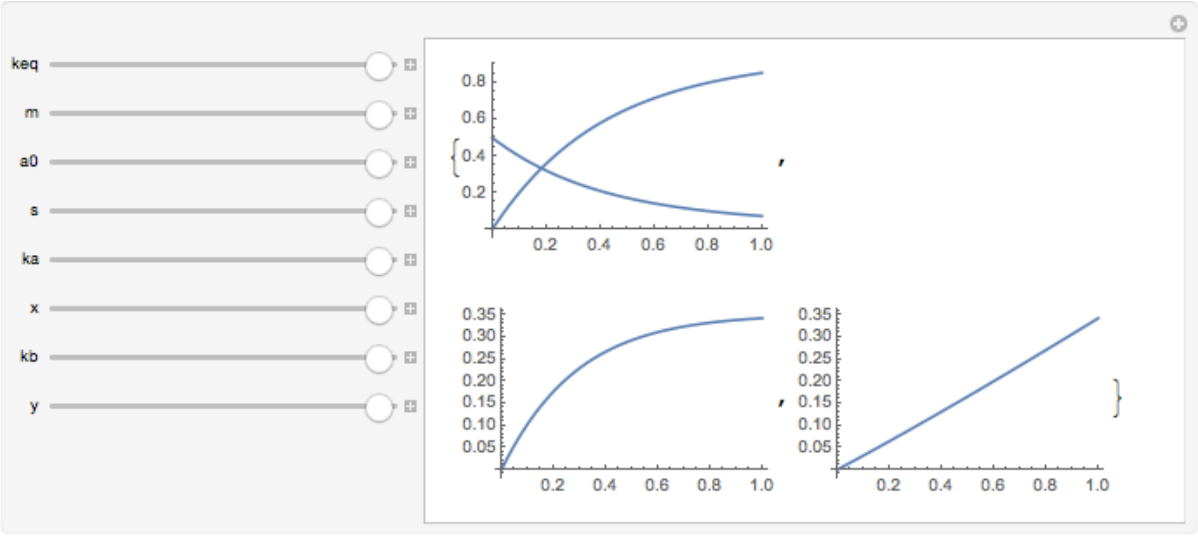

To extract a simulated order in a particular component, the FindFit function is applied to arrayed data according to the assumed power function $y = ax^b$.

```
FindFit[Table[{«component to vary»,«function to fit»},{«component to vary»,«increment»,«final value»,«increment»}],«v1»*«v2»^«v3»,{«v1»,«v3»},«v2»]
```

Solvent order, for example:

```
FindFit[Table[{s,(ka*s^x*a2+kb*s^y*a2^(1/2))/.{a2->1/8 (4 a0+keq s^m-Sqrt[keq] s^(m/2) Sqrt[8 a0+keq s^m]),a->1/4 (-keq s^m+Sqrt[keq] s^(m/2) Sqrt[8 a0+keq s^m])}},{s,0.005,1,0.005}],a*d^b,{a,b},d]
```

We construct the final mechanistic model in *Mathematica* using eq 16 and the rate data (*vide infra*) with the following input:

```
Manipulate[{Plot[{(k8*s*a2s2+k9*s^n*a2s2+k10*a2s2^0.5+k11*s^(n+1)*a2s2^0.5)/.a2s2->1/8 (4 a0+keq s^4-Sqrt[keq] s^2 Sqrt[8 a0+keq s^4]),(a (12.3-s)^m/(1+b*(12.3-s)^m)+c) (k8*s*a2s2+k9*s^n*a2s2+k10*a2s2^0.5+k11*s^(n+1)*a2s2^0.5)/.a2s2->1/8 (4 a0+keq s^4-Sqrt[keq] s^2 Sqrt[8 a0+keq s^4])},{s,0,12.3},PlotRange->{0,5},AxesLabel->{"[THF] (M)","\!\(\*SubscriptBox[StyleBox[\"k\",\nFontSlant->\"Italic\"], \(obsd\)]\) hexane"},PlotLegends->{"hexane","toluene"}],StringForm["LiHMDS order: ``",Round[bb/.FindFit[Table[{a0,(k8*s*a2s2+k9*s^n*a2s2+k10*a2s2^0.5+k11*s^(n+1)*a2s2^0.5)/.a2s2->1/8 (4 a0+keq s^4-Sqrt[keq] s^2 Sqrt[8 a0+keq s^4])},{a0,0.0005,0.25,0.0005}],aa*x^bb,{aa,bb},x],0.01]],Plot[(a (12.3-s)^m/(1+b*(12.3-s)^m)+c) (k8*s*a2s2+k9*s^n*a2s2+k10*a2s2^0.5+k11*s^(n+1)*a2s2^0.5)/.a2s2->1/8 (4 a0+keq s^4-Sqrt[keq] s^2 Sqrt[8 a0+keq s^4]),{a0,0,0.25},AxesLabel->{"[LiHMDS] (M)","\!\(\*SubscriptBox[StyleBox[\"k\",\nFontSlant->\"Italic\"], \(obsd\)]\)"}],Plot[{k8*s*a2s2,k9*s^n*a2s2,k10*a2s2^0.5,k11*s^(n+1)*a2s2^0.5}/.a2s2->1/8 (4 a0+keq s^4-Sqrt[keq] s^2 Sqrt[8 a0+keq s^4]),{s,0,12.3},PlotRange->{0,5},AxesLabel->{"[THF] (M)","Contributions to \!\(\*SubscriptBox[StyleBox[\"k\",\nFontSlant->\"Italic\"], \(obsd\)]\) hexane"}],Plot[(a (12.3-s)^m/(1+b*(12.3-s)^m)+c) {k8*s*a2s2,k9*s^n*a2s2,k10*a2s2^0.5,k11*s^(n+1)*a2s2^0.5}/.a2s2->1/8 (4 a0+keq s^4-Sqrt[keq] s^2 Sqrt[8 a0+keq s^4]),{s,0,12.3},PlotRange->{0,5},AxesLabel->{"[THF] (M)","Contributions to \!\(\*SubscriptBox[StyleBox[\"k\",\nFontSlant->\"Italic\"], \(obsd\)]\) toluene"}],Plot[(a (12.3-s)^m/(1+b*(12.3-s)^m)+c),{s,0,12.3},PlotRange->{0,1},AxesLabel->{"[THF] (M)","\!\(\*StyleBox[\"f\",\nFontSlant->\"Italic\"]\)\!\(\*StyleBox[\"(\",\nFontSlant->\"Italic\"]\)[S])"}]},{{keq,0.00022,"keq"},0,1},{{a0,0.1,"[A\!\(\*SubscriptBox[\(]\), \(0\)]\)"},0,1},{{k8,39.6,"k8"},0,100},{{k9,2.5*10^-5,"k9"},0,100},{{k10,0.2,"k10"},0,100},{{k11,5*10^-7,"k11"},0,100},{{n,6,"n"},0,10},{{a,-0.0000319,"a"},-1,1},{{b,0.0000336,"b"},0,1},{{c,1,"c"},0,10},{{m,4.81,"m"},0,10},{{s,12.3,"[S]"},0,12.3}]
```

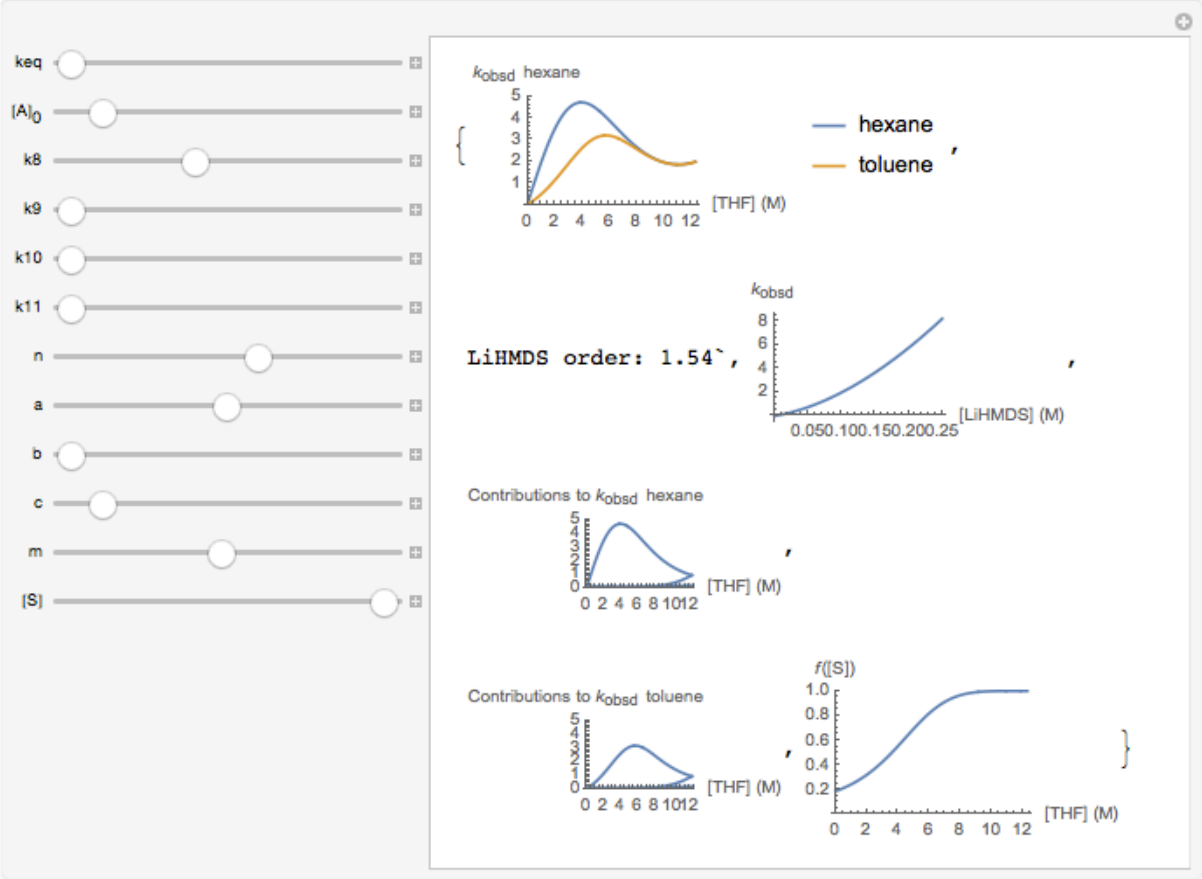

Note that the complexity in this system originates not from the ground state variation but instead in the number of transition states. One can similarly construct more elaborate schemes wherein multiple ground states are accessible.

v. Fitting in *IgorPro*

We illustrate eq 16 —ready to paste into *IgorPro*—for rate data analysis using unweighted least-squares fits:

```
f(s) = (a*(12.3-s)^m/(1+b*(12.3-s)^m)+c)*((k8*s+k9*s^n)*((4*a0+keq*s^4-
Sqrt(keq)*s^2*Sqrt(keq*s^4+8*a0))/8)+(k10+k11*s^(n+1))*((4*a0+keq*s^4-
Sqrt(keq)*s^2*Sqrt(keq*s^4+8*a0))/8)^0.5)
```

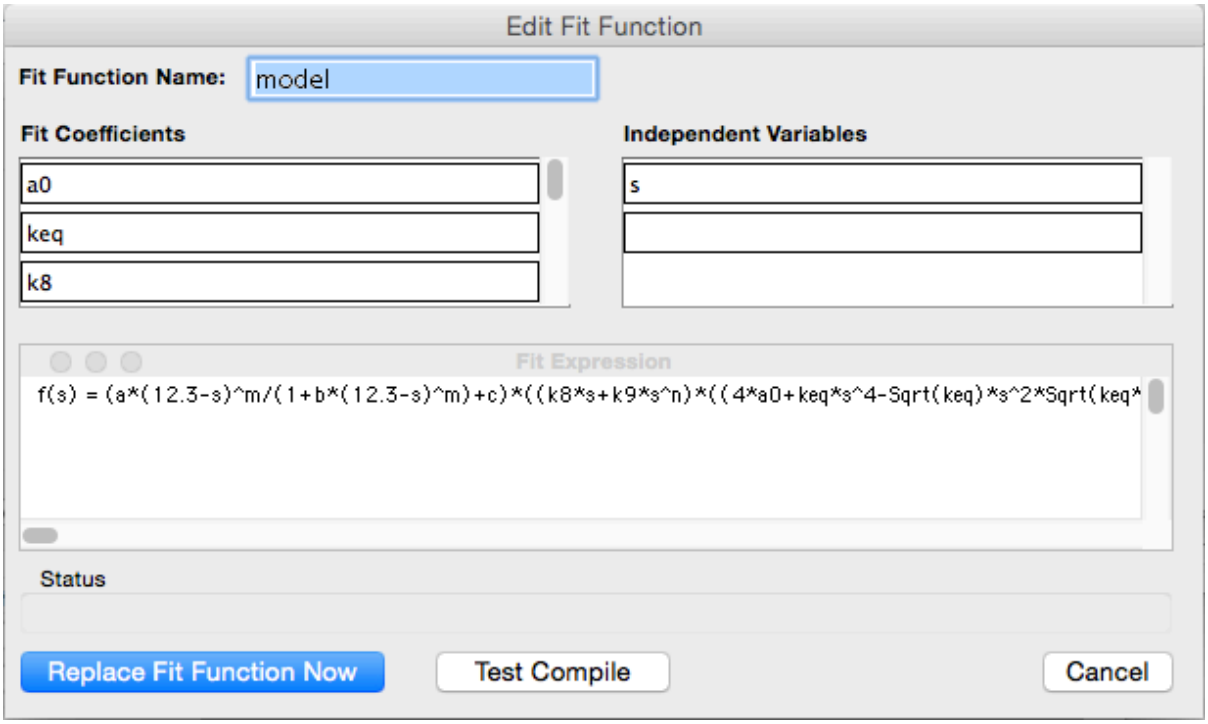

vi. Alternative Simulation Strategy

Although the description considered above is correct, it cannot readily extend to pairwise equilibrating systems of higher aggregates (*i.e.* pentamer/trimer). To appreciate where the problem lies consider the following equilibrium:

$$\mathrm{A}_m\mathrm{S}_n + (my/x - n)\ \mathrm{S} \overset{K_{\mathrm{eq}}}{\rightleftharpoons} m/x\ \mathrm{A}_x\mathrm{S}_y$$

Converting this expression to an equilibrium constant definition (and accounting for the mass balance $[\mathrm{A}]_0 = m[\mathrm{A}_m\mathrm{S}_n] + x[\mathrm{A}_x\mathrm{S}_y]$) follows:

$$K_{\mathrm{eq}} = \frac{\left[\mathrm{A}_x\mathrm{S}_y\right]^{\frac{m}{x}}}{\left[\mathrm{A}_m\mathrm{S}_n\right]\left[\mathrm{S}\right]^{\frac{my}{x}-n}} = \frac{\left[\mathrm{A}_x\mathrm{S}_y\right]^{\frac{m}{x}}}{\left(\frac{\left[\mathrm{A}\right]_0}{m} - \frac{x\left[\mathrm{A}_x\mathrm{S}_y\right]}{m}\right)\left[\mathrm{S}\right]^{\frac{my}{x}-n}}$$

Rearranging the expression above gives:

$$\frac{\left[\mathrm{A}_x\mathrm{S}_y\right]^{\frac{m}{x}}}{K_{\mathrm{eq}}\left[\mathrm{S}\right]^{\frac{my}{x}-n}} + \frac{x\left[\mathrm{A}_x\mathrm{S}_y\right]}{m} - \frac{\left[\mathrm{A}\right]_0}{m} = 0$$

Extracting the roots affiliated with this equation is impossible for $m/x \geq 5$; selecting appropriate closed-form roots that are analytically tractable for other cases is often prohibitive. An alternative strategy is to differentiate the expression above with respect to $[\mathrm{A}]_0$:

$$\frac{m\left[\mathrm{A}_x\mathrm{S}_y\right]^{\frac{m}{x}-1}}{xK_{\mathrm{eq}}\left[\mathrm{S}\right]^{\frac{my}{x}-n}}\frac{\mathrm{d}\left[\mathrm{A}_x\mathrm{S}_y\right]}{\mathrm{d}\left[\mathrm{A}\right]_0} + \frac{x}{m}\frac{\mathrm{d}\left[\mathrm{A}_x\mathrm{S}_y\right]}{\mathrm{d}\left[\mathrm{A}\right]_0} - \frac{1}{m} = 0$$

Continue by isolating $d[A_xS_y]/d[A]_0$:

$$\frac{d\left[A_xS_y\right]}{d\left[A\right]_0} = \frac{1}{\frac{m^2\left[A_xS_y\right]^{\frac{m}{x}-1}}{xK_{eq}\left[S\right]^{\frac{my}{x}-n}} + x}$$

The differential equation above describing $[A_xS_y]$ is well suited for numerical solution (with the trivial boundary condition $[A_xS_y](0) = 0$) that can be implemented either with NDSolveValue or with an explicit finite-difference sum.

Using NDSolveValue to generate the ordered set $\{[A_mS_n],[A_xS_y]\}$ requires the following code:

```
NDSolveValue[{y'[v]==1/(m^2*y[v]^(m/x-1)/(x*keq*s^(m*y/x-n))+x),y[0]==0},{a0/m-
x*y[a0]/m,y[a0]},{v,0,10},MaxSteps->1000]
```

A visually tractable output of $[A_mS_n]$ and $[A_xS_y]$ vs $[A]_0$ and $[S]$ can be achieved with the following code:

```
Manipulate[{Plot[NDSolveValue[{z'[v]==1/(m^2*z[v]^(m/x-1)/(x*keq*s^(m*y/x-
n))+x),z[0]==0},{a0/m-x*z[a0]/m,z[a0]},{v,0,10},MaxSteps->5000],{s,0,12.3},PlotRange-
>{0,a0}],Plot[NDSolveValue[{z'[v]==1/(m^2*z[v]^(m/x-1)/(x*keq*s^(m*y/x-
n))+x),z[0]==0},{a0/m-x*z[a0]/m,z[a0]},{v,0,10},MaxSteps-
>5000],{a0,0,0.3}]},{{keq,0.0001,"keq"},0.0001,10},{{m,2,"m"},1,10},{{n,2,"n"},0,10},{{x,1,
"x"},1,10},{{y,3,"y"},0,10},{{a0,0.1,"a0"},0,10},{{s,10,"s"},0,12.3}]
```

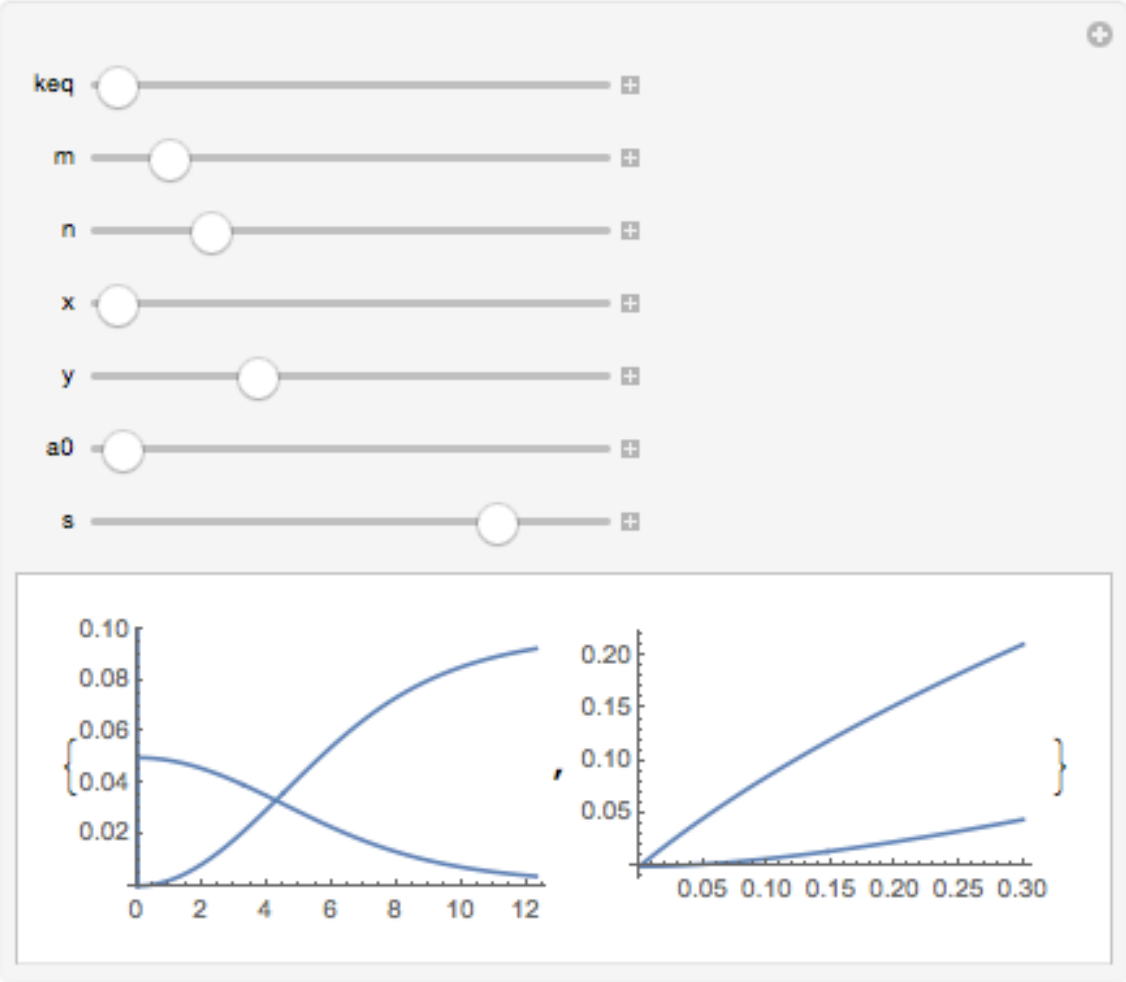

One may achieve a similar outcome employing (sometimes at greater computational cost) finite-difference summation:

```
t=0;Do[t=t+i*1/(m^2*t^(m/x-1)/(x*keq*s^(m*y/x-n))+x),a0/i];t//N
```

The above expression approximates the value of $[A_xS_y]$ by executing the discrete sum shown below (i is the increment step size and x is the index of summation):

$$\left[\mathrm{A}_x\mathrm{S}_y\right]_z = \sum_{z=1}^{[\mathrm{A}]_0/i} \frac{i}{\dfrac{m^2\left[\mathrm{A}_x\mathrm{S}_y\right]_{z-1}^{\frac{m}{x}-1}}{xK_{\mathrm{eq}}\left[\mathrm{S}\right]^{\frac{my}{x}-1}} + x}$$

Casting the above into executable *Mathematica* code entails the following:

```
Manipulate[{Plot[{a0/m-x/m(t=0;Do[t=t+i*1/(m^2*t^(m/x-1)/(x*keq*s^(m*y/x-
n))+x),a0/i];t//N),t=0;Do[t=t+i*1/(m^2*t^(m/x-1)/(x*keq*s^(m*y/x-
n))+x),a0/i];t//N},{s,0,12.3},PlotRange->{0,a0}],Plot[{a0/m-x/m(t=0;Do[t=t+i*1/(m^2*t^(m/x-
1)/(x*keq*s^(m*y/x-n))+x),a0/i];t//N),t=0;Do[t=t+i*1/(m^2*t^(m/x-1)/(x*keq*s^(m*y/x-
n))+x),a0/i];t//N},{a0,0,0.3}]},{{keq,0.0001,"keq"},0.0001,10},{{m,2,"m"},1,10},{{n,2,"n"},0,
10},{{x,1,"x"},1,10},{{y,3,"y"},0,10},{{a0,0.1,"a0"},0,10},{{s,10,"s"},0,12.3},{{i,0.001,"i"},0,
0.1}]
```

One can implement the above sum in *Microsoft Excel* according to the following VBA macro:

```
Sub SolveSystem()
'
' SolveSystem Macro
Range("F1").Select
    ActiveCell.FormulaR1C1 = "=R[5]C[2]/R[3]C[2]"
    Range("F2").Select
    ActiveCell.FormulaR1C1 = _
        "=R[4]C[2]/(RC[2]^2*R[-1]C^(RC[2]/R[2]C[2]-1)/(R[2]C[2]*R[-1]C[2]*RC[-
4]^(RC[2]*R[3]C[2]/R[2]C[2]-R[1]C[2]))+R[2]C[2])+R[-1]C"
    Range("F3").Select

    Dim i
    Range("J6").Select
    ActiveCell.FormulaR1C1 = "=ROUNDDOWN(R[-4]C[-9]/RC[-2],0)"
    Dim j

    j = ActiveCell.Value - 2

    For i = 1 To j
    Range("F2").Select
    Application.CutCopyMode = False
    Selection.Copy
    Range("F1").Select
    Selection.PasteSpecial Paste:=xlValues, Operation:=xlNone, SkipBlanks:= _
        False, Transpose:=False
    Range("D5").Select
    Next i

    Range("F2").Select
    Application.CutCopyMode = False
    Selection.Copy
    Range("E2").Select
    Selection.PasteSpecial Paste:=xlValues, Operation:=xlNone, SkipBlanks:= _
        False, Transpose:=False
    Range("D2").Select
    Application.CutCopyMode = False
    ActiveCell.FormulaR1C1 = "=RC[-3]/RC[4]-R[2]C[4]*RC[1]/RC[4]"
    Range("F1:F2").Select
    Range("F2").Activate
    ActiveCell.FormulaR1C1 = ""
    Range("F1").Select
    ActiveCell.FormulaR1C1 = ""
    Range("J6").Select
```

```
    ActiveCell.FormulaR1C1 = ""
    Range("E3").Select
End Sub

Sub CreateSheet()
'
' CreateSheet Macro
'
    Range("A1").Select
    Application.CutCopyMode = False
    ActiveCell.FormulaR1C1 = "[A]0"
    Range("B1").Select
    ActiveCell.FormulaR1C1 = "[S]"
    Range("D1").Select
    ActiveCell.FormulaR1C1 = "[AmSn]"
    Range("E1").Select
    ActiveCell.FormulaR1C1 = "[AxSy]"
    Range("G1").Select
    ActiveCell.FormulaR1C1 = "Keq"
    Range("A2").Select
    ActiveCell.FormulaR1C1 = "0.1"
    Range("B2").Select
    ActiveCell.FormulaR1C1 = "2"
    Range("G2").Select
    ActiveCell.FormulaR1C1 = "m"
    Range("G3").Select
    ActiveCell.FormulaR1C1 = "n"
    Range("G4").Select
    ActiveCell.FormulaR1C1 = "x"
    Range("G5").Select
    ActiveCell.FormulaR1C1 = "y"
    Range("G6").Select
    ActiveCell.FormulaR1C1 = "increment"
    Range("H1").Select
    ActiveCell.FormulaR1C1 = "0.0001"
    Range("H2").Select
    ActiveCell.FormulaR1C1 = "2"
    Range("H3").Select
    ActiveCell.FormulaR1C1 = "2"
    Range("H4").Select
    ActiveCell.FormulaR1C1 = "1"
    Range("H5").Select
    ActiveCell.FormulaR1C1 = "3"
    Range("H6").Select
    ActiveCell.FormulaR1C1 = "0.001"
```

```
    Range("A1").Select
End Sub
```

Chart A.5.2. Transition structures and activation energies.

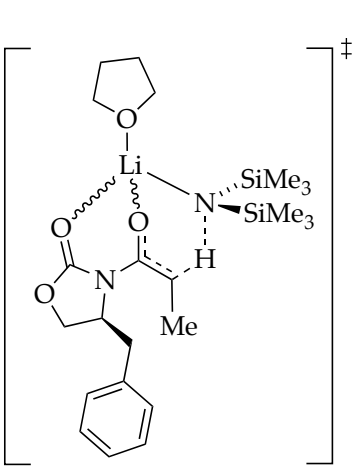

11

[AS•**9**]‡

$\Delta G^{‡}_{anti}$ = 16.9 kcal/mol
$\Delta G^{‡}_{syn}$ = 19.4 kcal/mol

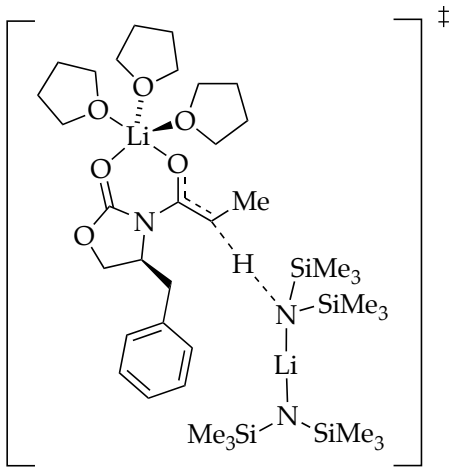

12

[A_2S_3•**9**]‡

$\Delta G^{‡}_{anti}$ = 17.2 kcal/mol
$\Delta G^{‡}_{syn}$ = 22.8 kcal/mol

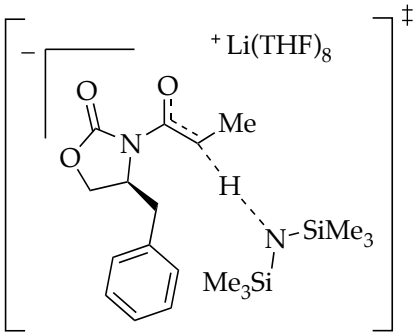

13

[AS_8•**9**]‡

$\Delta G^{‡}_{anti}$ = Not determined [a]
$\Delta G^{‡}_{syn}$ = Not determined [a]

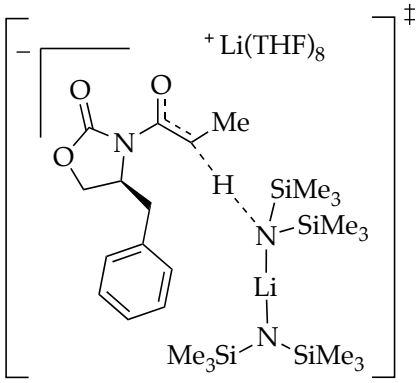

14

[A_2S_8•**9**]‡

$\Delta G^{‡}_{anti}$ = Not determined [a]
$\Delta G^{‡}_{syn}$ = Not determined [a]

[a] The anionic fragment of the transition structures was studied using $^{+}Li(THF)_{3–4}$. Transition (and ground state) structures containing $^{+}Li(THF)_{n\geq5}$ do not converge; these have a bias towards tetrahedral Li. However, there is precedence for hypersolvated ^{+}Li in the literature, including crystallographic and rate data.[S2] Our data strongly supports octasolvated transition structures **13** and **14** (*vide infra*).

Other potential transition structures and activation energies:

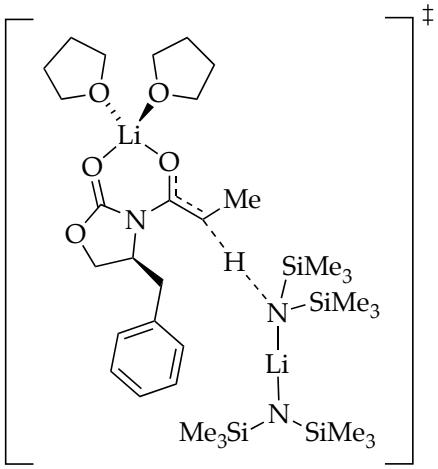

15

$[A_2S_2•\mathbf{9}]^‡$

$\Delta G^‡_{anti}$ = 21.9 kcal/mol
$\Delta G^‡_{syn}$ = 26.8 kcal/mol

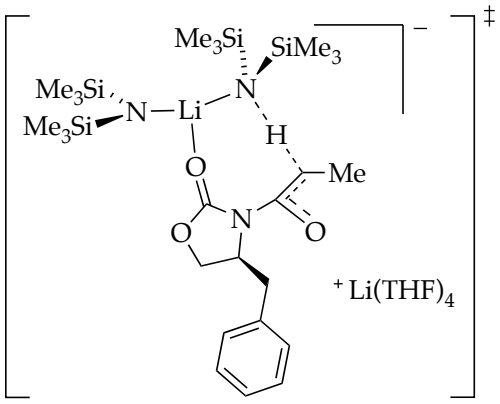

18

$[A_2S_4•\mathbf{9}]^‡$

$\Delta G^‡_{anti}$ = 32.5 kcal/mol
$\Delta G^‡_{syn}$ = 29.4 kcal/mol

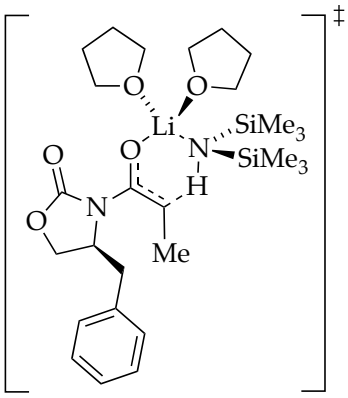

19

$[AS_2•\mathbf{9}]^‡$

$\Delta G^‡_{anti}$ = 17.9 kcal/mol
$\Delta G^‡_{syn}$ = 18.3 kcal/mol

III. Rate studies

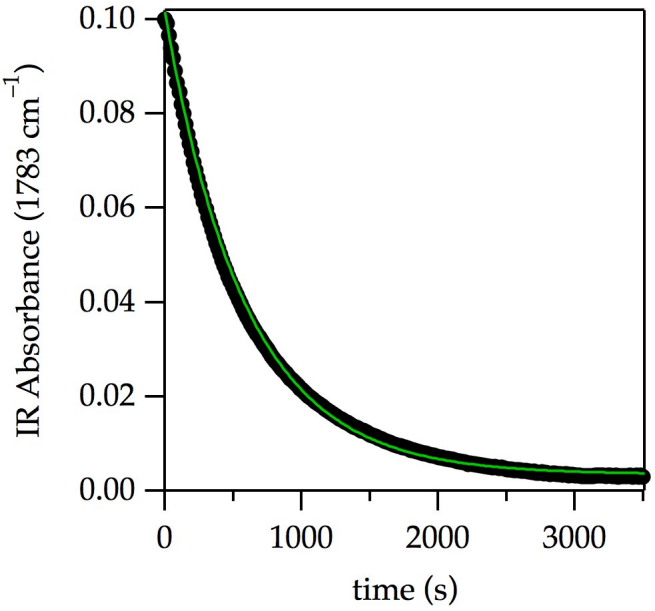

Figure A.5.7. Lithiation of oxazolidinone **9** with equimolar LiHMDS in neat THF at –78 °C showing the loss of **9**. The decay was fit to the first-order function $f(t) = a + be^{-kt}$ [a = (3.48 ± 0.09) × 10^{-3}; b = (9.81 ± 0.02) × 10^{-2}; k = (1.699 ± 0.008) × 10^{-3} s^{-1}]. The origin of the fit to the first-order function in the stoichiometric enolization stems from a non-linear relation between IR absorbance and [**9**] at > 0.015 M of **9** (deviation from Beer's law).

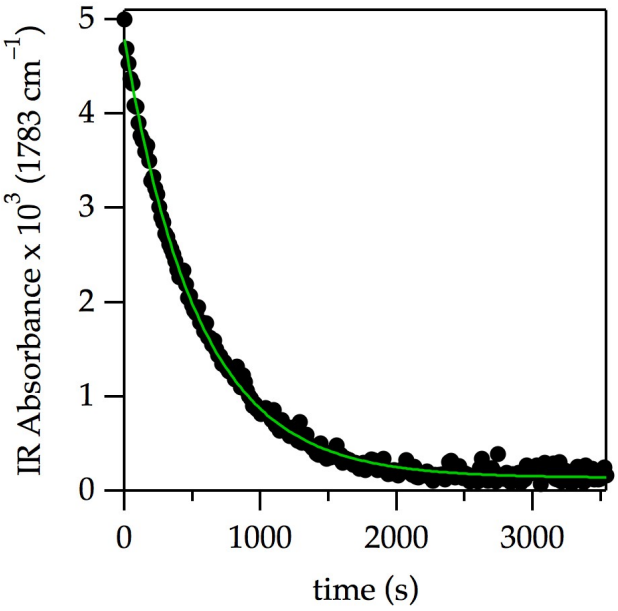

Figure A.5.8. Lithiation of 0.0050 M oxazolidinone **9** with 0.10 M LiHMDS in neat THF at –78 °C showing the loss of **9** (pseudo-first-order conditions). The decay was fit to $f(t) = a + be^{-kt}$ [$a = (1.37 \pm 0.06) \times 10^{-4}$; $b = (4.65 \pm 0.02) \times 10^{-3}$; $k = 1.85 \pm 0.02) \times 10^{-3}$ s^{-1}].

Table A.5.1. k_{obsd} for the enolization of oxazolidinone **9** with 0.10 M LiHMDS at various concentrations of **9** in neat THF at –78 ºC.

[**9**] (M)	$k_{obsd} \times 10^3$ (s^{-1}) [a]
0.001	1.86 ± 0.09
0.002	1.70 ± 0.03
0.003	2.10 ± 0.03
0.004	1.65 ± 0.01
0.005	1.85 ± 0.02
0.010	1.52 ± 0.02

[a] Average = 1.8 ± 0.1

Table A.5.2. k_{obsd} for the enolization of oxazolidinone **9** with 0.10 M LiHMDS at various concentrations of **9** and 1.0 M THF–hexane at –78 ºC.

[**9**] (M)	$k_{obsd} \times 10^3$ (s^{-1}) [a]
0.002	2.26 ± 0.09
0.003	2.1 ± 0.1
0.004	1.72 ± 0.05
0.005	1.75 ± 0.05
0.006	1.81 ± 0.03

[a] Average = 1.9 ± 0.2

* For individual runs, the error represents the error of the fit. For replicated runs, the error represents the standard deviation. This is true for *every single kinetic run.* *

Solvent orders

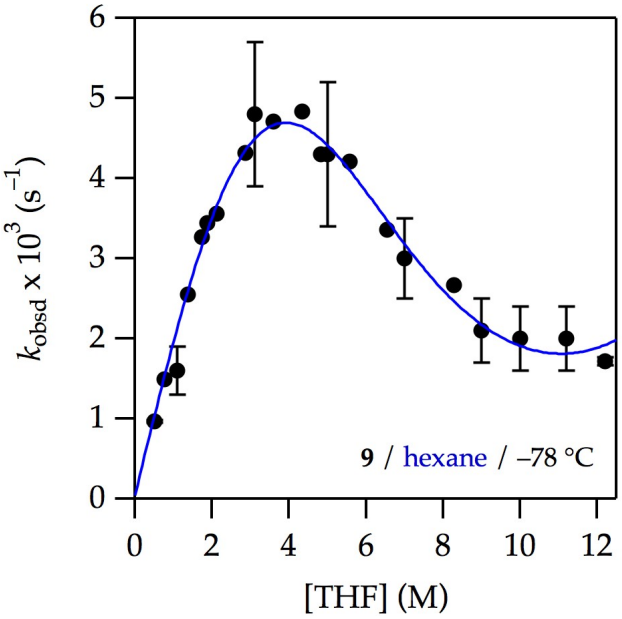

Figure A.5.9. Plot of k_{obsd} vs [THF] for the enolization of 0.0050 M oxazolidinone **9** with 0.10 M LiHMDS at various concentrations of THF in hexane at –78 ºC. The curve depicts the result of an unweighted least-squares fit to eq 16 ($[A]_0$ is set at 0.10; K_{eq} = (2.3 ± 0.2) × 10^{-4}; k_8 = (3.9 ± 0.1) × 10^{-2}; k_9 = (2 ± 10) × 10^{-8}; k_{10} is set to 2.0 × 10^{-4}; k_{11} = (5 ± 4) × 10^{-10}).

[THF] (M)	$k_{obsd}^{1} \times 10^3$ (s^{-1})	$k_{obsd}^{2} \times 10^3$ (s^{-1})	$k_{obsd}^{3} \times 10^3$ (s^{-1})	$k_{obsd}^{4} \times 10^3$ (s^{-1})	$k_{obsd}^{avg} \times 10^3$ (s^{-1})
0.50		0.95 ± 0.02		0.99 ± 0.01	0.97 ± 0.02
0.76		1.49 ± 0.03			
1.1	1.85 ± 0.07			1.40 ± 0.09	1.6 ± 0.3
1.4		2.55 ± 0.04			
1.7		3.27 ± 0.06			
1.9		3.44 ± 0.07			
2.1			3.56 ± 0.05		
2.9			4.32 ± 0.06		
3.1	5.5 ± 0.1			4.2 ± 0.2	4.8 ± 0.9
3.6			4.71 ± 0.07		
4.3			4.83 ± 0.08		
4.8			4.30 ± 0.07		
5.0	4.90 ± 0.06			3.61 ± 0.03	4.3 ± 0.9
5.6			4.21 ± 0.06		
6.5			3.36 ± 0.04		
7.0	3.36 ± 0.04			2.63 ± 0.04	3.0 ± 0.5
8.3			2.67 ± 0.04		
9.0	2.33 ± 0.03			1.81 ± 0.02	2.1 ± 0.4
10.0	2.31 ± 0.04			1.70 ± 0.01	2.0 ± 0.4
11.2	2.28 ± 0.02			1.68 ± 0.02	2.0 ± 0.4
12.2	1.68 ± 0.01			1.76 ± 0.01	1.72 ± 0.05

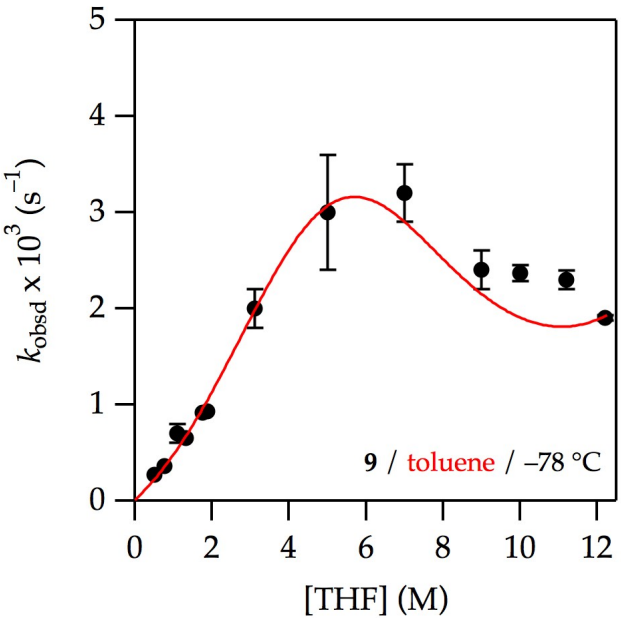

Figure A.5.10. Plot of k_{obsd} vs [THF] for the enolization of 0.0050 M oxazolidinone **9** with 0.10 M LiHMDS at various concentrations of THF in toluene at –78 ºC. The curve depicts the result of an unweighted least-squares fit to eq 16 (All parameters carried over from the fit from Figure A.5.9; additionally, $a = -3.19 \times 10^{-5} \pm 0$; $b = 3.36 \times 10^{-5} \pm 0$, c is set at 1.0, $m = 4.81 \pm 0$).

[THF] (M)	$k_{obsd}^{1} \times 10^3$ (s^{-1})	$k_{obsd}^{2} \times 10^3$ (s^{-1})	$k_{obsd}^{3} \times 10^3$ (s^{-1})	$k_{obsd}^{avg} \times 10^3$ (s^{-1})
0.51		0.271 ± 0.002		
0.76		0.363 ± 0.002		
1.1	0.59 ± 0.01	0.537 ± 0.008	0.731 ± 0.004	0.6 ± 0.1
1.4		0.655 ± 0.008		
1.7		0.92 ± 0.01		
1.9		0.93 ± 0.01		
3.1	1.85 ± 0.02		2.15 ± 0.02	2.0 ± 0.2
5.0	2.59 ± 0.05		3.51 ± 0.03	3.0 ± 0.6
7.0	3.00 ± 0.04		3.39 ± 0.03	3.2 ± 0.3
9.0	2.28 ± 0.03		2.59 ± 0.02	2.4 ± 0.2
10.0	2.43 ± 0.03		2.32 ± 0.02	2.37 ± 0.08
11.2	2.40 ± 0.02		2.24 ± 0.03	2.3 ± 0.1
12.2	1.92 ± 0.01		1.88 ± 0.03	1.90 ± 0.03

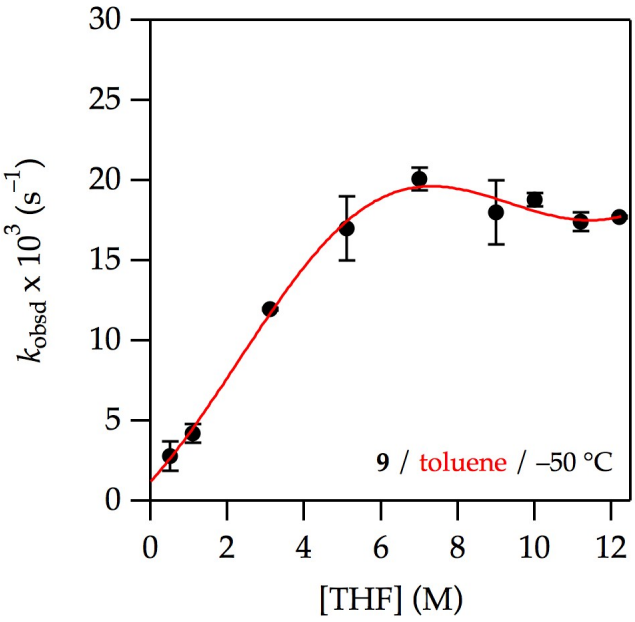

Figure A.5.11. Plot of k_{obsd} vs [THF] for the enolization of 0.0050 M oxazolidinone **9** with 0.10 M LiHMDS at various concentrations of THF in toluene at –50 ºC. The curve depicts the result of an unweighted least-squares fit to eq 16 ($[A]_0$ is set at 0.10; $K_{eq} = (1.0) \times 10^{-4}$; $k_8 = (2.5) \times 10^{-1}$; $k_9 = (7.8) \times 10^{-8}$; $k_{10} = (2.7) \times 10^{-2}$; $k_{11} = (2.8) \times 10^{-9}$; $a = (-9.7) \times 10^{-3}$; $b = (1.1) \times 10^{-2}$; $c = (0.83)$; $m = 2.2$).

[THF] (M)	$k_{obsd}^{1} \times 10^3$ (s^{-1})	$k_{obsd}^{2} \times 10^3$ (s^{-1})	$k_{obsd}^{avg} \times 10^3$ (s^{-1})
0.50	2.12 ± 0.03	3.40 ± 0.05	2.8 ± 0.9
1.1	3.78 ± 0.06	4.62 ± 0.06	4.2 ± 0.6
3.1	12.0 ± 0.5	11.9 ± 0.3	11.97 ± 0.07
5.1	16.3 ± 0.8	18.7 ± 0.5	17 ± 2
7.0	21 ± 1	19.6 ± 0.6	20.1 ± 0.7
9.0	16.8 ± 0.9	19.9 ± 0.7	18 ± 2
10.0	19 ± 1	18.6 ± 0.3	18.8 ± 0.4
11.2	17.0 ± 0.8	17.8 ± 0.5	17.4 ± 0.6
12.2	17.0 ± 0.5	18 ± 1	17.7 ± 0.09

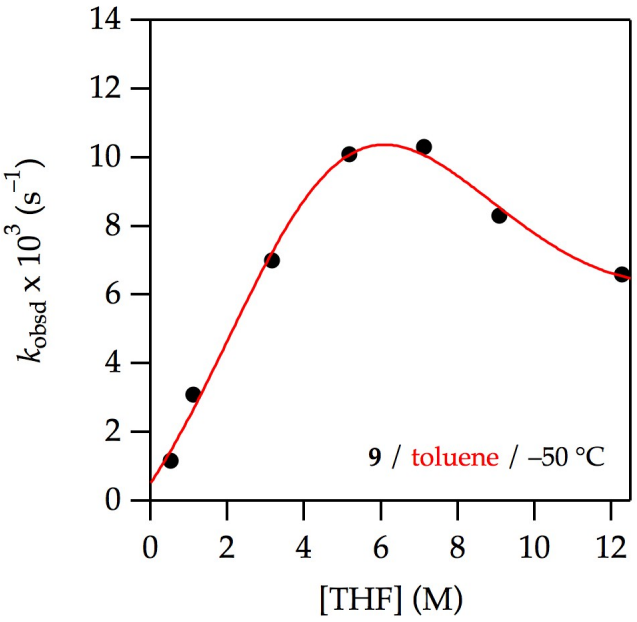

Figure A.5.12. Plot of k_{obsd} vs [THF] for the enolization of 0.0050 M oxazolidinone **9** with 0.050 M LiHMDS at various concentrations of THF in toluene at –50 ºC. The curve depicts the result of an unweighted least-squares fit to eq 16 ($[A]_0$ is set at 0.05; K_{eq} is set at 1.0×10^{-4} ; $k_8 = (2.7) \times 10^{-1}$; $k_9 = (7.9) \times 10^{-7}$; $k_{10} = (1.4) \times 10^{-2}$; $k_{11} = (0.0)$; $a = (-1.9) \times 10^{-3}$; $b = (2.0) \times 10^{-3}$; c is set at 1 ; m is set to 3).

[THF] (M)	$k_{obsd} \times 10^3$ (s^{-1})
0.52	1.17 ± 0.02
1.1	3.10 ± 0.09
326	7.0 ± 0.3
5.2	10.1 ± 0.4
7.1	10.3 ± 0.2
9.1	8.3 ± 0.2
12.3	6.6 ± 0.1

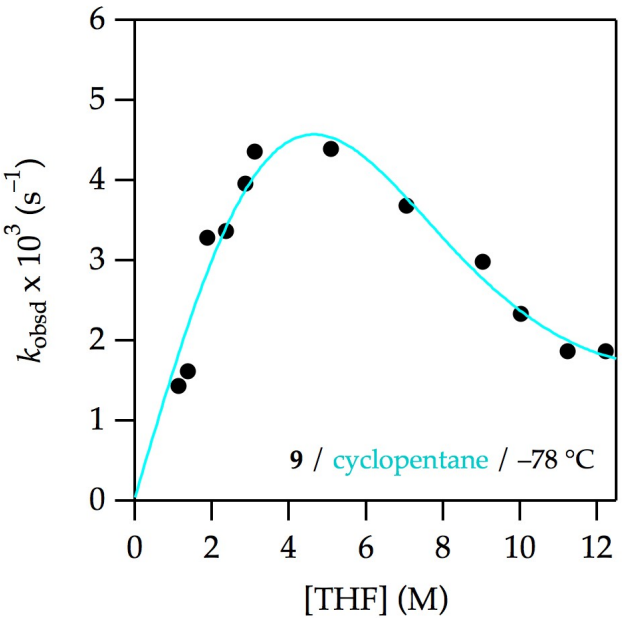

Figure A.5.13. Plot of k_{obsd} vs [THF] for the enolization of 0.0050 M oxazolidinone **9** with 0.10 M LiHMDS at various concentrations of THF in cyclopentane at –78 ºC. The curve depicts the result of an unweighted least-squares fit to eq 16 ($[A]_0$ is set at 0.10; $K_{eq} = (1.2 \pm 0.3) \times 10^{-4}$; $k_8 = (3.3 \pm 0.2) \times 10^{-2}$; $k_9 = (2.9) \times 10^{-8}$; k_{10} is set at 2.0×10^{-4}; $k_{11} = (6.0) \times 10^{-11}$.

[THF] (M)	$k_{obsd}{}^1 \times 10^3$ (s^{-1})	$k_{obsd}{}^2 \times 10^3$ (s^{-1})
1.1	1.43 ± 0.02	
1.4		1.62 ± 0.03
1.9		3.28 ± 0.04
2.4		3.37 ± 0.05
2.9		3.96 ± 0.06
3.1	4.36 ± 0.04	
5.1	4.39 ± 0.09	
7.0	3.68 ± 0.06	
9.0	2.98 ± 0.05	
10.0		2.33 ± 0.03
11.2		1.87 ± 0.03
12.2	1.87 ± 0.02	

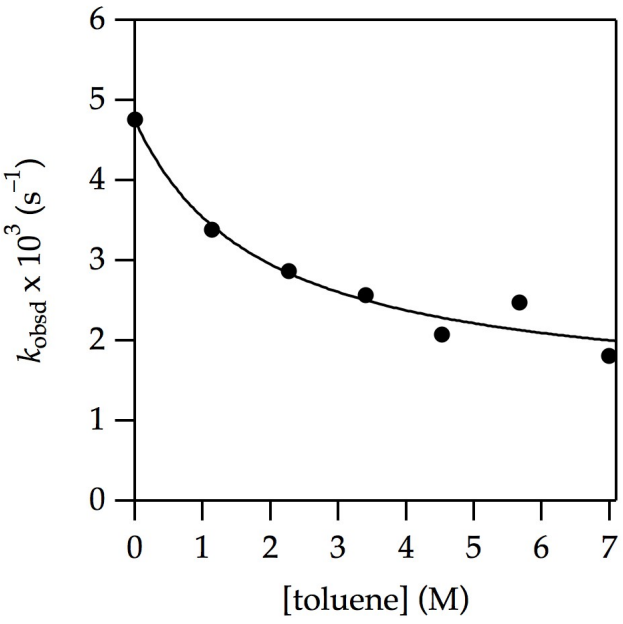

Figure A.5.14. Plot of k_{obsd} vs [toluene] for the enolization of 0.0050 M oxazolidinone **9** with 0.10 M LiHMDS at various concentrations of toluene in 3.1 M THF–hexane at –78 ºC. The curve depicts the result of an unweighted least-squares fit to $f(x) = (a + bx)/(1 + cx)$, ($a = (4.7 \pm 0.2) \times 10^{-3}$, $b = (7 \pm 5) \times 10^{-4}$, $c = 0.5 \pm 0.2$).

[toluene] (M)	$k_{obsd} \times 10^3$ (s^{-1})
0	4.8 ± 0.1
1.1	3.39 ± 0.05
2.3	2.87 ± 0.04
3.4	2.57 ± 0.03
4.5	2.08 ± 0.03
5.7	2.48 ± 0.03
7.0	1.81 ± 0.02

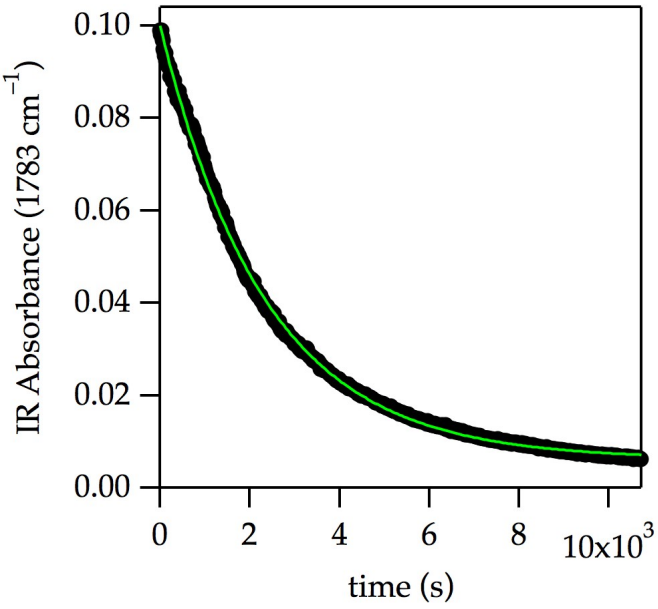

Figure A.5.15. Lithiation of oxazolidinone **9**-d_2 with equimolar LiHMDS in neat THF at –78 °C showing the loss of **9**-d_2. The decay was fit to the first-order function $f(t) = a + be^{-kt}$ [$a = (6.17 \pm 0.06) \times 10^{-3}$; $b = (9.44 \pm 0.01) \times 10^{-2}$; $k = (4.27 \pm 0.01) \times 10^{-4}$ s^{-1}]. The origin of the fit to the first-order function in the stoichiometric enolization stems from a non-linear relation between IR absorbance and [**9**] at > 0.015 M of **9** (deviation from Beer's law).

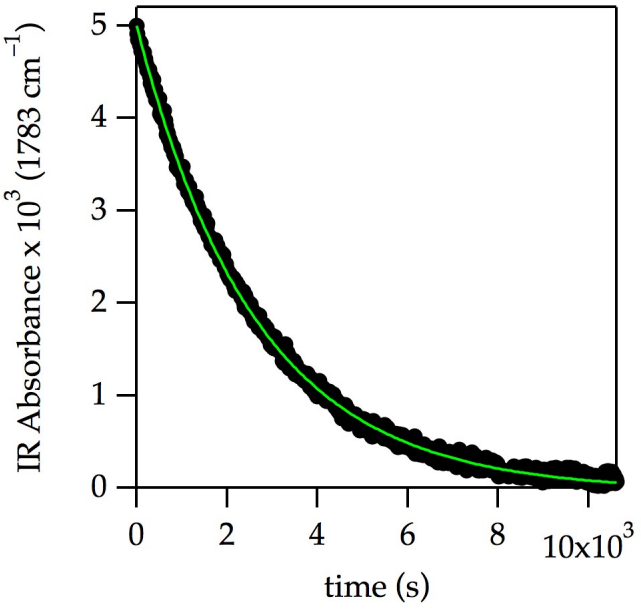

Figure A.5.16. Lithiation of 0.0050 M oxazolidinone **9**-d_2 with 0.10 M LiHMDS in neat THF at –78 °C showing the loss of **9**-d_2 (pseudo-first-order conditions). The decay was fit to $f(t) = a + be^{-kt}$ [$a = (-3.7 \pm 0.6) \times 10^{-5}$; $b = (5.03 \pm 0.06) \times 10^{-3}$; $k = (2.55 \pm 0.01) \times 10^{-4}$ s^{-1}].

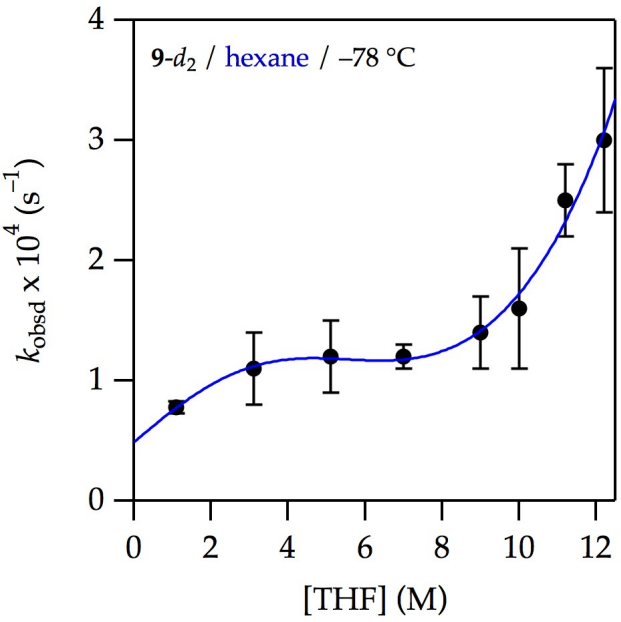

Figure A.5.17. Plot of k_{obsd} vs [THF] for the enolization of 0.0050 M oxazolidinone **9**-d_2 with 0.10 M LiHMDS at various concentrations of THF in hexane at –78 ºC. The curve depicts the result of an unweighted least-squares fit to eq 16 ($[A]_0$ is set at 0.10; $K_{eq} = (1.1 \pm 1) \times 10^{-4}$; $k_8 = (5 \pm 4) \times 10^{-4}$; $k_9 = (8) \times 10^{-9}$; $k_{10} = (2 \pm 1) \times 10^{-4}$; $k_{11} = (7 \pm 3) \times 10^{-11}$).

[THF] (M)	$k_{obsd}^{1} \times 10^4$ (s^{-1})	$k_{obsd}^{2} \times 10^4$ (s^{-1})	$k_{obsd}^{avg} \times 10^4$ (s^{-1})
1.1	0.750 ± 0.003	0.817 ± 0.003	0.78 ± 0.05
3.1	0.911 ± 0.009	1.30 ± 0.01	1.1 ± 0.3
5.1	0.934 ± 0.005	1.37 ± 0.01	1.2 ± 0.3
7.0	1.132 ± 0.007	1.267 ± 0.006	1.2 ± 0.1
9.0	1.182 ± 0.004	1.578 ± 0.009	1.4 ± 0.3
10.0	1.22 ± 0.01	1.90 ± 0.02	1.6 ± 0.5
11.2	2.27 ± 0.01	2.695 ± 0.009	2.5 ± 0.3
12.2	2.55 ± 0.01	3.44 ± 0.02	3.0 ± 0.6

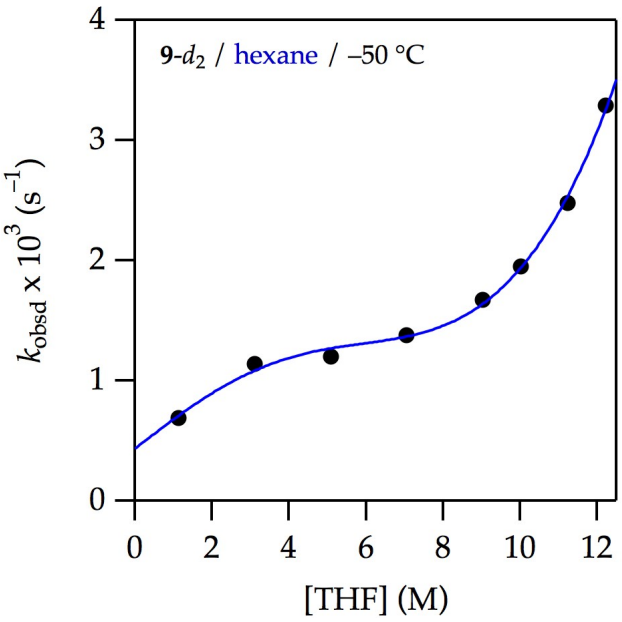

Figure A.5.18. Plot of k_{obsd} vs [THF] for the enolization of 0.0050 M oxazolidinone **9**-d_2 with 0.10 M LiHMDS at various concentrations of THF in hexane at –50 ºC. The curve depicts the result of an unweighted least-square fit to eq 16 ($[A]_0$ is set at 0.10; $K_{eq} = (5 \pm 4) \times 10^{-5}$; $k_8 = (5 \pm 2) \times 10^{-3}$; $k_9 = (5 \pm 5) \times 10^{-8}$; $k_{10} = (1.9 \pm 0.6) \times 10^{-3}$; $k_{11} = (4 \pm 1) \times 10^{-10}$).

[THF] (M)	$k_{obsd} \times 10^3$ (s^{-1})
1.1	0.69 ± 0.03 [a]
3.1	1.14 ± 0.04 [a]
5.1	1.20 ± 0.08 [a]
7.0	1.38 ± 0.02
9.0	1.67 ± 0.09
10.0	1.95 ± 0.02
11.2	2.48 ± 0.04
12.2	3.29 ± 0.07

[a] A reaction burst was observed by IR during the first 2–5 minutes of monitoring. After excluding the burst data points from the plot, the decays afforded unweighted least-squares fits to the first-order function $f(t) = a + be^{-kt}$. Extended ^{6}Li NMR and IR studies at different **9**-d_2 and THF concentrations were performed, but the origin of the burst is still unknown. However, the k_{obsd} were reproducible regardless of the presence, absence, or extent of the reaction burst.

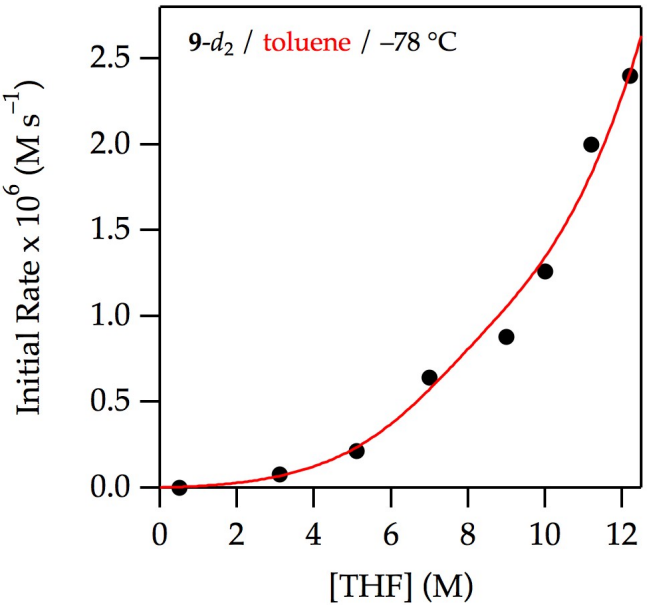

Figure A.5.19. Plot of initial rates vs [THF] for the enolization of 0.0050 M oxazolidinone **9**-d_2 with 0.10 M LiHMDS at various concentrations of THF in toluene at –78 ºC. The curve depicts the result of an unweighted least-squares fit to eq 16 (All parameters carried over from the fit from Figure A.5.17; additionally, a = (–2) × 10^{-4}; b = (1) × 10^{-4}, c = 1.57 ± 0.07, m = (5.0)).

[THF] (M)	Initial Rate × 10^6 (M s^{-1})
0.50	[a]
3.1	0.076 ± 0.002
5.1	0.215 ± 0.005
7.0	0.64 ± 0.06
9.0	0.88 ± 0.06
10.0	1.26 ± 0.08
11.2	2.0 ± 0.4
12.2	2.4 ± 0.1

[a] No reaction was observed after 2.5 hours of monitoring by IR.

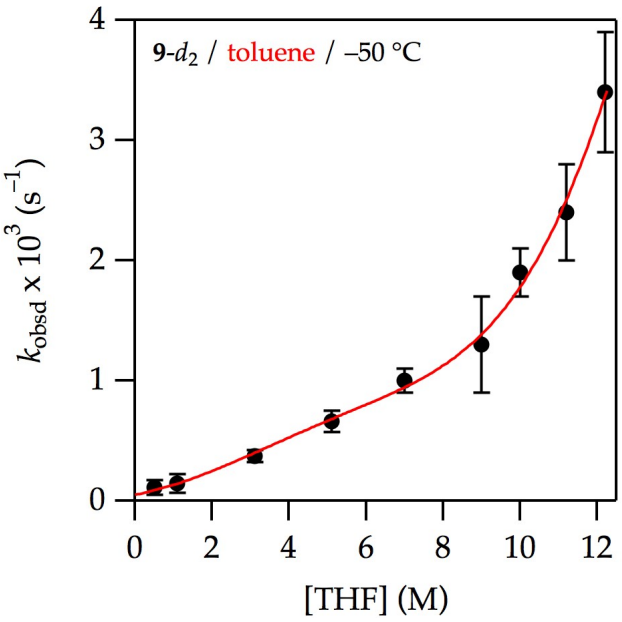

Figure A.5.20. Plot of k_{obsd} vs [THF] for the enolization of 0.0050 M oxazolidinone **9**-d_2 with 0.10 M LiHMDS at various concentrations of THF in toluene at –50 ºC. The curve depicts the result of an unweighted least-squares fit to eq 16 (All parameters carried over from the fit from Figure A.5.18; additionally, a = (–4) × 10^{-2}; b = (9) × 10^{-3}, c = (1.04), m = 1.3).

[THF] (M)	$k_{obsd}^{1} \times 10^3$ (s^{-1})	$k_{obsd}^{2} \times 10^3$ (s^{-1})	$k_{obsd}^{avg} \times 10^3$ (s^{-1})
0.50	0.153 ± 0.001	0.0642 ± 0.0005	0.11 ± 0.06
1.1	0.139 ± 0.002	0.1500 ± 0.0005	0.145 ± 0.08
3.1	0.331 ± 0.002	0.407 ± 0.001	0.37 ± 0.05
5.1	0.602 ± 0.007	0.724 ± 0.006	0.66 ± 0.09
7.0	0.866 ± 0.004	1.05 ± 0.01	1.0 ± 0.1
9.0	1.04 ± 0.01	1.64 ± 0.02	1.3 ± 0.4
10.0	1.72 ± 0.02	2.02 ± 0.03	1.9 ± 0.2
11.2	2.14 ± 0.02	2.66 ± 0.03	2.4 ± 0.4
12.2	3.71 ± 0.05	3.06 ± 0.03	3.4 ± 0.5

LiHMDS orders

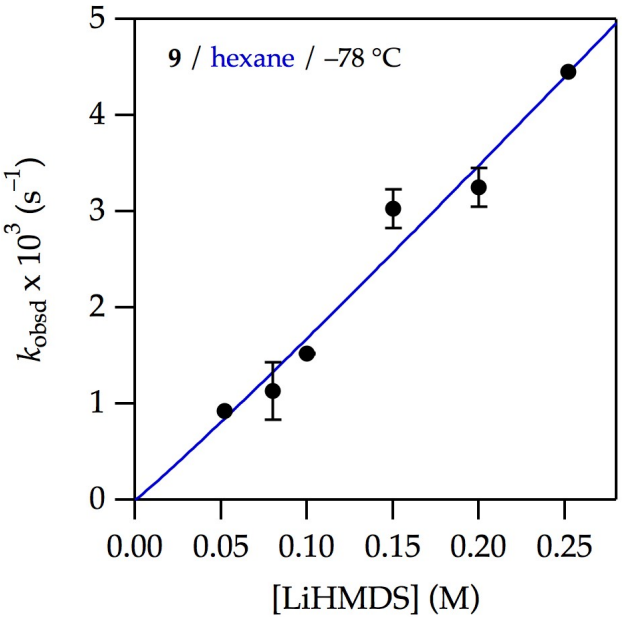

Figure A.5.21. Plot of k_{obsd} vs [LiHMDS] for the enolization of 0.0050 M oxazolidinone **9** at various concentrations of LiHMDS and 1.0 M THF–hexane at –78 ºC. The curve depicts the result of an unweighted least–squares fit to $k_{obsd} = k[\text{LiHMDS}]^n$ ($k = (1.9 \pm 0.4) \times 10^{-2}$ s^{-1}; $n = 1.1 \pm 0.1$).

[LiHMDS] (M)	$k_{obsd}^{1} \times 10^3$ (s^{-1})	$k_{obsd}^{2} \times 10^3$ (s^{-1})	$k_{obsd}^{avg} \times 10^3$ (s^{-1})
0.052		0.93 ± 0.02	
0.080	0.92 ± 0.04	1.34 ± 0.05	1.1 ± 0.3
0.10	1.51 ± 0.04	1.52 ± 0.05	1.52 ± 0.01
0.16	3.20 ± 0.09	2.86 ± 0.09	3.0 ± 0.2
0.21	3.4 ± 0.1	3.1 ± 0.1	3.2 ± 0.2
0.25	4.5 ± 0.2		

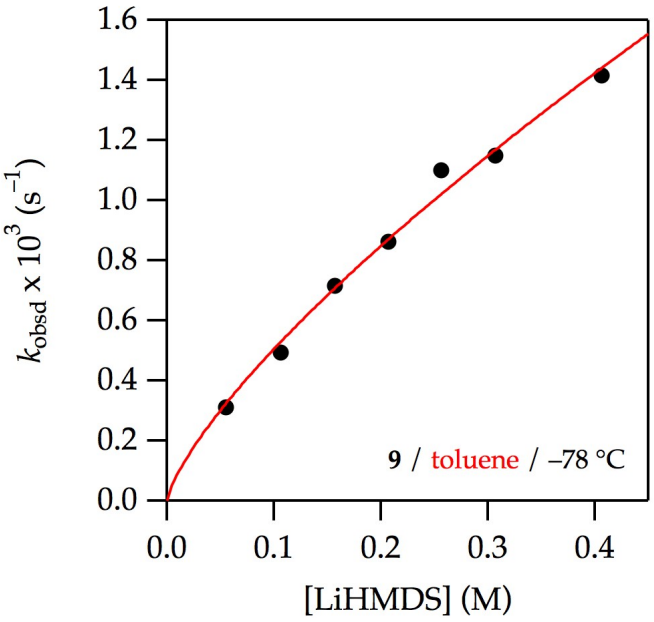

Figure A.5.22. Plot of k_{obsd} vs [LiHMDS] for the enolization of 0.0050 M oxazolidinone **9** at various concentrations of LiHMDS and 1.0 M THF–toluene at –78 ºC. The curve depicts the result of an unweighted least-squares fit to $k_{obsd} = k[\text{LiHMDS}]^n$ ($k = (2.8 \pm 0.2) \times 10^{-3}$ s^{-1}; $n = 0.75 \pm 0.04$).

[LiHMDS] (M)	$k_{obsd} \times 10^3$ (s^{-1})
0.055	0.311 ± 0.002
0.11	0.494 ± 0.006
0.16	0.717 ± 0.006
0.21	0.863 ± 0.008
0.26	1.10 ± 0.01
0.31	1.15 ± 0.01
0.41	1.42 ± 0.03

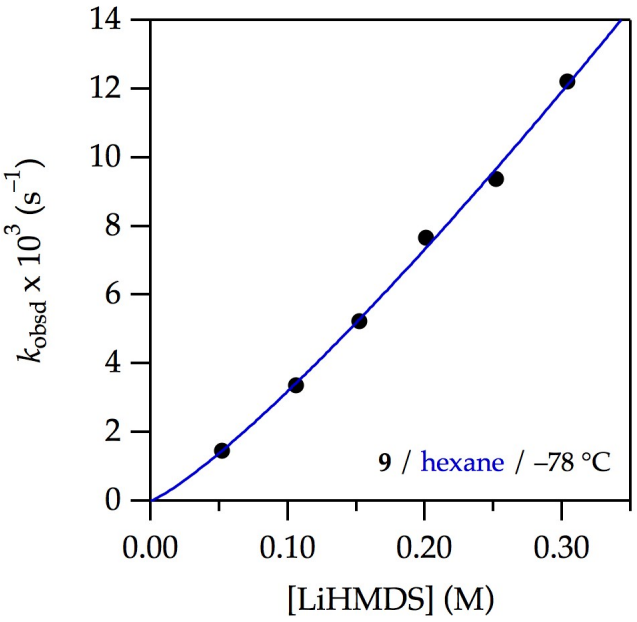

Figure A.5.23. Plot of k_{obsd} vs [LiHMDS] for the enolization of 0.0050 M oxazolidinone **9** at various concentrations of LiHMDS and 7.1 M THF–hexane at –78 ºC. The curve depicts the result of an unweighted least-squares fit to $k_{obsd} = k[\text{LiHMDS}]^n$ ($k = (5.1 \pm 0.3) \times 10^{-2}$ s^{-1}; $n = 1.20 \pm 0.04$).

[LiHMDS] (M)	$k_{obsd} \times 10^3$ (s^{-1})
0.052	1.46 ± 0.01
0.11	3.36 ± 0.04
0.15	5.24 ± 0.07
0.20	7.7 ± 0.1
0.25	9.4 ± 0.1
0.30	12.2 ± 0.3

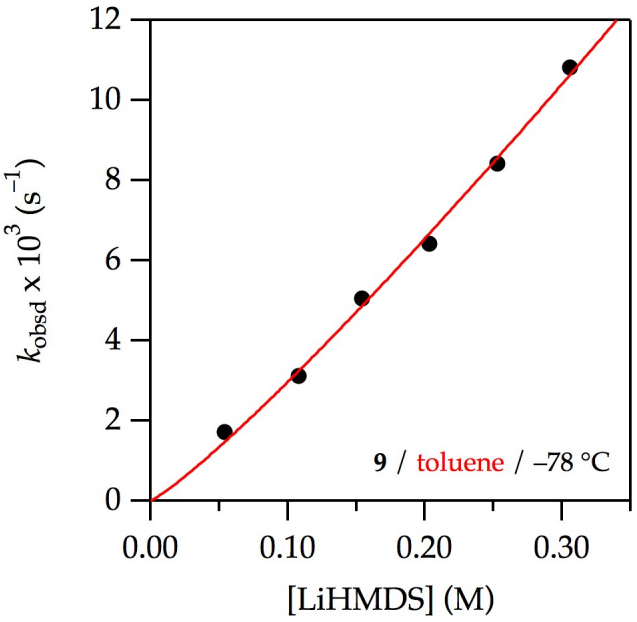

Figure A.5.24. Plot of k_{obsd} vs [LiHMDS] for the enolization of 0.0050 M oxazolidinone **9** at various concentrations of LiHMDS and 7.1 M THF–toluene at –78 ºC. The curve depicts the result of an unweighted least-squares fit to $k_{obsd} = k[\text{LiHMDS}]^n$ ($k = (4.1 \pm 0.3) \times 10^{-2}$ s^{-1}; $n = 1.14 \pm 0.05$).

[LiHMDS] (M)	$k_{obsd} \times 10^3$ (s^{-1})
0.054	1.72 ± 0.02
0.11	3.12 ± 0.04
0.15	5.05 ± 0.08
0.20	6.4 ± 0.1
0.25	8.4 ± 0.2
0.31	10.8 ± 0.4

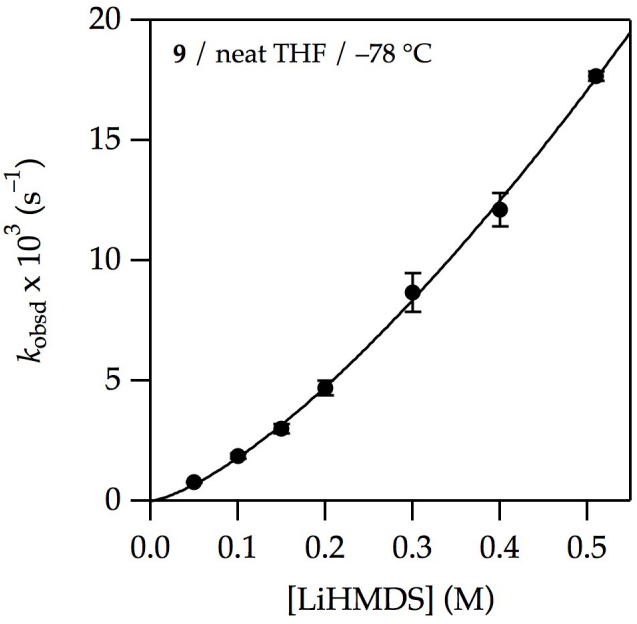

Figure A.5.25. Plot of k_{obsd} vs [LiHMDS] for the enolization of 0.0050 M oxazolidinone **9** at various concentrations of LiHMDS in neat THF at –78 ºC. The curve depicts the result of an unweighted least-squares fit to $k_{obsd} = k[\text{LiHMDS}]^n$ ($k = (4.5 \pm 0.1) \times 10^{-2}$ s^{-1}; $n = 1.40 \pm 0.03$).

[LiHMDS] (M)	$k_{obsd}^1 \times 10^3$ (s^{-1})	$k_{obsd}^2 \times 10^3$ (s^{-1})	$k_{obsd}^{avg} \times 10^3$ (s^{-1})
0.050	0.75 ± 0.01	0.798 ± 0.004	0.78 ± 0.03
0.10	1.80 ± 0.02	1.949 ± 0.009	1.9 ± 0.1
0.15	2.82 ± 0.05	3.17 ± 0.03	3.0 ± 0.2
0.20	4.48 ± 0.06	4.91 ± 0.07	4.7 ± 0.3
0.30	8.1 ± 0.2	9.3 ± 0.1	8.7 ± 0.8
0.40	11.6 ± 0.4	12.6 ± 0.4	12.1 ± 0.7
0.51	18 ± 1	17.5 ± 0.3	17.7 ± 2

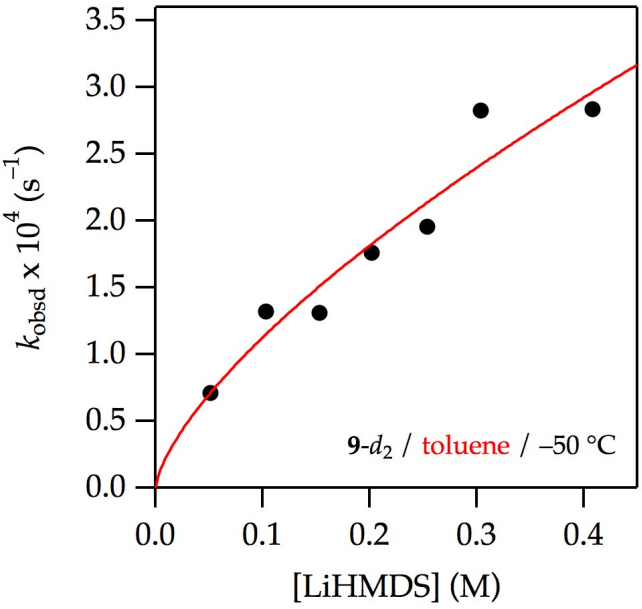

Figure A.5.26. Plot of k_{obsd} vs [LiHMDS] for the enolization of 0.0050 M oxazolidinone **9**-d_2 at various concentrations of LiHMDS and 1.0 M THF–toluene at –50 ºC. The curve depicts the result of an unweighted least-squares fit to $k_{obsd} = k[\text{LiHMDS}]^n$ ($k = (5.5 \pm 0.8) \times 10^{-4}$ s^{-1}; $n = 0.7 \pm 0.1$).

[LiHMDS] (M)	$k_{obsd} \times 10^4$ (s^{-1})
0.051	0.708 ± 0.003
0.10	1.32 ± 0.01
0.15	1.31 ± 0.01
0.20	1.76 ± 0.02
0.25	1.957 ± 0.009
0.30	2.82 ± 0.02
0.41	2.83 ± 0.03

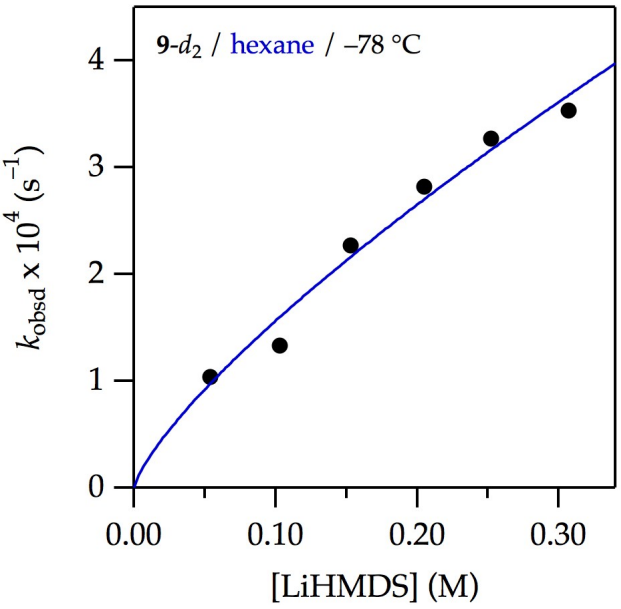

Figure A.5.27. Plot of k_{obsd} vs [LiHMDS] for the enolization of 0.0050 M oxazolidinone **9**-d_2 at various concentrations of LiHMDS and 3.1 M THF–hexane at –78 ºC. The curve depicts the result of an unweighted least-squares fit to $k_{obsd} = k[\text{LiHMDS}]^n$ ($k = (9 \pm 1) \times 10^{-4}$ s^{-1}; $n = 0.76 \pm 0.08$).

[LiHMDS] (M)	$k_{obsd} \times 10^4$ (s^{-1})
0.054	1.036 ± 0.006
0.10	1.333 ± 0.008
0.15	2.27 ± 0.01
0.20	2.82 ± 0.01
0.25	3.27 ± 0.03
0.31	3.53 ± 0.02

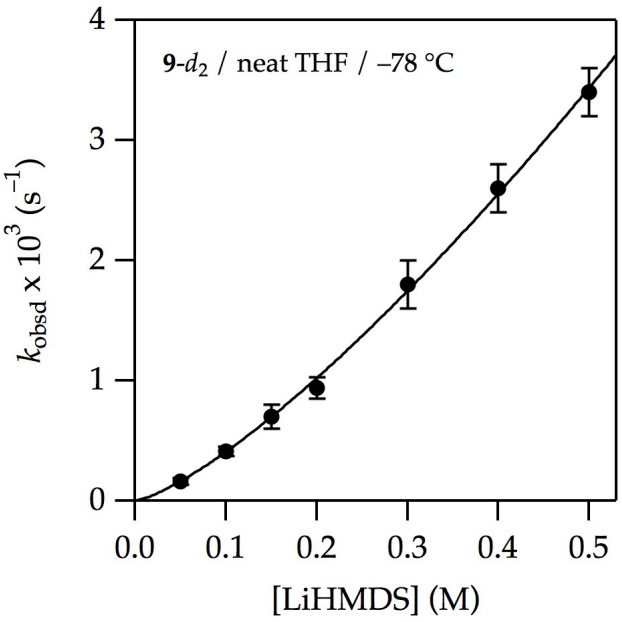

Figure A.5.28. Plot of k_{obsd} vs [LiHMDS] for the enolization of 0.0050 M oxazolidinone **9**-d_2 at various concentrations of LiHMDS in neat THF at –78 ºC. The curve depicts the result of an unweighted least-squares fit to $k_{obsd} = k[\text{LiHMDS}]^n$ ($k = (8.6 \pm 0.3) \times 10^{-3}$ s^{-1}; $n = 1.32 \pm 0.03$).

[LiHMDS] (M)	$k_{obsd}^1 \times 10^3$ (s^{-1})	$k_{obsd}^2 \times 10^3$ (s^{-1})	$k_{obsd}^{avg} \times 10^3$ (s^{-1})
0.050	0.139 ± 0.001	0.1812 ± 0.0008	0.16 ± 0.03
0.10	0.385 ± 0.005	0.440 ± 0.02	0.41 ± 0.04
0.15	0.605 ± 0.006	0.748 ± 0.004	0.7 ± 0.1
0.20	0.873 ± 0.008	0.998 ± 0.006	0.94 ± 0.09
0.30	1.66 ± 0.02	1.95 ± 0.01	1.8 ± 0.2
0.40	2.48 ± 0.04	2.78 ± 0.03	2.6 ± 0.2
0.50	3.26 ± 0.06	3.50 ± 0.06	3.4 ± 0.2

Isotope effects

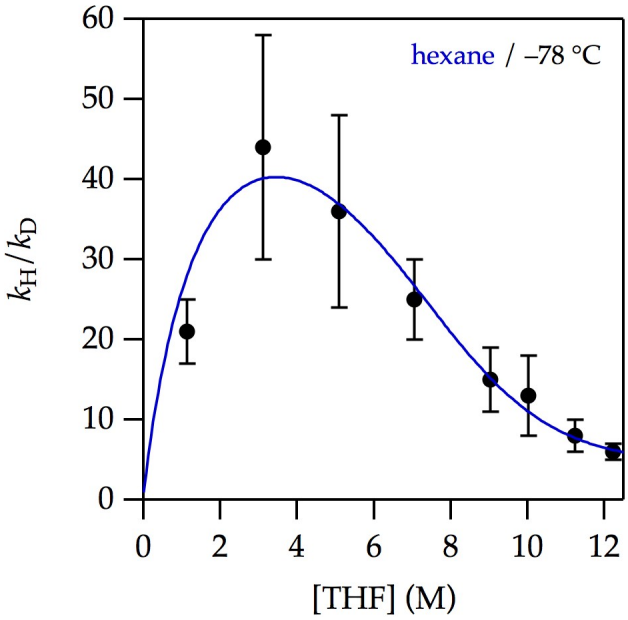

Figure A.5.29. Plot of k_H/k_D vs [THF] for the enolization of 0.0050 M oxazolidinones **9**-d_2 and **9** with 0.10 M LiHMDS at various concentrations of THF in hexane at –78 ºC. The curve depicts the result of an unweighted least-squares fit to $f(x) = (eq^H\ 16)/(eq^D\ 16)$ using the values derived from the least-squares fits to eq 16 on Figures 9 and 17 (contributions to k_H and k_D, respectively).

[THF] (M)	k_H/k_D
1.1	21 ± 4
3.1	44 ± 14
5.1	36 ± 12
7.1	25 ± 5
9.0	15 ± 4
10.0	13 ± 5
11.2	8 ± 2
12.2	6 ± 1

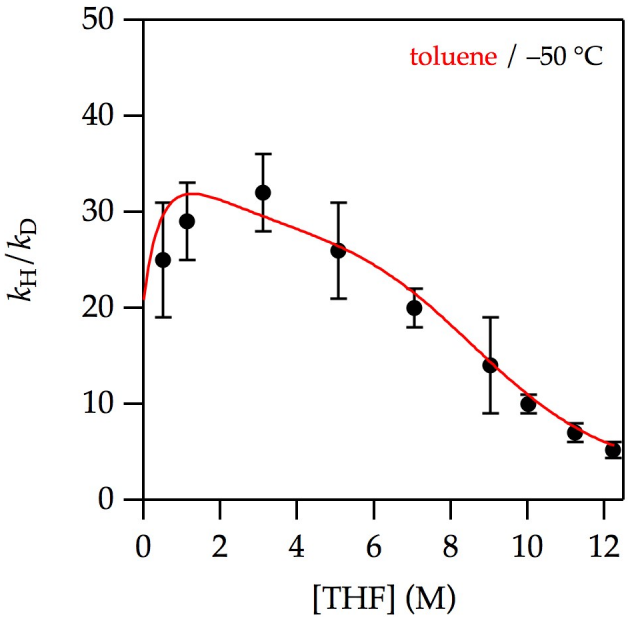

Figure A.5.30. Plot of k_H/k_D vs [THF] for the enolization of 0.0050 M oxazolidinones **9**-d_2 and **9** with 0.10 M LiHMDS at various concentrations of THF in toluene at –50 °C. The curve depicts the result of an unweighted least-squares fit to $f(x) = (\text{eq}^H\ 16)/(\text{eq}^D\ 16)$ using the values derived from the least-squares fits to eq 16 on Figures 11 and 20 (contributions to k_H and k_D, respectively).

[THF] (M)	k_H/k_D
0.50	25 ± 6
1.1	29 ± 4
3.1	32 ± 4
5.1	26 ± 5
7.1	20 ± 2
9.0	14 ± 5
10.0	10 ± 1
11.2	7 ± 1
12.2	5.2 ± 0.8

Probing for isotope effects using biphasic kinetics

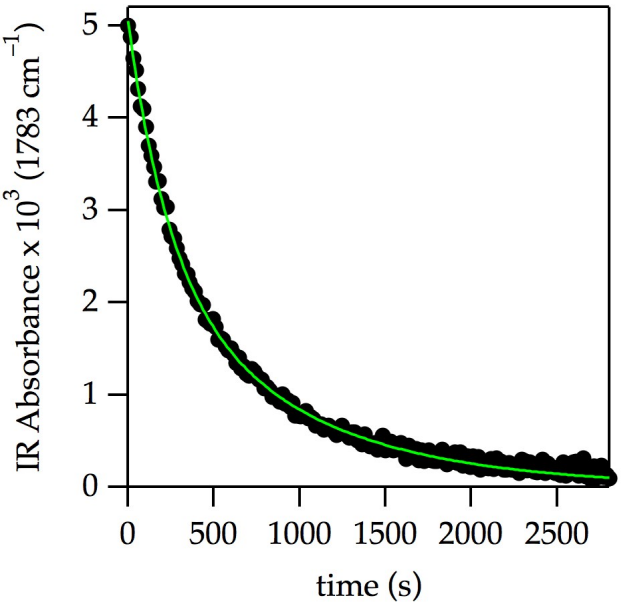

Figure A.5.31. Biphasic decay for the enolization of a 1:1 mixture of oxazolidinones **9**-d_2 and **9** (total concentration = 0.0050 M) with 0.10 M LiHMDS in neat THF at –78 ºC. The decay was fit to $f(t) = a[(\exp(-k_H t) + (\exp(-k_D t)]$, $a = (2.52 \pm 0.01) \times 10^{-3}$, $k_H = (4.24 \pm 0.09) \times 10^{-3}$ s^{-1}, $k_D = (1.1149 \pm 0.008) \times 10^{-3}$ s^{-1}; $\boldsymbol{k_H/k_D = 3.8}$.

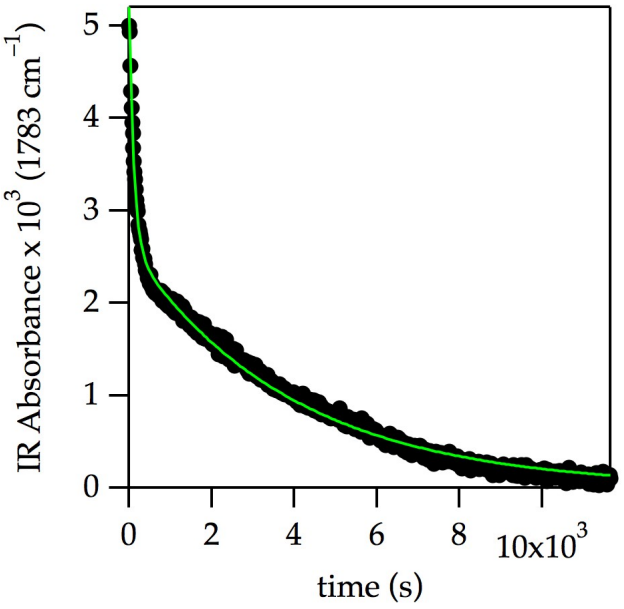

Figure A.5.32. Biphasic decay for the enolization of a 1:1 mixture of oxazolidinones **9**-d_2 and **9** (total concentration = 0.0050 M) with 0.10 M LiHMDS in 3.1 M THF–hexane at –78 ºC. The decay was fit to $f(t) = a[(\exp(-k_H t) + (\exp(-k_D t)]$, $a = (2.617 \pm 0.009) \times 10^{-3}$, $k_H = (8.5 \pm 0.2) \times 10^{-3}$ s^{-1}, $k_D = (2.55 \pm 0.01) \times 10^{-4}$ s^{-1}; $\boldsymbol{k_H/k_D = 33}$.

Contributions of individual enolization pathways to k_{obsd}

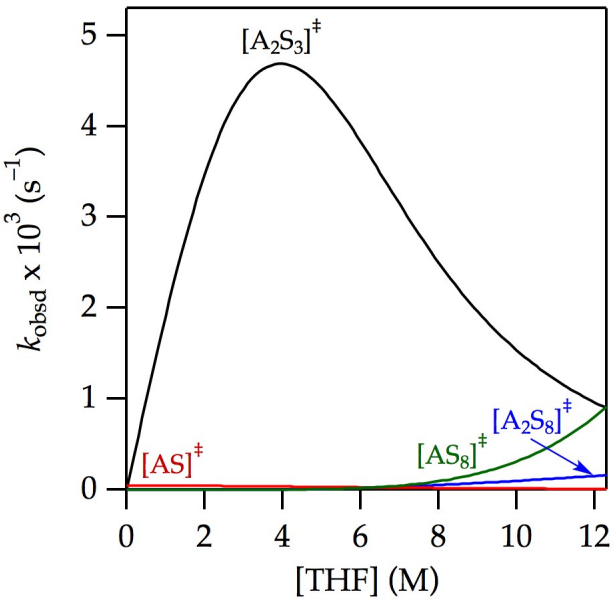

Figure A.5.33. Contributions of **$[A_2S_3]^‡$**, $[AS]^‡$, $[A_2S_8]^‡$, and $[AS_8]^‡$ for the enolization of oxazolidinone **9** in THF–hexane at –78 °C from Figure A.5.9 (see caption).

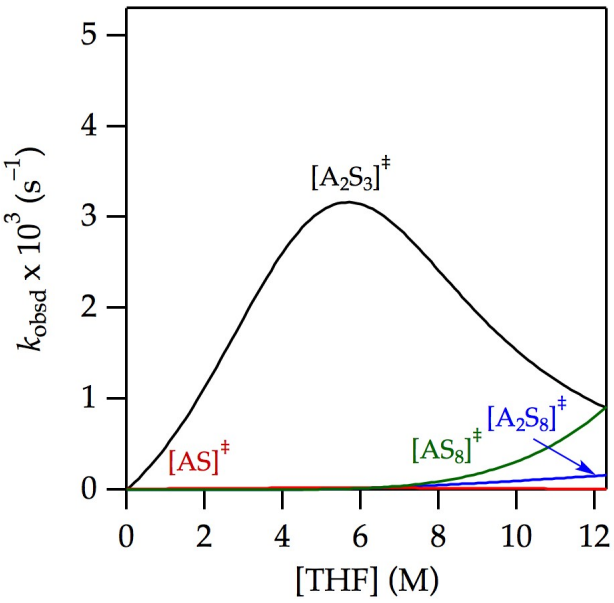

Figure A.5.34. Contributions of **$[A_2S_3]^‡$**, $[AS]^‡$, $[A_2S_8]^‡$, and $[AS_8]^‡$ for the enolization of oxazolidinone **9** in THF–toluene at –78 °C from Figure A.5.10 (see caption).

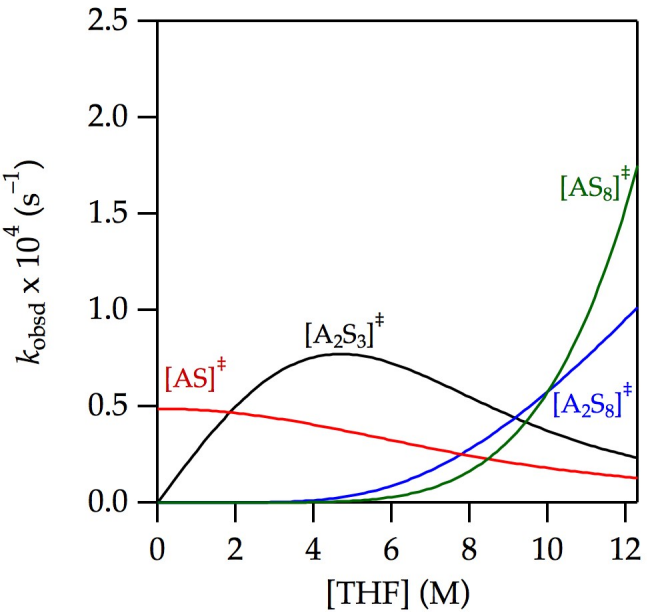

Figure A.5.35. Contributions of **$[A_2S_3]^‡$**, $[AS]^‡$, $[A_2S_8]^‡$, and $[AS_8]^‡$ for the enolization of oxazolidinone **9**-d_2 in THF–hexane at –78 °C from Figure A.5.17 (see caption).

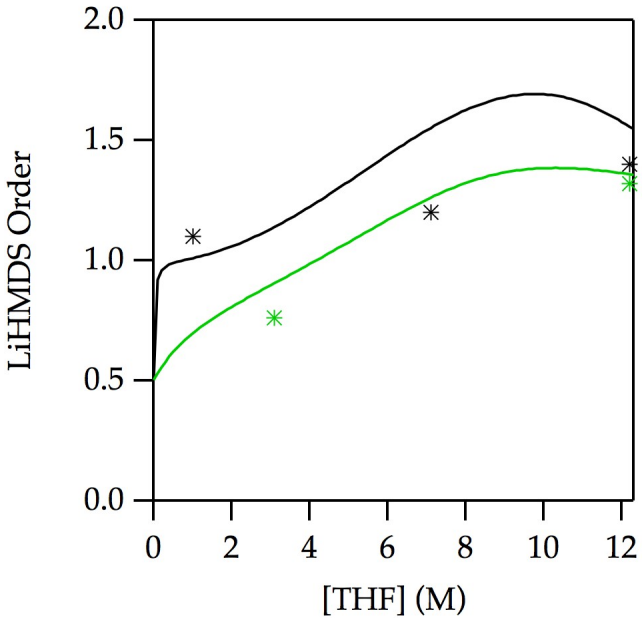

Figure A.5.36. Predicted LiHMDS order vs THF concentration for **9** (black trace overlaid on observed orders) and **9**-d_2 (green trace overlaid on observed orders). All parameters were carried over from the fits in Figures 9 and 17.

VII. Appendix A

Revisiting the LiHMDS-mediated enolization of 2-methylcyclohexanone

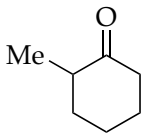

3

i. Rate studies

By including constraints applied by the dependencies on THF concentration, and cosolvent choice, the subset of mechanisms required to *fit all data* reduces to one (eq 17) that is described by eq 18. This is true for *all* fits on plots of k_{obsd} vs [S] (S = THF) for the enolization of 2-methylcyclohexanone **3**.

$$\tfrac{1}{2}\,A_2S_2 + S \rightleftharpoons AS_2 + \mathbf{3} \xrightarrow{k} [AS_2\bullet\mathbf{3}]^{\ddagger} \tag{17}$$

$$k_{obsd} = f\left(\left[S\right]\right)\left\{\left(k\left[S\right]\right)\left(\frac{4\left[A\right]_0 + K_{eq}\left[S\right]^4 - \sqrt{K_{eq}}\left[S\right]^2\sqrt{8\left[A\right]_0 + K_{eq}\left[S\right]^4}}{8}\right)^{\frac{1}{2}} + \right. \tag{18}$$

$$\text{where } f\left(\left[S\right]\right) = \begin{cases} 1 \text{ for hexane} \\ \dfrac{a\left(12.3 - \left[S\right]\right)^m}{1 + b\left(12.3 - \left[S\right]\right)^m} + c \text{ for toluene} \end{cases}$$

Eq 18 is the general equation used for the unweighted least-squares fits on all the plots of k_{obsd} vs [S] for the enolization of 2-methylcyclohexanone **3**.

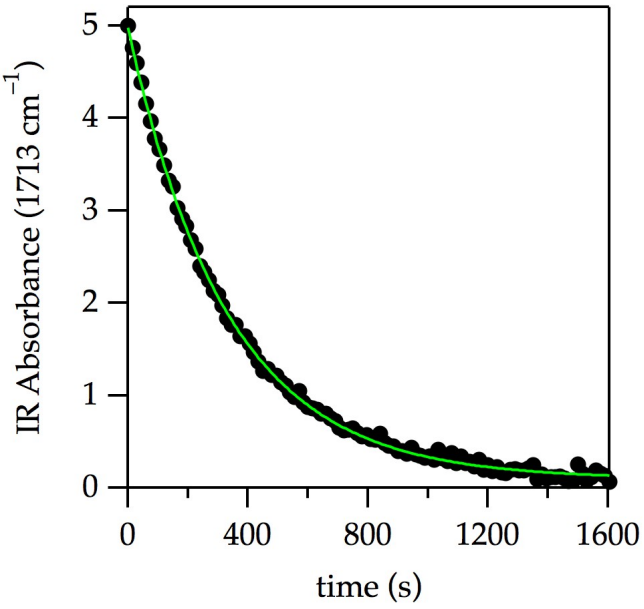

Figure A.5.37. Lithiation of 0.0050 M 2-methylcyclohexanone **3** with 0.10 M LiHMDS and 9.0 M THF–hexane at –78 °C showing the loss of **3** (pseudo-first-order conditions). The decay was fit to $f(t) = a + be^{-kt}$ [$a = (9.5 \pm 0.8) \times 10^{-5}$; $b = (4.88 \pm 0.02) \times 10^{-3}$; $k = (3.02 \pm 0.02) \times 10^{-3}$ s^{-1}].

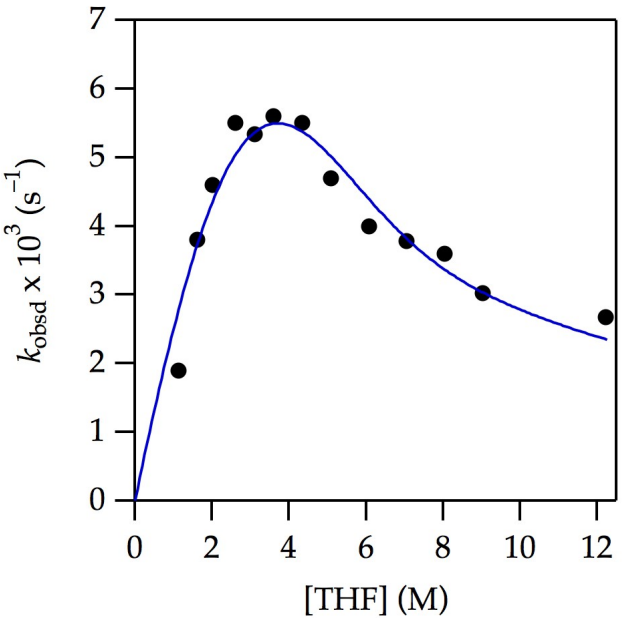

Figure A.5.38. Plot of k_{obsd} vs [THF] for the enolization of 0.0050 M 2-methylcyclohexanone **3** with 0.10 M LiHMDS at various concentrations of THF in hexane at –78 °C. The curve depicts the result of an unweighted least-squares fit to eq 18 ($[A]_0$ is set at 0.10; $K_{eq} = (1.7 \pm 0.3) \times 10^{-2}$; $k = (2.4 \pm 0.1) \times 10^{-2}$).

[THF] (M)	$k_{obsd}{}^1 \times 10^3$ (s^{-1})	$k_{obsd}{}^2 \times 10^3$ (s^{-1})
1.1	1.90 ± 0.01	
1.6		3.8 ± 0.1
2.0	4.6 ± 0.2	
2.6		5.5 ± 0.2
3.1	5.34 ± 0.08	
3.6		5.6 ± 0.2
4.3		5.5 ± 0.2
5.1	4.7 ± 0.1	
6.1		4.0 ± 0.1
7.0	3.78 ± 0.05	
8.0		3.6 ± 0.1
9.0	3.02 ± 0.02	
12.2	2.67 ± 0.02	

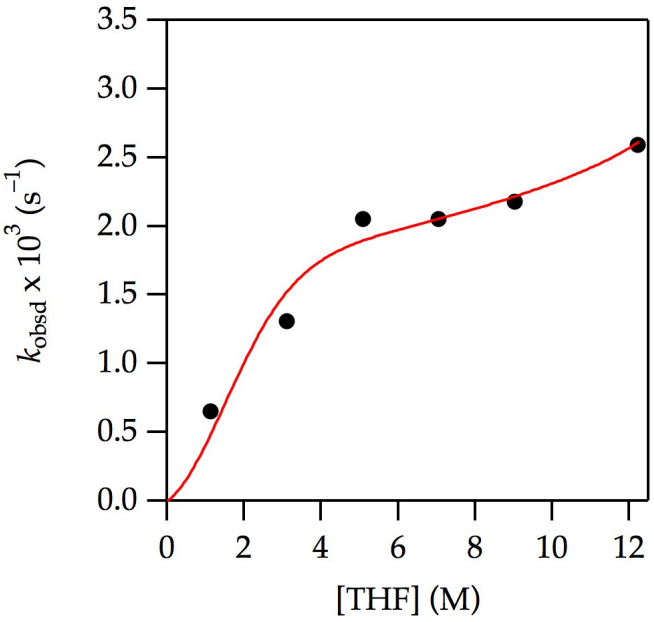

Figure A.5.39. Plot of k_{obsd} vs [THF] for the enolization of 0.0050 M 2-methylcyclohexanone **3** with 0.10 M LiHMDS at various concentrations of THF in toluene at –78 °C. The curve depicts the result of an unweighted least-squares fit to eq 18 (All parameters carried over from the fit from Figure A.5.38; additionally, $a = (-8 \pm 7) \times 10^{-2}$; $b = (8 \pm 6) \times 10^{-2}$, $c = (5.58 \pm 0.5) \times 10^{-1}$, $m = 1.0 \pm 0.8$).

[THF] (M)	$k_{obsd} \times 10^3$ (s^{-1})
1.1	0.65 ± 0.02
3.1	1.31 ± 0.03
5.1	2.05 ± 0.06
7.0	2.05 ± 0.07
9.0	2.18 ± 0.09
12.2	2.59 ± 0.05

Enolization of **3** in THF/toluene was previously studied, and the data was fitted to the equation $f(x) = (a + bx)/(1 + cx)$.[S3] Our values are equal to the ones previously determined within experimental error. Data from ref S3 was succesfully fitted using eq 18 with the same parameters presented above (see figure caption).

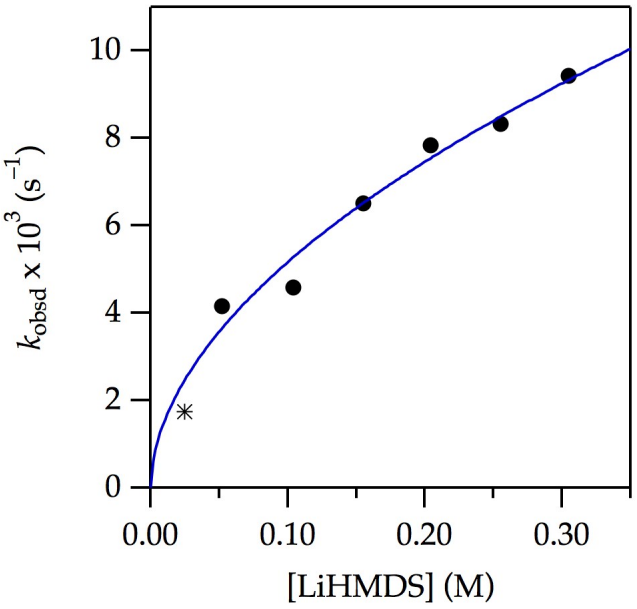

Figure A.5.40. Plot of k_{obsd} vs [LiHMDS] for the enolization of 0.0050 M 2-methylcyclohexanone **3** at various concentrations of LiHMDS and 2.0 M THF–hexane at –78 ºC. The curve depicts the result of an unweighted least-squares fit to $k_{obsd} = k[\text{LiHMDS}]^n$ ($k = (1.7 \pm 0.2) \times 10^{-2}$ s^{-1}; $n = 0.53 \pm 0.06$). The * denotes a measured point that was not included in the fit.

[LiHMDS] (M)	$k_{obsd} \times 10^3$ (s^{-1})
0.026	1.7 ± 0.5 *
0.052	4.16 ± 0.07
0.10	4.6 ± 0.2
0.15	6.5 ± 0.2
0.20	7.8 ± 0.4
0.25	8.3 ± 0.3
0.30	9.4 ± 0.9

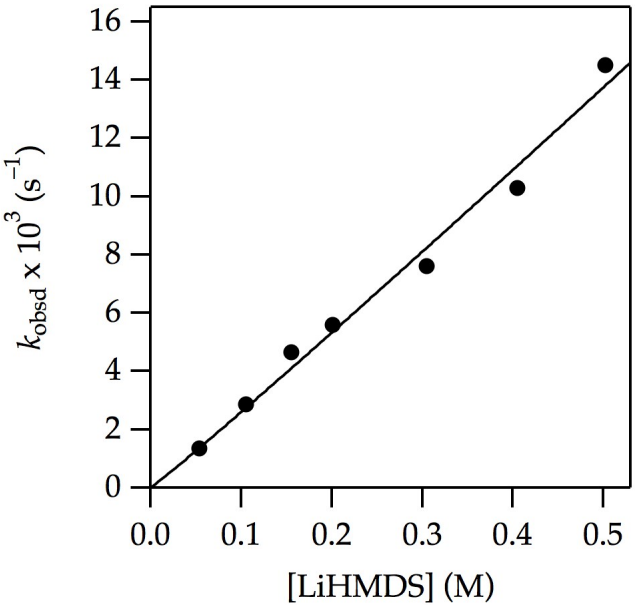

Figure A.5.41. Plot of k_{obsd} vs [LiHMDS] for the enolization of 0.0050 M 2-methylcyclohexanone **3** at various concentrations of LiHMDS in neat THF at –78 ºC. The curve depicts the result of an unweighted least-squares fit to $k_{obsd} = k[\text{LiHMDS}]^n$ ($k = (2.8 \pm 0.2) \times 10^{-2}$ s^{-1}; $n = 1.03 \pm 0.08$).

[LiHMDS] (M)	$k_{obsd} \times 10^3$ (s^{-1})
0.055	1.35 ± 0.01
0.10	2.86 ± 0.04
0.15	4.66 ± 0.09
0.20	5.6 ± 0.1
0.30	7.6 ± 0.2
0.40	10.3 ± 0.5
0.50	14.5 ± 0.8

Chart A.5.3. Substrates, transition structures and activation energies.

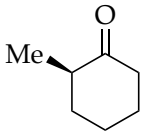

3$_{ax}$

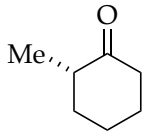

3$_{eq}$

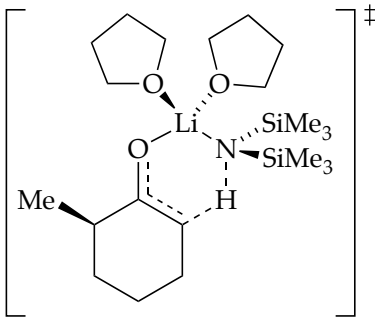

20$_{ax}$

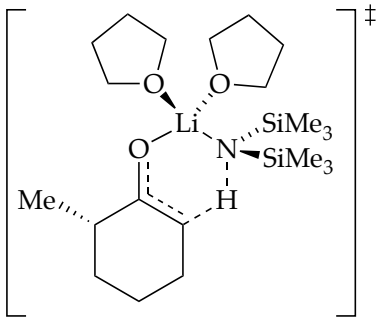

20$_{eq}$

[AS$_2$•**3**$_{ax}$]‡

$\Delta G^{‡}_{anti}$ = 10.9 kcal/mol
$\Delta G^{‡}_{syn}$ = 10.5 kcal/mol

[AS$_2$•**3**$_{eq}$]‡

$\Delta G^{‡}_{anti}$ = 10.4 kcal/mol
$\Delta G^{‡}_{syn}$ = 12.9 kcal/mol

Chapter 6

Lithium Diisopropylamide: Non-Equilibrium Kinetics and Lessons Learned about Rate Limitation

Lithium Diisopropylamide: Non-Equilibrium Kinetics and Lessons Learned about Rate Limitation

Abstract

The kinetics of lithium diisopropylamide (LDA) in tetrahydrofuran under non-equilibrium conditions are reviewed. These conditions correspond to a class of substrates in which the rates of LDA aggregation and solvation events are comparable to the rates at which various fleeting intermediates react with substrate. Substrates displaying these reactivities, by coincidence, happen to be those that react at tractable rates on laboratory timescales at –78 °C. In this strange region of non-limiting behavior, rate-limiting steps are often poorly defined, sometimes involve deaggregation and at other times include reaction with substrate. Changes in conditions routinely cause shifts in the rate-limiting steps, and autocatalysis is prevalent and can be acute. The studies are described in three distinct portions: (1) methods and strategies used to deconvolute complex reaction pathways, (2) the resulting conclusions about organolithium reaction mechanisms, and (3) perspectives on the concept of rate limitation reinforced by studies of LDA in tetrahydrofuran at –78 °C under non-equilibrium conditions.

Lithium diisopropylamide (LDA), a highly reactive and selective Brønsted base, stands among the most prominent reagents in organic synthesis.[1] A survey of 500 total syntheses revealed that LDA is one of the most commonly used reagents.[2] In the world of structural and mechanistic organolithium chemistry in which solvent-dependent aggregation and mixed aggregation impart enormous structural and mechanistic

complexity,[3] LDA has appeal for the study of structure–reactivity relationships owing to its relative structural simplicity: it exists exclusively as disolvated dimers in most coordinating solvents.[4] That said, tetrahydrofuran (THF)-mediated deaggregation of LDA, depicted in Scheme 6.1 (**1**–**6**), exemplifies only a few of the many structural forms that can occur fleetingly in solution at full equilibrium. Include the plethora of possible mixed aggregates formed from LDA and other lithium salts (LiX), and it is clear that even the simplest organolithium reagent offers the potential for breathtaking mechanistic complexity.[5]

Scheme 6.1. Simplified deaggregation of LDA dimer to monomer. Reproduced from ref 8e. Copyright 2011 American Chemical Society.

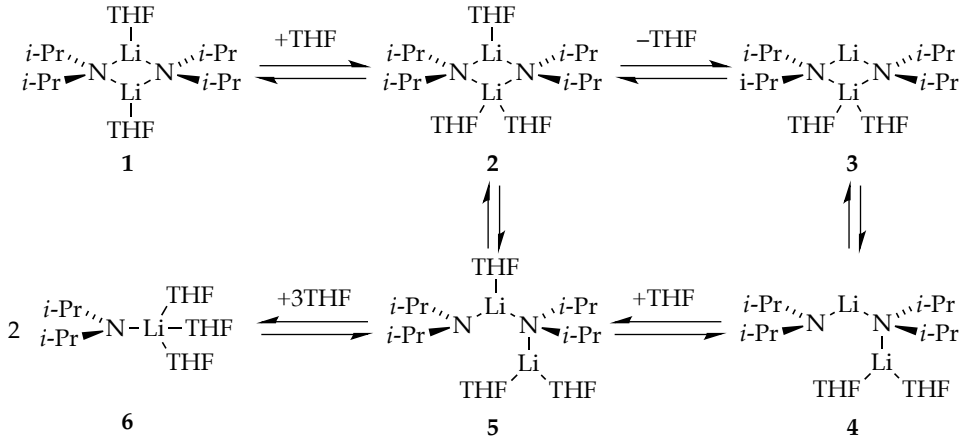

This review of the chemistry of LDA is our second. The first described investigations that probed mechanistic pathways—nearly a dozen amide–solvent stoichiometries in the rate-limiting transition states—that become available when LDA

solvated by standard coordinating solvents reacts with various electrophiles.[6,7] We thought we were nearing a logical end point, but that proved to be premature. We had assiduously avoided studying metalations at –78 °C based on the misguided notion that dry ice–acetone baths would provide inadequate temperature control. Reevaluating this bias, we discovered an extraordinary coincidence that forms the foundation of this review: LDA-mediated metalations in THF at –78 °C—conditions that are of singular importance in organic synthesis—occur at nearly the rates at which the aggregates in Scheme 6.1 exchange. The resulting mechanistic complexity proved high even by organolithium standards, and the effort expended to understand metalations under such non-equilibrium conditions would have been difficult to justify for reagents of lesser importance. This base was the iconic LDA, however.

Eight publications form the core of this second review.[8] LDA, however, is only one part of a three-part story. Section 1 is a tutorial that delineates the methods and tactics used to untangle the interwoven mechanistic pathways, in particular, when rate-limiting steps routinely change. These strategies and principles are generally applicable to the deconvolution of complex ensembles of mechanisms. Section 2 summarizes the specifics of LDA-mediated metalations under non-equilibrium conditions. Rather than re-adjudicating the cases, we merely summarize observations that are of potential interest to mechanistic organolithium and synthetic chemists. Section 3 focuses on seemingly simple notions of rate limitation emanating from rate studies that may be counterintuitive and possibly even difficult to accept. We begin by illustrating why this particular subset of LDA-mediated metalations is so strange.

Background. LDA-mediated metalations as well as all other organolithium reactions can be described using three scenarios (Figure 6.1). The dimensionless concept of reactivity in Figure 6.1 can be construed as the reaction temperature required to monitor a reaction on laboratory timescales using standard kinetic methods. Complexity, also a dimensionless entity, will become clear in the forthcoming description of scenario 3.

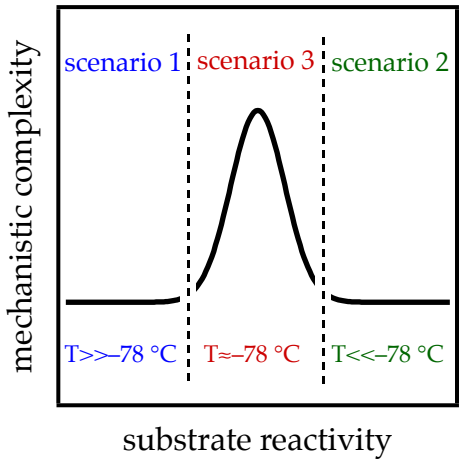

Figure 6.1. Abstract depiction of mechanistic complexity in the limit of fast aggregate exchange (scenario 1), aggregate non-exchange (scenario 2), and non-equilibrium aggregate exchange (scenario 3).

Scenario 1: Fast aggregate exchange. In the limit that all aggregates rapidly equilibrate on the timescales of subsequent metalations, the mechanistic course of a reaction is dictated by the lowest barrier of the LDA-mediated proton transfer (Scheme 6.2). We rely heavily on the shorthand shown in the inset in Scheme 6.2 to simplify forthcoming discussions. For example, A_2S_2 refers to a disolvated dimer such as **1**, [A_2S_n*] connotes a spectroscopically invisible dimer of solvation number *n*, and

$[A_2S_n(ArH)]^‡$ corresponds to a transition structure for the metalation of an arene, ArH, of $A_2S_n(ArH)$ stoichiometry. LDA/THF-mediated metalations of relatively unreactive substrates are comfortably monitored from –55 °C to room temperature. Substrates necessarily undergo rate-limiting proton transfers, which display large (sometimes *very* large) primary kinetic isotope effects (KIEs).[9] Although the multitude of substrate-solvent combinations have revealed almost a dozen stoichiometrically distinct monomer- and dimer-based mechanisms,[6] one or two mechanisms usually dominate for any given substrate–solvent combination.

Scheme 6.2. Reactions of LDA via parallel pathways

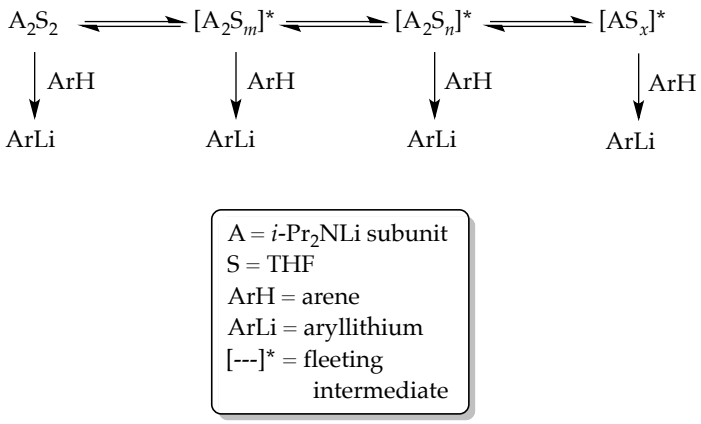

Scenario 2: Aggregate non-exchange. In the limit that an organolithium reagent reacts with substrate rapidly *relative to the rate that aggregates exchange*, only the observable aggregates are available to react (Scheme 6.3). (Solvent exchanges *may* remain rapid on the reaction timescales.) After seminal studies by McGarrity and co-workers[10,11] using rapid injection NMR spectroscopy, Reich[12] investigated a number of

organolithium reactions under conditions in which two or more aggregates are observable at the non-exchange limit. The rates were fast, and the requisite temperatures were typically much lower than –100 °C. Although the technical challenges of carrying out these reactions were considerable, the rate studies were simple: they measured the relative rates at which each observable form disappears. Fleeting intermediates were not germane.

Scheme 6.3. Reactions of aggregates that do not exchange.

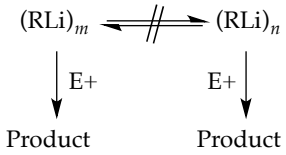

Scenario 3: Non-equilibrium aggregate exchange. There is a fateful level of substrate reactivity—a narrow temperature range required to monitor reactions on normal laboratory timescales—at which the barriers to LDA aggregate–aggregate exchanges are comparable to the barriers that fleeting structural forms react with substrates. Imagine that the equilibria in Scheme 6.1 are *not* fully established on the timescales of a metalation. In this non-limiting regime, the rate-limiting steps often become poorly defined with an affiliated spike in mechanistic complexity (Figure 6.1). Moreover, any of the fleeting intermediates could react with substrate via rate-limiting deaggregation, substrate complexation, or proton transfer (Scheme 6.4). The most viable mechanism for proton transfer could lie behind an insurmountable barrier to deaggregation.

Scheme 6.4. Rate limiting aggregation, complexation or proton transfer.

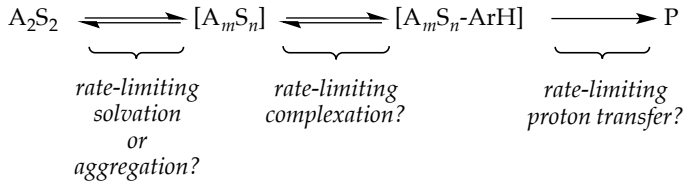

With an irony that will be lost on few, this fateful twilight zone corresponding to scenario 3 for LDA/THF-mediated metalations is centered on substrates that react on laboratory timescales (half-lives of minutes) at –78 °C. Under this non-limiting regime, rate-limiting deaggregations are commonplace. Traces of LiX—particularly LiCl—catalyze reactions at parts per million levels with marked changes in mechanisms, rates, and rate laws. LDA generated in situ from LiCl-contaminated *n*-butyllithium can have reactivities that are >100 times that of LiCl-free commercial LDA. Traces of added Et_3N-HCl bring commercial LDA to parity with LDA generated in situ. Unlike metalations in scenario 1 in which unreactive LDA–LiX mixed aggregates are autoinhibiting,[6] the resulting LiX salts cause autocatalysis under scenario 3. Plots of substrate concentration versus time display unusual curvatures in place of standard first- or second-order decays. Reactions can manifest rate-limiting deaggregations in which, paradoxically, *the rates depend on the choice of substrate but not on their concentrations (manifesting linear decays).* Simple isotopic substitution can completely change the mechanism and affiliated rate law. Relentlessly shifting rate-limiting steps resulting from seemingly inconsequential changes in reaction conditions, although confounding at the outset,

proved pivotal in unlocking insights into the reaction mechanisms and nuances of rate limitation.

1. Methods and Strategies. LDA-mediated reactions under conditions in which observable and fleeting forms are at full equilibrium (Scenario 1) are easily examined using traditional kinetic methods based on the equilibrium approximation with flooding techniques[13] or the method of initial rates.[14] These strategies were summarized in our 2007 review.[6] Non-equilibrium kinetics are more demanding, however. In this section, we provide a tutorial on our methods and strategies as well as some foundational principles of rate limitation that are easily overlooked or misunderstood. Throughout the review, illustrative simulations are used rather than the actual raw data with fits. The mathematics underlying the simulations are archived in supporting information.

1.1. Analytical Tools. A combination of ^{6}Li, ^{15}N, and ^{19}F NMR spectroscopies[4,15,16] and in situ IR spectroscopy[17] were used to determine the solvation and aggregation states of observable intermediates and monitor reaction rates. Isotopic labeling shows whether a proton transfer is rate limiting but, as our results demonstrate, offers far more than that. The method of initial rates assumes special importance because substrate decays often deviate from first order. Numerical methods are critical owing to pervasive non-limiting behaviors.

The importance of synergies cannot be overstated. Synthetic organic and physical organic chemistries together underpin this review. Classical and numerical kinetics methods are used in tandem to tease apart complex mechanisms. Kinetics and density functional theory (DFT) computational methods[18] are mutually supportive: the

computational methods offer insights that can elude experimental observations, whereas the rate data constrain the computational methods to address precise questions and comparisons.

1.2. Saturation Kinetics. Plots of initial rates or pseudo-first-order rate constants (k_{obsd}) versus the concentration of a substrate or other reagent can show first-order (or higher-order) dependence at low concentration and independence at high concentration. These so-called saturation kinetics are illustrated in Figure 6.2. Saturation behavior emerges in two mathematically interchangeable but chemically distinct ways.

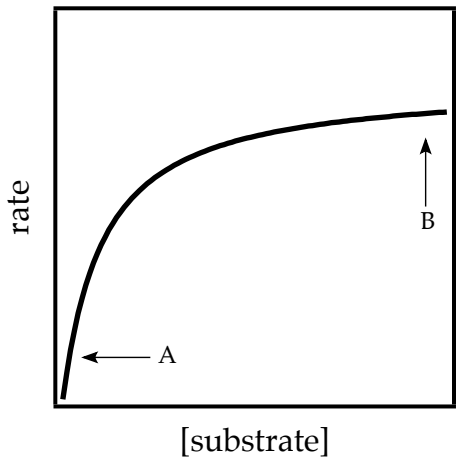

Figure 6.2. Saturation kinetics. A and B correspond to regions of substrate-concentration-dependent and substrate-concentration-independent regions.

The most prevalent origin of saturation kinetics is akin to that in Michaelis–Menten enzyme kinetics,[19] in which the catalyst is uncomplexed by the "substrate" at low substrate concentrations and becomes fully saturated, forming an *observable* substrate–catalyst complex, at high concentrations (eqs 6.1 and 6.2).[20]

Saturation Kinetics Case 1: Shifting Ground State (Michaelis–Menten Kinetics)

$$\text{reagent} + \text{substrate} \underset{k_{-1}}{\overset{k_1}{\rightleftharpoons}} \text{reagent–substrate} \xrightarrow{k_2} \text{product} \quad (6.1)$$

$$\text{d[product]}/\text{d}t = k_1k_2[\text{reagent}][\text{substrate}]/(k_{-1} + k_2[\text{substrate}]) \quad (6.2)$$

Saturation Kinetics Case 2: Shifting Rate-Limiting Step

$$\text{reagent} \underset{k_{-1}}{\overset{k_1}{\rightleftharpoons}} [\text{intermediate}] \xrightarrow{k_2[\text{substrate}]} \text{product} \quad (6.3)$$

$$\text{d[product]}/\text{d}t = k_1k_2[\text{reagent}][\text{substrate}]/(k_{-1} + k_2[\text{substrate}]) \quad (6.4)$$

An alternative, far less common form of saturation kinetics occurs when the change in substrate concentration is accompanied by a shift in the rate-limiting step (eqs 6.3 and 4).[21] Saturation occurs as the substrate concentration becomes sufficiently high to trap the fleeting intermediate efficiently. Note that cases 1 and 2 are mathematically interchangeable yet mechanistically unrelated. Case 2-type saturation dominates our investigations of non-equilibrium kinetics.

1.3. What Defines a Rate-Limiting Step? Consider a variation of case 2 using a mechanism for the A_2S_2-mediated metalation of ArH via a fleeting (high-energy) isomeric form, [A_2S_2*], to give ArLi (eq 6.5). The rate law is described by eq 6.6. To maintain focus on rate limitation, we chose an example that does not require formal deaggregation, additional solvation, or explicit substrate complexation. Rate limitation can be considered from a number of perspectives as follows.

$$A_2S_2 \underset{k_{-1}}{\overset{k_1}{\rightleftharpoons}} [A_2S_2^*] \xrightarrow{k_2[ArH]} ArLi \qquad (6.5)$$

$$d[ArLi]/dt = k_1k_2[A_2S_2][ArH]/(k_{-1} + k_2[ArH]) \qquad (6.6)$$

(1) Rate limitation is dictated by barrier heights (Figure 6.3). Proton transfer is rate limiting when its barrier is high relative to that of deaggregation (Figure 6.3; red). Conversely, deaggregation is rate limiting when the proton transfer barrier is low relative to that of deaggregation (Figure 6.3; blue).

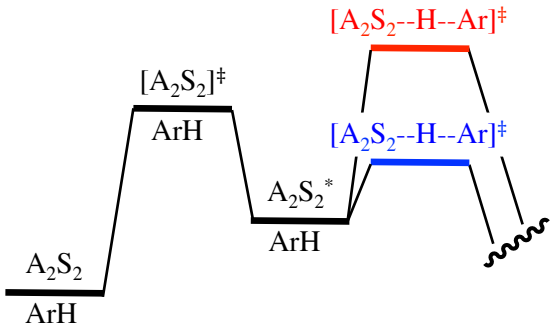

Figure 6.3. Reaction coordinate diagram for a dimer-based metalation showing rate-limiting proton transfer (red) and rate-limiting deaggregation (blue).

(2) The proton transfer in eq 6.5 can be viewed as being dictated by the *fate* of fleeting intermediate A_2S_2* by placing it in the context of the rate law (eq 6.6). If A_2S_2* readily returns to starting material and only rarely proceeds to product—if $k_2[ArH] << k_{-1}$—then A_2S_2–A_2S_2* equilibrium is fully established, and the relatively infrequent proton transfer limits the rate (see Figure 6.3; red). The rate law in eq 6.6 reduces to eq 6.7, showing first-order dependence on substrate. Loss of ArH versus time follows a simple first-order decay (Figure 6.4, curve A). By contrast, if the proton transfer is fast relative

to reaggregation—if k_2[ArH] >> k_{-1}—intermediate A_2S_2* is converted to product each time it forms (Figure 6.3; blue). The rate law reduces to eq 6.8 and shows zeroth-order substrate dependence (Figure 6.4; blue).

$$d[ArLi]/dt = (k_1k_2/k_{-1})[A_2S_2][ArH] \quad (6.7)$$

$$d[ArLi]/dt = k_1[A_2S_2] \quad (6.8)$$

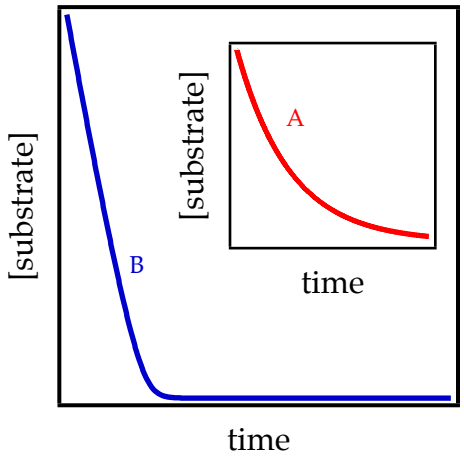

Figure 6.4. Decays of substrate ArH according to eqs 6.5 and 6.6 assuming rate-limiting proton transfer (k_2[ArH]/k_{-1} = 0.1; curve A) and rate-limiting deaggregation (k_2[ArH]/k_{-1} = 10; curve B).

(3) The substrate concentration dependence transitioning from first to zeroth order is manifested in plots of substrate concentration versus time. At low substrate concentration, the proton transfer is rate-limiting and manifests a standard exponential decay (Figure 6.4, curve A). At high substrate concentrations, the zeroth-order substrate dependencies display linear decays (Figure 6.4, curve B). Moreover, linear decays of ArH

are independent of initial concentration (Figure 6.5 and eq 6.8). Slight curvatures arise at depleting concentrations of ArH as the proton transfer begins to limit the rate (see Figure 6.5).

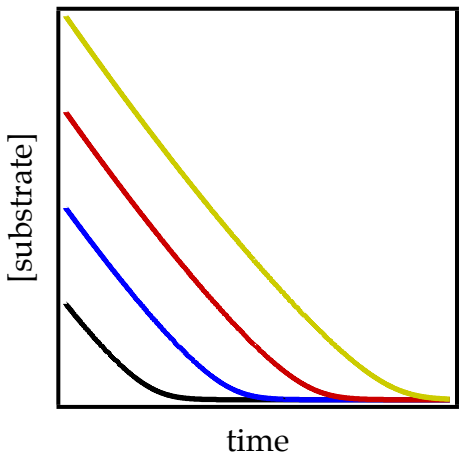

Figure 6.5. Zeroth-order decays at various initial starting concentrations of ArH showing parallel decays and the onset of rate-limiting proton transfer (curvatures) at low ArH concentration.

There is an awkward non-limiting region in which the barriers for deaggregation and proton transfer are comparable. Fleeting intermediate A_2S_2* proceeds to product and back to starting material with equal fidelity: k_2[ArH] ≈ k_{-1}. This phenomenon occurs in the highly curved (fall-off) region of Figure 6.2. The rate law in eq 6.6 does not reduce to a simple limiting form, and the resulting profile resembles an exponential decay but does not fit a first-order function. This non-limiting behavior is prevalent in metalations by LDA/THF at –78 °C.

Throughout the sections below, we cite instances of shifting rate-limiting steps.[21,22] Saturation behaviors are central to these observations. In principle, a rate-

limiting deaggregation obscures critical post-rate-limiting steps. In practice, many strategies allow us to peer over or beyond the horizon (*vide infra*).

1.4. Comments on Reaction Coordinate Diagrams. Thermochemical depictions of reaction coordinates such as those in Figure 6.3 are popular pedagogical tools of introductory chemistry courses. We find them useful to discuss non-equilibrium kinetics as well, but they are fraught with risk. Several basic principles must be adhered to for meaningful discussion.

(1) *All energy levels must be fully balanced*. Energy levels must share a common empirical formula. The balancing can be left implicit to eliminate clutter but at great peril.

(2) *Reaction coordinate diagrams necessarily represent a single snapshot of a dynamic picture.* Changes in reaction parameters—concentration, temperature, or substrate—cause the relative energies to change, and energies change continuously as a reaction proceeds. Despite some drawbacks, these reaction variables offer control over the energies. Raising the LDA concentration, for example, lowers the barriers of the more highly aggregated intermediates and transition structures relative to those of the less aggregated forms. Lowering the THF concentration raises the energies of more highly solvated forms relative to those of less solvated forms. Deuteration introduces zero-point energy (ZPE) contributions in all minima as well as in the often overlooked transition states.

(3) *Discussion of mechanism is dangerous at the murky interface where prose meets thermochemistry.* Bear with us as we try to avoid taking excessive linguistic liberties.

1.5. Multidimensionality of Rate Laws. Much the way reaction coordinate diagrams are slices of a complex picture, rate laws do not reflect a single scenario. The case of saturation kinetics arising from a shifting reaction order in one species (such as the substrate in Section 1.2), for example, is often affiliated with shifting orders in other species. Thus, reaction orders for all other species must be measured at the two limits corresponding to rate-limiting proton transfer and rate-limiting deaggregation. We frequently determine the orders in LDA at different THF concentrations to track THF-concentration-dependent changes in mechanism. In cases in which catalysis is involved (*vide infra*), detailed rate studies—full rate laws—with and without catalyst are imperative. Non-equilibrium kinetics are so sensitive to changes in conditions that even an isotopic substitution (*vide infra*) ostensibly used to measure a simple KIE demands an autonomous rate law. Similar to other multidimensional imaging techniques, probing a complex mechanism requires multiple slices through the data.

1.6. Serial versus Parallel Pathways. We often observe instances in which two aggregation events appear to be competing for rate limitation as evidenced by non-integer LDA orders;[6,8] competing dimer- and tetramer-based aggregation events akin to those in Section 2.8 are emblematic. A composite LDA order between first and second order implicates two pathways of comparable barriers either in series (Figure 6.6) or in parallel (Figure 7). Increasing LDA concentration stabilizes the more highly aggregated tetramer-based transition structure relative to the dimer-based transition structure. In the serial case (Figure 6.6), tetramer stabilization causes the dimer-based barrier to be rate limiting and the rate law to converge on dimer-like dependencies (rate = $k[A_2S_2]^1[S]^1$). By contrast, in the parallel sequence (Figure 6.7), analogous lowering of the tetramer-

based barrier diverts the chemistry through the tetramer-based pathway with an affiliated tetramer-like rate law (rate = $k[A_2S_2]^2[S]^1$).

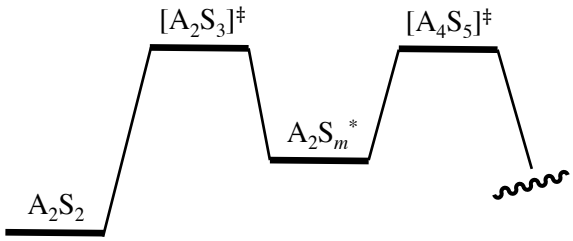

Figure 6.6. Thermochemical picture for two barriers in series. Solvents and LDA needed to balance the stoichiometries have been omitted.

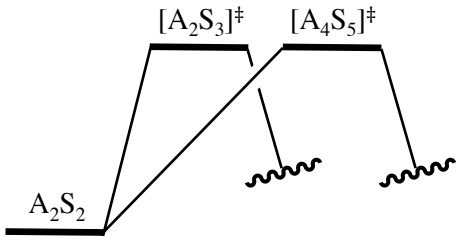

Figure 6.7. Thermochemical picture for two barriers in parallel. Solvents and LDA to balance the stoichiometries have been omitted.

1.7. Autocatalysis. LDA/THF-mediated metalations at –78 °C under *non-equilibrium conditions* are markedly autocatalytic: the reactions are accelerated by the products formed.[23,24] Autocatalysis has two critical prerequisites: (1) the reaction must be susceptible to catalysis, and (2) the product must be a catalyst. We have documented autocatalysis as well as LDA-mediated metalations that fail to autocatalyze because one of the two prerequisites was not satisfied.[8]

Autocatalysis is detectable in decays of substrate versus time (Figure 6.8). Low levels cause a slight straightening (curve B) relative to a first-order decay (curve A).

Autocatalysis by ArLi formation during during an ortholithiation, for example, offsets the deceleration owing to the loss of ArH titer. Beware that mild autocatalysis (curve B) is easily confused with superimposed first- and zeroth-order decays (Figure 6.4). Stronger autocatalysis (curve C) can be equally confusing. For example, in our first detailed study (see Section 2.1), autocatalysis produced nearly perfect linear decays that were not zeroth order.[8a] We routinely probe for mild autocatalysis using a standard control experiment. At the end of an experiment using excess organolithium reagent, a second aliquot of substrate is added. Autocatalysis is evidenced by acceleration relative to the first aliquot. Pronounced autocatalysis, by contrast, appears as sigmoidal decays (Figure 6.8, curve D, inset). Even mild autocatalysis affords sigmoidal curvature when superimposed on an otherwise *zeroth*-order decay.

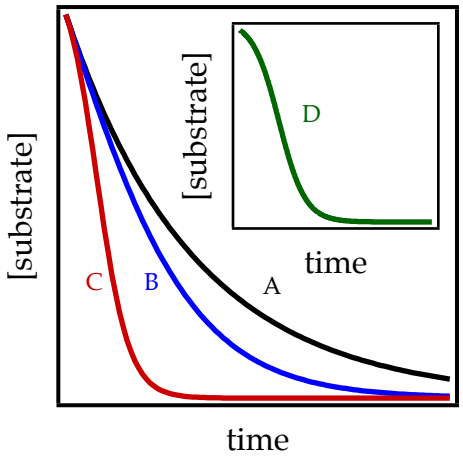

Figure 6.8. Varying degrees of autocatalysis superimposed on first-order decays: curve A, none; curve B, mild; curve C, medium; curve D, strong.

1.8. Salt Effects and Saturation Kinetics. What processes are the various LiX salts catalyzing? In a word, deaggregation. Several steps in the deaggregation shown in Scheme 6.1 are susceptible to catalysis, but usually the net effect is to shift the rate-limiting step from LDA deaggregation to proton transfer. Figure 6.9 illustrates initial rates versus catalyst concentration showing first- and second-order saturation kinetics. (Both have been observed.) It might be tempting to invoke Michaelis–Menten-like behavior in which LDA and LiX form a reactive mixed aggregate that becomes the observable form at saturation, but saturation is attained at low LiX concentration (often <5%) relative to the concentration of LDA.

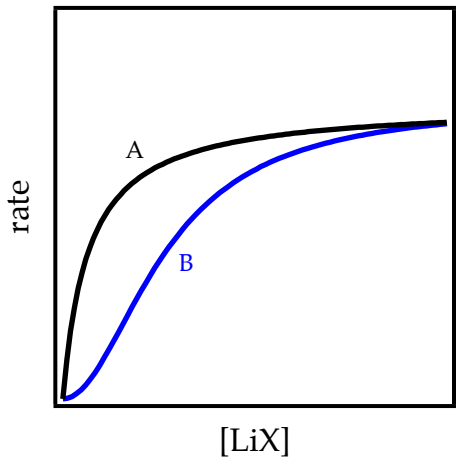

Figure 6.9. Simulation of catalysis showing first-order (curve A) and second-order (curve B) saturation kinetics.

Catalysis of dimer-to-monomer conversion is the most prevalent salt effect under non-equilibrium conditions (eq 6.9) and, thus, is used emblematically here. The rate law is described by eq 6.10. We have overtly excluded the THF dependencies on both the

uncatalyzed and catalyzed deaggregation for this illustration. The algebraic complexity in eq 6.10 stemming from deaggregation and the requisite use of the quadratic equation disappears in the various limits (eqs 6.11–13).

$$1/2\ A_2S_2 \underset{k_{-1}+k_{-cat}[LiX]}{\overset{k_1+k_{cat}[LiX]}{\rightleftharpoons}} [AS_m^*] \xrightarrow{k_2[ArH]} ArLi \tag{6.9}$$

$$\frac{d[ArLi]}{dt} = k_2[ArH]\frac{-k_2[ArH] + \sqrt{\left(k_2[ArH]\right)^2 + 16\left(k_1 + k_{cat}[LiX]\right)\left(k_{-1} + k_{-cat}[LiX]\right)\left[A_2S_2\right]}}{4\left(k_{-1} + k_{-cat}[LiX]\right)} \tag{6.10}$$

$$d[ArLi]/dt = k_1[A_2S_2][ArH]^0 \tag{6.11}$$

$$d[ArLi]/dt = (k_1+k_{cat}[LiX])[A_2S_2][ArH]^0 \tag{6.12}$$

$$d[ArLi]/dt = (k_1k_2/k_{-1})[A_2S_2]^{1/2}[ArH] \tag{6.13}$$

In the absence of catalyst, a rate-limiting deaggregation manifests a first-order dependence on A_2S_2 owing to an $[A_2S_2]^‡$ rate-limiting transition structure and a zeroth-order substrate dependence (Figure 6.5). The rate law reduces to the simplest form (eq 6.11). Adding low concentrations of LiX causes acceleration reflected by $k_1+k_{cat}[LiX]$ while the deaggregation remains rate limiting (eq 6.12). The mechanistic details of catalysis (including THF and catalyst concentration dependencies) are ascertained by taking a slice of the multidimensional rate law (see Section 1.5), but we bypass them here. At high catalyst concentrations (although <5% in most cases), the pre-equilibrium

becomes fully established, and additional catalysis has no effect on the measured rate of metalation (eq 6.13). The mechanism at saturation includes a rate-limiting proton transfer and is probed by ascertaining the LDA and THF concentration dependencies. One would expect to find no isotope effect in the absence of catalyst ($k_H/k_D = 1.0$) and a substantial isotope effect at full catalysis ($k_H/k_D >> 1.0$). That story proves more complex (Section 1.13.)

Figure 6.10 underscores additional points. Strong and weak catalysis are represented by curves A and B, respectively. Although a less effective catalyst requires higher loading, the limiting rate at saturation is the same. *Fully established aggregate–aggregate equilibration affords rates that are independent of catalyst structure.* The commonality of rates shows a commonality in the intermediates. Curve C, by contrast, shows an altogether different metalation rate at full saturation. *The catalyst that produces curve C is necessarily catalyzing a deaggregation that differs from those in curves A and B.* The rate laws measured at the plateaus reveal the differences.

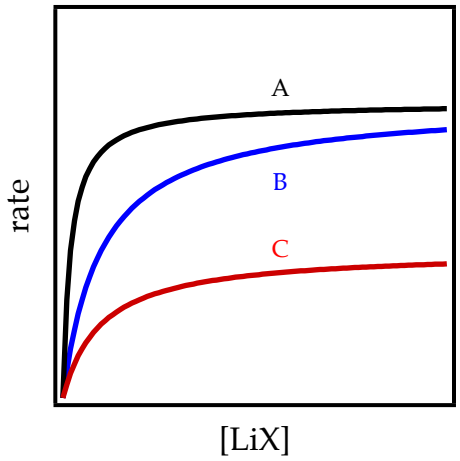

Figure 6.10. Saturation behavior for LiX catalysts. Curve A is a strong catalyst, curve B is a weak catalyst, and curve C corresponds to catalysis of a different deaggregation step than those of curves A and B.

1.9. Catalysis: Acceleration versus Rate Limitation. LiX catalysts serve two seemingly related roles: accelerating a reaction by catalyzing an otherwise rate-limiting deaggregation and shifting the rate-limiting step from deaggregation to proton transfer. It goes without saying that catalyzing a slow (rate-limiting) deaggregation—(k_{-1} + k_{cat}[LiX]) in eq 6.9—accelerates that reaction. However, recall that rate limitation is determined by the fate of the fleeting intermediate (AS_m* in eq 6.9). In the absence of catalyst, monomer proceeds to product with high efficacy—k_{-1}[AS_m*] << k_2[ArH]—rendering deaggregation rate limiting. By contrast, the LiX catalyst shifts the rate-limiting step to the proton transfer by accelerating the *reaggregation* of LDA monomer to dimer such that (k_{-1} + k_{-cat})[AS_m*] >> k_2[ArH]. In short, *catalyzing the forward step—the deaggregation—accelerates the reaction, whereas catalyzing the reverse step—the reaggregation—shifts the rate-limiting step.*

1.10. Peering beyond Rate-Limiting Steps. In principle, rate-limiting deaggregation renders all subsequent steps, including the critical proton transfers, invisible to scrutiny. The discussion to this point, however, shows that this is not altogether true. For years, we chose to study sluggish substrates to ensure that the reaction with LDA was slow, and the various aggregated forms were in full equilibrium. In essence, we were shifting the rate-limiting step by attenuating the proton transfer rate. The catalysis described above shows how under non-equilibrium conditions, we can reduce the barrier to deaggregation, revealing the previously concealed proton transfer. (Recall the caveat in Section 1.4 that the barriers visualized in reaction coordinate diagrams are anything but constant.) Changing THF concentration can lower the barrier to any THF-dependent step relative to those that are not dependent. Deuteration alters the relative barriers to metalations and deaggregations in ways that are discussed separately below. Finally, a variety of competitions allow us to probe reactions of substrates with post-rate-limiting fleeting intermediates without lowering or bypassing the obstructing barrier.

1.11. Relative Rate Law. Whereas the rate law provides the stoichiometry of the transition state relative to the reactants, a relative rate law provides the stoichiometries of transition structures relative to one another. For example, the relative proportions of two products might be independent of LDA concentration and linearly dependent on THF concentration, which shows that the two product-determining transition structures differ by a single THF ligand. The relative rate law assumes special importance for documenting the origins of minor impurities or selectivities when the influence of the minor pathway on the rates cannot be measured directly.[8d,25]

Relative rate laws also provide useful insights about non-equilibrium kinetics in which the key proton transfers of regioselective orthometalations occur in post-rate-limiting steps. Whereas measuring the observable metalation rates versus THF and LDA concentration reveals the stoichiometry of the rate-limiting deaggregation, the dependencies on the *product distribution* reflect the *relative* solvation and aggregation states of the competing post-rate-limiting metalations. This notion of relative rate law is similar to the principles underlying competitive and intramolecular isotope effects.

1.12. Isotope Effects: Variants. The most common application of deuterium substitution in rate studies is to confirm a rate-limiting proton transfer,[9] but isotope effects are even more powerful for probing complex mechanisms. Their utility in studying LDA-mediated metalations under conditions of shifting rate-limiting steps proved far more central than we imagined. In this section, we explore three types of KIEs that are often erroneously considered interchangeable.[9e] Section 1.16 considers nuances that we did not fully appreciate at the outset.

(1) Intermolecular Isotope Effects. The most standard isotope effect is to measure rate constants for protonated and deuterated substrates (ArH and ArD) independently (eq 6.14) to afford a KIE emblematic of rate-limiting proton transfer. The disappearance of substrate over time will follow first-order decays with very different rates. In the event of a rate-limiting deaggregation and post-rate-limiting proton transfer (eq 6.8), k_H/k_D will be equal to 1.0. According to the saturation curve in Figure 6.2, $k_H/k_D >> 1.0$ at low ArH (ArD) concentrations, and $k_H/k_D = 1.0$ at high concentrations. An isotope effect of unity will likely show linear (zeroth order) decays for ArH and ArD that are superimposable.

Analogously, under catalyzed conditions (Figure 6.9), low catalyst loading affords a $k_H/k_D \approx 1.0$, and at high loadings (saturation), $k_H/k_D >> 1.0$.

$$\text{ArH} \xrightarrow{A_2S_2} \text{ArLi} \xleftarrow{A_2S_2} \text{ArD} \qquad (6.14)$$

(2) Intramolecular Isotope Effects. A mixed isotopologue in which symmetry-equivalent sites are protonated and deuterated is used to measure an intramolecular isotope effect by analyzing the isotopic content of quenched products (eq 6.15).[26] The merit of the intramolecular isotope effect is that regardless of whether the proton transfer is rate limiting or post-rate limiting, the isotopically sensitive selectivity will be manifested by a preference for proton rather than deuterium extraction. Moreover, an *inter*molecular isotope effect of unity and a large *intra*molecular isotope effect confirm a post-rate-limiting proton transfer.

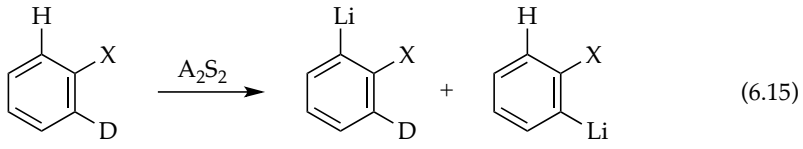

(6.15)

(3) Competitive Isotope Effects. Isotope effects measured when two substrates compete in a single vessel (eq 6.16) show similarities to, but are not interchangeable with, intramolecular and intermolecular isotope effects. They seem straightforward because they involve monitoring of the isotopic content of the starting materials and products in quenched products. They also risk misinterpretation, however.

$$\mathrm{ArH + ArD} \xrightarrow{\mathrm{A_2S_2}} \mathrm{ArLi} \qquad (6.16)$$

In the event of rate-limiting proton transfer, both ArH and ArD disappear via first-order decays and display large k_H/k_D values mirroring the intermolecular isotope effect. A rate-limiting deaggregation and post-rate-limiting proton transfer, by contrast, produce what we call biphasic kinetics (Figure 6.11 and Scheme 6.5).[8c,f,g] The fleeting A_mS_n* intermediate is efficiently and selectively scavenged by ArH and shows the characteristic zeroth-order linear decay discussed in Section 1.3. The induction period for ArD loss occurs because ArD does not appreciably scavenge A_mS_n* until ArH has been consumed, after which the slopes of ArD and ArH decay are comparable ($k_H/k_D \approx 1$). The curvature arising from the dilution of ArH is often acutely more visible in the decay of the much less efficient trapping by ArD. *Deuteration shifts the rate-limiting step.*

Scheme 6.5. Post-rate-limiting proton transfer leading to biphasic kinetics (Figure 6.11). Reproduced from ref 8f. Copyright 2013 American Chemical Society.

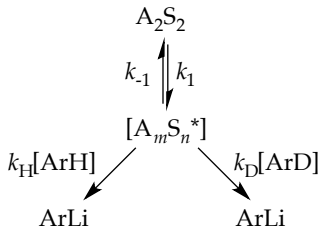

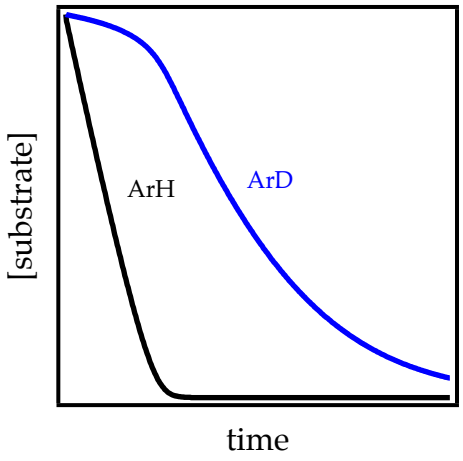

Figure 6.11. Plot showing preferential metalation of ArH over ArD corresponding to $k_H/k_D = 24$.

1.13. Isotope Surrogates. In one case study described below, LDA reacts via a 1,4-addition rather than a proton transfer (see Section 2.3), and in this and many other instances, a detailed mechanistic study lacks the probative power of primary deuterium isotope effects (Chart 6.1). One might be tempted to turn to secondary deuterium isotope or heavy-atom isotope effect[9] strategies similar to those of Singleton and co-workers,[27] but the appeal of these approaches is attenuated (for us at least) by the complexity of the system. Although not for purists, an alternate strategy that is seriously underutilized is the use of surrogates.

Imagine varying the size of the R groups in Chart 6.1 enough to perturb reactivity but insufficiently to impart mechanistic change. In the 1,4-addition example below, we used *n*-alkyl and cyclohexyl and, by coincidence, imposed a relative reactivity of 7:1 (the value often associated with primary KIEs). The analog of the intermolecular isotope effect showed superimposable zeroth-order decays of the two substrates consistent with a

rate-limiting deaggregation. The analog of the competitive isotope effect—monitoring the loss of the two concurrently—revealed relative rates of 7 along with biphasic kinetics (as in Figure 6.11), which are both consistent with a structurally sensitive post-rate-limiting addition. How would one confirm the presumed absence of a deep-seated mechanistic change with the change in substituent? The relative rate law (see Section 1.11) would largely put that issue to rest.

Chart 6.1. Reactions that do not involve proton transfer

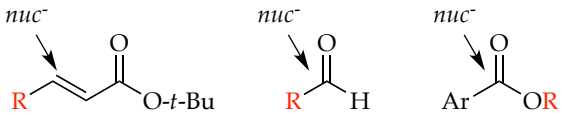

1.14. Role of Substrate Complexation. Along the reaction coordinate, the substrate probably complexes to a fleeting intermediate, which is followed by proton transfer (eq 6.17). The mechanism has several possibilities, each affording a different limiting scenario as follows.

$$A_2S_2 \underset{k_{-1}}{\overset{k_1}{\rightleftharpoons}} [A_mS_n^*] \underset{k_{-2}}{\overset{k_2[ArH]}{\rightleftharpoons}} [A_mS_n(ArH)^*] \xrightarrow{k_3} ArLi \qquad (6.17)$$

(i) The proton transfer corresponding to k_3 is rate limiting ($k_3 << k_{-2}$). This reaction is a standard metalation with aggregates (at least those shown) at full equilibrium as described in our previous review.[6]

(ii) The second step corresponding to substrate complexation is rate limiting with a subsequent rapid proton transfer. This sequence would manifest all the trappings of a normal metalation including a first-order dependence on substrate, but no intermolecular isotope effect would occur ($k_H/k_D = 1.0$). As described, there would be a large intramolecular isotope effect but *no* competitive isotope effect because the product distribution is dictated by an isotopically insensitive complexation step. Biphasic kinetics would not be observed.

(iii) In a third scenario in which the substrate is involved (even assists), a rate-limiting deaggregation followed by post-rate-limiting metalation would be difficult to distinguish from scenario ii. If, unlike in scenario ii, substrate exchange is fast before *proton transfer*, a large competitive isotope effect in conjunction with biphasic kinetics is observed. This scenario was observed during fluoropyridine metalations (see Section 2.6).

We are reminded that the three types of KIEs offer powerful probes of rate limitation as well as post-rate-limiting proton transfers. There is great risk in presuming that they are equivalent.

1.15. Isotope Effects: Roles of ZPE. The simplest (two-body) analysis of primary deuterium isotope effects shows that the rate differential emanates from the ZPE of ArD in the ground state, which is retained in all steps preceding the proton transfer but disappears in the transition state for proton transfer (Figure 6.12).[9] We use $[A_2S_2\text{--}H\text{--}Ar]^{‡}$ to keep the discussion stoichiometrically simple. It is widely held that KIEs maximize at a k_H/k_D of approximately 7 at 25 °C and at a k_H/k_D of up to 20 if adjusted to –78 °C. Notably, a KIE is implicitly an inherent property of the substrate and independent

of the mechanism of proton abstraction. Additional vibrations coupled to the vibration becoming the reaction coordinate are invoked to account for mechanism-dependent KIEs.

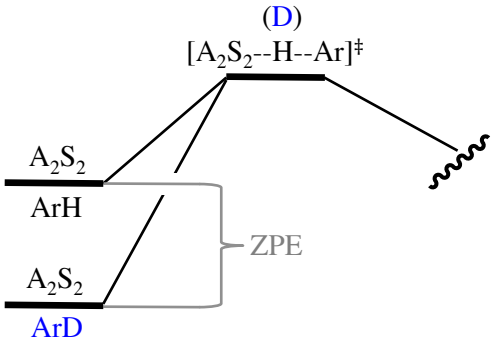

Figure 6.12. Two-body model showing the role of ZPE as a determinant of a primary KIE.

How does deuteration shift the rate-limiting step? It is tempting to assume that the barrier to transfer is higher, but the two-body model says that cannot be. By including a fleeting intermediate—A_2S_2* to maintain simplicity—we see that the ZPE retained in the *deaggregation* transition state causes the shift (Figure 6.13).

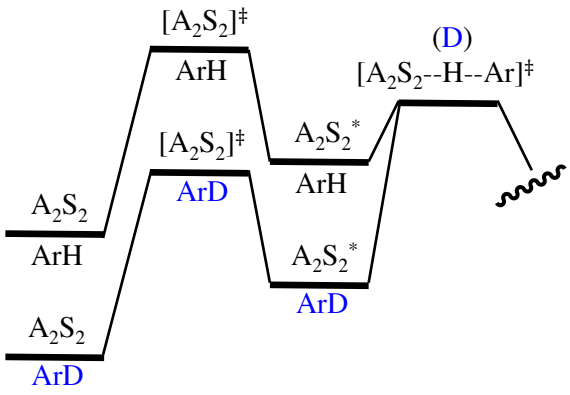

Figure 6.13. Contributions of isotopic substitution and ZPE to an *intermolecular* KIE and rate-limiting step using ArH and ArD measured independently.

Consider the two additional isotope effects from the thermochemical perspective. Figure 6.14 shows that the intramolecular isotope effect has no differential ZPE at any point leading up to the proton transfer. The origin of k_H/k_D is the retention of stabilizing ZPE associated with the C–D bond that promotes the abstraction of the proton. Note that, at least in theory, *proton and deuterium transfer could have different rate-limiting steps* (deaggregation in the former and deuterium transfer in the latter.) The competitive isotope effect (Figure 6.15) is similar in that ZPE retained in the rate-limiting *transition state* dictates the relative rates and the step that is rate limiting. The relative roles of ground-state and transition-state ZPEs are easily overlooked.

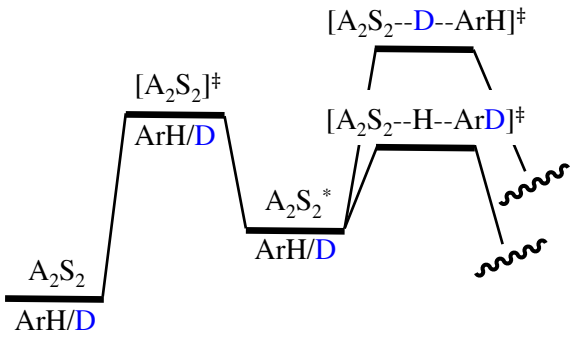

Figure 6.14. Contributions of isotopic substitution and ZPE to an *intramolecular* KIE on a monodeuterated substrate denoted ArH/D.

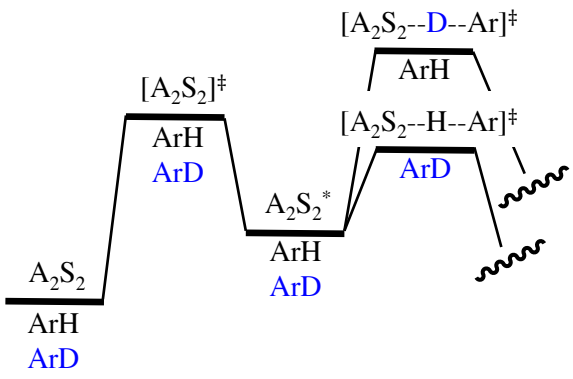

Figure 6.15. Contributions of isotopic substitution and ZPE to a *competitive* KIE using a mixture of ArH and ArD. All ground and transition states contain all three components.

1.16. Isotope Effects: Role of Tunneling. Organolithium-based metalations can manifest KIEs that exceed 50 for a variety of bases and conditions.[8,28] A number of instances emerge in the LDA-mediated ortholithiations described in Section 2. Their magnitudes and considerable mechanism-dependent variations influence rate limitation markedly. To explain these isotope effects, we join the ranks of those who have invoked tunneling.[9] We have little interest in discussing the origins of this predilection beyond noting that isotopically sensitive tunneling in the transition state favoring proton transfer (Figure 6.16) would work in concert with ZPE in a multiplicative relationship in the ground states to produce large KIEs.

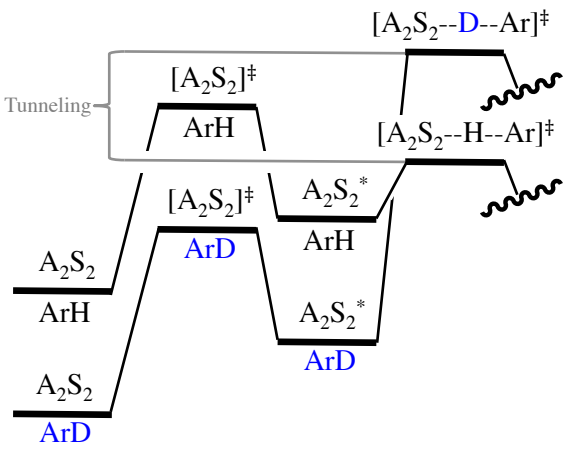

Figure 6.16. ZPE and tunneling as determinants of an *intermolecular* KIE and rate-limiting step.

2. Case Studies. This section describes studies showing how the rates of LDA aggregate exchanges influence reactivity and selectivity under non-equilibrium conditions. The studies are largely chronological, capturing the evolution of our understanding, and are placed in the context of the tutorial in Section 1 without re-adjudicating the cases.

We first detected strange rate behavior during the detailed rate studies of the LDA/THF-mediated lithiations of 16 imines.[29] The most reactive imine—that requiring dry ice–acetone bath at –78 °C to monitor the rates—showed distorted decays in the form of an unusual lack of curvature within the first several half-lives (Figure 6.8). We noted it and ignored it. The ortholithiation of carbamates forced an attitude correction, which is where the story begins.

2.1. Arylcarbamate Lithiations. The metalation of carbamate **7** by LDA/THF at –78 °C under second-order conditions (1:1 ArH to base) followed an apparent first-order decay to the exclusion of observable mixed aggregates (eq 6.18).[10a] We appeared to have

discovered the simplest organolithium reaction to date, but it should have followed a *second*-order decay. Pseudo-first-order conditions or any conditions with a modest excess of LDA paint an altogether different picture (Figure 6.17) in which linear loss of starting material and the formation of ArLi product is followed by the *delayed* appearance of mixed aggregates. The final mechanistic model is summarized in Scheme 6.6.

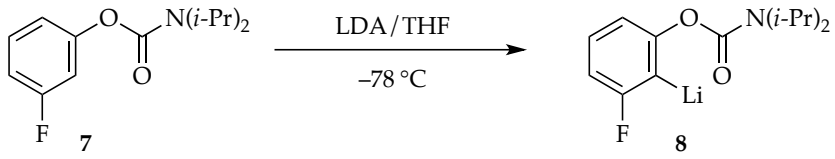

(6.18)

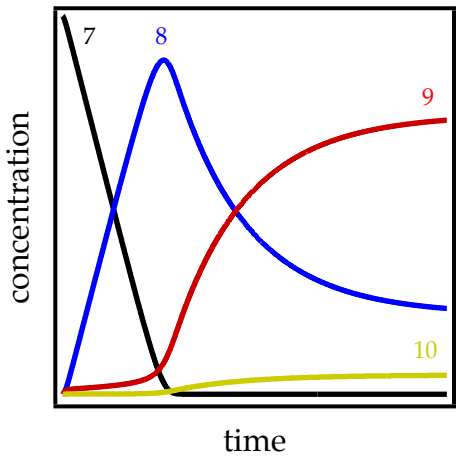

Figure 6.17. Simulated plots of concentration versus time for the reaction of **7** (black trace) with lithium diisopropylamide in tetrahydrofuran at –78 °C. The functions derive from a mathematical model based on Scheme 6.6.

Scheme 6.6. Mechanism of carbamate ortholithiation. Reproduced from ref 8a. Copyright 2008 American Chemical Society.

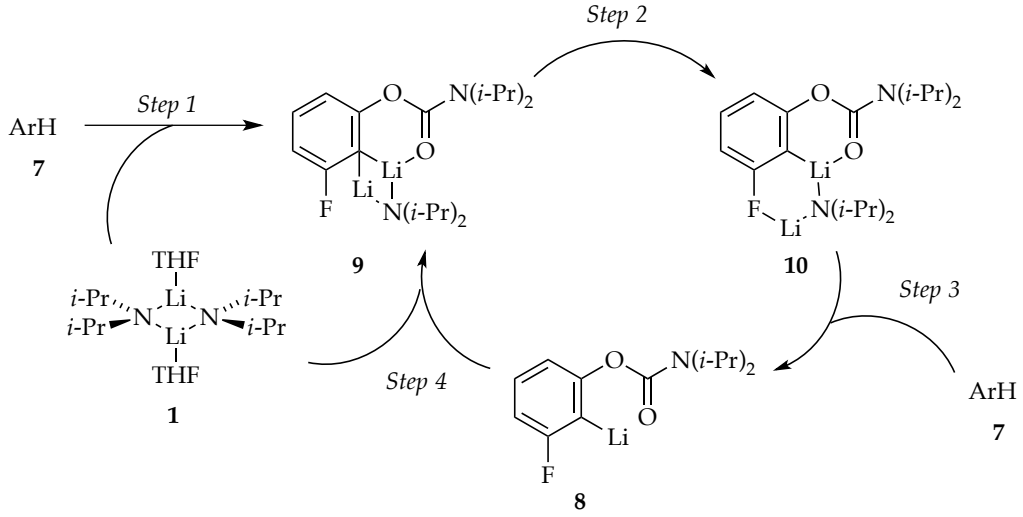

The decays proved paradoxical in that the linearity suggested a zeroth-order dependence on substrate (see Section 1.3), but the slopes were concentration-*dependent* (Figure 6.18) rather than parallel (Figure 6.5), which suggested an approximate first-order dependence. Changing the THF concentration or inserting a deuterium afforded sigmoidal behavior showing that autocatalysis was at play (see Section 1.7). The linearity stemmed from a remarkable coincidence in which an upwardly curving decay was precisely offset by downward curvature imparted by autocatalysis.

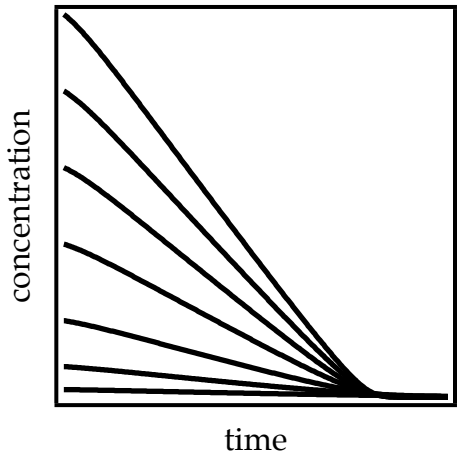

Figure 6.18. Simulations of plots showing concentration versus time for various initial concentrations of carbamate **7**. The original paper simply displayed independent linear fits.[8a]

The mechanistic hypothesis in Scheme 6.6 underscores a number of oddities. An LDA-dimer-based metalation (step 1) affords cyclic mixed dimer **9** (step 1) and low concentrations (3%) of mixed dimer **10**. *However*, LDA–ArLi mixed aggregates **9** and **10** are consumed rapidly by substrate and therefore persist *only after carbamate 7 is completely consumed*. Moreover, the **9**–**10** equilibrium (step 2) is *not fully established on the timescale of the metalation* (step 3); minor isomer **10** is far more reactive and can be selectively depleted with an aliquot of **7**. Autocatalysis stemmed from the conversion of LDA dimer **1** to mixed dimers (step 4) via a mixed-trimer-based transition structure. The mathematical model based on Scheme 6.6 was effective at fitting data over a range of conditions. Moreover, the model was *not* "sloppy" (subject to large variations); many plausible models failed to fit the data.

The overarching themes of this first study are that aggregates are not rapidly (fully) equilibrating in THF at –78 °C on the laboratory timescales of the metalations, and

catalysis by LiX is significant. We noted with some prescience, however, that the model was "vulnerable to revision." Indeed, a small isotope effect within the range expected for a primary isotope effect was reinvestigated in the context of a subsequent study[8d] and shown to be a fraction of a much larger KIE because *proton transfer was only partially rate limiting*. Deuteration to measure k_H/k_D was, unbeknownst to us at the time, imparting fundamental mechanistic changes. Only in retrospect did we realize that the linear decays attributed to autocatalysis superimposed on an exponential decay also include contributions from a true zeroth-order term. We also noted, "it almost goes without saying that an autocatalytic organolithium reaction necessarily involves highly reactive mixed aggregates." Although technically true, the mixed aggregates do *not* necessarily mediate proton transfer.[23] Such retrospective adjustments to the models and experimental reinvestigations became the norm: each case study offered a more nuanced view and often prompted reevaluation of preceding work.

2.2. Ortholithiations: A Survey. As multiple investigators within our laboratory began exploiting a newfound confidence in –78 °C baths, strange rate behaviors began emerging, paradoxical ones at that. We had discovered during the carbamate lithiations that traces of LiCl markedly influence rates. A survey of a dozen arenes found that metalations of many, but not all, arenes are autocatalyzed and highly susceptible to LiCl catalysis.[8b] With LiCl catalysis, *all metalations showed standard pseudo-first- or second-order decays.* Subsequent studies showing catalysis by as little as 100 ppm LiCl eventually showed that multiply recrystallized LDA containing <0.02% LiCl *was not pure enough*,[8b] prompting us to modify a literature procedure to generate LiCl-free LDA.[8c]

On a practical level, rumors that commercially available LDA is inferior to LDA prepared from *n*-butyllithium were traced to the absence of LiCl in commercial LDA, which ironically is almost indistinguishable from analytically pure LDA. Deaggregation-limited lithiations using commercial LDA are markedly accelerated by generating traces of LiCl in situ (eq 6.19).[31]

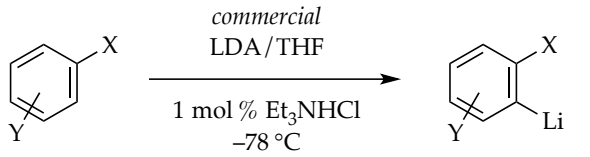

(6.19)

The window of substrate reactivity in which the anomalies clustered was confusing at the time. Highly reactive and notably unreactive substrates were insensitive to catalysis, prompting us to create the progenitor to Figure 6.1. A half dozen other LiX salts accelerate ortholithiations from 2-fold to 300-fold. What we did not know at the time was that the salts do not necessarily catalyze the same process (*vide infra*).

2.3. Conjugate Additions. As part of an attempt to study g-deprotonations of unsaturated esters, we achieved clean 1,4-addition (eq 6.20)[8c] akin to that observed by Schlessinger and co-workers[32] and exploited its synthetic potential for other lithium amides.[33] The conjugate addition offered one of the more interesting probes into the non-equilibrium kinetics of LDA and confirmed that the effects transcend proton transfer.

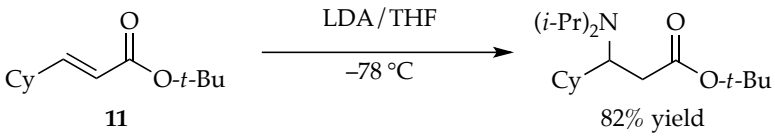

11

82% yield

(6.20)

Monitoring the 1,4-addition under pseudo-first-order conditions revealed new and unusual curvatures—Figure 6.19 is emblematic but only one of a multitude of flavors—that led to the mechanism shown in Scheme 6.7. The time dependencies shown in Figure 6.19 include a number of striking features: (1) the linear loss of starting material *superficially* akin to that noted in carbamate metalations proved to be true zeroth-order decay (see Section 1.3); (2) homodimeric enolate **14** *overshoots* its equilibrium population, reaching an apex at the point that starting ester **11** is consumed; (3) mixed dimer **16** formation appears to decelerated and then accelerate abruptly at that same point, eventually attaining an equilibrium population; and (4) the absence of an induction period shows that mixed dimer **16** is *not* uniquely the precursor to homodimer **14**.

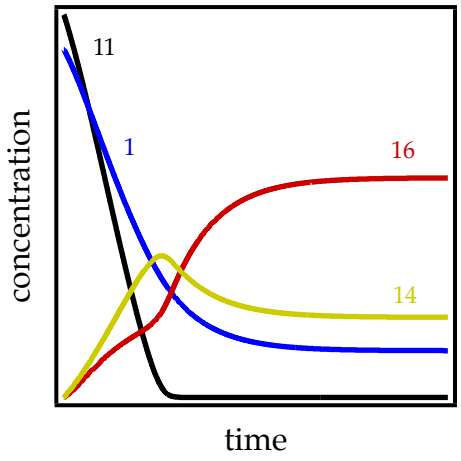

Figure 6.19. Simulated time-dependent concentrations of ester **11**, lithium diisopropylamide dimer **1**, enolate homodimer **14**, and mixed dimer **16**. The functions are from the model described in Scheme 6.7.

Scheme 6.7. Mechanism of 1,4-addition. Reproduced from ref 8c. Copyright 2010 American Chemical Society.

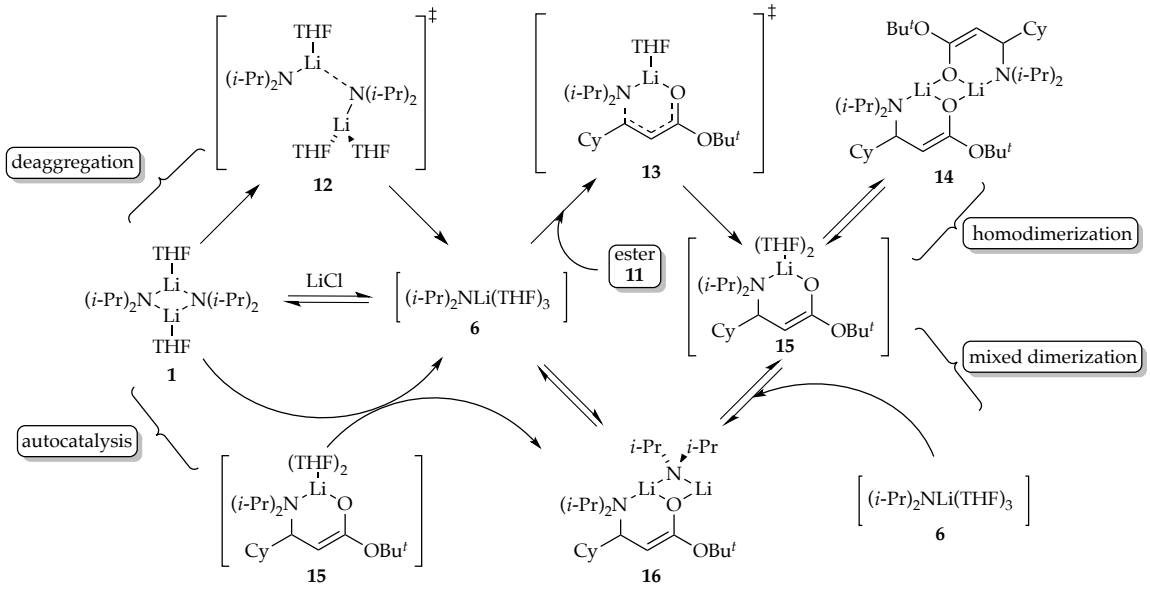

Rate and computational studies filled in the details in Scheme 6.7 and afforded the final model that fit multiple and highly variable time-dependent behaviors akin to those in Figure 6.19. The zeroth order in ester **11** was traced to a trisolvated-dimer-based rate-limiting deaggregation; **12** is one of several possibilities. Enolate monomer **15**, formed via monosolvated-monomer-based transition structure **13**, reacts with one of three species: (1) a second equivalent of **15** to form homodimer **14**, (2) LDA monomer **6** to form mixed dimer **16**, or (3) LDA dimer **1** to form mixed dimer **16** and regenerate LDA monomer **6**. This third process is the source of low but detectable levels of autocatalysis. Owing to slow aggregate exchange and the rapid consumption of monomer **6**, many of the species in Scheme 6.8 are not in fully established equilibria until ester **11** is consumed. A 100-fold acceleration by LiCl was traced to the facile equilibration of dimer

1 with highly reactive monomer **6**, shifting the rate-limiting step to 1,4-addition rather than deaggregation and greatly simplifying the reaction coordinate.

The nature of catalyzed deaggregation unfolded slowly and had many subtleties, as described in Section 2.7. As noted in Section 1.7, autocatalysis has two immutable requirements: (1) the reaction must be susceptible to catalysis, and (2) the product must be a viable catalyst. In this case, enolate monomer **15** rather than, for example, dimer **14** appears to be the catalyst, but its concentrations remain too low to be highly autocatalytic. Homodimer **14** reenters the cycle via mixed dimer **16** but also quite slowly. Notably, the scenario in which LDA dimer (A_2) is converted sequentially to mixed dimer (AX) and enolate homodimer (X_2) is grossly oversimplified:

$$A_2 \Rightarrow AX \Rightarrow X_2$$

Also, whereas mixed dimer **16** reacts demonstrably faster than LDA homodimer **1**, **16** does not appear to react directly with ester **11**; it serves as a kinetically facile source of LDA monomer. This may have been the case for the LiCl mixed aggregates in the carbamate studies described in Section 2.1

2.4. Ortholithiation of 1-Chloro-3-(trifluoromethyl)benzene. Another generic ortholithiation first reported by Schlosser (eq 6.21)[34] manifests substrate-independent rates, shifting rate-limiting steps, autocatalysis, and LiCl catalysis—key hallmarks of a reaction under the auspices of rate-limiting aggregation events.[8d]

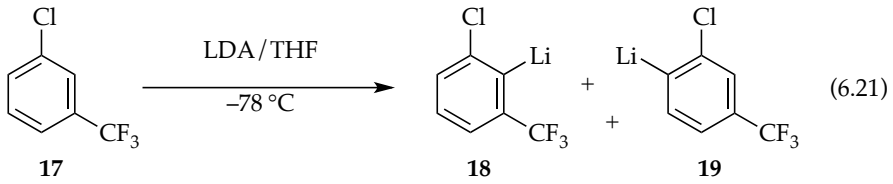

(6.21)

The results from rate studies are summarized in Scheme 6.8. In the uncatalyzed lithiations, rate-limiting deaggregation occurs via an $[A_2S_2]^{\ddagger}$-based rate-limiting deaggregation rather than the $[A_2S_3]^{\ddagger}$ variant observed for the 1,4-additions. This reaction can only occur if the post-rate-limiting reaction for the ortholithiation and 1,4-addition occur from different intermediates that are not at equilibrium. Shifting rate-limiting steps by changing concentrations and using deuterated isotopologues with large and variable isotope effects (k_H/k_D = 30–60) showed that the dimer-based rate-limiting deaggregation event is followed by post-rate-limiting dimer-based lithiations differing by one THF ligand (suggested by DFT computations to be **20** and **21**).

Scheme 6.8. Mechanism of carbamate ortholithiation. Reproduced from ref 8d.

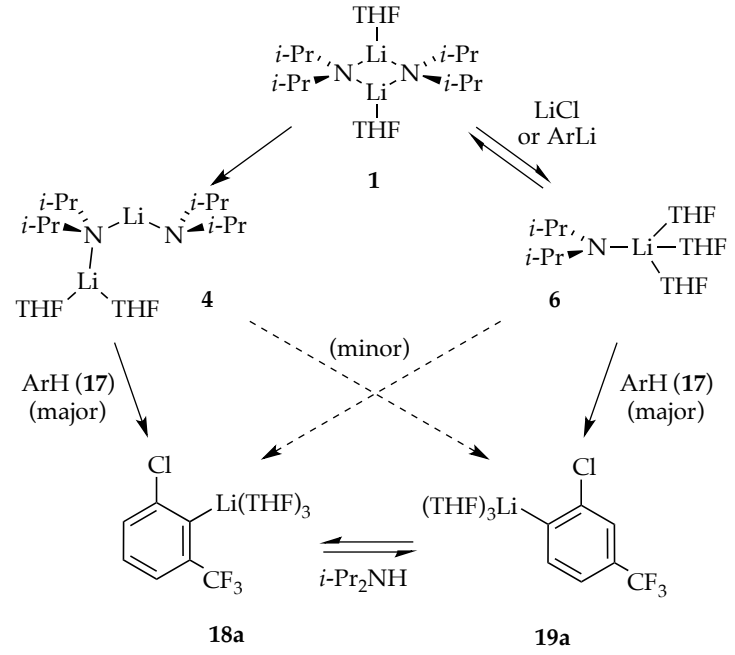

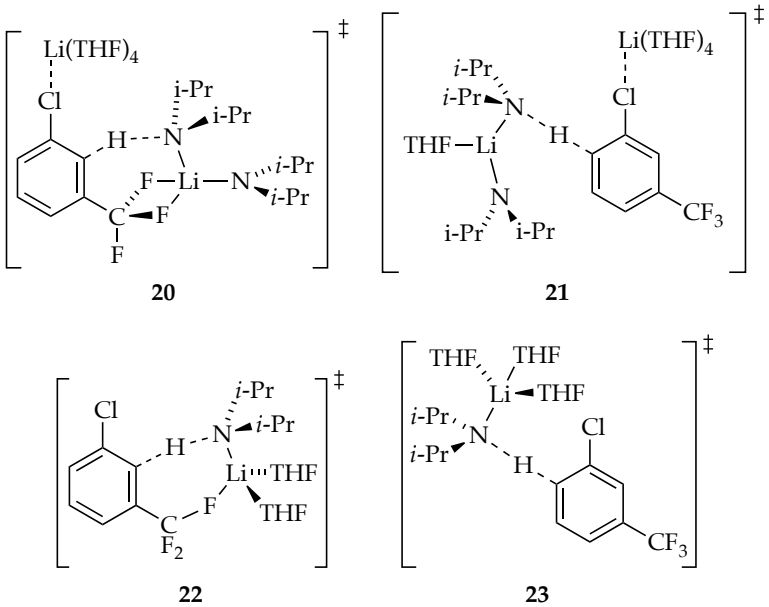

ArLi-derived autocatalysis or the markedly more efficient LiCl catalysis diverts the reaction through reversibly formed fleeting monomer **6** and monomer-based transition structures **22** and **23**, thereby affording the opposite regioselectivity favoring **19a**. The catalyst-independent regioselectivity implicates a common intermediate. It is ironic and amusing that aryllithium **18a** is the major isomer of the dimer-based metalation and a 6-fold more effective autocatalyst than **19a**, yet **18a** then promotes the formation of **19a**.

A complicating isomerization of **18a** and **19a** is superimposed on the non-equilibrium and equilibrium kinetics.[35] The isomerization is mediated by diisopropylamine via LDA monomers as expected from the principle of microscopic reversibility.[36] The conclusion section describes whimsical and contrasting views of the chemistry through the lenses of mechanistic organolithium and synthetic organic chemistry.

2.5. LDA Deaggregation: A Computational Study. The growing number of rate-limiting solvation or aggregation steps dictating metalation rates and selectivities prompted a detailed computational study of the conversion of LDA dimer **1** to monomer shown in Scheme 6.1.[8e] Figure 6.20 is the expanded version of Scheme 6.1 but with transition structures as well as ensembles of conformational isomers (shaded in gray) arising from rotations about the isopropyl groups. (Note that the rigorous equation balancing discussed in Section 1.4 is omitted to minimize clutter.) Of special note, the barriers crudely approximate a monotonic rise with the final fragmentation to monomers corresponding to the highest barrier. The shaded conformational ensembles spanning a broad energy range are entered and exited through "portals" via various conformers showing substantially different energies. We also introduced the notion that bridging

THF ligands (**24** and **25**) may be important motifs in critical fragmentation steps (eq 6.22).[37] To the best of our knowledge, this detailed analysis is the first for an organolithium deaggregation. It might have benefitted from the algorithmic methods for searching complex surfaces developed recently by Zimmerman and co-workers.[38]

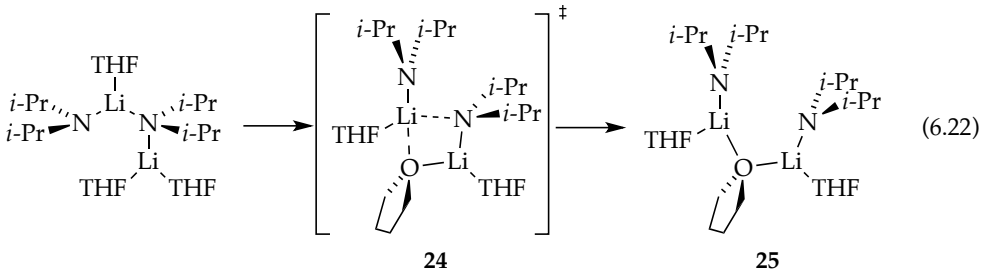

(6.22)

The "washboard"-like surface in Figure 6.20 shows some analogy with examples in enzymology in which barriers of nearly equal energy are legion.[39] With unreactive substrates in which all forms of LDA are at equilibrium (Figure 6.1, Scenario 1), all intermediates are accessible. Only a couple—often only one—dominate the reaction coordinate. However, if substrates react rapidly with fleeting intermediates in post-rate-limiting steps—if they react via barriers lower than those corresponding to aggregate–aggregate exchanges—fundamentally different mechanisms are separated by subtle factors.

Recall that during the metalations of **17**, the monomer-based pathway made possible through catalysis was far more efficient than the dimer-based metalations dominating in the absence of catalysis. Even when deuteration causes dimer-based lithiations to involve rate-limiting proton transfer, more efficient monomer-based

metalations are precluded by a barrier for final cleavage of dimer to monomer that is simply too high. In principle, even a conformational barrier could preclude access to an intermediate that might offer a more viable path for metalation. We do not take the energies in Figure 6.20 seriously, but exploring the process markedly shaped our thinking. Unbeknownst to us at the time, restricting our focus to only dimeric intermediates en route to monomers was an error (vide infra).

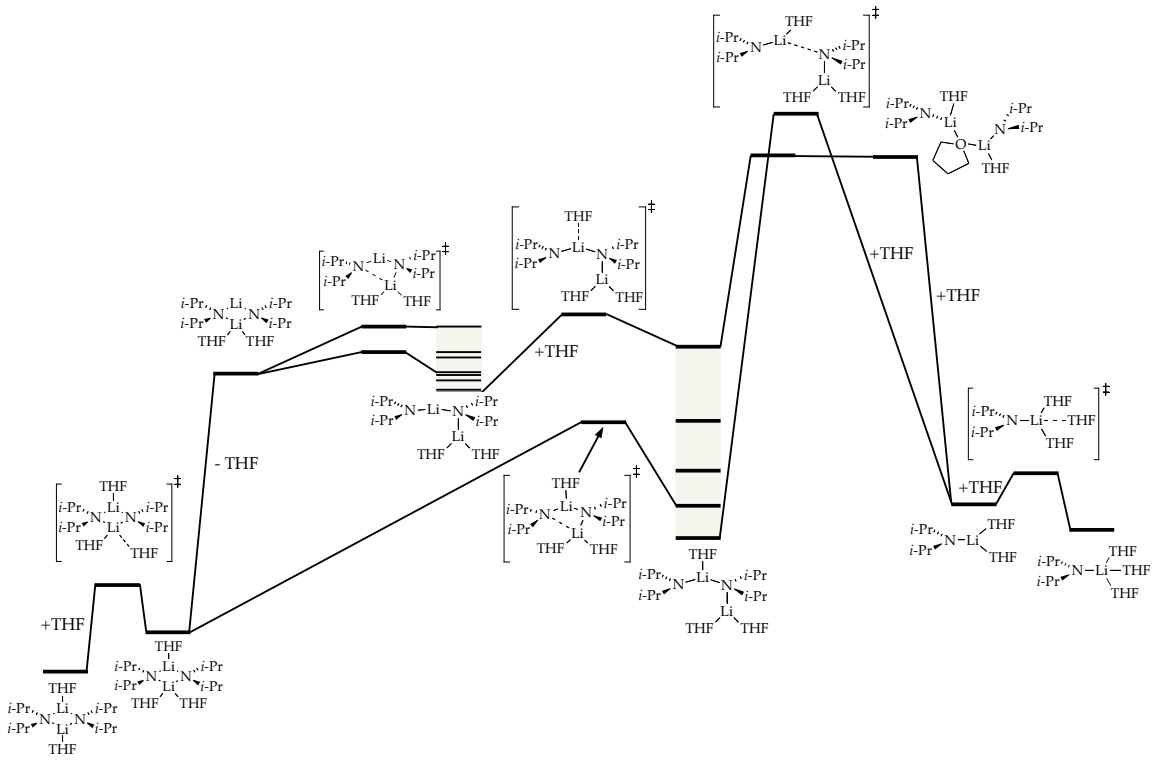

Figure 6.20. DFT-calculated mechanisms for the deaggregation of lithium diisopropylamide dimer to monomer. The shaded areas correspond to ensembles of discrete conformers. Reproduced from ref 8e. Copyright 2011 American Chemical Society.

2.6. Ortholithiation of 2-Fluoropyridines. Lithiations of 2-fluoropyridines (eq 6.23)[40,41] proved to be among the most challenging within the series because they revealed all of the trappings of non-equilibrium kinetics—autocatalysis, LiCl catalysis, rate-limiting and partially rate-limiting deaggregations (Scheme 6.9), strange time-dependent decays of substrates, and biphasic kinetics in the competitive KIE (see Section 1.12). It also included some subtleties that would not be understood until subsequent studies were completed.[8g,h]

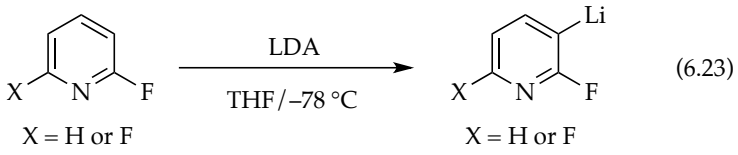

(6.23)

Substrate-dependent rates accompanied by post-rate-limiting proton transfer (Scheme 6.9, path *i*) attest to either rate-limiting complexation or pyridine-assisted deaggregation (see Section 1.14). Moreover, the growing awareness that each substrate in the case studies offers unique probes of different portions of a very complex deaggregation surface was reinforced by evidence of a high-order dependence on LDA implicating a *tetramer-based aggregation event* (Scheme 6.9, path *ii*). The role of LDA tetramers resurfaces and is fleshed out in Section 2.9, augmented by additional experimental support. Autocatalysis by ArLi and catalysis by LiCl were traced to A_2X_2 mixed-tetramer-based mechanisms (paths *iii* and *iv*), which we discuss in the next section. Under full LiCl catalysis—at full saturation as shown in Figure 6.9 (see Section

1.8)—the metalation proceeds via disolvated-monomer-based transition structure **26**, which is strongly supported computationally.

Scheme 6.9. Mechanism of 2-fluoropyridine ortholithiation. Reproduced from ref 8f. Copyright 2013 American Chemical Society.

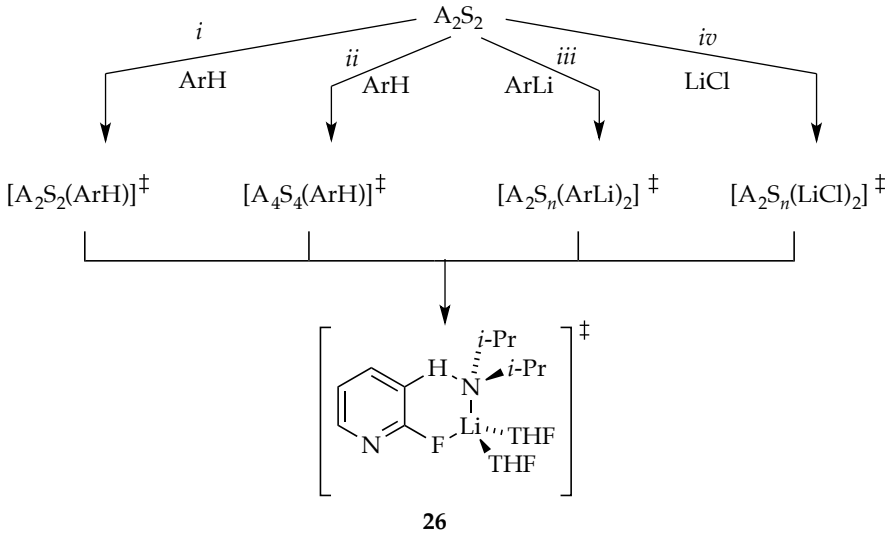

26

We had missed a critical part of the story. Previous evidence showed that autocatalysis by ArLi and catalysis by LiCl share common monomer-based intermediates. Pyridine lithiations offered evidence that the two salts catalyze different pathways (see Figure 6.10), but we did not fully understand the implications until we undertook studies of 1,4-difluorobenzene lithiations (*vide infra*).[8g] A discussion of ArLi-autocatalyzed and LiCl-catalyzed deaggregation proceeding via mixed tetramers segues to the next section describing our accumulated thoughts on the mechanism of catalysis.

2.7. Mechanism of Catalyzed Deaggregation. Our understanding of catalyzed deaggregation was assembled piecemeal and is presented as a single picture in this section. Rate studies were used to ascertain the stoichiometry of the rate-limiting transition structures for LiCl- and ArLi-catalyzed metalations. The mechanisms appear to be salt- and substrate-dependent. In some instances, a first-order dependence on LiX implicates an $[A_2X]^‡$ mixed trimer stoichiometry, whereas in others, an $[A_2X_2]^‡$ mixed tetramer is suggested. The saturation kinetics discussed in Section 1.8 are the norm. Given assignments of ArLi as trisolvated monomers and a more limited understanding of LiCl structure, even solvation numbers were assigned, albeit tentatively. We consider two basic types of mechanisms for catalyzed deaggregation as follows.

(1) Triple-ion-like species such as **27**, with chloride playing a role as a highly dipolar ligand (Scheme 6.10), carry some appeal. We may have detected such a chloride adduct of lithium 2,2,6,6-tetramethylpiperidide years ago.[42] A second-order dependence on LiCl suggested a complex gegenion, maybe a cationic triple ion.[43] The bridging THF in computationally viable **28** is a motif that we find highly appealing as central to the final aggregate scission.

Scheme 6.10. Lithium chloride-catalyzed LDA deaggregation via triple ions. Reproduced from ref 8f. Copyright 2013 American Chemical Society.

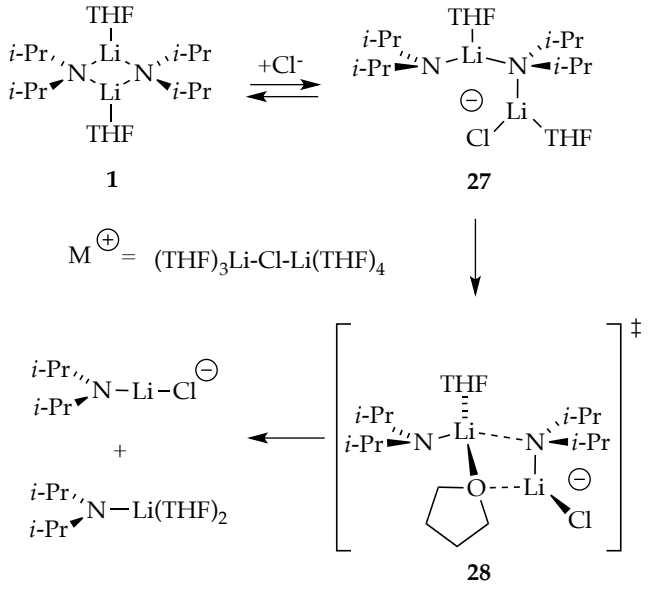

(2) An alternative and potentially more general model involves intermediate three- and four-rung ladders (Scheme 6.11).[44] This laddering could be considered a form of associative substitution. Whereas dissociating two high-energy monomers from a dimer carries an inherently high thermochemical penalty, dissociating a single monomer from the end of ladder **29** or **32** may be less costly.[45] Alternatively, the facile dissociation of two mixed dimers (**31**) from ladder **30** also seems credible. This laddering model was examined computationally on several occasions.[8g,h] We return to it in the context of tetramer-based LDA chemistry.

Scheme 6.11. Lithium chloride-catalyzed LDA deaggregation via ladders. Reproduced from ref 8f. Copyright 2013 American Chemical Society.

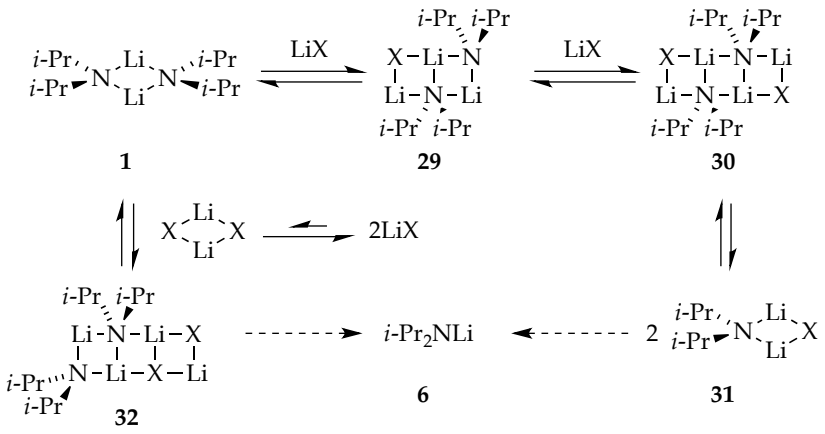

2.8. Ortholithiation of 1,4-Difluorobenzene. The ortholithiation of 1,4-difluorobenzene (eq 6.24)[46] underscored the ease with which rate-limiting steps can shift.[8g] Isotope effects played a prominent role in this process (see Sections 1.15 and 1.16). We also exploited reaction coordinate diagrams (Figure 6.21) to describe the various *experimentally detectable* barriers. Recall, however, that such diagrams are riddled with intellectual traps (see Section 1.4) in which any change in reaction conditions, including changes with percent conversion, alters the diagram. These diagrams are living, breathing depictions in which the version shown represents merely a snapshot. The implicit balancing of equilibria are omitted to minimize clutter, again placing the model at risk for misinterpretation.

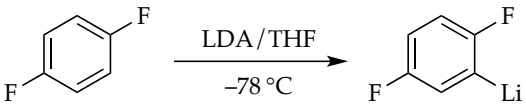

(6.24)

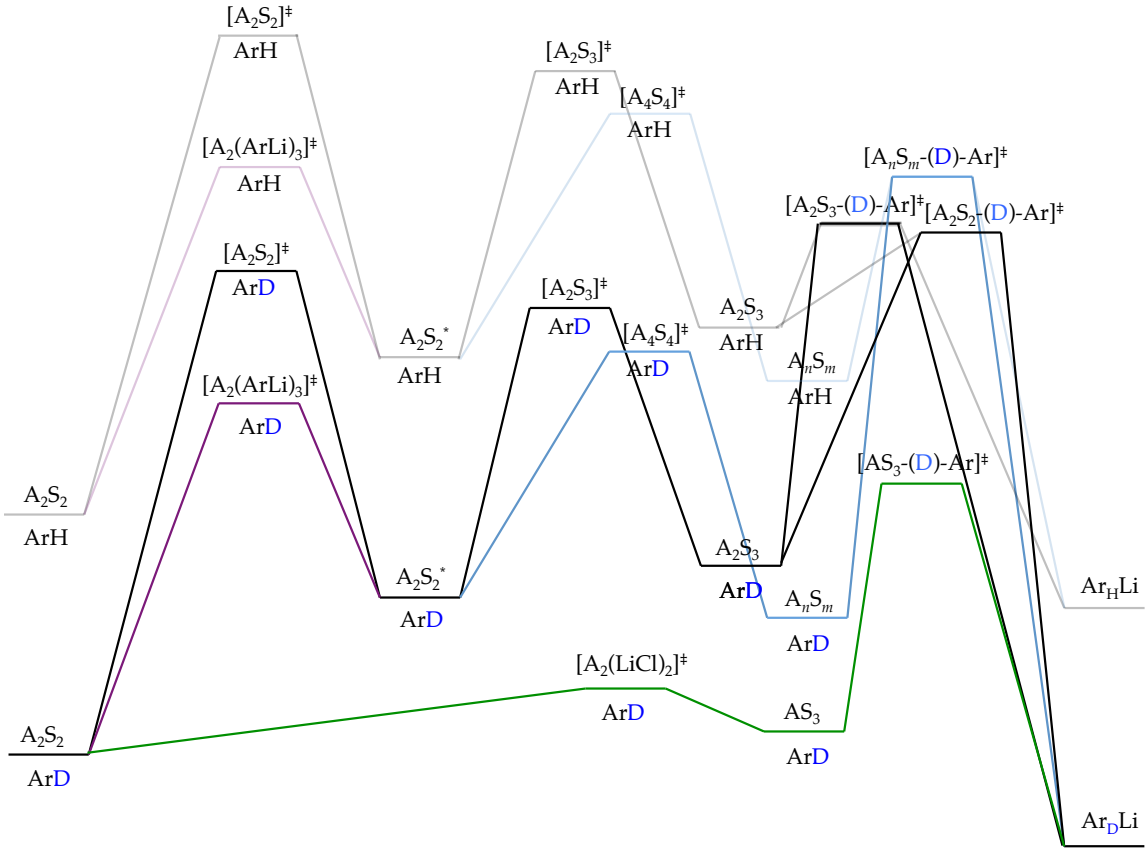

Figure 6.21. Snapshot of an experimentally determined reaction coordinate diagram for the metalation of 1,4-difluorobenzene (eq 6.24). Reproduced from ref 8g. Copyright 2014 American Chemical Society.

In the uncatalyzed variant, the previously detected rate-limiting deaggregation via disolvated dimer, $[A_2S_2]^{‡}$, dominates. Autocatalysis by ArLi-catalyzed *partial* deaggregation allowed us to peer beyond this first barrier to observe a *different* rate-

limiting *aggregation* event via a tetrasolvated tetramer, $[A_4S_4]^{‡}$. The deuterated substrate in conjunction with large isotopic sensitivities in the transition states (see Section 1.16) revealed rate-limiting deuterium transfer via a combination of tri- and tetrasolvated dimers, $[A_2S_2(ArD)]^{‡}$ and $[A_2S_3(ArD)]^{‡}$, which guided by DFT computations, are depicted as **33** and **34**, respectively. Lithium chloride, by contrast, catalyzes the deaggregation to monomer, affording rate-limiting monomer-based transition structure **35**. In this study, a dimer-based proton transfer is observed because the more efficient monomer-based mechanism is unavailable in the absence of catalyst.

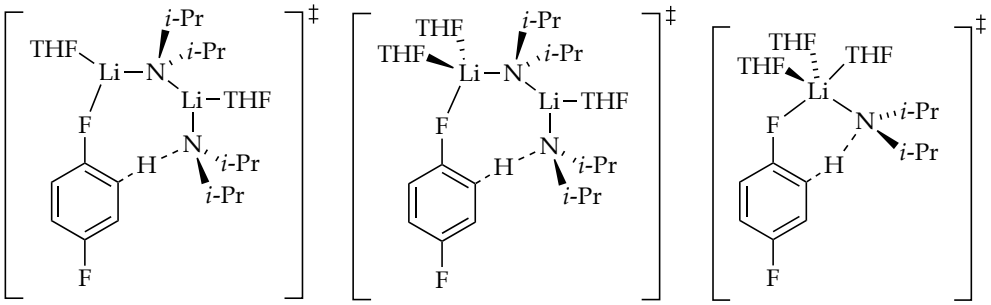

33 **34** **35**

2.9. LDA Deaggregation Revisited: Role of Tetramers. Dependencies of LDA significantly exceeding unity attest to the presence of tetramer-based rate-limiting steps. We must confess to having no idea that this scenario was even possible at the outset. After 30 years of studying the chemistry of LDA, we finally determined the rates and mechanisms of LDA subunit exchange by (1) analyzing the line shape of the coalescence of the ^{6}Li triplet of [^{6}Li,^{15}N]LDA as a function of concentration, and (2) monitoring the rate at which [^{6}Li]LDA and [^{6}Li,^{15}N]LDA form the mixed isotopologue *on laboratory timescales* (eq 6.25).[8g] In both instances, the data support a combination of dimer-to-

monomer *dissociative* exchange (see Section 2.5 and eq 6.26) and dimer-to-tetramer *associative* exchange (eq 6.27). We offer the ladder-based pathway illustrated in Scheme 6.12 in which we have taken a few simplifying liberties. Computational support was challenging owing to the severe steric demands of the ladders that often subvert the DFT method, but we obtained a computationally viable sequence that may suffer from unnecessary complexity.[8g]

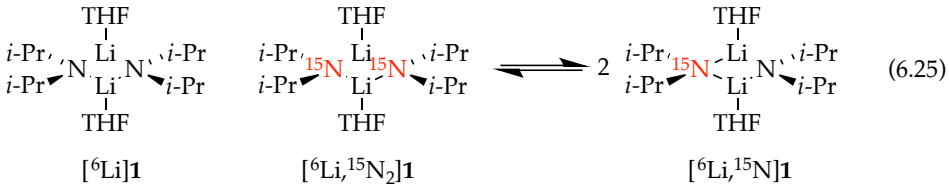

(6.25)

$$A_2 + A_2 \rightleftharpoons 2A + 2A \rightleftharpoons 2AA \qquad (6.26)$$

$$A_2 + A_2 \rightleftharpoons A_2A_2 \rightleftharpoons 2AA \qquad (6.27)$$

Scheme 6.12. LDA deaggregation via tetrameric ladders. Reproduced from ref 8f. Copyright 2013 American Chemical Society.

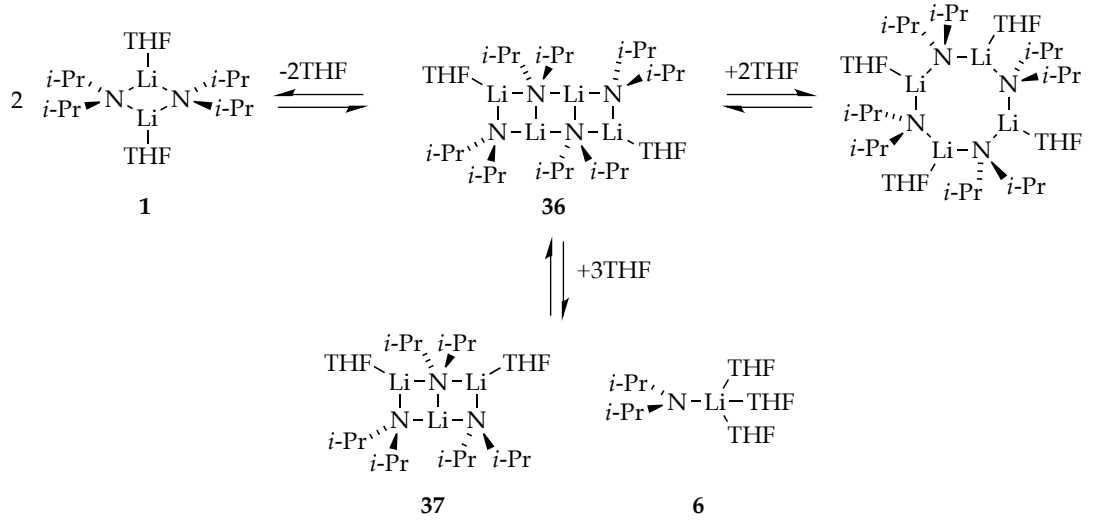

The overall exchange rate showing half-lives of minutes at –78 °C was much slower than previously believed but was clearly predicted from the non-equilibrium conditions. The tetramer-based subunit exchange had a number of notable features. Associating two dimers to form tetrameric ladder **36** avoids the thermochemically challenging problem of generating two high-energy monomers via a single transition structure.[47] A ladder fragment such as **37** can be viewed as a leaving group as well as the source of a second monomer. Moreover, the principle of microscopic reversibility[36] suggests that the process in reverse—the aggregation of monomers to form dimers—proceeds via monomer–monomer self-association *and* the far less obvious sequential association of two monomers with LDA dimer **1** to form four-rung ladders followed by the dissociation to 2 equiv of **1**. Last, we showed that, as expected, LiX salts such as LiCl accelerate the subunit exchange consistent with their influence on deaggregation-limited metalation rates.

2.10. Ortholithiation of 1,4-bis(Trifluoromethyl)benzene. Studies of the metalation in eq 6.28[34] showed features similar to those of 1,4-difluorobenzene described in Section 2.8.[8h]

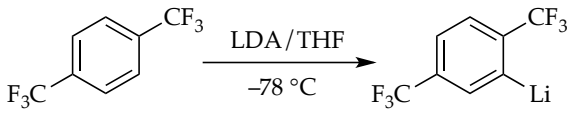

(6.28)

The results summarized in Scheme 6.13 reveal a combination of rate-limiting dimer- and tetramer-based aggregation events competing for dominance.[48] With the aid of isotopic substitution to shift the rate-limiting steps, we showed that the dimer- and tetramer-based deaggregations are followed by dimer-based metalations. Unusually low levels of autocatalysis foreshadowed oddities.

Scheme 6.13. Mechanism of LDA-mediated ortholithiation of 1,4-bis(trifluoromethyl)benzene. Reproduced from ref 8h. Copyright 2015 American Chemical Society.

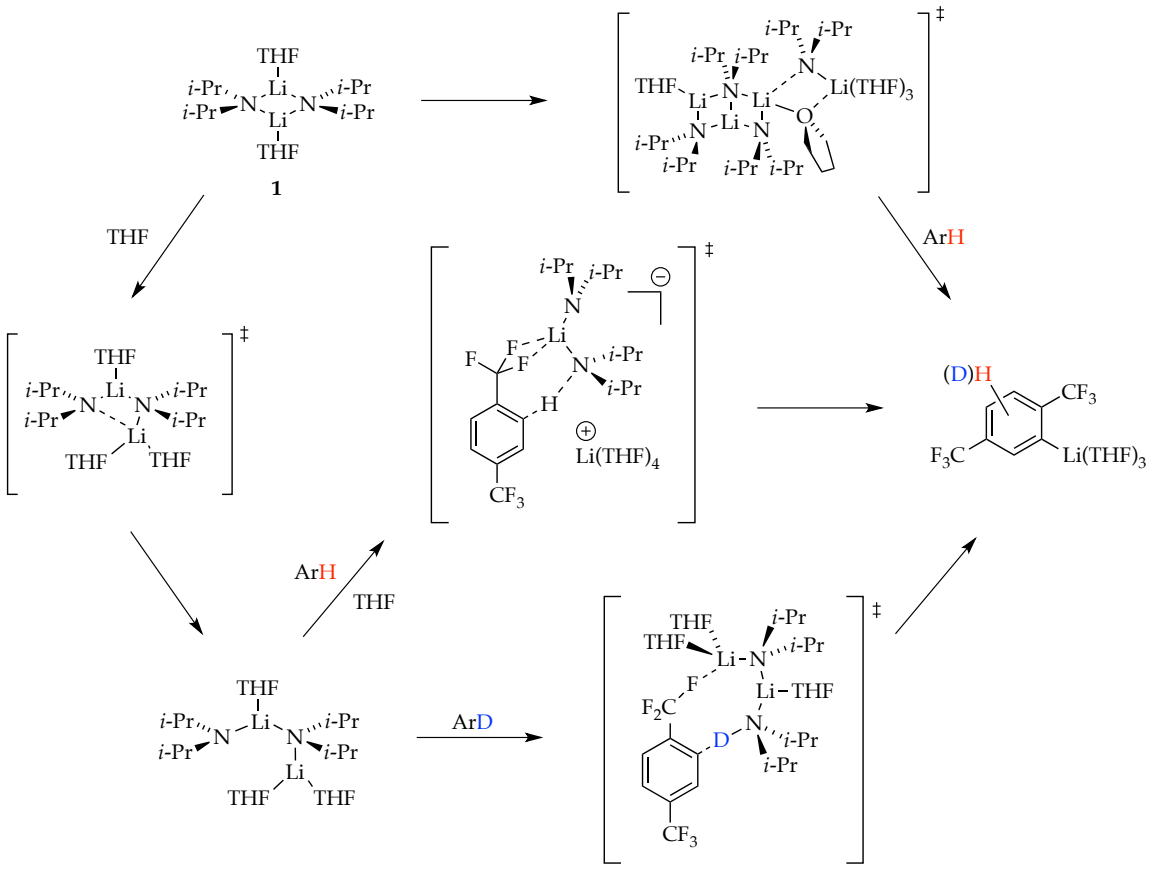

This final foray into non-equilibrium kinetics added one more jarring result to assure us that our understanding remains incomplete. We discovered that at –78 °C, LiCl had *no measurable effect on the metalation rate* (Figure 6.22, scenario 2). This result was unprecedented within the series. For obscure reasons, we examined the influence of LiCl at elevated temperature (–42 °C) and found that catalytic LiCl produced a small but still significant *inhibition* of the metalation—a factor of 2 (Figure 6.22, scenario 1). On first

inspection, 5% catalyst imparting a 2-fold inhibition defies common sense given that inhibitors under equilibrium conditions are necessarily stoichiometric. The results became surreal when dropping the temperature to –95 °C revealed LiCl catalysis, albeit at muted levels (Figure 6.22, scenario 3).

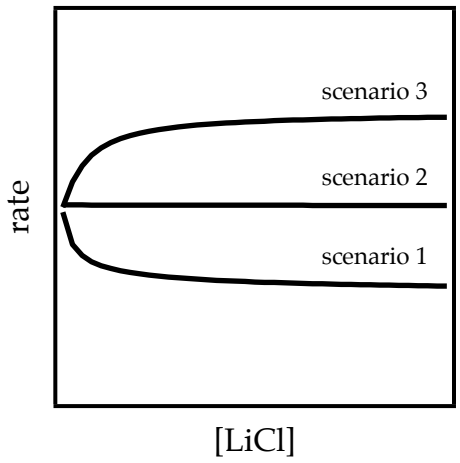

Figure 6.22. Plot of initial rate versus LiCl concentration showing catalyzed inhibition (scenario 1), no change in rate (scenario 2), and catalyzed acceleration (scenario 3).

How does one account for the influence of LiCl that ranges from catalyzed inhibition to catalyzed acceleration by merely adjusting the temperature? The key to constructing a model for catalyzed inhibition *even as a proof of principle* was noting the complex interplay between the LiCl-catalyzed monomer-based metalation and uncatalyzed dimer-based metalation. The critical portion of an otherwise complex mechanism and mathematical model is the reaction flux via the dimer-based metalation, which creates aryllithium and a low steady-state population of LDA monomer (AS_3) that is rapidly scavenged by ArH (eq 6.29). We identified three limiting scenarios: (1) if the

monomer population generated from the dimer-based metalation is *below* the equilibrium population, LiCl-catalyzed dimer-monomer equilibration increases the steady-state concentration to equilibrium levels and increases the reaction rate; (2) if the monomer population generated from the dimer is *above* the equilibrium population, LiCl catalysis accelerates the reaggregation to dimer with a consequent rate reduction (inhibition); and (3) if the monomer population generated from the dimer-based metalation is at the equilibrium population, LiCl-catalyzed monomer-dimer equilibration has no effect on the monomer population and thus no effect on the ortholithiation rate. These three conditions are met at –95 °C, –42 °C, and –78 °C, respectively. We find analogy of the catalyzed inhibition to photodesensitizers (fluoorescence quenchers) or anti-knock agents in gasoline to be useful constructs,[49,50] as they are also non-equilibrium processes that can be influenced by an external agent (catalyst) to reestablish equilibria.

$$A_2S_2 + ArH + 4S \longrightarrow ArLiS_3 + [AS_3] \qquad (6.29)$$

3. Rate Limitation: Some Additional Thoughts. Struggles to understand LDA-mediated reactions under non-equilibrium conditions underscored aspects of rate limitation that we either had thought about only superficially or worse, had no understanding of whatsoever. We failed to grasp, for example, the pragmatic consequences of ZPE and tunneling in transition states. In this final section, we present an eclectic mix of ideas tied together by rate limitation. Some will seem self-evident, whereas others may be counterintuitive.

3.1. Commensurate Barriers. The mechanistic complexity of the chemistry in this review stems from a series of activation barriers that are, energetically, nearly equivalent. This topic has received surprisingly little attention.[22] Imagine, in the abstract, a surface that has, for the sake of discussion, a 10.0 kcal/mol barrier versus one with two sequential barriers of 10.0 kcal/mol each (Figure 6.23). Does fleeting intermediate *I* influence the reaction rate, or is the rate dictated by the energy of the highest barrier, which is 10.0 kcal/mol with or without *I*? In short, intermediate *I* imparts a two-fold rate suppression. Having overcome the first 10.0 kcal/mol barrier, *I* has a 50% probability of exiting to product. In fact, the rate suppression caused by *n* equal energy barriers is proportional to 1/*n* (supporting information). Thus, the existence of *I* makes the effective barrier >10 kcal/mol.

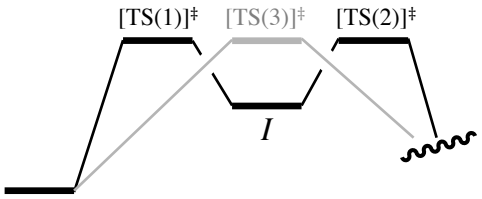

Figure 6.23. Superimposed single and double barriers of equal energies.

Now imagine that the second barrier is incrementally lower by 0.2 kcal/mol (Figure 6.24, top). Is the first barrier now rate limiting and the second barrier of no consequence? Again, the answer is no. The probability of *I* proceeding to product is now

>50%, but the probability of returning to starting material remains significant (42% at 25 °C).

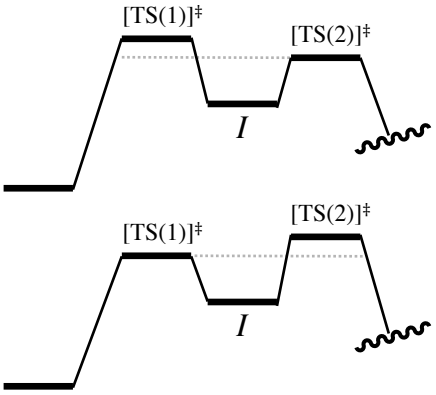

Figure 6.24. Double barriers in which the second barrier is slightly lower (top) and the first barrier is slightly lower (bottom).

It is less intuitive when the first barrier is slightly lower (Figure 6.24, bottom), but the rate suppression is identical whether the lower barrier precedes or succeeds the highest barrier. Given a series of barriers of similar but unique energies (eq 6.30), an expression for the effective barrier can be written (eq 6.31; supporting information). One should probably hope never to need this calculation.

$$\mathrm{C} \underset{k_{-1}}{\overset{k_1}{\rightleftharpoons}} \mathrm{I}_1 \underset{k_{-2}}{\overset{k_2}{\rightleftharpoons}} \ldots \underset{k_{-n}}{\overset{k_n}{\rightleftharpoons}} \mathrm{P} \qquad (6.30)$$

$$-\frac{\mathrm{d}[\mathrm{C}]}{\mathrm{d}t} = \frac{[\mathrm{C}]_0}{\sum_{m=1}^{n} \frac{1}{k_m \prod_{i=1}^{m-1} \frac{k_i}{k_{-i}}}} \qquad (6.31)$$

3.2. Complex-Induced Proximity Effect. There is an exceedingly popular theory of ortholithiations and related directed metalations called the complex-induced proximity effect or CIPE.[51] As the theory goes, pre-complexation of a substrate to a functional group brings the base and proton proximate, which facilitates the reaction (eq 6.32).

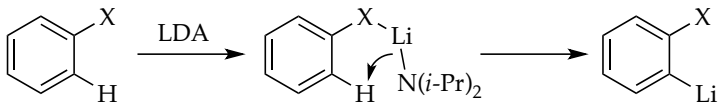

pre-complex (6.32)

We (and others) have challenged this theory at a foundational level and will now amplify our concerns.[6,52] The arguments made were twofold to which we now add a third:

(1) The energy required to proceed from the ground state to the rate-limiting transition state is a state function; it is path-independent. The existence of an intermediate en route does not affect the relative energies (which is fortunate for kineticists).

(2) Should such a “pre-complex” be so stable as to become observable, the putative merits offered by proximity are offset by the lowering of the ground state with consequent *increase* in the overall barrier height.

(3) We now add the scenario in which the barrier leading to the fleeting "pre-complex" is close to the barrier for proton transfer. Per the discussion in Section 3.1, the existence of the fleeting intermediate retards the metalation rate as much as twofold.

The notion that complexation facilitates a metalation has nothing to do with proximity. Metal–ligand interactions accelerate the metalation if, and only if, they stabilize the *transition state* for proton transfer.

3.3. Mixed Aggregation Effects and the Principle of Detailed Balance. The principle of detailed balance should, in our opinion, be one of the foundational principles emphasized in organic chemistry.[53] It is especially useful when considering complex systems that otherwise defy intuition. The principle states that, given an ensemble of species at equilibrium (eq 6.33), each individual equilibrium is maintained.

$$\mathrm{A} \rightleftharpoons \mathrm{B} \rightleftharpoons \mathrm{C} \qquad (6.33)$$

If, for example, an additional equilibrium is attached by adding reagent X to afford CX (eq 6.34), the concentration of *all* species in the original equilibrium will *diminish* according to the principles of equilibrium.

$$\mathrm{A} \rightleftharpoons \mathrm{B} \rightleftharpoons \mathrm{C} \overset{\mathrm{X}}{\rightleftharpoons} \mathrm{CX} \qquad (6.34)$$

The inhibition described in Section 2.10 arose from catalyzing an equilibrium that was not fully established in the absence of catalyst. Given an ensemble already at equilibrium, adding 5 mol % LiCl to form a 1:1 mixed aggregate would cause a 5 mol % concentration depletion of the original ensemble and an affiliated 5% reduction in the reaction rate, not 50%. *Inhibition of systems at equilibrium are inherently stoichiometric.* A corollary is that the attachment of an additional equilibrium to *any* of the species in the ensemble depletes *all* species in the ensemble: forming CX rather than BX or AX in no way attests to a mechanistic importance of C rather than A or B.

The principle of detailed balance offers insights into the consequences of heterogeneous media. It is tempting to infer that the rate of reaction of a partially soluble reagent or substrate will *necessarily* increase if one introduces an additive, X, that solubilizes the reagent (eq 6.35). The complexent could be a lithium salt, such as LiCl, added to form a soluble mixed aggregate or a polar solvent that may, but does not necessarily, coordinate directly to A. The concentration of the species denoted $A_{solution}$ necessarily remains constant as $AX_{solution}$ forms until the A_{solid} is consumed. The reaction rate of A increases only if an independent reactive pathway is available to $AX_{solution}$. Dissolving a substrate by ligation is inherently stabilizing and will not influence the reaction rate unless the transition state is disproportionately stabilized.

$$A_{solution} \rightleftharpoons A_{solid} \overset{X}{\rightleftharpoons} AX_{solution} \qquad (6.35)$$

3.4. Termolecular Reactions. In this final section, we pick a fight, and a risky one at that. We suggested earlier that LDA monomers reaggregate sequentially, associating two LDA monomers with a dimer to form a tetramer, which then dissociates to two dimers (see Section 2.9). We now ask the seemingly blasphemous question: can these three associate in a single step? The answer is no: assembling three fragments does not occur as a single-step—*termolecular*—reaction (eq 6.36) but rather proceeds through two sequential bimolecular reactions.

Try the following: ask a chemist *why* such three-component associations necessarily proceed via sequential *bimolecular* steps (eqs 6.37 and 6.38). The answer will, without fail in our experience, be some variant of "the probability of bringing three species together in one place to achieve termolecularity is simply too low." In short, termolecular reactions via $[A—B—C]^{‡}$ are widely accepted to be entropically disfavored. But is this true?

Termolecular

$$A + B + C \longrightarrow [A\text{--}B\text{--}C]^{‡} \longrightarrow ABC \qquad (6.36)$$

sequential bimolecular

$$A + B \longrightarrow [A\text{--}B]^{‡} \longrightarrow AB \qquad (6.37)$$

$$AB + C \longrightarrow [AB\text{--}C]^{‡} \longrightarrow ABC \qquad (6.38)$$

Using the principle of microscopic reversibility, consider the reaction in reverse: the dissociation of ABC via $[AB\text{--}C]^{‡}$ is entropically favored as evidenced both experimentally and theoretically.[54] Dissociation of ABC via $[A\text{--}B\text{--}C]^{‡}$ should be entropically even more favored, should it not? Thus, scaled relative to ABC as a common reference point, $[A\text{--}B\text{--}C]^{‡}$ is entropically favored relative to $[AB\text{--}C]^{‡}$. In fact,

unimolecular dissociation of a large *n*-mer to *n*-monomers would be stupendously favored entropically. *$[A\text{--}B\text{--}C]^{‡}$ is unfavorable because each partial bond represents significant enthalpic cost as the number of bonds rises.* We add that, at the high-temperature limit, termolecular reactions would be highly favored and *n*-mers could indeed dissociate to *n* monomers unimolecularly.

Conclusion

Studies of LDA-mediated metalations under non-equilibrium conditions have provided a mechanistic complexity that rivals that of any homogeneous organometallic mechanism. The story unfolded owing to the efforts of a half dozen Ph.D. researchers. The big question is simple: was it worth it? A referee once suggested that such a question is inappropriate. To the contrary, that question should be asked of *any* scientific pursuit. We answer affirmatively and give five reasons: (1) the prominence of LDA in both academic and industrial organic synthesis easily justifies understanding its most intimate details; (2) probes of how LiX salts deaggregate are almost nonexistent; (3) partially and fully rate-limiting deaggregations and other non-equilibrium events have measurable consequences on the chemistry of LDA in THF at –78 °C; (4) such transitional regions of reactivity in which rates for key aggregation events and reactions of the fleeting structural forms with substrates necessarily exist for *any* organolithium reagent–solvent combination; and (5) the methods and strategies outlined in Section 1 are potentially generalizable to any complex mechanistic study. This review represents our last word on non-equilibrium kinetics as it pertains to the chemistry of LDA (or so we hope), but it is by no means the last word on the topic in the larger picture. Early results suggest that

reactions of lithium enolates may be particularly influenced by the rates at which aggregates exchange, not just the existence of those aggregates.

Chapter 6 References and Footnotes

1. (a) Bakker, W. I. I.; Wong, P. L.; Snieckus, V. *Lithium Diisopropylamide.* In *e-EROS Encyclopedia of Reagents for Organic Synthesis*; Paquette, L. A., Ed.; John Wiley: New York, 2001. (b) Eames, J. Product Subclass 6: Lithium Amides. In *Science of Synthesis*; Snieckus, V., Ed.; Thieme; New York, 2006; Vol. 8a, p 173.

2. Reich survey: http://www.chem.wisc.edu/areas/reich/syntheses/syntheses.htm

3. (a) Seebach, D. *Angew. Chem. Int. Ed. Engl.* **1988**, *27*, 1624. (b) Reich, H. J. *Chem. Rev.* **2013**, *113*, 7130.

4. Collum, D. B. *Acc. Chem. Res.* **1993**, *26*, 227.

5. Tchoubar, B.; Loupy, A. *Salt Effects in Organic and Organometallic Chemistry*; VCH: New York, 1992.

6. Collum, D. B.; McNeil, A. J.; Ramírez, A. *Angew. Chem. Int. Ed.* **2007**, *46*, 3002.

7. The rate law provides the stoichiometry of the transition structure relative to that of the reactants: Edwards, J. O.; Greene, E. F.; Ross, J. *J. Chem. Educ.* **1968**, *45*, 381.

8. (a) Singh, K. J.; Hoepker, A. C.; Collum, D. B. *J. Am. Chem. Soc.* **2008**, *130*, 18008. (b) Gupta, L.; Hoepker, A. C.; Singh, K. J.; Collum, D. B. *J. Org. Chem.* **2009**, *74*, 2231. (c) Ma, Y.; Hoepker, A. C.; Gupta, L.; Faggin, M. F.; Collum, D. B. *J. Am. Chem. Soc.* **2010**, *132*, 15610. (d) Hoepker, A. C.; Gupta, L.; Ma, Y.; Faggin, M. F.; Collum, D. B. *J. Am. Chem. Soc.* **2011**, *133*, 7135. (e) Hoepker, A. C.; Collum, D. B. *J. Org. Chem.* **2011**, *76*, 7985. (f) Gupta, L.; Hoepker, A. C.; Ma, Y.; Viciu, M. S.; Faggin, M. F.; Collum, D. B. *J. Org. Chem.* **2013**, *78*, 4214. (g) Liang, J.; Hoepker, A. C.; Bruneau, A. M.; Ma, Y.; Gupta, L.; Collum, D. B. *J. Org. Chem.* **2014**, *79*, 11885. (h) Liang, J.; Hoepker, A. C.; Algera, R. F.; Ma, Y.; Collum, D. B. *J. Am. Chem. Soc.* **2015**, *137*, 6292.

9. (a) Kohen, Amnon, and Hans-Heinrich Limbach, eds. *Isotope effects in chemistry and biology*. CRC Press, 2005. (b) Bell, R. P. *The Tunnel Effect in Chemistry*; Chapman & Hall: New York, 1980. (c) Carpenter, B. K. *Determination of Organic Reaction Mechanisms*; Wiley: New York, 1984. (d) Caldin, E. F. *Chem. Rev.* **1969**, *69*, 135. (e) For an excellent discussion of the various isotope effects from a decidedly thermochemical perspective, see: Simmons, E. M.; Hartwig, J. F. *Angew. Chem., Int. Ed. Engl.* **2012**, *51*, 3066

10. McGarrity, J. F.; Ogle, C. A. *J. Am. Chem. Soc.* **1985**, *107*, 1810.

11. (a) Thomas, A. A.; Denmark, S. E. *Science* **2016**, *352*, 329. (b) Bertz, S. H.; Cope, S. K.; Hardin, R. A.; Murphy, M. D.; Ogle, C. A.; Smith, D. T.; Thomas, A. A.; Whaley, T. N. *Organometallics* **2012**, *31*, 7827.

12. (a) Reich, H. J. *J. Org. Chem.* **2012**, *77*, 5471. (b) Jones, A. C.; Sanders, A. W.; Sikorski, W. H.; Jansen, K. L.; Reich, H. J. *J. Am. Chem. Soc.* **2008**, *130*, 6060. (c) Plessel, K. N.; Jones, A. C.; Wherritt, D. J.; Maksymowicz, R. M.; Poweleit, E. T.; Reich, H. J. *Org. Lett.* **2015**, *17*, 2310.

13. Espenson, J. H. *Chemical Kinetics and Reaction Mechanisms*, 2nd ed.; McGraw-Hill: New York, 1995.

14. Casado, J.; Lopez-Quintela, M. A.; Lorenzo-Barral, F. M. *J. Chem. Educ.* **1986**, *63*, 450.

15. For a review of structural studies using ^{19}F NMR spectroscopy, see: (a) Gakh, Y. G.; Gakh, A. A.; Gronenborn, A. M. *Magn. Reson. Chem.* **2000**, *38*, 551. (b) McGill, C. A.; Nordon, A.; Littlejohn, D. *J. Process Anal. Chem.* **2001**, *6*, 36. (c) Espinet, P.; Albeniz, A. C.; Casares, J. A.; Martinez-Ilarduya, J. M. *Coor. Chem. Rev.* **2008**, *252*, 2180.

16. Review of ^{6}Li NMR spectroscopy: Günther, H. *J. Brazil. Chem.* **1999**, *10*, 241.

17. (a) Rein, A. J.; Donahue, S. M.; Pavlosky, M. A. *Curr. Opin. Drug Discovery Dev.* **2000**, *3*, 734. (b) Eisenbeis, S. A.; Chen, R.; Kang, M.; Barrila, M.; Buzon, R. *Org. Process Res. Dev.* **2015**, *19*, 244, and references cited therein.

18. Frisch, M. J. et al. *GaussianVersion 3.09*; revision A.1; Gaussian, Inc.: Wallingford, CT, 2009.

19. Frey, P. A.; Hegeman, A. D. *Enzymatic Reaction Mechanisms*; Oxford University Press: New York, 2007; Chapter 2.

20. (a) Kristian, K. E.; Iimura, M.; Cummings, S. A.; Norton, J. R.; Janak, K. E.; Pang, K. *Organometallics* **2009,** *28,* 493. (b) Yi, C. S.; Zeczycki, T. N.; Lindeman, S. V. *Organometallics* **2008,** *27,* 2030. (c) Wijeratne, G. B.; Corzine, B.; Day, V. W.; Jackson, T. A. *Inorg. Chem*. **2014**, *53*, 7622.

21. (a) Schneider, K. J; van Eldik, R. *Organometallics* **1990**, *9*, 1235. (b) Byers. P. K.; Canty, A. J.; Crespo, M.; Puddephatt, R. J.; Scott, J. D. *Organometallics* **1988**, *7*, 1363. (c) Jordan, R. F.; Norton, J. R. *J. Am. Chem. Soc*. **1982**, *104*, 1255. (d) Belt, S. T.; Grevels, F-W.; Klotzbücher, W. E.; McCamley, A.; Perutz, R. N. *J. Am. Chem. Soc*. **1989**, *111*, 8373. (e) Brown, T. L.; Bellus, P. A. *Inorg. Chem.* **1978**, *17*, 3726. (f) Minniti, D.; Alibrandi, G.; Tobe, M. L.; Romeo, R. *Inorg. Chem*. **1987**, *26*, 3956. (g) Durak, L. J.; Lewis, J. C. *Organometallics* **2013**, *32*, 3153.

22. (a) Dumesic, J. A. *J. Catalysis*. **1999**, *185*, 496. (b) Campbell, C. T. *J. Catalysis*. **2001**, *204*, 520. (c) Dumesic, J. A. *J. Catalysis*. **2001**, *204*, 525. (d) Meskine, H.; Matera, S.; Scheffler, M.; Reuter, K.; Metiu, H. *Surface Science* **2009**, *603*, 1724. (e) Campbell,

C. T. *Topics in Catalysis* **1994**, *1*, 353. (f) Stegelmann, C.; Andreasen, A.; Campbell, C. T. *J. Am. Chem. Soc.* **2009***, 131*, 8077.

(g) Barański, A. *Solid State Ionics* **1999**, *117*, 123. (g) Kozuch, S.; Shaik, S. *Acc. Chem. Res.* **2011**, *44*, 101.

23. (a) Besson, C.; Finney, E. E.; Finke, R. G. *J. Am. Chem. Soc.* **2005,** *127,* 8179. (b) Besson, C.; Finney, E. E.; Finke, R. G. *Chem. Mater.* **2005,** *17,* 4925. (c) Huang, K. T.; Keszler, A.; Patel, N.; Patel, R. P.; Gladwin, M. T.; Kim-Shapiro, D. B.; Hogg, N. *J. Biol. Chem.* **2005**, *280*, 31126. (d) Huang, Z.; Shiva, S.; Kim-Shapiro, D. B.; Patel, R. P.; Ringwood, L. A.; Irby, C. E.; Huang, K. T.; Ho, C.; Hogg, N.; Schechter, A. N.; Gladwin, M. T. *J. Clin. Invest.* **2005**, *115*, 2099. (e) Tanj, S.; Ohno, A.; Sato, I.; Soai, K *Org. Lett.* **2001**, *3*, 287. (f) Barrios-Landeros, F.; Carrow, B. P.; Hartwig, J. F. *J. Am. Chem. Soc.* **2008**, *130*, 5842.

24. (a) Bissette, A. J.; Fletcher, S. P. *Angew. Chem. Int. Ed.* **2013**, *52*, 12800. (b) Espenson, J. H. *Chemical Kinetics and Reaction Mechanisms*, 2nd ed.; McGraw-Hill: New York, 1995, p. 190.

25. Houghton, M. J.; Huck, C. J.; Wright, S. W.; Collum, D. B. *J. Am. Chem. Soc.* **2016**, *138*, 10276.

26. Adam, W.; Krebs, O.; Orfanopoulos, M.; Stratakis, M.; Vougioukalakis, G. C. *J. Org. Chem.* **2003**, *68*, 2420 and references cited therein.

27. Gonzalez-James, O. M.; Kwan, E. E.; Singleton, D. A. *J. Am. Chem. Soc.* **2012**, *134*, 1914 and references cited therein.

28. (a) Ma, Y.; Breslin, S.; Keresztes, I.; Lobkovsky, E.; Collum, D. B. *J. Org. Chem.* **2008**, *73*, 9610. (b) Rennels, R. A.; Rutherford, J. L.; Collum, D. B. *J. Am. Chem. Soc.* **2000**, *122*, 8640. (c) Anderson, D. R.; Faibish, N. C.; Beak, P. *J. Am. Chem. Soc.* **1999**, *121*, 7553. (d) Meyers, A. I.; Mihelich, E. D. *J. Org. Chem.* **1975**, *40*, 3158.

29. Liao, S.; Collum, D. B. *J. Am. Chem. Soc.* **2003**, *125*, 15114.

30. We discuss the varieties of salt effects on reaction rates in ref 6c.

31. Barr, D.; Snaith, R.; Wright, D. S.; Mulvey, R. E.; Wade, K. *J. Am. Chem. Soc.* **1987**, *109*, 7891.

32. Herrman, J. L.; Kieczykowski, G. R.; Schlessinger, R. H. *Tetrahedron Lett.* **1973**, *15*, 2433.

33. Davies, S. G.; Smith, A. D.; Price, P. D. *Tetrahedron: Asymmetry* **2005**, *16*, 2833.

34. Mongin, F.; Desponds, O.; Schlosser, M. *Tetrahedron Lett.* **1995**, *37*, 2767.

27. (a) Mongin, F.; Schlosser, M. *Tetrahedron Lett*. **1997**, *38*, 1559. (b) Cottet, F.; Schlosser, M. *Eur. J. Org. Chem*. **2004**, 3793.

36. The principle of microscopic reversibility must be applied with caution: (a) Blackmond, D. G. *Angew. Chem. Int. Ed.* **2009**, *48*, 2648. (b) Krupka, R. M.; Kaplan, H.; Laidler, K. J. *J. Chem. Soc., Faraday Trans.* **1966**, *62*, 2754. (c) Chandrasekhar, S. *Res. Chem. Intermed.* **1992**, *17*, 173. (d) Burwell, R. L.; Pearson, R. G. *J. Phys. Chem.* **1966**, *70*, 300.

37. Representative examples of structurally characterized bridging THF ligands: (a) Pratt, L. M.; Merry, A.; Nguyen, S. C.; Quanb, P.; Thanh, B. T. *Tetrahedron* **2006**, *62*, 10821. (b) Clegg, W.; Liddle, S. T.; Mulvey, R. E.; Robertson, A. *Chem. Commun.* **1999**, 511. (c) Boche, G.; Boie, C.; Bosold, F.; Harms, K.; Marsch, M. *Angew. Chem. Int. Ed.* **1994**, *33***,** 115. (d) Daniele, S.; Drost, C.; Gehrhus, B.; Hawkins, S. M.; Hitchcock, P. B.; Lappert, M. F.; Merle, P. G.; Bott, S. G. *J. Chem. Soc., Dalton Trans.* **2001**, 3179. (e) Chivers, T.; Fedorchuk, C.; Parvez, M. *Inorg. Chem.* **2004**, *43*, 2643. (f) Briand, G. G.; Chivers, T.; Parvez, M. *J. Chem. Soc., Dalton Trans.* **2002**, 3785.

38. Zimmerman, P. M. *J. Computational Chem.* **2015**, *36*, 601.

39. (a) Lonsdale, R.; Harvey, J. N.; Mulholland, A. J. *Chem. Soc. Rev*. **2012**, *41*, 3025. (b) Bahnson, B. J.; Klinman, J. P. *Methods Enzymol*. **1995**, *249*, 373. (c) Hong, Y. J.; Tantillo, D. J. *Nature Chem.* **2009**, *1*, 384.

40. (a) Schlosser, M. *Angew. Chem. Int. Ed.* **2005**, *44*, 376. (b) Schlosser, M.; Rausis, T. *Eur. J. Org. Chem.* **2004**, 1018. (c) Kuethe, J. T.; Zhong, Y.-L.; Alam,M.; Alorati, A. D. Beutner, G. L.; Cai, D.; Fleitz, F. J.; Gibb, A. D.; Kassim, A.; Linn, K.; Mancheno, D.; Marcune, B.; Pye, P. J.; Scott, J. P.; Tellers, D. M.; Xiang, B.; Yasuda, N.; Yin, J.; Davies, I. W, *Tetrahedron* **2009**, *65*, 5013. (d) Güngör, T.; Marsais, F.; Queguiner, G. *J. Organomet. Chem.* **1981**, *215*, 139.

41. (a) Fort, Y. *2-Fluoropyridine* In *e-EROS Encyclopedia of Reagents for Organic Synthesis*; John Wiley & Sons, NewYork; 2001. (b) Bhardwaj, P.; Forgione, P. *2,6-Difluoropyridine.* In *e-EROS Encyclopedia of Reagents for Organic Synthesis*; John Wiley & Sons, NewYork; 2001.

42. Romesberg, F. E.; Collum, D. B. *J. Am. Chem. Soc.* **1994**, *116*, 9198.

43. (a) Evans, W. J.; Broomhall-Dillard, R. N. R.; Ziller, J. W. *J. Organomet. Chem.* **1998**, *569*, 89. (b) Klingebiel, U.; Tecklenburg, B.; Noltemeyer, M.; Schmidt-Baese, D.; Herbst-Irmer, R. *Z. Naturforsch. B Chem. Sci.* **1998**, *53*, 355.

44. Mulvey, R. E. *Chem. Soc. Rev.* **1991**, *20*, 167.

45. For examples of lithium amide mixed ladders, see: (a) Williard, P. G.; Hintze, M. J. *J. Am. Chem. Soc.* **1987**, *109*, 5539. (b) Mair, R. S.; Clegg, W.; O'Neil, P. A. *J. Am. Chem.*

Soc. **1993**, *115*, 3388. (c) Engelhardt, L. M.; Jacobsen, G. E.; White, A. H.; Raston, C. L. *Inorg. Chem.* **1991**, *30*, 3978. (d) Williard, P. G.; Hintze, M. J. *J. Am. Chem. Soc.* **1987**, *109*, 5539.

46. For an example of the butyllithium-based ortholithiation of arene **1**, see: Coffer, P. K.; Dillon, K. B.; Howard, J. A. K.; Yufit, Dmitry S.; Zorina, N. V. *J. Chem. Soc., Dalton Trans.* **2012**, *41*, 4460.

47. Tetrameric lithium amide ladders: (a) Armstrong, D. R.; Barr, D.; Clegg, W.; Mulvey, R. E.; Reed, D.; Snaith, R.; Wade, K. *J. Chem. Soc.*, *Chem. Commun.* **1986**, 869. (b) Gardiner, M. G.; Raston, C. L. *Inorg. Chem.* **1996**, *35*, 4047. (c) Vestergren, M.; Eriksson, J.; Hilmersson, G.; Hakansson, M. *J. Organomet. Chem.* **2003**, *682*, 172. (d) Boche, G.; Langlotz, I.; Marsch, M.; Harms, K.; Nudelman, N. E. S. *Angew. Chem.* **1992**, *104*, 1239.

48. For crystallographically characterized examples of lithium amide ladder structures showing open-dimer-like subunits, see: Armstrong, D. R.; Barr, D.; Clegg, W.; Hodgson, S. M.; Mulvey, R. E.; Reed, D.; Snaith, R.; Wright, D. S. *J. Am. Chem. Soc.* **1989**, *111*, 4719.

49. (a) Lakowicz, Joseph R. *Principles of Fluorescence Spectroscopy, 3rd edition*; Springer Science; New York, NY, 2006. (b) Eftink, M. R. *Fluorescence Quenching:*

Theory and Applications. In *Topics in Fluorescence Spectroscopy* Vol 2; Lakowicz, Joseph R., Ed.; Springer Science; New York, NY, 2002.

50. (a) Linteris, G. T.; Rumminger, M. D.; Babushok, V. I. *Progress in Energy and Combustion Science*. **2008**, *34*, 288. (b) Casias, C. R.; McKinnon, J. T. *Combust. Sci. Technol.* **1996**, *116-117*, 289. (c) Benson, S. W. *J. Phys. Chem*. **1988**, *92*, 1531.

51. Whisler, M. C.; MacNeil, S.; Snieckus, V.; Beak, P. *Angew. Chem. Int. Ed.* **2004**, *43*, 2206.

52. For similar concerns about the language of the complex-induced proximity effect, see: van Eikema Hommes, N. J. R.; Schleyer, P. v. R. *Angew. Chem. Int. Ed. Engl.* **1992**, *31*, 755.

53. Alberty, R. A. *J. Chem. Educ.* **2004**, *81*, 1206.

54. Anslyn, E. V; Dougherty, D. A. *Modern Physical Organic Chemistry*; University Science Books; Sausalito, California, 2006.

Chapter 6 Appendix

I. Simulation Protocols

Generic Scheme.

Assuming the generic scheme

$$\mathrm{A} \underset{k_{-1}}{\overset{k_1}{\rightleftharpoons}} \mathrm{B} \xrightarrow{k_2[\mathrm{C}]} \text{product}$$

an expression for [B] at a steady state follows.

$$[\mathrm{B}] = \frac{k_1[\mathrm{A}]}{k_{-1} + k_2[\mathrm{C}]}$$

From this expression one readily obtains the rate law for consumption of C.

$$-\frac{\mathrm{d}[\mathrm{C}]}{\mathrm{d}t} = \frac{k_1 k_2[\mathrm{A}][\mathrm{C}]}{k_{-1} + k_2[\mathrm{C}]}$$

II. Simulations

All figures were generated in Igor Pro® using simulated data from Wolfram Mathematica®. Following each figure is a chemical scheme and demarcated Mathematica code that can be copied and directly executed to recreate the plots. The figure numbers correspond to those in the manuscript.

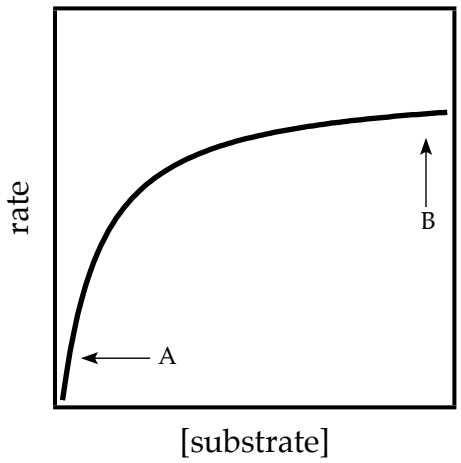

Figure A.6.1. (Figure 6.2 in manuscript) Saturation kinetics. A and B correspond to regions of substrate-concentration-dependent and substrate-concentration-independent regions.

$$\mathrm{A} \underset{k_{-1}}{\overset{k_1}{\rightleftharpoons}} \mathrm{B} \xrightarrow{k_2[\mathrm{C}]} \text{product}$$

$$\frac{\mathrm{d}[\mathrm{A}]}{\mathrm{d}t} = -k_1[\mathrm{A}] + k_{-1}[\mathrm{B}]$$

$$\frac{\mathrm{d}[\mathrm{B}]}{\mathrm{d}t} = k_1[\mathrm{A}] - k_{-1}[\mathrm{B}] - k_2[\mathrm{B}][\mathrm{C}]$$

$$\frac{\mathrm{d}[\mathrm{C}]}{\mathrm{d}t} = -k_2[\mathrm{B}][\mathrm{C}]$$

```
sol[k1_, kn1_, k2_, a0_, c0_] :=   NDSolve[{a'[t] == -k1*a[t] + kn1*b[t],     b'[t] ==
k1*a[t] - kn1*b[t] - k2*b[t]*c[t], c'[t] == -k2*b[t]*c[t],     a[0] == (a0 kn1)/(k1 + kn1),
b[0] == (a0 k1)/(k1 + kn1),     c[0] == c0}, {a, b, c}, {t, 0, 1000}]

Manipulate[{Plot[-c'[10] /. sol[k1, kn1, k2, a0, c0], {c0, 0, 0.1},     PlotRange -> {0,
0.0001}]}, {{k1, 0.001, "k1"}, 0,    10}, {{kn1, 1, "kn1"}, 0, 10}, {{k2, 1000, "k2"}, 0,
10}, {{a0, 0.1, "a0"}, 0, 10}, {{c0, 0.01, "c0"}, 0, 0.1}]

Export["table.xls",   Table[-c'[10] /. sol[0.001, 1, 100, 0.1, x], {x, 0, 0.1, 0.001}]]
```

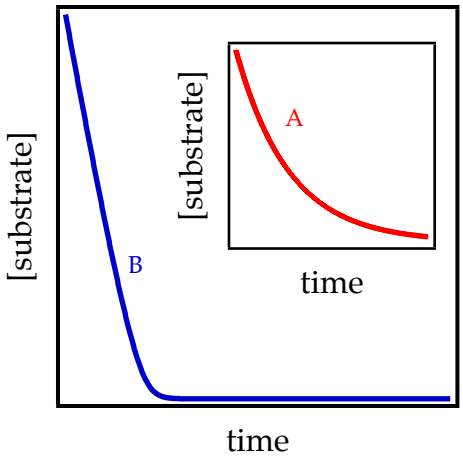

Figure A.6.2. (Figure 6.4 in manuscript) Decays of substrate ArH according to eqs 5 and 6 assuming rate-limiting proton transfer (k_2[ArH]/k_{-1} = 0.1; curve A) and rate-limiting deaggregation (k_2[ArH]/k_{-1} = 10; curve B).

$$\mathrm{A} \underset{k_{-1}}{\overset{k_1}{\rightleftharpoons}} \mathrm{B} \xrightarrow{k_2[\mathrm{C}]} \text{product}$$

$$\frac{d[A]}{dt} = -k_1[A] + k_{-1}[B]$$

$$\frac{d[B]}{dt} = k_1[A] - k_{-1}[B] - k_2[B][C]$$

$$\frac{d[C]}{dt} = -k_2[B][C]$$

```
sol[k1_, kn1_, k2_, a0_, c0_] :=   NDSolve[{a'[t] == -k1*a[t] + kn1*b[t],     b'[t] ==
k1*a[t] - kn1*b[t] - k2*b[t]*c[t], c'[t] == -k2*b[t]*c[t],     a[0] == (a0 kn1)/(k1 + kn1),
b[0] == (a0 k1)/(k1 + kn1),     c[0] == c0}, {a, b, c}, {t, 0, 10000}]

Export["table.xls", {Table[    Evaluate[c[t] /. sol[0.0001, 1, 10, 0.1, 0.01]], {t, 0, 50000,
10}], Table[    Evaluate[c[t] /. sol[0.0001, 1, 1000, 0.1, 0.01]], {t, 0, 5000,      1}]}]
```

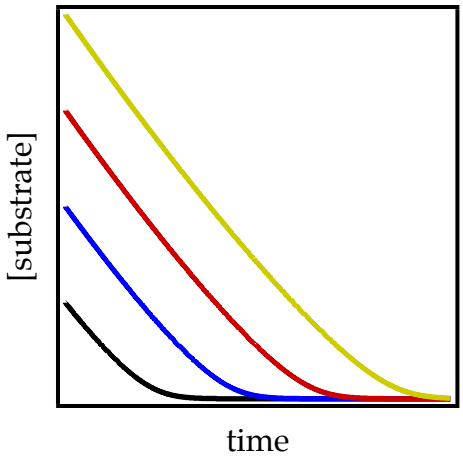

Figure A.6.3. (Figure 6.5 in manuscript) Zeroth-order decays at various initial starting concentrations of ArH showing parallel decays and the onset of rate-limiting proton transfer (curvatures) at low ArH concentration.

$$\mathrm{A} \underset{k_{-1}}{\overset{k_1}{\rightleftharpoons}} \mathrm{B} \xrightarrow{k_2[\mathrm{C}]} \text{product}$$

$$\frac{\mathrm{d}[\mathrm{A}]}{\mathrm{d}t} = -k_1[\mathrm{A}] + k_{-1}[\mathrm{B}]$$

$$\frac{\mathrm{d}[\mathrm{B}]}{\mathrm{d}t} = k_1[\mathrm{A}] - k_{-1}[\mathrm{B}] - k_2[\mathrm{B}][\mathrm{C}]$$

$$\frac{\mathrm{d}[\mathrm{C}]}{\mathrm{d}t} = -k_2[\mathrm{B}][\mathrm{C}]$$

```
sol[k1_, kn1_, k2_, a0_, c0_] :=   NDSolve[{a'[t] == -k1*a[t] + kn1*b[t],     b'[t] ==
k1*a[t] - kn1*b[t] - k2*b[t]*c[t], c'[t] == -k2*b[t]*c[t],     a[0] == (a0 kn1)/(k1 + kn1),
b[0] == (a0 k1)/(k1 + kn1),     c[0] == c0}, {a, b, c}, {t, 0, 10000}]

Export["table.xls",  { Table[Evaluate[c[t] /. sol[0.00001, 0.1, 1000, 0.1, 0.001]], {t, 0,
5000, 1}], Table[Evaluate[c[t] /. sol[0.00001, 0.1, 1000, 0.1, 0.002]], {t, 0,     5000, 1}],
Table[Evaluate[c[t] /. sol[0.00001, 0.1, 1000, 0.1, 0.003]], {t, 0,     5000, 1}]}]
```

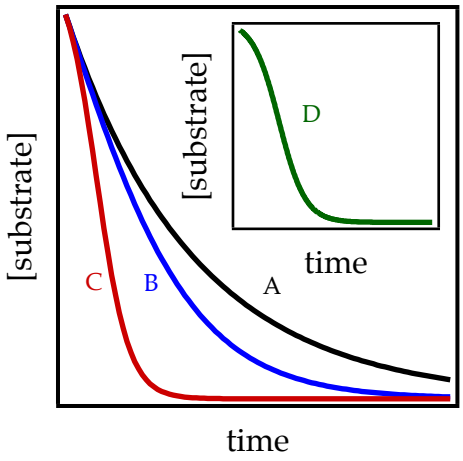

Figure A.6.4. (Figure 6.8 in manuscript) Varying degrees of autocatalysis superimposed on first-order decays: curve A, none; curve B, mild; curve C, medium; curve D, strong.

$$\mathrm{A} \xrightarrow{k_1} \mathrm{B}$$

$$\mathrm{A} \xrightarrow{k_2[\mathrm{B}]} \mathrm{B}$$

$$\frac{\mathrm{d}[\mathrm{A}]}{\mathrm{d}t} = -k_1[\mathrm{A}] - k_2[\mathrm{A}][\mathrm{B}]$$

$$\frac{\mathrm{d}[\mathrm{B}]}{\mathrm{d}t} = k_1[\mathrm{A}] + k_2[\mathrm{A}][\mathrm{B}]$$

```
sol[k1_, k2_, a0_] :=   NDSolve[{a'[t] == -k1*a[t] - k2*a[t]*b[t],     b'[t] == k1*a[t] +
k2*a[t]*b[t], a[0] == a0, b[0] == 0}, {a,     b}, {t, 0, 1000}]

Export["table.xls",   {Table[Evaluate[a[t] /. sol[0.1, 0, 0.1]], {t, 0, 60, 0.3}],
Table[Evaluate[a[t] /. sol[0.1, 1, 0.1]], {t, 0, 60, 0.3}], Table[Evaluate[a[t] /. sol[0.1, 5,
0.1]], {t, 0, 60, 0.3}]}]
```

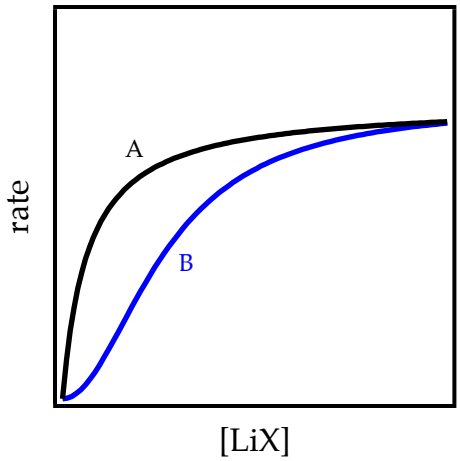

Figure A.6.5. (Figure 6.9 in manuscript)Simulation of catalysis showing first-order (curve A) and second-order (curve B) saturation kinetics.

$$\text{rate} = \frac{ax^n}{1+ax^n}$$

```
Export["table.xls", {Table[1*x^1/(1 + 1*x^1), {x, 0, 10, 0.1}], Table[0.2*x^2/(1 + 0.2*x^2), {x, 0, 10, 0.1}]}]
```

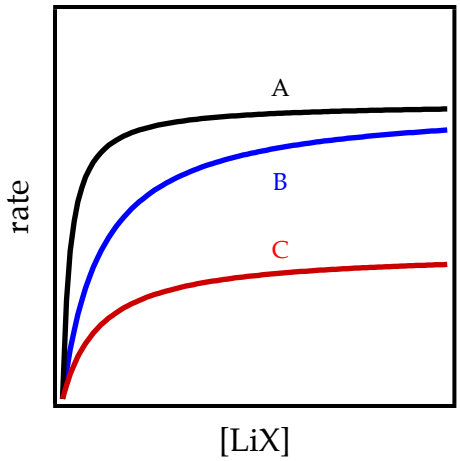

Figure A.6.6. (Figure 6.10 in manuscript) Saturation behavior for LiX catalysts. Curve A is a strong catalyst, curve B is a weak catalyst, and curve C corresponds to catalysis with a different deaggregation step than those of curves A and B.

$$\text{rate} = \frac{ax^n}{1 + ax^n}$$

```
Export["table.xls", {Table[5*x^1/(1 + 5*x^1), {x, 0, 10, 0.1}], Table[0.2*x^1/(1 + 0.2*x^1), {x, 0, 10, 0.1}], Table[0.5*x^1/(1 + 1*x^1), {x, 0, 10, 0.1}]}]
```

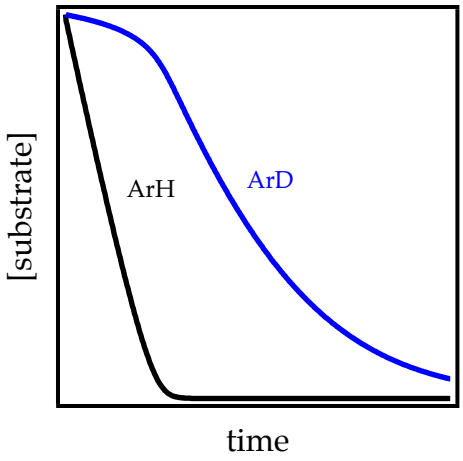

Figure A.6.7. (Figure 6.11 in manuscript) Plot showing preferential metalation of ArH over ArD corresponding to $k_H/k = 24$.

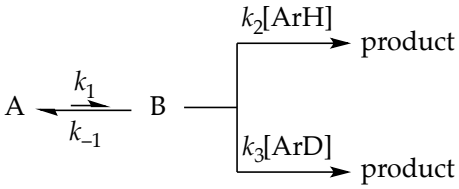

$$\frac{d[A]}{dt} = -k_1[A] + k_{-1}[B]$$

$$\frac{d[B]}{dt} = k_1[A] - k_{-1}[B] - k_2[B][ArH] - k_3[B][ArD]$$

$$\frac{d[ArH]}{dt} = -k_2[B][ArH]$$

$$\frac{d[ArD]}{dt} = -k_3[B][ArD]$$

```
sol[k1_, kn1_, k2_, k3_, a0_, h0_, d0_] :=  NDSolve[{a'[t] == -k1*a[t] + kn1*b[t],
b'[t] == k1*a[t] - kn1*b[t] - k2*b[t]*h[t] - k3*b[t]*d[t],    h'[t] == -k2*b[t]*h[t], d'[t] == -
k3*b[t]*d[t],    a[0] == (a0 kn1)/(k1 + kn1), b[0] == (a0 k1)/(k1 + kn1),    h[0] == h0,
d[0] == d0}, {a, b, h, d}, {t, 0, 10000}]

Manipulate[  Plot[Evaluate[{h[t], d[t]} /. sol[k1, kn1, k2, k3, a0, h0, d0]], {t,    0, 1000}],
{{k1, 0.0001, "k1"}, 0, 1}, {{kn1, 1, "kn1"}, 0,    1}, {{k2, 24000, "k2"}, 0, 1}, {{k3,
1000, "k3"}, 0,    1}, {{a0, 0.1, "a0"}, 0, 1}, {{h0, 0.001, "h0"}, 0,    1}, {{d0, 0.001,
"d0"}, 0, 1}]

Export["table.xls",  Flatten[Table[    Evaluate[{h[t], d[t]} /.      sol[0.0001, 1, 24000,
1000, 0.1, 0.001, 0.001]], {t, 0, 2000,     1}], 1]]
```

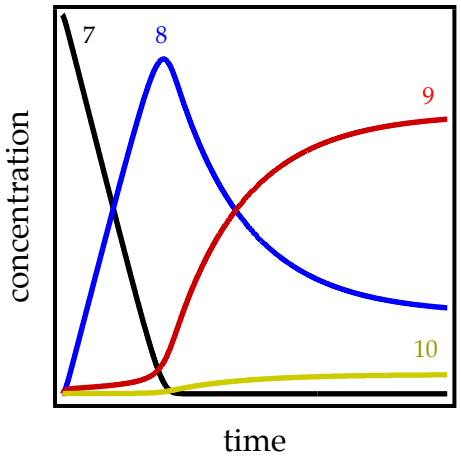

Figure A.6.8.(Figure 6.17 in manuscript) Simulated plots of concentration versus time for the reaction of 7 (black trace) with lithium diisopropylamide in tetrahydrofuran at –78 °C. The functions derive from a mathematical model based on Scheme 6.

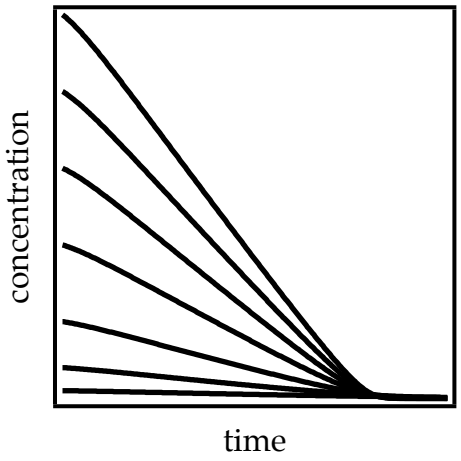

Figure A.6.9. (Figure 6.18 in manuscript) Simulations of plots showing concentration versus time for various initial concentrations of carbamate **7**. The original manuscript simply displayed independent linear fits.

$$\frac{\mathrm{d}[\mathrm{ArH}]}{\mathrm{d}t} = -k_1[\mathrm{ArH}][\mathrm{A}_2] - k_3[\mathrm{A{\cdot}ArLi}^*][\mathrm{ArH}]$$

$$\frac{\mathrm{d}[\mathrm{ArLi}]}{\mathrm{d}t} = -k_4[\mathrm{ArLi}][\mathrm{A}_2] + k_{-4}[\mathrm{A{\cdot}ArLi}][\mathrm{A}_2]^{0.5} + 2k_3[\mathrm{A{\cdot}ArLi}^*][\mathrm{ArH}]$$

$$\frac{\mathrm{d}[\mathrm{A{\cdot}ArLi}]}{\mathrm{d}t} = k_1[\mathrm{ArH}][\mathrm{A}_2] - k_2[\mathrm{A{\cdot}ArLi}] + k_{-2}[\mathrm{A{\cdot}ArLi}^*] + k_4[\mathrm{ArLi}][\mathrm{A}_2] - k_{-4}[\mathrm{A{\cdot}ArLi}][\mathrm{A}_2]^{0.5}$$

$$\frac{\mathrm{d}\left[\mathrm{A{\cdot}ArLi}^{*}\right]}{\mathrm{d}t} = k_2\left[\mathrm{A{\cdot}ArLi}\right] - k_{-2}\left[\mathrm{A{\cdot}ArLi}^{*}\right] - k_3\left[\mathrm{A{\cdot}ArLi}^{*}\right]\left[\mathrm{ArH}\right]$$

$$\left[\mathrm{A}_2\right] = \frac{\left[\mathrm{A}\right]_0 - \left[\mathrm{ArLi}\right]}{2} - \left[\mathrm{A{\cdot}ArLi}\right] - \left[\mathrm{A{\cdot}ArLi}^{*}\right]$$

```
sys[k1_, k2_, kn2_, k3_, k4_, kn4_, a0_, s0_] :=  NDSolve[{arh'[t] == -k1*arh[t]*a2[t] -
k3*aarlis[t]*arh[t],    arli'[t] == -k4*arli[t]*a2[t] + kn4*aarli[t]*a2[t]^0.5 +      2
k3*aarlis[t]*arh[t],    aarli'[t] ==     k1*arh[t]*a2[t] - k2*aarli[t] + kn2*aarlis[t] +
k4*arli[t]*a2[t] -      kn4*aarli[t]*a2[t]^0.5,    aarlis'[t] == k2*aarli[t] - kn2*aarlis[t] -
k3*aarlis[t]*arh[t],    a2[t] == a0/2 - 0.5*arli[t] - aarli[t] - aarlis[t], arh[0] == s0,    arli[0]
== aarli[0] == aarlis[0] == 0}, {arh, arli, aarli, aarlis,    a2}, {t, 0, 2000}]

Manipulate[ Flatten[Table[   Evaluate[{arh[t], arli[t], aarli[t], aarlis[t]} /.      sys[k1, k2,
kn2, k3, k4, kn4, a0, s0]], {t, 0, 2000, 1}],   1], {{k1, 0.020495, "k1"}, 0, 1}, {{k2,
0.09695, "k2"}, 0,   1}, {{kn2, 1.4131, "kn2"}, 0, 1}, {{k3, 828.12, "k3"}, 0,   1}, {{k4,
0.0461, "k4"}, 0, 1}, {{kn4, 0.0027294, "k1"}, 0,   1}, {{a0, 0.1, "a0"}, 0, 1}, {{s0,
0.0074, "s0"}, 0, 1}]

Export["carbamate.xls",«insert table from above»]

Manipulate[{Flatten[   Table[Evaluate[     arh[t] /. sys[k1, k2, kn2, k3, k4, kn4, a0,
0.001]], {t, 0, 200,      0.5}]], Flatten[   Table[Evaluate[     arh[t] /. sys[k1, k2, kn2, k3,
k4, kn4, a0, 0.004]], {t, 0, 200,      0.5}]], Flatten[   Table[Evaluate[     arh[t] /. sys[k1,
k2, kn2, k3, k4, kn4, a0, 0.01]], {t, 0, 200,      0.5}]], Flatten[   Table[Evaluate[     arh[t]
/. sys[k1, k2, kn2, k3, k4, kn4, a0, 0.02]], {t, 0, 200,      0.5}]], Flatten[   Table[Evaluate[
arh[t] /. sys[k1, k2, kn2, k3, k4, kn4, a0, 0.03]], {t, 0, 200,      0.5}]], Flatten[
Table[Evaluate[     arh[t] /. sys[k1, k2, kn2, k3, k4, kn4, a0, 0.04]], {t, 0, 200,      0.5}]],
Flatten[   Table[Evaluate[     arh[t] /. sys[k1, k2, kn2, k3, k4, kn4, a0, 0.05]], {t, 0, 200,
0.5}]]}, {{k1, 0.020495, "k1"}, 0, 1}, {{k2, 0.09695, "k2"}, 0,   1}, {{kn2, 1.4131,
"kn2"}, 0, 1}, {{k3, 828.12, "k3"}, 0,   1}, {{k4, 0.0461, "k4"}, 0, 1}, {{kn4, 0.0027294,
"k1"}, 0,   1}, {{a0, 0.5, "a0"}, 0, 1}, {{s0, 0.0074, "s0"}, 0, 1}]

Export["carbamate.xls",«insert table from above»]
```

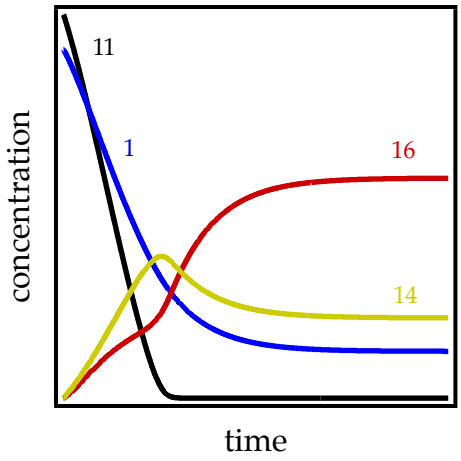

Figure A.6.10. (Figure 6.19 in manuscript) Simulated time-dependent concentrations of ester **11**, lithium diisopropylamide dimer **1**, enolate homodimer **14**, and mixed dimer **16**. The functions are from the model described in Scheme 7.

$$\frac{d[\text{ester}]}{dt} = -k_2[\text{A}][\text{ester}]$$

$$\frac{d[\text{A}_2]}{dt} = -k_1[\text{A}_2] + k_{-1}[\text{A}]^2 - k_3[\text{A}_2][\text{E}] + k_{-3}[\text{A}_2][\text{AE}]$$

$$\frac{d[\text{A}]}{dt} = 2k_1[\text{A}_2] - 2k_{-1}[\text{A}]^2 - k_2[\text{A}][\text{ester}] + k_3[\text{A}_2][\text{E}] - k_{-3}[\text{A}][\text{AE}] - k_4[\text{A}][\text{E}] + k_{-4}[\text{AE}]$$

$$\frac{d[\text{AE}]}{dt} = k_3[\text{A}_2][\text{E}] - k_{-3}[\text{A}][\text{AE}] + k_4[\text{A}][\text{E}] - k_{-4}[\text{AE}]$$

$$\frac{d[\text{E}]}{dt} = k_2[\text{A}][\text{ester}] - k_3[\text{A}_2][\text{E}] + k_{-3}[\text{A}][\text{AE}] - k_4[\text{A}][\text{E}] + k_{-4}[\text{AE}] - 2k_5[\text{E}]^2 + 2k_{-5}[\text{E}_2]$$

$$\frac{d[\text{E}_2]}{dt} = k_5[\text{E}]^2 - k_{-5}[\text{E}_2]$$

```
sol[k1_, kn1_, k2_, k3_, kn3_, k4_, kn4_, k5_, kn5_, a0_, s0_] :=  NDSolve[{est'[t] == -k2*a[t]*est[t],  a2'[t] == -k1*a2[t] + kn1*a[t]^2 - k3*a2[t]*e[t] + kn3*a[t]*ae[t],  a'[t] ==  2 k1*a2[t] - 2 kn1*a[t]^2 - k2*a[t]*est[t] + k3*a2[t]*e[t] -  kn3*a[t]*ae[t] - k4*a[t]*e[t] + kn4*ae[t],  ae'[t] ==  k3*a2[t]*e[t] - kn3*a[t]*ae[t] + k4*a[t]*e[t] - kn4*ae[t],  e'[t] ==  k2*a[t]*est[t] - k3*a2[t]*e[t] + kn3*a[t]*ae[t] - k4*a[t]*e[t] + kn4*ae[t] - 2 k5*e[t]^2 + 2 kn5*e2[t],  e2'[t] == k5*e[t]^2 - kn5*e2[t], a2[0] == a0/2, est[0] == s0,  a[0] == ae[0] == e[0] == e2[0] == 0}, {est, a2, a, ae, e, e2}, {t,  0, 20000}]

Manipulate[  Flatten[Table[  Evaluate[{est[t], a2[t], ae[t], e2[t]} /.  sol[k1, kn1, k2, k3, kn3, k4, kn4, k5, kn5, a0, s0]], {t, 0,  20000, 10}], 1], {{k1, 0.000070944, "k1"}, 0, 1}, {{kn1, 267.46, "kn1"}, 0, 1}, {{k2, 223.44, "k2"}, 0,  1}, {{k3, 0.33594, "k3"}, 0, 1}, {{kn3, 0.84648, "kn3"}, 0,  1}, {{k4, 910.74, "k4"}, 0, 1}, {{kn4, 0.00051948, "k1"}, 0,  1}, {{k5, 451.57, "k5"}, 0, 1}, {{kn5, 0.0080254, "kn5"}, 0,  1}, {{a0, 0.1, "a0"}, 0, 1}, {{s0, 0.055, "s0"}, 0, 1}]

Export["ester.xls",«insert table from above»]
```

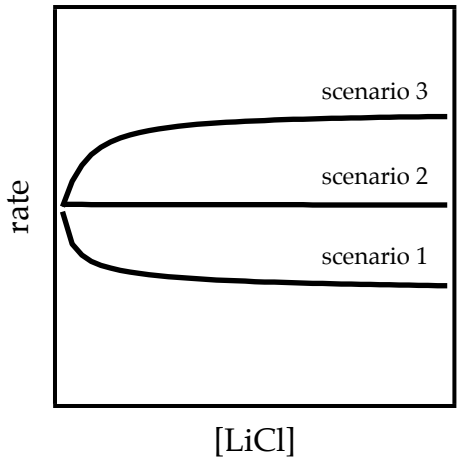

Figure A.6.11. (Figure 6.22 in manuscript) Plot of initial rate versus LiCl concentration showing catalyzed inhibition (scenario 1), no change in rate (scenario 2), and catalyzed acceleration (scenario 3).

$$\frac{\mathrm{d}[\mathrm{A}_2]}{\mathrm{d}t} = -k_1[\mathrm{A}_2] + k_{-1}[\mathrm{A}_2^*] - (k_2 + k_5[\mathrm{LiX}])[\mathrm{A}_2] + \left(k_{-2} + \frac{k_5 k_{-2}}{k_2}[\mathrm{LiX}]\right)[\mathrm{A}]^2$$

$$\frac{\mathrm{d}[\mathrm{A}_2^*]}{\mathrm{d}t} = k_1[\mathrm{A}_2] - k_{-1}[\mathrm{A}_2^*] - k_3[\mathrm{A}_2^*][\mathrm{S}]$$

$$\frac{\mathrm{d}[\mathrm{A}]}{\mathrm{d}t} = 2(k_2 + k_5[\mathrm{LiX}])[\mathrm{A}_2] - 2\left(k_{-2} + \frac{k_5 k_{-2}}{k_2}[\mathrm{LiX}]\right)[\mathrm{A}]^2 - k_4[\mathrm{A}][\mathrm{S}] + k_3[\mathrm{A}_2^*][\mathrm{S}]$$

$$\frac{\mathrm{d}[\mathrm{S}]}{\mathrm{d}t} = -k_3[\mathrm{A}_2^*][\mathrm{S}] - k_4[\mathrm{A}][\mathrm{S}]$$

```
sol[k1_, kn1_, k2_, kn2_, k3_, k4_, k5_, a0_, s0_, c_] :=  NDSolve[{a2'[     t] == -(k1) a2[t] + (kn1) a2s[t] - (k2 + k5*c) a2[       t] + (kn2 + k5*kn2/k2*c) a[t]^2,     a2s'[t] == (k1) a2[t] - (kn1) a2s[t] - k3*a2s[t]*s[t],     a'[t] ==      2 (k2 + k5*c) a2[t] - 2 (kn2 + k5*kn2/k2*c) a[t]^2 -       k4*a[t]*s[t] + k3*a2s[t]*s[t],     s'[t] == -k3*a2s[t]*s[t] - k4*a[t]*s[t],     a2[0] == (     4 a0 kn1 + (k2 kn1^2)/(k1 kn2 + kn1 kn2) - (      Sqrt[k2] kn1^(3/2) Sqrt[k2 kn1 + 8 a0 k1 kn2 + 8 a0 kn1 kn2])/(      k1 kn2 + kn1 kn2))/(8 (k1 + kn1)),     a2s[0] == (     4 a0 k1 + (k1 k2 kn1)/(k1 kn2 + kn1 kn2) - (      k1 Sqrt[k2] Sqrt[kn1] Sqrt[       k2 kn1 + 8 a0 k1 kn2 + 8 a0 kn1 kn2])/(k1 kn2 + kn1 kn2))/(     8 (k1 + kn1)),     a[0] == (-k2 kn1 +       Sqrt[k2] Sqrt[kn1] Sqrt[k2 kn1 + 8 a0 k1 kn2 + 8 a0 kn1 kn2])/(     4 (k1 kn2 + kn1 kn2)), s[0] == s0}, {a2, a2s, a, s}, {t, 0,     10000}]

Manipulate[  Table[-D[Fit[       Table[Evaluate[         Flatten[{t, s[t]} /.           sol[k1, kn1, k2, kn2, k3, k4, k5, a0, s0, c]]], {t, ti, tf,          10}], {1, x, x^2}, x], x] /. x -> 0, {a0, 0, 0.3,     0.001}], {{k1, 0.0005, "k1"}, 0, 10}, {{kn1, 0.5, "kn1"}, 0,    10}, {{k2, 1.*^-10, "k2"}, 0, 10}, {{kn2, 0.1, "kn2"}, 0,    10}, {{k3, 5, "k3"}, 0, 10}, {{k4, 33, "k4"}, 0, 10}, {{k5, 0.05, "k5"}, 0, 10}, {{a0, 0.3, "a0"}, 0,    1}, {{s0, 0.005, "s0"}, 0, 10}, {{c, 0, "c"}, 0,    0.01}, {{ti, 10, "ti"}, 0, 1000}, {{tf, 200, "tf"}, 0, 1000}]
```

III. Parallel versus Serial Barrier Order Dependence

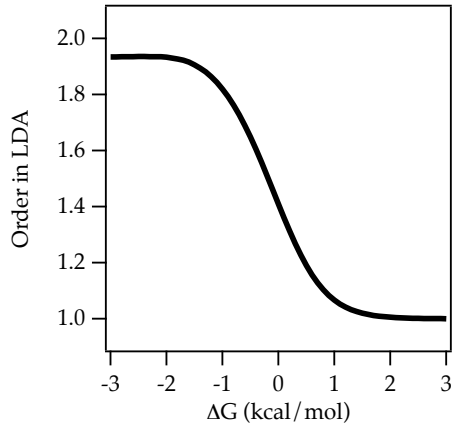

Figure A.6.12. Order in LDA versus ΔG (parallel)

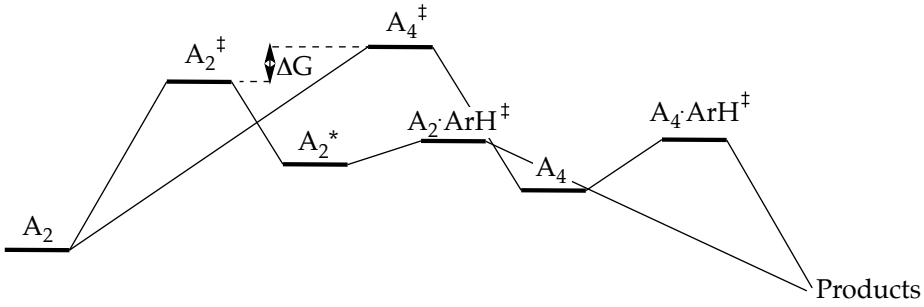

$$\frac{\mathrm{d}[\mathrm{A}_2]}{\mathrm{d}t} = -k_1[\mathrm{A}_2] + k_{-1}[\mathrm{A}_2^*] - 2k_1k_2[\mathrm{A}_2]^2 + 2\frac{k_1k_2}{K}[\mathrm{A}_4] + \frac{k_3}{2}[\mathrm{A}_2^*][\mathrm{S}] + \frac{3k_4}{2}[\mathrm{A}_4][\mathrm{S}]$$

$$\frac{\mathrm{d}[\mathrm{A}_2^*]}{\mathrm{d}t} = k_1[\mathrm{A}_2] - k_{-1}[\mathrm{A}_2^*] - k_3[\mathrm{A}_2^*][\mathrm{S}]$$

$$\frac{\mathrm{d}[\mathrm{A}_4]}{\mathrm{d}t} = k_1k_2[\mathrm{A}_2]^2 - \frac{k_1k_2}{K}[\mathrm{A}_4] - k_4[\mathrm{A}_4][\mathrm{S}]$$

$$\frac{\mathrm{d}[\mathrm{S}]}{\mathrm{d}t} = -k_3[\mathrm{A}_2^*][\mathrm{S}] - k_4[\mathrm{A}_4][\mathrm{S}]$$

```
Solve[{-k1*a2 + kn1*a2s == 0, -2 k2*k1*a2^2 + 2*k2*k1*a4/Keq == 0,    2 a2 + 2 a2s +
4 a4 == a0}, {a2, a2s, a4}]

sol2[k1_, kn1_, k2_, Keq_, k3_, k4_, a0_, s0_] :=   NDSolve[{a2'[t] == -k1*a2[t] +
kn1*a2s[t] - 2 k2*k1*a2[t]^2 +       2*k2*k1*a4[t]/Keq + 1/2 k3*a2s[t]*s[t] +
3/2*k4*a4[t]*s[t],     a2s'[t] == k1*a2[t] - kn1*a2s[t] - k3*a2s[t]*s[t],     a4'[t] ==
k2*k1*a2[t]^2 - k2*k1*a4[t]/Keq - k4*a4[t]*s[t],     s'[t] == -k3*a2s[t]*s[t] -
k4*a4[t]*s[t],     a2[0] == (-k1 - kn1 + Sqrt[      k1^2 + 2 k1 kn1 + kn1^2 + 4 a0 Keq
kn1^2])/(4 Keq kn1),     a2s[0] == (-(k1/Keq) - k1^2/(Keq kn1) + (      k1 Sqrt[k1^2 + 2
k1 kn1 + kn1^2 + 4 a0 Keq kn1^2])/(Keq kn1))/(     4 kn1), a4[0] == ((2 k1)/Keq +
k1^2/(Keq kn1) + 2 a0 kn1 + kn1/      Keq - Sqrt[k1^2 + 2 k1 kn1 + kn1^2 + 4 a0 Keq
kn1^2]/Keq - (      k1 Sqrt[k1^2 + 2 k1 kn1 + kn1^2 + 4 a0 Keq kn1^2])/(Keq kn1))/(     8
kn1), s[0] == s0}, {a2, a2s, a4, s}, {t, 0, 10000}]

Manipulate[{Plot[-s'[1] /.      sol2[k1, kn1, Exp[-4186.8 g/(8.314*195.13)], keq1, k3, k4,
a0,       s0], {a0, 0, 10}],    Plot[Evaluate[{s[t]} /.       sol2[k1, kn1, Exp[-4186.8
g/(8.314*195.13)], keq1, k3, k4, a0,       s0]], {t, 0, 1000}, PlotRange -> {0, 0.01}]},
{{k1, 0.00001,     "k1"}, 0, 10}, {{kn1, 10, "kn1"}, 0, 1000}, {{g, 0, "g"}, -10,    10},
{{keq1, 1.`*^-12, "Keq1"}, 0, 1000}, {{k3, 10000, "k3"}, 0,    1000}, {{k4, 1000000000,
"k4"}, 0, 1000}, {{a0, 0.1, "a0"}, 0,    1}, {{s0, 0.01, "s0"}, 0, 1}]

Flatten[Table[{g, a} /.     FindFit[Flatten[      Table[{10^a0, Log[-s'[0.1]]} /.
sol2[0.000001, 1, Exp[-4186.8 g/(8.314*195.13)], 1.`*^-12,          10000, 1000000000,
10^(a0), 0.01], {a0, -1, 1, 0.01}]],      a*Log[x] + b, {a, b}, x], {g, -3, 3, 1}], 0]
```

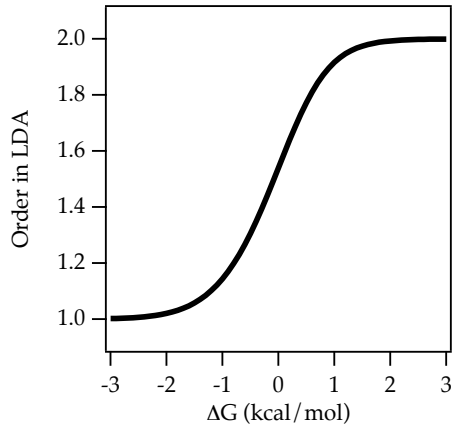

Figure A.6.13. Order in LDA versus ΔG (series)

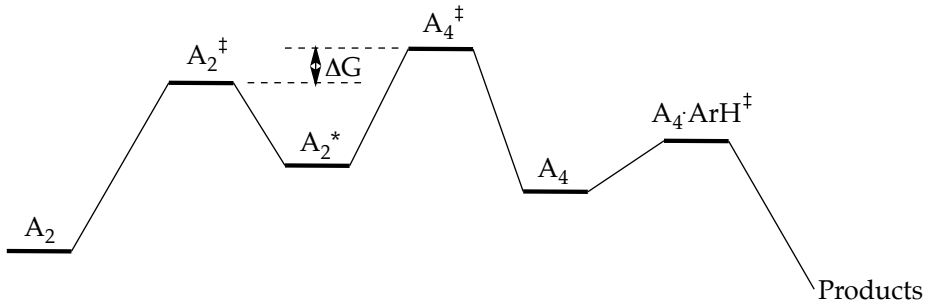

$$\frac{\mathrm{d}[\mathrm{A}_2]}{\mathrm{d}t} = -k_1[\mathrm{A}_2] + k_{-1}[\mathrm{A}_2^*] - k_{-1}k_2[\mathrm{A}_2][\mathrm{A}_2^*] + \frac{k_{-1}k_2}{K}[\mathrm{A}_4] + \frac{3k_3}{2}[\mathrm{A}_4][\mathrm{S}]$$

$$\frac{\mathrm{d}[\mathrm{A}_2^*]}{\mathrm{d}t} = k_1[\mathrm{A}_2] - k_{-1}[\mathrm{A}_2^*] - k_{-1}k_2[\mathrm{A}_2][\mathrm{A}_2^*] + \frac{k_{-1}k_2}{K}[\mathrm{A}_4]$$

$$\frac{\mathrm{d}[\mathrm{A}_4]}{\mathrm{d}t} = k_{-1}k_2[\mathrm{A}_2][\mathrm{A}_2^*] - \frac{k_{-1}k_2}{K}[\mathrm{A}_4] - k_3[\mathrm{A}_4][\mathrm{S}]$$

$$\frac{\mathrm{d}[\mathrm{S}]}{\mathrm{d}t} = -k_3[\mathrm{A}_4][\mathrm{S}]$$

```
Solve[{k1*a2 - kn1*a2s == 0, -k2*kn1*a2*a2s + k2*kn1/Keq1*a4 == 0,    2 a2 + 2 a2s +
4 a4 == a0}, {a2, a2s, a4}]

sol[k1_, kn1_, k2_, Keq1_, k3_, a0_, s0_] :=   NDSolve[{a2'[t] == -k1*a2[t] + kn1*a2s[t]
- k2*kn1*a2[t]*a2s[t] +       k2*kn1/Keq1*a4[t] + 3/2*k3*a4[t]*s[t],     a2s'[t] ==
k1*a2[t] - kn1*a2s[t] - k2*kn1*a2[t]*a2s[t] + k2*kn1/Keq1*a4[t],     a4'[t] ==
k2*kn1*a2[t]*a2s[t] - k2*kn1/Keq1*a4[t] - k3*a4[t]*s[t],     s'[t] == -k3*a4[t]*s[t],
a2[0] == (-k1 - kn1 + Sqrt[      k1^2 + 2 k1 kn1 + 4 a0 k1 Keq1 kn1 + kn1^2])/(4 k1
Keq1),     a2s[0] == (-(k1/Keq1) - kn1/Keq1 + Sqrt[      k1^2 + 2 k1 kn1 + 4 a0 k1 Keq1
kn1 + kn1^2]/Keq1)/(4 kn1),     a4[0] ==      1/(8 kn1) (k1/Keq1 + 2 a0 kn1 + (2
kn1)/Keq1 + kn1^2/(k1 Keq1) -         Sqrt[k1^2 + 2 k1 kn1 + 4 a0 k1 Keq1 kn1 +
kn1^2]/Keq1 - (        kn1 Sqrt[k1^2 + 2 k1 kn1 + 4 a0 k1 Keq1 kn1 + kn1^2])/(        k1
Keq1)), s[0] == s0}, {a2, a2s, a4, s}, {t, 0, 10000}]

Manipulate[{Plot[-s'[1] /.      sol[k1, kn1, Exp[-4186.8 g/(8.314*195.13)], keq1, k3, a0,
s0], {a0, 0, 10}],    Plot[Evaluate[{s[t]} /.       sol[k1, kn1, Exp[-4186.8
g/(8.314*195.13)], keq1, k3, a0,        s0]], {t, 0, 1000}, PlotRange -> {0, 0.01}],
Flatten[Table[{g, a} /.       FindFit[Flatten[        Table[Log[-s'[1]] /.          sol[k1, kn1,
Exp[-4186.8 g/(8.314*195.13)], keq1, k3, a0,           s0], {a0, 0.01, 10, 0.01}]], a*Log[x]
+ b, {a, b},        x], {g, -3, 3, 1}], 0]}, {{k1, 0.001, "k1"}, 0,    10}, {{kn1, 1000, "kn1"},
0, 1000}, {{keq1, 1, "Keq1"}, 0,    1000}, {{k3, 1000000000, "k3"}, 0, 1000}, {{a0, 0.1,
"a0"}, 0,    1}, {{g, 0, "g"}, -3, 3}, {{s0, 0.01, "s0"}, 0, 1}]

Flatten[Table[{g, a} /.     FindFit[Flatten[      Table[Log[-s'[1]] /.         sol[0.001, 1000,
Exp[-4186.8 g/(8.314*195.13)], 1, 1000000000,          a0, 0.01], {a0, 0.01, 10, 0.01}]],
a*Log[x] + b, {a, b},      x], {g, -3, 3, 0.1}], 0]
```

IV. Standard Steady State Treatment of Multiple Barriers in Series

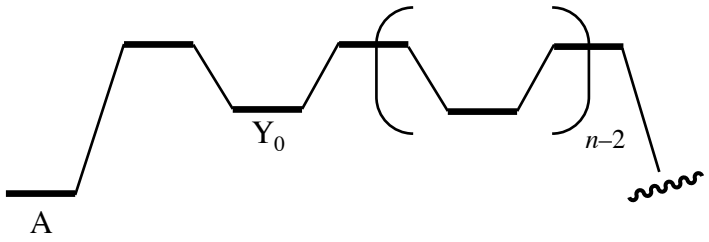

Assume the forward rate constant for conversion of A to Y_0 is k_1 and the reverse rate constant is k_{-1}. All intermediates Y_i are of the same energy; otherwise stated, they are pairwise interconverted with rate constant k_{-1}. The time-varying concentration of Y_i is:

$$\frac{d[Y_i]}{dt} = k_{-1}[Y_{i-1}] - 2k_{-1}[Y_i] + k_{-1}[Y_{i+1}]$$

Assuming a steady state has been reached $\frac{d[Y_i]}{dt} = 0$, and

$$[Y_{i-1}] = 2[Y_i] - [Y_{i+1}] \qquad (1a)$$

On shifting the index,

$$[Y_i] = 2[Y_{i+1}] - [Y_{i+2}] \qquad (1b)$$

From equation 1b, it follows that $[Y_{m-1}] = 2[Y_m]$ and generally that

$$[Y_{m-x}] = (x+1)[Y_m] \qquad (2)$$

The time-varying concentration of Y_0 is

$$\frac{d[Y_0]}{dt} = k_1[A] - 2k_{-1}[Y_0] + k_{-1}[Y_1]$$

Applying the steady state approximation to the former expression gives

$$[Y_0] = \frac{k_1[A] + k_{-1}[Y_1]}{2k_{-1}} \qquad (3)$$

Using equation 1b for $[Y_0]$ we find $[Y_0] = 2[Y_1] - [Y_2]$. Given that $\frac{[Y_2]}{[Y_1]} = \frac{m-1}{m}$ from equation 2, $[Y_0] = 2[Y_1] - \frac{m-1}{m}[Y_1] = \left(2 - \frac{m-1}{m}\right)[Y_1]$. Therefore,

$$[Y_1] = \frac{[Y_0]}{\left(2 - \frac{m-1}{m}\right)} \tag{4}$$

On combining equations 3 and 4,

$$[Y_0] = \frac{k_1[A] + k_{-1}\left(\frac{[Y_0]}{\left(2 - \frac{m-1}{m}\right)}\right)}{2k_{-1}}$$

Simplification of the above gives

$$[Y_0] = \frac{k_1[A]}{k_{-1}}\left(\frac{1}{2 - \frac{1}{2 - \frac{m-1}{m}}}\right)$$
$$= \frac{k_1[A]}{k_{-1}}\left(\frac{m+1}{m+2}\right)$$

To obtain an expression for the rate of consumption of [A] as a function of relevant rate constants and the number of barriers begin with the rate law for A and employ the preceding result:

$$\frac{d[A]}{dt} = -k_1[A] + k_{-1}[Y_0]$$
$$= -k_1[A] + k_{-1}\left(\frac{k_1[A]}{k_{-1}}\left(\frac{m+1}{m+2}\right)\right)$$
$$= -k_1\left(1 - \frac{m+1}{m+2}\right)[A]$$
$$= -k_1\left(\frac{1}{m+2}\right)[A]$$

Notice that the number of barriers is $m+2$, so we define $n=m+2$, and the above expression becomes

$$\frac{\mathrm{d}[\mathrm{A}]}{\mathrm{d}t}=-\frac{k_1}{n}[\mathrm{A}] \qquad (5)$$

Therefore, the rate of a process that proceeds through *n* barriers of equal activation energy relative to the ground state attenuates the rate associated with reactivity through a single such barrier by a factor of *n*.

Proof of equation 2:

We want to show that $[\mathrm{Y}_{m-x}]=(x+1)[\mathrm{Y}_m]$, so we provisionally assume that $[\mathrm{Y}_{m-x}]=(x+1)[\mathrm{Y}_m]$ and $[\mathrm{Y}_{m-(x-1)}]=x[\mathrm{Y}_m]$ are true. From equation 1a, we know that $[\mathrm{Y}_{i-1}]=2[\mathrm{Y}_i]-[\mathrm{Y}_{i+1}]$, so $[\mathrm{Y}_{m-(x+1)}]=2[\mathrm{Y}_{m-x}]-[\mathrm{Y}_{m-(x-1)}]=2(x+1)[\mathrm{Y}_m]-x[\mathrm{Y}_m]=(x+2)[\mathrm{Y}_m]$ and the proof is complete.

V. Arbitrary Height Barriers in Series

We want to derive a general expression for overall rate in terms of the microscopic rate constants and do so paralleling Wagner, C. *Advances in Catalysis*, **1970**, *21*, 323. Consider the scheme depicted below.

$$\mathrm{C} \underset{k_{-1}}{\overset{k_1}{\rightleftharpoons}} \mathrm{I}_1 \underset{k_{-2}}{\overset{k_2}{\rightleftharpoons}} \ldots \underset{k_{-n}}{\overset{k_n}{\rightleftharpoons}} \mathrm{P}$$

At each step, denote $K_i = k_i/k_{-i}$. Assume that a single rate-limiting step exists at position m, for which all preceding and subsequent steps are at equilibrium. By mass balance,

$$\left[\mathrm{I}_{m-1}\right]^* = \left[\mathrm{C}\right]\prod_{i=1}^{m-1} K_i$$

$$\left[\mathrm{I}_m\right]^* = \left[\mathrm{P}\right]\prod_{i=m+1}^{n} K_i^{-1}$$

Given that $K_{\mathrm{eq}} = \prod_{i=1}^{n} K_i$, a rate expression assuming exclusive rate-limitation at position m follows.

$$\begin{aligned} v_m^* &= k_m\left(\left[\mathrm{I}_{m-1}\right]^* - \frac{\left[\mathrm{I}_{m-1}\right]^*}{K_m}\right) \\ &= k_m\left(\left[\mathrm{C}\right]\prod_{i=1}^{m-1} K_i - \frac{\left[\mathrm{P}\right]\prod_{i=m+1}^{n} K_i^{-1}}{K_m}\right) \\ &= k_m\prod_{i=1}^{m-1} K_i\left(\left[\mathrm{C}\right] - \left[\mathrm{P}\right]\prod_{i=1}^{n} K_i^{-1}\right) \\ &= k_m\prod_{i=1}^{m-1} K_i\left(\left[\mathrm{C}\right] - \frac{\left[\mathrm{P}\right]}{K_{\mathrm{eq}}}\right) \end{aligned}$$

The overall rate at steady state is given by

$$v = v_m = k_m\left(\left[\mathrm{I}_{m-1}\right] - \frac{\left[\mathrm{I}_{m-1}\right]}{K_m}\right)$$

We are now in a position to relate v to the various v^*. Begin by finding the ratio $\frac{v_m}{v_m^*}$.

$$\frac{v_m}{v_m^*} = \frac{k_m\left(\left[\mathrm{I}_{m-1}\right] - \frac{\left[\mathrm{I}_m\right]}{K_m}\right)}{k_m\prod_{i=1}^{m-1}K_i\left(\left[\mathrm{C}\right] - \frac{\left[\mathrm{P}\right]}{K_{\mathrm{eq}}}\right)}$$

$$= \frac{\prod_{i=1}^{m-1}K_i^{-1}\left(\left[\mathrm{I}_{m-1}\right] - \frac{\left[\mathrm{I}_m\right]}{K_m}\right)}{\left(\left[\mathrm{C}\right] - \frac{\left[\mathrm{P}\right]}{K_{\mathrm{eq}}}\right)}$$

Sum over all $\frac{v_m}{v_m^*}$.

$$\sum_{m=1}^{n}\frac{v_m}{v_m^*} = \sum_{m=1}^{n}\frac{\prod_{i=1}^{m-1}K_i^{-1}\left(\left[\mathrm{I}_{m-1}\right] - \frac{\left[\mathrm{I}_m\right]}{K_m}\right)}{\left[\mathrm{C}\right] - \frac{\left[\mathrm{P}\right]}{K_{\mathrm{eq}}}}$$

$$= \frac{1}{\left[\mathrm{C}\right] - \frac{\left[\mathrm{P}\right]}{K_{\mathrm{eq}}}}\left(\sum_{m=1}^{n}\prod_{i=1}^{m-1}K_i^{-1}\left[\mathrm{I}_{m-1}\right] - \sum_{m=1}^{n}\prod_{i=1}^{m}K_i^{-1}\left[\mathrm{I}_m\right]\right)$$

note that $\left[\mathrm{I}_0\right]$ is $\left[\mathrm{C}\right]$ and $\left[\mathrm{I}_n\right]$ is $\left[\mathrm{P}\right]$

$$= \frac{1}{\left[\mathrm{C}\right] - \frac{\left[\mathrm{P}\right]}{K_{\mathrm{eq}}}}\left(\left[\mathrm{C}\right] + \sum_{m=2}^{n}\prod_{i=1}^{m-1}K_i^{-1}\left[\mathrm{I}_{m-1}\right] - \sum_{m=1}^{n-1}\prod_{i=1}^{m}K_i^{-1}\left[\mathrm{I}_m\right] - \frac{\left[\mathrm{P}\right]}{K_{\mathrm{eq}}}\right)$$

$$= \frac{1}{\left[\mathrm{C}\right] - \frac{\left[\mathrm{P}\right]}{K_{\mathrm{eq}}}}\left(\left[\mathrm{C}\right] + \sum_{m=1}^{n-1}\prod_{i=1}^{m}K_i^{-1}\left[\mathrm{I}_m\right] - \sum_{m=1}^{n-1}\prod_{i=1}^{m}K_i^{-1}\left[\mathrm{I}_m\right] - \frac{\left[\mathrm{P}\right]}{K_{\mathrm{eq}}}\right)$$

$$= \frac{\left[\mathrm{C}\right] - \frac{\left[\mathrm{P}\right]}{K_{\mathrm{eq}}}}{\left[\mathrm{C}\right] - \frac{\left[\mathrm{P}\right]}{K_{\mathrm{eq}}}}$$

$$= 1$$

With this trivial identity, proceed to find the overall reaction rate.

$$\sum_{m=1}^{n} \frac{v_m}{v_m^*} = \sum_{m=1}^{n} \frac{v}{v_m^*} = v \sum_{m=1}^{n} \frac{1}{v_m^*} = 1$$

Therefore,

$$v = \frac{1}{\sum_{m=1}^{n} \frac{1}{v_m^*}}$$

$$= \frac{1}{\sum_{m=1}^{n} \frac{1}{k_m \prod_{i=1}^{m-1} K_i \left([\mathrm{C}] - \frac{[\mathrm{P}]}{K_{\mathrm{eq}}} \right)}}$$

$$= \frac{[\mathrm{C}] - \frac{[\mathrm{P}]}{K_{\mathrm{eq}}}}{\sum_{m=1}^{n} \frac{1}{k_m \prod_{i=1}^{m-1} K_i}}$$

Under initial rate conditions, assume [P] ≈ 0 to give the expression below (equation 6.31 in Chapter 6)

$$-\frac{\mathrm{d}[\mathrm{C}]}{\mathrm{d}t} = \frac{[\mathrm{C}]_0}{\sum_{m=1}^{n} \frac{1}{k_m \prod_{i=1}^{m-1} K_i}}$$

Particular Cases.

1) *Equivalent–Energy Intermediates*

We examine the case where all intermediates in the conversion of C to P are of equal energy. This means $1 = K_2 = K_3 = \ldots = K_{n-1}$. Therefore,

$$-\frac{\mathrm{d}[\mathrm{C}]}{\mathrm{d}t} = \frac{[\mathrm{C}]_0}{\frac{1}{k_1} + \sum_{m=2}^{n} \frac{1}{k_m K_1}} = \frac{k_1[\mathrm{C}]_0}{1 + \frac{k_1}{K_1}\sum_{m=2}^{n} \frac{1}{k_m}} = \frac{k_1[\mathrm{C}]_0}{1 + k_{-1}\sum_{m=2}^{n} \frac{1}{k_m}}$$

2) *Equivalent–Energy Intermediates and Barriers of Equal Height*

$$-\frac{\mathrm{d}[\mathrm{C}]}{\mathrm{d}t} = \frac{k_1[\mathrm{C}]_0}{1 + k_{-1}\sum_{m=2}^{n} \frac{1}{k_{-1}}} = \frac{k_1[\mathrm{C}]_0}{1 + \sum_{m=2}^{n} 1} = \frac{k_1[\mathrm{C}]_0}{n}$$

3) *Differing Molecularity — Two Barrier Case*

$$\mathrm{A} \underset{k_{-1}}{\overset{k_1}{\rightleftharpoons}} \mathrm{I} \underset{k_{-2}}{\overset{k_2[\mathrm{S}]}{\rightleftharpoons}} \text{product}$$

Following the equation described in the previous section,

$$\frac{\mathrm{d}[\text{product}]}{\mathrm{d}t} = \frac{[\mathrm{A}]_0}{\sum_{m=1}^{n} \frac{1}{k_m \prod_{i=1}^{m-1} K_i}}$$

$$= \frac{[\mathrm{A}]_0}{\frac{1}{k_1} + \frac{1}{k_2[\mathrm{S}]\left(\frac{k_1}{k_{-1}}\right)}}$$

$$= \frac{k_1 k_2 [\mathrm{A}]_0 [\mathrm{S}]}{k_{-1} + k_2[\mathrm{S}]}$$

As expected from a standard steady state treatment.